Carbon Dioxide Capture for Storage in Deep Geologic Formations – Results from the CO_2 Capture Project

Volume 3

Advances in CO_2 Capture and Storage Technology Results (2004 – 2009)

Edited by

Lars Ingolf Eide
Stian Kristensens vei 33
N-1348 Rykkinn, Norway

cplpress
2009

Published in the UK by:

CPL Scientific Publishing Services Ltd trading as CPL Press
Tall Gables, The Sydings, Speen, Newbury, Berkshire RG14 1RZ, UK
Tel/Fax: +44 1635 569787 Email: press@cplpress.com http://www.cplpress.com/sps

for:

CO_2 Capture Project Phase 2 (CPP2) – http://www.co2captureproject.org

Chapters 21, 25, 26 and 27 were written with support of the US Department of Energy under Award Nos. DE-FC26-05NT422211 and DE-AC02-05CH11231.

The European Commission under the 6th Framework Programme (Contract 019972) co-funded work in chapters 6, 7, 8, 11, 12, 13, 14, 15 and 16.

The Research Council of Norway co-funded work in chapters 4, 9, 12 and 24.

The Canadian Federal Government's Climate Change Technology & Innovation (T&I) Program supported chapter 18.

First edition 2009

British Library Cataloguing in Publication Data
A catalogue record is available from the British Library

ISBN: 978-1-872691-49-7

Copies of this publication can be obtained via the CPL Press Online Bookshop: http://www.cplbookshop.com

Volumes 1 & 2 of this series were published by Elsevier BV ISBN: 0-08-044570-5 (2 volume set)

Printed in the UK by Antony Rowe Ltd

PREFACE

Gardiner Hill
Chairman CO_2 Capture Project Executive Board
BP plc, Sunbury-on-Thames, UK

The CO_2 Capture Project (CCP) is a collaborative partnership of eight of the world's leading energy companies and three government organizations. The initiative undertakes research and develops technologies to help make CO_2 capture and geological storage (CCS) a practical reality for reducing global CO_2 emissions and tackling climate change – one of the great international challenges of our time.

Since 2000, CCP has been at the very forefront of advancing CCS; a process that involves capturing the CO_2 emitted from industrial and energy-related sources and then securely storing the CO_2 deep underground in geological formations.

Phase 1 of CCP identified next generation capture technologies that had the potential to deliver performance and efficiency improvements resulting in close to a 50% reduction in the cost of CO_2 capture. It also pioneered a risk-based approach for geological site selection, operation and abandonment; and developed new CO_2 monitoring tools and the science behind CO_2 geological storage.

In Phase 2, CCP has continued to build on achievements in capture and storage. The culmination of this five year study is found in this book.

During this second phase, CCP, leveraging its combined expertise in the oil and gas industry, has worked in collaboration with governments, industry, world-leading academic institutions and environmental interest groups' The objective for capture technology was to further the development of the promising technologies identified during CCP1 with a view to realising the expected cost reductions, reducing the range of uncertainty around cost estimates and maturing at least one technology ready for subsequent demonstration. In the matter of geological storage, CCP2 has focused on the science and steps required to deliver secure CO_2 geological storage, with a leading programme examining well integrity.

Over this period of time there has also been a sea change in scientific, political and public opinion towards recognition of the need for swift, decisive action to reduce anthropogenic CO_2 emissions. This consensus is underlined by the most recent report from the Nobel Prize-winning Intergovernmental Panel on Climate Change (IPCC), which concluded that global CO_2 emissions need to be cut from current levels by 50-80% by 2050 to avoid the most damaging effects of climate change. At the same time, scientific and economic projections clearly demonstrate the pivotal role that fossil fuels will continue to play to meet the world's growing energy needs in the short to medium-term. The projections also suggest that renewable energy capacity cannot grow quickly enough to replace them.

A major acknowledgement for CCS came in July 2005, when the Carbon Sequestration Leadership Forum (CSLF) was endorsed by the G-8 Summit in its Gleneagles Plan of Action on Climate Change, Clean Energy and Sustainable Development, and identified it as a medium of cooperation and collaboration with key developing countries in dealing with greenhouse gases. The CSLF,

currently comprising 21 countries and the European Commission, is a Ministerial-level international climate change initiative whose mission is to facilitate the development and deployment of CCS technologies via collaborative efforts that address key technical, economic, and environmental obstacles. CCP is pleased to have been selected as a CLSF Recognized Project, which was a huge vote of confidence in the contribution that CCP would make.

The scale of the challenge facing the world is immense. There is no one technology option or 'magic bullet'. A portfolio of approaches including renewables, nuclear and energy efficiency measures is likely to be required to provide secure, affordable energy that does not negatively impact our environment. It is against this backdrop that CCS has been increasingly recognized as a critical technology that can be deployed now to reduce CO_2 emissions and ensure the world continues to benefit from fossil fuels.

CCS is a bridging technology that gives society time to deliver alternative energy sources at scale. CO_2 enhanced oil recovery (EOR) is already helping the oil industry recover oil and gas that would otherwise have been uneconomical. EOR combined with CO_2 storage will offer even greater advantages. CCS also provides an opportunity for rapidly industrializing countries like India and China, and major developed areas like the US, to use their abundant sources of low-cost coal to meet demands for energy while mitigating environmental impacts.

The IEA in their Energy Technology Perspectives June 08 report, believes that CCS could account for 19% of the total CO_2 emission reductions needed this century to stabilise climate change. With considerable thanks to CCP, it is now no longer a question of whether CCS is relevant, but of how it can be applied at scale and at a cost equal to or lower than the other low carbon energy alternatives.

The CCP's work both in its Phase 1 (2000-2003) and continuing into Phase 2 (2004-2009) has been focused on providing the scientific and technical understanding and know-how necessary to reassure that CO_2 can be securely stored and the costs of CO_2 capture can be reduced. Much of the focus has been on how this can be applied to power generation and the oil and gas industry itself, to reduce its own carbon footprint and associated operating costs. This focus will become even more necessary as we find ourselves living in an increasingly carbon constrained world.

The CCP Capture Team in Phase 2 has trialled a number of different capture technologies in refinery and gas fired power stations, building deep knowledge and learning while delivering significant cost reduction potential. Additionally, some of the capture technologies have been developed to the stage where they are now ready to be tested at pilot or demonstration scale. CCP's commitment to investing in next generation technology today is critical to CCS and ensures that the results of its work can apply to a wide variety of industrial applications and power sources, as well as those of the oil and gas industry.

The Project's Storage Monitoring and Verification Team have made considerable strides in scientific and operational understanding of two key facets of geological storage - well integrity and CO_2 storage site characterization. Additionally the extensive collective experience of each of the participants working in the project has been collated and published in early 2009 in a CCP Technical Publication entitled *"A Technical Basis for Carbon Dioxide Storage"*. This ground-breaking work is the definitive technical guide for potential CCS regulators, policy makers, operators and industry as to how CO_2 geological storage can be practically undertaken. The work is not just based on scientific and academic research and CCS demonstration projects but also the considerable expertise and operational data from analogous oil and gas operations held by each of the CCP's eight member companies. The report and detailed case studies further validate the fact that CO_2 can be – and is - safely stored in geological formations now. Alongside this, the Team has developed a Certification Framework to guide the evaluation of suitability of candidate sites in any given location. This consists of a platform for input of geological data, specialised tools to predict

behaviour of CO_2 in the subsurface and a tool to calculate risk. The simple and transparent results will be a useful tool to communicate with a range of stakeholders.

The Project's Policy and Incentives Team continued to work in close cooperation with the US Department of Energy and the European Commission and with environmental NGOs. The Project team has produced a number of important papers that highlight the need for early adopters of CCS to receive incentives and they have outlined positions on principles of storage certification, pipeline financing and long term storage liability. The required incentives reflect the commercial and technological costs of developing and pioneering any new mitigation technology.

This CCP2 publication presents the technical papers and findings from Phase 2 of the project in its entirety. The work is the combined effort of around 60 technology providers and academic institutions, key NGOs and each of the eight CCP member companies. A wide range of academic and commercial institutions, all subject to open and comprehensive peer review, have provided breakthrough thinking, concepts and technology. The views of external bodies, such as environmental groups and other associated NGOs, have also played a crucial role in shaping and reviewing work undertaken.

Through this international public–private collaboration, we believe CCP has made a significant impact in verifying technology for safe and secure geological storage of CO_2, influencing fit-for-purpose storage regulations and stimulating the next generation of capture technologies that can help drive down the costs of CCS.

The industrial participants in the CCP2 would like to thank all of the people who have worked so hard over the past 5 years from turning CCS from an interesting mitigation technology to something that is on the brink of commercial reality. Little would have been achieved without a huge degree of cooperation and hard work.

Our extended multi-disciplinary team and overall approach has ensured CCP is probably one of the most comprehensive scientific studies in the world on CCS. The Technology Advisory Board, which is made up of independent experts, played a key role in achieving this outcome. They provided an independent peer review of our work, ongoing assurance and advice to the CCP executive board, providing guidance on the direction of the research and verification that the project was making a unique and important contribution. I would personally like to thank the Technology Advisory board for their sage advice and commitment to help make CCP a comprehensive and highly credible technology research project.

Finally, I would like to formally thank the industrial participants – Chevron, ConocoPhilips, Eni, Petrobras, Shell, StatoilHydro, Suncor and BP – for their proactive engagement, unwavering commitment and strong leadership. Thanks are also due to our Associate participants, EPRI and Repsol YPF for their strong and valued support. Yet our partnership could not have made such outstanding progress without support from governments who worked with us and provided co-funding. Hence I formally want to recognise the US Department of Energy, Norway's Norges forskningsråd (Research Council of Norway) and the European Union (EU) for the role they planned in enabling CCP2 to accomplish its objectives and helping move forward the science and technology of CCS.

The Executive Board of CCP is confident that, with the level of expertise that the CCP has to hand, we are and will remain at the forefront of delivering the technical insight to making CCS a practical reality and thereby a major contribution to mitigating climate change.

Our efforts don't and can't stop with CCP2. We have made significant progress over the last eight years but there is still a long way to go. Every major oil, gas, chemical, power, pharmaceutical, steel and cement plant across the world has the potential to use and benefit from CCS. There are

even new ‘green’ technologies like Biofuels that could benefit from CCS. This is an industry that could still be growing in fifty years time.

As technologists and engineers we recognize the crucial role technology will continue to play. It will provide cost effective options and inform the policy debate. A CCS industry will need to continuously improve; Capture costs must diminish at pace through a mixture of “learning by doing” and application of next generations technologies, and new geological structures will need to be explored in such a way that builds confidence and reduces risk. But we also recognize that for CCS to be successful and deliver its full potential, we have to use our technical expertise and knowledge to demonstrate to consumers, NGOs and regulators that CO_2 has and can be securely stored in geological formations for millions of years.

ACKNOWLEDGEMENTS

Linda Curran, BP
Program Manager, CO_2 Capture Project Phase 2

The CO_2 Capture Project (CCP) is a unique collaborative technology development program in many aspects. Participants represent corporations, academia, governments, research institutions, policy makers, and individual contractors, all with in-depth insights to the needs and potential approaches to carbon capture and storage (CCS). These many contributors have come together to advance the development of new approaches and improve efficiencies of existing new technologies.

Beginning in 2000 with Phase 1, eight corporate partners engaged with governments to develop a unique program to advance the state of the art of Capture and Storage technologies. Phase 2 began in 2004 with 8 corporate members of the full program and two additional partners joining the Storage, Policies, and Communications efforts and 4 governments participating (EU, Research Council of Norway, UK Department of Trade and Industry, and US Department of Energy). The following corporate members have been the foundation for Phase 2 (8 Full members): BP, Chevron, ConocoPhillips, ENI, Petrobras, Shell, StatoilHydro, and Suncor, and two Associate members: EPRI and Repsol YPF. Members have provided both technical experts and funding to advance capture and storage technologies and policy development over the last five years. Each of the many individuals (90 research team members), and experts from over 40 contracted institutions have provided thousands of hours of their time and generously shared their knowledge, advancing the task of making CCS a reality. The efforts of the team leads -Ivano Miracca - Capture Team Lead (ENI), Scott Imbus - Storage Team Lead (Chevron), Arthur Lee - Policy Team Lead (Chevron), Iain Wright, Communications Team Lead (BP), and Torgeir Melien Economics Team Lead (StatoilHydro),– have been key to shaping the program and delivering the results. Additionally, many researchers from academic institutions and corporations, as well as independent consultants, have made contributions to the program. Executive Board members have provided key guidance to the Teams and made difficult choices throughout Phase 2 as the opportunities expanded. Governments have contributed through generously providing co-funding for a number of the technologies in the program.

The Advisory Board, led by Vello Kuuskraa has acted as challengers to the teams and independent mentors to the Executive Board and Program Manager, challenging proposals from the Teams, bringing new insights and opportunities to the technical work. Participants have been: Olav Bolland, Pierpaolo Garibaldi, Chris Higman, Larry Myer, Nick Riley, Dale Simbeck, and Sally Benson.

Sincere thanks to all reviewers of the technical contributions. Without their voluntary efforts the book would not have reached the standard we believe it has achieved.

This book describes the achievements of many collaborators and only a few have been named here. As we enter Phase 3 the challenges have become more visible than at the start of the effort thanks to the many contributors brought together by the CO_2 Capture Project.

Finally, special thanks to Lars Ingolf Eide, editor, who has managed the process of bringing together the documentation of the work by so many researchers and technology providers.

CONTENTS

Carbon Dioxide Capture for Storage in Deep Geologic Formations, Volume 3
L.I. Eide (Ed.)

INTRODUCTION

Lars Ingolf Eide[1] and Linda Curran[2]
[1]Stian Kristensens vei 33, N-1348 Rykkinn, Norway
[2]BP Alternative Energy 150 W. Warrenville Road, Naperville, IL 60563, USA

BACKGROUND

The CO_2 Capture Project (CCP) is an international cooperative partnership between industry, governments, academics and environmental interest groups. The project is focused on technology development to reduce the cost of CO_2 capture and to demonstrate that geological storage is safe and secure. CCP is a three stage technology development programme with overall objectives to:

- Deliver major cost reductions in the cost of Carbon Capture and Storage (CCS), relative to the 2000 baseline and make CCS cost competitive with other low or no carbon energy alternatives
- Demonstrate to external stakeholders that geological CO_2 storage is secure, measurable and verifiable.

Phase 1 of the programme, CCP1 (2000-2004), progressed capture technologies to proof of feasibility and defined and started closing key technical gaps within geologic storage of CO_2.

Phase 2 of the programme, CCP2 (2005-2009), brought forward the most promising capture technologies from CCP1, and some new ones, to reduce technical and cost uncertainties, scale-up operations by at least one order of magnitude and bring at least one capture technology to a "ready-for-pilot" stage. Other goals for CCP2 were to:

- Contribute to establish best practice for site characterization, process optimization, monitoring and verification and risk assessment for geologic storage of CO_2.
- Increase public acceptance and awareness of CCS.
- Expand economic/ infrastructure scenarios for the whole CCS value chain.
- Advance the science and expand the potential scope of implementation of CCS technologies through international industrial, academic and governmental co-operation.

Within the storage program, the objective of CCP2 was to further develop the most pressing storage issues, with emphasis on:

- Risk assessment and certification guidelines and protocols
- Wellbore integrity
- Geo-mechanical stability of reservoirs and caprocks

The full industry members in CCP2 are BP, Chevron, ConocoPhillips, Eni, StatoilHydro, Petrobras, Shell, and Suncor. Government agencies provided co-funding for select portions of the program. Two sub-programs are co-funded with the European Commission – Chemical Looping Combustion Gas Power (CLC GP) (Chapters 5 – 8 of this book) and CACHET (Chapters 10 – 16),one with the Research Council of Norway - Climit (Chapters 4, 9 and 24) and one with the US Department of Energy (DOE), (Chapters 25-27).

In addition to the co-funding with European and US funding sources, CCP2 participated in Phase 9 of the Canadian CANMET CO_2 R&D Consortium ENERGY Technology Centre program. This program included modeling of advanced supercritical oxy-coal plants, performance testing of a pilot

scale unit and investigation of phase change in CO_2 gas mixtures, testing of a novel oxy-fuel steam burner, development of a mercury removal process, and development of pulverized coal combustion processes for oil sands, and petroleum coke in air and oxygen enriched environments. A summary of the Phase 9 program is reported here in Chapter 18.

CCP2 has been a Carbon Sequestration Leadership Forum (CSLF) Recognized Project since September 2004, because it met the evaluation criteria of the CSLF for collaborative research, development, and demonstration projects that reflect the CSLF member countries priorities.

Phase 3 of the CCP programme (CCP3) is planned for the period 2009 – 2013. Phase 3 will continue to develop "ready for demo" selected technologies and target participation in capture and storage demonstrations. Scenarios that will provide the context for which technologies will be demonstrated and further developed are: 1. Natural Gas Combined Cycle (NGCC) power station; 2. Oil refinery (applying oxy-fired Fluidized Catalytic Cracker, FCC); and 3. Once Through Steam Generator (OTSG) for a heavy oil scenario. Within Storage, Monitoring and Verification (SMV) the main themes will be Storage Assurance research and development**,** Field Trials, and understanding stakeholder issues.

ABOUT THIS BOOK

This book is a collection of peer reviewed scientific papers that describe the technological advances made in CCP Phase 2. It is the third volume, following on from the first two, published in 2005, which summarized achievements in CCP1 [1,2]. This introductory chapter provides background on the development of CCP, including its structure, organization and technology selection process and a brief summary of CCP1 results.

Following this introduction, a paper by the Chair of the CCP Advisory Board (CAB), Vello Kuuskraa, summarizes the views and recommendations of the CAB. Thereafter follows a section devoted to CO_2 capture. There are 13 scientific papers, of which one, Chapter 18 by CanmetEnergy, is a collection of several shorter contributions rather than one long paper. In addition there are three non-scientific chapters and one concluding chapter. The non-scientific chapters include an overview of the entire capture program of CCP2 and introductions to the two projects co-funded with the European Union: Chemical Looping Combustion Gas Power (CLC GP) and Carbon Dioxide Capture and Hydrogen Production from Gaseous Fuels (CACHET). Following the technical capture papers is a paper with the performance and cost evaluations of 22 combinations of the CCP2 technologies and different applications (scenarios).

Thereafter follows a section on underground storage of CO_2. The section follows the same pattern as that on capture – an overview chapter of the program in the beginning followed by seven scientific papers and a concluding chapter.

The book ends with two chapters summarizing activities within Policy and Incentives (P&I) and Communications.

The scientific papers report on the results from work carried out under CCP2. Several of the capture technology projects were continuations of work carried out under CCP1. This must be kept in mind when reading the papers.

The CCP Executive Board and management as well as the editor have strived for a selection of papers of high scientific standard. All technical/scientific papers, except the contribution from CANMET, have been reviewed by at least two referees. All but three of the twenty reviewed papers, were reviewed by persons without connections to CCP. Only one paper was reviewed solely by persons employed by a CCP company. Overview and summary papers have not been reviewed.

All chapters of this book will be available for downloading as individual papers from the website http://www.co2captureproject.org

THE STRUCTURE OF THE CO_2 CAPTURE PROJECT

CCP2 has two levels of membership:

- Full membership for companies that take part in all CCP2 activities and have representation on the Executive Board and all working groups.
- Associate membership for companies that are focused on advances in CO_2 geological storage, policy development and stakeholder discussion and engagement. In addition to regular SMV and Policy meetings, Associate Participants participate in annual meetings of the CCP Executive and Technical Advisory Boards, NGO outreach meetings and public/government meetings. Associate Participants have opportunities to participate in future technology demonstrations. Associate members in CCP2 have been EPRI (Electricity Power Research Institute) and Repsol YPF.

Structure and Management Process

The structure of the CCP2 project is illustrated in Figure 1. The Project has technical teams staffed with experts from the participating companies and technology providers that work together to deliver the program results. These teams are focused on technology development to reduce the cost of CO_2 capture, demonstrate that geological storage is safe and secure, and communicate policy matters that will impact the effectiveness of CCS technology.

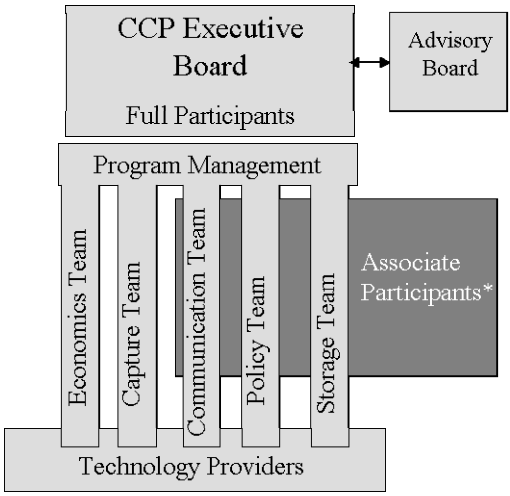

Figure 1. The CCP2 Project Structure.
* See text for definition of Associate Participants

Executive Board

The Executive Board consists of one member from each of the eight CCP2 full member companies and exercises overall control and governance of the program of work and prioritization of specific projects to be undertaken and funded by CCP2.

CCP2 Advisory Board

The CCP2 Advisory Board (CAB) consists of international technology experts selected by the Executive Board to provide independent advice and review of the CCP2 technology program. The CAB provides assurance for the quality and integrity of the technology program and challenges the Technical Teams and Executive Board to reach beyond short term needs to define an approach to technology development encompassing a broad range of industrial users of energy and fuel sources.

Program Management

The Project Manager provides direction to the teams for the delivery of the program goals within the overall budget and timeframe set by the Executive Board.

Technical Teams

Each of the technical teams was led by a designated Technical Team Leader. Technical Teams were formed by the Executive Board for the purpose of progressing development of technology in approved areas. Each Technical Team included at least one representative from each participating company. The teams regularly reviewed and compared the development of technologies, allowing the teams to prioritize and focus on the technologies with the best results for specific applications.

The technical teams were assigned the following tasks within their areas:

- Capture and Economics: advance technology development of the selected technologies; assess their performance, evaluate cost and compare the costs and benefits of various approaches to capture.
- Storage, Monitoring, and Verification: verify the feasibility of underground storage, and develop improved assessment, monitoring and verification methods.
- Communications: build awareness of technical developments among policy makers and interested stakeholders.
- Policy: assess the impact of proposed government policies and regulations on CO_2 capture and storage processes and costs.

Technology Providers

CCP2 engaged with Technology Providers to develop the CCP technical program. Technology providers include academic institutions, research companies, CCP2 participants, national laboratories and expert consulting firms.

Within the Capture and SMV teams, dedicated persons were given the responsibility to act as technical focal points for the Technology Providers.

CCS TECHNOLOGIES IN CCP

Technology Selection Process

The foundation for CO_2 Capture and Storage (CCS) technologies selected for CCP2 was laid in CCP1, where approximately 200 technologies were evaluated for potential application to full-scale development. The selection process is described in [1]. Here follows a brief summary:

The Phase 1 selection of technologies took place in two stages. First, numerous concepts being promoted by technology developers, researchers, and entrepreneurs were screened for their potential

in a Review and Evaluation (R&E) process. The criteria selected by the teams for the R&E stage were:

- Likelihood to achieve target cost reductions relative to existing (baseline) technology.
- Health, Safety, and Environmental performance requirements must be met. The technologies must be safe for workers and the environment. The technology must be robust to ensure that the plant will operate efficiently and have high availability for use.
- Relevance to Participants' emission sources: The technologies must have the potential to be applied to Participants' commercial operations without significant negative impact.
- Able to meet CCP's schedule: The technologies must be sufficiently well advanced to prove that the concept will work by the end of 2009. The preferred technology must be sufficiently developed to be ready for larger scale implementation by 2010-11.
- Acceptable to government and public stakeholders. Potential emissions must be understood and control methods available to limits currently defined. Ideally, one would like to identify a small number of full system-based capture technologies that could serve in many different industrial applications. Phase 1 revealed that none of the considered technologies would be likely to achieve this; also it indicated that no technology had been developed to a stage where one could be certain about the performance and cost. Therefore, the selection of technologies to be brought into the next step took place in the Analysis Phase, in which the goals were to:
    - Screen and rank technologies relative to CCP Key Success Criteria.
    - Select technologies for further development.
    - Decide budget allocations by:
        - Technology theme (pre-, post-, oxy-fuel combustion)
        - Technology theme for each Scenario
    - Agree slate of potential technology developers.
    - Agree process to access novel technologies.

The research, engineering and analysis phases (the main work of CCP1) provided strategic direction for the third and last activity of CCP1, the Technology Development Phase. The technologies that passed the Analysis Phase were funded for further development. The results are presented in 34 technical papers in [1].

CCP1 ACHIEVEMENTS - BACKGROUND FOR CCP2

Capture

In the Technology Development Phase, CCP1 commissioned around 35 engineering and/or research studies for further development and performance assessment of the selected technologies. The technologies were evaluated within four different application scenarios, Table 1. The capture technologies listed in Table 1 were compared to a state-of-the-art, post-combustion solution using amines (MEA) or, in the Canadian case, a state-of-the-art Integrated Gasification Combined Cycle (IGCC).

Table 1. CO_2 capture scenarios used in CCP1.

Application	Location	Fuel source	CO_2 source	Capture technology
Refinery	Europe	Hydrocarbon gas and liquids	Heaters and boilers	Oxy-fuel, Pre-combustion
Natural Gas Combine Cycle power plant	Western Norway	Natural gas	Large gas turbines	Post- and pre-combustion
Distributed turbines	Alaska North Slope	Natural gas	Small gas turbines	Pre-combustion
Gasification	Western Canada	Sold fuels, petroleum coke, coal	Steam, electricity and hydrogen coproduction	Advance capture solutions

Post-combustion approaches included integrated solutions, exhaust gas recycle and membrane contactors. The pre-combustion cases included membrane water gas shift (MWGS), sorption enhanced water gas shift (SEWGS) and a complete membrane based hydrogen reformer. The oxy-fuel approach included revamping heaters and boilers for burning the fuel in pure oxygen as well as the Chemical Looping Combustion (CLC) technology.

The studies revealed that significant cost reductions may be achievable. Pre-combustion technologies had the largest potential, with cost reductions between 44% and 60%, depending on technology, whereas post-combustion and oxy-fuel showed cost reduction potential in the ranges 43% - 54% and 38% - 48%, respectively.

Despite the extensive research and development behind the studies it became clear that the cost reductions are connected with large uncertainties, as none of the technologies were tested beyond laboratory scale, and some did not progress further than economic analysis studies. Additionally the uncertainty in the cost estimates was $\pm$ 30%.

Storage, Monitoring and Verification (SMV)

The Research & Engineering Phase of CCP1 produced state-of-the-art descriptions of the technologies, technical gaps needing additional work and recommendations that were carried into the Analysis Phase. The technologies were organized into the following areas:

- "Integrity" - assessing the competence of natural and engineered systems to retain CO_2 over extended periods.
- "Optimization" - strategies for improving the efficiency and economics of CO_2 transportation and storage.
- "Monitoring" - identification of techniques suitable for tracking CO_2 movement within (performance) and outside (leakage or seepage) the injection target.
- "Risk Assessment" - development of concepts, protocols and methodologies to quantify probability and impact of CO_2 leakage from storage sites.

The SMV program for the Technology Development stage was comprised of some 30 projects. The constellation of industry, academic and government programs addressing geological CO_2 storage considered risk-based approaches that entailed identifying technical questions and addressing them by leveraging the existing natural and industrial analog knowledge base and developing new R&D avenues. Whereas some projects were based on a specific asset or storage venue type, the applications developed are universally applicable.

CCP2 – FURTHER PROGRESS

The CCP2 Capture Technology portfolio

The CCP2 portfolio of capture technologies consists of seven pre-combustion technologies, two oxyfiring concepts and one post-combustion technology. The scenarios were reduced to two – a natural gas fired power plant in Northwest Europe and a refinery. The refinery scenario included studies of a fluidized catalytic cracker (FCC) in South America in addition to heaters and boilers in Northwest Europe. A summary of the CCP2 capture Programme is given in Chapter 2 of this book and the results of the different technology projects are reported in Chapters 3 – 18. The technologies may be grouped as follows:

- Technologies with completion date in 2008. These technologies received a major part or all of the funding from CCP2.
- Technologies with completion date in 2009. These technologies received funding from CCP2, the EU and the technology providers.

One major outcome of the CCP2 capture work is that the uncertainties in cost and performance that were still lingering from CCP1 have been reduced. Several of the technologies have now been produced at significantly larger scales and have been subjected to much longer and more realistic tests. In addition, improved manufacturing methods have made cost estimates more accurate and realistic. Although the improvement in uncertainty has not been quantified, it is fair to say that there is now a better understanding of the cost of CO_2 capture than existed at the completion of Phase 1 in 2004.

Although the uncertainties in cost and performance have been reduced in CCP2, the evaluations in Chapter 17 basically confirm the CCP1 estimates of CO_2-avoided costs and the ranking of the technologies. This raises the issue of what can be done to reduce the costs further. The Economics Team points out in Chapter 17 that there appears to be a relationship between high capture rate and low efficiency and that although this relationship may not hold for all technologies it would be worthwhile pursuing the cost implication for relevant technologies.

The CCP2 Storage Technology Portfolio

The CCP2 portfolio for storage, monitoring and verification (SMV) consists of seven technologies. Chapter 20 summarizes the technologies together with the participating R&D institutions and co-funding sources. The portfolio consists of 1) Certification Framework (CF), an integrated platform for site certification for CO_2 permitting, operation and decommissioning; 2) well integrity logging, sampling, modelling, history matching, and simulation of post-closure sealing capability over extended time periods; 3) testing the capability of standard logging tools to detect a sharp interface between free-phase CO_2 and brine; 4) coupling of geo-chemical and geo-mechanical models; 5) simulation of safe and effective operational constraints and monitoring for CO_2 injection in coal beds; and 6) a field test of airborne remote sensing technologies. Details of the study results are given in Chapters 21 - 27.

At the start of CCP2, site assessment and other regulatory developments were high on the international agenda. The integrity of wells that have been exposed to CO_2 over long periods was thought to be a potential CO_2 storage "showstopper" and there was a focus on coal beds as a major potential venue for CO_2 storage. The CCP Storage program has addressed these issues and significant progress has been achieved:

1. The CF contributed to the CO_2 and brine leakage-risk part of the process for licensing and permitting and has provided a useful set of guidelines and procedures for assessing the viability of a CO_2 storage site.

2. The examination of wells exposed over long time periods has indicated this likely is not a major issue. Phase 3 will provide additional focus on this question.

Furthermore, the SMV Program of CCP2 has made advances in the development of reservoir simulators that combine reactive transport with geo-mechanical analysis and in modelling and monitoring CO_2 injection in coal beds. The industry standard RST tool was evaluated for use in detecting the presence of CO_2 in saline waters, and an airborne multispectral imaging system was evaluated for detecting CO_2 and methane leakage from perforated pipelines.

REFERENCES

1. Thomas, D.C., ed., 2005. Carbon Dioxide Capture for Storage in Deep Geologic Formations - Results from the CO_2 Capture Project, Vol. 1: Capture and Separation of Carbon Dioxide from Combustion Sources, Elsevier Publishing, UK. 654 pp.
2. Benson, S.M., ed., 2005. Carbon Dioxide Capture for Storage in Deep Geologic Formations - Results from the CO_2 Capture Project, Vol. 2: Geologic Storage of Carbon Dioxide with Monitoring and Verification, Elsevier Publishing, UK. 678 pp.

Carbon Dioxide Capture for Storage in Deep Geologic Formations, Volume 3
L.I.Eide (Ed.)

Chapter 1

CCP2 ADVISORY BOARD REPORT: APPRAISING THE PERFORMANCE AND ACCOMPLISHMENTS OF THE CO_2 CAPTURE PROJECT - PHASE 2

Vello A. Kuuskraa
Advanced Resources International, Inc.
4501 Fairfax Drive, Suite 910, Arlington, VA 22203 USA

ABSTRACT: Since its inception in 2001, the CO_2 Capture Project (CCP) has pursued two main themes: (1) identify and further develop technologies that would lead to lower costs for capture of CO_2; and (2) improve the performance and public acceptance of CO_2 storage. In addition to overall management of the project by the CCP Executive Board (containing representatives from each of the participating companies), the CCP established an Advisory Board as part of its commitment to quality project management.

INTRODUCTION

During Phase I of the CO_2 Capture Project (CCP), which encompassed three years (mid-2001 to mid-2004), the CCP conducted in depth reviews of nearly 200 novel CO_2 capture technologies. Based on these reviews, CCP1 identified a handful of technologies for further appraisal and development. In parallel, CCP1 also sponsored a series of studies that helped highlight the high priority barriers facing CO_2 storage.

The purpose of Phase II of the CCP (operating from mid-2004 to mid-2009) has been to channel more intensive research and investigation on this handful of "preferred" CO_2 capture technologies as well as further pursue high priority topics for CO_2 storage, monitoring and verification. This introductory Chapter transmits the review by the Advisory Board of the performance and accomplishments of Phase 2 of the CCP.

The CCP2 Advisory Board past and current members include: Vello Kuuskraa, Chairman, Dale Simbeck, Chris Higman, Olav Bolland, Pierpaolo Garibaldi, Larry Meyer, Nick Riley and Sally Benson.

THE CCP2 CO_2 CAPTURE PROGRAM

The CCP2 Capture Program, budgeted at $25.7 million for its five years of effort, set forth three major objectives for the "preferred" CO_2 capture technologies that emerged from CCP Phase I assessments:

- Achieve "ready for field demonstration" for at least one technology
- Pursue scale-up of "preferred technologies" by at least one order of magnitude.
- Solve the critical technical issues and confirm the economics of the "preferred" technologies.

With respect to its three objectives, the Advisory Board finds that CCP2 has addressed and accomplished the following:

1. Oxy-Fuel CO_2 Capture Technology for Fluid Catalytic Cracking (FCC) in Refineries Is Being Made "Ready for Field Demonstration".
2. Two of the Novel CO_2 Capture Technologies - Hydrogen Membrane Reforming and Chemical Looping Combustion - Have Been Pursued at Larger Scale.
3. Achieving Lower Cost CO_2 Capture from Natural Gas Combined Cycle Units Remains a Challenge.

To provide a more comprehensive appraisal of CCP2 performance and accomplishments, the Advisory Board chose to address three questions:

- How effectively did the CCP2 achieve its objectives?
- How much has the CCP2 technology program contributed to advanced understanding of CO_2 capture science and deployment?
- To what extent has the CCP2 program led to a better understanding of the costs of implementing CO_2 capture technology today and in the future?

Oxy-Fuel CO_2 Capture Technology for Refinery FCC Units Is Being Made "Ready for Field Demonstration"

An important accomplishment by CCP2 has been the identification of oxy-fuel combustion as the preferred CO_2 capture technology for fluid catalytic cracking (FCC) units of petroleum refineries. The FCC unit typically is the largest single source of CO_2 emissions in petroleum refining, accounting for about half of overall emissions. A side-by-side economic and process performance assessment by CCP2 showed that oxy-firing would have significant cost savings compared to using a post-combustion process for capture of CO_2 emissions from the FCC unit of a refinery.

A field demonstration of oxy-fired CO_2 capture with FCC is scheduled to start in the second quarter of 2009 at the Petrobras refinery test unit, a 60 barrel a day FCC facility located in Brazil. As such, CCP2 is actively pursuing its main objective - - achieve "ready for field demonstration" status for at least one CO_2 capture technology.

Additional efforts are underway by the CCP to extend oxy-firing technology to other CO_2 emitting units of the refinery, namely in its heaters and boilers. Before proceeding, the Advisory Board recommends that the CCP conduct a rigorous "head-to-head" comparison of using pre, post and oxy-fuel for capture of CO_2 from refinery heaters and steam generation boilers. This would help establish the least cost and lowest CO_2 emissions option (including accounting for CO_2 emissions from the electricity used for producing oxygen).

Pursuing Scale-Up of Novel Technologies

The CCP, from its inception, has "reserved space" for higher risk, high impact technologies. During CCP2, the two most notable of the high risk, high impact technologies were: (1) membrane development for hydrogen membrane reforming (HMR), and (2) chemical looping combustion (CLC). Notable scale-ups have been achieved for both of these technologies, yet significant development challenges remain:

- While CCP's economic analysis still shows low CO_2 capture costs for hydrogen membrane reforming (HMR), numerous technical barriers remain, such as membrane performance at high temperatures, membrane embrittlement and membrane resistance to contaminants. Each of these barriers still requires continued research investments.

- Chemical looping combustion (CLC), facing temperature limitations on its oxygen carrying materials, may find its most useful CO_2 capture niche in lower temperature process heat applications such as generation of steam for in-situ heavy oil/oil sand recovery and for refinery processes. Further research investment in this area is also warranted.

The Advisory Board recommends that Phase III of the CO_2 Capture Project continue to pursue advances for these two high risk, high reward technologies. Successful research investment in advanced HMR and CLC could substantially reduce the costs of future CO_2 capture technologies directly applicable to the oil and gas industry.

Achieving Lower Cost CO_2 Capture Options for Natural Gas Combined Cycle Power Plants Remains a Challenge

The objective of identifying and further developing significantly lower cost CO_2 capture technology for Natural Gas Combined Cycle power generation has yet to be achieved. With advances in process integration and the commercial availability of larger scale amine units, the early economic advantage of CCP's BIT (Best Integrated Technology) development, including its push for increasing the CO_2 content of the flue gas with exhaust gas recirculation (EGR), has essentially evaporated. Rigorous economic analysis of the costs of CO_2 capture, prepared by both internal and external analysts, indicates that the BIT CO_2 capture option, even with 40% EGR, may not warrant its added complexities and capital costs.

The Advisory Board notes that, with advances in amine and other sorbent systems and improvements in processes integration, post-combustion capture of CO_2 from Natural Gas Combined Cycle power plants (NGCCs) may be the "preferred technology". A "head-to-head" cost and performance evaluation of post-combustion CO_2 capture technology offered by the top four to five vendors would provide valuable information on today's costs and performance, helping clarify the pathway toward the preferred CO_2 capture technology for NGCCs.

Conducting the proposed evaluation of emerging post-combustion CO_2 capture systems for NGCC as an initial task during Phase III would enable the CCP to more fully meet the objective – "confirm the economics of each selected technology."

Looking Ahead

When first formed, the CO_2 Capture Project provided one of the leading scientific efforts on a broad array of CO_2 capture technologies and applications. With the entry of additional companies, research institutes and technology vendors into the CO_2 capture industry, it is prudent for the CCP to narrow its focus, concentrating on CO_2 capture technologies of direct use by the oil and gas industry. In the view of the Advisory Board, the pursuit of lower cost CO_2 capture options for petroleum refineries and for steam generation are most appropriate. Continuing to pursue lower cost CO_2 capture technologies for NGCCs, chemical processes and poly-generation (including gasification of refinery "bottoms" and coke for production of hydrogen) is also recommended.

In the view of the Advisory Board, it is also timely to initiate larger-scale integrated CO_2 capture and storage field demonstrations, as further discussed under the CCP2 SMV program.

Certain of the initially selected "preferred technologies" appear to have barriers and lower potentials for cost savings than initially established by CCP1. While work by CCP2 has addressed some of these barriers, the recent economic analyses confirm that three of the previously identified "preferred technologies" provide only marginal gains in efficiency and costs, namely:

- Sorbent Enhanced Water Gas Shift. This technology still has high CO_2 capture and avoidance costs and contributes only a few percent toward improving energy efficiency.
- Membrane Water Gas Shift. This technology suffers from problems with membrane development, adds little to methane conversion rates and appears to have high costs.
- One Step Decarbonization. This technology introduces high complexity yet limited efficiency improvements for CO_2 capture with hydrogen production.

The Advisory Board recommends that the CCP no longer invest in these three "preferred technologies" but rigorously document the work performed by the CCP for use by future investigators.

THE CCP2 STORAGE, MONITORING AND VERIFICATION (SMV) PROGRAM.

The CCP2 SMV program has also achieved a series of important accomplishments. These accomplishments are particularly notable given the relatively modest budget of $5.3 million for its five years of effort. The key accomplishments by the SMV Program, discussed in more depth below, include the following:

1. The Well Integrity Program Has Led to Improved Understanding of the Containment Integrity of Existing and New CO_2 Storage Wells.
2. The Certification Framework Provides a Simplified Work Flow Protocol for Assessing CO_2 Storage Sites.
3. The SMV Program Has Transferred Valuable Technical Information on CO_2 Storage to the NGOs and the Public.

Well Integrity Program

At the top of the list of accomplishments is the Well Integrity Field Study that has addressed the risks that the presence of injected and stored CO_2 would have on the containment integrity of existing and newly drilled wells. The objective of this portion of the CCP2 SMV program was:

"Put the long-term wellbore integrity issue in proper perspective by assessing well materials alteration in CO_2-experience wells and projecting prospects for long-term stability."

Much of the impetus for this SMV program came from conflicting data and perceptions on well integrity in the presence of CO_2, ranging from laboratory studies showing rapid deterioration of traditionally used well cements to evidence of decades long well cement integrity experienced by CO_2 EOR operators in West Texas.

Of particular value has been the in-depth Case Study of a natural CO_2 production well at Sheep Mountain, Colorado, completed in the Dakota Sandstone at 4,561 feet (top of production zone). The well produced for a total of 20 years, at a rate of 7 Mcfd of CO_2 and 5 barrels of water during its first 13 years and intermittently during its final seven years. Some key data for the well are:

- The well was cased with 7-inch diameter carbon steel, K-55 grade, and cemented with a Portland Class H cement-fly ash system (containing 50% fly ash).
- The top of the cement (behind casing) was at 3,050' and extended 1,640' above the CO_2-bearing zone.
- Production tubing was a plastic-coated, K-55 grade, material that showed no signs of corrosion during its production life.

Using in-depth well diagnosis, the Case Study showed that, despite significant alteration of the cement, the well system continued to provide a competent barrier to pressure loss or migration of fluids or CO_2. For example, there was no observed casing pressure (which would indicate leakage

of CO_2 through the cement barrier) during the life of the well. In addition, while a major portion of the cement samples taken across the CO_2 reservoir had been converted to calcium carbonate, the fluid barrier was not compromised. The cement interface with the caprock and casing showed tight contacts and only very thin deposits of calcium carbonate. All twenty carbon steel casing samples were in excellent condition.

An important preliminary finding from the Case Study is that Portland-based cement systems, when properly placed, can create competent barriers to CO_2 leakage from wells. A second well integrity field Case Study, at the Buracica Field in Salvador State, Brazil, is still underway and will provide additional data on this important CO_2 storage issue.

The Well Integrity Program is planned to be continued in CCP3 and has an emphasis on additional well surveys and simulation of the effects of longer-term cement alteration processes on well integrity. The Advisory Board strongly supports the continuation of research on this important CO_2 storage topic.

Certification Framework

The purpose of the Certification Framework (CF) is to develop a workflow protocol for assessing CO_2 storage sites. The Certification Framework, developed during the initial year of CCP2, has been applied to two field sites - a hypothetical CO_2 storage project in the Texas Gulf Coast and an actual CO_2 storage project at Kimberlina, San Joaquin Basin of California. Based on feedback from these two case studies, the CF provided a useful set of guidelines and procedures for assessing the viability of a CO_2 storage site. However, the CF fell short in providing an acceptable probability-based risk assessment for CO_2 leakage.

Future plans, assuming success in obtaining funding from outside sources, include adding storage optimization and decommissioning to the CCP SMV Program. In the opinion of the Advisory Board, CO_2 storage optimization and storage site decommissioning are two topics that deserve high priority.

Other Accomplishments

Given its many years of experience and its in-depth scientific expertise, the oil and gas industry has much to offer to the CO_2 storage industry. The CCP2 SMV program has worked to assemble the available industry expertise and transmit it to the NGO and technical communities through a variety of initiatives:

- Presentations at numerous conferences and preparation of peer-reviewed papers (over 25) on the technical aspects of CO_2 storage.
- Preparation and publication of the high quality document, "Technical Basis for CO_2 Storage", that outlines the industry's technical recommendations for safely storing CO_2.
- Sponsorship of the annual North American and European forums, addressing the practice and risks of CO_2 storage.

In addition, the Advisory Board recommends that the CCP3 SMV program become pro-active in providing information on CCS to the media and the general public, to further build public acceptance for this important CO_2 mitigation option.

Other Technical Programs

In addition to the above, CCP2's SMV program has undertaken a number of smaller efforts including: improving the development of a coupled geochemical-geomechanical simulator; testing

the capability of the industry standard RST tool to detect the presence of CO_2 in saline waters; evaluating remote sensing capability to detect CO_2 and methane leakage from perforated pipelines; and assessing, using reservoir simulation, the operational trade offs of CO_2 storage and methane production from coal seams.

These efforts have helped advance the science and understanding of CO_2 storage, but are not planned to be further pursued in CCP3.

Looking Ahead

The CCP2 Advisory Board commends the CCP2 SMV Program for its high impact accomplishments and recommends continued efforts on well integrity, storage optimization, monitoring technology and subsurface processes. In addition, the Advisory Board recommends that the CCP3 SMV Program add two high priority topics to its list:

- CO_2 Purity Specifications for Transportation and Storage. With the new emphasis on using oxy-fuel based CO_2 capture technologies, the topic of acceptable CO_2 purity specifications takes on new importance. The Advisory Board recommends that the CCP3 SMV program address the topic - What should be the recommended CO_2 purity specifications for effective and safe CO_2 transportation and storage?
- Remediation of Existing and Abandoned Wells. Many of the most favorable CO_2 storage sites, including saline formations above and below existing oil fields, will have older wells that may penetrate the intended CO_2 storage horizon. The Advisory Board recommends that the CCP3 SMV program address the topic - What would constitute a set of "best practices" for remediating existing wells to be used for storing and monitoring CO_2?

Finally, given the remaining challenge of building public acceptance for CCS, particularly the long-term storage of CO_2, the Advisory Board recommends that the CCP3 SMV program engage in numerous field tests, including linking storage of CO_2 with its CO_2 capture demonstrations.

ACKNOWLEDGEMENTS

Vello Kuuskraa, Chairman, would like to thank each of the members of the CCP2 Advisory Board for their contributions to this paper as well as their most valuable guidance and participation during CCP2.

SECTION 1:
CO_2 CAPTURE

Carbon Dioxide Capture for Storage in Deep Geologic Formations, Volume 3
L.I.Eide (Ed.)

Chapter 2

INTRODUCTION TO THE CCP2 CAPTURE TECHNOLOGY PORTFOLIO

Ivano Miracca
Saipem S.p.A. (Eni), Viale De Gasperi 16, I-20097 San Donato Milanese, Italy

ABSTRACT: The portfolio of capture technologies in CCP2 is described, and achieved technical progress for each technology in the path toward commercialization is outlined.

INTRODUCTION

The CCP has been supporting development of CO_2 capture technologies with the target of cost reduction by at least 60% compared to year 2000 state-of-the-art. This paper aims to give a general overview of the capture activities in CCP2 (2004-2009), synthetically describing:

- The selected scenarios where application of CCP technologies has been evaluated.
- The technical progress achieved for each technology.
- The path for future development for the most promising technologies
- Lessons learnt and future outlook based on the CCP2 experience

Single chapters will be dedicated to the detailed description of each technology in CCP2, while a dedicated chapter will describe results from the economic evaluations.

THE PHASES AND SCENARIOS OF CCP

Since the year 2000 the CCP has gone through two phases, which may be defined as:

- CCP1 or the "Proof-of-concept" phase (2000-2004) where ~ 200 technologies were reviewed and ~ 10 achieved both technical proof-of-concept and economic validation in a scenario of interest to the member companies.
- CCP2 or the "Intensive development" phase (2004-2009), where the objective was to develop the most promising technologies from CCP1 to the "ready for a pilot plant" stage.

Four different scenarios were considered for application of technologies in CCP1:

- New-built natural gas Combined Cycle Gas Turbine (CCGT) 400 MW power station in Norway
- Retrofit of heaters and boilers system in a UK refinery (2 Mtons/year of CO_2)
- Retrofit of a network of gas turbines in Alaska (1.3 million tons/year of captured CO_2)
- New-built petcoke Integrated Gasification Combined Cycle (IGCC) unit (4.9 million tons/year of captured CO_2)

The extremely high costs of the Alaskan scenario make it an unlikely early deployment opportunity of Carbon Capture and Storage (CCS), while CCP1 showed that the additional costs for CCS in a gasification unit are negligible compared to the huge capital cost of the IGCC itself. In this case, cost reduction should target the gasification unit, rather than the capture technology and this type of

development is out of the scope of the CCP. As a consequence these two scenarios were not pursued anymore in CCP2.

Attention was rather focused on power generation from natural gas, recognizing this application as challenging, since the low concentration of CO_2 in the flue gas leads to higher capture costs compared to coal power generation, and power generation is likely to be the first industrial sector where CCS techniques will be commercially applied.

On the other side, the refinery scenario was made more flexible, assessing oil refinery as a multi-source of CO_2, and addressing each type of source with the most promising capture technology. Production of heavy oil or tar, though not directly included in Phase II, is a related application of growing interest where generation of the required steam will result in high levels of CO_2 emission. In this case, rather than retrofitting a whole set of process heaters and boilers, a new-built single unit was considered, with a specific capture unit. In another refinery sub-scenario capture of CO_2 from the regenerator effluent of a Fluid Catalytic Cracking (FCC) unit was considered, as this is the largest concentrated source of CO_2 in many refineries.

Scenarios in CCP2 were also made more flexible by using a "generic" location in a strongly industrialized site, where most needed utilities may be bought at a certain cost, rather than produced inside battery limits. The CCP2 scenarios are therefore:

- New-built CCGT 400 MW power station in NW Europe
- Refinery scenarios including three sub-scenarios:
    - Retrofit of a set of heaters and boilers to capture 2 Mtons/year of CO_2 using a centralized capture system.
    - New-built single boiler producing 210 tons/hour of steam.
    - Retrofit of the regenerator of a 62,000 bpd FCC unit.

POWER GENERATION FROM NATURAL GAS IN A COMBINED CYCLE

Description of considered technologies

The baseline case for this scenario is a post-combustion approach where flue gas containing ~ 4% vol. of CO_2 is washed by a monoethanolamine (MEA) unit (30% vol.). The capture rate of 86% was assumed as an optimum, though it is recognized that the cost/performance curve is quite flat in the 85-90% range of capture rates. At the time of CCP1 it was assumed that two parallel amine trains were needed to wash the effluent from a 400 MW CCGT power station. Engineering and construction progress over the last years are enabling major licensors to offer a single amine train to wash the effluent of CCGT power stations up to the capacity of 500-600 MW. Considering that amine washing of this size is not yet commercially proven (one order of magnitude scale-up is necessary), the CCP decided to retain the original baseline, adding the single train option as a sort of advanced baseline named BUT (Best Unintegrated Technology). When claims from technology providers will be proven, the BUT case might be considered as the new baseline, witnessing the general trend toward advancement of technologies, even if already relatively mature.

As reported by Choi et al. [1], the CCP and Nexant developed at the conceptual level an integrated post-combustion process scheme to minimize the costs of capture. This scheme was named "Best Integrated Technology" (BIT) and may in principle be applied to any post-combustion capture technology based on absorption of CO_2. The process flow diagram for BIT as applied to power generation is represented in Figure 1.

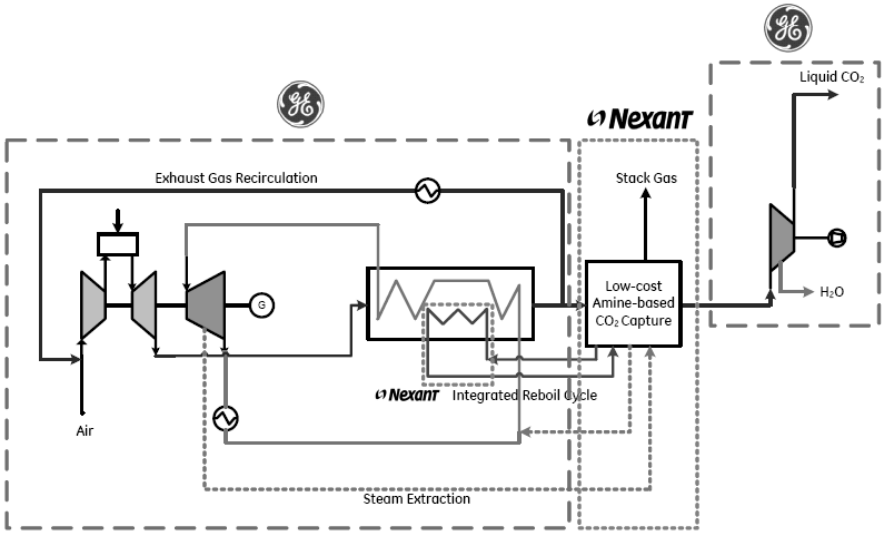

Figure 1. BIT process flow diagram.

The positive economic evaluation achieved in CCP1 was caused by two main items:

- Exhaust Gas Recycle (EGR) for the combined-cycle power plant of 50% of the flue gas stream, increasing the CO_2 concentration in the flue gas from the usual 4 vol. % to 10 vol. %. This led to the adoption of a single amine train, thus enhancing the advantage of the BIT case compared to the baseline.
- Integrating the Heat Recovery Steam Generator (HRSG) with the solvent reboilers to eliminate some reboiler shells from the capture plant and reduce net steam extraction to the capture plant.

EGR leads to lean combustion (~ 13% vol. of oxygen for 50% EGR) which may affect operation of the combustion chamber. The CCP has therefore collaborated with one of the main turbine vendors (General Electric) to investigate experimentally the feasibility and limitations of EGR and to update the BIT process scheme and evaluations. Tests with actual EGR were performed on a prototype combustion rig with ~1% thermal load of a full 9FB machine (1/6 of a can). The experimental setup included two combustors, water quenching, re-firing in second stage, piping and preheating. The tests have demonstrated EGR up to 35 % under relevant conditions for up to 30 hours and the feasibility of deploying EGR on Dry Low-NO_x (DLN) turbine, confirming good performance of the DLN nozzle. Modifications of existing equipment might allow demonstration of 40% EGR. Additional to flame stability, concentration of carbon monoxide in the flue gas is the main index used in the assessment. The revised BIT process scheme shows power generation efficiency close to 50% using a 30% wt. solution of MEA as solvent with a penalty of ~ 8 percentage points compared to the uncontrolled case. The use of more advanced new generation solvents may further reduce this gap. The next step for development of the EGR technology may be a full can test ($1/12^{th}$ of a 9F turbine) or a field demonstration retrofitting an existing E- or F-type machine. Results from the economic evaluations are however showing that the concept of EGR coupled to the MEA technology is only beneficial in the range where it results in high capex saving (one vs. two amine trains). This range is now shifted toward higher capacity (> 600 MW). Since 800MW is a typical size for a CCGT power station coupling two 9F machines in parallel, the EGR concept may still be

of interest for commercial application. Additionally, other solvents may have different ranges for the one vs. two trains issue or even different energy consumption for different concentrations of CO_2 in the flue gas.

As descriped in [2], a technology under development by StatoilHydro (at the time Norsk Hydro), Hydrogen Membrane Reforming (HMR), showed outstanding potential for long term cost reduction in CCP1 (53% efficiency – 24 $/ton capture cost). HMR is based on the development of novel, high temperature (~1000°C) ceramic membranes permeable to hydrogen and is applicable to pre-combustion decarbonization schemes for CO_2 Capture. This result did not purely come from the core technology under development, but was also associated to some non-conservative assumptions concerning high temperature gas-gas heat exchange, air extraction from the turbine and turbine inlet temperature. The work in CCP2 was therefore directed not only toward technical development of the membranes, but also to a revision of the process scheme, limiting non-conventional features. Updated process schemes include:

- Reduction in the overall membrane area: one or two stages of membrane reforming vs. three stages in CCP1. CO_2 capture is achieved in a conventional amine (MDEA) unit.
- Possible use of conventional turbines with the original three stage concept since the air extraction is reduced to < 20%
- Use of gas heated reformer in the one-stage concept to avoid metal dusting and turbine inlet temperature in an acceptable range for current machines.

The option of high temperature gas-gas heat exchange may however be feasible in prospect, since the development of the ceramic material of the membrane should also enable construction of ceramic heat exchangers. One of the new schemes is reported in Figure 2.

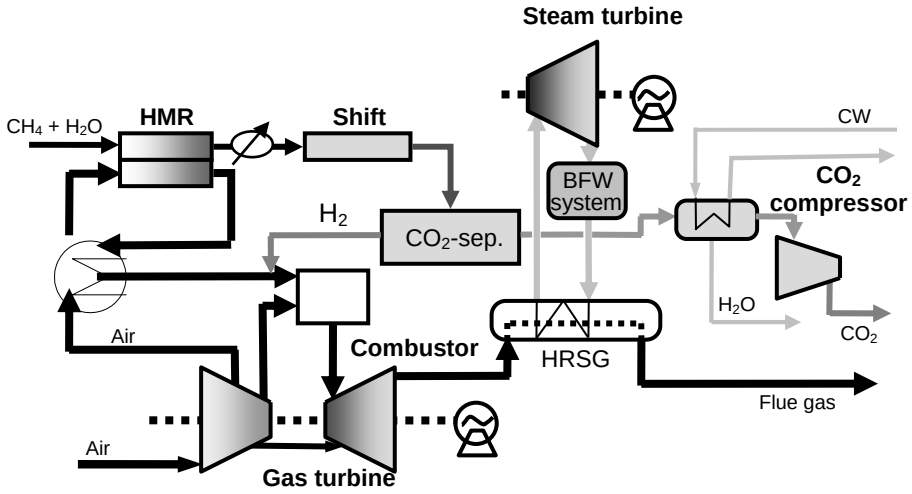

Figure 2. HMR process scheme with 1-stage of membrane reaction.

All new schemes have kept efficiencies in the 50% zone that may be competitive with the post-combustion capture. CO_2 capture costs were also confirmed as the lowest for CCGT scenario. During phase II, the membranes were scaled-up from 10 cm tubes (4 mm internal diameter) to 7x7 cm monoliths with 1.5 mm active channels. Smaller monoliths (2x2 cm) were tested under process conditions at 1000°C and 20 bars and methane conversion was close to equilibrium. The

HMR development has entered a 2-year program for qualification and optimization of the membrane materials. The following phase of development would be focused on design, construction and testing of a pilot unit.

CCP1 showed that pre-combustion may be the winner for the CCGT application in the long term. This result pushed the CCP toward a thorough investigation of novel radical concepts for pre-combustion power generation in the EU co-funded project CACHET (2006-2009), see [3]. Establishment of a state-of-the-art pre-combustion process scheme applicable in the very short term to this scenario was among the targets of CACHET. The selected technology by Technip was an air-fired autothermal reformer (air-ATR). Some technical assumptions were quite conservative to ensure possibility of early deployment:

- 50% vol. maximum hydrogen content of the stream to the turbine.
- Max. inlet turbine temperature of 300°C.
- Avoidance of gas-gas heat exchange in the zone of potential metal dusting.

The process efficiency was therefore limited to ~ 41%. Considering that CCGT power stations may currently achieve ~ 58% efficiency and post-combustion capture should results in a 8-10 percentage points of efficiency loss, it is clear that pre-combustion still has a long way to go before being competitive for this application. The activity of CACHET was therefore focused on the development of novel technologies for the production of hydrogen from natural gas and demonstrated that this route alone may not bring to the desired outcome. None of the process schemes based on novel technologies in CACHET showed efficiency > 48%, not favourable therefore to the expensive development of a long term technology. Combination with parallel advancement in the field of hydrogen burners (to burn more concentrated hydrogen streams) and smoothing of the gas-has heat exchange limitations would be necessary to give real prospects for future application of these technologies. The list of novel CACHET technologies is reported in Table 1 with a brief description of the main features.

Table 1. Novel CACHET technologies.

Technology	**Main Feature**	**Main technology provider(s)**
HyGenSys	Novel concept of Gas Heated Reforming	IFP
CLR (a)	Application of the concept of Chemical Looping Combustion to the production of syn-gas	Chalmers University, Vienna University of Technology, CSIC, Alstom Power Boilers
CLR (s)	Chemical Looping Combustion used as heat supply to a conventional steam reformer	Chalmers University, Vienna University of Technology, CSIC, Alstom Power Boilers
One Step Decarbonisation	Application of the concept of Chemical Looping Combustion to the water splitting reaction for direct production of hydrogen	Eni
Low temperature membrane reforming	novel steam reforming using metallic membranes permeable to hydrogen in the 500-600°C range	ECN, Sintef, Dalian Technical University

CACHET continued the development of two technologies already in the CCP portfolio during Phase I. These are medium-term separation technologies that may be integrated into existing process schemes for syngas production, specifically coupling the Water Gas Shift (WGS) reaction to a separation technique:

- Membrane Water Gas Shift (MWGS) coupling WGS to a noble metal hydrogen permeable membrane (not necessarily in the same vessel).
- Sorbent Enhanced Water Gas Shift (SEWGS) coupling WGS to a solid sorbent for CO_2 capture.

In both cases, the WGS reaction is driven to completion making CO_2 capture easier and cheaper. These technologies seem to be good candidates, coupling good economics to shorter development time.

MWGS is based on the development of ultra-thin palladium membranes started by Sintef in CCP1, as described by Klette et al. [4]. Very thin palladium layers (< 5µm) deposited on a stainless steel porous support are utilized to remove the hydrogen from the syn-gas produced by the reforming and the water gas shift reactions. Good performance of tubes a few centimetres long was demonstrated during Phase I in the water gas shift environment. During Phase II the membrane coated tubes have successfully been scaled-up. 50 cm long membranes have been successfully produced with palladium/silver using a two-step method in which the thin defect-free Pd-alloy film is prepared by sputtering deposition onto the 'perfect surface' of a silicon wafer. In a second step, the membrane is removed from the wafer and transferred onto a porous stainless steel support. A bench scale reactor module based on the scaled-up tubes with hydrogen production roughly equivalent to 4 - 8 kW has been constructed and tested at ECN. The next step of development should be a modular pilot unit in the 100 kW range in a non-integrated version of the technology (separate WGS reactors and membrane vessels), based on the modules developed in CACHET.

SEWGS, developed by Air Products in Phase I, uses a solid adsorbent able to preferentially adsorb CO_2 and thereafter applies pressure swing adsorption (PSA) and water gas shift (WGS) within a single vessel to simultaneously convert CO/H_2O to CO_2/H_2 and to capture CO_2. A complete process flow diagram for application to power generation is represented in Figure 3.

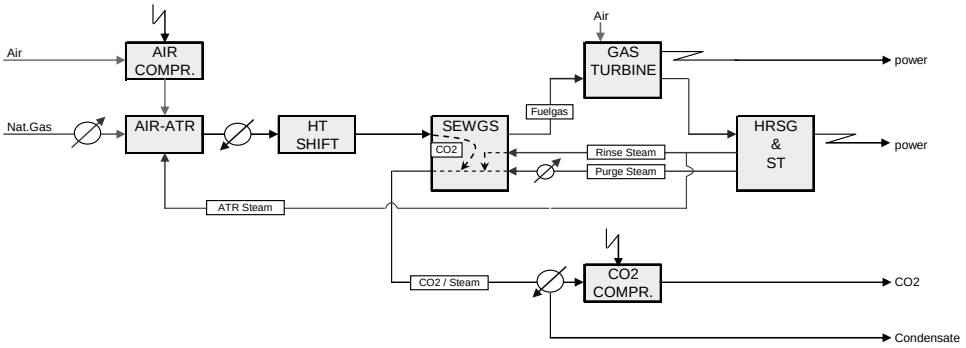

Figure 3. SEWGS process scheme.

In CCP1 suitable adsorbents (modified hydrotalcites) were developed and tested in a single laboratory reactor with alternating cycles of adsorption and desorption. In the frame of CACHET, a multi-column test rig (6 columns) representing a complete continuous commercial cycle has been

constructed at ECN. Columns are of the same height as future commercial columns (6 meters), so that further scale-up should be straightforward.

Both SEWGS and MWGS have potential to increase efficiency of the baseline by 3-6 percentage points. While this may not be enough to make these two pre-combustion concepts competitive in the short term, they may become important if all different types of technical advancement will be combined in a single process scheme. For instance, a preliminary study has shown that the combination of HMR and MWGS has the potential for a big additional benefit.

No purely oxy-fired cases were studied in CCP2 for the CCGT application, since availability of specifically developed gas turbines is considered as a necessity to implement this concept. Oxy-firing may however be considered in pre-combustion application for preparation of syngas through the use of oxygen-fired Autothermal Reforming (O2ATR) or Partial Oxidation (POX). The availability of novel techniques for cheaper oxygen production may therefore become an additional support to the development of competitive pre-combustion schemes.

Technology matrix used in the economic evaluations

The cases that were considered for economic evaluation, [5], in this scenario may be split into two categories:

- Cases that were simply updated from CCP1 for cost escalation (A cases)
- Cases developed in CCP2 using new technical information (B cases)

Table 2. Selected CCGT cases for cost updating from CCP1 (letters refer to the Economic screening in [5].)

Technology case	Description
A1 CCGT Ref. case Uncontrolled	CCP1 uncontrolled baseline
A2 CCGT w/capt Post BL	CCP1 controlled baseline using two parallel MEA trains for capture
A3 CCGT w/ capt Post BL low cost MEA	Engineering improvements to the MEA baseline (low cost machinery, structured packing etc.). Not commercially proven for this application.
A4 CCGT w/capt post BL low cost MEA integrated	Case A3 plus 50% EGR and integration of amine steam reboiler into the HRSG system. One MEA train.
A5 CCGT adv. tech. BIT	Case A4 with advanced solvent with lower regeneration energy.
A6 HMR	Process scheme with three membrane reactors in series and non conservative assumptions.
A7 SEWGS	Partially new case compared to CCP1, including some very conservative assumptions for purge and rinse gas consumption.

Table 3. New CCGT cases for economic evaluation developed in CCP2 (letters refer to the Economic screening in [5].)

Technology case	Description
B1 CCGT Ref. case Uncontrolled	CCP1 uncontrolled baseline A1 moved to a generic NW Europe location where all needed utilities may be bought rather than produced ISBL.
B2 MEA amine CLIMIT BL	Case A2 with the same modifications than B1.
B3 Adv Tech BUT no-EGR MEA	Retrofit case jointly developed by GE and Nexant including engineering development claimed by licensors. Single train of capture.
B4 Adv Tech BUT 40% EGR - MEA	Same as B3 with 40% EGR. Shows the pure effect of EGR on a single MEA train.
B5 Adv Tech BIT 40% EGR MEA	Same as B4 with complete integration between power island and capture train (new built).
B6 HMR-2	New process scheme with one stage of membrane reactionand low air extraction.
B7 HMR-GHR	More conservative HMR process scheme.
B8 ATR CACHET BL	Air–ATR CACHET pre-combustion baseline aligned to cost and economic CCP assumptions
B9 Adv Tech SEWGS AirATR	SEWGS CACHET case aligned to cost and economic CCP assumptions.
B10 Adv Tech MWGS	MWGS CACHET case aligned to cost and economic CCP assumptions.

CO_2 CAPTURE IN AN OIL REFINERY

Several sources contribute to the overall greenhouse gas emissions of an oil refinery. Their relative importance depends on the specific configuration of the selected refinery. Three major sources may however be identified:

- Steam boilers and process heaters
- Regenerator of the Fluid Catalytic Cracking (FCC) unit
- Hydrogen production

During Phase I the CCP studied the overall retrofit of a set of refinery heaters and boilers in a UK-based refinery fed with refinery gas, targeting capture of 2 Mt/year of CO_2, an amount roughly equivalent to the annual emission of a 600 MW CCGT power station [6]. This scenario assumed that a large centralized system should be deployed to either capture CO_2 directly or supply a different feedstock to the system to make capture easier. The main cases studied were:

- Post-combustion: MEA washing in a centralized unit collecting flue gas from all of the selected heaters and boilers.

- Oxy-firing: Cryogenic oxygen production (95% vol.) in two parallel units (3,300 t/day each), retrofitting heaters and boilers to oxy-combustion with exhaust gas recycle for temperature control. The capture section also included distributed and centralized purification units to achieve requested specs in terms of CO_2 purity.
- Pre-combustion: An oxygen-fired autothermal reformer coupled to advanced CO_2 separation (Membrane Water Gas Shift) supplying a rich-hydrogen stream (86% vol.) as fuel to process heaters and boilers.

The evaluation in CCP1 showed that both oxy-firing and pre-combustion showed a much lower CO_2 avoidance cost than the post-combustion case (35-40%). Oxy-firing achieved through a large centralized Air Separation Unit (ASU) and Flue Gas Recycle (FGR) may be considered as an alternative state-of-the-art option with minimal research needed (the retrofit of process heaters with appropriate burners may be considered as the task in need of more investigation). The development of novel technologies for air separation may further increase this advantage in the future, even if some additional costs for final purification of CO_2 might be added, depending on the specification requirements. The CCP2 consequently focused its refinery scenario evaluations on advanced technologies for oxy-firing, and on extension of the oxy-firing concept to other sources than heaters and boilers.

A sub-scenario considering a single new-built boiler producing 210 t/h of steam and emitting ~ 340 kt/year of CO_2 was introduced in CCP2 to properly evaluate the potential of a novel, advanced oxy-firing technique, such as Chemical Looping Combustion (CLC). Results from this sub-scenario may also be conveniently applied to steam production for the extraction of heavy oils or tar sands.

CLC is an approach to oxy-firing that is based on a solid carrier able to chemically adsorb oxygen from air (oxidation in the air reactor) and release it in the presence of a gaseous fuel (reduction in the fuel reactor) with immediate complete combustion. Central to the technology is a two-reactor system with continuous circulation of solids, as schematically shown in Figure 4.

From the safety point of view, CLC has the advantage of performing oxy-combustion without the presence of free gaseous oxygen. Complete air separation with co-production of pure nitrogen is not needed, decreasing the theoretical energy consumption. The CCP supported formation of a partnership, including Chalmers University of Technology, Consejo Superior de Investigaciones Cientificas (CSIC), Technical University of Vienna and Alstom Boilers, that brought the technology from the almost pure conceptual level in 2000 to development of a very active Ni-based oxygen carrier and demonstrated the operation of a 10 kw unit with continuous solid circulation at Chalmers (2003) in the EU GRACE Project, [7]. Development continued in Phase II in the frame of the EU co-funded project CLC GAS POWER, [8], with further scale-up to a 120 kW unit at the Vienna University and optimization and scale-up of carrier production. Although more extended runs on the Vienna unit in a future project are needed to assess mechanical and chemical durability of the carrier, the technology may be considered ready for another big step in the scale-up path. The preliminary design for a 10MW demonstration unit has been prepared as a deliverable of CLC GAS POWER [9].

The evaluations of CCP2 have confirmed that this approach may result in > 50% saving compared to post-combustion with MEA, even with conservative assumptions in terms of oxygen carrier replacement rate. A very competitive absolute cost in the 30-40 €/ton of CO_2 range is achievable by the CLC technology. Another interesting advantage in case of deployment in remote areas, as may happen in exploitation of heavy oils and tar sands, is that oxy-firing is achieved without the need of deploying specific oxygen production tools.

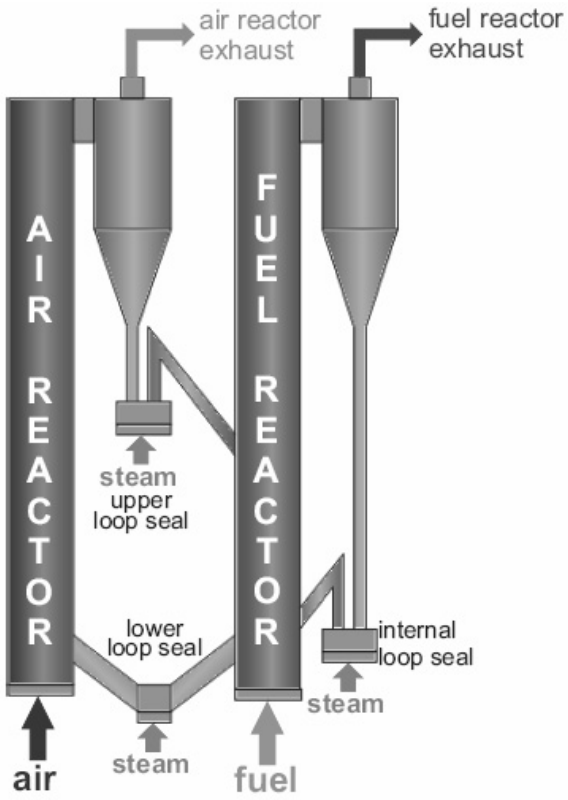

Figure 4. CLC conceptual dual reactor scheme.

The Fluid Catalytic Cracker (FCC) unit is the single largest emitter of CO_2 in most refineries. CO_2 is emitted through the regenerator exhaust, where coke, deposited on the catalyst, is burnt with air. Capturing CO_2 from this post-combustion stream is likely to be very expensive due to the low concentration and low pressure of flue gas stream. In the oxy-fired FCC catalyst regeneration concept, pure (95 to 99.5% vol.) oxygen instead of air is used to burn the coke in the regenerator and flue gas is partly recycled to avoid temperature runaway. Building on results from testing in a small pilot by Petrobras, one of the CCP member Companies, a study to develop a cost basis for a base case (post-combustion) and a set of oxy-fired cases for CO_2 storage from a FCC regenerator was awarded to Randall Technologies. The case considered retrofitting an existing unit operated by Petrobras at Landulpho Alves refinery. The unit capacity is 62,500 bpd of feedstock (an average size FCC unit) emitting about 1Mt/year of CO_2, roughly equivalent to a 300MW CCGT power station. The study confirmed that retrofitting an FCC regenerator to oxy-firing is technically feasible and economically advantageous when compared to post-combustion capture (about 50% reduction in CO_2 avoidance cost).

A complete list of the cases studied in the refinery scenarios is reported in Table 4.

Table 4. Cases for the refinery case (letters refer to the Economic screening in [5].)

Technology case	Description
C1 Reference refinery Heaters and boilers	CCP1 uncontrolled baseline with selected heaters and boilers fed with refinery gas and oil emitting 2 Mt/year of CO_2
C2 MEA amine refinery H&B with capture	State-of-the-art (2003) MEA washing applied to the C1 case cost updated to June 2008.
C3 MWGS adv. tech. refinery H&B	Pre-combustion retrofit of the refinery heaters and boilers using oxygen-fired autothermal reforming for syn-gas production and membrane water gas shift for advanced CO_2 separation. 2003 case cost updated to 2008.
C4 Oxy-FGR-ASU adv. tech. refinery H&B	Oxy-fired retrofit of the refinery heaters and boilers with cryogenic Air Separation Unit producing the required amount of 95% oxygen and Flue Gas Recycle to control operating temperature. 2003 case cost updated to 2008.
F1 New Refinery Gas Boiler	New built uncontrolled boiler producing 210 t/h of steam.
F2 MEA amine post baseline new refinery gas boiler	New built boiler F1 with CO_2 capture by MEA washing, assuming that a dedicated amine unit is built on purpose.
F5 Oxy-boiler 3 adv. tech. new refinery gas boiler	New built boiler F1 oxy-fired assuming oxygen supply from a large cryogenic ASU and dedicated purification units
F6 CLC1 adv. tech. new refinery gas boiler	New built CLC boiler incorporating CO_2 capture and assuming solid carrier replacement every 50,000 hours (optimistic case)
F7 CLC2 adv. tech. new refinery gas boiler	New built CLC boiler incorporating CO_2 capture and assuming solid carrier replacement every 8,000 hours (conservative case)
H1 Reference Case refinery FCC unit	Uncontrolled baseline. Existing FCC unit.
H2 MEA amine post baseline refinery FCC unit	CO_2 capture from FCC regenerator effluent by MEA washing.
H3 Oxyfuel 99.5% O_2 adv. tech. refinery FCC unit	CO_2 capture from regenerator effluent by oxy-firing (ASU incl. in capex) and Flue Gas Recycle.

CONCLUSION

The CCP has been a focal point for development of CCS technologies for oil and gas applications over the last decade. Development of technologies selected in the initial assessment was financially supported through the years and periodically reviewed by the CCP Capture Team, both technically and economically. The progress of technical development for the main technologies in the CCP portfolio, as well as the next possible step in development, is summarized in Table 5.

Table 5: Summary of CCP achievements

Technology/Year	Main Technology Providers	2000	2004	2008	Near Future
BIT (Best Integrated Post-Combustion Technology)	General Electric, Nexant		Conceptual study	1/6th of 9F turbine can testing	Full can testing or field demo
HMR (Hydrogen Membrane Reforming)	StatoilHydro	Concept	8cm single tube	7x7 cm monolith	Further material qualification before pilot
MWGS (Membrane Water Gas Shift)	Sintef, ECN, Dalian Research Institute	Lab scale fabrication technique for ultrathin Pd layers	Tested 2 cm long tubes	Tested modules with 50 cm long tubes	Pilot unit based on developed modules
SEWGS Sorbent Enhanced Water Gas Shift)	Air Peoducts, ECN	Sorbent screening	Single column testing	Multicolumn testing	Pilot unit
CLC (Chemical Looping Combustion)	Chalmers University, Alstom, TUV, CSIC	Small scale lab testing	10 kW circulating unit	120 kW circulating unit	1-10 MW unit

ACKNOWLEDGEMENTS

The author acknowledges the outstanding contributions of all members of the Capture Team in CCP2:

- BP: Richard Beavis, Jonathan Forsyth, Linda Curran in her role of Program Manager.
- Chevron: Daniel Chinn, Cliff Lowe, Karl Gerdes, Raja Jadhav
- ConocoPhillips: Steve Schlasner, Julio Rincon, Joe Cross, Jim Kimble.
- Petrobras: Gustavo Torres Moure
- Shell: Stefanie Brown-Roijen, Jan Assink, Tom Brownscombe, Evert Wesker
- StatoilHydro: Knut Ingvar Åsen, Torgeir Melien
- Suncor: Cal Coulter, Mark Bohm, Stephen Kaufmann

The CCP acknowledges contribution by the European Union, the Norwegian Council for Research and the U.S. Department of Energy. The CCP also wish to thank all technology providers involved in CCP projects for their continuing engagement, proactivity and fruitful efforts.

This Chapter contains figures, portions and excerpts that originally appeared in Energy Procedia Vol 1, Issue 1, Greenhouse Gas Control Technologies 9, Proceedings of the 9th International Conference on Greenhouse Gas Control Technologies (GHGT-9), 16-20 November 2008, Washington DC, USA, which was published by Elsevier Ltd.

REFERENCES

1. Choi, G.N., R. Chu, B. Degen, H. Wen, P.L. Richen and Chinn, D., 2005, CO_2 removal from power plant flue gas – cost efficient design and integration study. In: Thomas DC, (ed.). Carbon Dioxide Capture for Storage in Deep Geologic Formations – Results from the CO_2 Capture Project, Vol. 1, Oxford: Elsevier Ltd; 2005
2. Vigeland, B. and Åsen, K, 2005, Development of a Hydrogen Mixed Conducting Membrane Based CO_2 Capture Process. In: Thomas DC, (ed.). Carbon Dioxide Capture for Storage in Deep Geologic Formations – Results from the CO_2 Capture Project, 1, Oxford: Elsevier Ltd; 2005
3. Beavis, R. (2009) The Cachet Project, 2009 Introduction to CACHET, in Eide, L.I. (ed.) Carbon Dioxide Capture for Storage in Deep Geologic Formations, Volume 3. CPL Press; 2009
4. Klette, H., Raeder, H., Larring, Y., and Bredesen, R., 2005, GRACE: Development of supported palladium alloy membranes. In: Thomas DC, (ed.). Carbon Dioxide Capture for Storage in Deep Geologic Formations – Results from the CO_2 Capture Project, Vol. 1, Oxford: Elsevier Ltd; 2005
5. Melien, T. and Brown-Roijen,S., 2009 Economics, in Eide, L.I. (ed.) Carbon Dioxide Capture for Storage in Deep Geologic Formation, Volume 3. CPL Press; 2009
6. Allam, R., White, V., Ivens, N., Simmonds, M., 2005, The Oxyfuel Baseline: revamping heaters and boilers to Oxyfiring by Cryogenic Air Separation and Flue Gas Recycle. In: Thomas DC, (ed.). Carbon Dioxide Capture for Storage in Deep Geologic Formations – Results from the CO_2 Capture Project, Vol. 1, Oxford: Elsevier Ltd; 2005
7. Hurst, P. and. Miracca, I., 2005, Chemical Looping Combustion (CLC) Oxyfuel Technology Summary. In: Thomas DC, (ed.). Carbon Dioxide Capture for Storage in Deep Geologic Formations – Results from the CO_2 Capture Project, Vol. 1, Oxford: Elsevier Ltd; 2005
8. Assink, J. and Beal, C., 2009, Chemical Lopping Combustion (CLC) Technology Summary, in Eide, L.I. (ed.) Carbon Dioxide Capture for Storage in Deep Geologic Formation, Volume 3. CPL Press; 2009
9. Alstom Power Boilers, 2008 CLCGASPOWER Deliverable 8.1. Process and technology scale up package for industrial demonstration unit. EU Project CLC Gas Power, Project no. 019800

Carbon Dioxide Capture for Storage in Deep Geologic Formations, Volume 3
L.I. Eide (Ed.)

Chapter 3

OXY-COMBUSTION FOR CO_2 CAPTURE FROM FLUID CATALYTIC CRACKERS (FCC)

Leonardo F. de Mello[1], Gustavo T. Moure[1], Oscar R. C. Pravia[1], Loren Gearhart[2], Paul B. Milios[2]
[1]Petrobras – Research and Development Center (CENPES), Av. Horácio Macedo, 950 – Cidade Universitária, Rio de Janeiro 21941-915, Brazil
[2]Randall Gas Technologies, a Division of Lummus Technology, a CBI Company, Houston, Texas, USA

ABSTRACT: The oxy-combustion concept was studied for CO_2 capture from FCC units and compared to a post-combustion amine absorption technology. Two oxygen purities were considered for the oxy-combustion cases, namely 99.5% and 95%. All three processes were able to achieve the required specifications and recovery level, although there were differences in complexity and utility requirements. The post-combustion case showed a lower capital cost, but the smaller operational costs of the oxy-combustion cases strongly influenced the final CO_2 capture and avoided costs giving a better economical result. Besides that, the 99.5% O_2 oxy-combustion case was considered to be the simplest process for CO_2 capture and also the most efficient, since it presented the highest value of avoided CO_2 at lower costs.

INTRODUCTION

The oil refining industry is considered to represent a significant source of CO_2 emission when compared to other energy-related industrial activities. Many typical refining processes and units generate CO_2, examples of which are heaters, boilers, fluid catalytic cracking (FCC) and hydrotreating units. However, FCC units are considered to be one of the main sources of CO_2 emission in the refinery as a whole, representing as high as 40 to 45% of total emissions. Finding ways of efficiently capturing CO_2 from FCC units is an important step to mitigate CO_2 emissions in the refining industry.

THE FLUID CATALYTIC CRACKING PROCESS

The conventional catalytic cracking process was designed to convert heavy oil fractions, such as heavy vacuum gasoil (HVGO), to lighter, more valuable products, such as liquid petroleum gas (LPG) and gasoline.

A typical layout of an FCC unit may be seen in Figure 1. The heavy feed is injected in the base of the riser, where it is contacted with hot catalyst particles. The hot catalyst provides the necessary heat to vaporize the feed and catalyses the endothermic cracking reactions, which occur along the riser. During the reaction step, coke is formed and deposits on the surface of the catalyst particles, which become deactivated. When the solid-gas mixture reaches the top of the riser, a series of cyclones enable a fast catalyst-hydrocarbon product separation and the spent catalyst is sent to a stripping zone to remove some entrained hydrocarbon. To re-establish catalyst activity, the coke is burned with air in the regenerator and this raises the catalyst bed temperature. The catalyst is

maintained in a fluidized state and circulates from the riser to the regenerator and back, thus maintaining catalyst activity and thermal balance.

When the FCC unit is running on a full combustion mode (excess air in the regenerator), the low pressure, high temperature flue-gas from the regenerator typically contains around 10 to 20% CO_2. Since the feed may have N- and S-containing compounds, some of the nitrogen and sulfur end up in the coke and are oxidized to NO_x and SO_x species in the regenerator. The hot flue-gas is therefore usually a mixture of N_2, CO_2, O_2, H_2O and contaminants such as NO_x and SO_x. More information regarding the fluid catalytic cracking process may be found in the literature [1, 2].

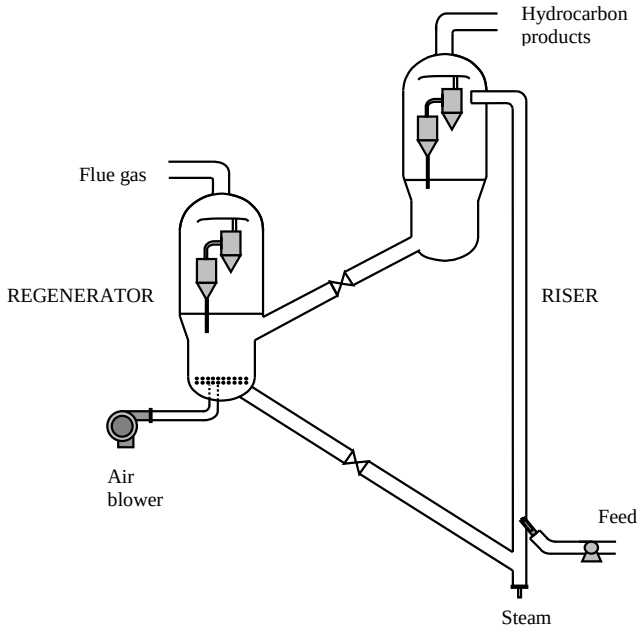

Figure 1. Fluid catalytic cracker.

OXY-COMBUSTION FOR CO_2 CAPTURE IN FCC UNITS

Due to very large volume flow rates, low pressure and low CO_2 content usually seen on FCC flue-gases, the oxy-combustion technology seems to be a good option for CO_2 capture.

Operating an FCC unit in the oxy-combustion mode implies substitution of air by pure O_2 in the regeneration step. In this way, the flue gas leaving the regenerator is absent of N_2 and is therefore a CO_2-rich mixture. However, to prevent temperature runaways during the combustion reaction and also to minimize fluidization problems some of the CO_2-rich flue gas must be recycled back to the regenerator. By using pure O_2 instead of air, the N_2/CO_2 post-combustion separation is avoided and the CO_2-rich flue gas needs only to be dehydrated and compressed. On the other hand, an air separation unit (ASU) is required to produce the oxygen. The oxy-combustion concept has been previously described in literature for coal gasification as well as for the FCC process [3, 4]. Although the concept has been described before, a thorough comparison between the oxy-combustion and post-combustion technologies has never been made for the fluid catalytic cracking process.

The work presented in this chapter is therefore a direct comparison between the oxy-combustion and post-combustion technologies applied to an FCC unit. An amine scrubber unit for CO_2 absorption was taken as the post-combustion technology option and chosen to be the base case of the study since it is considered as commercially proven technology.

Study basis

An existing 10,000 m^3/d resid FCC unit was taken as reference. Based on process data collected from the unit, mass and energy balance calculations were made to estimate flue gas composition for the unit operating in the oxy-combustion mode, considering two oxygen purity levels: 99.5% and 95%. Temperature, pressure and flue gas composition for the base and oxy-combustion cases are shown in Table 1. No air leakage was considered since the entire system works at positive pressure.

The flue gas recycle rate was established to maintain the same volume flow-rate as that of N_2 in air, so that O_2 concentration at the inlet of the regenerator in the oxy-combustion cases would be approximately the same as that of the base case (21%vol). The initial estimates presented in Table 1 were made considering that no pre-treatment for SO_x or NO_x removal were performed before the recycle and this is why there is a build-up of those contaminants when compared to the base case. However, a 3% by volume limit was established for the water content on the recycle stream. This limit was set to avoid an increase in partial pressure of water in the regenerator, and thus avoid a higher hydrothermal deactivation of the catalyst. This, however, implies in additional processing of the recycle stream, with the introduction of a cooler and separator, as well as an extra pressure drop. Although NO_x and SO_x are recycled to the regenerator, no impact on catalyst life is expected.

The operation of the FCC unit in the oxy-combustion mode greatly enhances the CO_2 content in flue gas and for the 99.5% pure O_2 case, the complete removal of water would lead to a 96% CO_2 gas stream. However, when 95% pure O_2 (contaminants are 3.5%Ar, 1.5%N_2) is used, the amount of inert (N_2 and Ar) in the flue-gas is higher and the removal of water takes the CO_2 content up to 91%.

CO_2 product specifications were established by CCP considering its application for enhanced oil recovery (EOR) and are shown in Table 2. A minimum of 90% CO_2 recovery was set to be achieved in each process. According to the data in Tables 1 and 2, it is clear that for the oxy-combustion case with 99.5% O_2, the dehydration and compression of the flue gas would be sufficient to meet the specifications, while for the 95% O_2 case, further processing would be needed for inert removal. The values on Table 1 for oxy-combustion are expected values for the flue gas at the outlet of the regenerator, prior to the third stage cyclones and turbo-expander

Table 1. Flue-gas composition and characteristics for base and oxy-combustion cases.

	Base case	**Oxy-combustion**	
		99.5% O_2	**95% O_2**
Total flow-rate (t/h)	556.5	773.7	767.1
Temperature (^oC)	690	690	690
Pressure (bar g)	2.45	2.45	2.45
Composition			
O_2 (%mol.)	2.7	2.7	2.7
CO_2 (%mol.)	13.5	87.3	82.31
H_2O (%mol.)	10.0	9.16	9.13
N_2 (%mol.)	72.9	0.17	1.67
Ar (%mol.)	0.85	0.39	3.90
CO (ppm)	9	9	9
SO_x (ppm)	378	2327	2195
NO_x (ppm)	81	524	494

Table 2. CO_2 product specification.

Component	Specification
CO_2	> 95%
H_2O	< 50 ppm
SO_2	no spec
NO_x	no spec
Inerts (N_2, Ar)	< 4 mol%
O_2	< 3 mol%
Temperature	< 60 ^oC
Pressure	150 bar g

Process descriptions

The CO_2 purification process flow diagrams for the base case and the two oxy-combustion cases are presented in Figures 2-4. All three cases have a waste heat steam generator, a SO_2 scrubber, a quench cooler, CO_2 compression and a dehydration system. The base case requires an amine scrubber unit for CO_2 absorption and the 95% O_2 oxy-combustion case requires a propane refrigeration system to concentrate the CO_2 and meet specification. Both oxy-combustion cases need an air separation unit to provide the oxygen.

Waste heat steam generator (WHSG)

The flue gas from the regenerator first goes through third stage cyclones for fines removal and then through a turbo-expander and emerges at around 1.2 bara and 560 ^oC. The WHSG receives these gases and is designed to produce high pressure steam (42 bara and 400 ^oC). Since the exhaust gas is corrosive, it is cooled down to about 220 ^oC, which is above the acid gas dew point.

SO_2 scrubber

The main purpose of the SO_2 scrubber was to bring the SO_2 concentration down to 7 ppmv ± 3 ppmv to allow a successful operation of the amine plant in the base case. To accomplish this, a limestone mixture was used and its reaction with SO_2 produces a waste by-product of $CaSO_4$. For the oxy-combustion cases, the SO_2 scrubber was also used to prevent sulfur poisoning of the molecular sieve beds in the dehydration step. This was done to avoid the beds from becoming a potential emission source of SO_2 during the regeneration step.

Amine plant

The amine plant considered for the base case used the Kerr-McGee CO_2 recovery technology, which has been commercially demonstrated in coal fired power plants. Basically, the technology uses an aqueous solution of mono-ethanolamine (MEA) to absorb CO_2, which is then regenerated by the application of heat obtained from low pressure steam. Contaminants such as SO_x and NO_x form heat stable salts with MEA, which may be partially recovered using soda ash and sodium sulfate in the reclaimer.

Air separation unit (ASU)

The air separation unit was designed to produce either a 99.5% or a 95% O_2 mixture at 20 ^oC and 3.9 bara. Part of the nitrogen waste stream from the ASU is used for the regeneration of the dehydration beds since it is a dry gas and no compression is required.

Dehydration

The dehydration of the CO_2 leaving the amine unit is accomplished by compression, cooling and separation of free water, followed by molecular sieve drying (Type 3A molecular sieve), composed of two vessels operating in a adsorption/regeneration cycle. The performance of the fixed-bed dryer improves as pressure increases and therefore it has been placed downstream of the third stage of CO_2 compression. The molecular sieve is regenerated with dry air at 2.4 bara, which is heated with high pressure steam. The water content in the leaving gas is less than 50 ppmv.

For the oxy-combustion cases, the main difference is that the molecular sieve is regenerated by dry nitrogen from the air separation unit, which is also heated with high pressure steam. For these cases, the dehydration unit is placed downstream the fourth stage CO_2 compression.

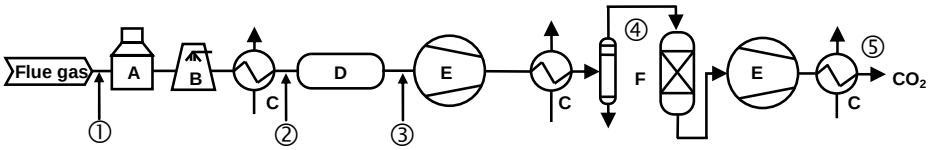

Figure 2. Process flow diagram for the base case: A – WHSG, B – SO_2 scrubber, C – coolers, D – amine plant, E – CO_2 compressors, F – dehydration unit.

CO_2 compression

For the base case, CO_2 is compressed from 1.8 bara to 151 bara by two two-stage centrifugal compressors. The hot gas from each stage of compression is cooled by a water-cooled heat exchanger to 35 ^oC where the process side of the exchangers is made of stainless steel due to corrosive conditions. Since the CO_2 from the amine unit is saturated with water vapor, it condenses in the first three after-coolers, separated in stainless steel scrubbers and then drained to waste water treatment.

For the oxy-combustion case with 99.5% O_2, the main difference is that CO_2 is compressed from 1.1 bara to 67 bara by two two-stage centrifugal compressors and a fifth stage compresses to 151 bara also with a centrifugal compressor. The 95% O_2 case uses two two-stage compressors to bring the CO_2 pressure from 1.1 bara to 62 bara and then a fifth stage elevates the pressure to 151 bara with a centrifugal pump.

In all cases, it was decided that the CO_2 compressors would be driven by electric motors.

Recycle compressors

The recycle compressors were considered on both oxy-combustion cases and replaced the existing air blower. This was done so since the air blower would not be adequate, as it was not designed to operate with the recycle gas composition, which would require different sealing and metallurgy.

The recycle gas is compressed by a two-stage centrifugal compressor from 1.1 bara to 3.9 bara. Two stages of compression were used because the discharge temperature of 170 ^oC for one stage exceeds what centrifugal compressor manufacturers recommend. The inter-stage cooler adjusts the water content to 3 %vol. by cooling the discharge of the first stage to 35 ^oC.

Although the air blower was driven by a steam turbine, it was decided that the recycle compressors used in the oxy-combustion cases would be driven by electric motors.

Propane refrigeration system

For the oxy-combustion case where a 95% oxygen mixture is used, a propane refrigeration system was considered since the flue gas for this case does not meet the specified minimum requirement of 95% CO_2 after dehydration. In this case, achieving the specification is accomplished by partially condensing the gas with propane chillers and venting the non-condensables.

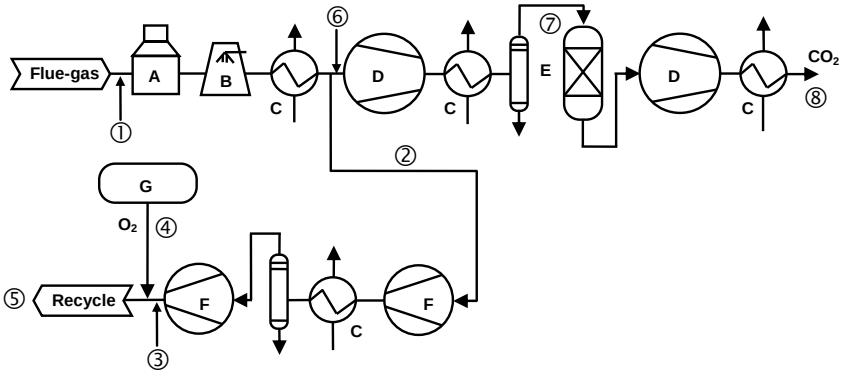

Figure 3. Process flow diagram for the 99.5%O_2 case: A – WHSG, B – SO_2 scrubber, C – coolers, D – CO_2 compressors, E – dehydration unit, F – recycle compressors, G – ASU.

Process calculations and performance

The calculations were performed considering that the oxy-combustion operation would have no effect on catalyst activity and cracking reactions, thus maintaining the same coke formation as in normal operation. For the oxy-combustion cases, the total volumetric flow rate entering the regenerator (flue gas recycle plus O_2 mixture from ASU) was made equal to the volumetric flow rate of air in the base case to minimize fluidization problems. Since CO_2 has a higher heat capacity than N_2, this would imply in more heat removed from the regenerator. However, the resid FCC unit taken as reference makes use of a cat-cooler to control the temperature of the catalyst bed in the regenerator and therefore this would result in a lower heat duty demand for the cat-cooler to keep the same temperature.

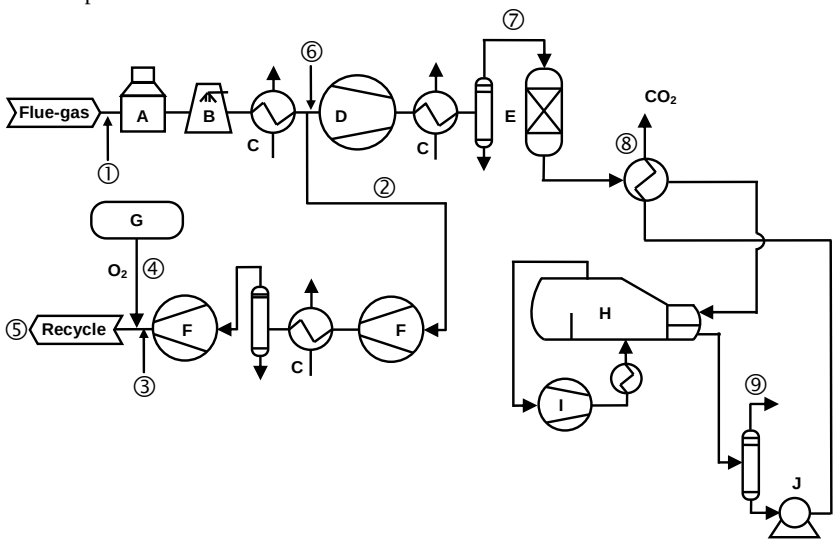

Figure 4. Process flow diagram for the 95%O_2 case: A – WHSG, B – SO_2 scrubber, C – coolers, D – CO_2 compressor, E – dehydration unit, F – Recycle compressors, G – ASU, H – propane chillers, I – propane compressor, J – CO_2 pump.

To keep the comparison of cases on a similar basis, the molar flow rate of CO_2 entering the amine plant for the base case and the molar flow rate of CO_2 entering the first stage compressors in the oxy-combustion cases were made equal. The CO_2 recycle rates for the oxy-combustion cases were 84.7 wt% and 83.8 wt% for the 99.5% O_2 and 95% O_2 respectively.

The main characteristics of each process, estimated from simulation runs are shown in Tables 3-5 and the final results are summarized in Table 6.

Table 3. Process calculations for the post-combustion base case.

	Stream (Figure 2)				
	①	②	③	④	⑤
Pressure (bara)	1.21	1.14	1.79	46.8	151
Temperature (^oC)	560	42	49	35	35
Total flow rate (t/h)	556.5	546.1	104.6	101.8	101.7
Composition (mol%)*					
CO_2	13.6	14.1	93.4	99.7	99.9
H_2O	10.1	7.4	6.5	0.3	<50 ppm
O_2	2.7	2.8	<0.1	<0.1	<0.1
N_2	73.6	75.8	<0.1	<0.1	<0.1

* trace components Ar, CO, SO_x, NO_x are not shown

Table 4. Process calculations for the 99.5% O_2 oxy-combustion case.

	Stream (Figure 3)							
	①	②	③	④	⑤	⑥	⑦	⑧
Pressure (bara)	1.21	1.14	3.94	3.9	3.9	1.14	66.7	151
Temperature (^oC)	560	39	104	20	93	39	35	35
Total flow rate (t/h)	784.5	662.6	653.3	98.5	751.8	119.0	116.0	115.9
Composition (mol%)*								
CO_2	87.0	87.8	93.2	-	77.6	87.9	95.8	96.1
H_2O	9.6	8.5	3.0	-	2.5	8.5	0.3	<50ppm
O_2	2.7	2.7	2.9	99.5	19.1	2.7	3.0	3.0
N_2	0.2	0.2	0.2	0.1	0.2	0.2	0.2	0.2

* Ar and trace components CO, SO_x, NO_x are not shown

Table 5. Process calculations for the 95.0% O_2 oxy-combustion case.

	Stream (Figure 4)								
	①	②	③	④	⑤	⑥	⑦	⑧	⑨
Pressure (bara)	1.21	1.14	3.94	3.9	3.9	1.14	61.7	151	37.6
Temperature (^oC)	560	39	106	20	94	39	35	28	23
Total flow rate (t/h)	776.8	648.9	639.4	103.4	742.8	125.1	121.8	106.1	15.7
Composition (mol%)*									
CO_2	82.2	83.1	86.2	-	72.3	83.1	90.4	95.1	62.4
H_2O	9.1	8.1	2.9	-	2.5	8.1	0.3	<50ppm	0
O_2	2.7	2.8	2.9	95	19.9	2.8	3.0	1.5	12.7
N_2	1.7	1.7	1.8	1.5	1.7	1.7	1.8	0.8	8.6

* Ar and trace components CO, SO_x, NO_x are not shown

The final CO_2 purity was greater for the base case because of the absorption technology applied considering the high selectivity of the MEA solution towards CO_2. On the other hand CO_2 recovery was lower, although it was above the specified limit. The 95% O_2 oxy-combustion case recovery was less than the 99.5% O_2 case because some of the CO_2 was vented to the atmosphere in the flash tank to meet the 95% purity requirement.

The different amount of product CO_2 reflects the choices made for the process conditions in each case. For example, the CO_2 recovery by the amine plant could have been increased, but the demand on the low pressure steam system (used for MEA regeneration) would have been much higher. The % CO_2 recovery for the 95% O_2 oxy-combustion case also could have been increased, but more compression would be required. It is important to emphasize that the process conditions were not necessarily optimized. Nevertheless, in all cases, the product CO_2 specifications and recovery were achieved. The 99.5% O_2 oxy-combustion case was considered to be the simplest since it meets the CO_2 specifications upon compression and dehydration.

Table 6. Summary of final results.

	Units	**Base Case**	**99.5%O_2**	**95%O_2**
CO_2 Purity	vol%	99.95	96.07	95.1
CO_2 Recovery	%	90.42	99.99	90.52
Product CO_2	ton/h	101.7	112.3	101.6

Major equipments costs

Table 7 summarizes the major equipments cost estimation for each case. The estimations are at a quality of ±30% and are based on 2007 pricing. The total installed costs are shown for the WHSG, the SO_2 scrubber, the amine plant and the ASU while the plant total cost includes equipment, material, freight, construction directs, indirect, home office engineering, insurance and profit for the recycle compression system, CO_2 compression, dehydration and propane refrigeration systems. Profit is based on 10% of Total Indicated Cost while contingency, escalation and taxes are excluded and are not part of total cost.

Table 7. Capital cost estimation (MM$).

	Base Case	**99.5%O_2**	**95%O_2**
WHSG	15.2	16.2	16.2
SO_2 Scrubber	23.7	23.7	23.7
Amine plant	59.8	-	-
ASU	-	83.1	78.8
Recycle compression	-	20.9	25.7
CO_2 compression	12.6	16.9	14.3
Dehydration	4.2	1.8	2.0
Propane refrigeration	-	-	3.5
Balance of plant	9.2	9.9	10.7
Home office engineering, insurance and profit	8.4	20.8	22.6
Plant total	34.4	70.3	78.8
Total	133.1	193.3	197.5

The oxy-combustion cases showed a 45% to 48% higher capital cost when compared to the post-combustion base case. The main reasons for this were the higher costs of the oxygen plant compared to the amine absorption plant and also the need for recycle compressors to replace the existing air blower. Although less pure oxygen lowers the ASU cost in the 95%O_2 case, the need for a propane refrigeration system and larger recycle compressors turned out to give an overall higher investment.

The capital costs in table 7 are the original values supplied by ABB Randall. The figures were elaborated by the CCP cost estimators. They may, therefore, differ somewhat from those given in [5].

Utility and chemical requirements and costs

All utility requirements and power demand were estimated and are summarized in Table 8. The cooling tower water flow was based on a 10 ^{o}C temperature rise and all steam consumed was assumed to be "imported" from the refinery whereas the high pressure (HP) steam produced in the WHSG would be "exported" back to the refinery. All new equipments were assumed to have electric motor drivers where needed and a 95% efficiency was assumed for these drivers.

While in the base case there is a great LP steam demand for the amine regeneration, the oxy-combustion cases require large amounts of power supply, mainly due to the air separation unit and the motor-driven recycle compressors. However, when the FCC unit operates in the oxy-combustion mode, the recycle compressors replace the existing air blower, which is driven by a HP steam turbine. Although the air blower is existing equipment, the high pressure steam consumed in its steam turbine driver has been considered in the utility requirements so the comparison between the different technologies could be made on the same basis. Therefore, an extra 140 t/h of HP steam used to drive the air blower has been included in the base case.

The estimated annual utility costs are also shown in Table 8. The oxy-combustion cases showed very close values and were approximately 61% lower than for the base case. These differences are mainly associated with the steam/power balance and how they are priced.

Table 8. Utility requirements and cost.

	Units	**Base case**	**99.5%O2**	**95%O2**
Water makeup	**m3/h**	67.5	59.8	59.8
Water blowdowns	**m3/h**	15.1	18.3	18.3
Cooling tower water	**m3/h**	13733	6918	7539
Steam demand				
HP	**t/h**	140	0.3	0.4
MP	**t/h**	0	2.3	2.4
LP	**t/h**	216.5	0	0
Steam produced				
HP – WHSG	**t/h**	78.7	103.6	102.2
Electrical power	**MW**	15.8	74.0	71.2
Final cost*	**MM$/y**	73.5	28.2	28.4

*values used for cost estimation: 0.14 $/m^3 (water); 24 $/t (HP steam); 18 $/t (MP and LP steam); 63 $/MWh (power).

The annual chemical requirements and costs are summarized in Table 9. The chemical requirements are mainly associated with limestone needed to react with SO_2 in the scrubber, MEA make-up, corrosion inhibitors, a filter aid to remove particulates, activated carbon to remove hydrocarbons, sodium carbonate to reclaim MEA and molecular sieve (type 3A) replacement in the dehydration

systems. The amount of disposal required for the base case is grater than for the oxy-combustion cases due to the large amount of waste material generated by the MEA reclaimer.

The limestone requirement is the same for all three cases since the SO_2 scrubber was placed before the flue-gas recycle. By doing this, only a very small amount of SO_2 is recycled back to the regenerator and almost no build-up is observed. Alternatively, the SO_2 scrubber could be placed in line 6 (refer to Figures 3 and 4), after the recycle of flue gas. This would reduce the scrubber size since almost 85 wt% of flue gas is recycled back to the regenerator.

The oxy-combustion alternatives showed 77% lower chemical requirements costs than the base case, although these values are not as significant in magnitude as those for utility costs.

Table 9. Chemical requirements and costs.

	Cost ($/kg)*	**Annual chemical requirement (t/year)**		
		Base Case	**99.5%O_2**	**95%O_2**
MEA (100%)	2.76	632	-	-
Corrosion inhibitor	6.61	49	-	-
Filter aid	2.76	67	-	-
Activated carbon	3.86	67	-	-
Sodium carbonate	0.56	556	-	-
Disposal	0.077	10,116	-	-
Mol sieve	3.86	4.8	5.4	5.9
Limestone (100%)	0.0195	5,364	5,364	5,364
Final cost (MM$/y)	-	3.73	0.86	0.86

*based on prices in the USA (2007)

As for capital investments the costs given in Tables 8 and 9 differ somewhat from the operational costs in [5].

Carbon balance and cost analysis

The main differences between the three cases studied are related to the CO_2 recovery obtained in each process and the steam/power balance, since the base case is highly intensive in steam demand while the oxy-combustion cases show larger power requirements. Since the production of steam and power are associated with additional CO_2 emission, the CO_2 recovery and energy balance may change relative CO_2 avoided values.

For the calculation of avoided CO_2, a net steam demand was considered, based on the steam consumed and produced in each case, according to the values in Table 8.

Typical CO_2 emission factors related to steam generation (0.12 t CO_2/t steam) and power generation (0.37 tCO_2/MWh) were used [6], considering natural gas industrial boilers and natural gas combined cycle (NGCC) power plants, respectively. The results are summarized in Table 10.

The 99.5% O_2 oxy-combustion case presented the highest amount of avoided CO_2, mainly due to its high CO_2 recovery. The large difference between the base case and the oxy-combustion cases are attributed to the steam/electricity balance and the efficiency of their production, which is reflected by the CO_2 emission factors. The choice to use electric motor drivers for new equipment may be seen as an advantage for the oxy-combustion cases since when the recycle compressors replace the existing air blower, the process as a whole becomes more efficient (less CO_2 is emitted in the process of promoting FCC CO_2 capture).

On the other hand, since the recycle compressors used in the oxy-combustion cases were chosen to have electric motor drivers, it would be reasonable to make a comparison considering that for the base case the blower was also electric motor driven. In this case, there would not be an extra 140 t/h steam demand, but an extra 29 MW power demand. The amount of avoided CO_2 for the oxy-combustion cases would not be changed, but for the base case it would now be 70.4 t/h. Nevertheless, the oxy-combustion cases would still show higher amounts of avoided CO_2.

Table 10. Avoided CO_2.

	Unit	**Values**		
		Base case	**99.5% O_2**	**95% O_2**
Total CO_2 from FCC	**t/h**	112.46	112.27	112.27
Product CO_2 (captured)	**t/h**	101.69	112.26	101.63
Net steam consumption	**t/h**	277.8	-101	-99.4
Steam-related CO_2 emission	**t/h**	33.3	-12.1	-11.9
Net power consumption	**MW**	15.8	74.0	71.2
Power-related CO_2 emission	**t/h**	5.85	27.38	26.34
Avoided CO_2	**t/h**	62.5	97.0	87.2

Based on the values obtained in the present study, it was possible to estimate and compare the CO_2 capture and avoided costs for each case. The full economic analysis is reported elsewhere [5] and only the relative contribution of capital investments and operational costs to the final CO_2 capture cost are summarized in Table 11. Despite the fact that the post-combustion base case showed a lower investment, the annual costs of utility and chemical requirements for the oxy-combustion cases were considerably lower and contributed with a higher weight to the final values. The oxy-combustion cases showed a 38 to 44% reduction in CO_2 capture costs compared to the base case and since the amount of avoided CO_2 was greater for both oxy-combustion cases, the reduction in the cost of avoided CO_2 was even higher.

The 99.5%O_2 oxy-combustion case presented the better overall economical result, which is in part attributed to its lower complexity and better efficiency.

Table 11. Relative capture and avoided costs.

	Relative contribution to total cost (% of total)		
	Base Case	**99.5%O_2**	**95%O_2**
CAPEX	18	41	42
OPEX	82	59	58
Total cost	**% change relative to base case**		
Capture	-	- 44	- 38
Avoided	-	- 61	- 56

CONCLUSIONS

FCC units usually are significant sources of CO_2 emissions in a refinery. In the study presented here, a comparison between post-combustion and oxy-combustion technologies for CO_2 capture from an FCC unit was performed. A mono-ethanolamine (MEA) absorption unit was considered as the post-combustion technology and referred to as the base case while for the oxy-combustion technology, two cases were considered with different oxygen purities (99.5% and 95%).

An existing 10,000 m^3/d FCC unit was taken as reference and a product CO_2 specification was established considering its use for enhance oil recovery (EOR). A minimum of 90% CO_2 recovery was set.

All three processes were able to achieve the required specifications and recovery level, although there were differences in complexity and utility requirements, especially concerning the steam/power balance of each process.

The base case was shown to be highly intensive in steam demand, mainly used in the amine regeneration step. The oxy-combustion cases however showed larger power requirements due to the air separation unit and the motor-driven recycle compressors. The energy demand for the CO_2 capture processes reflects in additional CO_2 emission and consequentially different amounts of avoided CO_2.

The 99.5% O_2 oxy-combustion case was considered to be the simplest process for CO_2 capture and also the most efficient, since it showed a lower chemical requirement, higher recovery and higher avoided amount of CO_2 when compared to the other cases. The trade-off between oxygen purity and energy demand does not seem to be advantageous since it reduces CO_2 recovery and increases process complexity.

Although the post-combustion base case showed a lower capital cost, the significantly smaller operational costs presented by the oxy-combustion cases strongly influenced the final CO_2 capture and avoided costs providing a better economical result for this alternative.

Finally, it is important to emphasize that as research is carried out, many other issues regarding the continuous operation of an FCC unit in the oxy-combustion mode must still be addressed. Examples of such issues include possible corrosion problems on existing equipment due to the high CO_2 content in the flue gas, impact of CO_2 recycle on thermal balance and catalyst attrition, impact of high CO_2 content on coke burn in the regenerator and also reliability of operation.

ACKNOWLEDGEMENT

The authors acknowledge the support of the CO_2 Capture Project Phase 2 (CCP2).

REFERENCES

1. Sadeghbeigi R. (2000) *Fluid Catalytic Cracking Handbook*, 2nd Ed., Butterworth-Heinemann (2000), Woburn, MA.
2. Wilson, J.W. (1997) *Fluid Catalytic Cracking Technology and Operations*, PennWell Publishing Company (1997), Tulsa, Oklahoma.
3. Singh D., Croiset E., Douglas P.L. and Douglas M.A. (2003), *Energy Conversion and Management*, 44 (2003) 3073.
4. Hegarty W.P. *Process for the Recovery and Recycle of Effluent Gas from the Regeneration of Particulate Matter with Oxygen and Carbon Dioxide*, US Patent No. 4 542 114 (1985).
5. Melien, T. and S. Brown-Roijen, 2009. Economics, in Eide, L.L. (ed.) 2009 Carbon Dioxide Capture for Storage in Deep Geologic Formations, Volume 3. CPL Press
6. Simbeck D. *First National Conference on Carbon Sequestration*, Washington DC, May 14 – 17, 2001.

Carbon Dioxide Capture for Storage in Deep Geologic Formations, Volume 3
L.I. Eide (Ed.)

Chapter 4

APPLICATION OF EXHAUST GAS RECIRCULATION FOR POST COMBUSTION CO_2 CAPTURE: EFFECT ON LEAN PREMIXED COMBUSTION

Ahmed M. ElKady, Andrei T. Evulet and Anthony R. Brand
General Electric, Global Research Center, Niskayuna, NY 12309, New York, USA

ABSTRACT: The capture and sequestration of CO_2 will be necessary to mitigate CO_2 emissions from fossil fuel (coal, oil, natural gas or biomass) power generation facilities in a carbon constrained world. Post combustion carbon capture is a viable technology alternative to reduce CO_2 emissions from power plants in the short term. The CO_2 concentration in the exhaust gases of natural gas fired power plants can be increased through exhaust gas recirculation (EGR). A joint CO_2 Capture Project (CCP) and GE study of the Best Integrated Technology (BIT) shows that EGR enables reduced exhaust gas flow to the post combustion capture plant and cost of the CO_2 capture. This chapter summarises the experimental work performed at General Electric Global Research Center, in collaboration with CCP, in order to better understand the risks of utilizing EGR in combination with dry low NO_x (DLN) combustors. A research combustor was developed for exploring the dry low emissions capability of nozzles to operate in low Oxygen environment. A series of experiments have been conducted at representative gas turbine pressures and temperatures, in an EGR test rig. Exhaust gas generated in a first stage, at pressure, is used to vitiate the fresh air to levels determined by cycle models. Experimental results include the effect of applying EGR on operability, efficiency and emissions performance under conditions of up to 40% EGR (low oxygen). Our findings confirm the feasibility of EGR for enhanced CO_2 capture, exceeding the expectations of operability and combustion efficiency predicted by models. In addition, we confirm benefits of NO_x reduction while complying with CO emissions in Dry Low NO_x Emissions combustors under low oxygen content oxidizer.

INTRODUCTION

Power Generation is considered to be responsible for more than half of total greenhouse emissions produced, particularly CO_2. The continuous use of fossil fuels for power generation will increase the CO_2 emissions in the form of flue gases mixed at the stack. In recent years development of CO_2 capture ready gas turbine cycles have included pre-combustion and post-combustion de-carbonization approaches. Because of the efficiency penalties imposed by CO_2 separation and capture on any cycle, the integration of these units with the power generation island is essential. One of these techniques, Exhaust Gas Recirculation (EGR) is an enabling technology for high efficiency, reduced-CO_2 power generation via reduction of flue gas volumetric flow and increase in concentration of CO_2. EGR can reduce the capital cost of CO_2 separation units by decreasing the flow of flue gases for treatment and increasing the CO_2 concentration by more than 50%. Hence, it is desirable to modify GE gas turbines such as the 9FB or the LMS100 for EGR operation. The issues associated with EGR are combustor operability, emissions (NO_x, CO) in vitiated air, turbomachinery performance with the altered working fluid, and efficiency penalties associated with the energy demand of the CO_2 removal unit. It is expected that EGR will provide about 25% reduction in the cost of CO_2 capture compared with standard retrofit options.

In order to capture and sequester the CO_2 emitted from natural gas-based power generation plants, three different main types of concepts may be considered:

- Separation of CO_2 from the exhaust gas of a standard gas turbine combined cycle (CC), using chemical absorption by amine solutions. It can either be performed with a direct contact between exhaust gas and absorbent, or with the use of membranes.
- Integrated Reformer Combined Cycle (IRCC) with natural gas de-carbonization, in which the carbon is removed prior to combustion and the fuel heating value is transferred to hydrogen. This concept can be applied for natural gas by reforming and water gas shift reaction followed CO_2 removal process.
- Oxyfuel gas turbine CC at near-stoichiometric combustion conditions with oxygen (> 90%+ purity) from an air separation unit as oxidizing agent, producing CO_2 and H_2O vapor as the combustion products and partially re-circulating the products into the combustor.

In all cases the CO_2 separation process needs to be integrated with the combined cycle and usually results in penalties associated with the efficiency of the plant. It is important therefore to minimize the energy (work) consumed for CO_2 capture. Today's state-of-the-art amine separation systems rely on gas separation processes with sizes highly dependent on the volumetric flow and the concentration of the CO_2 in the flue gas. A significant reduction in CO_2 separation plant capital cost results from increasing the CO_2 concentration while reducing the flow-rate of the flue gas.

Unfortunately very little data exist to verify the assumed risks associated with EGR for combustion, particularly at the elevated temperatures and pressures representative of gas turbines. Existing data are limited to experiments performed at atmospheric pressures [1] and ambient temperatures or with diffusion flames (e.g. boiler burners) or models and simulations of low oxygen combustor.

The modeling of combustion at low oxygen concentrations has been recently demonstrated to fail in predicting the emissions using existing mechanisms (such as GRI-Mech) [2]. Under the present collaboration with the CO_2 Capture Project (CCP) consortium, General Electric, Global Research Center (GE GRC) performed experimental work to better understand the issues related to Gas Turbine combustion with EGR.

Several studies in the past described some of the major risks of EGR in gas turbines to be the combustion efficiency and operability [1,2]. Bolland recommends EGR levels of no more than 40% [3]. This was justified by the Minimum Oxygen Content (MOC) requirement for the combustion air, which was predicted to be 16-18%. We determined that EGR levels of nearly 50% and oxygen levels at the combustor exit of ~2% may be achievable, for flame temperatures between 2750 and 2950 F, typical of combustors in use today, during phase 1 of the program described below.

In 2005 GE and CCP started a collaboration aimed at demonstrating the feasibility of using EGR for post-combustion carbon capture. Two main activities were conducted: a cycle performance of a 109FB power plant with incorporated EGR and in addition a small experimental program that was aimed at finding the limitations of exhaust gas recirculation in conjunction with lean premixed combustion of natural gas. The first collaboration between GE and CCP was the experimental work performed at GE GRC in 2006 in order to better understand the risks of using EGR in combination with a dry low emissions research nozzle by simulating the oxidizer compositions. GE performed a series of experiments in which inert gases such as N_2 and N_2/CO_2 were used to vitiate the fresh air to the levels determined by cycle models. Our findings confirmed the feasibility of EGR for ease of CO_2 capture, exceeding the expectations of operability and efficiency. In addition, we confirmed the benefits of NO_x reduction with Dry Low Emissions (DLE) combustors under lower oxygen content oxidizer. This phase was then closed with the conclusion that while combustion needs to be

demonstrated in more “realistic” EGR conditions, including minor and major species and with real 9FB nozzle, considerable potential exists for implementation of EGR with lean premixed nozzles.

This paper discusses the design and construction, operation and results obtained with an EGR rig much more complex than the first phase of the project. In summary, a two stage rig was proposed, then built and operated for characterization of a 9FB nozzle in much more realistic EGR conditions, including appropriate pressures, temperatures and oxidizer composition of both major and minor species. The second phase concluded in 2008 with a series of important conclusions regarding the feasibility of using up to 35% EGR in conjunction with Dry Low NO_x (DLN) for post-combustion capture at higher CO_2 concentrations, without the need to change significantly the combustion hardware. The experiment proved that NO_x and CO emissions are manageable with the current hardware and that further improvements may be obtained with minor changes.

EXPERIMENTAL

The experimental setup includes two combustors in series. The first combustor is used as exhaust gases generator; the exhaust gas is quenched, then cooled and dried. The cold exhaust gas is then mixed with preheated air to determine the expected vitiated air entering the secondary combustor. The latter is the nozzle of interest currently under investigation, namely the DLN2+ nozzle employed in the 9FB platform. Other nozzles can be tested as well, should the platform change (e.g. to a E class or aeroderivative, etc.) The test assembly is shown in Figures 1 and 2. The experiment involved operation of a DLN equipped first stage, which is a microturbine combustor, followed by Deionised (DI)-Water injection system to quench the exhaust gases from the 1st stage combustor exit to the designed heat exchangers inlet temperature. The heat exchangers cool down the exhaust gases to allow condensation of the DI-water and the water product from the 1st stage combustor. This water is 99%+ eliminated by using water moisture separators/drainers installed downstream of the heat exchangers. Finally the conditioned exhaust gas is mixed with the preheated air in the pre-chamber of the second combustor to simulate EGR oxidizer, including the major and minor species involved in re-circulation. The second stage can utilize any GE DLN or diffusion single nozzle premixer, for any class of GE gas turbine.

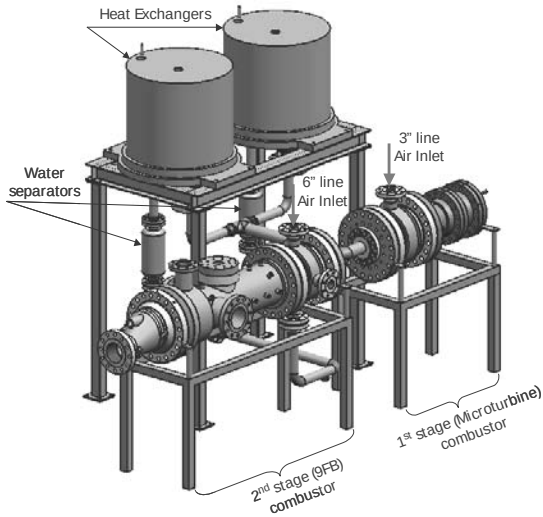

Figure 1. Test rig assembly.

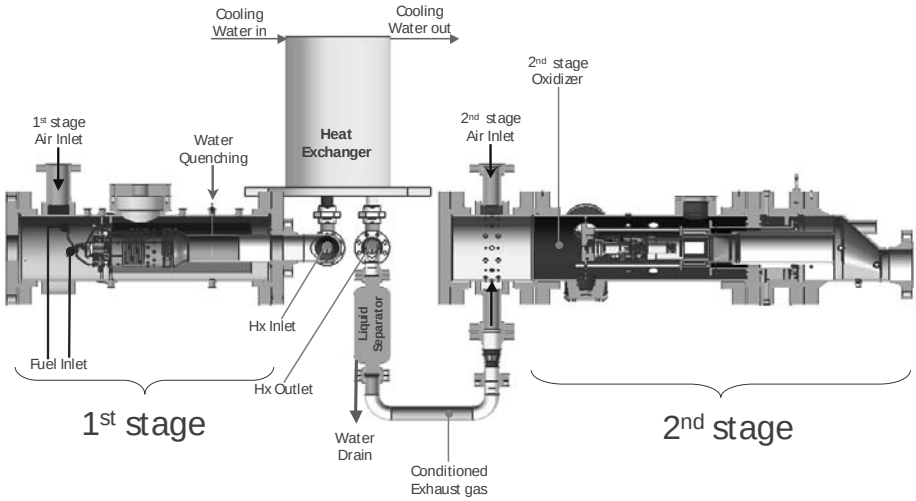

Figure 2. Schematic of experiment setup.

First Stage

The Microturbine combustor rig is a test vehicle that allows the study of performance of a prototype low-emissions combustion system at pressure with and without air preheat. The combustor allows for flexible operation from fully diffusion to fully premixed mode. The equipment is designed for high-pressure, high-temperature combustion experiments using natural gas fuel. The four-nozzle combustor is mounted within a 12" pressure vessel as shown in Figures 3a and 3b. Air and fuel are supplied to the test cell by facility systems. Air is fed through a 3" line, which is not preheated, designed for inlet air pressure at 200 psi at this stage. Ignition is achieved using a hydrogen torch mounted through the wall of the combustor test section. Burned gas is sampled and sent to a set of continuous gas analyzers for measurements of Unburned Hydrocarbons (UHC), CH_4, CO, CO_2, NO_x, and O_2.

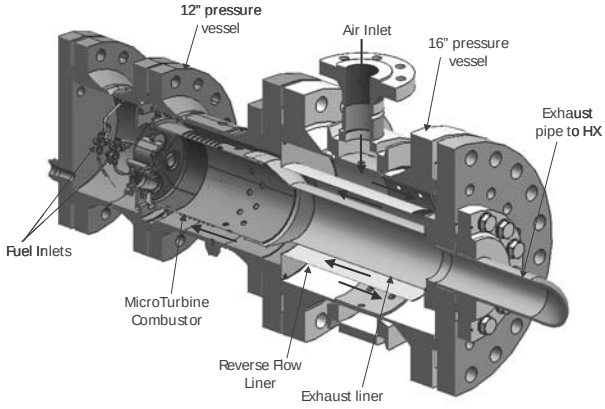

Figure 3a. First stage assembly.

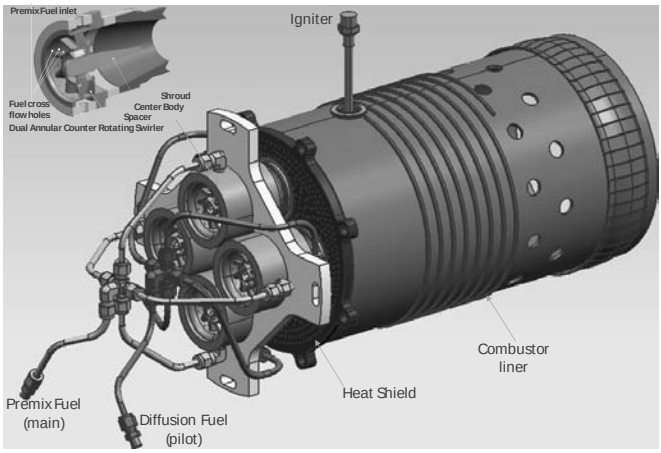

Figure 3b. First stage assembly.

All critical pressures, temperatures and flows are measured within the first stage. For safe operation the first stage is also instrumented with a set of vessel skin, combustor, and liner thermocouples, which are monitored in the control room as shown in Figure 4. Maximum inlet flow conditions for these tests are P_3 = 200 psia and T_{inlet} = 200 °F.

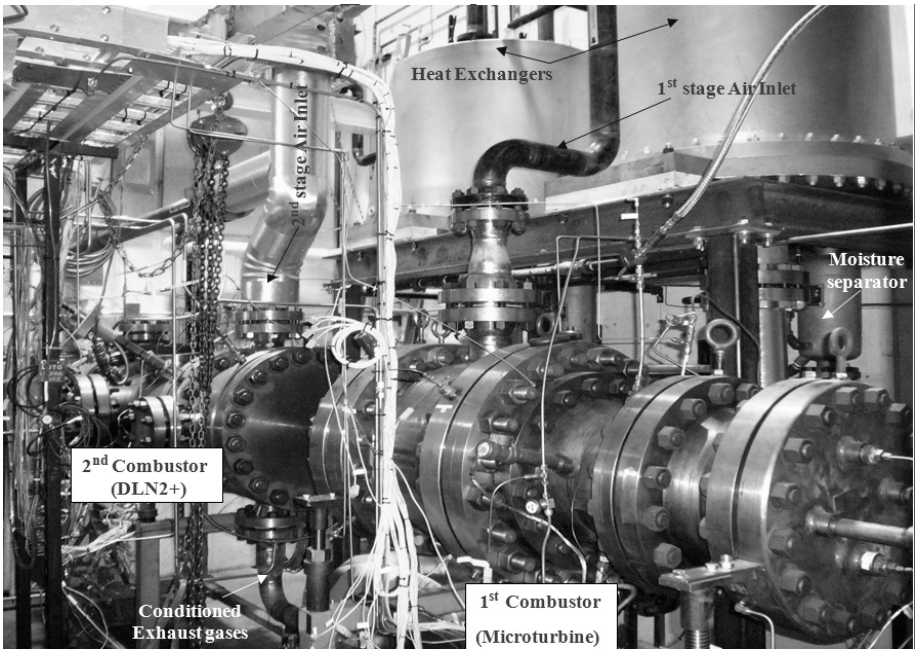

Figure 4. Test Rig.

DI water system

Treated water is needed to quench the products of combustion and cool it down from the flame temperature of 2500-3000 °F to 1200-1500 °F (Figure 5.) In the first set of experiments the DI water is needed to bring the exhaust gases to 1200 °F due to the limitation on the pipe used for delivering these gases to the heat exchangers. The DI water pump is currently rated for 5 gpm at 2500 psi.

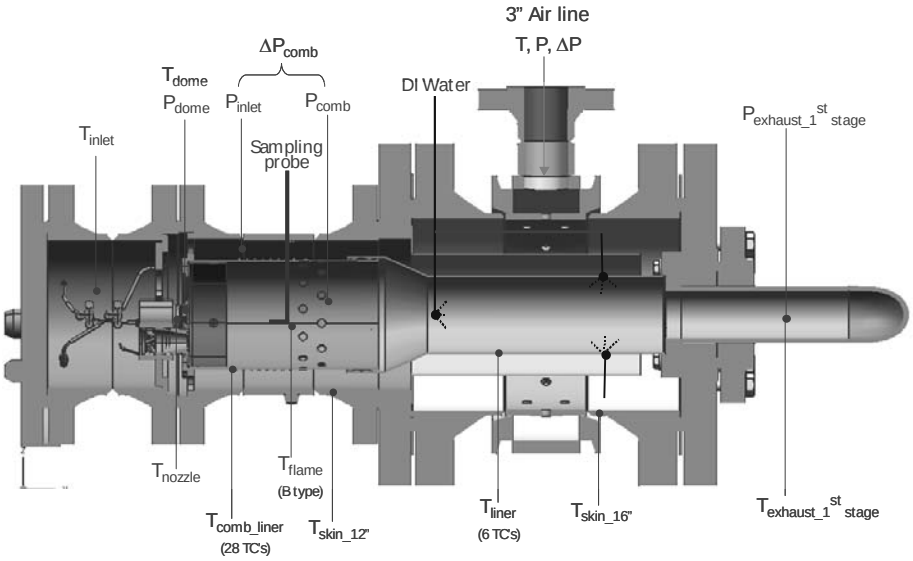

Figure 5. First stage instrumentation.

Heat Exchanger

Two heat exchangers are installed in parallel and designed to cool down the exhaust gases from 1500 °F to <100 °F with a designed gas flow rate of 2.0 lb/sec in the tube side per heat exchanger (for a total of 4 lb/sec.) Cooling water is provided through the water-cooling tower system with a required flow rate of 220 gpm (per HX) to cool the gases to the targeted temperature. The tube sides, shell sides and water jackets were hydro-tested at 850 psig, 110 psig, and 130 psig respectively. According to the manufacturer, the maximum allowable pressure (MAWP) in the tube side is 75 psi at max temperature of 500 °F. For the tube side the MAWP is 500 psi at 1000 °F. For safety reasons, the heat exchangers are monitored via thermocouples installed in the shell and tube sides. A pressure transducer is also mounted to the shell side. In addition, relief valves are mounted on the shell side of each heat exchanger and set to max. pressure of 80 psi.

Moisture separators /Drainers

Dry-Flo L1 moisture separators are installed at each heat exchanger outlet with a separation efficiency of 99%. The separators are rated to 500 psig at 650 °F. Drained water flows through Armstrong 33-LD free floating lever drain traps, which are rated at MAWP of 1000 psi at 100 °F. The trapped gases in the liquid drainer are vented back to the moisture separator.

Second Stage

The second stage (Figure 6) is designed for high pressure and high temperature combustion burning natural gas. The rig is designed to investigate the use of low oxygen oxidizer and its effect on operability and emissions.

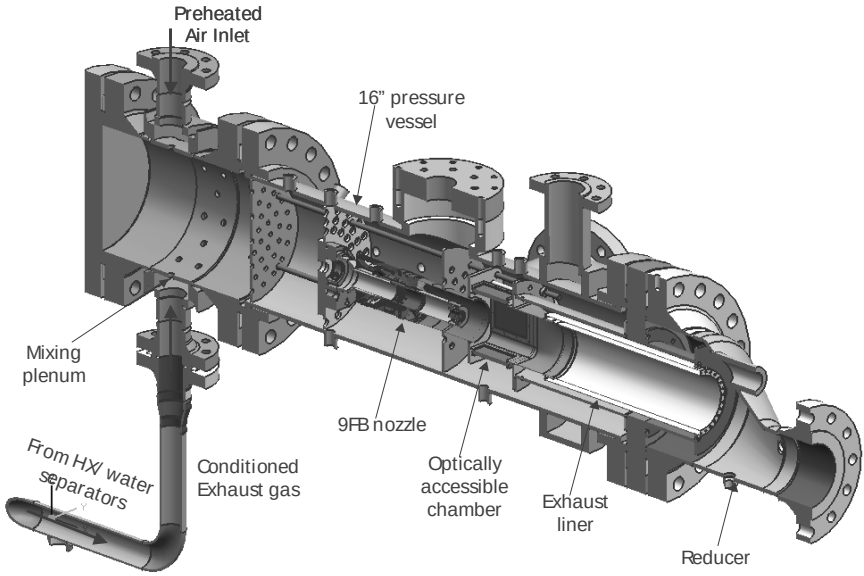

Figure 6. Second stage assembly.

The conditioned (dried and cooled) exhaust gases in each line of the heat exchangers are combined and flow through a Micromotion Coriolis flowmeter to meter the final gases mass flow and estimate the amount of water that is still in the exhaust gases. The conditioned gases pipe is instrumented with a pressure transducer and a thermocouple. The gases flow through the plenum of the second stage where it mixes with preheated air to reach the final mix temperature. The assembly of the second stage is shown in Figures 6 and 7a. The air supplied through the 6" boost line is overheated to >1100 °F, so that the final oxidizer mixture will be at about >700 °F, typical of the compressor discharge in a gas turbine. The boost line pressure will be adjusted to match the pressure of the conditioned exhaust gases. A gas sampling probe will be located just upstream of the fuel nozzle to determine the final mixture (oxidizer) composition. This sampling probe is mounted on a traverse system to check for the uniformity of the mixture before combustion. Typical results confirming uniformity of the major and minor species concentrations are shown in Figure 8.

The fuel nozzle and combustion chamber are mounted inside the 16" pressure vessel, which has visual access though quartz windows (not employed at this time.) Ignition is achieved using a hydrogen torch mounted through the wall of the combustor test section. The exhaust is directed into the facility exhaust tunnel.

Burned gas is sampled and sent to a set of continuous gas analyzers for measurements of UHC, CH_4, CO, CO_2, NO_x, and O_2. All critical pressures, temperatures and flows are measured within the test

cell. A schematic of the location of these measurements is shown in Figure 7a. Figure 7b shows the corresponding measurement point of the DLN can combustor. Maximum inlet flow conditions for these tests are P_3 = 200 psia and T_3 = 1100 °F.

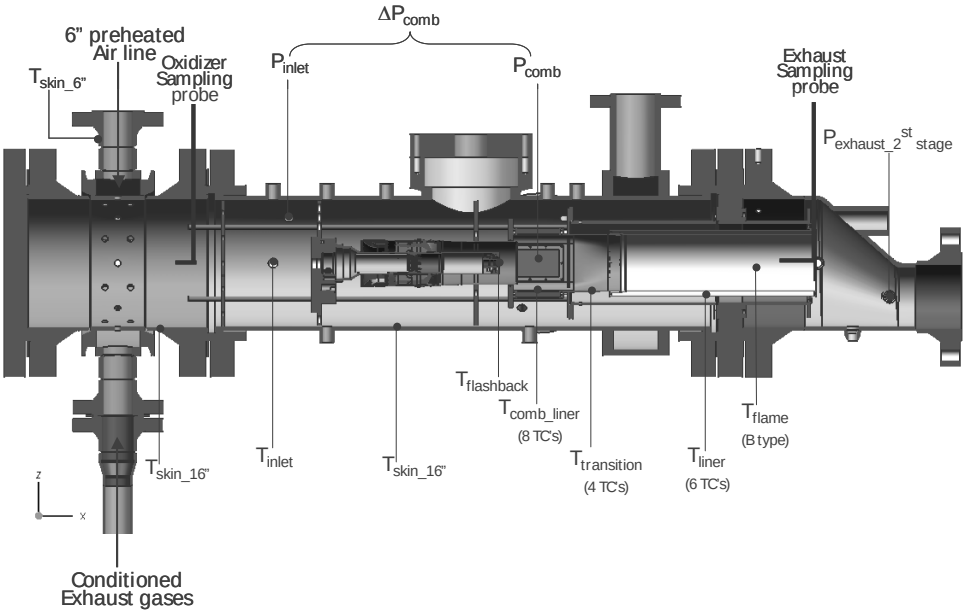

Figure 7a. Second stage instrumentation.

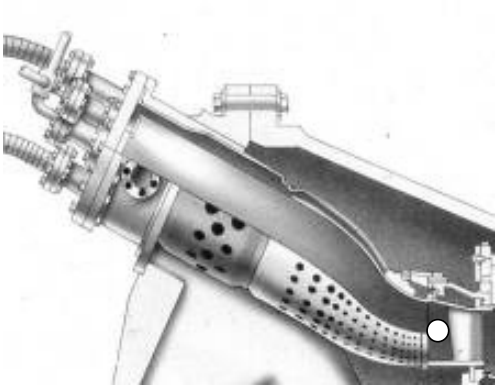

Figure 7b. Corresponding Full Can DLN System Containing Several as Tested Premixers.

Air System

The air compressors supply high-pressure air for combustion to the test cell through two air lines. The first air line is the 3" line which is not preheated, the other line is the 6" diameter boost line. Hot air flow is adjusted using two facility control valves upstream of the preheater. Orifice flow meters are provided to measure the flows through each of the control valves. The hot pipe is rated for 800 psi at 1200°F. The spool to the inlet pressure vessel of the second stage is rated at 600 psi @ 1100 °F. These pressures and temperatures cover most of GE's combustors air inlet (compressor discharge) conditions.

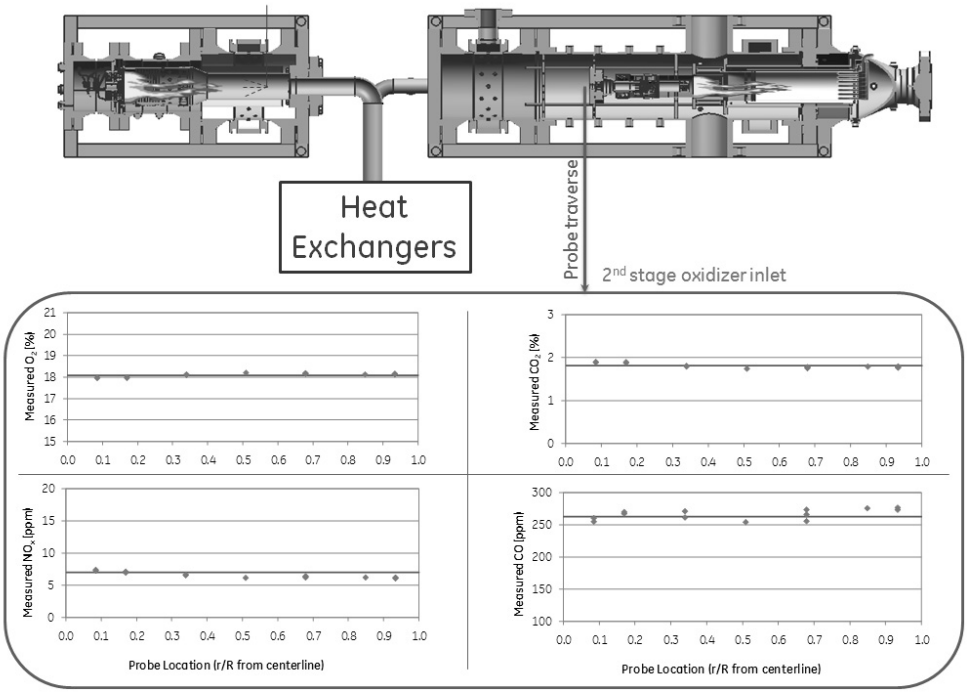

Figure 8. Oxidizer mixture uniformity at 2nd stage combustor inlet.

Fuel System

The natural gas system consists of a compressor that supplies high-pressure natural gas to the test cell. The natural gas supply includes four circuits to feed two fuel circuits per combustor. The fuel circuit P&ID is shown in Figure 9. Each stage is supplied with a diffusion (pilot) circuit and a premixed (main) circuit. No liquid fuel is used in this program.

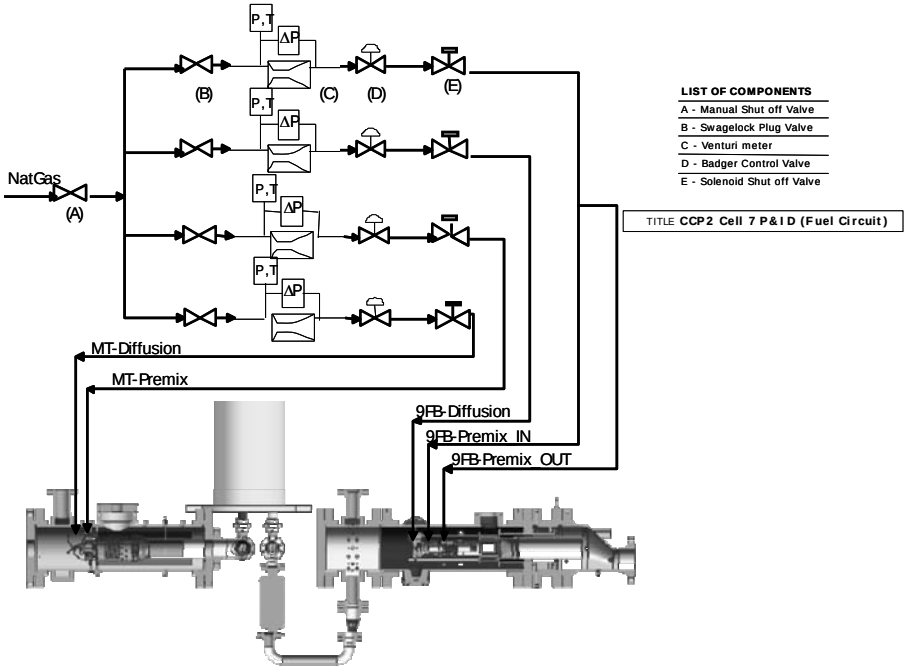

Figure 9. Fuel circuit P&ID.

Water System

Water is used to cool the post combustion section of the test stand and is sprayed into the burned gas through the use of a cooling ring and the sampling probe. The cooling ring injects water axially downstream and towards the wall. The sample probe, which is water-cooled, ejects the heated water axially downstream through a series of holes on the downstream edge of the probe.

Pressure Vessels

A number of pressure vessels are employed in this setup. They are all 16" vessels except for the micro-turbine vessel (first stage.) The micro-turbine pressure vessel is a 12" vessel containing the micro-turbine combustor. This vessel is ASME stamped to withstand 350 psia at 500°F. A transition flange between these two vessels is 600-pound flange. Carbon steel bolts are used and a 1000°F temperature limit must be observed for the bolts. A choked backpressure orifice in the exhaust section holds the pressure in the rig. Fine-tuning of the backpressure is achieved by controlling the water flows. The products of combustion are directed into the exhaust tunnel. There is a rupture disk (300 psi @ 1100°F) on the burst line that connects to the air supply line to assure vessel protection. This is the weakest link in the pressure rated system and will prevent the vessels from overpressure. The discharge line is directed outside the test cell.

Exhaust System

An orifice plate is used for controlling pressure drop across the second stage combustor. A facilities blower creates suction in the exhaust tunnel to insure that gases do not back flow into the test cell.

Gas Sampling System

Three gas-sampling probes are mounted in this experiment. The first, a water-cooled gas sampling probe with a single port is located downstream of the premixer within the 12" pressure vessel. There is another water cooled sampling probe located downstream the combustor of the second stage. The third sampling probe system is installed upstream of the second stage fuel nozzle to check for the oxidizer composition. The signals from the analyzers are recorded by the data acquisition system.

RESULTS AND DISCUSSION

All the data reported here were obtained at the following conditions:

- Combustor Pressure: 100-150 psia
- Pressure Drop Across secondary nozzle: 1-3 %
- T_3 (Inlet Temperature): 550-750 °F
- Pilot Fuel Circuit (diffusion): 0%

For all the emissions data plotted in following sections and in order to clarify the trends, data were curve fitted.

Measurement Details

The flame temperatures reported are based on the O_2 levels measured at the probe location at the time and location of measurement (first or second stage.) These values were compared to the thermodynamic equilibrium values and excellent agreement was found. In addition, flame temperatures based on the flows of air and natural gas (equivalence ratios) and airflow-splits (combustion versus bypass/cooling) also show good agreement. Temperatures at the inlet of the secondary combustor were obtained by mixing cold exhaust gas from the first stage with hot fresh air, overheated, as a countermeasure for determining the correct temperatures at the inlet of the premixer. The emissions of minor species (NO_x, CO and UHC) in the first stage were monitored to determine their evolution before and after the combustion in the second stage. It was found that in general NO_x and CO burn in the secondary combustor, resulting in acceptable levels of emissions. UHC are negligible, showing good efficiency of the combustion process up to 30% EGR. At this time there is no measurement of the condensed water to determine NO, CO or sulfur levels in the condensate. While there is a wealth of data collected, we report mainly data related to the condition of EGR levels of 25% and 30%.

Flame stability

The flame was in general very stable without using a pilot, even with the low levels of O_2 tested down to 17.8% in the oxidizer and 5.5% in the exhaust. No important acoustic instabilities were observed. It was determined that operation at Full Speed Full Load (FSFL) is an acceptable condition up to 30%, in absence of acoustic instabilities and with excellent efficiency of combustion. An attempt to produce 50% EGR data failed due to experimental constraints that considerably lowered temperatures of the vitiated air. Based on this initial finding, all our experiments were performed at fully premixed condition. Pilot operation was not explored, although it could be a beneficial addition for extending the operability of the combustor without NO_x degradation.

CO_2 emissions

The main goal of this phase was to demonstrate premixed combustion technology operability of a commercially available nozzle (9FB) and efficiency with real EGR produced in a separate combustion process. The most important emissions goal was to demonstrate that high levels of CO_2 may be achieved in the combustor without losses. High levels of CO_2 and low levels of O_2 resulting from combustion with EGR are successfully demonstrated for down to 17.8% O_2 in the oxidizer and 5.5% measured in the exhaust gas at the end of the second stage combustion (see Figure 10.) The

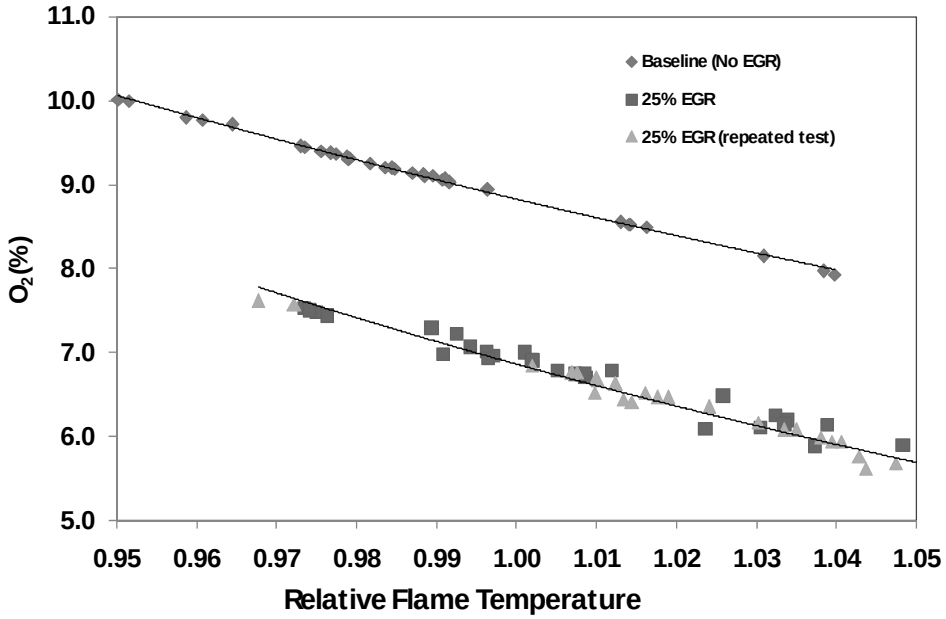

Figure 10. O_2 concentration at 25% EGR: baseline (no EGR) is used for comparison.

CO_2 emissions results for 25% EGR are presented in Figure 11. The levels of CO_2 produced in the first stage are shown in Figure 12. We demonstrated that CO_2 levels of more than 8% are achievable at the exit from the combustor. In Figure 11 the measured CO_2 levels are shown at different conditions and as function of flame temperature. The CO_2 in the vitiated air was up by 1.6% at 30% EGR, as shown in Figure 13. Given the linear behaviour, Figure 13 also suggests that the CO_2 levels expected as function of flame temperatures clearly will achieve the 9% CO_2 level at a flame temperature of 3000 °F and 35% EGR, and the 50% EGR at 2900 °F flame temperature will exceed 10.5% CO_2 in the primary zone, if we were able to test it. This conclusion is based on good CO emissions, its burnout and the linearity of the process, as shown in the 2006 report [4].

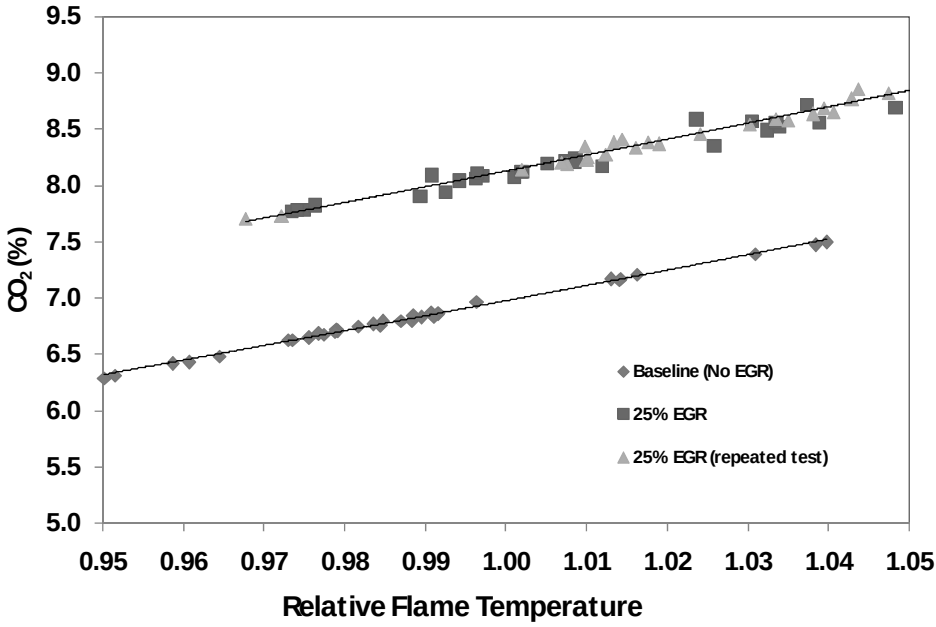

Figure 11. CO_2 concentration at 25% EGR: baseline (no EGR) is used for comparison.

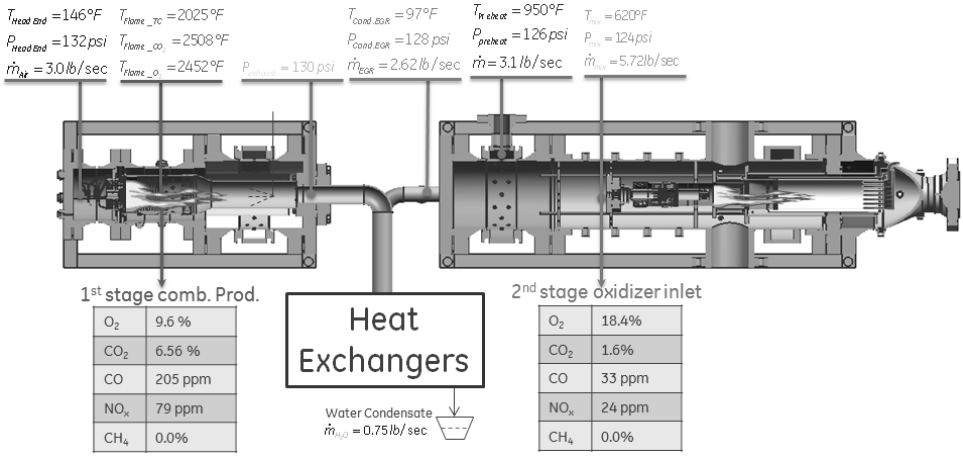

Figure 12. 25% EGR condition measurements at various stations.

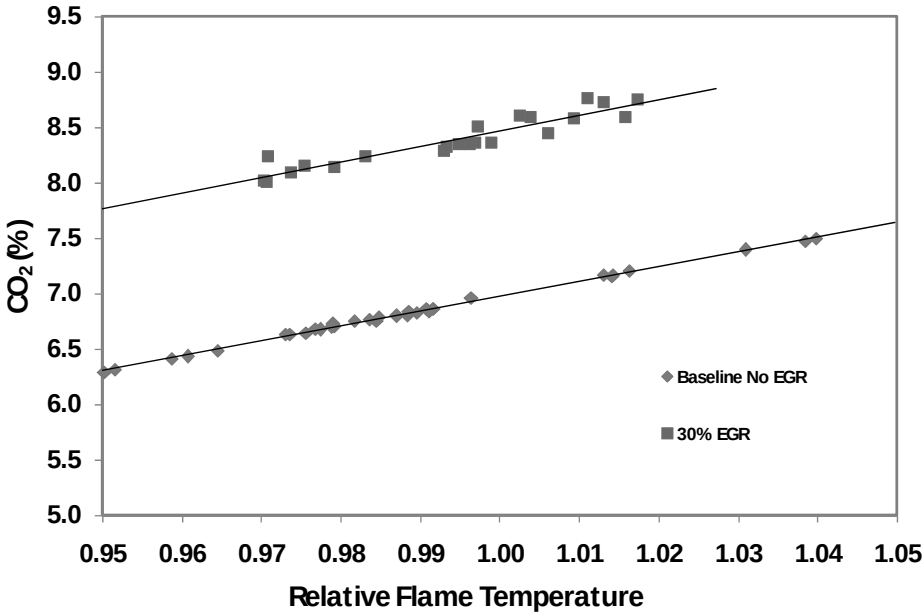

Figure 13. CO_2 concentration at the exit of the combustor at 30% EGR compared to baseline.

O_2 Levels

Figures 10 and 14 show the O_2 levels measured, compared to the baseline measurements. Figure 10 shows the lower oxygen levels obtained with increasing flame temperature and EGR levels of 25% in this case. The lowest oxygen level in this case is 5.5% leftover at 30% EGR and flame temperature of ~2950 F. At same temperature, a 35% EGR will produce roughly 4.6% O_2. Introduction of CO before combustion (from stage 1) should be mentioned here. The low levels of oxygen also result in less consumption of the CO and therefore emissions of CO may be higher due to the oxygen starvation of these flames. According to the phase 1 tests in 2006, however, we can predict that oxygen levels of lower than 2% are achievable, while still compliant with 25 ppm limit of CO emissions, even if some levels of CO are re-circulated.

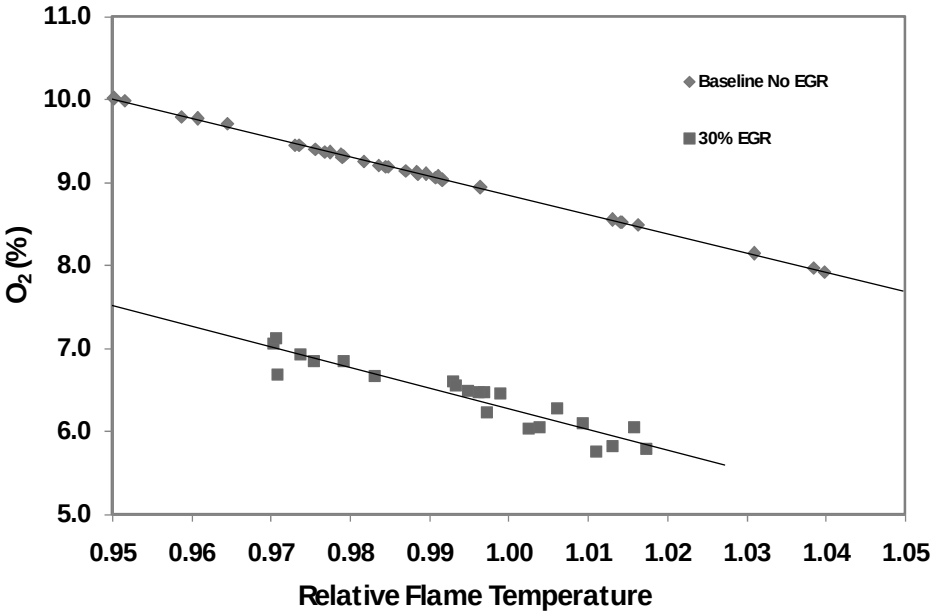

Figure 14. O_2 concentration measured at the exit of the combustor at 30% EGR, compared to baseline

NO_x emissions

It was found that the NO_x emissions are reduced via the reduction of oxygen in the combustion air, as explained in [4], even if NO_x is introduced at ppm levels in the vitiated air before combustion in the secondary stage. The NO_x reduction levels were considerable. NO_x levels will be preserved when compared to current performance with DLN. If full can (as opposed to single premixer) tests confirm the operability, it is possible to reduce the NO_x by more than 50% depending on the EGR levels and NO_x recirculation. Figure 15 shows the levels of reduction measured on a relative chart as function of temperature. This stays relatively linear with the amount of EGR introduced, as we discovered in previous studies. A reference temperature is chosen for the flame and relative numbers are reported on the abscissa.

Combustion Efficiency with EGR

EGR may induce loss of efficiency in completely combusting the fuel. The combustion efficiency can be measured based on the levels of unburnt hydrocarbons (e.g. methane) as well as incomplete burnout of intermediate species like CO, etc. Due to oxygen starvation and specific conditions, a gas turbine combustor designed for 21% O_2 air may not guarantee complete the oxidation reaction to CO_2 in EGR conditions, thus determining inefficiencies. However, for the lean premixed flames and conditions tested with up to 30% EGR as described in Table 1, the efficiencies remain high, similar to the ones in the baseline cases and complying with the CO emissions. This is also reflected by the good oxygen consumption described in the preceding section. An efficiency of combustion formula needs to be derived to account for introduction of CO_2 and CO as inert and fuel respectively, in the oxidizer.

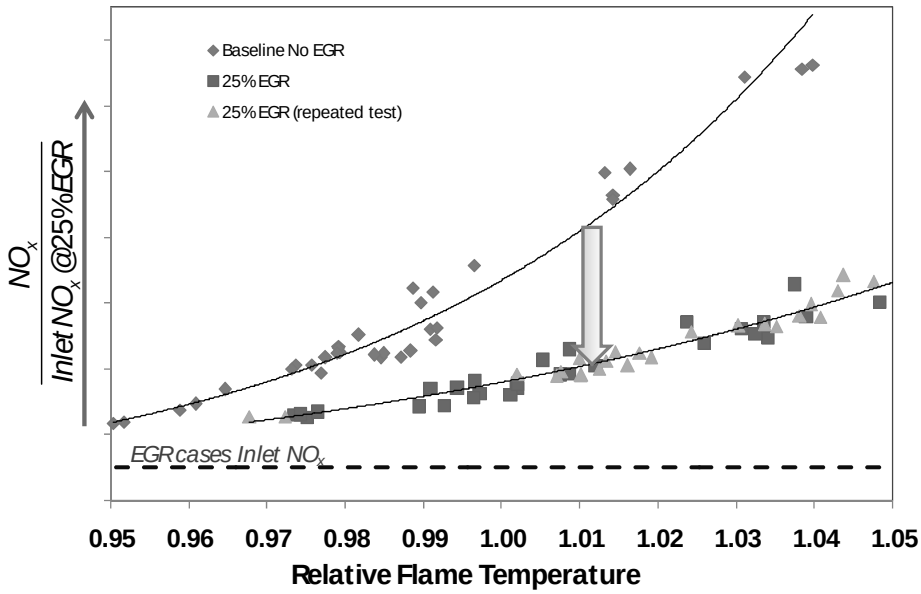

Figure 15. NO_x concentration at 25% EGR: baseline (no EGR) is used for comparison.

Table 1. Inlet oxidizer composition at different EGR levels.

EGR (%)	YO_2	YCO_2	YN_2
50	0.132	0.044	0.823
40	0.159	0.029	0.812
30	0.177	0.019	0.804
20	0.191	0.011	0.798
10	0.202	0.005	0.793
0	0.210	0.000	0.789

CO emissions

CO concentrations need to be kept to minimum levels, and it was reported by us and others that they are the main challenge in oxygen starved flames. CO will be produced due to lack of oxygen or limited residence time or low pressures and temperatures required to complete the oxidation reaction to CO_2. An explanation of these mechanisms was given in the first phase report [4].

Experimental data of CO emissions on a relative scale and raw numbers are presented as function of flame temperature and at 25% EGR condition in Figures 16 and 17**.** In the baseline case (0% EGR) CO concentrations rapidly climb at low flame temperatures and decrease with increasing the flame temperature to a minimum value at about 2900 °F due to the oxidation reaction CO + OH → CO_2 + H which becomes significant at temperatures in excess of 2300 °F. Beyond a flame temperature of 2750 °F the dissociation of CO_2 to CO takes place leading to increase in CO concentrations at combustor exit plane.

An interesting behavior was observed in the presence of modest original CO levels (before combustion) i.e. that the CO levels were in fact lower with CO doped before combustion (see Figure 16.) This demonstrates that CO burnout is real and that kinetics of CO oxidation is improved by a mechanism we currently investigate.

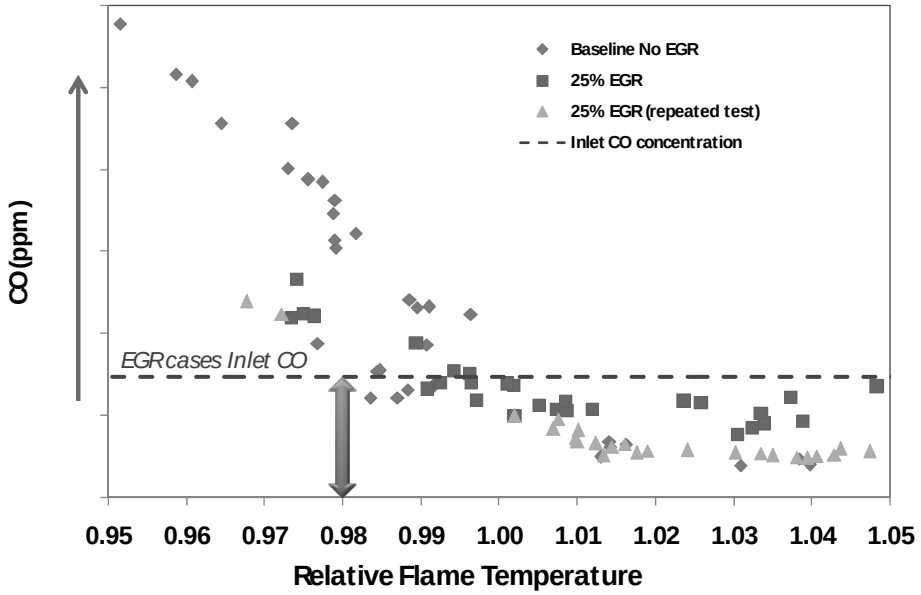

Figure 16. CO concentration at 25% EGR: baseline (no EGR) is used for comparison.

CO emissions measured were not an issue at the EGR levels tested (up to 30%). This shows that CO could be kept in check up to 30% EGR after which a change in emissions could be expected. We can predict at this point that at maximum measured EGR levels (slightly above 30%) and within flame temperature in the range of 2800-2900 °F, confirmation of the previous phase results is achieved, namely CO emissions will be kept in check. It is encouraging to see that the re-burn of NO_x and CO is occurring, thus the concerns of re-circulated build-up of CO and NO_x appear to be speculative up to the EGR levels tested.

In summary, the presence of EGR plus additional CO in the oxidizer, leads to low oxygen concentrations, which play a role in shifting as well as reducing the reaction rates, and reduce the local flame temperature, which is not in favor of the oxidation of CO to CO_2. In these tests however, no special CO issues were observed for up to 30% EGR conditions.

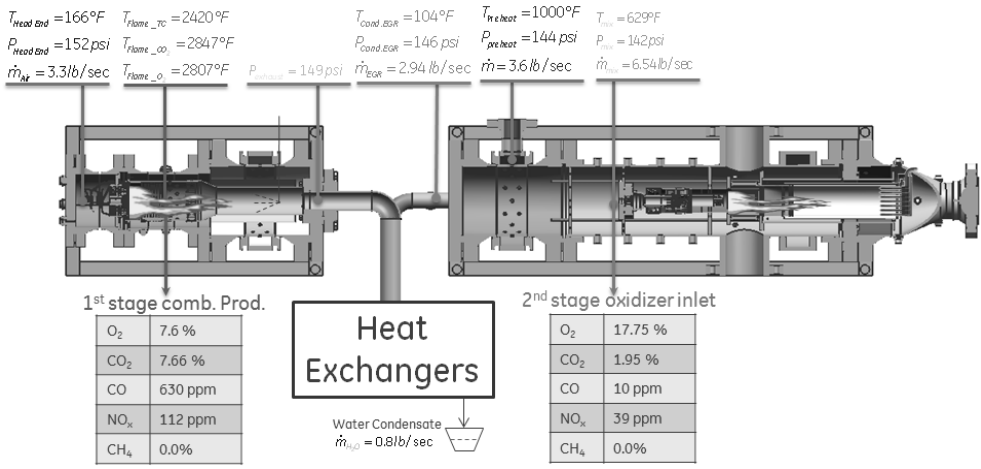

Figure 17. 30% EGR measurements at various stations.

CONCLUSION

A unique rig that allows measurement of real EGR, including minor species recirculation, has been built and successfully operated at the General Electric-Global Research Center (GE-GRC) facilities in Niskayuna, NY. Combustion tests in Exhaust Gas Recirculation conditions at representative pressures and temperatures have been completed using a commercial 9FB DLN nozzle. They confirm the feasibility of using current combustion technologies in low oxygen conditions determined by EGR of up to 30%, potentially feasible to up to 35%. Under carefully chosen conditions and with some design changes, this GE DLN gas turbine combustor nozzle can operate with high efficiencies and determine CO_2 levels of more than 8% by volume in the gas products. Our prediction is that with minor modifications in the combustor design and its operation, the EGR levels could be augmented to more than 40%. Hence we validate the results obtained in 2006 using a research, smaller Dry Low Emissions (DLE) nozzle and with simulated EGR (no minor species such as NO_x and CO in the oxidizer.) Good CO and NO_x emissions burnout is obtained. The CO levels are found to be the limiting factor for EGR but not before 30% EGR conditions. Current models may be updated with our current findings and allow for optimization of the EGR cycles for carbon capture. The next suggested step is to perform a full scale can (multi-nozzle) DLN combustion test to confirm our findings.

ACKNOWLEDGEMENTS

The authors are grateful to the CO_2 Capture Project (CCP) consortium for the opportunity to collaborate on a novel research area in combustion for gas turbines. We address special thanks to Dr. Daniel Chinn of ChevronTexaco for the fruitful collaboration and his support of this research project. This work would not have been possible without the support of Mr. Kelly Fletcher. Valuable cycle information was provided by Matthias Finkenrath and Cristina Botero of GE GRC Munich.

This Chapter contains figures that originally appeared in Energy Procedia Vol 1, Issue 1, Greenhouse Gas Control Technologies 9, Proceedings of the 9th International Conference on Greenhouse Gas Control Technologies (GHGT-9), 16-20 November 2008, Washington D , USA, which was published by Elsevier Ltd.

REFERENCES

1. Rokke, P.E., Hustad, J.E. EGR in Gas Turbines for reduction of CO_2 Emissions; Combustion Testing with Focus on Stability and Emissions, Intl. J. of Thermodynamics, Vol. 8, (4), Sept. 2005.
2. Evulet, A., GE GRC Internal Presentation, 2005.
3. Bolland, O. and Mathieu, P., "Comparison of Two CO_2 Removal Options in Combined Cycle Power Plants," Energy Convers. Mgmt Vol. 39, No. 16-18, pp. 1653-1663, 1998
4. Evulet, A., ELKady, A. M. and Brand, A. CCP2-3.1 report, 2006.

OTHER LITERATURE

1. Warnatz, J., Maas, U., Dibble, R.W. Combustion, 2nd edition, Springer Verlag, 1999
2. Dean, A. J., private communication.
3. Miller, J.A. and Bowman, C.T. Mechanism and Modeling of Nitrogen Chemistry in Combustion, Prog. Energy Combust. Sci., 15, pp287-338, 1989.
4. Correa, S. M., "Carbon Monoxide Emissions in Lean Premixed Combustion," *Journal of Propulsion and Power*. Vol.8, No. 6, 1992, pp. 1144-1151.
5. Lefebvre, A. H., Gas Turbine Combustion, 2nd ed., Taylor and Francis, Philadelphia, PA, 1998.
6. Baulch, D. L. and Drysdale, D. D., "An Evaluation of the Rate Data for the Reaction CO + OH → CO_2 + H," *Combustion and Flame*, Vol. 23, 1974, pp. 215-225.
7. Bowman, C. T., "Chemistry of Gaseous Pollutant Formation and Destruction," *Fossil Fuel Combustion*, edited by W. Bartok and A. F. Sarofim John Wiley & Sons, New York, 1991, pp. 215-260.
8. Westenberg, A. A. and deHaas, N., "Steady-State Intermediate Concentrations and Rate Constants. Some HO_2 Results," *Journal of Physical Chemistry*, Vol. 76, No. 11, 1972, pp. 1586-1593.
9. Westbrook, C. K. and Dryer, F. L., "Chemical Kinetics and Modeling of Combustion Processes," *Proceedings of the Combustion Institute*, Vol. 18, 1981, pp. 749-767.
10. Evulet, A., Elkady, A.M., Brand, A. and Chinn, D. "Performance of GE's Dry Low NO_X Combustors Utilizing Exhaust Gas Recirculation for Post-Combustion Carbon Capture", presented at GHGT9, Washington DC, November 2008.
11. Evulet, A., Elkady, A.M., Brand, A. and Chinn, D. "On the Performance and Operability of GE's Dry Low NO_x Combustors utilizing Exhaust Gas Recirculation for PostCombustion Carbon Capture", Energy Procedia, Volume 1, Issue 1, February 2009, Pages 3809-3816

Carbon Dioxide Capture for Storage in Deep Geologic Formations, Volume 3
L.I. Eide (Ed.)

Chapter 5

CHEMICAL LOOPING COMBUSTION (CLC) TECHNOLOGY SUMMARY

Jan Assink[1], Corinne Béal[2]
[1]Shell Global Solutions Int. BV, Amsterdam, The Netherlands
[2]Alstom Power Boilers, Paris, France

ABSTRACT: This chapter provides a general introduction and overview of the Chemical Looping Combustion CO_2-Ready Gas Power project, conducted with EU and CCP funding by a consortium composed by Chalmers University of Technology, Instituto de Carbonquimica (CSIC), Alstom Power Boilers, Vienna University of Technology, Tallinn University of Technology, and Shell Global Solutions. The contributions of the partners will be discussed further in following chapters.

INTRODUCTION

The chemical looping combustion (CLC) concept is based on the transfer of oxygen from combustion air to a fuel by means of a 'looping' oxygen carrier. The oxygen carrier is often a metal oxide. Central to the concept are the air reactor, where the oxygen carrier is oxidised, Equation 1, and the fuel reactor, where the oxygen carrier is reduced and the fuel is oxidised by the carrier Equation 2. For methane fuel and NiO as example of an oxygen carrier the reactions are listed:

$$Ni + ½\ O_2 \rightarrow NiO \qquad \text{Equation 1}$$

$$CH_4 + 4\ NiO \rightarrow CO_2 + 2\ H_2O \qquad \text{Equation 2}$$

$$CH_4 + 2\ O_2 \rightarrow CO_2 + 2\ H_2O \qquad \text{Equation 3}$$

The overall reaction of the concept, Equation 3, is the same as for stoichiometric combustion, and the total amount of heat evolved from reactions in Equations 1 and 2 is the same as for Equation 3. The temperatures of two reactors' exit streams, the circulating solids, and any heat transfer surface installed govern the heat balance. Temperatures envisaged are typically in the range of 850-950°C. More importantly, the exit gas stream from the fuel reactor contains mainly CO_2 and H_2O, and almost pure CO_2 is obtained when water is condensed. Thus this concept resembles the category of oxyfuel or oxyfiring, where a fuel is combusted with pure oxygen, e.g. obtained from an air separation unit. Recently for CLC also the qualifier of unmixed combustion is used: the combustion with air, avoiding the mixing of N_2 and CO_2 in a single flue gas stream.

The CO_2 Capture Project (CCP) R&D on Chemical Looping started in 2002 with a two-year programme. As part of the GRACE Project [1,2] the partnership between BP, Alstom Power Boilers, Chalmers University, Istituto de Carboquimica (CSIC), and Vienna University of Technology, was formed conducting an extensive program. It yielded the key result of Proof-of-Feasibility for the technology through operation of the 10 kW_{th} pilot unit at Chalmers, substantial progress on oxygen carrier screening, fluidisation aspects and first design study on commercial size installation.

A large number of oxygen carrier materials with Cu, Fe, Mn, or Ni and various support materials were screened, and evaluated on reactivity, strength, attrition, and agglomeration. The most promising carriers based on Cu, Fe and Ni were prepared on kg scale to be tested in a pilot plant. Two of them with Ni and Fe were tested in this 10 kW unit, and of these the Ni-based oxygen carrier was operated for 100 hours and provided the proof of concept, whereas the Fe-based carrier was operated for 17 hours only.

Two main concerns on the development of the solid oxygen carrier were concluded to be on the critical path for technology development:

- Chemical and mechanical aging, leading to attrition and loss of inventory and loss of performance of the oxygen carrier;
- Scale-up of manufacturing procedure.

These and other were the starting points for the Chemical Looping Combustion CO_2-Ready Gas Power project that started in 2006 and ended mid 2008.

CLC GAS POWER (CLC GP) PROJECT

The partners of the previous project, now under the coordination of Chalmers defined and executed the CLC GP project. A coherent plan was forged in which the numerous objectives were addressed in a balanced way. In addition, the Technical University of Talinn was attracted for their expertise on high temperature processes.

NiO was selected for scale-up and testing, since it came out as the best material from the previous project, with highest activity, and having operated successfully for 100 h. Moreover, the duration of the project and focus on carrier scale-up and process aspects did not allow for general material screening.

A brief summary of the programme covering the two “concerns” stated above, with references to the following chapters, is given:

- Preparation of oxygen carrier by spray drying of commercial available materials in two stages (30 kg and 300 kg batches) to support eventual testing in a pilot plant [3].
- Alternative carrier development by impregnation of a commercial porous support and preparation of a batch for testing (30 kg) [4].
- Long term integrity testing (1000 h) in the existing 10 kW unit, and dedicated testing of high temperature resistance of the oxygen carrier [3].
- Chemical aging with contaminants sulphur and hydrocarbons heavier than methane [4].
- Carrier mechanical attrition testing under realistic hydrodynamic conditions [3].
- Modelling of CLC reactors and overall process, including measuring the kinetics of the selected oxygen carriers.
- Pilot plant testing in a modified dual fluidised bed with a capacity of 100-200 kW, to meet more closely hydrodynamic conditions of a commercial unit [5].
- Conceptual design of a next phase demonstration unit of 10-50 MWe. This work package also included a first environmental assessment and an update of the GRACE full scale CLC boiler cost model [2].

Without pre-empting the findings reported in the chapters to come, nearly all objectives of the programme listed above were met successfully. Moreover, this project can be characterised as learning by doing: Oxygen carriers were screened and developed by two partners, supported by an external contractor (VITO) [3,4]. Variations in composition were investigated to improve the

performance. Five partners were involved in hot testing at high temperatures (800-1190°C) of oxygen carrier samples for dedicated purposes.

Various topics surfaced during the research, e.g. the defluidisation phenomena [3] during the material screening work, the observed performance of the first batches of carrier in the 10 kW unit, design and safety aspects of the 120 kW pilot plant that had to be newly designed and built, and the conversion versus capacity trends observed [5]. Some of them were related to the small scale of research, the non-optimum design, need for experience, others may contribute to further insight in the near future. In some areas further analysis and/or modelling is needed to verify the theories that have been proposed. This holds for the pilot plant testing and the demonstration unit design. The latter could partly use available test results from the pilot plant. The industrial demonstration unit further was sized on general CFB criteria. A simple arrangement drawing is depicted in Figure 1. The safety and environmental implications of using NiO as active component in the oxygen carrier were not fully resolved in the first environmental assessment. NiO was concluded not to be a showstopper. However, for a commercial application it was recommended to reduce particle emissions to a minimum.

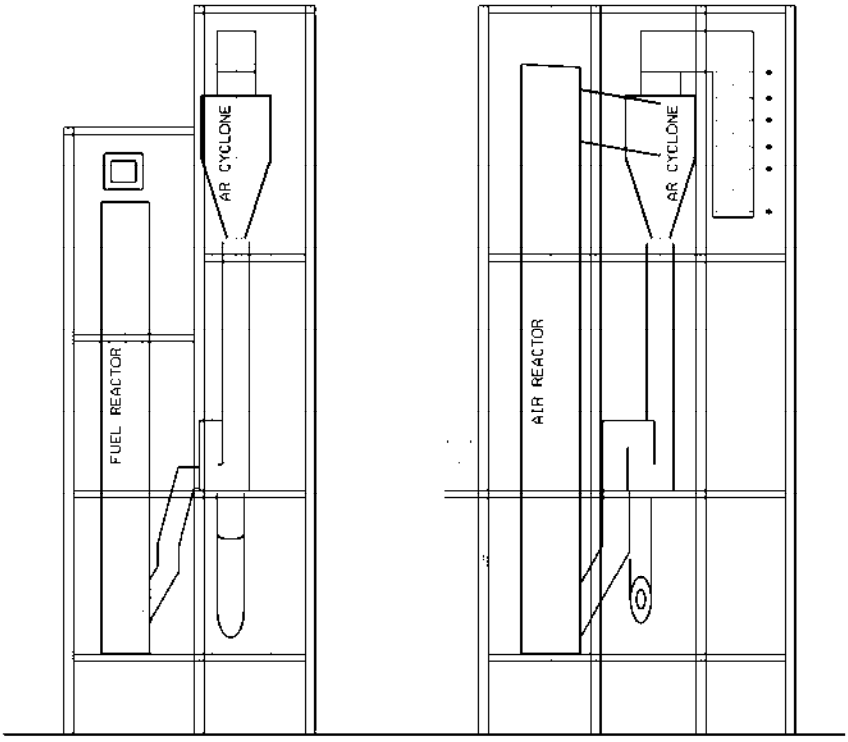

Figure 1. Preliminary general arrangement of 10 MWe CLC dual CFB.

In summary, the project with the pro-active partners led by Chalmers has achieved its objectives. On material development oxygen carrier has been prepared using commercial available materials and methods. Representative testing at various scales and including at 120 kW pilot plant scale provided valuable data on performance under various normal and off-normal conditions, and input for future scale up. All in all this technology is well positioned for further development and demonstration.

TECHNOLOGY OUTLOOK

How does this Chemical-Looping Combustion technology compare with other Chemical Looping technologies? At few occasions challenges were made such as:

- Only pressurised CLC with combined cycle can achieve high gas to power efficiency.
- Apply the technology for solid fuels such as coal etc. For these fuels, the steam boiler power systems compete with integrated gasification combined cycle concept.

For its first designated application, replacing a refinery boiler, the technology would seem a viable option [6]. Next to ascertain that this type of application has sufficient potential and probability of success to justify the development efforts for technology developers and energy industry. The pressurised CLC and solid fuel CLC are under development elsewhere. Timelines are different, and for solids fuel also the oxygen carrier material will most likely be different.

Another longer term outlook for chemical looping is the one where partial oxidation of the fuel is targeted with help of an oxygen carrier, either for syngas, hydrogen or power production. This is one of the so-called Chemical-Looping Reforming concepts that has been addressed in the CACHET project, and is found elsewhere in this book [7].

ACKNOWLEDGEMENTS

Chemical-Looping Combustion CO_2-Ready Gas Power (CLC GP) is a EU-financed research-project, Contract Number 019800. The project was also part of Phase 2 of the CO_2 Capture Project (CCP2) through Shell.

REFERENCES

1. Hurst, p. and Miracca, I, 2005. Chemical looping Combustion (CLC) Oxyfuel Technology, in Thomas, D. C. (ed.) 2005. Carbon Dioxide Capture for Storage in Deep Geologic Formations – Volume 1, Elsevier.
2. Morin, J-X. and Beal, C., 2005. Chemical Looping Combustion of refinery Fuel Gas with CO_2 Capture, in Thomas, D. C. (ed.) 2005. Carbon Dioxide Capture for Storage in Deep Geologic Formations – Volume 1, Elsevier.
3. Linderholm, C., Lyngfelt, A., Beal, C., Trikkel, A., Kuusik, R., Jerndal, E. and Mattisson, T. 2009. Chemical Looping Combustion with natural gas using spray-dried NiO-based oxygen carriers, in Eide, L.I. (ed.) 2009, Carbon Dioxide Capture for Storage in Deep Geologic Formations, Volume 3, CPL Press.
4. Adánez, J., García-Labiano, F., Abad, A., de Diego, L., Gayán, P. and Dueso, C., 2009, NiO-based oxygen carriers impregnated on Al_2O_3-based materials for Chemical Looping Combustion, in Eide, L.I. (ed.) 2009, Carbon Dioxide Capture for Storage in Deep Geologic Formations, Volume 3, CPL Press.
5. Pröll, T., Kolbitsch, P., Bolhàr-Nordenkampf, J. and Hofbauer, H., 2009 Demonstration of Chemical Looping Combustion at relevant operating conditions, in Eide, L.I. (ed.) 2009, Carbon Dioxide Capture for Storage in Deep Geologic Formations, Volume 3, CPL Press.
6. Melien, T. and Brown-Roijen, S., 2009 Economics, in Eide, L.I. (ed.) 2009, Carbon Dioxide Capture for Storage in Deep Geologic Formations, Volume 3, CPL Press.
7. Rydén, M., Lyngfelt, A., Schulman, A., de Diego, L., Adánez, J., Ortiz, M., Pröll, T., Bolhár-Nordenkampf, J., and Kolbitsch, P., 2009, Developing chemical looping stean reforming and chemical looping autothermal reforming, in Eide, L.I. (ed.) 2009 Carbon Dioxide Capture for Storage in Deep Geologic Formations, Volume 3, CPL Press.

Carbon Dioxide Capture for Storage in Deep Geologic Formations, Volume 3
L.I. Eide (Ed.)

Chapter 6

CHEMICAL LOOPING COMBUSTION WITH NATURAL GAS USING SPRAY-DRIED NiO-BASED OXYGEN CARRIERS

Carl Linderholm[1], Anders Lyngfelt[1], Corinne Béal[3], Andres Trikkel[2], Rein Kuusik[2], Erik Jerndal[1], Tobias Mattisson[1]
[1]Chalmers University of Technology, 41296 Göteborg, Sweden
[2]Tallinn University of Technology, Ehitajate 5, 19086 Tallinn, Estonia
[3]Alstom Power Boilers, 23/25 Ave. Morane Saunier, 92 364 Meudon La Forêt, France

ABSTRACT: The work presented in this chapter demonstrates the economical feasibility of making a good oxygen carrier from commercial raw materials using a commercial production method, i.e. spray-drying.

A batch fluidized-bed reactor was used for an extensive screening of many NiO-based oxygen carriers. This screening process led to the production of two major particle batches, which were used in continuous chemical looping experiments. High-temperature experiments in a batch-fluidized bed verified the thermal durability of the particles. The most important result presented here concerns long-term operation (> 1000 h) of a 10-kW_{th} chemical looping combustor using spray-dried NiO-based oxygen carriers. Conversion of the fuel was good, and increased with (a) decreased circulation, and (b) increased fuel-reactor temperature. Combustion efficiency close to 99% was accomplished using these spray-dried particles. At the end of the test series, the continuous loss of fine material was 0.003%/h, which corresponds to a particle life time of 33000 h. No decrease in reactivity was seen during these long-term tests. The fuel used in the experiments was natural gas and methane.

INTRODUCTION

In order to bring chemical looping combustion (CLC) technology to the commercial level, it is primarily necessary to demonstrate that oxygen carriers can be produced with commercial methods and with materials available at reasonable cost, and secondly to verify the durability of these materials in long-term operation. Although there have been several investigations in continuous reactors earlier [1,2,3,4], the duration of the tests were often limited and most of the oxygen carrier particles were produced with non-commercial and expensive methods.

The purpose of the work presented here was to produce a number of minor batches of NiO-based particles; identify the best-performing spray-dried particle through an extensive screening process in a batch fluidized-bed reactor; produce a larger batch of this particle; evaluate this oxygen carrier by subjecting it to (a) a CLC environment for > 1000 h, (b) high-temperature testing, and (c) attrition tests.

The work presented here was part of the EU project CLC Gas Power (CLC GP), which is described in [5] along with a brief summary of the CLC technology. Other work under CLC GP can be found in [6,7].

PRODUCTION AND SCREENING OF OXYGEN CARRIERS

In the first phase of the project approximately 40 different oxygen carriers based on NiO with $NiAl_2O_4$ were prepared by freeze granulation [8]. Here, different commercially available NiO and α-Al_2O_3 powders were used in the preparation stage. The oxygen carrier materials were investigated with respect to parameters important for CLC, such as reactivity under alternating oxidizing and reducing conditions, mechanical strength and defluidization phenomena. The most promising materials were then prepared by VITO in Belgium using spray-drying, a commercial method of particle production. The produced particles were first evaluated in a 300-W_{th} CLC reactor system, and finally subjected to long-term testing in a 10-kW_{th} chemical looping combustor. Some tests were also performed in a 15 kW_{th} attrition rig. Pröll et al. [6] describes the operation of a 100 kW_{th} CLC pilot constructed in Vienna, which used the same kind of spray-dried, NiO-based materials.

Particle production using industrial methods

Oxygen-carrier particles with high sphericity, good free-flowing properties and homogeneity on the micro-scale, were prepared by the industrial spray-drying method, using commercial raw materials. In order to do so, a powder mixture of NiO, α-Al_2O_3 or $MgAl_2O_4$ and in some cases with addition of MgO and $Ca(OH)_2$ were dispersed in deionised water with the necessary organic additives. A further description of the raw materials used can be found in the papers by Jerndal et al. [9,10] Appropriate amounts of the above materials were weighed before being suspended in deionised water. The suspension was homogenized either by milling in a planetary ball mill for small quantities or by means of a horizontal attrition mill for larger amounts. The water-based suspension was continuously stirred with a propeller blade mixer while being pumped to the 2-fluid spray dry nozzle, positioned in the lower cone part of the spray drier (type 6.3 -SD, Niro, Denmark). After spray drying, the fraction between 106 and 212 μm was separated from the rest of the spray dried product by sieving the chamber fraction. In order to obtain oxygen carrier particles with sufficient mechanical strength, sintering was performed in air at top temperatures in the range of 1300°C to 1500°C for 4 hours, using high-temperature furnaces (Entech, Sweden; Bouvier).

Oxygen carrier screening

The oxygen carriers produced by freeze-granulation and spray-drying were tested with respect to physical properties, chemical composition, performance during reducing and oxidizing conditions as well as rate of reduction. The reactivity investigation was carried out in a batch fluidized bed reactor where the oxygen carriers were exposed to alternating CH_4 and 5% O_2. The oxygen carriers prepared by spray-drying displayed a remarkable similarity to oxygen carriers prepared from the same raw material by freeze-granulation [10]. Almost all of the oxygen carriers prepared showed very high reactivity with methane. The mechanical strength and defluidization behavior varied between the tested materials. The defluidization of these oxygen carriers was most likely to occur for highly reduced particles, at low fluidizing velocities. The apparent density and crushing strength of the oxygen carriers could be increased by increasing the sintering temperature. However, the fraction of unreacted CH_4 was fairly unchanged when the sintering temperature was increased. The apparent density and crushing strength could also be increased by increasing the sintering time. Furthermore, increasing the sintering time resulted in a clearly improved conversion of CH_4.

A material based on Novamet refractory grade NiO and Almatis 3000SG Al_2O_3 was chosen to be produced for initial large-scale production. This material, referred to as N-VITO, had a combination of high reactivity with methane, high mechanical strength and low tendency for defluidization. SEM images of fresh N-VITO particles can be seen in Figure 1.

It was also found that the addition of MgO or the use of $MgAl_2O_4$ as support material improved the methane conversion. Therefore, an additional large batch of material was produced, which was similar to the N-VITO oxygen carrier, but with $5\%_{mass}$ MgO added during the preparation stage, hence the denotation N-VITOMg.

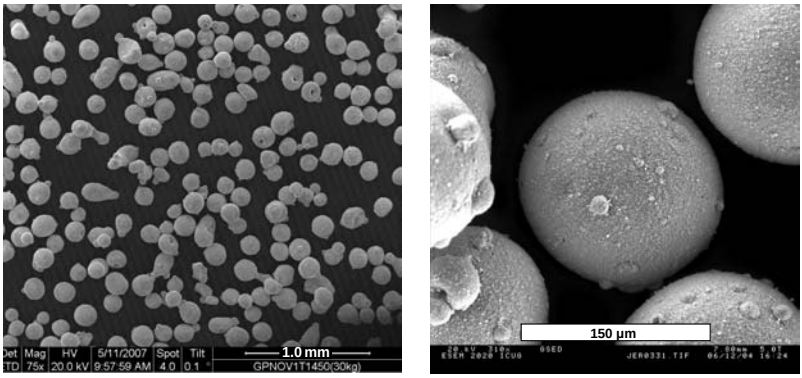

Figure 1. SEM images of fresh N-VITO particles.

Investigations of particle mixtures

It was found that N-VITO had good oxygen-transport characteristics, but that methane conversion could be improved by the addition of MgO [9]. The particle with MgO addition, on the other hand, showed excellent methane conversion coupled to decreased oxygen-transport capability, especially at lower temperature. Therefore it was decided to investigate the performance of a mixed batch, i.e. $50\%_{mass}$ N-VITO and $50\%_{mass}$ N-VITOMg, in a batch fluidized-bed as well as a small CLC unit.

Experiments in the batch reactor evaluated the performance of the two different spray-dried particles; individually and mixed. The $50/50_{mass}$-mixture of the two particles resulted in a potent oxygen-carrier batch with the desired qualities [11]. Results from the batch tests are depicted in Figure 2. The solids conversion, X, is defined as the ratio of the amount of available oxygen present in the carrier and the amount of available oxygen present in the carrier when fully oxidized,

$$X = \frac{m_{actual} - m_{red}}{m_{ox} - m_{red}} \qquad \text{Equation 1}$$

where m_{actual} is the actual mass of the carrier in its partially oxidized state, m_{ox} is the mass of the sample when fully oxidized, and m_{red} the mass of the sample in the fully reduced form.

The batches were exposed alternately to 5% O_2 in N_2 and 100% CH_4, thus simulating the cyclic conditions of a chemical looping combustion system. The experimental temperature is either 850°C (Figure 2a) or 950°C (Figure 2b). The same temperature is used for both oxidation and reduction. It should be noted that of the three oxygen-carrier systems, N-VITOMg has the highest fuel conversion to CO_2 at high X, N-VITO has the highest fuel conversion to CO_2 at low X, whereas the mixture displays the highest CO_2 yield at "medium" particle conversion. This is most evident at 850°C.

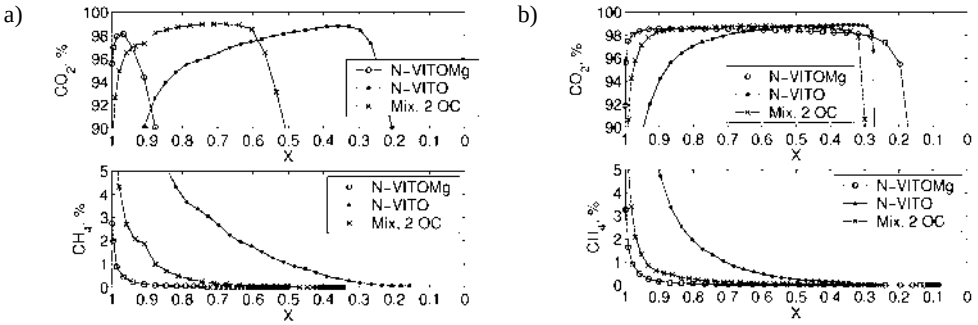

Figure 2. Fractions of CO_2 and CH_4 in batch-reactor tests. a) 850°C, b) 950°C. [11]

Experiments at 315 W in the small continuous unit were conducted in order to verify the results from the batch tests. N-VITO was used “alone” in one experimental series, and in another it was mixed with an equal mass share N-VITOMg. Results showed that the operation was more stable and that better fuel conversion was achieved when the mixture of the two oxygen carrier particles was used. With the mixture, the methane fraction in the exhaust gas could be brought down to < 0.1% while still maintaining a low CO fraction at the outlet of the fuel reactor. In other words, during optimal fuel conversion, the composition of carbon containing gases from the FR was around 99% CO_2, 0.1% CH_4 and 0.9% CO.

ATTRITION RIG

A 15 kW_{th} CLC pilot of has been built by Alstom in order to qualify the attrition rate of different types of particles. This rig is representative of attrition in industrial operating conditions and especially of high-velocity attrition processes. It is based on two integrated circulating fluidized beds.

In order to better understand some aspects of the design of the attrition pilot, a preliminary test rig in ambient operating conditions ("cold-flow model") has been built. This model has transparent walls allowing the visualization of solids flow. It has been designed in such a way that its fluid dynamic conditions could be rather close to those used in the hot attrition pilot. Figure 3 displays the cold-flow model.

Description of the hot attrition rig

The hot attrition rig consists mainly of two integrated fluidized bed reactors: the fuel reactor (FR) and the air reactor (AR) with their associated equipments: cyclone and seal-pot. The fuel reactor is fluidized by a mixture of natural gas and CO_2, the air reactor is fluidized by air. High-efficiency cyclones at the top of the reactors separate oxygen carriers from the gas stream. The collected solids fall through a down-comer to a seal-pot with a double outlet: one bringing the solids back to the same reactor, one bringing the solids to the second reactor. The seal pots are fluidized with CO_2. The hot flue gas leaving the AR and FR cyclones are cooled, filtered by a cyclone and then analyzed. The air reactor and the fuel reactor are electrically heated to maintain the required operating temperatures. The attrition rig is shown in Figure 4.

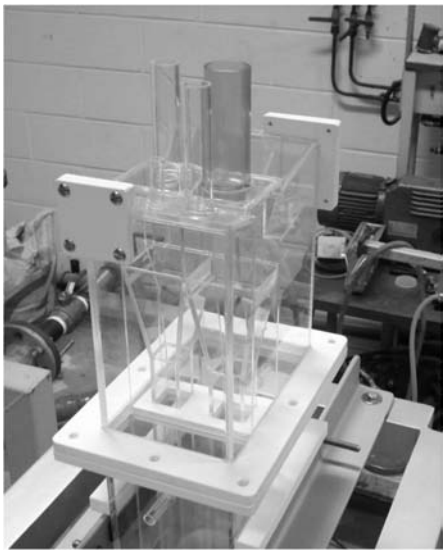

Figure 3. Cold-flow model.

Figure 4. Attrition rig.

Experimental and results

Four different oxygen carriers have been tested: two products prepared by spray-drying; one product prepared by impregnation and one prepared by freeze-granulation. The conducted tests allowed characterization of the optimal operating conditions concerning methane conversion to CO_2 in the Circulating Fluidized Bed (CFB) CLC pilot. Some trends regarding material properties could be recognized (reactivity, attrition, ageing). Methane conversion of about 99% was reached during stable conditions in the best cases. The production of fines during a 30-h test period was small: less than 1/2000 of total solids mass per hour.

LONG-TERM INTEGRITY TESTING IN A 10-kW REACTOR SYSTEM

From the screening phase of the project the N-VITO particle sintered at 1450°C was selected to be investigated for long-term operation (> 1000 h) with natural gas and study changes with respect to reactivity and physical characteristics of the particle. This study was performed in Chalmers 10 kW unit, and 1016 h of fuel operation were achieved [12]. The first 405 h were accomplished using a single batch of N-VITO. The last 611 h were achieved using a $50/50_{mass}$-mixture of the first batch, i.e. particles taken from the previous 405 h of operation, and a second batch (N-VITOMg), which was very similar in composition but with an addition of MgO, as described above. The gas conversion was generally high, see Figure 5. The fraction of unreacted CH_4 was 2-4% using the N-VITO batch, but decreased to below 1% after addition of the new particles, as can be seen in Figure 5. Combustion efficiency close to 99% was accomplished using the particle mixture, which is also shown in Figure 5. The combustion efficiency is defined here as a function of the amounts and lower heating values of the unreacted gases, compared to those of the fuel input.

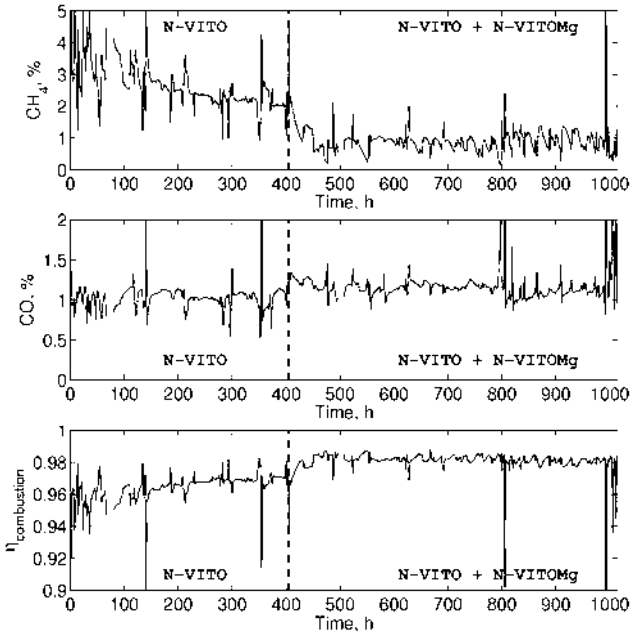

Figure 5. Fractions of CH_4 and CO plotted along with the combustion efficiency against time. [12]

No decrease in reactivity of the oxygen carrier was seen during the test period. No gas leakage between the reactors was detected. Agglomeration of particles occurred on some occasions. The agglomerates were soft, and could be crushed and reintroduced into the reactor system. During the 1016 h of experiments in the 10 kW unit, the loss of fines decreased slowly throughout the test period. An estimated particle life time of 33000 h was calculated from the loss of fines [12].

The particle attrition rate in the 10 kW pilot should be comparable to that expected in a full-scale unit, considering the velocities in the reactor system. The velocity in the riser is approximately 3 m/s, the cyclone inlet velocity is approximately 7 m/s, and the velocity at the outlet of the air distribution nozzles in the air reactor reaches a maximum of 40 m/s. Hence, the maximum nozzle outlet velocity is higher than the corresponding one in a large-scale system, while velocities in the riser and at the cyclone inlet are somewhat lower than in a large-scale system.

HIGH-TEMPERATURE EXPERIMENTS

It is important that the oxygen carriers have the ability to withstand high temperatures. Hence, thermal resistance of several of the most promising oxygen carrier samples was tested using a ceramic fluidized-bed reactor [13]. It was shown that in reducing atmosphere the spray-dried N-VITO particles started to agglomerate at 1125 °C and defluidized at 1150°C. The particles doped with 5% MgO, i.e. N-VITOMg, did not form agglomerates and did not defluidize in any of the tests up to 1175-1190°C, neither in oxidizing nor reducing conditions.

It can be seen in Figure 6 that at 1150°C molten phase is present on the surface of the particles. Several cuts along the cross-section were made to find exactly the level of some connection between the agglomerated particles. As can be seen in Figure 6, the bridges formed between the particles are quite small, which may explain the weakness of the agglomerates – they can be very easily crushed. The composition of the connecting bridge corresponds to pure Ni phase, as determined by EDX.

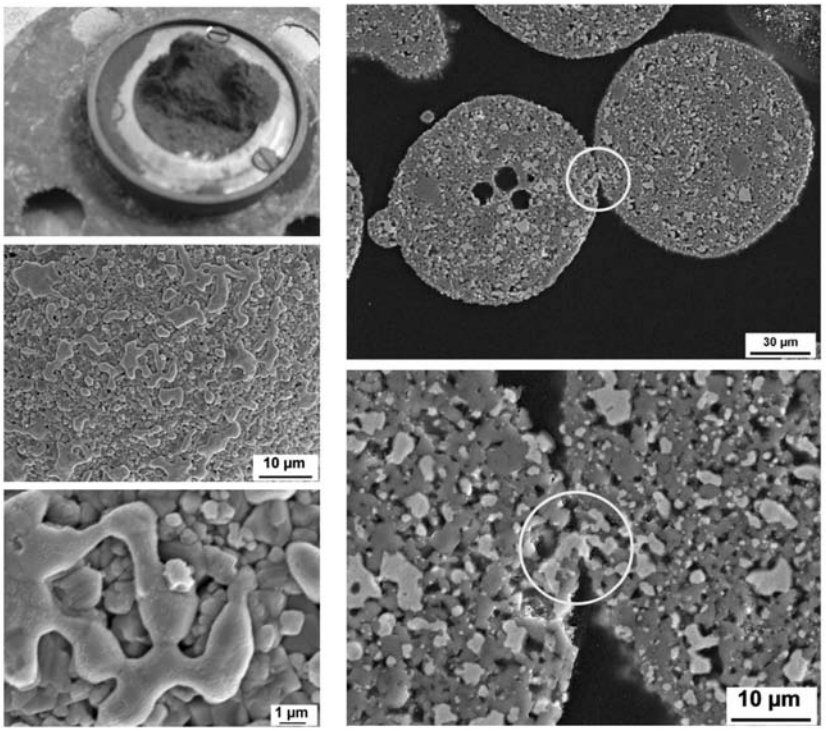

Figure 6. Particles which defluidized at 1150°C. Top left: agglomerate on the gas distributor; Left: surface of a particle; Right: cross section of two particles connected with a "bridge". [13]

CONCLUSIONS

The work presented here has shown that it is possible to produce a good oxygen carrier from commercial raw materials using spray-drying. The addition of MgO or $MgAl_2O_4$ to the support material of the oxygen carrier proved beneficial for the methane conversion. The most important finding presented here is the successful long-term operation (> 1000 h) using NiO-based particles manufactured by spray-drying of commercial raw materials.

ACKNOWLEDGEMENTS

The work described in this chapter was carried out within the EU-financed research-project CLC GP (Chemical- Looping Combustion CO_2-Ready Gas Power), Contract Number 019800. The project was also part of Phase 2 of the CO_2 Capture Project Phase 2 (CCP2) through Shell. The particles were supplied by VITO (Flemish institute for technological research) in Belgium.

This Chapter contains figures that originally appeared in Energy Procedia Vol 1, Issue 1, Greenhouse Gas Control Technologies 9, Proceedings of the 9th International Conference on Greenhouse Gas Control Technologies (GHGT-9), 16-20 November 2008, Washington DC, USA, which was published by Elsevier Ltd.

REFERENCES

1. Lyngfelt, A., and Thunman, H. Construction and 100 h of operational experience of a 10-kW chemical looping combustor. Chapter 36 in *Carbon Dioxide Capture for Storage in Deep Geologic Formations - Results from the CO_2 Capture Project, Volume 1 – Capture and Separation of Carbon Dioxide From Combustion Sources.* Ed.: Thomas, D. Elsevier Science, London 2005, pp. 625-646.
2. Ryu, H. J., Bae, D. H., and Jin, G. T. 2003. Effect of temperature on reduction reactivity of oxygen carrier particles in a fixed bed chemical looping combustor. *Kor J Chem Eng* 20:960–966.
3. de Diego, L. F., García-Labiano, F., Gayán, P., Celaya, J., Palacios, J. M., Adanez, J. 2007. Operation of a 10 kW_{th} chemical looping combustor during 200 h with a CuO-Al_2O_3 oxygen carrier. *Fuel* 86:1036-1045.
4. Linderholm, C., Abad, A., Mattisson, T., Lyngfelt, A. 2008. 160 h of chemical looping combustion in a 10 kW reactor system with a NiO-based oxygen carrier. *International Journal of Greenhouse Gas Control* 2:520-530.
5. Assink, J. and Beal, C. 2009. Chemical looping combustion (CLC) technology summary, in Eide, L.I. (ed.) 2009, Carbon Dioxide Capture for Storage in Deep Geologic Formations, Volume 3. CPL Press.
6. Pröll, T., Kolbitsch, P., Bolhàr-Nordenkampf, J. and Hofbauer, H. 2009. Demonstration of Chemical Looping Combustion at relevant operating conditions, in Eide, L.I. (ed.) 2009, Carbon Dioxide Capture for Storage in Deep Geologic Formations, Volume 3. CPL Press.
7. Adánez, J., García-Labiano, F., Abad, A., de Diego, L., Gayán, P. and Dueso, C. 2009. NiO based oxygen carriers impregnated on Al2O3-based materials for chemical looping Combustion, in Eide, L.I. (ed.) 2009, Carbon Dioxide Capture for Storage in Deep Geologic Formations, Volume 3. CPL Press.
8. Jerndal, E., Mattisson, T. and Lyngfelt, A. 2008. Investigation of Different $NiO/NiAl_2O_4$ Particles as Oxygen Carriers for Chemical -Looping Combustion. *Accepted for publication in Energy&Fuels*.
9. Jerndal, E., Mattisson, T., Thijs, I., Snijkers, F., and Lyngfelt, A. 2008. NiO particles with Ca and Mg based additives produced by spray-drying as oxygen carriers for chemical-looping combustion. GHGT-9: 9th International Conference on Greenhouse Gas Control Technologies, 16-20 November 2008.
10. Jerndal, E., Mattisson, T., Thijs, I., Snijkers, F., Lyngfelt, A. 2008. Investigation of $NiO/NiAl_2O_4$ Oxygen Carriers for Chemical Looping Combustion Produced by Spray-Drying. *Submitted for publication*.
11. Linderholm, C., Jerndal, E., Mattisson, T., Lyngfelt, A. 2008. Investigation of Ni-based mixed oxides in a 300 W chemical looping combustor. *Submitted for publication.*
12. Linderholm, C., Mattisson, T., Lyngfelt, A. 2009. Long-term integrity testing of spray-dried particles in a 10-kW chemical looping combustor using natural gas as fuel. *Accepted for publication in Fuel.*
13. Kuusik, R., Trikkel, A., Lyngfelt, A., Mattisson, T. 2008. High temperature behaviour of NiO-based oxygen carriers for Chemical Looping Combustion. GHGT-9: 9th International Conference on Greenhouse Gas Control Technologies, 16-20 November 2008.

Carbon Dioxide Capture for Storage in Deep Geologic Formations, Volume 3
L.I. Eide (Ed.)

Chapter 7

DEMONSTRATION OF CHEMICAL LOOPING COMBUSTION AT RELEVANT OPERATING CONDITIONS

T. Pröll, P. Kolbitsch, J. Bolhàr-Nordenkampf and H. Hofbauer
Vienna University of Technology, Institute of Chemical Engineering,
Getreidemarkt 9/166, 1060 Vienna, Austria

ABSTRACT: A pilot plant for chemical looping combustion (CLC) of gaseous fuels has been designed, built and operated. The system is designed for natural gas at a fuel power of 120 kW and a global excess air ratio of 1.1. It consists of two interconnected circulating fluidized bed (CFB) reactors. The primary CFB reactor, which represents the air reactor for CLC, determines global solids circulation of the dual fluidized bed reactor system. The secondary CFB reactor is operated as the fuel reactor in the sense of CLC and may be optimized with respect to gas-solids contact. Gas phase leakages between the reactors are effectively prevented using steam fluidized loop seals. In order to keep the desired operating temperature, heat is withdrawn from the reactor system via cooling jackets attached to the air reactor. Solids samples taken out of the loop seals during operation were analyzed to determine the mean degree of oxidation after each reactor and of the global solids circulation rate. Experimental runs are reported in the range of 60-145 kW fuel power and at operating temperatures in the range of 800-950°C. High global solids circulation rates up to 1.8 kg/s (13 kg/MJ_{th}) are observed. The heights of the two riser reactors are relatively low, however, the results show satisfactory fuel conversion using a nickel oxide based oxygen carrier. The system may be a suitable candidate for further scale up to industrial size.

INTRODUCTION

Chemical looping combustion (CLC) is a method of indirect combustion where fuel and air are never mixed. The concept has therefore been classified as “unmixed combustion” and belongs to second generation carbon capture processes [1]. Metal oxides are used to selectively transport oxygen from air to fuel in the solid phase. If a suitable metal oxide is used as the oxygen carrier, the CLC system can be operated in such a way that the exhaust gas of the fuel reactor ideally consists of CO_2 and H_2O only and allows for subsequent water condensation, compression, and storage of pure CO_2. The energy-consuming gas-gas separation steps that are characteristic for the three main first generation carbon capture routes post combustion capture (CO_2 separation from flue gas), pre-combustion capture (CO_2 separation from syngas) and oxyfuel combustion (air separation) are inherently avoided. Therefore, CLC is discussed as one of the most energy-efficient approaches to carbon capture from power production or as chemical looping reforming (CLR) for fuel upgrading [2]. CLC is a typical dual fluidized bed technology where chemically active bed material, that is most suitably a metal oxide, is circulated between two reaction zones that are separated with respect to the gas phase. It was initially proposed as early as 1954 for production of pure CO_2 from any oxidizable carbonaceous material [3]. Then, the concept was studied theoretically as a means to improve the reversibility of combustion [4–6]. CLC has since then been identified as a promising technology for CO_2 capture from power plants, where 100% carbon capture can be achieved without a significant energy penalty [7–12]. With respect to CLC reactor system development, there has only been a limited research focus on scalability to industrial size. In addition to further

improvement of particles, optimization of CLC reactor systems suitable for scale-up may gain importance in CLC technology development.

The work presented here was part of the EU project CLC Gas Power (CLC GP) [13], of which operation of CLC under relevant conditions and in a scalable system was one of the main objectives. Other work under CLC GP can be found in [14,15].

THE DUAL CIRCULATING FLUIDIZED BED REACTOR SYSTEM

The basic requirements for Dual Circulating Fluidized Bed (DCFB) CLC systems include

- A high rate of global solids circulation which is required in order to provide enough oxygen for fuel combustion and to keep the temperature difference between air reactor and fuel reactor reasonably small.
- Excellent gas–solids contact in both reactors that is required to obtain satisfactory gas conversion. This is especially true for the fuel reactor where significant amounts of unconverted fuel will hardly be tolerable in industrial applications.
- Low particle attrition rates that are appreciated especially if expensive oxygen carriers are used.

The concept studied here represents a combination of the existing practice in CLC technology, where a bubbling fluidized bed fuel reactor is integrated within the solids return loop of a circulating fluidized bed air reactor [16], with the idea of using two scale-up ready circulating fluidized bed reactors for both air reactor and fuel reactor. In the dual circulating fluidized bed (DCFB) system according to Figure 2, the two CFB reactors are interconnected via a fluidized loop seal in the bottom region of the reactors (lower loop seal). The solids transport capacity of the air reactor determines global solids circulation. The solids are separated from the air reactor exhaust stream in a cyclone separator and pass over through a fluidized loop seal (upper loop seal) into the fuel reactor. From there, the global solids loop closes via the lower loop seal. The fuel reactor features a circulation loop in itself (fuel reactor cyclone and internal loop seal) and may be optimized with respect to good gas–solid contact and low particle attrition rates.

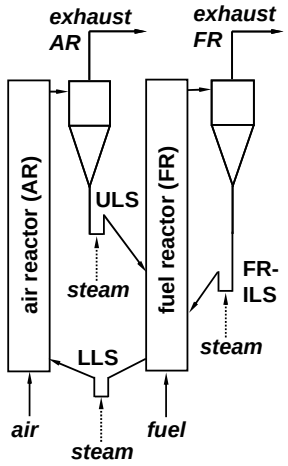

Figure 1. Dual circulating fluidized bed (DCFB) reactor system
(ULS=upper loop seal, LLS=lower loop seal, FR-ILS= fuel reactor internal loop seal).

The global circulation rate can be controlled by staged fluidization of the air reactor. This is common practice in CFB technology. The direct hydraulic connection of the two CFB reactors allows stable solids distribution in the overall system. Imposing moderate pressure differences between the two reactors changes the theoretical solids levels in the system. This can be done by changing the backpressure from the exhaust gas lines, allowing active control of the solids hold-up in each reactor.

A cold flow model of the DCFB unit has been operated prior to construction of the hot pilot plant. The results show a high rate of global solids circulation between air reactor and fuel reactor in the range of an air reactor net solids flux of 60-100 $kg \cdot m^{-2} \cdot s^{-1}$. Staged fluidization of the air reactor allows active control of the global circulation. The pressure profiles measured in the cold flow model indicate a fast fluidized regime in the air reactor and a pronounced dense bottom region with a relatively lean upper zone in the fuel reactor [17].

EXPERIMENTAL

Design of the 120 kW pilot plant

The DCFB pilot plant for CLC of gaseous fuels has been designed and built with the hot commissioning phase completed in early 2008. The operating parameters of the design case of the pilot plant are reported in Table 1.

In order to remove the heat released from combustion and to control the system temperature independently from the global air ratio, the air reactor shell is equipped with cooling jackets. These cooling jackets are operated with air and humidified air as coolants. The cyclone separators are designed according to Hugi and Reh [18]. The loop seals are fluidized with steam in nominal operation and could be switched to air fluidization during start-up and shut-down.

Table 1. Design case operating parameters of the 120 kW CLC pilot plant.

Parameter	Unit	Air reactor	Fuel reactor
reactor height	m	4.1	3.0
reactor inner diameter	mm	150	159
inlet gas flow	Nm^3/h	138.0	12.0
outlet gas flow	Nm^3/h	113.9	35.9
temperature in reactor	K	1213	1123
design fluid for calculation		depleted air	H_2O/CO_2 = 2/1
particle size	µm	120	
particle apparent density	kg/m^3	3200	
particle sphericity	-	0.99	
Archimedes number		7.55	9.13
superficial velocity	m/s	7.32	2.08
ratio U/U_{mf}	-	1280.4	315.4
ratio U/U_t	-	15.5	3.8
fuel power (natural gas)	kW	120	
lower heating value of fuel	MJ/kg	48.8	
design air/fuel ratio λ	-	1.2	
design global circulation rate	kg/s	0.76	

The exhaust gas streams of the two reactors are cooled separately to about 300°C and analyzed on-line to evaluate the conversion of the fuel as well as the leakages of the loop seals. The cooled exhaust gas streams pass valves which allow for imposing defined backpressure on each reactor. The exhaust gas streams are then mixed and sent to a natural gas fired post combustion unit, cooled again, filtered and sent to the chimney. Solids samples are collected from the upper and the lower loop seal during operation. This allows accurate interpretation of experimental results (oxygen carrier oxidation states and solids circulation rate).

Oxygen carrier used

The oxygen carrier particles used in the 120 kW pilot plant have been developed within the project by Chalmers University of Technology, Sweden and manufactured by the Flemish Institute for Technological Research (VITO), Belgium. A first batch of particles, oxygen carrier A (OC-A), is based on NiO and α-Al_2O_3. After sintering the particles consist of NiO and inert $NiAl_2O_4$. A second batch of Ni-based oxygen carrier (OC-B) was provided with the basic ingredients NiO, α-Al_2O_3 and MgO. Here, $MgAl_2O_4$ is additionally present after sintering. In the experiments shown here, a 50:50 (mass based) mixture of OC-A and OC-B is used. More information regarding these oxygen carriers can be found in [14].

RESULTS AND DISCUSSION

Chemical looping combustion performance quantification

The most important performance criterion of CLC systems is the degree of fuel conversion in the fuel reactor and the selectivity of the reactions to yield CO_2. The conversion of a fuel species is generally defined as

$$X_i = 1 - \frac{\dot{n}_{FRout} \cdot y_{i,FRout}}{\dot{n}_{FRin} \cdot y_{i,FRin}} \qquad \text{Equation 1}$$

The CO_2 yield from the fuel reactor is defined according to

$$\gamma_{CO_2} = \frac{\dot{n}_{FRout} \cdot y_{CO_2,FRout}}{\dot{n}_{FRin} \cdot \sum_i \left(\xi_{C,i} \cdot y_{i,FRin} \right)} \qquad \text{Equation 2}$$

The average degree of oxidation of the oxygen carrier particles is defined as

$$X_S = 1 - \frac{m_{ox} - m}{m_{ox} \cdot R_0} \qquad \text{Equation 3}$$

where the oxygen transport capacity R_0 is defined as the relative mass decrease when bringing the particles to a most reduced form:

$$R_0 = \frac{m_{ox} - m_{red}}{m_{ox}} \qquad \text{Equation 4}$$

X_S can be determined from solids samples by comparison of mass to mass after full oxidation and is a relevant parameter in order to characterize chemical looping operation. Detailed information on solids sampling has been reported by Kolbitsch et al. [19].

Baseline case for variations

The baseline case for the fuel reactor temperature and fuel input is specified in Table 2. In terms of fuel power and global air/fuel ratio, the conditions deviate slightly from the design case reported in Table 1. The solids inventory present in the two reactors can be determined from the pressure difference between the bottom and top of the reactors. These values for the baseline case are shown in Table 3.

Table 2. Nominal operating conditions for parameter variations.

Parameter	Unit	Value
fuel power input	kW	145
global stoichiometric air ratio λ	-	1.1
fuel reactor temperature	°C	900

Table 3. Actual solids inventory.

Parameter	Unit	Air reactor	Fuel reactor
solids inventory	kg	11	22
specific solids inventory	kg/MW	75	150

Variation of the operating temperature

The fuel reactor temperature was varied between 800°C and 950°C. Four points were operated for at least 30 minutes to obtain steady state conditions at least with respect to temperature and gas phase compositions. Average values over the last 10 minutes of each steady state point are sampled for evaluation. Figure 2a shows the global solids circulation rate and the degree of oxidation for the temperature variation runs. As expected, fluid dynamics and, thus, the solids circulation rate are not significantly influenced by temperature. The degree of oxidation X_S is generally far from fully oxidized particles, namely in the range of 0.5.

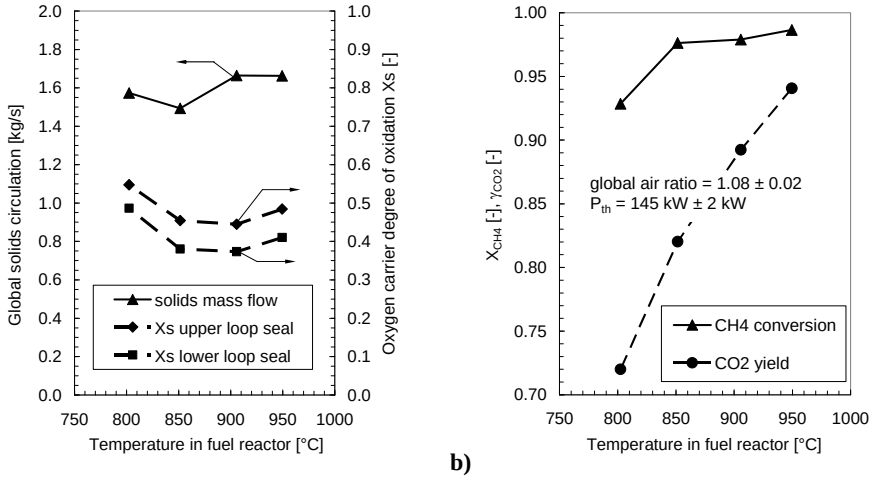

Figure 2: Variation of operating temperature: a) Solids circulation and degree of oxidation; b) Methane conversion and CO_2 yield.

This is a result of the relatively low particle residence time in both reactors and can be expected in the same way for large scale facilities [20]. It is observed that the trend for X_S shows a minimum between 850 and 900°C. This is especially interesting in combination with gas phase conversion data of the same run shown in Figure 2b.

While the CH_4 conversion is high above 850°C and significantly drops only for the point at 800°C, the CO_2 yield shows a high sensitivity towards temperature in the whole range. This means that even though the degree of carrier oxidation is increased at lower temperatures the CO_2 yield drops. Since there are only three carbon-containing species CH_4, CO and CO_2, the gap between CH_4 conversion and CO_2 yield reflects the net yield of CO. According to Figure 2b, the CO yield decreases with increasing temperature, an effect that can be attributed to increased reactivity of the oxygen carrier with increasing temperature. It must be mentioned that, due to generally high solids circulation rates, the temperature of the air reactor is only a few degrees (less than 10 K) higher than the temperature in the fuel reactor in all the temperature variation runs shown here.

Variation of the fuel power input

The fuel power input (i.e. the fuel flow rate) to the fuel reactor was varied while the operating temperature of the fuel reactor and the global stoichiometric air to fuel ratio were kept constant. The results of these series of runs are shown in Figure 3. The air flow into the air reactor increases with increasing fuel load because of the constant air to fuel ratio. Therefore, the air reactor entrainment increases and leads to the observed increase in global solids circulation rate (Figure 3a). The degree of oxygen carrier oxidation is relatively high at low load. A possible explanation for this behaviour is that the gas solids contact is getting specifically better in the fuel reactor with increasing load. At high load, the decreased global degree of oxidation indicates that the air reactor reactivity can potentially limit the process. The fuel conversion performance of the system during the power variation run is reported in Figure 3b. Generally, CH_4 conversion was somewhat lower and the CO_2 yield somewhat higher than in the corresponding point (900°C, 140 kW) during the temperature variation run (Figure 2). A possible explanation is that the degree of oxidation of the solids was higher in the fuel power variation run than in the temperature variation run (compare Figure 2a to 3a) by about 0.1. The reason for this could perhaps be found the "operating history" of the particles, but here is room for further research.

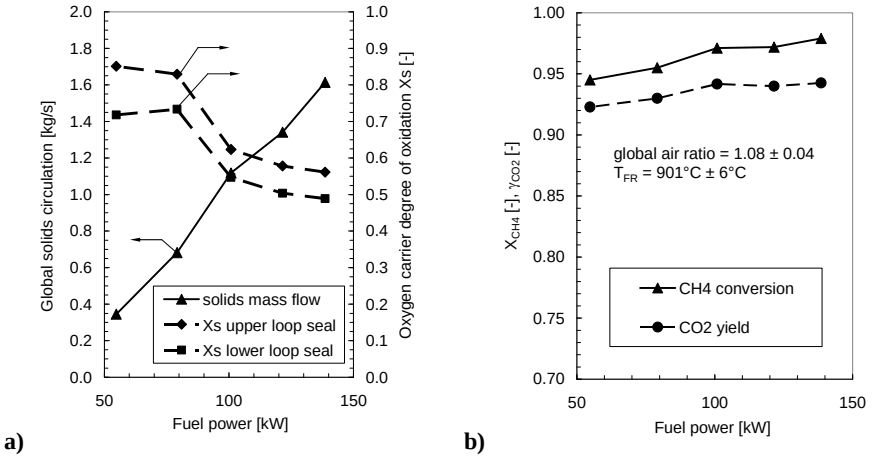

Figure 3: Variation of fuel power input: a) Solids circulation and degree of oxidation; b) Methane conversion and CO_2 yield.

A most interesting behaviour of the investigated system is observed during the power variation runs. Both the CH_4 conversion and the CO_2 yield increase with increasing fuel power. A maximum is not reached within the investigated operating range. The most likely explanation for this behaviour is that at increased fuel power, the increased gas–solids contact in the fuel reactor (due to an improved fluidization regime) over-compensates the reduced specific solids inventory. Another point is that, because of the increased global circulation rate at increased fuel power, the solids residence time is reduced and more surface-oxygen is available in the fuel reactor that is easier accessible for reactions. Obviously, with further increasing fuel power, there must be a point where either CH_4 conversion or CO_2 yield reaches a maximum. Experiments at higher fuel power than 150 kW at the pilot plant, however, will require adaptation of the cooling system and a larger natural gas compressor.

CONCLUSIONS

Chemical looping combustion (CLC) with gaseous fuels has been successfully demonstrated at a scale of 145 kW fuel power. A CLC system has been designed that consists of two circulating fluidized bed reactors interconnected in the way that only the air reactor determines the global solids circulation rate (dual circulating fluidized bed – DCFB). The system was operated at 900°C and at a global stoichiometric air to fuel ratio of 1.1. A designed NiO-based oxygen carrier was used during the experiments. The specific solids inventories in air and fuel reactor are 75 kg/MW and 150 kg/MW, respectively. Variations of operating temperature show a strong correlation between operating temperature and CO_2 yield while the primary conversion of CH_4 is less dependent on temperature. Variations of the fuel power input (i.e. of the fuel flow rate) at constant air to fuel ratio and temperature show that both CH_4 conversion and CO_2 yield are increasing with increasing load. This means that, in the range operated and with this specific oxygen carrier, performance increased with increasing fuel power even though the specific solids inventory decreased. Further investigation is required to determine optimized operating conditions for the pilot plant. It is important to observe that the riser heights of the reactors in the pilot plant are limited because of the laboratory clearance (net height fuel reactor: 3.0 m, air reactor: 4.1 m). It is anticipated that fuel conversion improves for industrial scale with riser heights of 12-20 m. As a general conclusion, the dual circulating fluidized bed system can be considered as a candidate for a next scale demonstration of CLC.

ACKNOWLEDGEMENTS

This work is part of the EU financed project CLC GAS POWER (FP6 Contract No. 019800), coordinated by Chalmers University of Technology. The project is also part of Phase 2 of CO_2 Capture Project (CCP2) through Shell.

NOTATION

m	mass	kg
$\dot{n}$	molar flow	$mol \cdot s^{-1}$
P_{th}	fuel power	W
R_0	oxygen transport capacity (mass specific)	$kg \cdot kg^{-1}$
T	temperature	K
U	superficial velocity	$m \cdot s^{-1}$
U_{mf}	(superficial) minimum fluidization velocity	$m \cdot s^{-1}$
X	chemical conversion based on initial quantity	–
X_S	solids conversion (i.e. degree of oxidation)	–
y	mole fraction in gas phase	$mol \cdot mol^{-1}$

Greek symbols

γ	chemical yield	–
λ	global stoichiometric air to fuel ratio	–
ξ_C	stoichiometric factor of carbon in fuel molecule	–

Indices

AR	air reactor
FR	fuel reactor
i	refers to chemical species
ox	refers to fully oxidized conditions
red	refers to fully reduced conditions

REFERENCES

1. Lyon R.K., Cole J.A. Unmixed combustion: An alternative to fire. *Combust. Flame.* 2000;121(1–2):249–261.
2. Bolland O. *Fundamental Thermodynamic Approach for Analysing Gas Separation Energy Requirement for CO_2 Capture Processes.* At: 8th International Conference on Greenhouse Gas Control Technologies (GHGT-8), Trondheim, Norway, 2006. Available online: folk.ntnu.no/obolland/pdf/GHGT8_Review_Lecture_Olav_Bolland.pdf
3. Lewis W.K., Gilliland E.R. *Production of pure carbon dioxide.* United States Patent No. 2665972, 1954.
4. Knoche K.F., Richter H. Verbesserung der Reversibilität von Verbrennungsprozessen, *Brennstoff-Wärme-Kraft.* 1968;20:205–210 (in German).
5. Richter H., Knoche K.F. Reversibility of combustion processes, efficiency and costing. Second Law analysis of processes. *ACS Symp. Ser.* 1983;235:71–85.
6. Ishida M., Zheng D., Akehata T. Evaluation of a chemical-looping-combustion power-generation system by graphic exergy analysis. *Energy.* 1987;12:147–154.
7. Ishida M., Jin H. A novel combustor based on chemical-looping reactions and its reaction kinetics. *Journal of Chemical Engineering of Japan.* 1994;27:296–301.
8. Ishida M., Jin H. A new advanced power-generation system using chemical-looping combustion. *Energy.* 1994;19:415–422.
9. Ishida M., Jin H. CO_2 recovery in a power plant with chemical looping combustion. *Energy Conversion and Management.* 1997;38(Suppl. 1):187–192.
10. Lyngfelt A., Leckner B., Mattisson T. A fluidized bed combustion process with inherent CO_2 separation, Application of Chemical Looping Combustion, *Chem. Eng. Sci.* 2001;56:3101–3113.

11. Wolf J., Anheden M., Yan J. *Performance Analysis of Combined Cycles with Chemical Looping Combustion for CO_2 Capture.* In: Proceedings of 18th Pittsburg Coal Conference, December 3–7, Newcastle, NSW, Australia, Session 23. 2001.
12. Ryu H.-J., Bae D.-H., Jin G.-T. *Chemical-looping combustion process with inherent CO_2 separation; Reaction kinetics of oxygen carrier particles and 50kWth reactor design.* In: The World Congress of Korean and Korean Ethnic Scientists and Engineers, Seoul, Korea. 2002:738–743.
13. Assink, J. and Beal, C., 2009, Chemical looping combustion (CLC) technology summary, in Eide, L.I. (ed.) 2009 Carbon Dioxide Capture for Storage in Deep Geologic Formations,, Volume 3. CPL Press
14. Linderholm C., Lyngfelt A., Trikkel A., Kuusik R., Jerndal E. Chemical Looping combustion with natural gas using spray-dried NiO-based oxygen carriers, 2009, in Eide, L.I. (ed.) 2009, Carbon Dioxide Capture for Storage in Deep Geologic Formations, Volume 3. CPL Press
15. Adánez, J., García-Labiano, F., Abad, A., de Diego, L., Gayán, P. and Dueso, C., 2009, NiO-based oxygen carriers impregnated on Al2O3-based materials for Chemical Looping Combustion, in Eide, L.I. (ed.) 2009, Carbon Dioxide Capture for Storage in Deep Geologic Formations, Volume 3. CPL Press
16. Lyngfelt A., Thunman H. Chemical-looping combustion: Design, construction and 100 h of operational experience of a 10 kW prototype. In: Thomas D (Ed.), Carbon Dioxide Capture for Storage in Deep Geologic Formations – Results from the CO_2 Capture Project: Vol. 1 – Capture and Separation of Carbon Dioxide from Combustion, Elsevier, London. 2004.
17. Pröll T., Rupanovits K., Kolbitsch P., Bolhàr-Nordenkampf J., Hofbauer H. Cold flow model study on a dual circulating fluidized bed (DCFB) system for chemical looping processes. *Chem. Eng. Technol.* 2009;32(3):418-424.
18. Hugi E., Reh L. Design of cyclones with high solids entrance loads. *Chem. Eng. Technol.* 1998;21(9):716-719.
19. Kolbitsch P., Bolhàr-Nordenkampf J., Pröll T., Hofbauer H. Characterization of chemical looping pilot plant performance via experimental determination of solids conversion. *Energy Fuels* 2009;23(3):1450-1455..
20. Kolbitsch P., Pröll T., Hofbauer H. Modeling of a 120kW chemical looping combustion reactor system using a Ni-based oxygen carrier. *Chem. Eng. Sci.* 2009;64:99-108.

Carbon Dioxide Capture for Storage in Deep Geologic Formations, Volume 3
L.I. Eide (Ed.)

Chapter 8

NiO-BASED OXYGEN CARRIERS IMPREGNATED ON Al_2O_3–BASED MATERIALS FOR CHEMICAL LOOPING COMBUSTION

Juan Adánez, Francisco García-Labiano, Alberto Abad, Luis de Diego,
Pilar Gayán and Cristina Dueso
Instituto de Carboquímica (CSIC), Department of Energy and Environment,
Miguel Luesma Castán 4, 50018 Zaragoza, Spain

ABSTRACT: The performance of Chemical Looping Combustion (CLC) systems using NiO-based oxygen carriers (OC) prepared by impregnation on Al_2O_3-based materials has been analyzed. γ-Al_2O_3, θ-Al_2O_3, α-Al_2O_3, $MgAl_2O_4$ and $CaAl_2O_4$ were used as supporting material. Low attrition rates and avoidance of agglomeration were found for all oxygen carriers. However, OCs prepared with γ-Al_2O_3 showed low reactivity because of the formation of the low reactive $NiAl_2O_4$ spinel compound. Higher reactivity was found for the rest of supports because the amount of $NiAl_2O_4$ was lower for α-Al_2O_3 and $MgAl_2O_4$ or even suppressed when $CaAl_2O_4$ was used as support. A NiO-based (18 wt% NiO) OC supported on α-Al_2O_3 was used in a continuously operated 500 W_{th} CLC system to burn CH_4 or gaseous mixtures of CH_4 with light hydrocarbons (C_2-C_3). All hydrocarbons were fully converted. Also the effect of minor amounts of H_2S in the fuel gas was also investigated. Deactivation of OC particles by sulphide formation was observed, and sulphur was emitted mainly as SO_2 from the air reactor. Nevertheless, the OC was regenerated after H_2S was removed. In all cases, agglomeration or carbon deposition related problems were not observed.

INTRODUCTION

In a chemical looping combustion (CLC) process, two interconnected fluidized bed (FB) reactors are used to burn a fuel (natural gas, syngas, coal, etc.) with inherently CO_2 capture. An oxygen carrier (OC) is continuously circulating between both reactors, transferring oxygen from air to the fuel. In the first reactor, so called fuel reactor (FR), the OC is reduced by the fuel gas to a lower oxidation state, being CO_2 and H_2O the reaction products. In the second reactor, so called air reactor (AR), the reduced OC is regenerated with air to its initial state. Thus, air and fuel are never mixed and the CO_2 can be easily recovered from the FR outlet gas without energetic losses [1].

In general, the OC is based on a metal oxide, e.g., CuO, NiO, CoO, Fe_2O_3, or Mn_3O_4, which is supported on an inert material, such as Al_2O_3, SiO_2 or TiO_2. Screenings to find appropriate combinations for metal and support material have been done in the past [1-3]. An OC must show high reaction rate, high conversion to CO_2 and H_2O, resistance against carbon deposition, avoidance of agglomeration and sufficient durability in successive cycles. The cost of the OC, and environmental and health aspects are also critical. For NiO-based particles, a review of suitable OCs was done by Adánez et al. [4]. NiO-based OCs have shown to be very reactive [5] with full CH_4 conversion in CLC systems. However, the reaction is not fully selective towards CO_2 and H_2O, but thermodynamic limitations results in small amounts of CO and H_2 in the FR exhaust gas. Moreover, for NiO-based OCs it must be specially analyzed the risk for carbon deposition, because metallic Ni

catalyzes the methane decomposition, or the sulphide formation if sulphur is present in the fuel gas. When Al_2O_3 was used as support material, the NiO-based OCs showed low attrition rates, avoidance of carbon deposition and no agglomeration problems. In most of the cases the reduction of NiO/Al_2O_3 particles was limited by the partial transformation of NiO into $NiAl_2O_4$ spinel compound, which has poor reactivity for CLC. However, high reactivity and low $NiAl_2O_4$ formation was found in some cases using mechanical mixing or impregnation methods or using chemically modified Al_2O_3 as support.

The objective of this work was to test the suitability of several NiO-based OCs prepared by impregnation on Al_2O_3–based materials for methane combustion in a CLC system. The performance of a promising OC selected from the prepared materials was analyzed in a 500 W_{th} CLC system. Methane and mixtures CH_4+C_2H_6 or CH_4+C_3H_8 were used as fuel gas. Moreover, the effect of operating conditions, such as the OC/fuel ratio and FR temperature, as well as the presence of sulphur in the fuel gas, on the OC performance was analyzed.

The work presented here was part of the EU project CLC Gas Power (CLC GP), which is described in [6] along with a brief summary of the CLC technology. Other work under CLC GP can be found in [7,8].

PREPARATION AND SELECTION OF THE OXYGEN CARRIERS

The NiO-based OC were prepared by impregnation on different Al_2O_3-based supports. These materials were physically and chemically characterized. Their reactivity during successive reduction and oxidation cycles was investigated for methane conversion in TGA. Gas product distribution, attrition and defluidization phenomena were also analyzed in a batch-mode FB.

Preparation of oxygen carriers

Several NiO-based oxygen carriers were prepared by ambient incipient wet impregnation (AIWI) at room temperature or by hot incipient wet impregnation (HIWI) at 353 K. A detailed description of the preparation method can be found elsewhere [9,10]. The materials for the support were γ-Al_2O_3, θ-Al_2O_3, α-Al_2O_3, $MgAl_2O_4$ and $CaAl_2O_4$. Commercial γ-Al_2O_3 particles of +100-300 μm were used as initial material. θ-Al_2O_3 and α-Al_2O_3 were obtained by calcination of the γ-Al_2O_3 particles at 1373 and 1423 K for 2 hours, respectively. $MgAl_2O_4$ and $CaAl_2O_4$ particles of +100-500 μm were prepared by the extruding commercial $MgAl_2O_4$ powder or a mixture of γ-Al_2O_3 and $CaCO_3$ powder, respectively. Also, chemically modified γ-Al_2O_3 supports were prepared by impregnation with magnesium nitrate or calcium nitrate solutions. For OC production, the support material was impregnated using a nickel nitrate solution and sintered for 1 h at temperatures ranging from 773 to 1373 K. Table 1 shows the list of the OC particles prepared. Particles with NiO content ranging from 10% to 38% could be achieved with additions of impregnations steps. The samples were designated with the NiO weight content (%), and the inert used as support. Also the preparation method and the final calcination temperature are given in the abbreviation for each OC. In the cases that γ-Al_2O_3 was modified by a thermal pre-treatment, the temperature at which this step was carried out is indicated in brackets. For example, Ni18αAl:HI:1223 means an OC with a 18% NiO on α-Al_2O_3 prepared by HIWI method and calcined at 1223 K. The crushing strength values of fresh OCs were in the range 2-5, which can be considered enough high for a OC, and it increases as the calcination temperature increases, being the highest values for particles impregnated on α-Al_2O_3.

Reactivity of the oxygen carrier materials

To analyze the reactivity of the OCs, five cycles of reduction and oxidation were carried out in a thermogravimetric analyzer (TGA) under well-defined conditions. The experiments were carried out at 1223 K using 15 vol.% CH_4 and 20 vol.% H_2O to avoid carbon formation (N_2 balance). Because of massive experimental run conducted for this work, it is not shown the reactivity data for every OC in this paper, but all of them corresponded to typical shapes which are shown in Figure 1.

Oxidation was very fast, usually obtaining complete conversion in less than 15 s in all cases with conversion-time curves fitting the "a" pattern in Figure 1. The oxidation was roughly affected by the OC type: a small decrease in the reaction rate was observed when the NiO content in the OC increased. On the contrary, reduction of the OC varied depending on the support material. Thus, the reactivity analysis was focused on the reduction reaction. The OCs usually stabilized after the first cycle, for which the reduction reaction rate was slower. Reactivity pattern for fresh samples and reacted samples after 5 redox cycles is showed in Table 1, using the notation presented in Figure 1.

Table 1. XRD phases and reactivity pattern as described in Figure 1 for the OC studied in this work.

Ref	Oxygen carrier	Imp. (1)	XRD phases in the oxidized OCs		Reactivity pattern	
			fresh	reacted(2)	fresh	reacted(2)
1	Ni21γAl:AI:773	2	γ-Al_2O_3, NiO	γ-Al_2O_3, NiO, $NiAl_2O_4$	a*	b
2	Ni21γAl:AI:1073	2	γ-Al_2O_3, NiO	γ-Al_2O_3, NiO, $NiAl_2O_4$	a*	b
3	Ni21γAl:AI:1223	2	γ-Al_2O_3, $NiAl_2O_4$	γ-Al_2O_3, NiO, $NiAl_2O_4$	c	b
4	Ni21γAl:AI:1273	2	γ-Al_2O_3, $NiAl_2O_4$	γ-Al_2O_3, NiO, $NiAl_2O_4$	c	b
5	Ni21γAl:AI:1373	2	γ-Al_2O_3, $NiAl_2O_4$	γ-Al_2O_3, NiO, $NiAl_2O_4$	c	b
6	Ni20γAl:AI:1223(1073)	2	γ-Al_2O_3, $NiAl_2O_4$	γ-Al_2O_3, NiO, $NiAl_2O_4$	c	b
7	Ni19γAl:AI:1223(1223)	2	γ-Al_2O_3, $NiAl_2O_4$	γ-Al_2O_3, NiO, $NiAl_2O_4$	c	b
8	Ni16θAl:AI:1223(1373)	2	α-Al_2O_3, NiO, $NiAl_2O_4$	α-Al_2O_3, NiO, $NiAl_2O_4$	a*	a*
9	Ni11αAl:AI:1223	2	α-Al_2O_3, NiO, $NiAl_2O_4$	α-Al_2O_3, NiO, $NiAl_2O_4$	a*	a
10	Ni26αAl:AI:1223	5	α-Al_2O_3, NiO, $NiAl_2O_4$	α-Al_2O_3, NiO, $NiAl_2O_4$	a*	a
11	Ni38αAl:AI:1223	10	α-Al_2O_3, NiO, $NiAl_2O_4$	α-Al_2O_3, NiO, $NiAl_2O_4$	a*	a
12	Ni10αAl:HI:1223	1	α-Al_2O_3, NiO, $NiAl_2O_4$	α-Al_2O_3, NiO, $NiAl_2O_4$	a*	a
13	Ni18αAl:HI:1223	2	α-Al_2O_3, NiO, $NiAl_2O_4$	α-Al_2O_3, NiO, $NiAl_2O_4$	a*	a
14	Ni25αAl:HI:1223	3	α-Al_2O_3, NiO, $NiAl_2O_4$	α-Al_2O_3, NiO, $NiAl_2O_4$	a*	a
15	Ni20Mg5γAl:AI:1223	2	γ-Al_2O_3, $MgAl_2O_4$, $NiAl_2O_4$	$MgAl_2O_4$, NiO, $NiAl_2O_4$	b*	b
16	Ni20Mg9γAl:AI:1223	2	γ-Al_2O_3, $MgAl_2O_4$, $NiAl_2O_4$	$MgAl_2O_4$, NiO, $NiAl_2O_4$	b*	b
17	Ni14Ca9γAl:AI:1223	2	γ-Al_2O_3, $CaAl_4O_7$, $NiAl_2O_4$	$CaAl_4O_7$, NiO, $NiAl_2O_4$	b*	b
18	Ni20$MgAl_2O_4$:AI:1223	2	$MgAl_2O_4$, NiO	$MgAl_2O_4$, NiO	a**	a**
19	Ni11$CaAl_2O_4$:AI:1223	2	$CaAl_4O_7$, $CaAl_2O_4$, NiO	$CaAl_4O_7$, $CaAl_2O_4$, NiO	a	a

(1) Number of impregnation steps
(2) Particles after 5 redox cycles

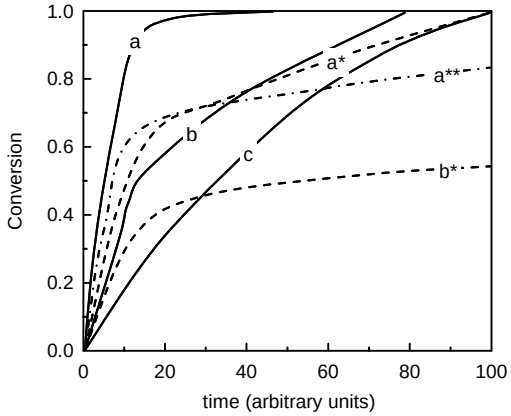

Figure 1. Typical conversion curves obtained during reactivity testing, used for notation in Table 1.

The OC particles impregnated on γ-Al_2O_3 showed low reactivity because all the nickel was as $NiAl_2O_4$, which has poor reactivity, except for particles calcined at the lower temperatures (OCs: 1-2 in Table 1). In all of those particles (OCs: 1-7) the more reactive free NiO appeared after the first full reduction, and reactivity increased. This fact was because $NiAl_2O_4$ is decomposed during reduction. During subsequent oxidation, a fraction of Ni^{2+} develops again the $NiAl_2O_4$ phase, and the rest forms free NiO [4]. A similar situation was found for OCs impregnated on γ-Al_2O_3 chemically modified support (OCs 15-17), but the $NiAl_2O_4$ was more difficult to reduce during the first cycle. For fresh particles impregnated on α-Al_2O_3 the reactivity was higher because some nickel appeared as free NiO, independently of the preparation method (AIWI or HIWI) or the NiO content (OCs: 9-14). In these cases, the conversion curves has an initial step very fast, corresponding to the NiO reduction, followed by a sharp decrease of the reaction rate corresponding to the $NiAl_2O_4$ reduction. After the first redox cycle, most of nickel was as free NiO, and the reactivity was very high with a solid conversion X_r = 95% in less than 15 s (curve "a" in Figure 1). For OC 8 on θ-Al_2O_3, α-Al_2O_3 was formed during calcination. Its reactivity was between that for particles on γ-Al_2O_3 and α-Al_2O_3. To minimize the interaction of the nickel with Al_2O_3, $MgAl_2O_4$ and $CaAl_2O_4$ were used as support material. High reactivity was observed for these samples (OCs 18-19), although higher conversion were obtained using $CaAl_2O_4$ as support. XRD analysis showed that most of the NiO impregnated was as free NiO, although $MgAl_2O_4$ was undistinguished of the $NiAl_2O_4$ by XRD. Reactivity data of OC 18 seems to indicate that some $NiAl_2O_4$ could be formed.

Redox multi-cycles tests were carried out in a batch fluidized bed to determine the gas product distribution for each OC, as well as to analyze the fluidization behaviour of the oxygen carriers with respect to attrition and agglomeration phenomena [9,10]. The tests were normally carried out at 950 ºC with an inlet superficial gas velocity into the reactor of 0.1 m/s. The composition of the gas was 25 vol.% CH_4 in N_2 during reduction and 10–15% O_2 in N_2 during oxidation. The reduction periods were varied between 120 and 300 s. The oxidation periods necessary for complete oxygen carrier oxidation varied between 600 and 1800 s. Each oxygen carrier was exposed to more than 50 reduction/oxidation cycles.

It was found that with the OCs prepared on γ-Al_2O_3 without chemical deactivation the CH_4 combustion was mainly selective towards the formation of H_2 and CO. On the contrary, with OCs

prepared on α-Al_2O_3, $MgAl_2O_4$ and $CaAl_2O_4$, the CH_4 was almost completely converted to CO_2 and H_2O, with CO and H_2 concentrations close to the thermodynamic equilibrium of NiO-CH_4. Thus, the formation of $NiAl_2O_4$ affects negatively to the methane combustion selectivity towards CO_2 and H_2O. In any case, methane was not observed during reduction period, indicating the existence of catalytic activity of the OC towards the methane reforming reaction. Moreover, it was found that none of the samples agglomerated or defluidized, and the elutriation rate was low, in the range 0.02-0.05 % per hour from cycles 20 to 100.

OCs impregnated on α-Al_2O_3, $MgAl_2O_4$ or $CaAl_2O_4$ have high content of free NiO, and they have high selectivity towards CO_2 and H_2O. The preparation method, AIWI or HIWI, has no relevance on their performance in a CLC system, but HIWI has the benefit of requiring less impregnation steps to reach the desired NiO amount in the particles. It is necessary to point out that an increase in the NiO content means a higher oxygen transport capacity and a higher rate of oxygen transference.

OXYGEN CARRIER TEST IN A 500 W_{th} CHEMICAL LOOPING COMBUSTOR

From above considerations, Ni18αAl:HI:1223 (OC 13 in Table 1) was found to be a promising OC to be used in CLC [11]. To analyze its behavior in a CLC system, this material was tested in a 500 W_{th} CLC plant where particles are continuously circulated between two fluidized beds, corresponding to the air (AR) and fuel (FR) reactors, similar to a circulating fluidized bed.

Figure 2 shows the schematic diagram of the atmospheric Chemical looping Combustor used in this work. The FR (1) consisted in a bubbling fluidized bed (0.05 m i.d.) with a bed height of 0.1 m. In this reactor the fuel gas reacts with the oxygen carrier to give CO_2 and H_2O. The solids reduced in the FR were then transported to the AR (3) through a U-shaped fluidized loop seal (2). The fluidization gas in the loop seal was nitrogen. The AR consisted of a bubbling fluidized bed (0.05 m i.d.) with a bed height of 0.1 m, followed by a riser (4) of 0.02 m i.d. and 1 m height. Secondary air can be introduced at the top of the bubbling bed to help particle entrainment. The oxidized carrier was recovered by a high-efficiency cyclone (5), and sent to a solids reservoir (7) setting the solids ready to be fed to the FR. Leakage of gas between both reactors was prevented by the presence of the U-shaped loop seal (2) and the solids reservoir (7). The regenerated oxygen carrier returned to the FR by gravity through a solids valve (8) which controlled the flow rates of solids entering the FR. A diverting solids valve (6) located below the cyclone allowed the measurement of the solids flow rates at any time. So, this design allowed to control and to measure the solids circulation flow rate between both reactors. The fines produced by fragmentation/attrition in the plant were recovered in filters (9) located downstream of the AR and FR. Because of the compact size of the system, this facility can be used to test several promising oxygen carriers using smaller amounts of solids than in larger facilities. Typically, the total solids inventory in the system was 1.5 kg.

The prototype was provided with several tools of measurement and system control. Thermocouples and pressure transducers located at different points of the plant showed the current operating conditions in the plant at any time. The AR and FR temperatures were controlled separately. Accurate flow rates of feeding gases were obtained by means of specific mass flow controllers. The gas outlet streams of the AR and FR were drawn to respective on-line gas analyzers to get continuous data of the gas composition. The outlet gas from the FR was composed by N_2, CO_2, H_2O, and unburnt CO and H_2. The composition of gases from the AR was N_2 and unreacted O_2. If carbon formation on particles occurs in the FR, also CO and CO_2 could appear in the AR because of its combustion by air.

A more detailed description of the CLC system and the operating conditions can be found elsewhere [4]. The CLC prototype was easy to operate and control, and the steady state for each operating conditions was reached in less than 10 min.

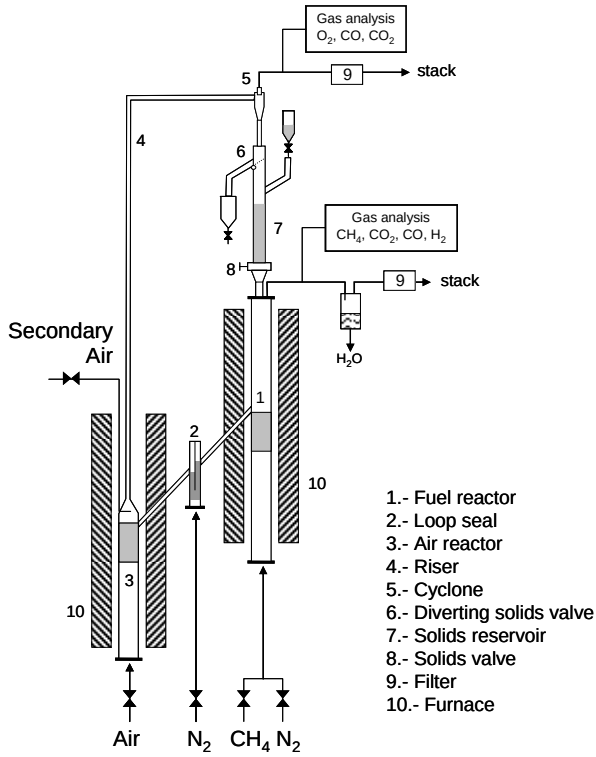

Figure 2. Schematic diagram of the 500 W_{th} CLC prototype.

Methane combustion performance

The effect of operating conditions, such as the OC/fuel ratio and the FR temperature, on the combustion efficiency has been analyzed during tests using CH_4 as fuel gas. The OC/fuel ratio was defined as $\phi = F_{NiO}/4F_{CH_4}$, where F_{NiO} is the total molar flow of Ni and F_{CH_4} is the inlet molar flow of CH_4 in the FR. A value of $\phi = 1$ corresponds to the stoichiometric NiO-CH_4 ratio. The combustion efficiency, η_c, was defined as the ratio of the oxygen reacted in the FR to the oxygen consumed by the gas if the fuel gas were completely converted to CO_2 and H_2O.

Figure 3(a) shows the effect of the ϕ value on the combustion efficiency at several temperatures. A total of 100 h of operation were fulfilled with the same OC batch. Full conversion of CH_4 was obtained in all tests, but H_2 and CO concentrations increased as the solids circulation rate decreased. A maximum value for efficiency of 99%, which is close to the equilibrium value (~ 99.5%) [4], was obtained for ϕ of about 3 for the three temperatures tested. When the ϕ value is decreased, the combustion efficiency decreases because the average reactivity of particles in the FR decreased [12]. Higher η_c values were obtained at higher temperatures as a consequence of the higher OC reactivity.

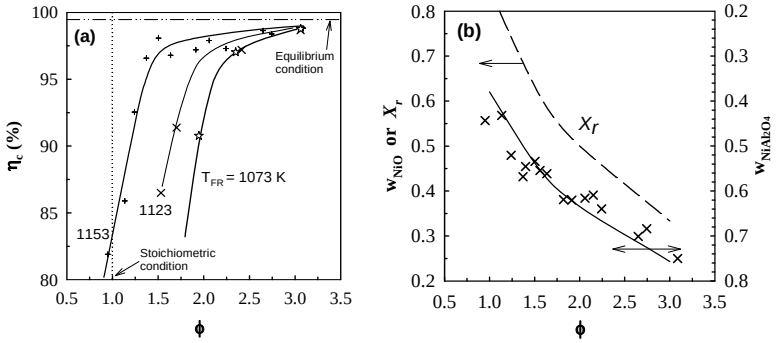

Figure 3. Effect of OC/fuel ratio, ϕ, on (a) the combustion efficiency, η_c, and (b) on the fraction of free NiO, w_{NiO}, and $NiAl_2O_4$, $w_{NiAl2O4}$, in the particles. Captions for Figure 3(b): fraction of NiO reduced in the FR, i.e. X_r (— — —); w_{NiO} and $w_{NiAl2O4}$ found during experimental test in the 500 W_{th} CLC unit (✕); w_{NiO} and $w_{NiAl2O4}$ when a 75% of the metallic Ni formed in the FR is oxidized towards free NiO and a 25% towards $NiAl_2O_4$ (——).

The relative fraction of NiO and $NiAl_2O_4$ for different samples of solids taken from the CLC system was obtained through TPR analysis. Figure 3(b) shows these fractions as a function of the OC/fuel ratio. It can be seen that upon increasing the ϕ value, an increase of the relative abundance of $NiAl_2O_4$, $w_{NiAl2O4}$, was observed at the expense of decreasing free NiO phase, w_{NiO}, (symbols "○" in Figure 3b). This fact was due to the lower extent of reduction reached in the FR, X_r, with an increase of the ϕ value. Moreover, the fraction of free NiO is lower than the fraction of metallic Ni produced in the FR, i.e. X_r. This result suggests that when reduced Ni in the FR is oxidized in the AR, a fraction of them (70-80%) is oxidized to NiO, whereas the rest is transformed into the $NiAl_2O_4$ phase. This behavior likely could be extended to other Ni-based materials prepared by impregnation on α-Al_2O_3 or γ-Al_2O_3. In the last case, the fraction of metallic Ni oxidized to $NiAl_2O_4$ should be higher because of the higher tendency to form $NiAl_2O_4$ when using γ-Al_2O_3 as support material.

Fate of the presence of sulphur and light hydrocarbons in the fuel gas

The effect of other minor compounds present in the fuel gas, as sulphur or light hydrocarbons (LHC), on the performance of a Ni-based OC have been also analyzed in the 500 W_{th} CLC system. The OC used was Ni19αAl:HI:1223 [13], that is similar than the OC above used, but sintered for 2 hours. To analyze the effect of the presence of LHC in the fuel gas, experiments carried out using a 30% CH_4 were compared to experiments where a 10% CH_4 was replaced by 5.7% C_2H_6 or 4.0% C_3H_8. Several tests were carried out varying the OC/fuel ratio and the temperature during 40 h of operation. In all cases, the best combustion efficiencies were obtained for CH_4 as fuel gas, and slightly decreased when C_2H_6 or C_3H_8 were present, likely because the OC was slightly more reactive with CH_4 [14]. No unconverted hydrocarbons were observed at any circumstance, but some CO and H_2 were also measured at the FR outlet. The amount of H_2 and CO increased, and therefore η_c decreased, as the OC/fuel ratio or FR temperature decreased. Combustion efficiencies close to equilibrium values were obtained for ϕ > 3. Although usually LHC have a higher tendency than CH_4 to carbon deposition, no carbon formation was observed.

The gaseous fuel (natural gas, refinery gas, etc.) may contain different amounts of sulphur compounds. Using NiO-based OCs, the formation of Ni_3S_2 is thermodynamically favourable at

typical FR conditions [13], which could lead to OC deactivation or defluidization problems because of its low melting point (1062 K). To evaluate the risks associated to the presence of sulphur in the fuel gas, an experimental investigation during 35 h of continuous operation was carried out with H_2S concentration between 100 and 1000 vppm. The temperature in the AR was 1223 K and in the FR was 1103 K or 1143 K.

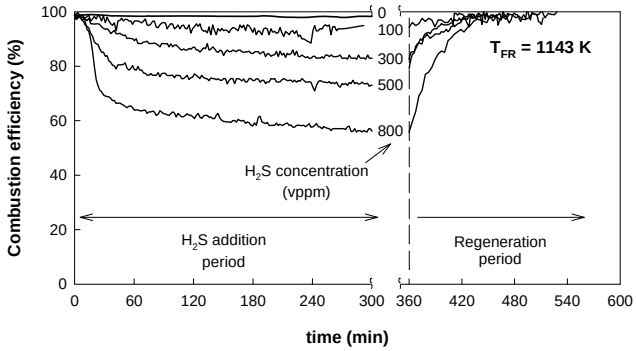

Figure 4. Combustion efficiency evolution during the tests with H_2S feeding.

Starting from a steady state, combustion efficiency slowly decreases after H_2S feeding until a constant value is reached, as it can be seen in Figure 4. The combustion efficiency decreased as the H_2S concentration increased. Main part of sulphur was released from the AR as SO_2. Sulphur was transferred from the fuel gas to the AR through the formation of Ni_3S_2, which oxidizes and decomposes in the AR into NiO and SO_2. However, some sulphur accumulated in the OC as Ni_3S_2 or $NiSO_4$. The sulphur accumulation could be favoured in the 500 W_{th} CLC system because the riser temperature was low enough (<1073 K) to favour the re-sulphation of the OC. Also, an insufficient residence time to decompose the nickel sulphide in the AR could have some relevance on the sulphur accumulation. After OC deactivation, unconverted CH_4 appeared likely because the presence of sulphur in the OC prevents the catalytic activity of the metallic Ni on CH_4 reforming. However, carbon deposition or agglomeration problems were not found in any case. Figure 4 also shows the combustion efficiency evolution after H_2S is removed from the FR feeding gas. It is observed that the OC recovered their initial combustion capacity after a combustion period of 1-2 h without H_2S addition. The regeneration was almost complete in all cases.

CONSIDERATIONS ABOUT DESIGN CRITERIA

A CO_2 capture efficiency of 100% could be reached in a CLC system using the Ni18αAl:HI:1223 OC. An estimation of the solids inventory for this OC gives a value of about 600 kg/MW_{th}, which is in line to other OCs but with higher Ni content [4]. The OC/fuel ratio is estimated to be in the range ϕ = 2-8 in a CLC system, limited by the riser transport capacity and the needs to transfer heat and oxygen [4]. Carbon formation and agglomeration did not happen and no operational problems are expected in an industrial CLC plant related to the use of this OC, neither for CH_4 combustion, and neither by the presence of LHC or H_2S in the fuel gas. These conclusions were supported by experimental work done in a continuous CLC facility, where a continuous flow of LHC and H_2S were added in the gases fed to the FR [13,14]. When sulphur was present in the fuel gas, sulphur accumulation in the OC would be avoided if the riser temperature in a CLC plant was high enough to oxidize and decompose the Ni_3S_2 formed in the FR. Main part of the sulphur fed into the system

likely would exit as SO_2 from the AR. Thus, not treatment of the flue gas downstream the FR will be necessary, but SO_2 emissions from AR could exceed the legislation limits [13]. Therefore, the more realistic option would be to avoid sulphur entering to the CLC system.

CONCLUSIONS

The oxygen carriers (OCs) prepared by AIWI or HIWI methods on α-Al_2O_3, $MgAl_2O_4$ and $CaAl_2O_4$ showed very high reactivity and selectivity towards CO_2 and H_2O for the CLC process. On the contrary, the reactivity of OCs supported on γ-Al_2O_3 was lower because of the formation of the low reactive $NiAl_2O_4$. Generally, the OC reactivity increased after a first reduction because the fraction of $NiAl_2O_4$ was reduced. A promising NiO-based OC (18 wt% NiO) prepared by HIWI on α-Al_2O_3 was selected to be tested in a 500 W_{th} CLC reactor. About 175 h of experience during continuous operation was gained. The effect of the FR temperature and the OC/fuel ratio was analyzed for CH_4 and gas mixtures of CH_4+C_2H_6 or CH_4+C_3H_8. The relative amount of NiO and $NiAl_2O_4$ varied with the OC/fuel ratio, which affected its reactivity. The OC showed enough high resistance to attrition, oxygen transport capacity and oxygen transference rate to be used in a CLC system. Carbon deposition, agglomeration or exiting hydrocarbons were not observed, being the only unconverted gases H_2 and CO. The presence of C_2H_6 or C_3H_8 had low effect on the CLC performance. However, deactivation of OC particles by sulphide formation was observed when H_2S was added to fuel gas. Even so, the OC was regenerated after H_2S was removed.

ACKNOWLEDGEMENTS

The work described in this chapter was carried out within the EU-financed research-project CLCGP (Chemical looping Combustion CO_2-Ready Gas Power), Contract Number 019800, with funding from the CO_2 Capture Project Phase 2 (CCP2) through Shell.

This Chapter contains figures that originally appeared in Energy Procedia Vol 1, Issue 1, Greenhouse Gas Control Technologies 9, Proceedings of the 9th International Conference on Greenhouse Gas Control Technologies (GHGT-9), 16-20 November 2008, Washington DC, USA., which was published by Elsevier Ltd.

REFERENCES

1. M.M. Hossain, H.I. de Lasa, Chemical-looping combustion (CLC) for inherent CO_2 separations—a review, *Chem. Eng. Sci.* **63** (2008) 4433.
2. J. Adánez, F. García-Labiano, L.F. de Diego, P. Gayán, A. Abad, J. Celaya, (2005) Development of Oxygen Carriers for Chemical-Looping Combustion. In: Carbon Dioxide Capture for Storage in Deep Geologic Formations-Results from the CO_2 Capture Project (Ed. by Thomas, D., Benson, S.) Vol. 1 Chapter 34 pp 587-604. Elsevier Ltd.
3. M. Johansson, T. Mattisson, A. Lyngfelt, Comparison of oxygen carriers for chemical-looping combustion, *Thermal Science* **10** (2006) 93.
4. J. Adánez, C. Dueso, L.F. de Diego, F. García-Labiano, P. Gayán, A. Abad, Methane combustión in a 500 W_{th} Chemical-Looping Combustión System Using an Impregnated Ni-Based Oxygen Carrier, *Energy & Fuels* **23** (2009) 130.
5. T. Mattisson, M. Johansson, A. Lyngfelt, The use of NiO as an oxygen carrier in chemical-looping combustion, *Fuel* **85** (2006) 736.

6. Assink, J. and Beal, C., 2009 Chemical Looping Combustion (CLC) technology summary, in Eide, L.I. (ed.) 2009, Carbon Dioxide Capture for Storage in Deep Geologic Formations, Volume 3. CPL Press
7. Linderholm C., Lyngfelt A., Trikkel A., Kuusik R., Jerndal E. Chemical Looping Combustion with natural gas using spray-dried NiO-based oxygen carriers, 2009, in Eide, L.I. (ed.) 2009, Carbon Dioxide Capture for Storage in Deep Geologic Formations, Volume 3. CPL Press
8. Pröll, T., Kolbitsch, P., Bolhàr-Nordenkampf, J. and Hofbauer, H., 2009 Demonstration of Chemical Looping Combustion at relevant operating conditions, in Eide, L.I. (ed.) 2009, Carbon Dioxide Capture for Storage in Deep Geologic Formations, Volume 3. CPL Press.
9. P. Gayán, L.F. de Diego, F. García-Labiano, J. Adánez, A. Abad, C. Dueso, Effect of support on reactivity and selectivity of Ni-based oxygen carriers for chemical-looping combustión, *Fuel* **87** (2008) 2641.
10. P. Gayán, C. Dueso, A. Abad, J. Adánez, L.F. de Diego, F. García-Labiano, NiO/Al_2O_3 oxygen carriers for chemical-looping combustion prepared by impregnation and deposition-precipitation methods, *Fuel* **88** (2009) 1016.
11. J. Adánez, F. García-Labiano, L.F. de Diego, P. Gayán, A. Abad, Transportador de oxígeno de NiO/Al_2O_3 para combustión indirecta de gas con captura inherente de CO_2. Procedimiento de obtención del mismo y su uso. Patent Nº PCT/ES2008/070146 (2007) Spain
12. A. Abad, J. Adánez, F. García-Labiano, L.F. de Diego, P. Gayán, J. Celaya, Mapping of the range of operational conditions for Cu-, Fe-, and Ni-based oxygen carriers in chemical-looping combustion, *Chem. Eng. Sci.* **62** (2007) 533.
13. F. García-Labiano, L.F. de Diego, P. Gayán, J. Adánez, A. Abad, C. Dueso, Effect of Fuel Gas Composition in Chemical-Looping Combustion with Ni-Based Oxygen Carriers. 1. Fate of Sulfur, *Ind. Eng. Chem. Res.* **48** (2009) 2499.
14. J. Adánez, C. Dueso, L.F. de Diego, F. García-Labiano, P. Gayán, A. Abad, Effect of Fuel Gas Composition in Chemical-Looping Combustion with Ni-Based Oxygen Carriers. 2. Fate of Light Hydrocarbons, *Ind. Eng. Chem. Res.* **48** (2009) 2509.

Carbon Dioxide Capture for Storage in Deep Geologic Formations, Volume 3
L.I. Eide (Ed.)

Chapter 9

THE HYDROGEN MEMBRANE REFORMER PRE-COMBUSTION GAS POWER CYCLE

Jens B. Smith, Knut I. Aasen, Kjersti Wilhelmsen and Daniel Käck
StatoilHydro, Forskningsparken, NO-3909 Porsgrunn, Norway

ABSTRACT: The development of the Hydrogen Membrane Reformer (HMR) pre-combustion power cycle started in 2001 when the CO_2 Capture Project (CCP) and the Research Council of Norway decided to support the project. The main focus areas were development of a hydrogen mixed conducting membrane and a pre-combustion gas power cycle utilising said membrane material. During the current HMR phase, an interesting new concept of the CCP1 HMR reactor has been developed. The core unit is a syngas reactor based on the hydrogen membrane which converts methane and steam into syngas. The hydrogen separation membrane makes the reactor self-sufficient with CO_2-free heat by combustion of hydrogen at the membrane sweep side. The reactor utilises conventional CO-shift and CO_2 capture by amine scrubbing, producing pure hydrogen fuel. Parallel to redesigning the HMR process, the first small-scale monolith modules have been fabricated and tested under realistic process conditions, demonstrating steam reforming and hydrogen flux close to equilibrium and flux model, respectively.

INTRODUCTION

The overall aims of the current Hydrogen Membrane Reformer project phase were to develop dense Hydrogen Mixed Conducting Membranes (HMCM) with sufficient H_2 transport rates and stability under normal steam reforming conditions, and further develop a techno-economically viable (Pre-Combustion De-Carbonization) PCDC process applying said materials. The project extends the materials and process development work conducted under the CO_2 Capture Project Phase 1 (CCP1): "Hydrogen Membrane Reformer Technology" [1]. The Norwegian Research Council and the CCP partners funded the project.

Technology concept

HMR is a pre-combustion CCS technology based on a hydrogen selective ceramic membrane, which separates hydrogen from synthesis gas. During the earlier phases the results have been promising, and the current focus has been on improvements in the process and reactor design, and scale-up and testing of membrane modules. The work has been organised under four different tasks:

- Task 1 – Process design optimisation. Further optimisation of the phase 1 HMR process with focus on avoiding large heat transfer and air extraction from the gas turbine that is outside vendor's experience.
- Task 2 – Reactor system modelling and design. Optimisation of the earlier reactor design and a safety and regularity analysis including start-up and shut-down procedures for the HMR full scale pre-combustion power plant.

- Task 3 – Membrane module development and fabrication. Optimisation of membrane composition based on flux measurements and modelling. Development of medium scale powder production methodology and sealing materials. Production of membrane module parts (including tubes, monoliths and flow distributors) and assembly of tubular and small scale monolith membrane modules.
- Task 4 – Test of small scale monoliths and catalyst tests. Test of small scale hydrogen mixed conducting membrane modules (tubular and small monoliths) under real process conditions. This includes tests of membrane and steam reforming catalyst co-performance.

The HMR technology is based on StatoilHydro IPR covering ceramic membrane materials, reactor design and process design [1,2].

TASK 1 PROCESS DESIGN OPTIMISATION AND COSTING

In the novel 400 MW HMR pre-combustion gas power cycle developed during the first phase of CCP (CCP1), the membrane reformer system replaces the traditional steam methane reformer (SMR) for production of hydrogen fuel (40-50 mol% hydrogen). Figure 1 is a simplified diagram showing the idea of the Hydrogen Membrane Reforming (HMR) power process.

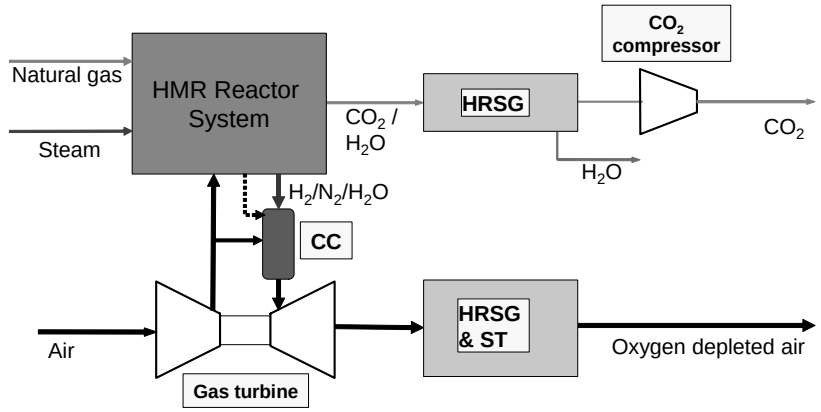

HRSG: Heat Recovery Steam Generation, ST: Steam Turbine

Figure 1. The HMR Pre-Combustion Process.

The novel membrane reactor concept combines steam methane reforming and a hydrogen mixed conducting membrane in a 3 stage process (Figure 2).

The first stage is a steam methane reformer section where more than 90% of the hydrocarbons in the feed gas are converted to syngas. A minor part of the produced hydrogen is transported through the membrane to react with air extracted from the gas turbine, generating sufficient heat for the endothermic steam methane reforming. The second and third steps are for production of hydrogen and heat, respectively. Unconverted methane from stage 1 is converted to CO_2 and H_2 in stage 2 and manly all CO from stage 2 is shifted to H_2 and CO_2 in stage 3. This is a very efficient process concept since the "CO_2 separation" is done without any heat consumption and CO_2 can be fed to the compressor at elevated pressure (> 15 bar) saving compressor duty.

The concept, however, relies on high air extraction (> 60%) from the gas turbine which is outside vendor's experience. About 80% of the extracted air is used to recover heat generated in stage 3. It has therefore been a target of the current project phase to develop HMR concepts using a more conventional gas turbine setup with air extraction ratios below 20%.

Based on information from APCI and Siemens it may, however, be possible to modify gas turbines for air extraction up to about 55% [3].

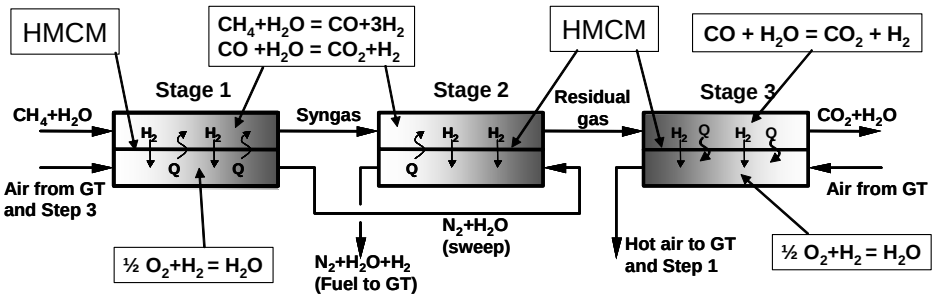

Figure 2. The 3-stage hydrogen membrane reactor.

The original 3-stage HMR process has therefore been re-estimated using a supplementary air compressor to supply additional compressed air.

In addition two new HMR process concepts were developed and evaluated against the slightly modified 3-stage concept. The new concepts need supplementary CO_2 removal and the heat transfer is significantly reduced by avoiding stage 3. An amine (MDEA) based process was used in this study but other CO_2 removal concepts (e.g. using physical solvents) could be beneficial in some of the concepts.

The 2 stage HMR concept with MDEA based CO_2 removal

In order to reduce heat transfer and GT air extraction a process without stage 3 was developed. A simplified process flow diagram is shown in Figure 3.

The air flow to the membrane reactor operates both as an oxygen source for combustion of hydrogen and as a sweep gas to pick up hydrogen and cool the membrane system (second stage). The hydrogen combustion in the first membrane stage supplies the reforming reaction with heat.

The disadvantage is that all CO_2 must be removed in the MDEA plant. All CO_2 therefore must be recompressed from low pressure. However, since hydrogen is extracted from HMR stage 2 the partial pressure of CO_2 downstream the water gas shift unit becomes very high. The fraction of CO_2 will exceed 50 mol% compared to around 25-30 % mol% in conventional oxygen blown Autothermal Reformers (ATRs). A quite efficient MDEA plant thus can be used and other CO_2 separation concepts may also be attractive. Since no air is needed to cool the HMR stage 3 the air extraction ratio will be reduced to around 11%. The performance of the different HMR concepts is summarized in Table 1.

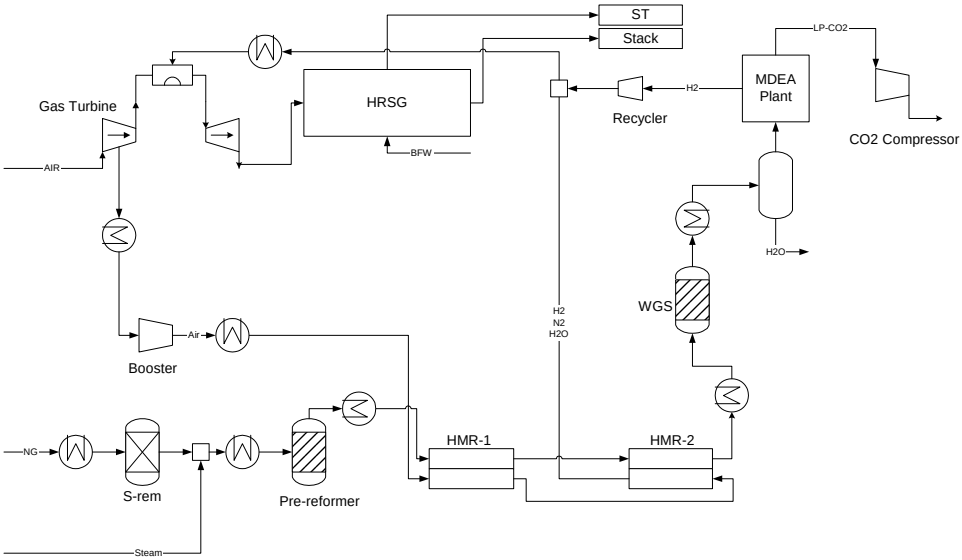

Figure 3. The 2 stage HMR concept with MDEA based CO_2 removal.

The 1 stage HMR concept with MDEA based CO_2 removal

In order to further reduce process complexity, a process with only the syngas generator (HMR stage 1) was developed. Since HMR stage 2 is eliminated the syngas is processed in conventional shift and CO_2 removal units. A simplified flow sheet is shown in Figure 4.

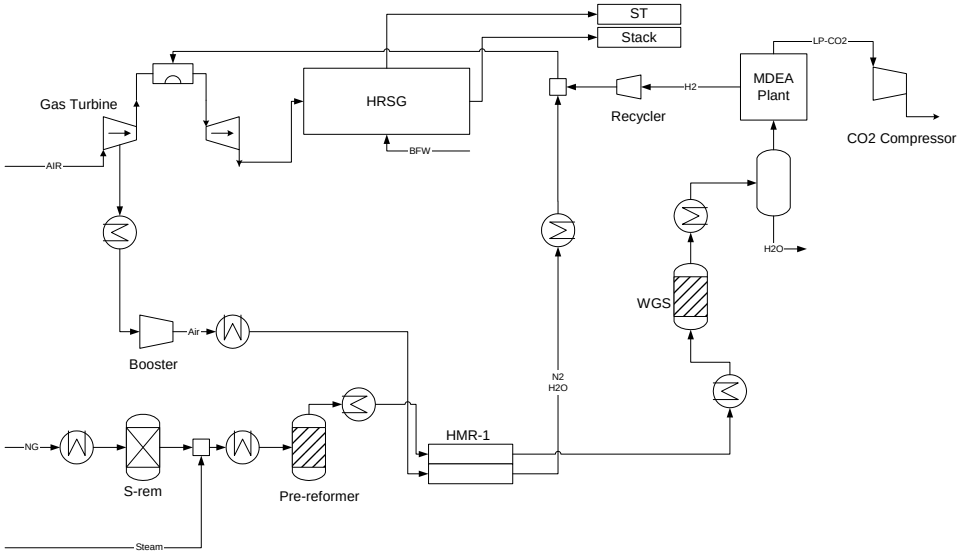

Figure 4. The 1 stage HMR concept with MDEA based CO_2 removal.

The composition of the syngas generated in HMR-1 is similar to syngas generated in an oxygen blown ATR reactor. This process is quite efficient since the air used to combust permeated hydrogen in principle can be fed directly into the gas turbine. This stream contains no or very little oxygen and it is suggested to mix it with purified hydrogen from the MDEA plant. Conventional gas turbines cannot burn pure hydrogen and the oxygen depleted gas from the HMR reactor is a perfect diluent.

Comparison of performance data

The performance of the selected HMR concepts is summarized in table 1.

Table 1. Performance of the selected HMR concepts.

		1 stage HMR	**2 stage HMR**	**3 stage HMR**
Fuel gas input	MW	745.05	745.05	706.49
CO_2 captured	%	87.9	92.7	98.7
Net power output	MW	372.95	375.57	375.82
Net efficiency	%	50.1	50.4	53.2

In the two cases including the MDEA plant (1 and 2 stage HMR) CO_2 is recovered at low pressure. This gives higher power consumption for CO_2 compression. In addition some of the LP steam is used in the CO_2 stripper reboiler. Introducing more conventional CO_2 capture technology thus will reduce efficiency by around 3%-points and less CO_2 will be captured. A possible way to increase the CO_2-recovery is to increase the S/C-ratio. The energy efficiency, however, will be further reduced. If the S/C-ratio is increased from 2.0 to 2.1 in the HMR 1 stage process, efficiency will drop to 49.7%, but the CO_2 capture will increase to about 91%.

Modification of the HMR 1 stage process

HMR alternative (1 stage) initially had some heat exchangers operating under metal dusting conditions (400 – 800 ºC) which may be very challenging. These exchangers, however, was replaced by a Gas Heated Reformer (GHR) that is designed to operate under metal dusting conditions. A GHR will also allow more heat to be transferred from the syngas to the natural gas and steam mixture feed gas. The GHR is proven technology (S/C > approx. 2) and is offered by Johnson Matthey.

Preheating of pre-reformed gas to 750 ºC is not proven technology, but is required for processes based on ionic transport membranes since the materials will have too low flux at lower inlet temperatures. Both preheating of gas and air will cause materials temperatures as high as 900 ºC and the feasibility of operation under these conditions remains to be demonstrated. Use of ceramic heat exchangers similar to the HMR-design is one obvious option to solve these challenges. In the cost evaluation presented in chapter 16 high temperature metal alloys has been used in all high temperature heat exchangers.

The HMR process developed in CCP2 also assumed a very high GT combustor inlet temperature of up to 670 ºC. This is well outside GT vendor's experience. The process is therefore re-estimated reducing the dilution of hydrogen (with the hot O_2 depleted air stream) to around 59%. This will reduce the fuel inlet temperature to 400 ºC which is still on the high side, but likely more realistically achievable in the future. The NO_x formation may increase to levels similar to a conventional natural gas fired CCGT. The above described changes will reduce the power plant

efficiency from 50.1% to 49.7% with the capture rate unchanged. A detailed PFD of the slightly revised process is shown in Figure 5.

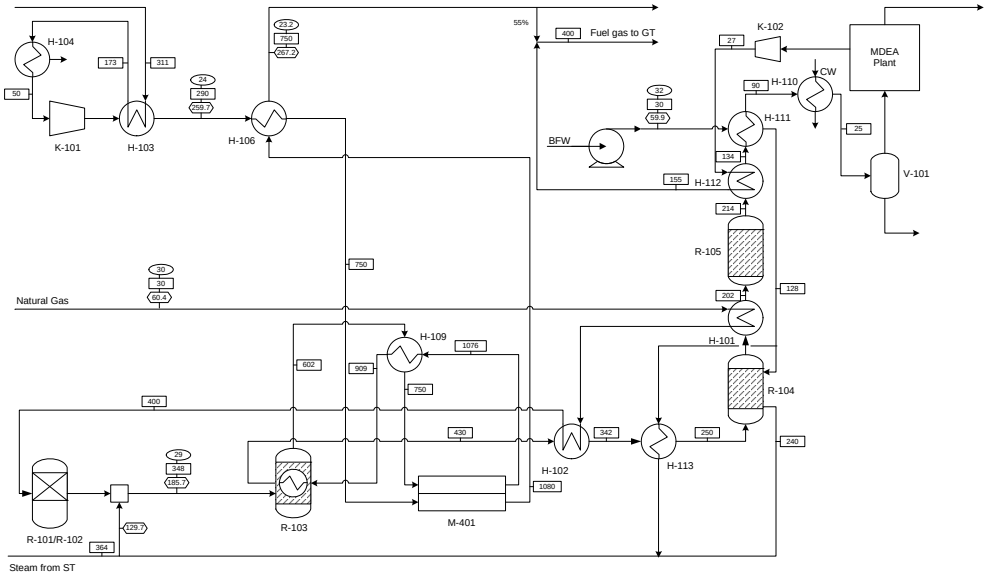

Figure 5. Modified 1 stage HMR concept with GHR

A cost and performance evaluation of 1 stage HMR with and without GHR is given in [4]. The cost of SCR is not included there, as it has not been concluded that this is a feasible option.

The rest of the oxygen depleted air (not used to dilute the hydrogen fuel) is mixed with the air from the GT compressor. This will increase the compressed air temperature by 30ºC to 441ºC. The main reason for the drop in efficiency is that some of the heat used for fuel gas preheating in the revised concept will be used for process steam generation. Process steam generation is increased by 21.2 t/hr to 59.9 t/hr.

TASK 2 REACTOR SYSTEM MODELLING AND DESIGN

The heart of the HMR reactor system is the multi channel monolithic membrane structures.

By use of a patented manifold system two different fluids (gases) can be fed in/out of all the channels of the monolith and distributed according to a chess board pattern flow. The chess pattern flow distribution enables all available internal walls to be utilized as active membrane walls. In the HMR process the monolith walls are a proton transporting ceramic membrane and the surface of the wall are coated with a catalyst for the steam-methane reforming reaction. The endothermic steam-methane reforming reaction produces a hydrogen rich synthesis gas ($CO + H_2$). Hydrogen is transported from reforming side, through the membrane, to the sweep or combustion side. The heat produced by burning the hydrogen is utilized directly by the reforming reaction. In an industrial sized process a large number of monolithic unit blocks are needed. The numbers of monoliths are dependent upon the hydrogen transport capacity (flux) and the available area of each monolith.

A reactor model developed by SINTEF in CCP phase 1 and modified by StatoilHydro during phase 2 has been used to estimate temperature profiles, concentration profiles, hydrogen flux and required

membrane area and volume for the different cases. The necessary membrane volumes are summarised in Table 2, indicating significant reduction in membrane volume by reducing the number of stages. This again will have a great impact on the membrane system costs.

The work described in this paper has led to significantly better knowledge and insight into how to design a monolith based membrane reactor, and has shown that the membrane reactor cost could be more than 400% higher than previously estimated. The multi stage processes with high membrane area requirement therefore became less economically attractive, and the 1 stage process turned out to be the most cost efficient process even though the efficiency is lower.

Table 2. Membrane volume needs.

	Stage 1 (m^3)	Stage 2 (m^3)	Stage 3 (m^3)	Total (m^3)
1 stage HMR	16.9	-	-	16.9
2 stage HMR	16.6	95.3	-	111.9
3 stage HMR	15.9	124.6	67.5	208.0

The sizing of the HMR reactor system is based on the estimated process flow data and membrane volume figures. This information has been used to calculate the number of membrane module stacks as well as detailed design solutions.

The membrane stack itself is an assembly made up of monoliths, choke plates, flow distributor plates and manifold heads. All parts are permanently sealed together with glass ceramics or co-sintered and arranged in containers (e.g. 50 stacks per container) that can be loaded into a pressure vessel (Figure 6).

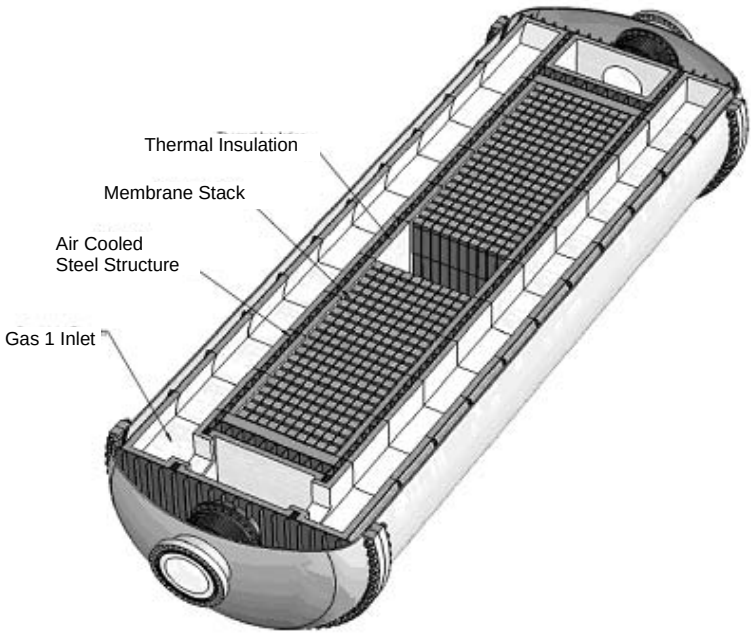

Figure 6. Inside the HMR reactor.

The stacks are connected to each other with a ceramic/metallic sealing device, allowing each membrane stack to individually move and rotate within certain limits due to thermal expansion or to compensate for manufacturing differences in each individual membrane stack. An air cooled spring generates the necessary force for the sealing device. This will maintain gas tightness between the different flows.

The HMR reactor has been designed with functionality to handle the high temperature of the process flows. In addition to the air cooled springs, each container is surrounded by an air cooled steel structure allowing "cold" air from the gas turbine to cool the pressure vessel.

Scale-up of the reactor can be done by increasing the length of the reactor according to the number of stacks needed (assuming that all membrane stacks have the same height). In case of an unpractical length (> 500 stacks) the reactor is divided into two or more vessels.

Summary process and reactor development

The original HMR process with three membrane stages shows reduced potential compared with the results from CCP1 caused by a significantly higher (about 400%) membrane reactor cost. This is mainly due to better knowledge and insight into design of monolith based membrane reactors learned by parallel in-house ceramic membrane projects. Step 2 and 3 become very expensive due to the large membrane area needed in these stages.

An alternative process flow sheet has been developed omitting the expensive stages 2 and 3. This study indicates that this HMR concept is the lowest cost solution among all the evaluated HMR cases.

The results are conclusive and it is recommended to concentrate on the development of the one stage hydrogen membrane reformer syngas reactor concept.

Main advantages compared with the original 3 step process:

- Membrane volume < 10%
- GT air extraction reduced from 60% to 11%
- Almost pure hydrogen may be extracted from the process (nitrogen/steam is mixed in after separation of CO_2)
- Reduced membrane reactor development costs. Only the syngas reactor step needs to be developed (potential for application in other processes e.g. methanol, hydrogen, ammonia etc.)
- High hydrogen flux less critical (low membrane area requirement)
- Reduced complexity and risk in general

The main disadvantages are:

- Reduced efficiency (alternative CO_2 removal techniques developed in parallel CCP projects, however, may improve efficiency)
- Reduced CO_2 capture. Additional process steps may improve CO_2 capture but costs may increase.

Safety and regularity

The safety and regularity of a HMR pre-combustion gas power plant has been considered by treating unexpected process upsets like gas turbine trips and reactor shut down, as well as safety aspects of reactor design (i.e. membrane module leakages). It was not meant as a final answer, but more as an initial guidance for how the complex HMR power plant may be controlled. Any negative effect on

environment and health as a consequence of amine emission is considered outside the scope of the analysis.

The HMR pre-combustion gas power plant may be considered an ordinary combined cycle power plant with an additional HMCM reformer unit. During start-up the "ordinary" combined cycle gas power plant will first be put into operation with the gas turbine running on natural gas rather than hydrogen. The hydrogen membrane reformer unit will be started gradually by increasing the temperature and pressure carefully. Finally, when the membrane modules are under process temperature and pressure, natural gas will be introduced into the reformer unit, and hydrogen production starts. The gas turbine fuel will gradually be shifted from natural gas to hydrogen. During shut-down the same schedule as for start-up will be followed, only in reverse order.

With this type of integration between the combined cycle gas power plant and the hydrogen membrane reformer unit, the HMR power plant may be run on natural gas if the membrane modules trip, making the power production more reliable. The integration relies on robust and trustworthy tools for detection of disturbances and trips, but at the present maturity level these are not considered yet. They are however completely necessary to enable safe operation and maximum on stream time for the power plant.

The safety aspects of the HMR power plant were also treated in a "what if" analysis, where possible failure situations and their influence on the reactor and power generation were discussed. With the technology still under development the analysis gave important input to further work on the reactor and plant integration system. Although no show stoppers were identified, the analysis left several questions which have to be addressed in coming phases of the development work, especially the effects of leakage and material failure in the reactor.

TASK 3 MEMBRANE MODULE DEVELOPMENT AND FABRICATION

During CCP1 tubular membrane modules with approximately 15 cm^2 membrane surface were fabricated and tested. For the current phase a main ambition was to up-scale the membrane modules and to implement the monolith design with checkerboard flow pattern of the process and sweep gas. To reach the target it was necessary to improve the sinterability of the ceramic HMCM powder and to demonstrate/evaluate large-scale powder production. A sealing material being compatible with the hydrogen membrane material to allow thermal cycling of the modules had to be developed, and a catalyst had to be integrated in the monolith module to facilitate the steam methane reforming in the process channels. Two different approaches were followed

- Fabrication of small-scale test modules with a 10 cm long square channelled monolith with choke plates and flow distributors at each end. The monolith had 21 process channels with steam reforming catalyst and 16 sweep channels with membrane (50 µm thickness). The total membrane area was 100 cm^2. The modules were tested in-house under real HMR conditions.

- Fabrication of a pilot-scale monolith with 400 channels and outer dimension 5x5x5cm^3. With membrane deposited in each second channel the total membrane area was 600 cm^2. The monolith was not used for module fabrication (or testing), i.e. the only purpose was to demonstrate pilot-scale monoliths.

Sinterability

To increase the sinterability of the HMCM powder, and simplify the fabrication of gas impervious membrane layers, several sintering aid additives have been tested. These were selected according to the criteria thermodynamic stability, sinterability and hydrogen flux, and only materials with

structural similarity to the HMCM were considered. Since only small amounts of sintering aid were allowed, maximum 4 mol%, the thermodynamic stability of the HMCM was expected to be little influenced.

All together, 6 different sintering aids (SA) have been considered, but the early screening, based on sintering properties, during the CCP1 extension phase left only 4 candidates, i.e. SA3, SA4, SA5 and SA6. These were further evaluated by flux measurements of membrane disks with 0-4 mol% sintering aid. The flux was measured using concentration cells at 1 bar absolute pressure connected to gas chromatographs for gas phase analysis. The process gas was a mixture of hydrogen and helium (to detect leakages), whereas the sweep gas was argon. The process and sweep gases were moisturised, containing 2 volume % steam. Unfortunately, the data show a very high scatter, showing no systematic difference between the different sample categories (based on version and concentration of sintering aid). Figure 7 shows the measured hydrogen fluxes transformed into estimates of the hydrogen flux for a 20 µm thick membrane at 1000 °C and process conditions. According to the model the target flux is reached for some of the samples, whereas others have too low flux. The main problem is however the lack of repeatability within the different groups, and it is therefore hard to draw any conclusion from these flux measurements.

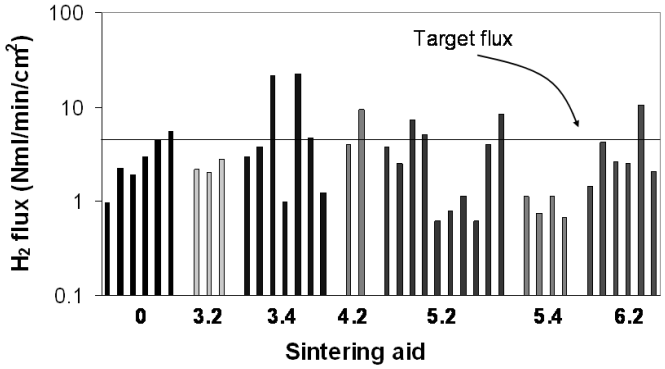

Figure 7. Hydrogen flux model predictions based on flux measurements on disks.
Numbers on x-axis are indicating type of sintering aid and mole %, i.e. 3.2 is SA3 – 2 mole %.
0 is representing the pure HMCM.

An explanation of the variation may be found in the fabrication route used for the disk samples. To achieve gas impervious membrane disks, the samples were sintered at very high temperature (1600-1700 °C), resulting in disks with typical thickness and diameter 2 mm and 10 mm, respectively. After sintering the samples were cooled rapidly to room temperature without time for equilibration with the surrounding atmosphere, leaving a high concentration of intrinsic defects like Schottky defects (cation and anion vacancies). Since equilibration of such defects relies on slow cation diffusion, whereas proton diffusion is fast, the intrinsic defects trapped in the HMCM disks may have dissolved extra water, increasing the concentration of mobile protons in the HMCM samples and hence the hydrogen flux. At typical flux measurement temperatures (800-1000 °C) the samples will re-equilibrate gradually, and the hydrogen flux decreases gradually until the sample is once again in equilibrium with the atmosphere. This was not taken into account when measuring the hydrogen flux of the 40 disk samples with the sintering aids, but on later occasions it has been demonstrated that equilibration at 1000 °C may need several weeks, and reduce the hydrogen flux by more than 50 % . For thin supported membranes (30-50 µm) this is not considered a problem since the bulk will equilibrate much more easily.

Since stability measurements were not part of the study and the flux data were without trends, the sinterability/ease of fabrication was left as the primary selection criteria. Since SA3.2 (SA3 – 2 mole %) and SA4.2 were the least effective of the chosen sintering aids, and SA6.2 is a 2 phase system these should not be pursued further. The remaining compositions with 2% SA5 and 4 % SA3 (5.2 and 3.4) were consequently recommended for further flux measurements on supported membrane structures under simulated process conditions. Composition 5.2 would be preferred over 3.4 due to the lower amount of sintering aid, introducing less compositional changes to the membrane host material. However, the very high flux measured in two of the SA3.4 membranes motivates the selection of both compositions for future measurements using thin supported membranes.

Medium scale powder production

Earlier experience with the HMR project showed that HMCM powders produced by spray pyrolysis had inferior sinter activity compared to powders produced in the laboratory by batch synthesis (citrate method). The particle size distributions appeared very similar by laser scattering, but the primary particles of the citrate powder were smaller. The agglomeration of the spray pyrolysis powder was also different, with more developed bridging between particles. See Figure 8.

For HMR applications in a full scale pre-combustion power plant only continuous methods like spray pyrolysis have the capacity for large-scale powder production. Demonstration of large-scale production of HMCM powder with small particle size and good sintering properties at minimum rate 1 kg/day was therefore targeted. The development work showed that spray pyrolysis could be applied, provided that calcination in vacuum and milling followed as next steps. The sintering properties of a powder batch with 2 mol% sintering aid were investigated in a dilatometer. Densities of >95% (compared to the theoretical density defined by unit cell dimension and molecular mass), which normally is sufficient for reaching gas imperviousness, was achieved by sintering in air atmosphere at >1700 °C and in moistened dilute hydrogen at 1600 °C. It can therefore be concluded that the development of a medium scale method for producing sufficiently sinterable powders has been accomplished.

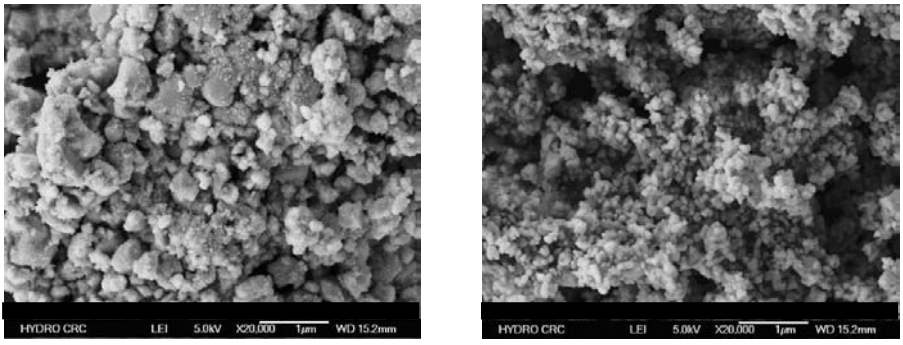

Figure 8. SEM pictures of powders produced by spray pyrolysis (left) and the citrate method (right).

Development of sealing material

For a HMR reactor to operate effectively, it is important to prevent leakage between the two separate gas streams entering and leaving the reactor module. Since the HMR module is built up from many components, i.e. gas manifolds, choke plates and monolith sections, it is important that the joints between these components are gas-tight. One of the crucial tasks in the HMR project has

therefore been to develop sealing materials and methods of their application so that HMR modules could be constructed and tested.

The specific requirements for candidate sealing materials are;

- Close match in thermal expansion coefficient with the membrane material
- Excellent flow and seal formation behaviour
- Good match in chemical compatibility with the membrane material
- Good high temperature microstructural stability
- Good chemical stability under reducing and oxidising conditions at high temperature
- Ability to survive repeated heating to the temperature used in the joining/sealing operation

Based on these requirements and the successful application in other ceramic membrane systems, it was decided to concentrate the sealant materials development on crystallizing glasses (glass-ceramics). This type of sealant undergoes crystallization during the sealing cycle to form a material with improved refractoriness and, depending on chemical composition, also a good match in expansion characteristics to the membrane material. The increase in refractoriness which accompanies crystallization makes it possible to subject sealed components to repeated sealing cycles without softening of previously formed joints.

Dilatometric analyses indicated that that $CTE_{(20\text{-}1000°C)}$ (Coefficient of Thermal Expansion) of the membrane material was 10.0×10^{-6} K^{-1} and that the presence of sintering aid had no noticeable influence on the expansion behaviour. Having measured the CTE for the membrane material, a number of candidate glass-ceramic sealant materials which were known to have relatively close expansion characteristics were selected for evaluation. In total six different glass-ceramics were selected for testing in combination with the membrane material, all silicate based glass-ceramics from various glass-forming systems. These were further screened based on their CTE, flow characteristics and chemical compatibility with the HMCM.

Based on the sealant development work, it appears that a glass-ceramic from the $CaO\text{-}MgO\text{-}SiO_2$ system is a good choice as sealant for HMR module construction. The thermal expansion stability and chemical compatibility with the membrane material are excellent and long term operation at high temperature is not expected to be problematic. The flow characteristics are relatively good, but it would be an advantage if these could be improved as this would increase the ease and reliability of seal formation. One positive point with the sealing behaviour, however, is that the material begins to flow and can form a seal at lower temperatures that the other sealants that were examined. This has made it possible to seal monolith based HMR modules at temperatures below 1000°C, and this is a considerable advantage since it limits the degree to which catalysts applied to the monolith are likely to suffer loss of activity during the sealing cycle(s).

Catalyst selection

The steam reforming reaction in the process channels of the membrane module are dependant on an active catalyst to overcome otherwise slow kinetics. Rh, Ru and Ni are all active for steam reforming, and have been tested for application in the HMR membrane module. The working conditions of the HMR process are relative tough, including temperatures up to 1000 °C and 20 bar absolute pressure. The noble metals Rh and Ru have a high melting temperature and low vapour pressure, making them less exposed to deactivation than Ni. Rh and Ru also show higher activity towards steam reforming, and better coke resistance, but are also more expensive and less available. As an alternative, various doped modifications of the HMCM were also tested, but the activity was deemed to be insufficient for applications in the membrane modules.

For initial testing of the catalysts, the activity towards steam reforming at atmospheric pressure and 700-1000 °C was investigated together with different routes for application of the catalyst in the membrane modules. With respect to the latter, the study demonstrated that the metal catalyst may be deposited directly in the porous monolith support structure of the modules, following much the same procedure as for membrane coating, but with catalyst nitrate solution rather than suspension/slicker (Figure 9).

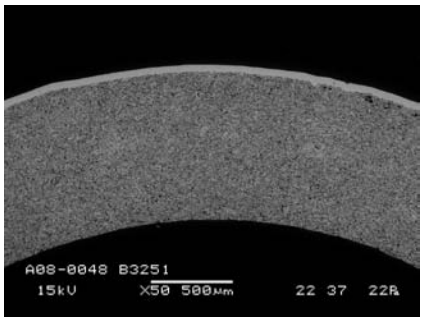

Figure 9. Cross section of porous support tube with an outer dense membrane layer. The catalyst is impregnated in the porous support structure, and may not be detected in the SEM micrograph.

Initial screening of the catalysts was performed using a quartz cell with connections to a gas chromatograph and a mass spectrometer. The catalyst impregnated supports were crushed and sieved to yield porous particles of fraction 0.5 – 1 mm, before the powder sample (10 g) was packed in the quartz tube, yielding a fixed bed configuration. During testing the steam to methane ratio was 2:1 and the residence time 0.25 s.

For each catalyst, the steam reforming activity with respect to methane conversion, *R*, and water gas shift, *S*, was studied as a function of temperature and catalyst loading. *R* and *S* are described, respectively, by,

$$R = \frac{[CO]+[CO_2]}{[CO]+[CO_2]+[CH_4]} \cdot 100\% \qquad \text{Equation 1}$$

$$S = \frac{[CO_2]}{[CO]+[CO_2]} \cdot 100\% \qquad \text{Equation 2}$$

where [-] is the measured concentration of each species. Figure 10 shows the degree of methane conversion and water gas shift for different loadings of Rh on the membrane support. For 0.5 and 0.01 wt% Rh, equilibrium is reached over the entire testing range, yielding almost 100 % methane conversion at temperatures above 800 °C. For these loadings the water gas shift also behaves according to equilibrium. For 0.001 wt % Rh, equilibrium is no longer established, i.e. much methane is left in the flue gas. Since this also leaves much steam, the CO/CO_2 ratio is shifted towards higher concentrations of carbon dioxide.

Similar behaviour was observed for Ru catalyst. For impregnation of the porous support with concentrations above 0.01 wt% Ru, equilibrium was reached over the entire temperature range. For Ni impregnation, 0.1 wt% Ni was necessary for reaching equilibrium conditions, demonstrating the inferior activity of Ni compared to noble metal catalysts. To determine the stability/rate of deactivation the Rh and Ru catalysts were also tested as a function of time using HMCM carriers with 0.01 wt% Rh and Ru. Already after 2 weeks the activity of the Ru containing sample was too

low for the gas mixture to reach equilibrium even at 1000 °C. The Rh containing sample proved to be more stable, and after 8 weeks the activity was still sufficient for equilibrium to be reached at 900-1000 °C.

Among the candidates tested, Rh had the best performance, but also for this material deactivation was demonstrated, but only for very low catalyst loading, i.e. 0.01 wt%. For the HMR modules higher concentrations would be needed to maintain sufficient catalytic activity, e.g. 0.5 wt%. With the high cost of Rh, it is thereby necessary to search for other catalyst materials, and Ni was selected for further testing too.

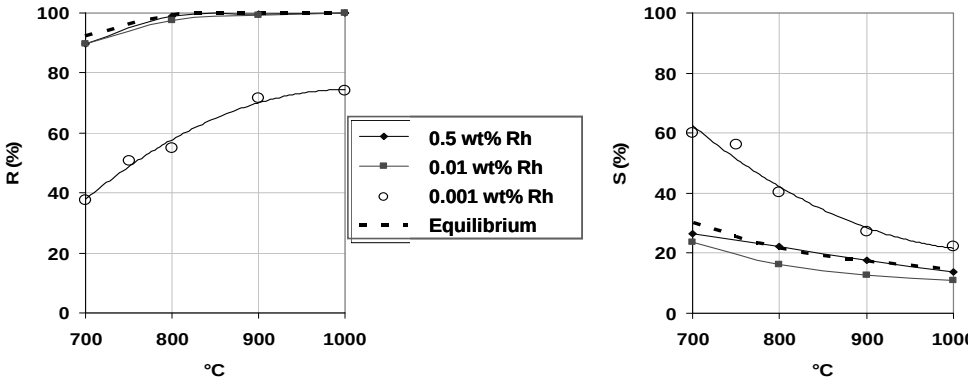

Figure 10. Methane conversion (left) and water gas shift (right) over Rh catalyst on the HMCM as a function of temperature. The steam to methane ratio is 2:1 and the residence time 0.25 seconds.

Small-scale monolith modules

Monoliths were made by extrusion of a plastic mixture of the ceramic membrane powder, water and organic material like pore former, binder and plasticizer. After extrusion the green monoliths were dried, and heated to 500 °C to remove the organic material. These steps were critical for the quality of the monoliths, yielding cracks if they were too rapid. To apply the membrane coating, the monoliths were pre-sintered at 1300 °C to secure the necessary handling strength. After pre-sintering each second monolith channel was blocked according to the chess pattern, and the monoliths were dip-coated by immersion in a slip of membrane powder, binder and ethyl acetate. The thickness of the membrane was proportional to the amount of powder precipitating from the slip, which again was influenced by the porosity of the substrate and the dipping time. After dip-coating, the monoliths were finally sintered at 1700 °C in moisturized dilute hydrogen (4%). Figure 11 shows an example of a cross-sectioned sintered monolith with the dense membrane in each second channel. The membrane is 50 µm thick, and located in the sweep channels. The steam reforming catalyst was deposited directly in the process channels by impregnation of the porous monolith walls with a catalyst nitrate solution followed by calcination at 1000 °C.

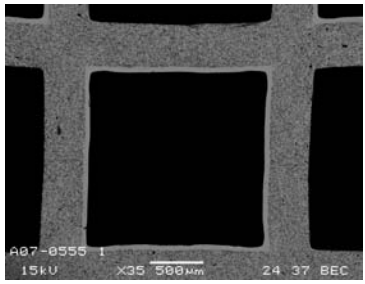

Figure 11. Scanning electron microscope picture of a cross sectioned monolith. The porous monolith has membrane coating (50 µm thickness) in each second channel.

Besides the sintered monolith, the small-scale monolith modules were made of two choke plates, two flow distributor plates and two top hats (Figure 12). The role of the choke plates was to create the necessary pressure drop along the module to secure gas supply to every channel. The flow distributor plates converted the process and sweep gas streams into multi-channel checkerboard flow pattern. Both choke plates and flow distributor plates were made from sintered, dense disks of the membrane material with machined patterns. The top hats were made of stabilized ZrO_2, and connected each test module to the rig. The different parts were assembled and sealed to each other by the glass ceramic sealing material. The process channels were available from the inside of the top hat, whereas the sweep channels were available from the outside, i.e. the sweep gas entered the module through the holes in the edge/side of the flow distributor. As seen from Figure 12, the modules also had two rings around the monolith. These were gas baffles, positioning the module inside the test reactor and forcing the sweep gas through the module rather than passing outside.

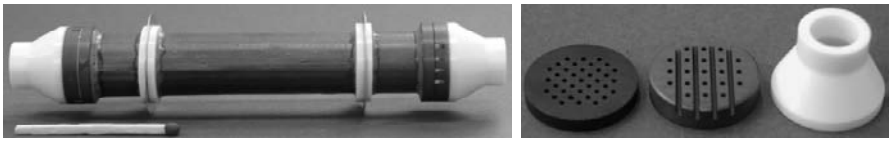

Figure 12. HMR small-scale test module, and a separate choke plate, flow distributor and top hat prior to module assembly.

The up-scaling of the small-scale monoliths to pilot-scale was demonstrated using a similar fabrication route. The pilot-scale monoliths were extruded with a 90x90 mm tool, having 25x25 square channels. Following a careful drying, burning and pre-sintering route the monoliths were pre-sintered at 1300 °C to yield a porous body with sufficient handling strength. Following membrane dip-coating, the monoliths were finally sintered in moisturized dilute hydrogen (4%) at 1700 °C, demonstrating fabrication of pilot-scale monoliths based on the same fabrication route as applied for the smaller test modules (Figure 13).

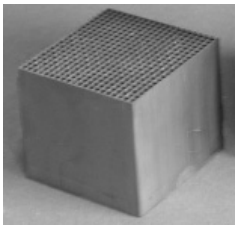

Figure 13. Sintered pilot-scale monolith (cut to 50x50x50 cm^3 to fit into sintering furnace).

TASK 4 TEST OF SMALL SCALE MONOLITHS AND CATALYST TEST

Figure 14 shows a sketch of the multi purpose test rig used for testing of the membrane modules under real HMR process conditions. The rig may be used for temperatures and pressures up to 1000 °C and 30 bar, respectively. It has two gas lines, one for the process side with N_2, H_2, CH_4 and H_2O(l) feed, and one for the sweep side with Air, Ar and H_2O(l). The water is evaporated at 150 °C in a pre-heater. The two gas mixtures are fed co-current to the reactor with maximum feed rate 3000 ml/min. Flue gas compositions are determined by gas chromatography (GC), and used for calculation of any leakage, hydrogen flux and steam reforming activity.

The membrane modules were tested at 20 bar total pressure and 1000-800 °C according to the test matrix in Table 3. The nitrogen addition to the process side was used for detection of any leakage to the sweep side during the measurements (assuming linear gas phase leakage and no contribution from Knudsen diffusion).

Table 3. Membrane module test matrices.

	Process side: 700 ml/min H_2 200 ml/min H_2O 100 ml/min N_2	**Process side:** 225 ml/min CH_4 675 ml/min H_2O 100 ml/min N_2	**Process side:** 300 ml/min CH_4 600 ml/min H_2O 100 ml/min N_2
Sweep Side: 800 ml/min Ar 200 ml/min H_2O	√	√	√

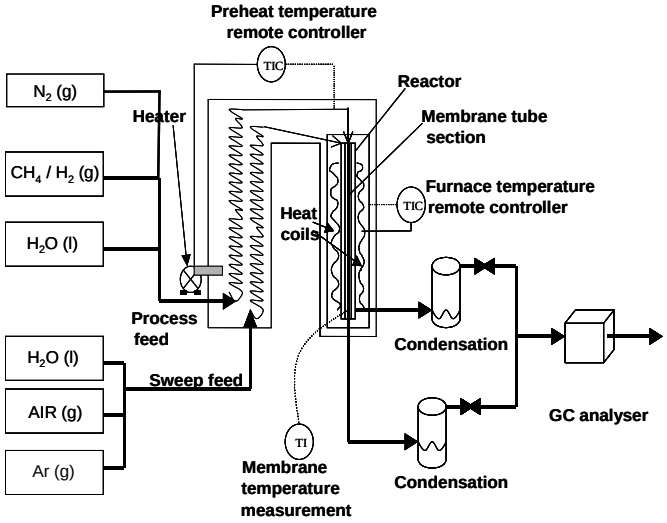

Figure 14. Sketch of the multi purpose test rig.

Figure 15 shows the flux and gas phase leakage of hydrogen at 800-1000 °C for a small-scale monolith module at 20 bar total pressure. The hydrogen leakage was calculated from the concentration of nitrogen in the sweep flue gas (0.5 %), and subtracted from the net amount of hydrogen (19-22%) to yield the hydrogen flux. The flux is significant, i.e. well above the hydrogen leakage.

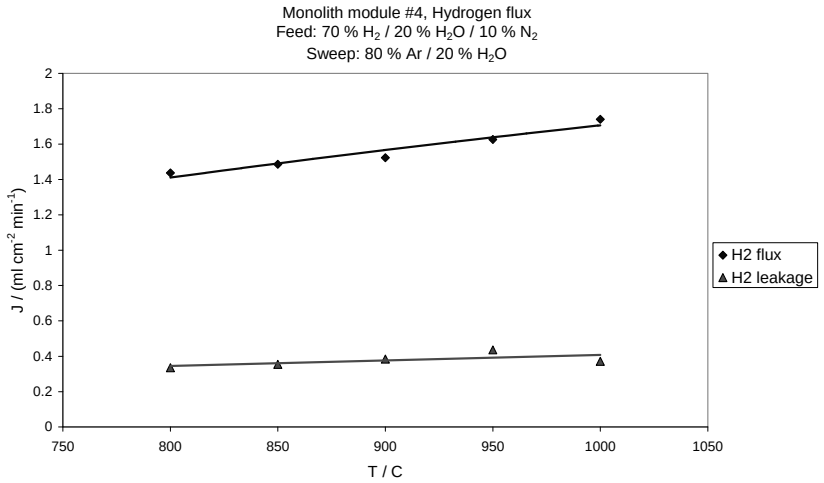

Figure 15. The flux (♦) and leakage (▲) of hydrogen as a function of temperature. The membrane thickness and area is 50 µm and 86 cm^2, respectively.

The steam reforming capacity of the small-scale test modules was tested for 3:1 and 2:1 steam to methane ratio (Figure 16). The conversion of methane increased with increasing temperature and steam to methane ratio, also favouring CO with respect to CO_2 at high temperatures. However, the activity of the catalyst was insufficient for reaching equilibrium. The monolith module contained 2.5 wt% Ni, which during the earlier measurements with crushed monolith samples had proven more than adequate for the reforming to reach equilibrium at even lower residence time (0.25 s). The availability of the catalyst, which was deposited in the porous monolith walls, is therefore questionable, and other techniques for catalyst deposition should probably be considered, e.g. coating with a porous layer of catalyst/carrier.

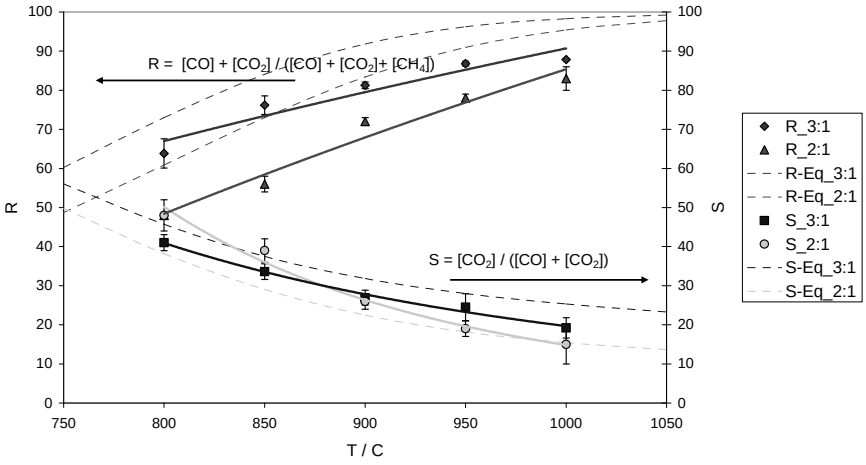

Figure 16. Steam reforming in a monolith module with 2.5 wt% Ni at 20 bar pressure and steam to methane ratio 3:1 and 2:1. The dotted curves represent equilibrium conditions. The residence time is 1.2 s.

During the steam reforming measurements the leakage across the membrane increased abruptly, and inspection of the module after ending the tests demonstrated severe cracking of the inlet zirconia cap, manifold and upper part of the monolith. Some coking was observed on the fracturing parts, but, no other secondary phase could be detected by X-ray diffraction (XRD). According to thermodynamic calculations coke formation is not to be expected. However, catalysts, and especially Ni, may promote coke deposition, especially for low steam to carbon ratios at high temperatures and pressures [5].

Discussion of test results

During the current HMR phase, 2 different small-scale monolith modules were tested, demonstrating relatively low hydrogen flux. The flux target for the HMR process is 5 ml cm^{-2} min^{-1} at 1000 °C under typical HMR conditions (20 bar total pressure), and earlier measurements with tubular membrane modules had demonstrated fluxes well above this (10-15 ml cm^{-2} min^{-1}) [1]. There may be several reasons for the failure to reach target flux for the small-scale monolith modules, among the most obvious are

- Insufficient porosity in the support monolith
- Leakages reducing the driving force

The difference in hydrogen chemical potential between the process and feed side is the driving force for hydrogen transport across the dense membrane. If the porosity of the support monolith is insufficient to allow free gas phase transport of hydrogen, the chemical potential of hydrogen drops across the support phase too, reducing the driving force for transport across the membrane. Compared to earlier measurements with tubular modules, the amount of sintering aid in the monolith supports has been increased to 3 wt% (compared to 2 wt% in the tubes) to match the sintering properties of the membrane layer and thereby avoid cracking. A side effect has been higher total sintering and less porosity in the monolith support, and the transport of hydrogen gas through the porous monolith may therefore have been impeded.

While the leakage of hydrogen (and nitrogen) from the process to the sweep side was low, there was a significant leakage of argon in the opposite direction, diluting the hydrogen mixture at the process side and reducing the driving force for hydrogen transport through the membrane. A possible way to counteract the argon leakage is to increase the feed rates of process and sweep gas, reducing the dilution at each side. The flux measurements were performed with only 1000 ml/min feeding rate at each side, while the test rig is designed for 3000 ml/min.

During earlier parts of the HMR project a flux model for calculation of membrane performance has been developed. Based on the experimental hydrogen gradient, assumed from the observed hydrogen flux and leakage of argon, the calculated flux also fails to reach flux target (Figure 17). The calculated flux is a factor 2 higher than the observed flux. One reason for the difference may be impeded gas transport in the porous support phase. However, taking the quality of the data into account, which is deteriorated by leakages and low gas feed rates, the agreement is reasonable at the present maturity level, and the prospects of demonstrating target flux should be good. To reach a better experimental foundation for the hydrogen flux it will be necessary to determine the gas phase transport in the support phase and to test modules without any leakages. However, this could not be performed within the scope of the present HMR phase, and have to be done later.

With respect to the steam reforming, the membrane modules were leaking too much to evaluate any effect of the hydrogen transport across the membrane for the final composition of the process gas. For a membrane module with proper sealing, the hydrogen transport would serve to drive the steam reforming equilibrium to the product side, increasing the conversion of methane to near 100 %.

On the other hand, the measurements have demonstrated that the catalyst may have too little activity when deposited in the walls of the porous support. If only a fraction of the catalyst is active, other techniques for applying the catalyst should be considered, e.g. a porous wash-coat layer of carrier and catalyst coated on the monolith channel walls at the membrane or support side. A wash coat would serve to locate the catalyst in a part of the module which is more highly exposed to the process gas species, possibly minimising the amount of catalyst and making more expensive materials like Rh a real choice.

Before piloting of the HMR technology should be considered, further evaluation of the HMCM stability (mechanic, thermodynamic and kinetic), hydrogen flux and catalyst behaviour is recommended. Further analyses of the safety aspects should also be pursued.

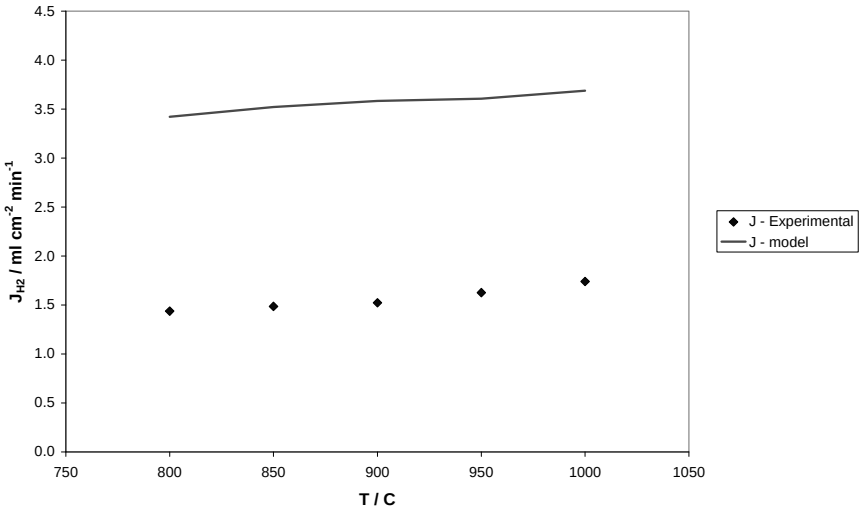

Figure 17. Comparison between the modelled and the experimental hydrogen flux.

CONCLUSION

A new and interesting concept for the HMR gas power plant has been developed and cost estimated. It is build around the syngas reactor (stage1) of the original HMR power plant, and produces a pure hydrogen fuel for the gas turbine. The CO_2 capture is only 88 %, but the net efficiency is 50 % with high potential for cost reduction compared to the original 3-stage HMR process.

New small-scale membrane modules have been produced and tested. The modules are made of a small porous monolith (37 channels) with manifold system for distributing process and sweep gas in checkerboard pattern. The membrane is deposited in the sweep gas channels. Flux measurements under realistic process conditions demonstrated hydrogen transport according to expectations. Steam reforming was also demonstrated, but failed to reach equilibrium even for relative high residence time. Due to cracking of the membrane modules, the co-performance of the hydrogen transport and steam reforming has not been evaluated.

A safety and regularity analysis of the HMR power plant identified no showstoppers, but the importance of careful interlocking, to prevent damage to the power plant as well as potentially dangerous situations, was pointed out.

ACKNOWLEDGEMENTS

StatoilHydro is grateful to the CO_2 Capture Project (CCP) and the Research Council of Norway for financing the development of the Hydrogen Membrane Reformer technology.

This Chapter contains figures that originally appeared in Energy Procedia Vol 1, Issue 1, Greenhouse Gas Control Technologies 9, Proceedings of the 9th International Conference on Greenhouse Gas Control Technologies (GHGT-9), 16-20 November 2008, Washington DC, USA, which was published by Elsevier Ltd.

REFERENCES

1. Vigeland B. and Åsen K., 2005. Development of a Hydrogen Mixed Conducting Membrane Based CO_2 Capture Process, in: Thomas, D., (ed), 2005. Carbon Dioxide Capture for Storage in Deep Geologic Formations - Results from the CO_2 Capture Project, Vol. 1: Capture and Separation of Carbon Dioxide from Combustion Sources, Elsevier Publishing, UK.
2. Smith J.B., Aasen K., Wilhelmsen K., Käck D., Risdal T., Berglund A., Østby A.S., Budd M., Bruun T. and Werswick B., 2008. Recent development in the HMR pre-combustion gas power cycle, *9th International Conference on Greenhouse Gas Control Technologies, Washington DC, November 2008.*
3. Stein V.E., Armstrong P. and Foster T., 2007. New Gas Turbine Integration Options for ITM Oxygen in Gasification Applications, *Gasification Technologies 2007, San Francisco, CA, 17 October 2007.*
4. Melien, T. and S. Brown-Roijen, 2009. Economics, in Eide, L.I. (ed.), 2009, Carbon Dioxide Capture for Storage in Deep Geologic Formations, Volume 3, CPL Press.
5. van Beurden P., 2004. On the Catalytic Aspects of Steam-Methane Reforming – A Literature Survey, ECN-I--04-003.

Carbon Dioxide Capture for Storage in Deep Geologic Formations, Volume 3
L.I. Eide (Ed.)

Chapter 10

INTRODUCTION TO CACHET A PRE-COMBUSTION TECHNOLOGY DEVELOPMENT PROGRAM CO-FUNDED BY THE EU AND CCP

Richard Beavis
BP, plc, Sunbury-on-Thames, UK

ABSTRACT: The European Union sponsored the development of several capture technologies through a program called CACHET (Carbon Dioxide Capture and Hydrogen Production from Gaseous Fuels). This program aimed to develop technologies, which will significantly reduce the cost of carbon dioxide (CO_2) capture from power generation and hydrogen (H_2) production. The primary objective was to reduce the cost of CO_2 capture by 50% compared to current costs. The project has focused on natural gas fuel, which is a major component of the world's energy systems.

BACKGROUND

One result of CCP1 was that pre-combustion technologies for CO_2 capture held high promise for significant reductions of CO_2 avoided costs. Pre-combustion therefore became the focus of CCP2. A strong and diverse international consortium of highly experienced research institutes, universities, energy businesses, engineering and manufacturing companies had decided to join forces to develop innovative technologies for hydrogen production from natural gas, with the objective to halving the cost of low-carbon energy. The consortium, called CACHET, had received funds from the European Commission and CCP2 was able to join the project as co-funder and active participant. The three-year CACHET program started in April 2006, with research in four promising technologies: advanced steam methane reforming, chemical looping, metal membranes and sorption enhanced water gas shift (SEWGS). The project also researched the integration of the CO_2 capture technologies with H_2 production systems for power generation and fuel applications.

OBJECTIVES OF THE CACHET PROJECT:

The project focused on a scenario with a natural gas fired nominal 400 MWe Combined Cycle Gas Turbine (CCGT) power plant with an optional pure H_2 side-stream. The project had two key objectives:

- Reduce the cost of CO_2 capture by 50% compared to state of the art
- Capture more than 90% of the CO_2 emitted

The goal was to advance technologies to be ready for pilot-unit testing and, if successful, selected pre-commercial demonstrations could then be developed, with commercial use foreseeable by ca. 2015-2020.

THE CACHET CONSORTIUM

Coordinated by BP, CACHET consisted of a strong and diverse international consortium comprising 28 research groups, from 4 continents and 17 countries and included:

- Oil & Gas Companies – BP, Shell, ENI, Chevron, ConocoPhillips, Suncor, Petrobras, StatoilHydro
- Electricity Utility Companies – Endesa, E.ON, Electricity Authority of Cyprus
- Engineering, Plant and Equipment and Contractors – Siemens, PDC, Air Products, Technip, Alstom, Meggitt
- R&D Institutes – ECN, IFP, Fraunhofer Umsicht, IETU, Dalian Institute of Chemical Physics, Sintef, CSIC
- Universities – Technical University of Vienna, Technical University of Sofia, National Technical University of Athens, Chalmers University

PROJECT STRUCTURE AND WORK PACKAGES

Technology development Work Packages

The four main technology areas include:

- Advanced Steam Reforming - Hydrogen Generation System (HyGenSys)
- Chemical Looping
- H_2 Permeable Metal Membranes (Integrated with reforming and water gas shift)
- Sorption Enhanced Water Gas Shift (SEWGS)

In addition these activities where also included:

- Technical optimisation and economics (including state of the art base case)
- Novel technology evaluation, HSE and dissemination

Hydrogen Generation System (HyGenSys)

The advanced steam methane reforming technology incorporates a convectively heated reformer integrated with a gas turbine. This new process arrangement with energy integration leads to generation of H_2 that is used as fuel in a CCGT plant to produce electric power.

The advanced HyGenSys concept was developed to increase the energy efficiency of the reforming process by integrating heat from the exhaust gas of a gas turbine. The novel reformer was designed to operate at elevated pressure on the exhaust gas side increasing heat transfer and facilitating a compact design.

The tasks undertaken to further develop the advanced technology include process studies to optimise and integrate the complete flow sheet, gas turbine selection, detailed mechanical reactor development, cost estimation, materials study, risk study, catalyst selection and cold mock-up to mimic both catalyst handling procedures. After three years of the project, sufficient work has been completed to understand the economic potential of the technology and sufficient design work completed to move to the next pilot plant scale for the HyGenSys concept.

Details of the advanced technology and the work performed in CACHET can be found in [1].

Chemical Looping Reforming

Chemical Looping (CL) technology has been developed rapidly in the last few years. CACHET considered how CL can produce syngas using three process variants. The first approach involves Chemical Looping Combustion (CLC) combined with autothermal reforming to directly produce syngas ($CLR_{(a)}$) . The second is CL with steam methane reforming, where CLC and steam methane reforming are integrated ($CLR_{(s)}$). The third process, One-Step Debonisation (OSD), features direct H_2 production with CO_2 capture.

These concepts are described [2]. The third process, One-Step Hydrogen, features direct H_2 production with CO_2 capture. The technology is based on the use of a circulating "RedOx" solid material that can be oxidised via water splitting, producing H_2 and reduced by a hydrocarbon fuel, producing CO_2. The process comprises a three-bed circulating fluid bed reactor. The solid material is partially oxidised with steam producing H_2, then fully oxidised with air in a second reactor before being reduced in the third reactor by reaction with the fuel. Details are given in [3].

Metal Membranes

The metal membranes work package has developed, tested and evaluated the potential of H_2 permeable palladium and palladium alloy membrane reactors to capture CO_2 either from syngas in a WGS reactor or directly from an integrated reformer to produce a H_2 rich gas stream that can be used in a CCGT. Integration of the H_2 selective membrane in the reactor allows H_2 to transfer from the feed-side to the permeate side by selective permeation through the membrane. The combination of reaction and separation in membrane steam reforming and/or membrane WGS shift offers higher conversion of the reforming and/or shift reactions.

The reforming reaction is strongly endothermic and with this technique can be forced to completion at lower temperature than normal (typically 500 to 600^{o}C). The program focused on membranes featuring a very thin membrane layer (ensuring high flux and low cost) applied to a porous support structure which will provide mechanical strength to the membrane. Using a dense metal membrane on a porous support ensures that the CO_2 cannot pass through the membrane and leaves the reactor in the raffinate stream at close to the feed pressure whereas the H_2 emerges in the permeate stream. The H_2 rich stream may be fed to a CCGT for power generation and the CO_2 can be dried and compressed for storage. The work undertaken in this project, described in [4] and [5], has included scale up, testing and lifetime tests of the membranes. A large multi-column unit has been built to demonstrate both combined separation/reforming and combined separation/shift.

Sorption Enhanced Water Gas Shift

The fourth technology area of CACHET features a Sorption Enhanced Water Gas Shift (SEWGS) process for the simultaneous production of hot, high pressure H_2 in catalytic shift reactors, with simultaneous adsorption of CO_2 on a high temperature adsorbent. The system operates in a cyclic manner with steam for adsorbent regeneration. State of the art processes for separation of H_2 from H_2/CO_2 mixtures include ambient temperature Pressure Swing Absorption (PSA) or liquid adsorbents, both chemical and physical. By arranging a number of reactors in parallel which are suitably sequenced, a continuous forward flow of H_2/steam can be maintained to the CCGT and a steady flow of CO_2/steam can also be maintained which goes to drying and compression. The work completed in the project included laboratory testing of a single reactor and a multi-bed reactor to demonstrate in the laboratory a practical continuously operating multi-bed switching reactor/adsorber system and to optimise the cycle. It also included optimisation and cost estimation activities. Details can be found in [6].

Novel Technologies

The consortium recognised that the world's research communities continue to progress forward in this area of research developing CO_2 capture technologies. This workpack surveyed 1901 patents and 160 references, all post 2002 English language publications with the objective of defining and benchmarking novel CO_2 capture concepts technologies with the four CACHET technologies.

Where the published data permitted, a more rigorous assessment was made on six selected technologies which appeared to be suitable for pre-combustion CO_2 capture from natural gas:

1. Sorption Enhanced Reforming
2. Alternative Chemical Looping concepts
3. Topchiev H_2 permeable membrane
4. High temperature proton conducting membranes
5. Microchannel reforming
6. CO_2 permeable membranes

The currently published data on CO_2 permeable membranes suggested that existing performance was insufficient to achieve the objectives. The assessment showed that Sorption Enhanced Reforming and High temperature proton conducting membranes and CO_2 permeable membranes all increased the energy efficiency beyond the CACHET base case, although none of these appeared to improve on the higher range of the efficiencies calculated for the CACHET technologies.

Optimisation and Integration Team

The Optimisation and Integration team has evaluated the benefits of combining combinations of the technologies whose performance characteristics are complimentary and may be integrated to achieve more substantial economic benefits. Initially 55 combinations were identified, of which 8 where believed to worthy of more detailed investigation. These included:

- HyGenSys – Sorption Enhanced Water Gas Shift (SEWGS)
- Chemical Looping Steam Reforming ($CLR_{(s)}$) – Membrane Water Gas Shift (MWGS)
- One Step Decarbonisation (OSD) – Membrane
- OSD – Membrane – MWGS
- Chemical Looping Autothermal Refoming ($CLR_{(a)}$) – SEWGS
- Integrated Membrane Reformer (MREF) – CLC
- MWGS – CLC
- $CLR_{(a)}$ – MWGS

Health, Safety and Environment

Technologies in all four areas have been assessed from a Health, Safety and Environmental (HSE) and economic perspectives. The team quantified emissions to air, water and land while dedicating particular focus to potential risks associated with metal dusting, nickel emissions (chemical looping), water usage, CO_2 venting and the formation of nickel tetra-carbonyl and during abnormal operation. IETU and Fraunhofer have concluded that all the HSE issues so far identified present no insurmountable barriers to the development of the technology. Good engineering and operational practices will facilitate safe long term operation.

SUMMARY OF RESULTS

The performance and cost results are summarized in Table 1. Note that the approach to costing the technologies applied in CACHET differs from that used by CCP and reported in [7]. The performances and costs in Table 1 must therefore be seen in relation to the baseline and the CACHET targets and not in absolute terms.

Table 1. Performance and cost summary of CACHET technologies.

	Reference	Base Case	HyGenSys	CLR(s)	CLR(a)	OSD	MemREF	MemWGS	SEWGS
Efficiency (%)	57.2	40.9	41.9	46.3	42.1	46.2	46.2	47.1	44.3
CACHET Target (49.05%)	49.05	49.05	49.05	49.05	49.05	49.05	49.05	49.05	49.05
Avoidance rate (%)	-	92.6	91	92	92.2	92.3	91.9	92.1	94.9
Capture rate (%)	-	94.8	93.4	93.5	94.3	93.8	93.5	93.5	96
CACHET Target (90% CO2 Avoided)	90	90	90	90	90	90	90	90	90
Cost of capture (€/t CO2)	-	82.1	77.1	81.5	101.2	88.1	96.1	65.9	75.9
Cost of avoidance (€/t CO2)	-	117.5	107.9	102.4	140.6	110.8	121.1	81.2	99.1
CACHET Target (€58.75/te)	58.75	58.75	58.75	58.75	58.75	58.75	58.75	58.75	58.75
Total fixed investment (€m)	194.9	461.8	587	562	586	534	530	476	468
Power output (MWe)	389.8	366	480	383	330	356	352	392	366.9
Break even electricity price (€/MWh)	55.9	86.6	82.7	81.3	94	84.2	87.4	74.4	81.3
Fixed Cost (€/MWh)	9	22	19.7	22.6	27.6	23.3	23.5	18.8	26.8
Variable Cost (€/MWh)	46.9	64.6	63	58.7	66.4	60.9	63.9	55.6	54.5
Specific Investment	0.50	1.26	1.22	1.47	1.78	1.50	1.51	1.21	1.28
CACHET Target (0.88 €M/Mwe)	0.88	0.88	0.88	0.88	0.88	0.88	0.88	0.88	0.88

HyGenSys = Hydrogen Generation System; CLR(s) = Chemical Looping Steam Reforming; CLR(a)= Chemical Looping Autothermal Reforming; OSD=One Step Decarbonisation; MemRef = Integrated Membrane Reformer; MemWGS = MWGS = Membrane Water Gas Shift; SEWGS = Sorption Enhanced Water Gas Shift

Table 2 shows the results of the combination study, which suggest that although some combinations can improve the efficiency by up to 2.6% pts, the benefits are outweighed by the capital cost increase.

All the CACHET technologies have improved the energy efficiency compared to the Base Case and all can achieve >90% CO_2 capture and avoidance. However all have increased the capital cost of the unit. The integrated membrane WGS technology is shown to have the lowest CO_2 capture cost, due to the highest efficiency and lowest investment cost. It remains to be seen what further improvements can be achieved when combining one or more of the CACHET technologies with e.g. the Hydrogen Membrane Reformer (HMR), [8].

Table 2. Changes in efficiency and costs when combining pairs of the program technologies.

Combined process	Process 1	Process 2	ΔEfficiency relative to Process 1	ΔEfficiency relative to Process 2	ΔProduction cost relative to Process 1	ΔProduction cost relative to Process 2	ΔCapitial cost relative to Process 1	ΔCapitial cost relative to Process 2
	[-]	[-]	[%]	[%]	[€/MWh]	[€/MWh]	[Mio€], TCI	[Mio€], TCI
HyGenSys - SEWGS	HyGenSys	SEWGS	0,26	2,66	n. a.	n. a.	n. a.	n. a.
CLR-s - MWGS	CLR-s	MWGS	0,00	-0,02	1,4	10,6	2	62
OSD-Mem	CLR-a	OSD	0,04	0,03	-4,6	-0,6	48	-8
OSD - MWGS	OSD-Mem	MWGS	0,00	-0,01	1,2	14,5	12	157
CLR-a - SEWGS	CLR-a	SEWGS	-5,00	-3,60	16,7	25,9	49	203
MREF-CLC	MREF	CLC	0,10	n. a.	6,0	n. a.	88	n. a.
MWGS-CLC	MWGS	CLC	-0,90	n. a.	10,8	n. a.	149	n. a.
CLR-a - MWGS	CLR-a	MWGS	No detailed investigation - parameter studies reveal: obviously no economic alternative					

The CACHET project has been an integrated part of CCP2 and an important contributor to enhancing CO_2 capture technologies. It has brought together researchers and engineers from academia, research institutes and industry in a constructive manner and paved way for further improvements through co-operations that might otherwise not have happened.

For more information, see www.CACHETCO2.eu and www.CO2CaptureProject.org

ACKNOWLEDGEMENTS

The CACHET project was funded by the European Commission under the 6th Framework (contract 019972). The consortium would like to thank the European Commission, supporters and co-workers within the CACHET project.

REFERENCES

1. F. Giroudière, J.L. Ambrosino, B. Fischer, D. Pavone, E. Sanz-Garcia, A. Le Gall, E. Soutif, H.Vleeming, 2009. HYGENSYS : A new process for power production with pr-combustion CO_2 capture, in L.I. Eide (ed.) 2009, Carbon Dioxide Capture for Storage in Deep Geologic Formations, Volume 3. CPL Press.
2. Magnus Rydén, Anders Lyngfelt[1], Alexander Schulman, Luis F. de Diego, Juan Adánez, María Ortiz, Tobias Pröll, Johannes Bolhàr-Nordenkampf, Philipp Kolbitsch, 2009. Developing Chemical Looping Steam Reforming and Chemical Looping Autothermal Refoming, in L.I. Eide (ed.) 2009, Carbon Dioxide Capture for Storage in Deep Geologic Formations, Volume 3. CPL Press.
3. Franco Mizia; Stefano Rossini; Mariangela Cozzolino; Ugo Cornaro, Stephen Tlatlik; Ingeborg Kaus; Egil Bakken; Yngve Larring, 2009. One Step Decarbonization, in L.I.Eide (ed.) 2009, Carbon Dioxide Capture for Storage in Deep Geologic Formation, Volume 3. CPL Press.
4. J.W. Dijkstra[1], D. Jansen, R.W. van den Brink, T.A. Peters, M. Stange, R. Bredesen, A. Goldbach, H.Y. Xu, A. Gottschalk, S. Tlatlik, A. Doukelis, 2009, Development of Hydrogen membrane reactors for CO_2 Capture, in L.I. Eide (ed.) 2009, Carbon Dioxide Capture for Storage in Deep Geologic Formation, Volume 3. CPL Press.
5. T. Peters, M. Stange and R. Bredesen, 2009, Development of thin Pd-23% Ag/Stainless Steel composite membranes for application in Water Gas Shift membrane reactors, in L.I. Eide (ed.) 2009, Carbon Dioxide Capture for Storage in Deep Geologic Formation, Volume 3. CPL Press.
6. Ed van Selow, Paul Cobden, Ruud van den Brink, Andrew Wright, Vince White, Peter Hinderink and Jeff Hufton, 2009, Pilot-scale Development of the sorption enhanced water gas shift process, L.I. Eide (ed.) 2009, Carbon Dioxide Capture for Storage in Deep Geologic Formation, Volume 3. CPL Press.
7. T. Melien and S. Brown-Roijen, 2009 Economics, in L.I. Eide (ed.) 2009, Carbon Dioxide Capture for Storage in Deep Geologic Formation, Volume 3. CPL Press.
8. B. Smith, Knut I. Aasen, Kjersti Wilhelmsen and Daniel Käck, 2009, The Hydrogen membrane reformer pre-combustion gas power cycle, in L.I. Eide (ed.) 2009, Carbon Dioxide Capture for Storage in Deep Geologic Formation, Volume 3. CPL Press.

Carbon Dioxide Capture for Storage in Deep Geologic Formations, Volume 3
L.I. Eide (Ed.)

Chapter 11

DEVELOPMENT OF HYDROGEN MEMBRANE REACTORS FOR CO_2 CAPTURE

J. W. Dijkstra[1], D. Jansen[1], R.W. van den Brink[1], T.A. Peters[2], M. Stange[2], R. Bredesen[2], A. Goldbach[3], H.Y. Xu[3], A. Gottschalk[4], S. Tlatlik[4], A. Doukelis[5]
[1]Energy research Centre of the Netherlands ECN, P.O. Box 1, 1755 ZG Petten, The Netherlands
[2]SINTEF Materials and Chemistry, P.O. Box 124, Blindern, 0314 Oslo, Norway
[3]Dalian Institute of Chemical Physics, 457 Zhongshan Road, Dalian, 116023, P.R. China
[4]Process Design Center GmbH, Joseph-von-Fraunhofer-Str. 20, 44227 Dortmund, Germany
[5]National Technical University of Athens, Heroon Polytechniou St9, Zografou, 15780 Athens, Greece

ABSTRACT: In the European FP6 research project CACHET palladium-based hydrogen membrane reactors for pre-combustion CO_2 capture from natural gas combined cycles have been developed. In the project both the electroless plating method used by DICP and the SINTEF two-stage membrane preparation method based on magnetron sputtering have been successfully up-scaled to produce membrane tubes with a length of 50 cm. The membranes have been tested extensively with hydrogen/nitrogen gas mixtures and with simulated feed gas for reforming and water gas shift conditions. Process design studies showed that both the Integrated Membrane Reformer Combined Cycle (MREF) and the Integrated Membrane Water Gas Shift Reactor Combined Cycle (MWGS) are able to capture virtually 100%. But due to economic reasons the current concepts have been designed to operate at 92% capture of the CO_2, having power generation efficiencies of 46.2% and 47.1%, respectively. For a full scale application, a reactor concept has been selected for a membrane reformer and water gas shift membrane reactor. This full scale reactor design has been used for the design of a bench scale Process Development Unit (PDU) with a capacity of testing up to 8 membranes of 50 cm length at the same time.

INTRODUCTION

This chapter presents the results of the CACHET work on development of hydrogen membrane reactors. The objective of the membrane work package in CACHET was to develop and evaluate the potential of H_2 membrane reactors using Pd or Pd/Ag membrane reactor technology for the pre-combustion capture of CO_2. These memb,ranes are integrated into reactors that are used in pre-combustion processes for CO_2 capture in natural gas combined cycles. An overview of the work is provided, with a special focus on reactor development. The work done on development of palladium-alloy membranes by magnetron sputtering, that was also part of this work package, is treated separately in [1]. The results of the economic evaluations are treated in [2].

The work has been done in close collaboration of the Energy Research Centre of the Netherlands (ECN), SINTEF from Norway, the Dalian Institute of Chemical Physics (DICP) from China, Process Design Center (PDC) from Germany and the National Technical University of Athens (NTUA) from Greece.

Hydrogen membrane reactors are considered an attractive technology for pre-combustion CO_2 capture in gas fired power stations. These integrated reactors combine the efficient conversion of natural gas or syngas into H_2 and CO_2, as well as their simultaneous separation (see Figure 1) [3].

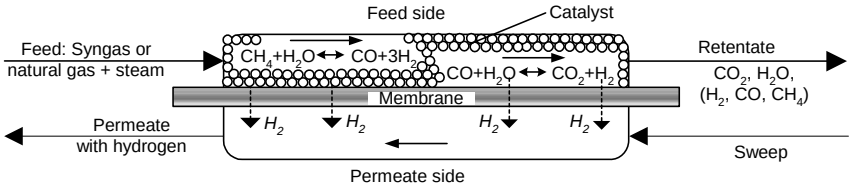

Figure 1. Working principle of a hydrogen membrane reactor for CO_2 capture.

The membrane reactor is integrated in a conventional power cycle, where the hydrogen is used for power generation, while the remaining gas stream contains mainly CO_2 and some non-recovered hydrogen, steam and other unconverted components at relatively high pressure. Subsequent condensation of the steam leaves concentrated CO_2 at high pressure, reducing the compression energy for transport and storage.

Concerning the development of this technology, multiple aspects have been considered. Membrane manufacturing (including supports and sealings) has been done to scale up the length of membranes. Membranes have been tested extensively to assess the performance and durability. Reactor concept selection and design has been done on a full-scale size and the results have been translated into a bench-scale Process Development Unit (PDU). Based on thermodynamic insights conceptual process design (process synthesis) was carried out to identify economically attractive process alternatives applying the membrane reactors.

PROCESS SYNTHESIS

The development of both membranes and the membrane reactor has been guided and supported by process synthesis and techno-economic analysis.

Two process schemes for H_2 membrane reactors integrated in natural gas combined cycles have been evaluated (see Figure 2):

(a) Integrated Membrane Reformer Combined Cycle (MREF) and
(b) Integrated Membrane Water Gas Shift Combined Cycle (MWGS).

At the start of the project preliminary performance criteria for the membranes were formulated as guidance for membrane development. These were based on capture cost data from open literature. Target CO_2 capture costs were used for estimating the allowable investments, which was then translated into a target permeance value. This study gave that apparent permeances of $1.3 – 1.6*10^{-6}$ $mol.m^{-2}.s^{-1}.Pa^{-1}$ would be required for MWGS, and $3.0 – 4.6*10^{-6}$ $mol.m^{-2}.s^{-1}.Pa^{-1}$ for MREF [4,5]. After that, detailed process synthesis and costing studies were done, based on experimental permeance data. These are treated in [2].

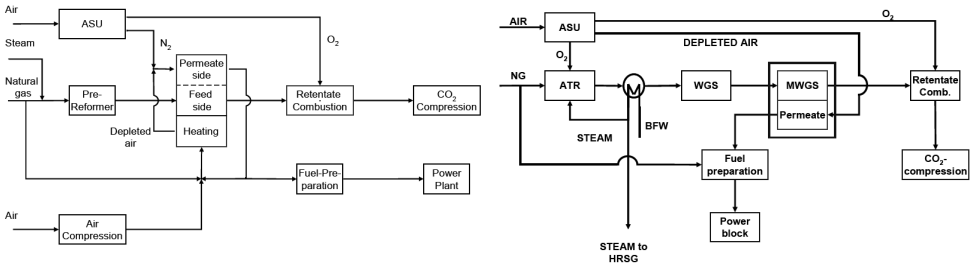

Figure 2. Process block schemes for (a) an Integrated membrane Reformer Combined Cycle (MREF) and for (b) an Integrated membrane Water Gas Shift Combined Cycle (MWGS).

MREF: The natural gas is preheated, desulfurized and mixed with steam. After adiabatic pre-reforming, the feed mixture is supplied to the reaction tubes of the key unit, the integrated membrane reformer. The conversion of the hydrocarbons (C_nH_m) by steam methane reforming (SMR) takes place at T = 600° C and p = 4.7 MPa (see Table 1). Syngas is generated; the water gas shift reaction (WGS) takes place consecutively. To support the SMR and the WGS reaction, the reaction product hydrogen is extracted from the reaction mixture selectively via the Pd-membrane. On the permeate side of the membrane, a mixture of nitrogen, CO_2 and steam serves as sweep gas. To achieve sufficient driving forces for the membrane separation the permeate side of the membrane is operated at 1 MPa, to reduce the requirement of membrane area with regard to economics.

Inside the reactor, heating is carried out to compensate for the endothermic heat of reaction. Bypassed natural gas and recovered hydrogen that is recycled to the heating section are combusted in presence of air. The combustion takes place at pressurized conditions; afterwards the flue gas is cooled down and used as sweep gas.

The permeate stream is prepared to be used as fuel gas for gas turbine use. The retentate stream released from the unit mainly consists of CO_2 and steam. Along with these minor fractions of combustible components like C_nH_m, H_2 and carbon monoxide are present. Thus to fulfill the specification for CO_2 storage, the mixture has to be treated in retentate combustion where the combustible components form CO_2 and steam. Heat and steam are recovered, CO_2 is conditioned for storage.

Table 1. Membrane reactor operating conditions

	MWGS	MREF
Inlet pressure	4.7 MPa	4.7 MPa
Feed side inlet/outlet temp	400/378° C	600/600° C
Feed $H_2/CO_2/CO/CH_4/H_2O$	0.56/0.18/0.05/0.01/0.19	0.053/0.023/0.0002/0.225/0.696
Mode of operation	Adiabatic, countercurrent	Isothermal, countercurrent

MWGS: Natural gas is converted into synthesis gas in an oxygen blown autothermal reformer (O_2-ATR). Steam is added to avoid coke formation. The reaction takes place at a pressure of 4.7 MPa (see Table 1). Downstream of the reformer, a high temperature pre-WGS is operated. CO and H_2O are converted into CO_2 and H_2 and a chemical equilibrium is virtually obtained. This reactor provides the feed for the water gas shift membrane reactor, which operates adiabatically at an inlet temperature of 400 °C. The outlet temperature of the syngas results from the heat balance, taking into account heat of reaction as well as the convective heat flows via feed and sweep-gas. Due to

superior driving force, the permeate is recovered at gas turbine inlet pressure. Additional pressurization is not required.

An air separation unit (ASU) is used to provide the oxygen used for the operation of the ATR. The ASU by-product N_2 is used as a sweep gas for the membrane reactor. The resulting permeate stream is directed to the gas turbine. The CO_2 present in the retentate is conditioned for storage.

Based on the concepts described detailed process simulations have been carried out in close collaboration between PDC, ECN, SIEMENS and NTUA. The Siemens V94.3 gas turbine performance has been calculated with the accounting for the impact of using hydrogen as a fuel and GT load limitations. The non-fired triple pressure single reheat steam cycle has been modeled in detail, incorporating import and export of steam from and to the capture section. The heat integration has been carried out. Based on the results of a pinch analysis, a heat exchanger network has been generated. Corrosion mechanisms like metal dusting have been considered.

Table 2 presents the calculated efficiencies based on the results of the process simulations. Technically 100% capture rate is possible to achieve. However, due to economic reasons the processes operate at reduced capture and therefore avoidance rate.

Table 2. Overall process performance.

	No-capture reference case	MWGS	MREF
Overall energy efficiency	57.2%	47.1%	46.2%
CO_2 capture rate	-	93.5%	93.5%
CO_2 avoidance rate	-	92.1%	91.9%

Among the membrane reactor processes investigated in CACHET, the MWGS case shows a significantly higher efficiency than the MREF case. Compared with the no-capture reference case (see [2]), the penalty of the MWGS process for capturing CO_2 amounts to 10.1%-points, the one of the MREF case to 11.0%-points. The required membrane surface area (taking permeances obtained from experimental data in gas mixtures at relevant temperature and pressure) for the MWGS case is much lower (4,000 m^2) than that of the MREF (20,000 m^2). The main reason for the lower surface area of MWGS case is the much higher partial pressure of hydrogen at the feed side, resulting in a much higher driving force for permeation.

Potential improvements of the MREF process include operating at a higher temperature. Increasing the temperature will shift the reforming reaction equilibrium towards a higher H_2 partial pressure at the feed side of the membrane reactor. Thus, this allows for operation of the sweep side at higher pressure without the need for recompression. This would allow for a higher efficiency, as well as for a lower membrane surface area.

The process design presented above has been used for an economic evaluation of both the MREF and MWGS processes, which is treated in [2].

MEMBRANE DEVELOPMENT

Within the project significant progress has been made in scaling up the length of the membranes. SINTEF produces 50 cm long Pd-23w%Ag membranes prepared by a two-step method in which first a thin defect-free Pd-alloy film is prepared by sputtering deposition onto a silicon wafer. In a second step, the membrane is removed from the wafer and transferred to a porous stainless steel support. SINTEF focuses on application of their membranes in the water gas shift membrane reactor at temperatures of around 400 °C. Please refer to [1].

DICP produces 50 cm long pure Pd membranes (Figure 3) on a ceramic support made by ECN and capped with new high temperature/high pressure seals (designed for 700 ^{o}C and 3.9 MPa), also provided by ECN. Prior to deposition of the Pd layer (2-15 μm) by electroless plating, the pores of the support tubes were pre-filled with an inorganic gel to obtain a smooth surface and prevent Pd from entering into the pore structures [6]. These pores were re-opened after completion of the Pd deposition by decomposing the gel at 500 ^{o}C in H_2, leaving a micro-porous ceramic residue behind. The DICP membranes can be applied in both water gas shift and steam reforming membrane reactors.

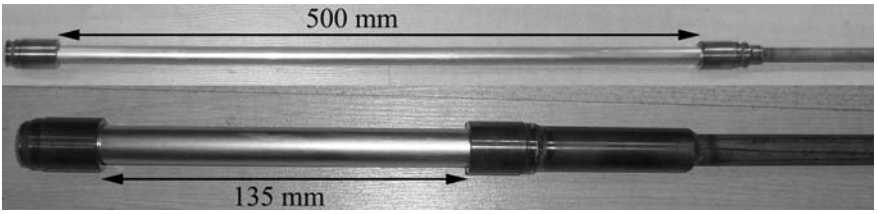

Figure 3. Pd membranes from DICP equipped with ECN's high pressure, high temperature seals.

MEMBRANE TESTING

DICP membranes have been tested extensively with hydrogen/nitrogen gas mixtures and with simulated feed gases for water gas shift and reforming. The pressure dependence of the single gas H_2 fluxes deviates from Sieverts' law with a typical pressure exponent of around 0.64 [7]. The 'linear' single gas H_2 permeance of DICP membranes with ca. 2 μm thick Pd layers is in the range of $7.2*10^{-6}$ to $9.7*10^{-6}$ mol·m^{-2}·s^{-1}·Pa^{-1} at 500 °C and 100 kPa pressure difference. At a 2.5 MPa pressure difference, it still amounts to $1.7*10^{-6}$ mol·m^{-2}·s^{-1}·Pa^{-1} at 400 °C and $2.5*10^{-6}$ mol·m^{-2}·s^{-1}·Pa^{-1} at 600 °C, which compares favourably with the CACHET target values for WGS and reforming applications, i.e. $1.3\text{-}1.6*10^{-6}$ mol·m^{-2}·s^{-1}·Pa^{-1} and $3.0\text{-}4.6*10^{-6}$ mol·m^{-2}·s^{-1}·Pa^{-1}, respectively [4,5]. The ideal H_2/N_2 selectivity of these membranes increased with temperature but decreased with pressure difference because of the non-linear increase of H_2 flux with pressure. At 400 °C it declined from 7000 to 2750 when the pressure difference was raised from 0.1 to 3.0 MPa. Membranes with such thin Pd layers are sufficiently stable for extended operation in the WGS temperature range, i.e. 350-450 °C as shown below. However, the discrepancy between thermal expansion coefficients of the ceramic substrate and the metal leads to increasing mechanical stress at higher temperatures, which may result in detachment of the Pd layer from the support or pinholes and fissures if the selective layer is very thin. Therefore, if temperatures approach and exceed 600 °C, application of Pd-type membranes in reforming probably will require membranes with thicker Pd layers, which exhibit significantly lower permeances. For example, the 'linear' permeance of Pd/ceramic composite membranes with ca. 11.5 μm thick Pd layers reached only $1*10^{-6}$ mol·m^{-2}·s^{-1}·Pa^{-1} at 500 °C and 1.5 MPa pressure difference which amounts to 40% the corresponding value of membranes with 2 μm thick Pd layers, i.e. $2.5*10^{-6}$ mol·m^{-2}·s^{-1}·Pa^{-1}. Ideal H_2/N_2 selectivity of composite membranes with 11.5 μm thick Pd layer ranged between 3400 and 7000 between 300 and 500 °C and pressure differences of 0.1-1.5 MPa. On the other hand, application of such membranes in the separation of syngas and steam reforming mixtures showed that H_2 permeation rates will remain significantly below values for pure hydrogen permeance mentioned above. This is caused by external mass flow restrictions in gas mixtures such as diffusion and concentration polarization near the membrane surface and by poisoning of the membrane surface by CO.

The stability of the DICP membranes during separation of various reformate mixtures was studied using short membranes [7]. Figure 4 shows the performance of an 8 cm long membrane with ca. 1.5 μm thick Pd layer (35.2 cm^2 area) during a 200 h test at 400 °C and 1.1 MPa feed pressure in an un-shifted reformate (ca. 58.9% H_2, 22.6% H_2O, 5.9% CO_2, 11.6% CO, balance: N_2, CH_4). H_2 recovery and purity remained practically constant at 88.7% and 99.9%, respectively, throughout the test. During a subsequent 100 day test with a shorter 4.2 cm long Pd membrane at 400 °C and 1.1 MPa feed pressure, H_2 purity also remained better than 99.9% while ca. 55% H_2 were recovered from reformate of similar composition [5]. Stable H_2 recovery (90%) and H_2 purity (99.95%) were also observed during a 500 h separation test under similar conditions, i.e. 400 °C and 1.1 MPa feed pressure, with a 10 cm long Pd membrane (ca. 5.5 μm thick Pd layer, 44 cm^2 area) using a dry WGS-shifted reformate (ca. 73.1% H_2, 24.4% CO_2, 0.5% CO, balance: N_2, CH_4).

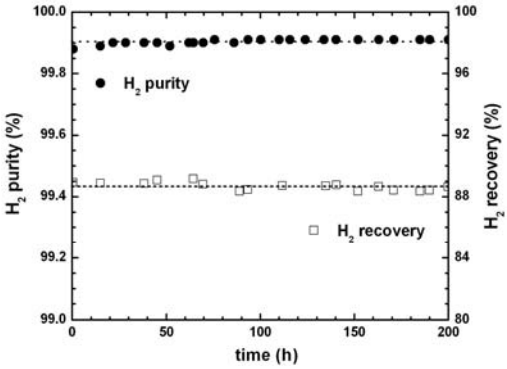

Figure 4. Reformate separation experiment with a DICP membrane [7]**.**

At ECN, two Pd membranes from DICP (both 3.5 μm thickness and fitted with ECN sealings, lengths respectively 8.3 cm and 13.9 mm) have successfully undergone durability testing. The membranes were in continuous operation at 450 °C for 14 days at atmospheric H_2 feed pressure wit daily permeance testing at 4-10 bar feed pressure. Subsequently successful temperature cycling in N_2 atmosphere and temperature cycling in atmospheric H_2 atmosphere (8-12 cycles, 450° C-150 °C with a ramp rate of 1 °C/min) was done. DICP has developed and tested thicker Pd membranes to enhance the long-term stability at operation temperatures of 600 °C because the degradation could go faster at this temperature in the reformate mixtures. Based on the stability tests performed so far it is concluded that membranes, sufficiently stable to be used for tests in a bench scale reactor, can be fabricated.

The long-term stability of Pd-23%Ag/stainless steel composite membranes has been examined in H2/N2 and WGS mixtures over periods exceeding one year. Based on these experiments, a membrane life time of several (1.6-2.5) years at T = 400°C is assessed. Pure H_2 permeance of SINTEF membranes up to $1.4*10^{-5}$ $mol \cdot m^{-2} \cdot s^{-1} \cdot Pa^{-1}$ at 400 °C have been obtained. Permeances in gas mixtures representative for the CACHET application are lower than those in pure H_2 due to the presence of mass transfer and surface effects on the hydrogen flux while measuring in gas mixtures [8]. Measurements by SINTEF in a typical water gas shift gas mixture showed H_2 permeances up to $8*10^{-7}$ $mol \cdot m^{-2} \cdot s^{-1} \cdot Pa^{-1}$ at 15% H_2 recovery. (See also [1]). This somewhat lower, but still is in the range of the cachet target value for MWGS of $1.3 – 1.6*10^{-6}$ $mol.m^{-2}.s^{-1}.Pa^{-1}$ given the uncertainty that is associated with the cost estimates from which the target values have been derived.

To conclude, the single gas H_2 permeance of the membranes produced by DICP and SINTEF are within the range required.. There is no absolute selectivity target for the membranes set within CACHET. However, to satisfy the target of capturing 90% of the CO_2, an (H_2/N_2) permselectivity in the order of 400 is needed [4]. Long-term stability testing at a feed pressure of 10 bars of the SINTEF membranes showed after 250 days process time H_2/N_2 selectivities of approximately 1000. In separation experiments at temperatures between 250 and 500 °C DICP membrane tubes with ECN seals showed ideal H_2/N_2 selectivities of at least 2500 at pressure differences up to 3 MPa. To conclude, both types of membranes have sufficient selectivity for capturing 90% of the CO_2.

CONCEPT SELECTION FOR FULL SCALE DESIGN

To decide about the design of a bench scale reactor to be constructed in the project, an assessment was first made about the preferred full scale reactor concept for implementation in a full scale combined cycle. Both applications correspond with several thousands of square meters of membrane surface area, which implies that multiple reactors must be used. The most important concepts found in literature for fixed bed membrane reformers are plate type membrane reactors from Tokyo Gas/MHI [8] and a fixed bed concept with membrane and heating tubes from Shell [9]. For membrane water gas shift reactors, the most important concepts are both shell-and-tube based concepts published by ECN [10] and BP [11]. On the basis of this concept inventory and an initial concept definition, a long list of design concepts has been made using a systematic design methodology [12], from which three promising concepts have been selected for final assessment. These concepts have been worked out for both reforming as well as water gas shift membrane reactors. The difference between reforming and water gas shift is primarily the absence of the heating zone in case of a water gas shift reactor. This makes the construction considerably more simple, which is especially noticeably in the manifolding.

The concepts selected for final assessment are:

- Catalyst in shell concept. A shell and tube based concept with catalyst in the shell. Membrane tubes are inserted into the shell and remove the hydrogen produced. In the case of a reformer, special burner tubes are also inserted in the catalyst bed. Manifolding is done using multiple tubesheets (Figure 5).
- Catalyst in annulus concept. A shell and tube based concept with catalyst in an annular space around the membrane. The advantage is that a better definition of the catalyst bed is obtained, with as a drawback a more complicated construction. In the case of a membrane reformer, special burners are placed in the shell of the reactor. Manifolding is done using multiple tubesheets (Figure 6).
- Box concept. This is based on a conventional steam methane reformer with membranes inserted in the reformer tubes, and manifolding using headers and pigtails. For reforming, conventional burners are placed in the box (Figure 7).

For evaluation, the multi-criteria scoring was done by a multi-disciplinary panel using a method developed by Kesselring [13]. Over 20 criteria were used in the assessment covering both manufacturing and use of the concepts.

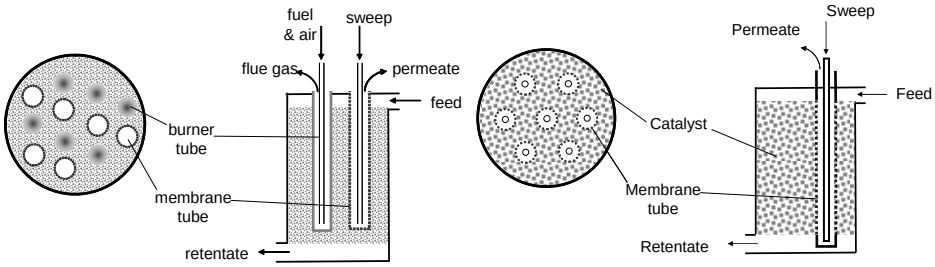

Figure 5. 'Catalyst in shell' designs for reforming (left) and for shift (right).

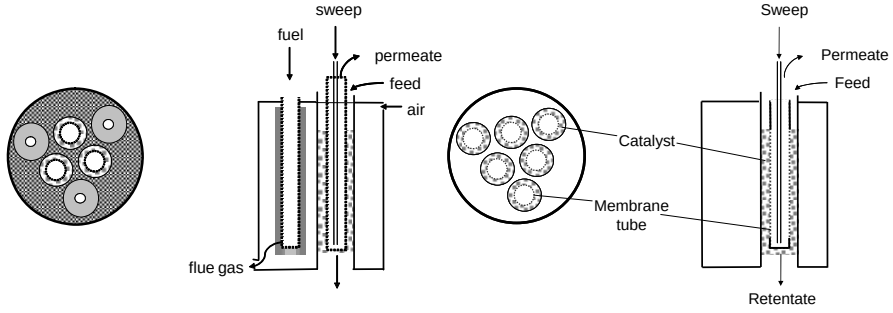

Figure 6. 'Catalyst in annulus' designs for reforming (left) and for shift (right).

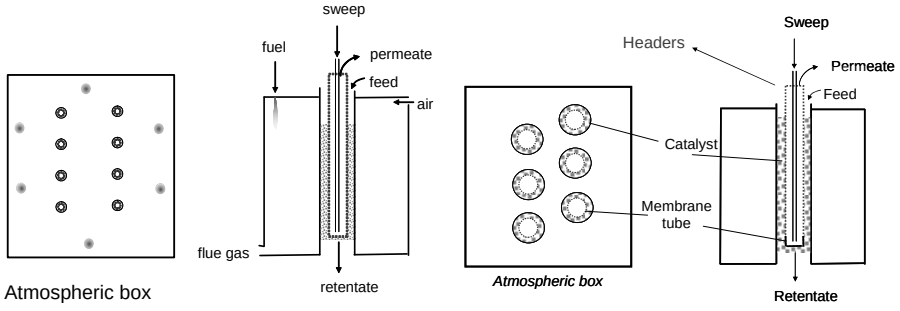

Figure 7. 'Box' concepts for reforming (left) and for water gas shift (right). Manifolding by means of headers (not shown).

For membrane reforming, the box concept was the best scoring concept in the analysis. This concept is derived from the design of a conventional steam reformer adapted for addition of membranes in the reformer tubes. The possibilities of operating the reformer box with heaters under pressure have not been considered explicitly. Strong points of this concept were the burner manufacturing and use, and issues related to failure and manufacturing aspects of the vessel/box. Weak points of this concept compared to the other membrane reactor alternatives are the membrane lifetime (due to the use of conventional burners giving a relative higher risk of hot-spots) and the complex manifolding.

For membrane water gas shift, the three concepts scored comparable in the multi-criteria analysis. More detailed information was required for a final selection. Especially the significance of mass

transfer limitations and the relative costs of manifolding were issues that were addressed as being important.

For MWGS, a sequential membrane and water-gas-shift catalyst set-up has the advantage of a lower reactor complexity (Figure 8). This set-up has consecutive conventional shift reactors and membrane permeators, using either of the three reactor concepts identified. Calculations indicated that for membrane water gas shift reactors 3-4 stages will give a sufficiently high CO conversion. For a sequential membrane steam reformer, however, up to 30 stages still gave insufficient methane conversion.

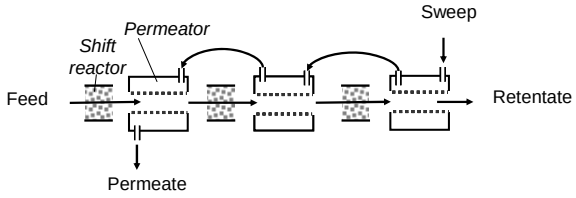

Figure 8. Sequential set-up for shift.

PROCESS DEVELOPMENT UNIT

The developed membranes will be tested under relevant process conditions in a Process Development Unit (PDU) for membrane reactor testing for both steam reforming and water-gas-shift (sequential and integrated). The PDU consists of two separate sections. The test rig provides gasses with the required composition, flow and process conditions, safely discards the used gasses and performs all necessary gas analyses. The second section, the membrane reactor, is a down-scaled simplified version of the box concept (Figure 7) but easy exchange of reactors is possible to test other concepts.

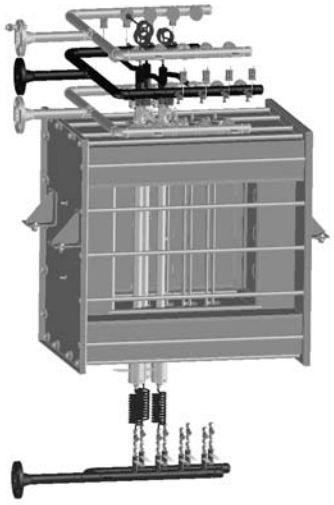

Figure 9. Isometric drawing of membrane reactor used in the Process Development Unit.

The currently connected membrane test reactor (Figure 9) is based on the box concept (Figure 7), following the results of the reactor concept selection for reforming. It is a downscaled version of a full-scale membrane reactor for steam methane reforming. It will however also provide information on the design of other concepts for membrane reforming. By not using any heating it can also be used as a water gas shift membrane reactor and by leaving out the catalyst as a test unit for the non-integrated shift and separation concept. The design features the same membrane tube/catalyst configuration as in the full-scale box concept, as well as its manifolding of multiple membranes. It has been simplified with respect to heating; burners are replaced by radiating electrical elements, placed in the walls. The reactor can consist of a maximum of 8 tubes (See Table 3). Each reactor tube can accommodate catalyst and membranes up to 50 cm length. The reactor will be tested at a scale of 3 tubes for shift to 8-tubes for reforming.

Supply of feed, sweep and removal of permeate gas is done at the top side of the reactors, using three manifolds. Using flange connections, membrane reactor tubes can be installed and removed easily. Spirally shaped lines have been used for flexibility. To allow for easy removal of reactor tubes from the oven, a compact gland packing has been used for the bottom retentate connection. This allows for pulling out one tube of the heated box in the upward direction. Individual removal allows for much easier mounting of membrane tubes in the reactor and for easier catalyst loading.

Table 3. PDU key data

	Value
Maximum temperature	600° C
Maximum pressure	40 bar
Maximum number/length of membranes	8 tubes/50 cm
Feed gasses	$H_2/CO/CO_2/H_2O/N_2$
Nominal H_2 production shift (3 membranes, 400° C)	6.7 kWth 9/2.2 Nm^3/hr
Nominal H_2 production reforming (8 membranes, 500° C)	2.5 kWth/0.8 Nm^3/hr
Operating range compared to nominal	25-400%
Configuration	Counter-current

The test rig was designed to operate membrane reactors at feed pressures and temperatures up to 40 bara and 600 ºC respectively. Feed gases consisting of CH_4, H_2, CO, CO_2 and H_2O with a flexible composition can be supplied at this pressure and temperature. The nominal hydrogen production capacity is 2.5 kWH_2 (0.8 Nm^3/hr) for reforming and 6.7 kWH_2 (2.2 Nm^3/hr) for shift. A 20-400% operating window relative to the nominal capacity is allowed. Gas analysis is done on the feed and product streams, as well as on samples from individual reactors. Reactor tube skin and catalyst temperatures are monitored for all reactors.

The PDU (Figure 10) will be used to demonstrate the feasibility of the reactor concept allowing experimental data to be taken for both design purposes and to improve process modeling. Experiments will be conducted to determine the effect of critical process variables (pressure, temperature, feed composition) on the reactor/membrane performance (conversion, permeability, permeate purity, heat transfer). The long term stability of the membrane and catalyst will also be verified. The results will provide robust design data that will form the basis for the future design in pilot-scale or full-scale.

Figure 10. Process Development Unit (PDU) for testing of membrane reactors for CO_2 capture.

OUTLOOK

Testing in the PDU will focus on demonstration of the feasibility of the reactor concept for pre-combustion CO_2 capture. It will be used to determine the effect of critical process variables (pressure, temperature, feed composition) on the process performance (conversion, permeability, permeate purity and heat transfer). The unit will also measure the membrane stability of up to eight individual membranes at the same time. Membrane lifetime or replacement frequency is a crucial parameter in determining the industrial applicability and costs of membrane reactors.

During separation of hydrogen from syngas and reformate mixtures, it became clear that mass transfer limitations are important issues to be addressed to optimize the reactor design [14]. Therefore 2-dimensional modeling of membrane reactors has been started. With the PDU validation of the reactor models can be done. More detailed reactor designs are to be made for a good assessment of the feasibility of reforming as well as shift. Also the issue of firing at elevated pressure in combination with the construction of the reformer reactor needs to be addressed. The PDU can be used for validation of these models and obtaining catalyst and membrane data under bench scale conditions.

To allow for better process efficiencies and lower costs, higher operating temperatures for reforming are required. Membrane stability at high operating temperatures of 600° C and above is however an issue that needs to be addressed. The prospects of using higher operating temperatures on process efficiency need to be addressed.

CONCLUSIONS

The results of CACHET have shown important progress in the development of Pd-based membrane reactors for pre-combustion CO_2 capture for natural gas combined cycles. Thin Pd-Ag membranes (2 µm thickness) on 50 cm long macro-porous (2 µm pore size) tubular stainless steel supports have been prepared by the SINTEF two-stage method. The performance of these Pd-alloy membranes are within the range of the required performance criteria derived for the integrated membrane Water Gas Shift Combined Cycle (MWGS) option. DICP produces 50 cm long pure Pd on ECN ceramic supports capped with new high ECN temperature/high pressure sealing. The performance of these Pd /ceramic membranes in reforming conditions is within the performance range needed for both the MWGS and the Integrated membrane Reformer Combined Cycles (MREF) option. However, for durability requirements, thicker membranes with significantly decreased permeance may be necessary in reforming applications.

Both SINTEF and DICP membrane tubes show sufficient selectivities to satisfy the CACHET target of capturing 90% of the CO_2 in a natural gas combined cycle power plant. Besides, based on long-term stability tests, it is concluded that stability of the membranes so far is sufficient for the membrane reactor test in the bench scale Process Development Unit.

For both the MWGS as well as the MREF a feasible process for power production with CO_2 capture have been designed. Process efficiencies of MREF and MWGS are 46.2% and 47.1%, respectively. The penalty for capturing CO_2 compared to the no-capture reference case of the MWGS process amounts to 10.2%-points, that of the MREF to 11.0%-points. The higher capture penalty of the MREF is mainly due to the fact that the H_2 product is at 1.0 MPa which means that cooling, compression and subsequent dilution with steam is required. The MWGS process is a much leaner and more straightforward process with a lower penalty.

For the MREF, the preferred reactor concept is the so-called box concept, derived from a conventional steam reformer. For the MWGS reactor, several feasible options were identified. A preference, however, exists for the sequential sub-type of the concepts that separates the reaction and separation steps.

A Process Development Unit has been constructed which features a scaled down version of the reactor concepts for integrated membrane steam reformer and integrated/sequential water gas shift. The reactor will be tested at a scale of 3 to 8 tubes of 50 cm length. These tests will produce input data for the efficiency and capture cost calculations and provide input for further technology development.

ACKNOWLEDGEMENTS

This research is financed by the European Union and the CO_2 Capture Project Phase 2 (CCP2) through the EU-6FP CACHET project (Contract no.: 019972) (www.CACHETCO2.eu), by the Dutch Ministry of Economic affairs (EZ) and the CATO project.

This Chapter is contains figures, portions and excerpts that originally appeared in Energy Procedia Vol 1, Issue 1, Greenhouse Gas Control Technologies 9, Proceedings of the 9th International Conference on Greenhouse Gas Control Technologies (GHGT-9), 16-20 November 2008, Washington DC, USA., which was published by Elsevier Ltd.

REFERENCES

1. T. Peters, M. Stange and R. Bredesen: Development of Thin PD-23%/AG/Stainless steel composite membranes for application in Water Gas Shift Membrane Reactors, in L.I. Eide (ed.): Carbon Dioxide Capture for Storage in Deep Geologic Formation, Volume 3, CPL Press 2009
2. T. Melien and S. Brown-Roijen: Economics, in L.I. Eide (ed.): Carbon Dioxide Capture for Storage in Deep Geologic Formation, Volume 3, CPL Press 2009
3. D. Jansen, P.P.A.C. Pex, J.W. Dijkstra and S.C.A. Kluiters, Membrane reactors: key technology for production of de-carbonised energy carriers, *The Seventh International Conference on Greenhouse Gas Control Technologies (GHGT-7)*, Vancouver, Canada 5th - 9th September, (2004).
4. A. Gottschalk, Pre-Combustion CO_2 Capture Technologies Treating Gaseous Fuels - EU-FP6-Project CACHET, *15th International Conference on the Properties of Water and Steam 2008 (15th ICPWS)*, Berlin, Germany, (7-11 September 2008), ISBN 978-3-931384-64-7.
5. Jansen, D., CACHET Hydrogen membrane reactors for pre-combustion CO_2 capture, *European Conference on CCS Research, Development and Demonstration, Oslo, Norway* (February 9-11, 2009).
6. S. F. Hou, K. Jiang, W.Z. Li, H.Y. Xu, L.X. Yuan, A metal palladium composite membrane or alloy palladium composite membrane and their preparation methods, *WO patent 2005/065806* (2005).
7. K. Jiang, A. Goldbach, C. Bao, C.Y. Yu and H.Y. Xu, *Proceedings of the 10th International Conference on Inorganic Membranes ICIM 10, Tokyo*, (2008), paper 1a07.
8. I. Yasuda, Y. Shirasaki, T. Tsuneki, T. Asakura, A. Kataoka, H. Shinkai and T. Yamaguch, Development of Membrane Reformer for Hydrogen Production from Natural Gas, *ICCMR-6*, (6-9 July 2004).
9. M.T. Miglin, A.N. Matzakos, S.L. Wellington, L.A. Clomburg, P. Veenstra, A. Munshi, R. Jean, G.W. Elliot and M.J. Groeneveld, Apparatus and process for production of high purity hydrogen, *Patent WO2004/022480* (2004).
10. P.T. Alderliesten and M. Bracht (1997), *An attractive option for CO_2 control in IGCC systems: water gas shift with integrated H_2/CO_2 separation (WIHYS) process; Phase 1: Proof of Principle; Final report CEC Project JOU2-CT92-0158*, ECN Energy research Centre of the Netherlands, ECN-C--97-097.
11. Middleton, P., Hurst, P. and Walker, P., *Grace: pre-combustion de-carbonisation hydrogen membrane study, In: Carbon Dioxide Capture for Storage in Deep Geologic Formations, Volume 1, Chapter 27* (ed. by D. C. Thomas, S. M. Benson), Elsevier (2005).
12. Pahl, G., Beitz, W. (1995) *Engineering Design: A Systematic Approach*, 5th Edition, Springer Verlag.
13. Kesselring, F. (1954) *Technische Kompsitionslehre*, Springer, Berlin.
14. T.A. Peters, M. Stange, H. Klette, R. Bredesen, High pressure performance of thin Pd-23%Ag/stainless steel composite membranes in water gas shift gas mixtures; influence of dilution, mass transfer and surface effects on the hydrogen flux, *Journal of Membrane Science*, 316 (2008) 119-127.

Carbon Dioxide Capture for Storage in Deep Geologic Formations, Volume 3
L.I. Eide (Ed.)

Chapter 12

DEVELOPMENT OF THIN PD-23% AG/STAINLESS STEEL COMPOSITE MEMBRANES FOR APPLICATION IN WATER GAS SHIFT MEMBRANE REACTORS

Thijs Peters, Marit Stange and Rune Bredesen
SINTEF Materials and Chemistry, P.O. Box 124 Blindern, N-0314, Oslo, Norway

ABSTRACT: In the current overview, we report the preparation and transport properties of tubular supported Pd-23%Ag membranes for application in WGS membrane reactors. Applying a H_2 feed pressure of 26 bars, one of the highest H_2 fluxes reported, 2477 $mL \cdot cm^{-2} \cdot min^{-1}$ (STP) or $6.1 \cdot 10^4$ kg $H_2 \cdot m^{-2} \cdot h^{-1}$, which corresponds to a permeance of $1.5 \cdot 10^{-2}$ $mol \cdot m^{-2} \cdot s^{-1} \cdot Pa^{-0.5}$, was measured at 400°C after an oxidative pre-treatment of the membrane surface. The low pressure (~ 2 bars) H_2/N_2 permselectivity obtained is higher than 7500, but decreases with pressure to 2900 at 26 bars feed pressure. In feed gas mixtures, however, the H_2 flux obtained is strongly limited by a combination of surface effects and gas phase diffusion limitations. The long-term stability of Pd-23%Ag/stainless steel composite membranes has been examined in H_2/N_2 and WGS mixtures over periods exceeding one year. Based on these experiments, a membrane life time of several (1.6-2.5) years at T = 400°C is assessed. Results suggest that life time increases considerably by reducing temperature in the 325-375°C range. To conclude, the performance of the Pd-alloy membranes in terms of flux, stability and separation efficiency shows that this type of membranes represent a very promising alternative to be applied in pre-combustion power generation cycles with carbon dioxide (CO_2) capture.

INTRODUCTION

Hydrogen (H_2) selective membranes are interesting candidates to be applied in H_2 and energy technology. In water gas shift (WGS) membrane reactors, for example, the membranes can be used to achieve pre-combustion decarbonisation in large-scale power generation or H_2 production with CO_2 capture. The current commercial availability of H_2 selective palladium-based (Pd-based) membranes and their utilization, however, are limited due to an unfavorable cost-performance combination. These membranes are available in the form of tubes or foils, which are relatively thick (20 μm or more). The H_2 flux, being inversely proportional to the thickness of the membrane, is therefore too low for most applications. For practical use, it is therefore necessary to develop membranes with a reduced thickness of the Pd layer.

SINTEF has developed a technique for the manufacturing of Pd-based H_2 separation membranes based on a two step process allowing a reduction in the membrane thickness. First, a defect free Pd-Ag alloy membrane is prepared by magnetron sputtering onto the 'perfect surface' of a silicon wafer. In a second step the film is removed from the wafer allowing the preparation of very thin membranes. These films may subsequently either be used self-supported or integrated with various supports of different pore size, geometry and size [1,2]. This allows for, for example, the preparation of very thin (approximately 2 μm) defect free high-flux membranes supported on macroporous substrates, which can be operated at elevated pressures [3]. Moreover, the magnetron sputtering technique allows for the preparation of homogeneous films using multi-component targets with good thickness and composition control [4].

In the European FP6 project CACHET (Carbon Dioxide Capture and Hydrogen Production from Gaseous Fuels), Pd-based membrane reactors for CO_2 capture are collaboratively being developed by Dalian Institute of Chemical Physics (DICP) from China, SINTEF from Norway, National Technical University of Greece, Process Design Centre (PDC), Energy research Centre of the Netherlands (ECN) from the Netherlands, and BP from the United Kingdom [5]. The objective is to develop and evaluate the potential of H_2 membrane reactors using Pd or Pd-alloy membrane technology for the capture of CO_2. H_2 membrane reactors are an attractive option for pre-combustion CO_2 capture in Natural Gas Combined Cycle (NGCC) power stations because they combine, all in one reactor, the efficient conversion of natural or reformatted gas into H_2 for power generation with capture of the remaining CO_2, a technology evaluated in CCP Phase 1 [6]. During CCP1 SINTEF developed very thin palladium layers (<5 μm) supported on porous stainless steel tubes with a length of approximately 4 cm. Good performance of membranes was demonstrated in the water gas shift environment. During CACHET/CCP2, the development at SINTEF has firstly focused on the reproducibility and up-scaling of the two-stage method up to a membrane length of 50 cm, and secondly the thorough evaluation of the membrane performance in different feed mixtures and process conditions. In the current overview, we report the preparation, up-scaling, and transport properties of tubular supported Pd-23%Ag membranes. Effects on the H_2 flux caused by H_2 dilution, concentration polarization due to mass transfer limitations, and adsorption effects, were particularly addressed, while the long-term stability of Pd-23%Ag/stainless steel composite membranes has been examined in H_2/N_2 and WGS mixtures over periods of up to almost one year.

EXPERIMENTAL PART

Pd-23%Ag film preparation

Unsupported palladium alloy films were prepared by sputtering using a CVC 601 magnetron sputtering apparatus. The films were sputtered from a Pd-23%Ag target onto polished silicon single crystal substrates. The vacuum chamber was pumped down to ~10^{-6} Torr before introducing the argon (Ar) sputtering gas into the system. Typically, after a sputtering time of around 2 hours a final nominal film thickness of ~2 μm was obtained.

Membrane preparation and up-scaling

After sputtering, the palladium film was removed manually from the silicon substrate and transferred to tubular macroporous stainless steel substrates. During the application, the Pd-23%Ag film was wrapped along the stainless tube. An overlap region of the films provided direct sealing between subsequent wrapped films. The Pd film – Si substrate interface side of the as-grown film served as the feed side and the Pd film growth side as the permeate side of the membrane during testing. Sealing was obtained by clamping the film to the dense stainless steel tube-end [7]. The tubular porous 316L stainless steel (PSS®) Accusep™ supports were supplied by Pall Corporation, USA. The support diameter and wall thickness of the support were 11.85 and 0.48 mm, respectively. The average pore size of the support was 2 μm. An intermetallic diffusion barrier was deposited on the porous stainless steel prior to application of the Pd film for some of the membranes investigated. Due to confidentiality we are unfortunately not able to reveal more information concerning the properties of the intermetallic diffusion barrier layer coating. Membranes with a length of up to 50 cm were prepared. This is shown in Figure 1. The production method used has no limitation in terms of membrane length as subsequent films wrapped on the tubes are sealed by interdiffusion in the overlapping regions.

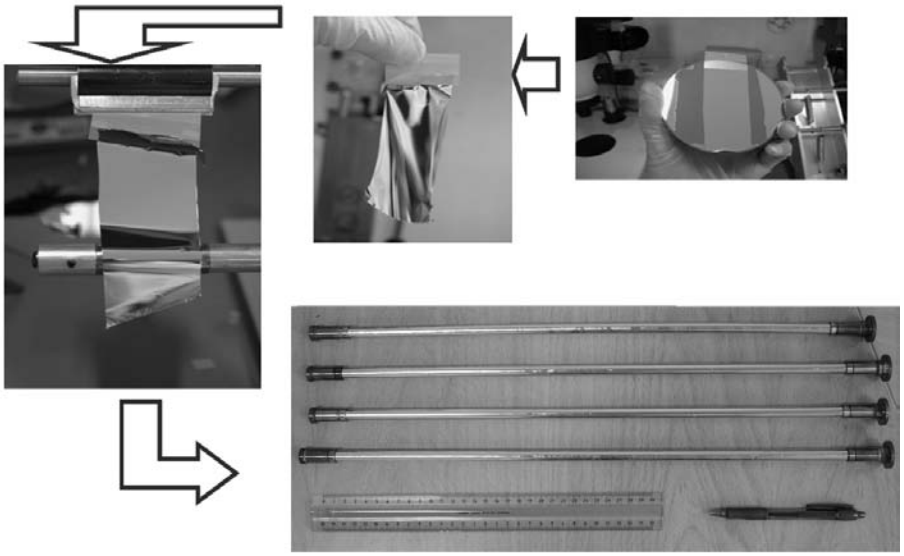

Figure 1. Membrane development and up-scaling, (a) Pd-23%Ag film prior to removal from the silicon wafer; (b) unsupported Pd-23%Ag film; (c) Pd-23%Ag film during wrapping on the tubular porous stainless steel (PSS®) support; (d) Four long (50 cm) composite Pd–23%Ag/stainless steel composite membranes.

Hydrogen permeation measurements

The tubular-supported palladium membrane was tested in a unit designed and constructed for high-pressure membrane permeability testing. The supported palladium membrane was placed inside a 316L stainless steel module (inside diameter 19 mm) allowing the membrane to be tested with counter-current flow. The feed and permeate feed flow rates were controlled by automated mass flow controllers (Bronkhorst High-Tech). The feed flow of water was regulated using a liquid mass flow controller (Bronkhorst High-Tech). The tank was pressurized with nitrogen (N_2) to force water into an evaporator before mixing with other gases prior to entering the membrane module. At the retentate side, the steam was condensed in a water trap, before the gas was analysed by a GC (Varian Inc., CP-4900). During CACHET the membrane test gas supply infrastructure and membrane test station were upgraded enabling the experimental verification of long membranes at high pressures.

The membrane was heated from room temperature to 300°C at a rate of 2°C/min in a N_2/Ar atmosphere (99.999%) before H_2 was introduced (99.995%). The pressure at the feed side of the membrane was controlled by a back pressure controller (Bronkhorst High-Tech). The gases at the feed and permeate side were analysed by a gas chromatograph (GC) (Varian Inc., CP-4900). Fluxes were calculated from the measured permeate H_2 concentration and the calibrated flow of Ar sweep gas. A counter-current sweep was applied. The permeate side of the membrane was kept at atmospheric pressure during the whole experiment. The H_2 permeance was calculated by dividing the H_2 flux by the average H_2 partial pressure difference over the membrane. The separation factor of the membrane was defined as the ratio of the permeance of the faster moving component (H_2) compared to the slower. In this calculation we have assumed for simplicity that $n = 1$. A high feed flow rate (up to 10 NL·min^{-1} corresponding to a linear gas velocity of 0.95 m·s^{-1}) was used in order

to reduce effects due to gas phase diffusion and H_2 depletion along the length of the membrane module. Sweep flow rates of 1.0 NL·min^{-1} are used. The effect of CH_4 (99.95%), CO_2 (99.95%) and CO (99.97) on the hydrogen flux was investigated by substitution for N_2, while keeping the H_2 content constant at 50%. Thermal treatment of the membrane in air was carried out by simply opening the feed, retentate, sweep, and permeate connections of the membrane module, respectively, after flushing the module with N_2 and Ar, allowing air to enter the system, at 400°C for 3 days. Subsequently, the connections were re-connected followed by sufficient flushing prior to H_2 introduction. The long-term stability of the membranes was investigated at low feed flow rates, *i.e.* high H_2 recovery, in order to prevent consumption of large quantities of gas. The flux stability was also studied under WGS conditions (57.5% H_2, 18.7% CO_2, 3.8% CO, 1.2% CH_4 and 18.7% steam) over a period of 75 days at different operation temperatures, and a feed pressure of 10 bars.

RESULTS AND DISCUSSION

Hydrogen permeation performance

In Figure 2 we first give the H_2 flux obtained in pure H_2 as feed as a function of the square root of the H_2 partial pressure difference before and after thermal treatment in air. A plot using n = 0.5 rather than n = 1 is chosen, because bulk diffusion is believed to be the most dominant step.

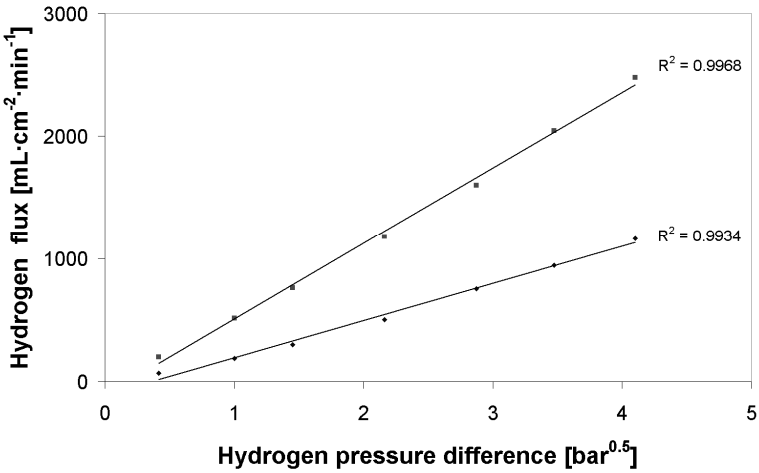

Figure 2. Obtained H_2 flux as a function of the square root of the H_2 pressure difference before and after thermal pre-treatment in air, T = 400°C.

Before and after the air pre-treatment, a H_2 flux of 1162 and 2477 mL·cm^{-2}·min^{-1}, respectively, was obtained at 26 bar feed pressure indicating a more than doubling of the H_2 permeance. This agrees with the enhancement previously obtained at low H_2 pressures (~ 0.1-0.5 bar) for thin, free-standing Pd/Ag23% membranes after heat treatment in air [8,9]. The corresponding H_2 permeance, after air pre-treatment, obtained at 26 bars equals $1.5 \cdot 10^{-2}$ mol·m^{-2}·s^{-1}·Pa$^{-0.5}$. The H_2 permeance and flux obtained at 26 bars feed pressure reported in this study is roughly double as high as any value previously reported in literature [10], which can be attributed to the use of a thin Pd-23%Ag layer supported on a macroporous support. Assuming viscous flow in the support, the contribution of the macroporous stainless steel support to the total resistance for mass transport is less than 5% under the conditions applied [3]. Allowing the value of n to float between 0.5 and 1, in order to obtain the

best fit between the fluxes, equation 1 gives a best fit for *n* equal to 0.792 and 0.633 before and after air treatment, respectively.

$$\left(p_{H_2^{ret}}^{n} - p_{H_2^{perm}}^{n} \right) \qquad \text{Equation 1}$$

A decrease in *n*-value was also found by Guazzone *et al.* after surface activation using air oxidation for a pure Pd membrane with a thickness of 19 μm [11]. In their study, the *n*-value ranged between 0.64 and 0.68 over the entire studied temperature range (300–500°C) prior to surface activation, while the *n*-value was equal to 0.58 at 250°C after oxidation. However, the *n*-value at 500°C had the same values as the *n*-values prior to surface activation. The decrease of the *n*-value could indicate that the diffusional rate limitation becomes prevailing over surface rate limitations after air treatment. This is consistent with other studies on self-supported membranes at low H_2 pressure, which have shown that air treatment increases the H_2 flux in parallel to increasing surface roughness, and grain size [8,12]. In order to correct for the support resistance the actual H_2 pressure drop of the Pd film was obtained by subtracting the pressure drop over the support determined in single component measurements [13,14]. For example, for the H_2 flux of 2046 $mL \cdot cm^{-2} \cdot min^{-1}$, obtained at a feed pressure of 20 bars, the H_2 pressure drop over the support is determined to be 0.86 bars. After correction for the support resistance a best fit for *n* equal to 0.631 has been obtained, see Figure 3, indicating that, even after pre-treatment of the membrane surface in air, an ideal value for bulk diffusion control of $n = 0.5$ can not be obtained.

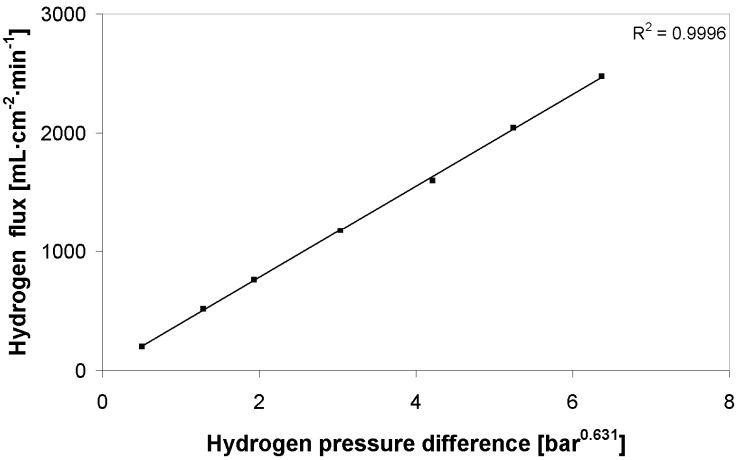

Figure 3. Obtained H_2 flux after oxidation as a function of the H_2 pressure difference to the power 0.631, $T = 400$°C. The H_2 partial pressure difference over the membrane has been corrected for the support resistance.

This value for *n* is, although maybe by coincidence, identical to the one obtained in the study of Morreale *et al.* [15] who studied the H_2 permeability of ~1 mm thick pure Pd membranes at H_2 pressures up to 27.6 bars. It should be noted that a linear relationship between the hydrogen flux and the square root of the hydrogen partial pressure difference over the membrane suggests that the product $S \times D$ is constant over the entire hydrogen pressure range investigated. Assuming bulk diffusion rate control, our results suggest that $S \times D$ does not follow such ideal relationship. It is,

however, not surprising that $S \times D$ could have a slight dependence on the pressure over the large applied feed pressure. For example, it has been shown that the H_2 diffusivity increases with the concentration of dissolved H_2 [16,17]. In addition, it has been claimed [18] that the H_2 solubility could increase with increasing pressure in a non-ideal solution where dissolved H_2 atoms form attractive forces towards one another. A concentration of H_2 atoms greater than that predicted by the Sieverts' constant from low-pressure solubility data may then occur. It is thus possible that the product of the diffusion coefficient and the solubility increases with H_2 pressure [15]. Logically, the net mathematical effect, keeping $S \times D$ constant as a function of pressure, is an increase in the *n*-value with increasing H_2 pressure.

Separation performance

The H_2/N_2 permselectivity of the membrane, defined as the ratio of the H_2 flux and N_2 flux obtained from single gas permeation experiments after the heat treatment in air, is depicted in Figure 4 as a function of pressure.

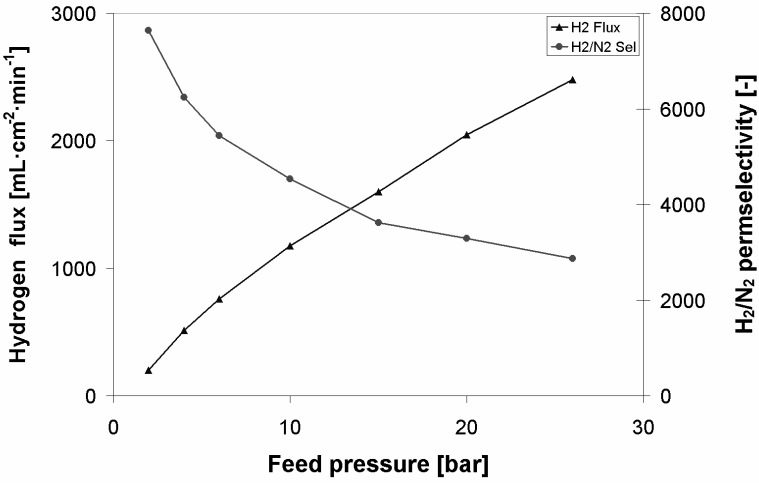

Figure 4. Obtained H_2 flux and H_2/N_2 permselectivity after oxidation as a function of the feed pressure, T = 400°C.

At a feed pressure of 26 bars, a N_2 permeance as low as $2.3 \cdot 10^{-9}$ mol·m^{-2}·s^{-1}·Pa^{-1} is obtained leading to a H_2/N_2 permselectivity of 2900 at this feed pressure. It must be specified that the air treatment of the membrane did not increase the leak rate of the membrane. Instead, a slightly lower N_2 permeance was obtained directly after air treatment. This might tentatively be explained by significant microstructural changes and formation of a thin PdOx layer on the surface closing pinholes [19]. The slight decrease in N_2 permeance, however, was cancelled out after the reduction of the surface during the H_2 permeation measurements. The obtained H_2/N_2 permselectivity decreases with an increase in feed side pressure. This is caused by an increasing contribution of unselective viscous flow through the sealing or pinholes present in the membrane with an increase in feed side pressure. Nonetheless, no hysteresis in permselectivity was observed when the pressure drop was decreased indicating that these thin membranes, supported on macroporous supports, withstand these high pressure drops. The high-pressure separation performance of the supported Pd-23%Ag membranes described in this study is superior as compared to results described in literature.

For example, Collins and Way obtained a H_2/N_2 permselectivity of 380 at a transmembrane pressure of 15 bars using a pure Pd membrane with a nominal thickness of 11.4 μm at 550°C [20]. At a total pressure drop of 28 bars, Rothenberger *et al.*, obtained a H_2/He selectivity of 12 using a Pd membrane with a nominal thickness of 21.3 μm for a feed stream composed of 90% H_2 and 10% He [21], while Pex *et al.*, obtained a H_2/N_2 permselectivity of 130 for 80 cm long Pd-Ag membranes with a Pd thickness of 3-5 μm at a feed pressure and temperature of 26 bars and 450°C, respectively [22]. Slightly higher permselectivities, 220, were obtained at a feed pressure of 10 bars. The high selectivity obtained for the membranes prepared in this study can be attributed to the preparation method, in which a palladium film is first prepared on the perfect surface of a silicon wafer by means of magnetron sputtering. By this, defects in the palladium film originating from a porous, typically non-defect free, support are minimised. It should be pointed out that the sealing technology employed also makes such performance possible.

Performance in mixtures

The H_2 flux obtained in mixtures of H_2 with other gases is influenced by several factors reducing either the effective H_2 partial pressure difference or the dissociative adsorption of H_2 on the palladium surface including:

i) H_2 dilution on the feed side by the presence of other gases components,
ii) H_2 depletion of the bulk feed due to H_2 removal along the length of the membrane module,
iii) The build-up of a H_2-depleted concentration polarization layer adjacent to the membrane surface due to gas phase mass transport limitation,
iv) Possible competitive adsorption of other gas components on the membrane surface.

To understand the relative importance of effects i-iv in various gas mixtures at elevated pressures, we have performed an analysis of systematic permeation studies in order to separate the different contributions. Our approach has been in a simple manner to estimate the effect on the flux of different rate limiting processes, as gas dilution, concentration polarization, adsorption, and transport through the composite membrane. Such understanding is vital in further development and use of this type of membranes for integration in steam reforming and WGS reactors.

Addition of inert component

It is generally accepted that, for short periods of exposure, N_2 has non or only very weak adsorption on Pd-alloy surfaces [23]. We regard therefore N_2 as an inert in the subsequent experiments. At 26 bar feed pressure a H_2 flux of 1223 $mL \cdot cm^{-2} \cdot min^{-1}$ or 8.4 $mol \cdot m^{-2} \cdot s^{-1}$ was obtained, corresponding to a permeance of $6.4 \cdot 10^{-3}$ $mol \cdot m^{-2} \cdot s^{-1} \cdot Pa^{-0.5}$ (Note, this value is obtained applying a membrane without air pre-treatment). In contrast to the high flux in pure H_2, a feed mixture of 50%H_2+50%N_2 gives only a maximum H_2 flux of 230 $mL \cdot cm^{-2} \cdot min^{-1}$ at 26 bar pressure. The calculated H_2 permeance and H_2 to N_2 separation factor are $1.7 \cdot 10^{-3}$ $mol \cdot m^{-2} \cdot s^{-1} \cdot Pa^{-0.5}$ and 1400, respectively. The effect of feed flow rate on flux is significant, but levels off at high rates as shown in Figure 5. At the maximum feed flow rate employed, only about 15% of the H_2 is recovered through the membrane indicating that H_2 depletion along the length of the module can not be the single cause for the lower H_2 flux obtained.

The large reduction in H_2 flux on changing the feed from pure H_2 to 50%H_2 in N_2 can also not be explained by simple gas dilution effects. We suggest that the high rate of H_2 removal causes the build-up of a H_2-depleted concentration polarization layer adjacent to the membrane. This polarization layer resulting from insufficient mass transport in the gas phase lowers the effective H_2 partial pressure difference which consequently results in a reduced H_2 flux. The value for the H_2 permeance, determined from measurements in pure H_2, enables calculation of the actual H_2 partial

pressure at the membrane surface. Based on this an estimation of the expected H_2 partial pressure reduction due to concentration polarisation can be made. Accordingly, the partial pressure reduction due to depletion was calculated on basis of the difference in the initial H_2 concentration in the feed and the measured H_2 concentration in the retentate. Figure 6 illustrates the expected flux reduction due to dilution, depletion, and concentration polarization as a function of the total feed pressure. In the calculation a linear depletion of H_2 in the feed gas along the membrane length was assumed.

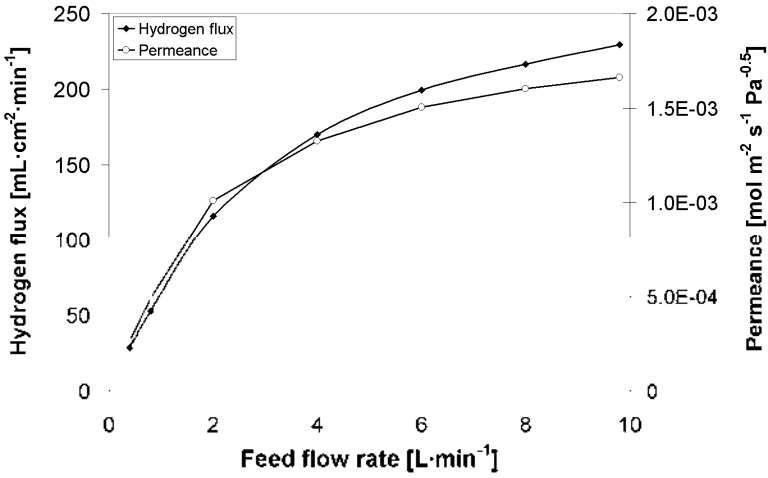

Figure 5. H_2 flux and calculated permeance in 50% H_2/ 50% N_2 as a function of the total feed flow rate. T = 400°C, P_{feed} = 26 bar. Copyright Elsevier, 2008. Reproduced by permission. Adapted from reference [3].

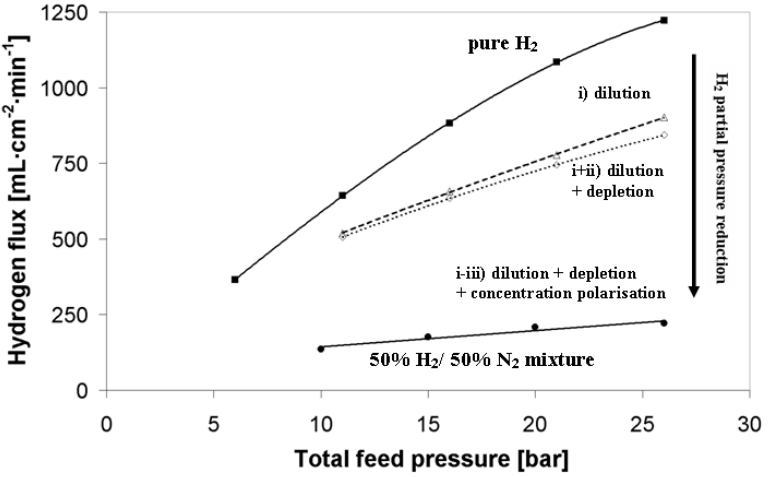

Figure 6. H_2 flux in pure H_2 and 50% H_2/ 50% N_2 as a function of the feed pressure. The estimated flux reduction due to dilution, and dilution and depletion as a function of total feed pressure is indicated. T = 400°C, V_{feed} = 8 NL·min^{-1}. Copyright Elsevier, 2008. Reproduced by permission. Adapted from reference [3].

The H_2-depleted concentration polarization layer adjacent to the membrane is responsible for the major part of the total pressure drop, while the relative importance of the actual H_2 pressure drop over the membrane constitutes only a small fraction, and decreases with increasing applied feed pressure. Depletion was not found to be substantial which can be explained by the fact that only about 15-20% of the H_2 is recovered through the membrane.

Effect of CH_4, CO and CO_2 on the hydrogen flux

Figure 7 shows the relative decrease in H_2 flux compared to an equimolar mixture of H_2/N_2 by replacing N_2 with an equal amount of either methane (CH_4), CO_2 or carbon monoxide (CO) at a feed pressure and temperature of 20 bars, and 400°C, respectively. Compared to CO and CO_2, CH_4 shows almost no H_2 flux inhibition. CH_4 is expected to have insignificant surface adsorption and may for short period measurements therefore be regarded as an inert. The significant, but still very different effects of CO and CO_2 we believe are attributed to surface adsorption.

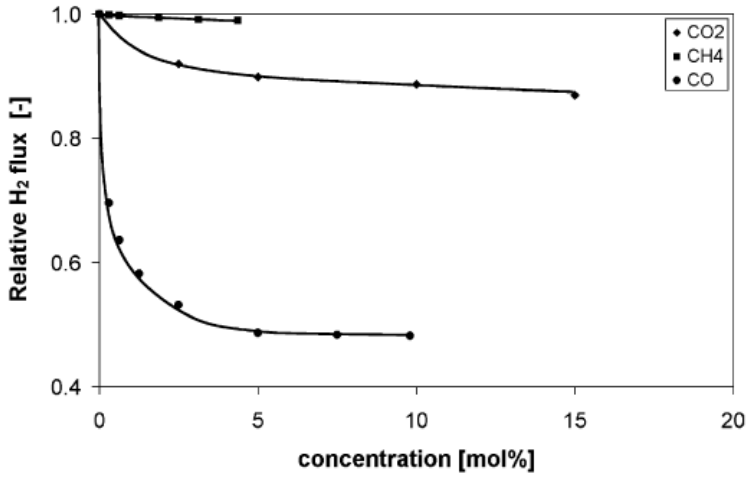

Figure 7. Relative H_2 permeation as a function of the CO, CO_2, and CH_4 concentration. T = 400°C, P_{feed} = 20 bar, V_{feed} = 8 NL·min^{-1}. The reference flux is 208 mL·cm^{-2}·min^{-1} obtained in 50% H_2/ 50% N_2 at 20 bar feed pressure. Copyright Elsevier, 2008. Reproduced by permission. Adapted from reference [3].

For CO adsorption, saturation appears to be approached at some 4-5 mol% CO in the gas giving a relative reduction of about 60%. Already at very low CO concentration a large flux reduction effect is accomplished under the present high pressure conditions. This is contradicting to previous studies [24] reporting that the effect of CO adsorption is insignificant above ~300-350°C. More surprisingly maybe, the decrease in H_2 permeation after the introduction of CO_2 seemingly indicates that even this molecule is capable of blocking H_2 dissociation sites on the palladium surface at 400°C. Inhibitive effects of CO_2 have previously also been observed at temperatures up to 450°C for thin (<5 µm) Pd membranes [23,25]. In these studies it was suggested that the inhibitive effect was attributed to the formation of CO by the reverse water gas shift (rWGS) reaction [25].

Overview of concentration polarisation and sorption effects in different gas mixtures

Figure 8 illustrates the estimated partial pressure drop for sustaining the flux by three major processes; gas diffusion to the membrane feed surface, transport through the Pd-Ag23wt.%, and transport through the porous steel support, respectively. The gas phase limitations imply a need for improving membrane and module design, and an optimisation of feed flow conditions to reduce the thickness of the H_2-depleted layer. The example using a Pd-based membrane may also be used to illustrate the problem of surface reaction rate limitation. Adsorption of other gas molecules on the surface hinders H_2 incorporation, and therefore reduces flux. The effect is particularly strong for CO, which is illustrated in Figure 8. A comparison with the high flux situation with only an inert molecule present shows that the importance of gas phase diffusion limitation is drastically reduced. This illustrates that the operation of highly permeable Pd-based membranes (or Group IV and V membranes with Pd-catalyst layer) in WGS conditions is strongly affected by a combination of surface effects and gas phase diffusion limitations. Thus, if the surface adsorption effect could be reduced, the expected flux increase will be limited by gas phase diffusion. It should be noted, however, that the relative contribution depends on a number of parameters as membrane material and thickness, support material and porosity, operating temperature and pressure etc., which should be determined experimentally and serve as input for module design modelling [26]. The design and operational implications set by gas phase diffusion limitations are not limited to the case of Pd-based membranes, but to all highly permeable and selective gas separation membranes.

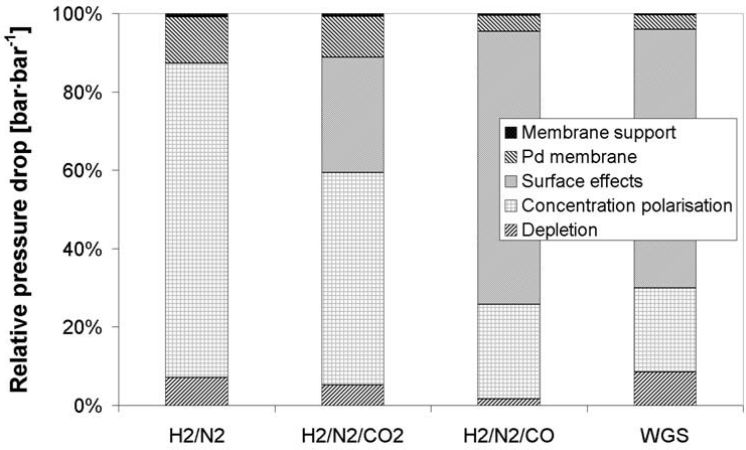

Figure 8. H_2 pressure drop due to depletion, concentration polarisation, surface effects, transport in the palladium membrane and porous support, compared to the total H_2 partial pressure drop. (a) H_2:N_2 = 50:50; (b) H_2:N_2:CO_2 = 50:25:25; (c) H_2:N_2:CO = 50:45:5; (d) H_2:CO_2:H_2O:CO:CH_4 = 60:19:16:4:1. P_{feed} = 20 bar, T = 400°C.

Application of membranes in the non-integrated membrane WGS concept

The H_2 permeability under WGS conditions has been examined using simulated WGS mixtures containing 60, 30 or 10 mol% of H_2. The exact compositions of the different simulated WGS feed mixtures are shown in Table 1.

Table 1. Typical gas compositions entering the three membrane separation units [27].

Gas	WGS-1 [%]	WGS-2 [%]	WGS-3 [%]
H_2	60.2	30	10
CO_2	19.2	40.5	60
H_2O	15.4	25	25.5
CO	4	2	2
CH_4	1.2	2.5	2.5

The measured hydrogen flux and calculated permeance under three simulated WGS conditions are depicted in Table 2. The hydrogen flux and permeance in pure hydrogen, and 50% H_2/ 50% N_2 mixture are given for comparison. In Figure 9 the estimated relative H_2 pressure drops are shown for the 3 WGS conditions. The results suggest that inhibiting adsorption increases for conditions WGS-1 < WGS-2 < WGS-3.

Table 2. Membrane performance obtained in pure H_2, 50% H_2/ 50% N_2 mixture, and WGS compositions 1-3. T = 400°C, P_{feed} = 20 bar, $V_{feed, WGS}$ = 5 NL·min^{-1}. Reproduced by permission. Adapted from reference [3]).

Characteristic	Units	H_2	H_2/N_2	WGS-1	WGS-2	WGS-3
H_2 concentration	mol%	100	50	55	28	10
H_2 flux	mL·cm^{-2}·min^{-1}	990	208	110	53	13
H_2 permeance	mol·m^{-2}·s^{-1}·Pa$^{-0.5}$	$6.2\cdot10^{-3}$	$1.8\cdot10^{-3}$	$8.3\cdot10^{-4}$	$5.9\cdot10^{-4}$	$2.7\cdot10^{-4}$

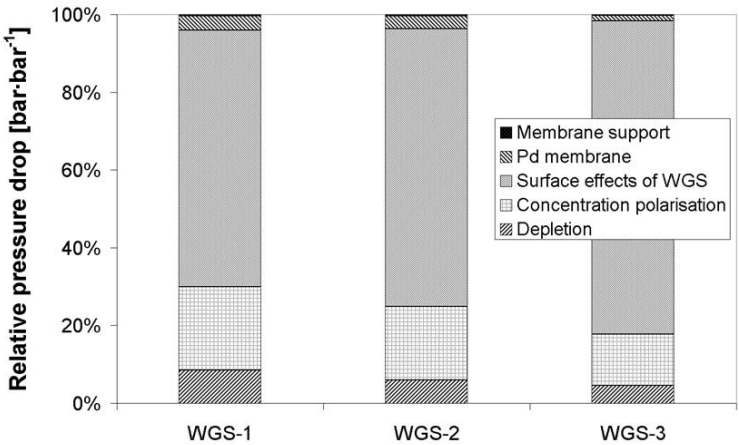

Figure 9. H_2 pressure drop due to depletion, concentration polarisation, WGS surface effects, transport in the palladium membrane and porous support, compared to total H_2 partial pressure drop as a function of the applied feed pressure. WGS 1-3, T = 400°C, P_{feed} = 20 bar, V_{feed} = 5 NL·min^{-1}. Copyright Elsevier, 2008. Reproduced by permission. Adapted from reference [3].

The H_2 pressure drop due to transport through the membrane is insignificant for all conditions. Water vapour may also adsorb on the Pd surface [25,28], and furthermore, various degrees of mutual interaction of different gas species affecting adsorption have been reported [29]. Despite the complex situation, the main conclusion remains that surface effects of WGS-related gases are responsible for the major part of the total pressure drop. The actual H_2 pressure drop over the composite membrane becomes insignificant for H_2 removal from WGS mixtures. Bulk depletion decreases with decreasing flux at constant feed flow rate. Furthermore, concentration polarisation increases in importance with increasing flux. To investigate the effect of H_2 depletion along the length of the membrane on the H_2 flux, the WGS-1 feed flow rate was varied, see Figure 10.

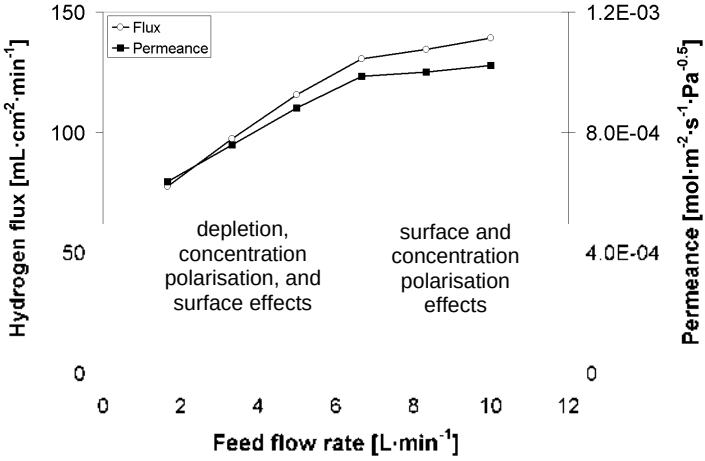

Figure 10. Membrane performance obtained in WGS-1 as a function of feed flow rate. T = 400°C, P_{feed} = 20 bar. Copyright Elsevier, 2008. Reproduced by permission. Adapted from reference [3].

From Figure 10 it can be seen that initially both the obtained H_2 flux and permeance increase with the total feed flow rate, but flattens out at the highest feed flow rates employed. At low feed flow rates, the increase of H_2 flux can be attributed to the decreasing effect of H_2 depletion. At high feed flow rates, the H_2 flux continues to increase at a lower rate due to the decreased effect of H_2 depletion of the feed along the membrane module resulting in a higher H_2 partial pressure on the shell-side [30]. At the maximum feed flow rate applied, the H_2 recovery is only equal to 15% which means that a fairly constant H_2 partial pressure exists along the axial direction of the membrane module. This is in comparison with the large variation in H_2 partial pressure at low feed flow rates. The polarisation effect is expected to be contributing to flux reduction at all H_2 partial pressures, and thus feed flow rates [2,3]. The H_2 permeance obtained at the maximum feed flow rate equals $1.0 \cdot 10^{-3}$ $mol \cdot m^{-2} \cdot s^{-1} \cdot Pa^{-0.5}$.

Long term stability

Long-term stability in H_2/N_2 mixtures

The long-term stability of the supported Pd-23%Ag membranes was monitored over a period of 100 days using a feed gas mixture of 50% H_2 + 50% N_2. On the porous stainless steel support applied in these measurements, an intermetallic diffusion barrier was deposited prior to application of the Pd film. The H_2 and N_2 fluxes were measured while the temperature and pressure were systematically

varied between 350-450°C and 5-20 bars, respectively. The observed fluxes of H_2 and N_2 as a function of process time under different operating conditions are given in Figure 11.

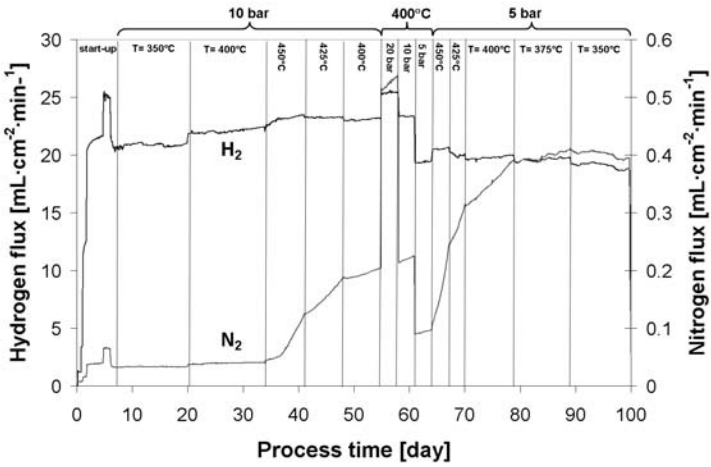

Figure 11. Long-term stability showing the H_2 and N_2 fluxes through the membrane as a function of time, temperature and pressure. Feed mixture: 50% H_2 + 50% N_2.
Note the large difference in scale of H_2 and N_2 flux. Copyright Elsevier, 2009.
Reproduced by permission. Adapted from reference [31].

Initially, a stable membrane performance was obtained by applying a feed pressure up to 10 bars and temperature up to 400°C during more than one month. However, after the subsequent increase in operation temperature to 450°C, the N_2 leakage flux increases drastically. The decrease in operating temperature to 400°C did not stabilize the N_2 leakage. Similarly, the rate of N_2 leakage was increased by increasing the feed pressure from 10 to 20 bars. By subsequently decreasing the pressure down to 5 bars and temperature down to 375°C, the N_2 leakage flux stabilises again. Most surprisingly, however, the N_2 leakage flux is found to increase fairly linear as a function of time at constant temperature and pressure. After operating the membrane for 100 days at T = 350-450°C and P_{feed} = 5-20 bars, the N_2 permeance had increased from its initial value of $4 \cdot 10^{-10}$ mol·m^{-2}·s^{-1}·Pa^{-1} to a maximum of $7 \cdot 10^{-9}$ mol·m^{-2}·s^{-1}·Pa^{-1}. The H_2/N_2 permselectivity still lies around 500, based on a H_2 permeance equal to $3.0 \cdot 10^{-6}$ mol·m^{-2}·s^{-1}·Pa^{-1}, which shows that the membrane is still highly selective towards H_2.

Similar leakage behaviour in these temperature ranges was reported by Guazzone and Ma for Pd composite membranes [32]. Based on experimental results, they identified pinhole formation mechanisms. It was proposed that leak formation and growth are related to inhomogeneous sintering and that pinhole formation and growth of pinholes started at about 400 – 450°C. According to this investigation, the formation of new and small pinholes can increase the leak rate as a function of time at a given temperature (450°C and above).

In order to investigate the membrane material stability and the sources of leakage, a thorough material characterization was performed after removing the Pd-23%Ag membrane from the PSS support. The microstructure of the membrane, changes in surface topography, chemical composition, both at the surface and in the bulk, and mechanical defects as possible sources of leakage were studied. Post-process characterisation shows a considerable grain growth and of micro-strain relaxation in the Pd-23%Ag membrane after the prolonged permeation experiment.

Changes in surface area are relatively small. An example of grain development from very fine to much bigger grains during heat treatment and testing is given by the dark field TEM images shown in Figures 12(a) and 12(b).

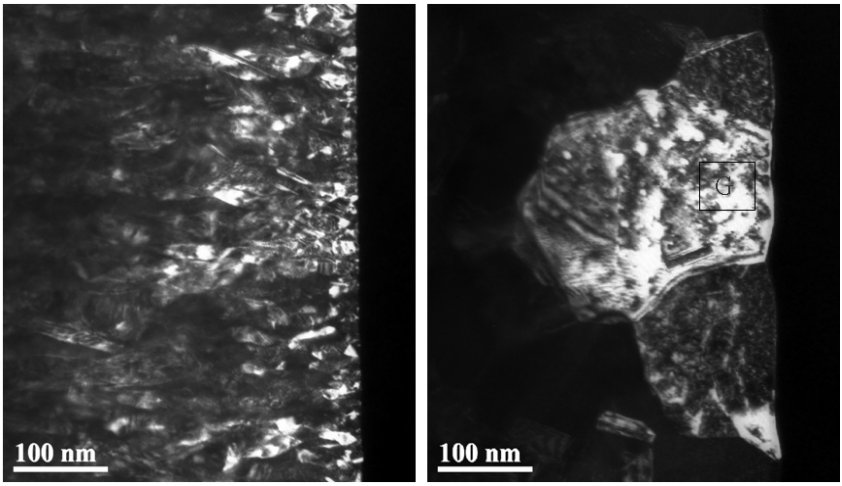

Figure 12. TEM dark field images showing microstructure near/at the silicon wafer surface of (left) as-grown sample, and (right) feed surface of the tested sample. The surfaces are the right edges in the images. Copyright Elsevier, 2009. Reproduced by permission. Adapted from reference [31].

In Figure 12(a), individual fine grains close to the original membrane/wafer interface can be seen, whereas Figure 12(b) shows the much coarser-gained region in the tested membrane. The grain marked "G" is close to a diffraction condition. Other grains in the dark field view are not showing strong diffraction contrast. The grain marked 'G' in Figure 12(b) has a diameter of 200 nm as compared to the tiny grains of the as-grown sample with an average grain size of ~10-20 nm near the surface shown in Figure 12(a). Compared to the as-grown membranes, some segregation of Ag to the membrane surfaces is observed after the 100 days testing as found by XPS and AES, results not shown. The formation of pinholes, however, is identified as the main source for the increased N_2 leakage during testing at higher temperature, see Figure 13. The topography of the feed surface shown in Figure 13(a) and (b) contains some bulged areas which are almost uniformly spread throughout the membrane. These bulged areas have been formed on the membrane surface due to a high and uneven stress distribution, while following the surface topography of the porous support during the high pressure operation. These bulged areas on the membrane surface are seemingly prone to pinhole formation since the observed pinholes appeared at such sites. A magnified image from one of these areas is shown in Figure 13(c). Figure 13(d) displays an example of nano-sized pinholes, whereas, Figure 13(e) displays a micro-sized pinhole. A magnified image of Figure 2(e) is shown in Figure 13(f). This pinhole has a diameter of about 5 μm. Pinholes at this size, however, were very rarely found in the membrane.

It is likely that an inhomogeneous stress distribution, originating from hydrogen dissolution, mismatch in thermal expansion coefficient, and mechanical pressure, causes some areas to reach above their local critical mechanical strength. The elevated operation temperature allows the material to release the excess energy through, *e.g.*, processes as plastic deformation, grain sliding and creep, which subsequently leads to microstructural changes and pinhole formation [33].

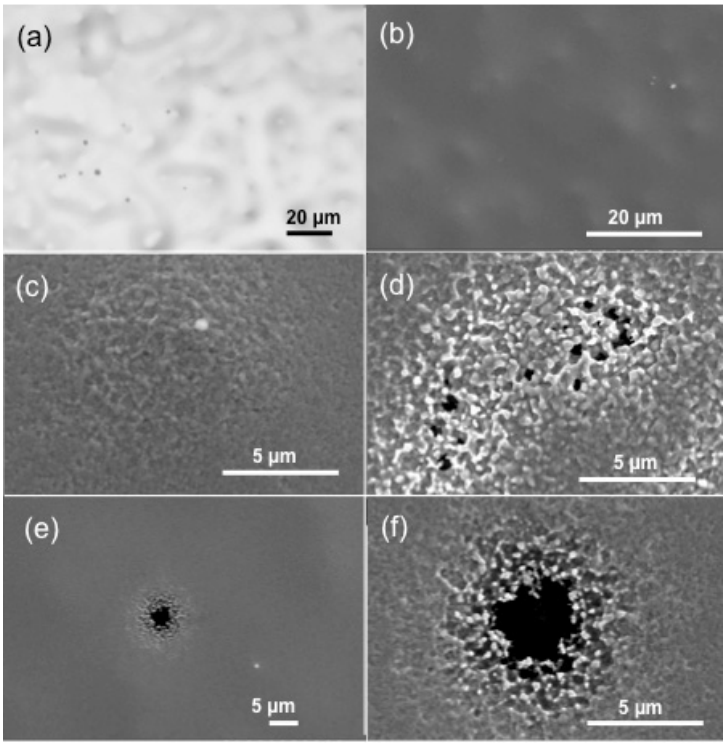

Figure 13. Optical and SEM images of the feed surface of the tested membrane:
(a) Optical image of the surface topography (b) SEM image of the surface topography
(c) magnified SEM image of one of the bulged site shown in (b), and
(d)-(f) show SEM images of pinholes at different magnifications.
Copyright Elsevier, 2009. Reproduced by permission. Adapted from reference [31].

Another membrane was tested for periods of up to one year at a feed pressure of 10 bars, at temperature varying between 325 and 425°C using H_2/N_2 or WGS as feed condition (Figure 14 and 15), and shows stable performance ($T \leq 350$°C). The support used for this membrane was a bare porous stainless steel support tube. In Figure 14 the first 250 days of process (H_2/N_2 as feed) is shown. Initially, a stable membrane performance was obtained by applying a feed pressure up to 10 bars and temperature up to 350°C during more than two months. However, after the subsequent increase in operation temperature to 400°C, the N_2 leakage increases indicating that pinholes started to appear on the membrane surface at this temperature. During the subsequent 175 days stable operation was obtained at 325°C. The N_2 flux was measured at $3 \cdot 10^{-9}$ $mol \cdot m^{-2} \cdot s^{-1} \cdot Pa^{-1}$, giving a H_2/N_2 permselectivity of around 1000, even after 250 days of operation. After around 260 days of process the feed to the membrane was changed to WGS conditions applying a feed pressure of 10 bars.

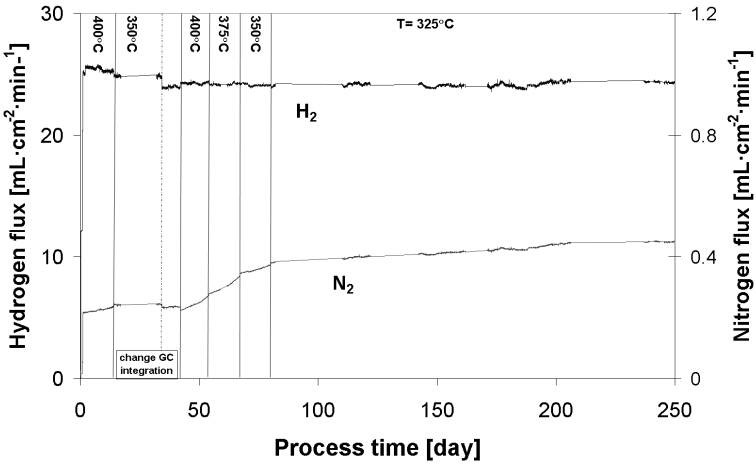

Figure 14. Long-term stability showing the H_2 and N_2 fluxes through the membrane as a function of time and temperature. Feed mixture: 50% H_2 + 50% N_2. Feed pressure = 10 bars. Note the large difference in scale of H_2 and N_2 flux.

Long-term stability in WGS mixtures

The long-term stability of the supported Pd-23%Ag membranes during the exposure to WGS conditions (H_2:CO_2:H_2O:CO:CH_4 = 57.5:18.7:18.7:3.8:1.2) was monitored over a period of around 65 days. The fluxes were measured while the temperature was systematically varied between 325-425°C. The observed fluxes of H_2 and N_2 as a function of process time under different operating conditions are given in Figure 15.

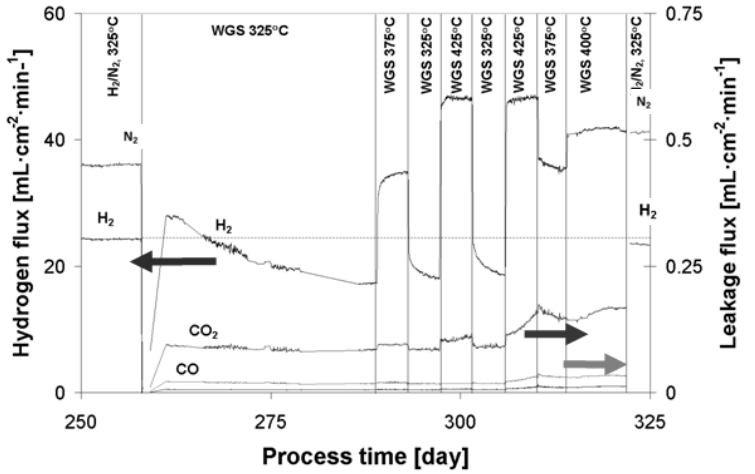

Figure 15. Long-term stability showing the H_2, CO and CO_2 fluxes through the membrane as a function of time and temperature. Feed mixture: H_2:CO_2:H_2O:CO:CH_4 = 57.5:18.7:18.7:3.8:1.2. Feed pressure = 10 bars. Note the large difference in scale of H_2 and CO and CO_2 fluxes.

An initial fairly constant H_2 and N_2 flux in the equimolar feed of H_2 and N_2, was changed into a decreasing H_2 flux on changing the feed to WGS conditions at 325°C. Note that these values cannot be compared directly with each other as the H_2 concentration in the feed mixtures is different. For a period of nearly 50 days, however, the leakage does not increase at temperatures between 325 and 425°C showing that exposure of the membrane to WGS conditions instead of H_2/N_2 does not severely alter membrane life-time. Instead, it seems that the membranes are more stable in WGS compared to H_2/N_2, most probably because of the effect of steam counteracting carbonaceous surface deposits [28,34]. The decreasing H_2 flux can be explained by coke formation of the membrane surface, a process which seems to be reversible as the flux is recovered after an increase in operating temperature. After 320 days of process the WGS feed was cut off and the H_2 and N_2 permeation rates were tested again at 325°C and 10 bars of feed pressure. Both the H_2 and N_2 flux were close to their initial values. The N_2 flux was measured now at $3 \cdot 10^{-9}$ $mol \cdot m^{-2} \cdot s^{-1} \cdot Pa^{-1}$, giving a H_2/N_2 permselectivity of 1000, even after almost one year of operation. To our knowledge this is the first time that the stability of thin (<5 μm) supported Pd-alloy membranes is examined over a prolonged period (almost one year) at a relative high feed pressure (<20 bars). Recent data reported by Matzakos show stable operation under actual steam-reforming conditions for 6000 h using a composite porous stainless steel palladium membrane [35]. However, no information on the membrane thickness and operating pressure was given. Recently, Tosti *et al.*, have published stability data obtained over a period of 12 months using thin wall permeator tubes produced by diffusion welding of Pd-Ag foils [36]. Although these rolled membranes are relatively thick (125 μm) for practical use, they showed complete H_2 selectivity for the whole period. The applied feed pressure, however, was only up to 2 bars.

Life-time estimation

For deployment of these Pd membranes in CO_2 capture processes, to achieve pre-combustion decarbonisation in large-scale power generation or H_2 production, preliminary process calculations have suggested a needed H_2/CO_2 separation factor of 100 [37]. In terms of H_2 to N_2 permselectivity, this would correspond to a value of around 400 due to the absence of mass transfer and surface effects on the H_2 flux while measuring in pure gases, which causes the H_2 flux to drop with a factor of around 4 [3]. Thus, based on the results obtained in this work (more specifically the data presented in Figure 11), and the assumption that the membranes are maintained in operation until the H_2/N_2 permselectivity drops below a value of 400, one may estimate the membrane operating life-time. In Table 3 and 4 we have estimated the time period to reach H_2/N_2 permselectivity of 400 based on the observed linear increase in N_2 permeance.

Table 3. Increase in N_2 leakage flux and life-time estimate as a function of temperature. Feed mixture: 50% H_2 + 50% N_2; Feed pressure = 10 bar. Copyright Elsevier, 2009. Reproduced by permission. Adapted from reference [31].

Temperature [°C]	**dN_2 flux [mL·cm^{-2}·min^{-1}·week^{-1}]**	**Pure H_2 flux [mL·cm^{-2}·min^{-1}]**	**Max. N_2 flux [mL·cm^{-2}·min^{-1}]**	**Life-time [years]**	**Based on data in Figure**
450	0.083	1400	3.5	0.8	11
425	0.056	1200	3	1.0	11
400	0.019	1000	2.5	2.5	11
325	0.003	400	1	7.1	14

Table 4. Increase in N_2 leakage flux and life-time estimate as a function of feed pressure. Feed mixture: 50% H_2 + 50% N_2; T = 400°C. Copyright Elsevier, 2009. Reproduced by permission. Adapted from reference [31].

Feed pressure [bar]	dN_2 flux [mL·cm^{-2}·min^{-1}·week^{-1}]	Pure H_2 flux [mL·cm^{-2}·min^{-1}]	Max. N_2 flux [mL·cm^{-2}·min^{-1}]	Life-time [years]	Based on data in Figure
20	0.061	2000	5	1.6	11
10	0.028	1200	3	2.1	11
5	0.015	700	1.75	2.2	11

From Table 3 it can be seen that a membrane life-time of 2.5 years is estimated if the membrane is operated at 400°C, even after the initial onset of N_2 flux increase caused during membrane operation at 450°C. This value matches very well with the life-time of commercially available low/medium temperature WGS catalysts. Operating the membrane at temperatures higher than 400°C, however, gives a rapid decrease in membrane life-time. Stability increases with thickness, therefore thicker Pd-23%Ag membranes (>2 μm), or alternatively other Pd-alloy compositions, for which temperature stability is enhanced, are needed above 400°C. Although the increase in N_2 flux is enhanced at increasing pressure, this does not have a dramatic influence on the expected life-time of the membrane as the H_2 flux is also increased due to the larger H_2 partial pressure difference over the membrane. At 400°C a membrane life-time of 1.6 and 2.2 years is estimated at operating pressures of 20 and 5 bars, respectively. The slight difference between the values for 400°C and 10 bars in Table 3 and 4 can be explained by the order of the measurement. The value given in table 3 is obtained after operation of the membrane at 20 bars of feed pressure, a pressure during which pinholes are generated at a larger rate. Consequently, the leakage rate increase obtained afterwards is larger than before the high pressure testing explaining the slight difference in membrane life-time given in Table 3 and 4. The results in Table 3 and 4 suggest that thermal activation is more important than mechanical stress in the temperature-pressure region investigated. Exposure of the membrane to WGS instead of H_2/N_2 conditions does not severely alter membrane life-time. Rather, it seems that the membranes are more stable in WGS compared to H_2/N_2, most probably because of the effect of steam as shown in Figure 15. In addition, the H_2/N_2 and WGS mixtures, long-term tests in presence of a catalyst and trace contaminants such as H_2S and COS are needed in order to fully evaluate the potential for broader application in WGS-MR.

CONCLUSIONS

During the CACHET program SINTEF has made significant progress on several areas; (i) development of longer membranes, (ii) laboratory facility upgrading, and (iii) membrane testing under different operating conditions and time scale. The membranes can now be made up to 50 cm long, a more than 20 times increase in effective length since the start of CACHET. The long-term testing of the membranes has lead to increased understanding of membrane stability and membrane behaviour under various gas mixtures, and operation pressures and temperatures.

For the highly selective ~ 2 μm thick Pd-23%Ag composite membranes, a H_2 flux reaching ~ 2477 mL·cm^{-2}·min^{-1} at 25 bar differential pressure was achieved. This corresponds to a permeance of $1.2 \cdot 10^{-2}$ mol·m^{-2}·s^{-1}·Pa$^{-0.5}$. The low pressure (~ 2 bars) H_2/N_2 permselectivity obtained is higher than 7500, while a H_2/N_2 permselectivity equal to 2900 has been obtained at a feed pressure of 26 bars. The permeance in mixtures and WGS conditions, however, was considerably reduced due to

concentration polarisation and CO surface poisoning. The relative contribution depends on parameters as membrane material and thickness, support material and porosity, operating temperature and pressure etc., and should be determined in experimental testing.

The long-term stability of Pd-23%Ag/stainless steel composite membranes has been examined in H_2/N_2 mixtures as a function of both temperature and feed pressure. During continuous operation, the membrane shows a good stability at 400°C while the N_2 leakage increases very slowly at a temperature of 450°C (P_{feed} = 10 bar). After 100 days of operation (P_{feed} = 5-20 bars, T = 350-450°C), the N_2 permeance equals $7.0 \cdot 10^{-9}$ $mol \cdot m^{-2} \cdot s^{-1} \cdot Pa^{-1}$, which indicates that the H_2/N_2 permselectivity still lies around 500, based on a H_2 permeance equal to $3.0 \cdot 10^{-6}$ $mol \cdot m^{-2} \cdot s^{-1} \cdot Pa^{-1}$. Despite the generation of small pinholes, a membrane life-time of several (1.6-2.5) years (T = 400°C) is estimated for the experimental conditions employed. The results suggest that the lifetime increases considerably by reducing temperature to the temperature region 325-375°C. A stable performance was also obtained in WGS conditions for a period exceeding two months for a membrane operating at 10 bars at temperatures between $325 \leq T \leq 425$°C. To conclude, the performance of the Pd-alloy membranes in terms of flux, stability and separation efficiency shows that these type of membranes represent a very promising alternative to be applied in pre-combustion power generation cycles and H_2 production with carbon dioxide (CO_2) capture. An economic assessment of CO_2 avoidance cost is in Chapter 11 in this volume.

ACKNOWLEDGEMENTS

This research is financed by the European Union, the CO_2 Capture Project (CCP), and the Research Council of Norway (RCN) through the following programs, CCP/RCN-Renergi 2004/2005 (Contract No: C04043 and 5299775), RCN-Nanomat (Contract no: 158516/S10), and the EU-6FP CACHET project, (Contract no.: 019972) (www.cachetco2.eu). We would thankfully acknowledge Pall Corp. for providing the membrane supports.

REFERENCES

1. R.Bredesen, Klette,H., US Patent 6,086,729, 11-7-2000
2. A.L.Mejdell, T.A.Peters, M.Stange, H.J.Venvik, R.Bredesen, Performance and application of thin Pd-alloy hydrogen separation membranes in different configurations, Journal of the Taiwan Institute of Chemical Engineers 40 (2009) 253-259.
3. T.A.Peters, M.Stange, H.Klette, R.Bredesen, High pressure performance of thin Pd-23%Ag/stainless steel composite membranes in water gas shift gas mixtures; influence of dilution, mass transfer and surface effects on the hydrogen flux, Journal of Membrane Science 316 (2008) 119-127.
4. B.McCool, G.Xomeritakis, Y.S.Lin, Composition control and hydrogen permeation characteristics of sputter deposited palladium-silver membranes, Journal of Membrane Science 161 (1999) 67-76.
5. www.cachetco2.eu, 2008.
6. H.Klette, H.Raeder, Y.Larring, R.Bredesen, Carbon Dioxide Capture for Storage in Deep Geologic Formations, Elsevier Science, Amsterdam, 2005, pp. 377-384.
7. H.Klette, Bredesen,R., Slotfeldt-Ellingsen,D., International Patent Application, WO 2008/039080, 2008
8. A.L.Mejdell, H.Klette, A.Ramachandran, A.Borg, R.Bredesen, Hydrogen permeation of thin, free-standing Pd/Ag23% membranes before and after heat treatment in air, Journal of Membrane Science 307 (2008) 96-104.

9. J.N.Keuler, L.Lorenzen, Developing a heating procedure to optimise hydrogen permeance through Pd-Ag membranes of thickness less than 2.2 micrometer, Journal of Membrane Science 195 (2002) 203-213.
10. J.D.Way, Proceedings of the 10th international conference on inorganic membranes, Tokyo, Japan, 2008.
11. F.Guazzone, E.E.Engwall, Y.H.Ma, Effects of surface activity, defects and mass transfer on hydrogen permeance and n-value in composite palladium-porous stainless steel membranes, Catalysis Today 118 (2006) 24-31.
12. A.Ramachandran, A.Mejdell, T.A.Peters, M.Stange, H.J.Venvik, A.Borg, R.Bredesen, Proceedings of the 10th international conference on inorganic membranes, Tokyo, Japan, 2008.
13. G.Xomeritakis, Y.S.Lin, Fabrication of a thin palladium membrane supported in a porous ceramic substrate by chemical vapor deposition, Journal of Membrane Science 120 (1996) 261-272.
14. H.Li, H.Xu, W.Li, Study of n value and alpha/beta palladium hydride phase transition within the ultra-thin palladium composite membrane, Journal of Membrane Science 324 (2008) 44-49.
15. B.D.Morreale, M.V.Ciocco, R.M.Enick, B.I.Morsi, B.H.Howard, A.V.Cugini, K.S.Rothenberger, The permeability of hydrogen in bulk palladium at elevated temperatures and pressures, Journal of Membrane Science 212 (2003) 87-97.
16. G.L.Holleck, Diffusion and solubility of hydrogen in palladium and palladium-silver alloys, The Journal of Physical Chemistry 74 (1970) 503-511.
17. S.Uemiya, N.Sato, H.Ando, E.Kikuchi, The water gas shift reaction assisted by a palladium membrane reactor, Ind. Eng. Chem. Res. 30 (1991) 585-589.
18. R.E.Buxbaum, A.B.Kinney, Hydrogen transport through tubular membranes of palladium-coated tantalum and niobium, Ind. Eng. Chem. Res. 35 (1996) 530-537.
19. W.M.Tucho, J.C.Walmsley, M.Stange, A.Ramachandran, H.J.Venvik, R.H.Mathiesen, A.Borg, R.Bredesen, R.Holmestad, Microstructural studies of self-supported (1.5-10 micrometer) Pd/23wt.%Ag hydrogen separation membranes subjected to different heat treatments, Submitted (2009).
20. J.P.Collins, J.D.Way, Preparation and characterization of a composite palladium-ceramic membrane, Ind. Eng. Chem. Res. 32 (1993) 3006-3013.
21. K.S.Rothenberger, A.V.Cugini, B.H.Howard, R.P.Killmeyer, M.V.Ciocco, B.D.Morreale, R.M.Enick, F.Bustamante, I.P.Mardilovich, Y.H.Ma, High pressure hydrogen permeance of porous stainless steel coated with a thin palladium film via electroless plating, Journal of Membrane Science 244 (2004) 55-68.
22. P.P.A.C.Pex, Y.C.v.Delft, L.A.Correia, H.M.v.Veen, D.Jansen, J.W.Dijkstra, 7th Netherlands' Catalysis and Chemistry Conference, Noordwijkerhout, The Netherlands, 2006.
23. K.Hou, R.Hughes, The effect of external mass transfer, competitive adsorption and coking on hydrogen permeation through thin Pd/Ag membranes, Journal of Membrane Science 206 (2002) 119-130.
24. H.Amandusson, L.G.Ekedahl, H.Dannetun, Hydrogen permeation through surface modified Pd and PdAg membranes, Journal of Membrane Science 193 (2001) 35-47.
25. F.C.Gielens, R.J.J.Knibbeler, P.F.J.Duysinx, H.D.Tong, M.A.G.Vorstman, J.T.F.Keurentjes, Influence of steam and carbon dioxide on the hydrogen flux through thin Pd/Ag and Pd membranes, Journal of Membrane Science 279 (2006) 176-185.
26. A.Caravella, G.Barbieri, E.Drioli, Concentration polarization analysis in self-supported Pd-based membranes, Separation and Purification Technology 66 (2009) 613-624.
27. P.Middleton, P.Hurst, G.Walker, Carbon Dioxide Capture for Storage in Deep Geologic Formations, Elsevier Science, Amsterdam, 2005, pp. 409-425.

28. A.Unemoto, A.Kaimai, K.Sato, T.Otake, K.Yashiro, J.Mizusaki, T.Kawada, T.Tsuneki, Y.Shirasaki, I.Yasuda, Surface reaction of hydrogen on a palladium alloy membrane under co-existence of H_2O, CO, CO_2 or CH_4, International Journal of Hydrogen Energy 32 (2007) 4023-4029.
29. A.Li, W.Liang, R.Hughes, The effect of carbon monoxide and steam on the hydrogen permeability of a Pd/stainless steel membrane, Journal of Membrane Science 165 (2000) 135-141.
30. W.P.Wang, S.Thomas, X.L.Zhang, X.L.Pan, W.S.Yang, G.X.Xiong, H2/N2 gaseous mixture separation in dense Pd/alpha-Al2O3 hollow fiber membranes: Experimental and simulation studies, Separation and Purification Technology 52 (2006) 177-185.
31. T.A.Peters, W.M.Tucho, A.Ramachandran, M.Stange, J.C.Walmsley, R.Holmestad, A.Borg, R.Bredesen, Thin Pd-23%Ag/stainless steel composite membranes: Long-term stability, life-time estimation and post-process characterisation, Journal of Membrane Science 326 (2009) 572-581.
32. F.Guazzone, Y.H.Ma, Leak growth mechanism in composite Pd membranes prepared by the electroless deposition method, Aiche Journal 54 (2008) 487-494.
33. W.Mekonnen, B.Arstad, H.Klette, J.C.Walmsley, R.Bredesen, H.Venvik, R.Holmestad, Microstructural characterization of self-supported 1.6 [mu]m Pd/Ag membranes, Journal of Membrane Science 310 (2008) 337-348.
34. A.Unemoto, A.Kaimai, K.Sato, T.Otake, K.Yashiro, J.Mizusaki, T.Kawada, T.Tsuneki, Y.Shirasaki, I.Yasuda, The effect of co-existing gases from the process of steam reforming reaction on hydrogen permeability of palladium alloy membrane at high temperatures, International Journal of Hydrogen Energy 32 (2007) 2881-2887.
35. A.Matzakos, Presentation at the 2006 NHA Annual Meeting - Fuel Cells Topical - Innovations in Fuel Processing Session, 2006.
36. S.Tosti, A.Basile, L.Bettinali, F.Borgognoni, F.Chiaravalloti, F.Gallucci, Long-term tests of Pd-Ag thin wall permeator tube, Journal of Membrane Science 284 (2006) 393-397.
37. P.P.A.C.Pex, Y.C.van Delft, Carbon Dioxide Capture for Storage in Deep Geologic Formations, Elsevier Science, Amsterdam, 2005, pp. 307-319.

Carbon Dioxide Capture for Storage in Deep Geologic Formations, Volume 3
L.I. Eide (Ed.)

Chapter 13

PILOT-SCALE DEVELOPMENT OF THE SORPTION ENHANCED WATER GAS SHIFT PROCESS

Ed van Selow[1], Paul Cobden[1], Ruud van den Brink[1], Andrew Wright[2], Vince White[2], Peter Hinderink[3] and Jeff Hufton[4]
[1] Energy research Centre of the Netherlands, Westerduinweg 3, PO Box 1, Petten, 1755 ZG, The Netherlands
[2] Air Products PLC, Hersham Place Technology Park, Molesey Road, Walton-on-Thames, Surrey, KT12 4RZ, UK
[3] Process Design Center BV, Catharinastraat 21f, PO Box 7052, NL-4800 GB Breda, The Netherlands
[4] Air Products and Chemicals Inc., 7201 Hamilton Blvd., Allentown, PA 18195, USA

ABSTRACT: Development efforts for the Sorption Enhanced Water Gas Shift process conducted from 2006-2009 under the CACHET project are described. The project has been focused on experimental testing, process model development, power generation process simulation and integration, and economic evaluation/comparison. The new technology is well suited for high temperature hydrogen decarbonisation from natural gas-based syngas, and offers the potential of 17% lower cost of avoided CO_2 than competitive conventional technology. The new process has been demonstrated in a cyclic multicolumn test unit, but performance has not yet reached levels predicted through modelling and required for economic value. A review of the experimental system and modeling assumptions are necessary to uncover and resolve the issues hindering performance.

INTRODUCTION

The Process

The Sorption Enhanced Water Gas Shift (SEWGS) process is a novel pre-combustion decarbonisation technology that has the potential to reduce CO_2 capture costs versus conventional removal processes such as amine scrubbing [1,2].

The process combines CO_2 adsorption with the water-gas-shift (WGS) reaction:

$$CO + H_2O \rightleftharpoons CO_2 + H_2 \qquad \text{Equation 1}$$

The process is executed with multiple vessels filled with a mixture of high temperature WGS catalyst (iron-chrome) and CO_2 adsorbent. When syngas (containing H_2, CO_2, CO, H_2O, CH_4, and inerts) is fed at high pressure and temperature (c. 30 bara, 400 ºC), CO_2 is removed by the sorbent. By Le Chatelier's principle, the reaction in Equation 1 is shifted to the right-hand-side, thereby completely converting the CO and maximizing the production of H_2. This effectively removes CO and CO_2 from the feed gas, producing a high pressure, hydrogen rich product stream. Eventually though, the capacity of the adsorbent is saturated and CO_2 begins to show up in the product stream (breakthrough). At a predetermined level of CO_2 breakthrough, the bed is taken off-line and regenerated. Specific process steps are conducted for regeneration (based on pressure swing), and this produces a low-pressure byproduct stream rich in CO_2. By using multiple beds and properly

staggering the process cycle, the inherently dynamic process can mimic a continuous one, with essentially constant feed and product/byproduct streams.

The SEWGS process is particularly attractive for pre-combustion decarbonisation applications. Here the desire is to convert as much CO in the syngas to H_2 as possible and then separate the CO_2 from the H_2. The H_2 can then be fed to a gas turbine to generate power, while the CO_2 is sequestered. Conventional approaches to this problem require multiple cooling steps. The first is to cool the hot gas from the high temperature WGS reactor to around 200 °C to carry out a second low temperature WGS reaction to achieve the required conversion of CO. Further cooling is then necessary to enable the capture of CO_2 by absorption with an amine solution. The H_2-rich stream is then typically reheated before it is combusted in a gas turbine.

A more elegant and straight forward approach is offered by incorporating the SEWGS process. Partially shifted syngas from the high temperature WGS reactor is fed to a SEWGS unit, and a hot, high pressure, hydrogen rich product stream is directly produced. This H_2-rich product can be fed directly to a gas turbine at around 400 °C. This removes the inefficiency of cooling/heating of the H_2 that is an inherent part of the conventional process. In addition, proper execution of the SEWGS technology can yield a CO_2 byproduct stream at sufficient purity for direct sequestration.

A major goal of this work was to develop overall power generation flowsheets utilizing the new SEWGS technology and estimate the potential economic advantages of this approach. A simplified schematic of such a process is illustrated in Figure 1. Syngas is generated from natural gas and steam in an air-blown autothermal reformer (ATR). It exits the reformer and is cooled down using a waste heat boiler (WHB) to generate steam. The syngas then passes through a high temperature WGS reactor (HTS) to convert as much CO as possible via the reaction in Equation 1. The reaction is thermodynamically limited though, so the gas stream exiting the reactor contains 2–6% CO. It is fed directly to the SEWGS process at a temperature around 350-450 °C. The SEWGS unit then simultaneously drives the WGS reaction to completion whilst separating the CO_2 from the H_2-rich fuel gas.

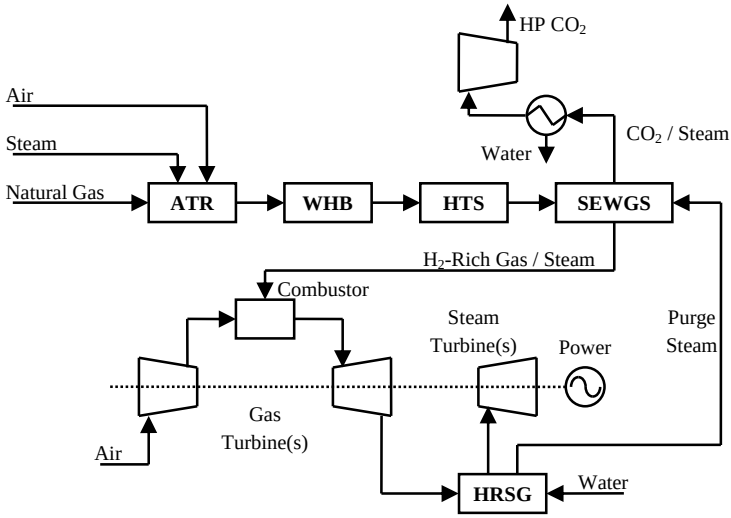

Figure 1. Schematic of Power Generation Process Incorporating SEWGS.

The H_2-rich fuel gas is diluted and combusted directly in a gas turbine to generate power. The resulting excess heat is used to generate steam via the HRSG (heat recovery steam generator). Some of this steam is used in the SEWGS unit, but the bulk is used to generate extra power in a steam turbine.

A stream of relatively pure CO_2 is obtained by cooling the low-pressure byproduct stream from the SEWGS unit and condensing out steam. The CO_2 stream can then be compressed for subsequent sequestration.

Details of the SEWGS process cycle are critical in defining how well the process will operate, e.g., it determines steam consumption, SEWGS bed size, and product and byproduct gas purity. A CO_2-rinse SEWGS cycle was proposed by Allam et al. [1], and it is illustrated in Figure 2. The top diagram shows the evolution of bed pressure in Reactor 1 during the cycle. The arrows in the middle drawing schematically indicate flow inputs and outputs from Reactor 1 during the cycle. The lower diagram is a cycle table, which specifies the sequence of process steps for each of the eight reactors in the SEWGS assembly.

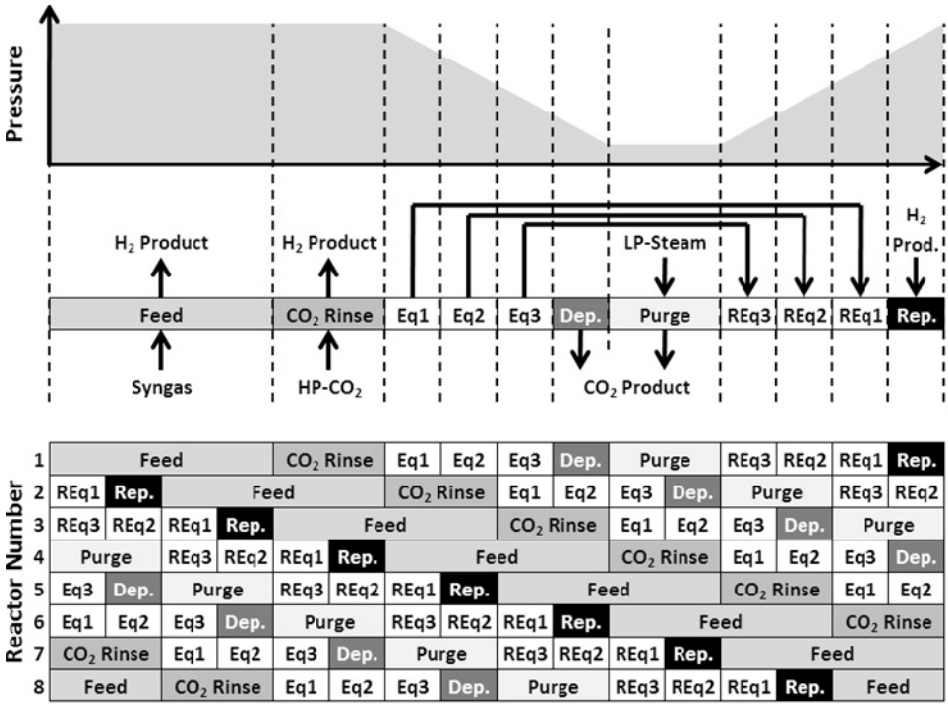

Figure 2. Process Steps for the Cocurrent CO_2 Rinse SEWGS Cycle.

The hydrogen product gas is produced during the 'Feed' step. High purity, high pressure CO_2 is partially flushed through the reactor during the 'CO_2 Rinse' step to displace some of the gas within the voids of the adsorbent/catalyst bed. The bed is then pressure equalised with other vessels to recover compression energy ('Eq1', 'Eq2', 'Eq3' steps) before finally being fully depressurized ('Dep.' step). After depressurisation, the adsorbent is regenerated by passing purge gas through the reactor to help facilitate desorption of CO_2 from the adsorbent ('Purge' step). Steam is the most logical purge fluid as it is readily available from the steam turbine and can be easily separated from

the CO_2 byproduct stream. The dried and compressed CO_2 byproduct stream is then sent offsite for sequestration, although a portion of the compressed gas must be recycled for the rinse step. After regeneration, the vessel receives a series of pressure equalization flows ('REq3', REq2', REq1' steps) and is repressurised with hydrogen product to the syngas feed pressure ('Rep.' step) and the cycle repeats.

Sufficient CO_2 rinse gas must be added so that at the end of the last equalisation step, the majority of the H_2-rich void gas in the bed is recovered. Without this step, a substantial quantity of void gas would end up in the CO_2 byproduct stream. This would reduce the byproduct gas purity and decrease the amount of hydrogen rich product gas available for power production. Unfortunately, using CO_2 is costly as it comes from compressing part of the low-pressure byproduct stream.

Ying et al. [3] proposed a cycle using counter-current steam for rinsing rather than co-current CO_2. Contrary to the CO_2 rinse cycle, the rinse steam ('H_2O Rinse' step in Figure 3) is supplied to the H_2-product end of the bed to maintain a high CO_2 concentration at the feed end – the effluent gas is recycled to another bed on the feed step. The power penalty for this approach is that the high pressure rinse steam is extracted from the steam turbine.

Integration of the various unit operations in the above power production process is critical for effective utilization of the SEWGS technology. The SEWGS process requires steam and (sometimes) power for operation, so effective sources must be found. The hot effluent streams (especially the CO_2 byproduct) can also be a source of thermal energy available for exchange with other streams in the plant. Understanding the tradeoffs between the two proposed SEWGS process cycles was a desired outcome of this work.

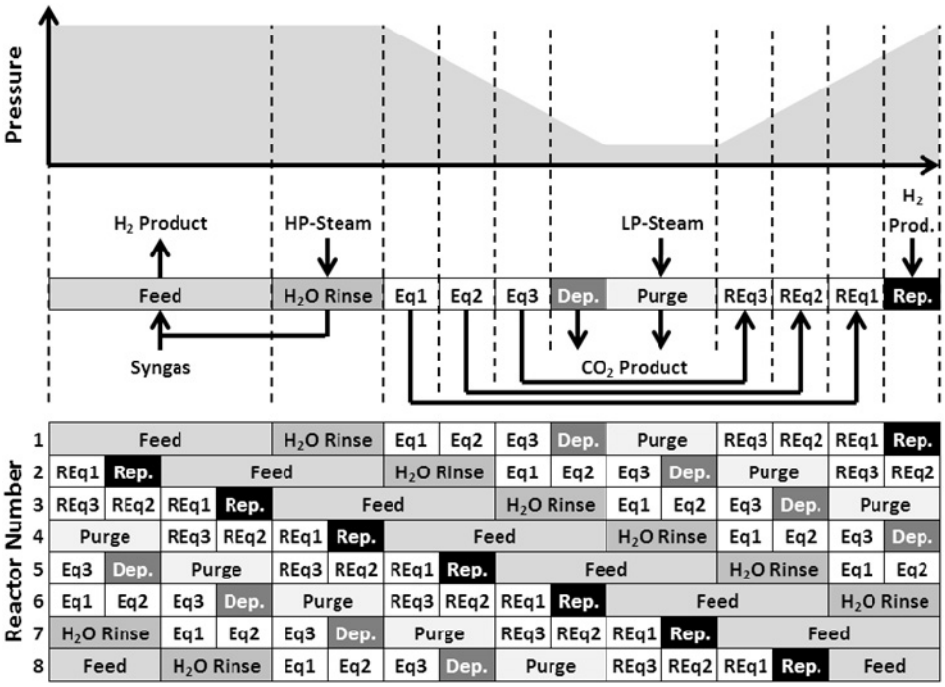

Figure 3. Process Steps for the Countercurrent Steam Rinse SEWGS Cycle.

Objective and Organization of the Work

The work described in this paper was part of the CACHET Program [4], a major pre-combustion project funded by the EU with support from the CO_2 Capture Project Phase 2 (CCP2).The major goals of the SEWGS part of CACHET were threefold: 1) experimentally demonstrate the SEWGS process under extended cyclic conditions, in both a single vessel and a multicolumn system, 2) develop a SEWGS process model which can describe the experimental results and can be used for optimization and scale-up, and 3) develop highly integrated power generation process flowsheets incorporating the SEWGS technology and evaluate relative performance and economics.

A multi-organizational team was assembled for this task. Experimental work was conducted at the Energy Research Centre of the Netherlands (ECN), SEWGS modelling was completed by Air Products Limited (APL), and overall power process modelling and economic evaluation was carried out by Process Design Center (PDC). The National Technical University of Athens (NTUA) provided support for power block design. Valuable input was also obtained from the various members of the CACHET technical team.

EXPERIMENTAL EQUIPMENT

Single Column Unit

In the first year of the project, a single reactor (2 m length x 38 mm ID) unit was built and operated at ECN for developing the SEWGS technology. It was designed for operation at up to 31 bara and 550 ºC. Feed gas consisted of synthetic mixtures containing H_2, CO_2, CO, N_2 and H_2O. The system was routinely used to measure breakthrough performance (e.g., measure composition of effluent gas as function of time after introduction of feed gas) as well as very simple cycle experiments (consisting of feed, countercurrent depressurization, countercurrent steam purge, countercurrent repressurisation). The latter experiments were used to obtain estimates of the CO_2 working capacity of the adsorbent. More detailed description of this unit is available in van Selow et al. [5].

Multicolumn Unit

A multi-column test rig was also constructed at ECN in order to characterize process performance under expected industrial conditions and process cycles. The unit was designed to handle 0.2 kgmole/hr feed flow, or roughly 1/150,000th of the total flow from an anticipated industrial system. It consisted of 6 reactors (6 m length x 38 mm ID) individually heat traced and insulated for operation up to 31 bara and 550ºC. One reactor had six thermocouples positioned at 0.5, 1, 2, 3, 4, and 5 m from the feed end. Syngas feed consisted of synthetic mixtures generated from bottled gas sources. Gas superficial velocities were targeted to be similar to those expected in the field. A large assembly of automated valves (48 in total) were present at the top and bottom of the columns, permitting operation of all steps of the steam rinse and CO_2 rinse cycles. As such, each column could be operated independently, or the assembly of columns could be continuously cycled via a Programmable Logic Controller (PLC) unit for continuous production of H_2 product and CO_2 byproduct. Gas analysis for the CO_2 product is by Ametek ProLine process mass spectrometer and for the H_2 product by ABB Advance Optima nondispersive IR. Process analysis was conducted by monitoring the composition of the effluent streams and, for cyclic experiments, evaluating average product and byproduct compositions, carbon capture fractions, H_2 recovery, and effective CO_2 working capacity of the adsorbent.

The multicolumn test rig was capable of doing top-to-top equalisations (i.e., beds connected at the H_2-product end) but not bottom-to-bottom equalisations (i.e., connecting beds at the syngas feed end). This was a limitation for the countercurrent steam rinse operation, as expansion of gas during

top-top pressure equalizations would not push void gases out of the vessel. A high H_2 recovery can only be achieved by flushing through the entire vessel with steam before the equalisation steps. This is not a particularly efficient mode of operation, but it was felt that modelling the data would permit extrapolation to bottom-to-bottom mode of operation.

More detailed description of the multi-column unit is available in van Selow et al. [6].

Materials

Two samples of CO_2 sorbent, designated as HTC1 and HTC2, were utilized in this work. Both consisted of 20 wt% K_2CO_3 promoted hydrotalcite pellets (4.8 mm diameter x 4.5 mm length) obtained from Sasol (PURALOX MG70). They differed primarily in their bulk density and crush strength, as indicated in Table 1. The high temperature WGS catalyst pellets were of a commercial Fe-Cr type and were obtained from an external supplier.

Table 1. Characteristics of Hydrotalcite CO_2 Adsorbents.

Source	Bulk density (g/cm^3)	Radial Crush Strength (N)
HTC1	0.39	33
HTC2	0.66	62

THEORETICAL MODELS

SEWGS Model

A robust SEWGS model was developed to help decipher experimental data from the test units and develop estimates of industrial performance. The model was based on similar theoretical framework as Air Products internal adsorption process simulator described by Kumar et al. [7], although a new, more efficient algorithm was written to solve the model equations. It uses the finite-volume technique with a stiff-ordinary-differential-equation solver to solve the coupled mass, momentum and energy balances for an adsorber over time. Boundary conditions are changed throughout the simulation to mimic the different steps within an adsorption cycle. Solutions obtained over many cycles can be used to determine the desired cyclic steady-state performance.

Prior to the CACHET project, work [2] on the K_2CO_3-impregnated hydrotalcite material yielded an adsorption isotherm for CO_2 based on the dual-site Langmuir form [8]. The isotherm was retained in this work, although the isotherm expression was multiplied by a scaling factor, F_I, to permit convenient fitting of the model to experimental data:

$$q_{CO_2} = F_I \left\{ \frac{m_1 b_o \exp\left(\frac{\Delta H_b}{RT}\right) P_{CO_2}}{1 + b_o \exp\left(\frac{\Delta H_b}{RT}\right) P_{CO_2}} + \frac{m_2 d_o \exp\left(\frac{\Delta H_d}{RT}\right) P_{CO_2}}{1 + d_o \exp\left(\frac{\Delta H_d}{RT}\right) P_{CO_2}} \right\} \qquad \text{Equation 2}$$

During the course of this work it became apparent that water can also adsorb onto the hydrotalcite, especially at higher partial pressures. This was accounted for in the model via a single-site Langmuir isotherm:

$$q_{H_2O} = \frac{mg_0 \exp\left(\frac{\Delta H_w}{RT}\right) P_{H_2O}}{1 + g_0 \exp\left(\frac{\Delta H_w}{RT}\right) P_{H_2O}} \qquad \text{Equation 3}$$

Carbon dioxide and steam were assumed to adsorb independently.

The linear driving force mass transfer model with constant mass transfer coefficient, k, was used to characterize transport of CO_2 into the adsorbent:

$$\frac{d\overline{q}}{dt} = k\left(\overline{q}^* - \overline{q}\right) \qquad \text{Equation 4}$$

The value of k can be varied to match the model to the experimental breakthrough curves. The rate of reaction on the high temperature WGS catalyst was modelled with the equations given by Rase [9]. This expression is valid only for steady state reactors, and will not account for any dynamic behaviour manifested in the SEWGS process (e.g., initial chemisorption of components on regenerated catalyst).

Power Process Model

Various power generation process flow diagrams loosely consistent with the simplified schematic in Figure 1 were constructed and simulated with ASPEN software. At a high level, the flow diagrams contained two process sections – a 'syngas production and separation' section (including air-blown autothermal reactor, high temperature WGS reactor, SEWGS unit, CO_2 compressor) and a 'powerblock' section (including gas turbine, heat recovery steam generation and steam turbines). Key parameter assumptions in both sections are listed in Table 2.

Table 2. Key Assumptions in ASPEN Process Simulations.

ATR steam/carbon = 1.4
ATR O_2/NG = 0.742
ATR CH_4 conversion 97%
3 steam levels – 120 bara, 30 bara, 4 bara
Gas turbine inlet T = 400 °C, P = 28 bara
Gas turbine = Siemens V94.3

Heat integration was generally isolated within the two sections, except for the heating of boiler feed water or steam generation for the power block. There was no process gas heat exchange between the two sections. Heat transfer from process streams was limited to raising steam when the potential for metal dusting was present (syngas at 400 °C or higher).

Capital and operating costs were evaluated via conventional approaches. The most uncertain cost component was the estimated installed capital cost for the SEWGS unit, as it is 'first of a kind' equipment and the mechanical design is not very well defined.

The various power generation schemes were simulated and the overall energy efficiency, power production cost, and cost of CO_2 avoided was determined and compared to the CACHET base case.

RESULTS

The single column unit was operated during the first year of the program to confirm that the CO_2 adsorbent could effectively remove CO_2 under extended cyclic operation, to generate adsorption data for process modeling, and to demonstrate the combined adsorption + reaction process under the CO_2 rinse and steam rinse cycles. The SEWGS process model was developed at this time as well, and model parameters were extracted from the experimental data. The model was then used to find optimized SEWGS performance points that minimized the cost of carbon capture for the power generation process. These data provided an estimate of the magnitude of savings possible with this new technology.

It also provided the incentive to push forward with further study of the SEWGS process under more realistic conditions (continuous cycling with industrial-scale feed rates, multiple beds and all relevant process steps). The multicolumn unit was constructed in the second year and operated in the later part of the third year. The results were compared with the predictions from the process model, and used to define forward directions for technology development.

Single Column Data

The experimental results from the single column unit have been thoroughly described by van Selow et al [5], so only a brief outline is provided here. This section will instead focus on the modeling and simulation results that evolved from this data.

Breakthrough Tests: Adsorbent only

The first set of experiments was conducted with packed adsorbent only and a feed gas of 20% CO_2 in N_2/H_2O at 28 bar, 400 °C. The column was first regenerated with flowing N_2 until all CO_2 was removed, and then was saturated with N_2/H_2O at the feed gas temperature and pressure. Results of this breakthrough test are illustrated in Figure 4 (all compositions on a dry basis), where the y-axis is the dry CO_2 mole fraction in the effluent divided by the dry CO_2 mole fraction in the feed.

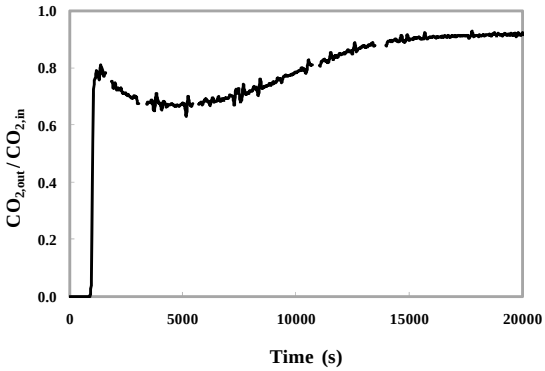

Figure 4. Breakthrough of CO_2 in Single Column Unit with Adsorbent Only.

Carbon dioxide breakthrough occurs at around 16 minutes, corresponding to a CO_2 adsorption capacity of 1.4 mmole/g. Breakthrough is followed by a long tail that lasts a number of hours. Carbon dioxide is continually being removed from the adsorbent during this time, albeit at a relatively low rate. It has been postulated [5] that this slow uptake is associated with bulk reaction of CO_2 to form $MgCO_3$. The initial uptake during the pre-breakthrough period is rapid and is thought to be associated with interaction of CO_2 with the surface of the adsorbent. Maximizing the extent of this rapid process will provide the largest benefits to the SEWGS process.

The SEWGS process model was used to simulate the thermal and mass transfer fronts exhibited in these tests. The isotherm model of Eqn 2 was capable of capturing the form of the entire breakthrough curve if the value of F_1 and k were 0.685 and 0.05 1/s, respectively (Figure 5). The relatively low value of F_1 is attributable to the influence of the bulk $MgCO_3$ reaction. The magnitude of the mass transfer coefficient is similar to values reported by Lee et al. [10].

Figure 6 shows experimental in-bed temperatures versus the model predictions for the adsorbent-only breakthrough experiment. The heat transfer coefficient between the reactor and the environment has been adjusted so the average temperature in the bed at the point of breakthrough is equal between the model and the experiment. There is a significant difference in the maximum temperature peaks, but otherwise agreement is reasonable. The discrepancy can be the result of combinations of an inadequate heat transfer model (which lumps together thermal capacity of packed column and column walls), improper solid packing heat capacity, inaccurate mass transfer rate parameter for CO_2, wrong isotherm shape, and/or artefacts introduced by the heat tracing temperature controllers. More work would be necessary to obtain more quantitative fit to the data.

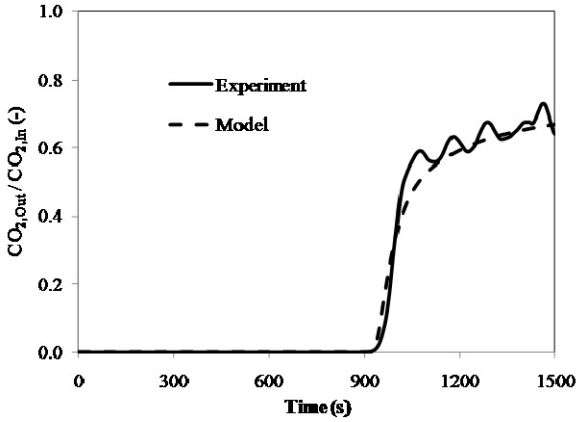

Figure 5. Adsorbent-Only Breakthrough Test – Experimental Data and Model.

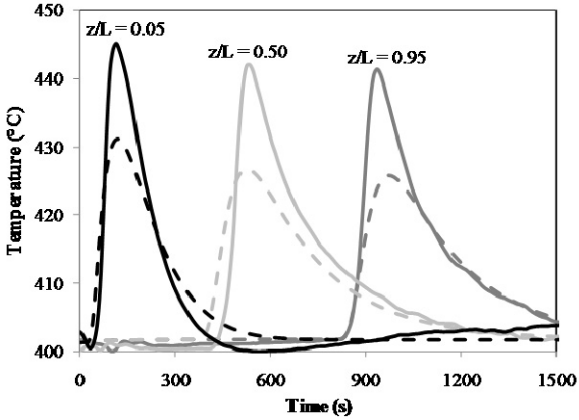

Figure 6. Temperature Profiles for Adsorbent-Only Breakthrough Test.

Breakthrough Test: Adsorbent/Catalyst

A mixture of HTC1 and WGS catalyst in 5:1 volume ratio was packed in the single column unit, the catalyst was reduced, and a breakthrough test was conducted with a feed gas consisting of 16% CO_2 / 10% CO / 16% H_2O / 58% H_2. The effluent gas compositions are plotted in Figure 7 as the solid lines. Initially only N_2 exits the reactor (the initial pressurization gas). It is followed by a substantial volume of essentially pure H_2 between 140 and 370 seconds. Carbon dioxide is removed by the adsorbent, CO is reacted to CO_2 and removed, leaving behind only H_2. Carbon dioxide and CO exit the bed together after 370 seconds. Also shown in Figure 7 is the best-fit of the model (dashed lines) with an F_1 value of 1.01 and a mass transfer coefficient of 0.18 s^{-1}. The model provides a reasonable qualitative description of the data, although the final values for the CO_2 and CO concentrations are not matched particularly well (this is believed to be partially attributable to inaccurate steam flow in this test). The model predicts concentrations consistent with water-gas-shift reaction equilibrium, and similar experiments in all columns in the multi-column rig yield compositions essentially at or slightly below shift equilibrium.

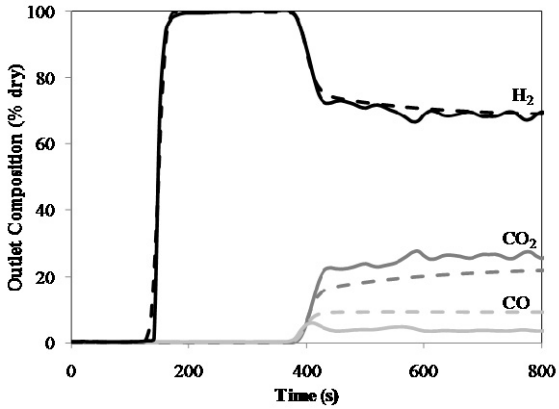

Figure 7. Adsorbent and Catalyst Breakthrough Test with Syngas Feed Gas

Single Bed Cyclic Experiments

Experiments were then carried out to determine the performance of the materials under a simplified SEWGS cycle consisting of feed, rinse, countercurrent depressurisation, countercurrent purge and countercurrent repressurisation steps. The rinse step involved either supplying CO_2 in a cocurrent direction in respect to the feed direction, or steam in a countercurrent direction with respect to the feed direction.

The most significant output from these tests was the experimental verification that the HTC1 adsorbent could achieve a cyclic steady state. There was concern that the bulk reaction component could act to continually decrease the adsorbent working capacity to diminishing levels. Instead, cycling the adsorbent-only system for 500 cycles with the CO_2 rinse cycle yielded a stable working capacity of 0.29 mmole/g. Similar tests with a steam rinse cycle over 1400 cycles produced a working capacity of 0.66 mmole/g. These results are described in great detail by van Selow et al. [5]

Attempts were made to match average product gas CO_2 content and product gas composition profiles taken from the above cyclic experiments (at cyclic steady state) with the SEWGS process model. For the CO_2 rinse case, qualitative agreement was obtained by adjusting k to 0.024 1/s, roughly half the value from the breakthrough tests. The experimental composition profiles show a

sharper CO_2 increase than the model, though, suggesting the isotherm expression in the model overestimates CO_2 capacity during rinse. This will lead to a conservative model (predicts higher CO_2 rinse flows than necessary). For the steam cycles, the average CO_2 content of the product gas was matched with the model when the k values were 0.026 – 0.029 1/s. Surprisingly, the effluent profiles were not described well, as the model predicts rapid increase of CO_2 in the product gas at the end of the rinse step which is not observed in the experiments. This will lead to conservative predictions of performance when hydrogen product purity must be maintained.

Based on the above results, full-scale system predictions with either a steam- or CO_2-rinse SEWGS cycle were based on a mass transfer coefficient of 0.026 s^{-1}, F_I = 0.685, and the reaction rate calculated as described by Rase [9].

Adsorbent Stability

Another key finding from the single column unit was that the mechanical stability of the HTC1 adsorbent is limited to only a few thousand high pressure cycles. Spent adsorbent from both the adsorbent-only and catalyst/adsorbent campaigns was fractured and powdered throughout the entire reactor. Interestingly, the CO_2 sorption capacity remained high during these tests. This is a critical issue for the SEWGS process as friable materials with limited crush strength will lead to valve sealing issues and failures. This topic is currently under further investigation.

Power Simulations based on Single Column Data

Using the results from the single column tests, the model was updated to predict designs for large-scale SEWGS units. This basically required changing the heat loss parameters so the simulated vessels operated adiabatically. The decision was also made to incorporate the higher bulk density of the second batch of hydrotalcite material (HTC2) for the modelling exercise.

The process cycles illustrated in Figures 2 and 3 were simulated. In each case, an 8-bed system was chosen with feed split between two beds at any one time. The 'provide equalisation' steps (Eq1, Eq2 and Eq3 in Figures 2 and 3) are carried out in the same direction as the rinse step.

The Appendix contains very insightful plots of the partial pressure of each component along the bed at the end of each process step. Rinse gas fills part of the bed and then expands during depressurisation steps to push the rest of the H_2-rich void gas into another bed. With the CO_2-rinse case, however, the amount of supplied rinse gas must be limited to prevent CO_2 transfer to the top of another bed. This limits the amount of void gas that can be flushed out. With the steam rinse cycles there is no such limitation as contaminating the product end of the bed with steam is not an issue. Therefore, achieving a higher degree of separation and a high purity CO_2 byproduct stream is less of a challenge for the steam-rinse case.

The steam rinse and CO_2 rinse cycle models were run with varying bed length, cycle time, rinse flow rate and purge flow rate. Each variable was given three different values, resulting in 3^4=81 simulations for each cycle model. The results were fit with a combined quadratic interpolation so that the performance at intermediate operating conditions could be estimated. A model characterizing operating and capital cost of the whole power production process as a function of the SEWGS operating parameters was developed using tie points from specific economic assessments conducted by the PDC. The model used for interpolating the SEWGS simulation results was then combined with the power process costing model so that the effect of changing the bed length, cycle time, rinse flow rate and purge flow rate, on overall power economics could be evaluated. An optimisation routine was set up to vary the SEWGS parameters so that the cost of CO_2 avoided was minimised, while guaranteeing at least 95% carbon capture and a 98% purity CO_2 byproduct stream.

Table 3 compares the performance of the CACHET base case power generation process (air Auto Thermal Reforming, air-ATR) with the estimated performance of the optimised SEWGS designs for the two different cycles. Net power production was 367 MW. The SEWGS approaches yield roughly 4 percentage point increase in overall process efficiency compared to the CACHET base case. Estimated unit costs for CO_2 capture and avoidance of the SEWGS designs compared to other CCP2 technologies are given in [11]. The results show that the CO_2-rinse cycle is a more expensive option than the steam-rinse case. This is due to the higher rinse flow requirements necessary to account for the adsorption of CO_2, and the extra purge steam required to remove this additional CO_2 from the bed. The results also suggested that rigorous economic evaluation of the steam rinse SEWGS process was warranted. The results of this rigorous evaluation, also listed in Table 3, are within the accuracy of the approximate evaluations.

Table 3. Comparison of Modelled SEWGS Cycles with Base Case.

		Rigorous Evaluation of Base Case (Air-ATR)	Approximate Evaluation of CO_2-Rinse SEWGS	Approximate Evaluation of H_2O-Rinse SEWGS	Rigorous Evaluation of H_2O-Rinse SEWGS
Overall Efficiency	%	40.9	44.6	45.0	44.3
H_2 Recovery	%	-	99.5	99.5	99.6
Carbon Capture	%	94.7	97.2	95.8	96.0

Multicolumn Data

The next phase of work was to investigate SEWGS process performance in the multicolumn test unit. All six reactors were loaded with a homogenous mixture of sorbent (HTC2) and catalyst. The catalyst volume fraction was 15%, and it was reduced per vendor instructions.

Breakthrough tests with syngas were completed in all six reactors. The tests confirmed that each reactor contained active catalyst and adsorbent, and all were packed fairly uniformly. Breakthrough capacities were 1.32 ± 0.11 mmol/g, which are similar to capacities measured in the single column unit. The CH_4 level in the product gas was 535 ± 140 ppm.

CO_2 Rinse Cycle

The CO_2 rinse cycle was the first SEWGS process tested on the multicolumn unit. Feed gas initially consisted of 54% H_2, 18% CO_2, 9% CO, and 19% H_2O (the N_2 flow controller had failed). Feed was at 30 bar, 400 °C, and purge steam to carbon in the feed was 2.0 mole/mole. A plot of the product gas and byproduct gas composition is illustrated in Figure 8. The amount of CO_2 rinse gas was adjusted at the indicated intervals. The results show that 1) the cycle can simultaneously produce relatively high purity CO_2 byproduct (85+%) and hydrogen product containing CO and CO_2 levels < 20% of the feed level, and 2) increasing the CO_2 rinse improves CO_2 byproduct purity at the expense of decreased carbon capture. It is also clear that the system has not yet achieved a cyclic steady state condition – this was generally difficult to achieve in the cyclic unit due to time constraints, long cycle times, and the slow approach to cyclic steady state due to bulk carbonate formation in the adsorbent. An illustration of the CO_2 byproduct purity and carbon capture ratio for these tests is shown in Figure 9.

A similar experiment was conducted once the N_2 controller was repaired. The impact of syngas dilution with 43% N_2 was to decrease the CO_2 byproduct purity (< 90%) and the carbon capture ratio (< 70%).

The byproduct CO_2 purity for the last cycles in Figure 8 is magnified in Figure 10 to show the average composition associated with the individual vessels. It is clear that a repetitive and dramatic reduction of purity is obtained for two of the reactors. This was determined to be caused by leaking valves, which allow impurity gases (H_2, N_2, CO) to infiltrate reactors during their low pressure purge and blowdown steps – these impurities then end up in the byproduct stream. Replacement of the leaking valves would increase the CO_2 byproduct purity to the 95% or better range.

The working capacity determined from the cyclic experiments was 0.17-0.21 mmole/g, which was substantially lower than obtained for the single column unit (0.29 mmole/g for adsorbent only tests, 0.34 mmole/g for adsorbent/catalyst tests). This could be due to the impact of pressure equalization steps in the cyclic unit which tend to move CO_2 towards the product end of the reactor and make CO_2 regeneration more difficult.

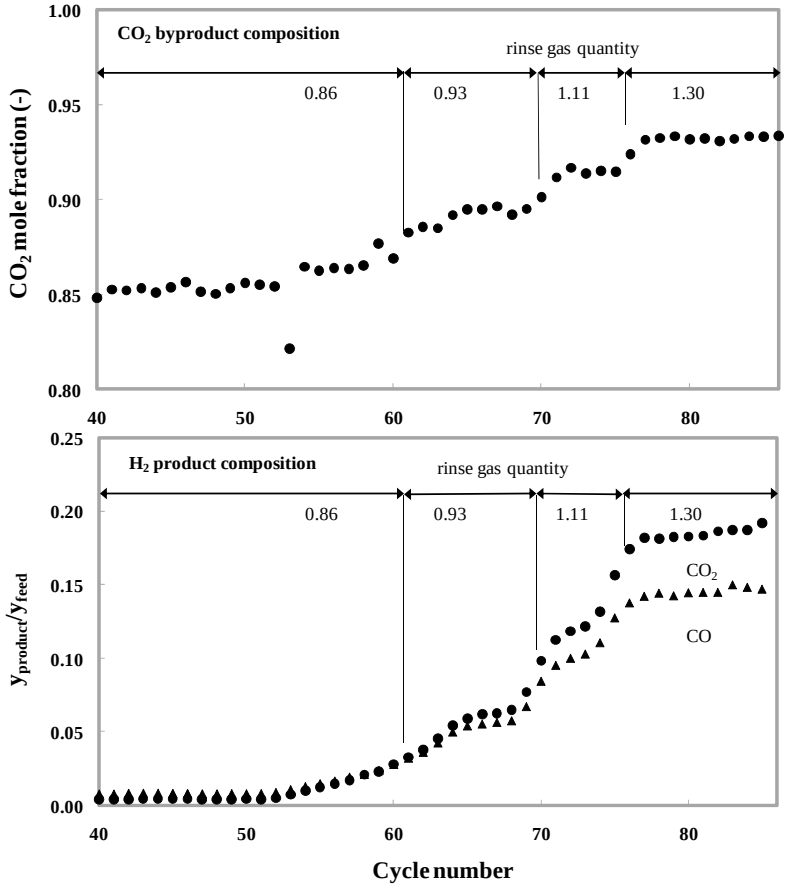

Figure 8. Byproduct Purity (bottom) and Product Purity (top) for CO_2 Rinse Cycle.

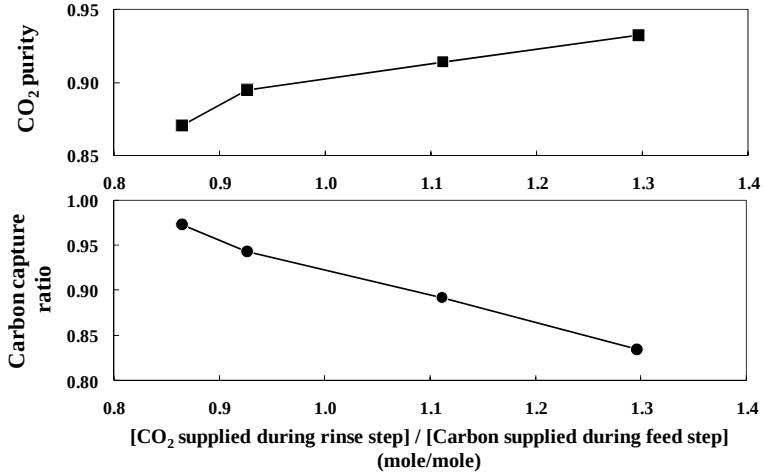

Figure 9. CO_2 Purity and Carbon Capture Ratio for CO_2 Rinse Cycles.

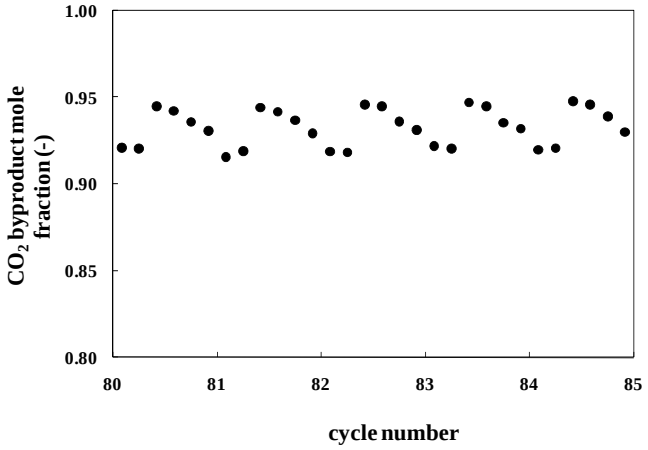

Figure 10. CO_2 Byproduct Purity Averaged over Each Reactor.

Steam Rinse Cycle

The countercurrent steam rinse cycle was tested with the same loading of adsorbent and catalyst. Figure 11 illustrates product gas and byproduct gas purity obtained for a sequence of roughly 75 cycles conducted with 1.6 moles of rinse steam per mole of carbon in the feed gas. Feed gas consisted of 37% H_2, 12% CO_2, 4% CO, 34% N_2 and 13% H_2O. The cycle is capable of rejecting the majority of CO and CO_2 from the hydrogen product gas while simultaneously producing 80% CO_2 byproduct. Hydrogen recovery was 98+%. Carbon capture and CO_2 byproduct purity are plotted versus the amount of steam rinse in Figure 12. Carbon capture ratios were less than 90%. The working capacity was 0.23 mmole/g.

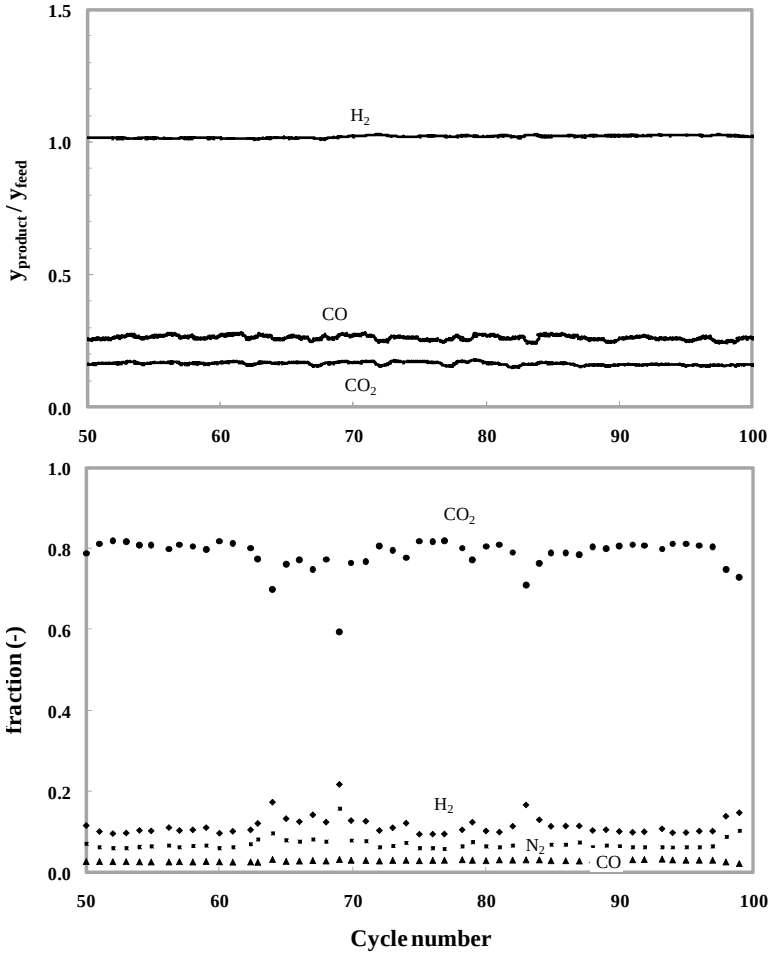

Figure 11. Byproduct Purity (bottom) and Product Purity (top) for Steam Rinse Cycle.

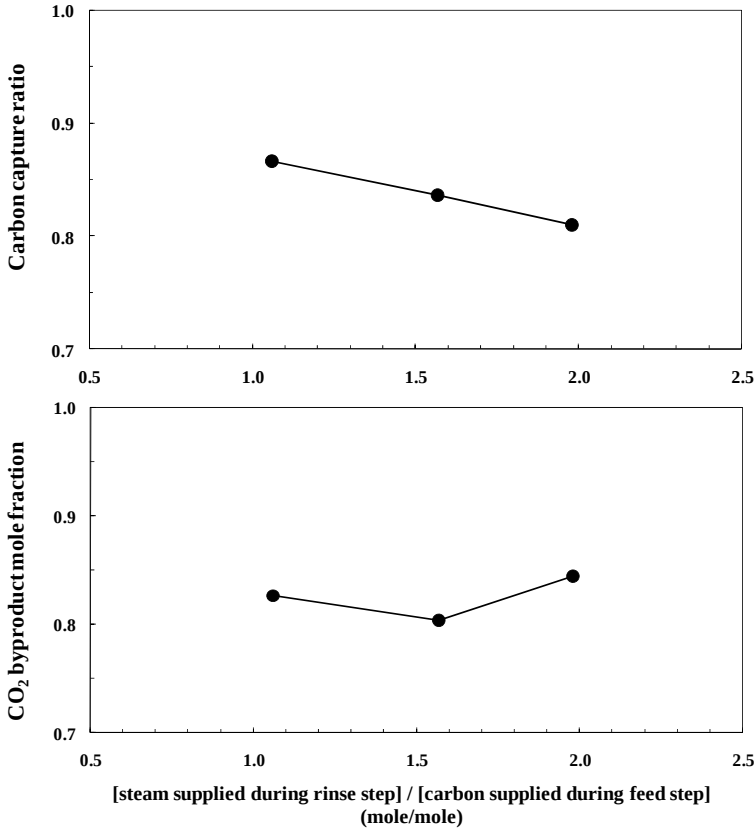

Figure 12. CO_2 Purity and Carbon Capture Ratio for Steam Rinse Cycle.

Process Simulation Shortfalls

The cyclic experimental data from the multicolumn unit were compared with model results. Use of the F_I and k values determined in the single column tests yielded poor predictions. It was found that the F_I value had to be reduced from 0.685 to 0.25 – 0.35 in order to match the H_2 product and CO_2 byproduct stream compositions for both the CO_2 rinse and steam rinse data. This represents a 40-70% drop in effective capacity compared to the single column results. This loss of performance could also be described by holding F_I at 0.685 and reducing k by about an order of magnitude.

The source of this discrepancy is not clear. Possible explanations are the use of different adsorbent materials, inability of the model to properly account for pressure equalization steps, influence of non-column void volumes on pressure equalization, valve leakage, or subtle differences between how the cycle experiment is conducted and how the model thinks the cyclic experiment is conducted. More work is needed to understand what is causing the issue and fix it, whether it is the assumptions in the model or the experimental data against which it is compared. The results suggest that both are contributing factors.

Comparison of the model and multicolumn experimental data suggests that some H_2 may be chemisorbing on or reacting with the catalyst during the feed step. It is then liberated (desorbed or

formed by catalyst oxidation by water) during the regeneration steps. Further investigation is also needed to understand this behaviour.

Updated Power Simulations based on Multicolumn Data

The relatively poor SEWGS performance obtained from the cyclic multicolumn experiments cannot meet the desired carbon capture and byproduct CO_2 purity specifications. A modified SEWGS model based on these data was used to estimate overall power generation performance, and both the CO_2 rinse and steam rinse cycle were now found to be more costly to operate than the base case amine system. It is therefore critical that the issues plaguing the multicolumn operation be addressed and resolved in the future.

CONCLUSIONS

In this project, we have tried to determine the potential of the SEWGS process through experimentation, simulation, and economic evaluations. Experimental data have been collected on a single bed unit to demonstrate an effective CO_2 adsorbent (K_2CO_3 promoted hydrotalcite). For the first time this material has been cycled under industrially relevant conditions for many cycles, and a cyclic steady state has been attained. Two different SEWGS process cycles, cocurrent CO_2 rinse and countercurrent steam rinse, have been identified and tested in the single bed unit. A powerful SEWGS process simulation tool has been developed and model parameters have been estimated by comparing with the experimental data. This tool has been coupled with rigorous ASPEN-based power generation process simulations in order to optimize the overall process performance. The results suggest that the SEWGS process has the potential to reduce the cost of CO_2 avoided in natural gas-based power generation systems by 15-20% for a 400 MW plant.

Unfortunately, demonstration of the desired level of cyclic performance has not been observed yet in the multicolumn test unit. It appears that it is time for a very detailed review of both the experimental unit as well as the SEWGS model to understand why this is the case. A series of fundamental experiments in the cyclic unit would likely expose these issues.

In addition to demonstration of the technology and model verification, there are some other key hurdles that need to be addressed. These include the observed limited mechanical stability of the adsorbent, the potential interaction of H_2/H_2O with the catalyst, imprecise modelling of both fast surface and slow bulk reaction processes characteristic of the CO_2 adsorbent, the relatively large impact of valve leakage on CO_2 byproduct purity, development of a detailed mechanical vessel design (and accurate cost), and verification of switch valve operations at high temperatures.

NOMENCLATURE

b_o	pre-exponential term for CO_2 adsorption on site 1 of dual site Langmuir model, 1/atm
d_o	pre-exponential term for CO_2 adsorption on site 2 of dual site Langmuir model, 1/atm
F_I	scaling factor for isotherm model, dimensionless
g_o	pre-exponential term for H_2O adsorption in Langmuir model, 1/atm
k	mass transfer coefficient, 1/s
m	monolayer capacity of adsorbent for H_2O in Langmuir model, mmole/g
m_1 , m_2	monolayer capacity of adsorbent for CO_2 in sites 1 and 2 of dual site Langmuir model, mmole/g
P_{CO_2}	partial pressure of CO_2 in gas phase, atm

P_{H_2O}	partial pressure of H_2O in gas phase, atm
$\bar{q}$	volume-averaged loading of CO_2 in an adsorbent pellet, mmole/g
$\bar{q}^*$	adsorbed-phase loading of CO_2 in equilibrium with gas concentration at pellet surface, mmole/g
q_{CO_2}	adsorbed phase loading of CO_2 on the adsorbent, mmole/g
q_{H_2O}	adsorbed phase loading of H_2O on the adsorbent, mmole/g
R	gas constant, 1.987 cal/mole/K
T	temperature, K
t	time, s
ΔH_b	heat of adsorption of CO_2 on site 1 of dual site Langmuir model, cal/mole
ΔH_d	heat of adsorption of CO_2 on site 2 of dual site Langmuir model, cal/mole
ΔH_w	heat of adsorption of H_2O in Langmuir model, cal/mole

ACKNOWLEDGEMENTS

Support from the European Commission and the CO_2 Capture Project Phase 2 (CCP2) is gratefully acknowledged. The authors would like to thank the CACHET work package technical team for their valuable suggestions.

Figure 1 of this Chapter originally appeared in Energy Procedia Vol 1, Issue 1, Greenhouse Gas Control Technologies 9, Proceedings of the 9th International Conference on Greenhouse Gas Control Technologies (GHGT-9), 16-20 November 2008, Washington DC, USA., which was published by Elsevier Ltd.

REFERENCES

1. R.J. Allam, R. Chiang, J.R. Hufton, P. Middleton, E.L. Weist, V. White, Development of the sorption enhanced water gas shift process, in D. C. Thomas and S. M. Benson (eds.), Carbon Dioxide Capture for Storage in Deep Geologic Formations, Volume 1. Elsevier Ltd, (2005) 227.
2. J.R. Hufton, R.J. Allam, R. Chiang, P. Middleton, E.L. Weist, V. White, Development of a process for CO_2 capture from gas turbines using a sorption enhanced water gas shift reactor system, *Proc. 7th Int. Conf. Greenhouse Gas Techn.* Vancouver, Canada (2004).
3. D.H.S. Ying, S. Nataraj, J.R. Hufton, J. Xu, R.A. Allam, S.J. Dulley, Simultaneous shift-reactive and adsorptive process to produce hydrogen, US Patent No 7354562 (2008).
4. Beavis, R., 2009. Introduction to CACHET, in Eide, L.I. (Ed.) 2009, Carbon Dioxide Capture for Storage in Deep Geologic Formations, Vol. 3. CPL Press.
5. E.R. van Selow, P.D. Cobden, P.A. Verbraeken, J.R. Hufton, R.W. van den Brink, Carbon capture by sorption enhanced water gas shift reaction process using hydrotalcite-based material", *Ind. Eng. Chem. Res.* **48**, 9 (2009) 4184.
6. E.R. van Selow, P.D. Cobden, R.W. van den Brink, J.R. Hufton, A. Wright, Performance of sorption-enhanced water-gas shift as a pre-combustion CO_2 capture technology, *Proc. 9th Int. Conf. Greenhouse Gas Techn*. Washington DC (2008).
7. R. Kumar, V.G. Fox, D.G. Hartzog, R.E. Larson, Y.C. Chen, P.A. Houghton, T. Naheiri, A versatile process simulator for adsorptive separations, *Chem. Eng. Sci.* **49** 18 (1994) 3115.
8. P.M. Mathias, R. Kumar, J.D. Moyer, Jr., J.M. Schork, S.R. Srinivasan, S.R. Auvil, O. Talu, Correlation of multicomponent gas adsorption by the dual-site Langmuir model. application to nitrogen/oxygen adsorption on 5A-zeolite, *Ind. Eng. Chem. Res.* **35** 7 (1996) 2477.

9. H.F. Rase (1977) *Chemical Reactor Design for Process Plants*, John Wiley and Sons.
10. K.B. Lee, M.G. Beaver, H.S. Caram, S. Sircar, Reversible chemisorption of carbon dioxide: simultaneous production of fuel-cell grade H_2 and compressed CO_2 from synthesis gas, *Adsorption* **13** (2007) 385.
11. Melien, T. and S. Brown-Roijen, 2009. Economics, in Eide, L.I. (Ed.) 2009, Carbon Dioxide Capture for Storage in Deep Geologic Formations, Vol. 3. CPL Press.

APPENDIX. REACTOR PROFILE PLOTS.

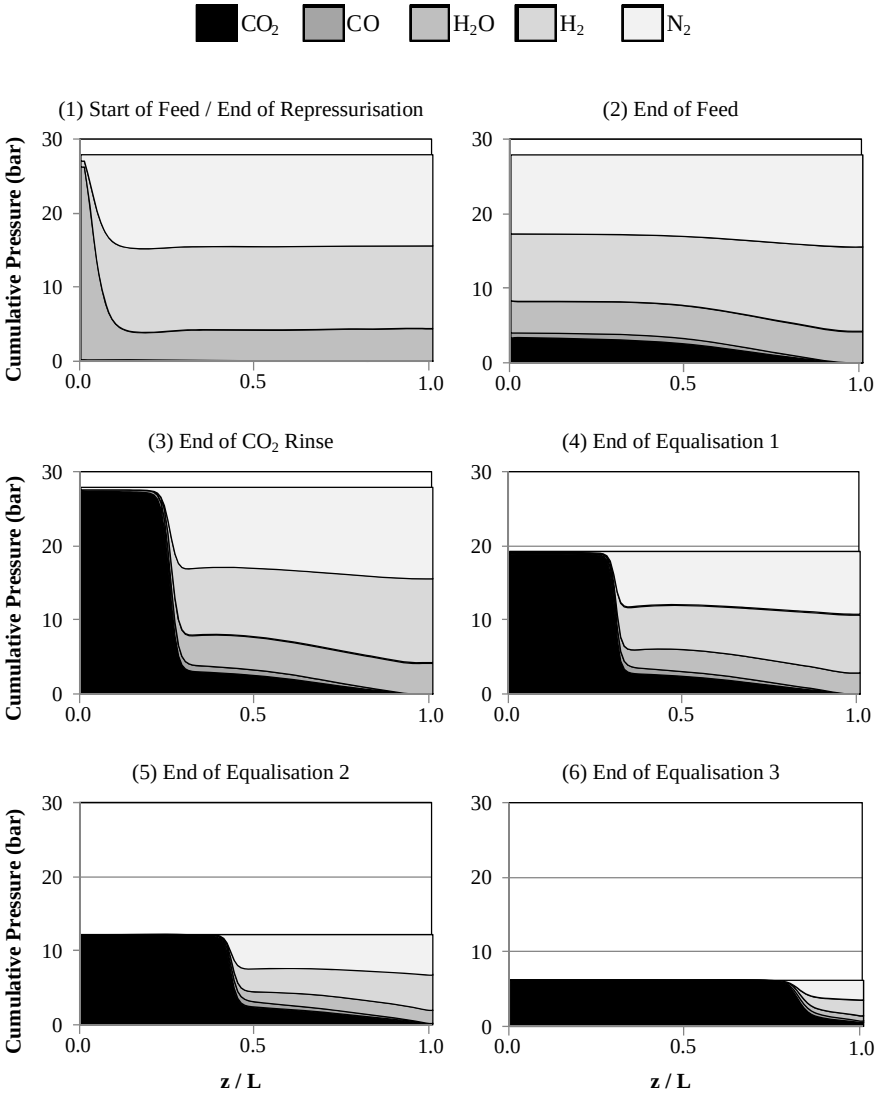

Simulation Results Showing Predicted Performance
of the SEWGS Cycle with a Co-Current CO_2-Rinse Step

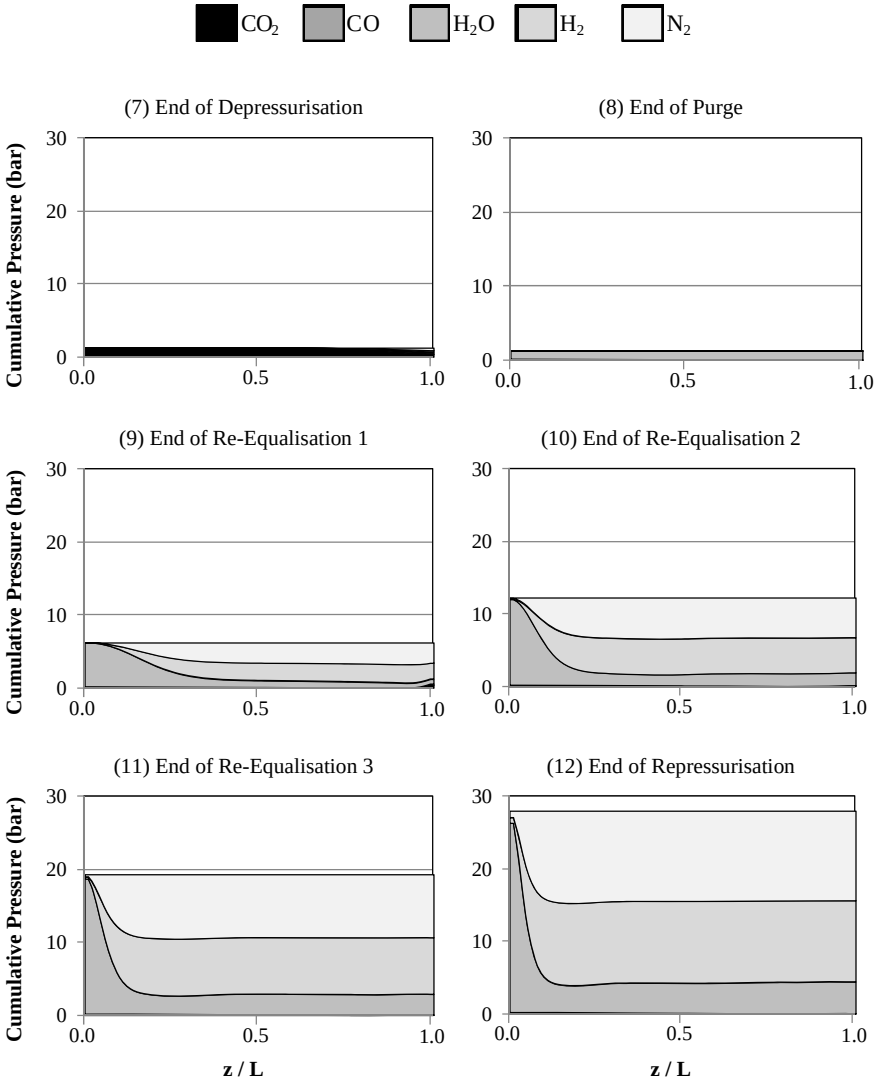

Simulation Results Showing Predicted Performance
of the SEWGS Cycle with a Co-Current CO_2-Rinse Step

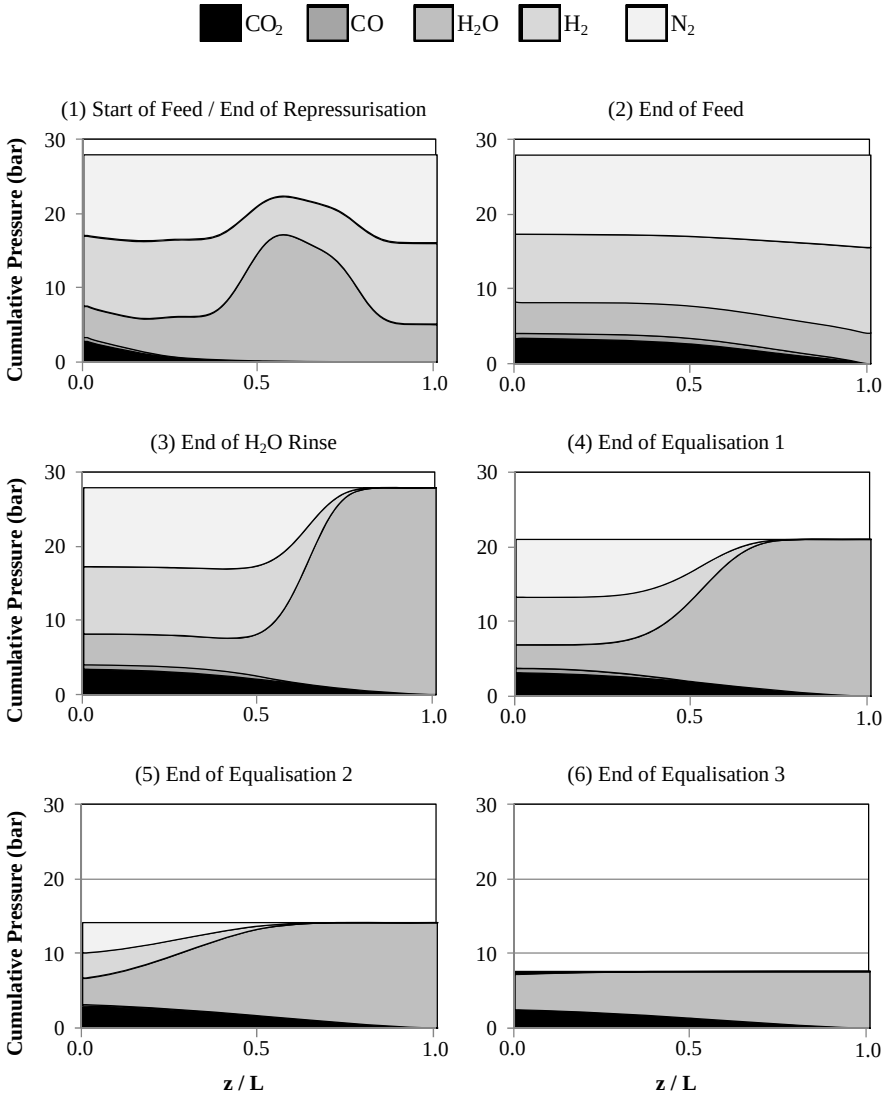

Simulation Results Showing Predicted Performance
of the SEWGS Cycle with a Counter-Current H_2O-Rinse Step

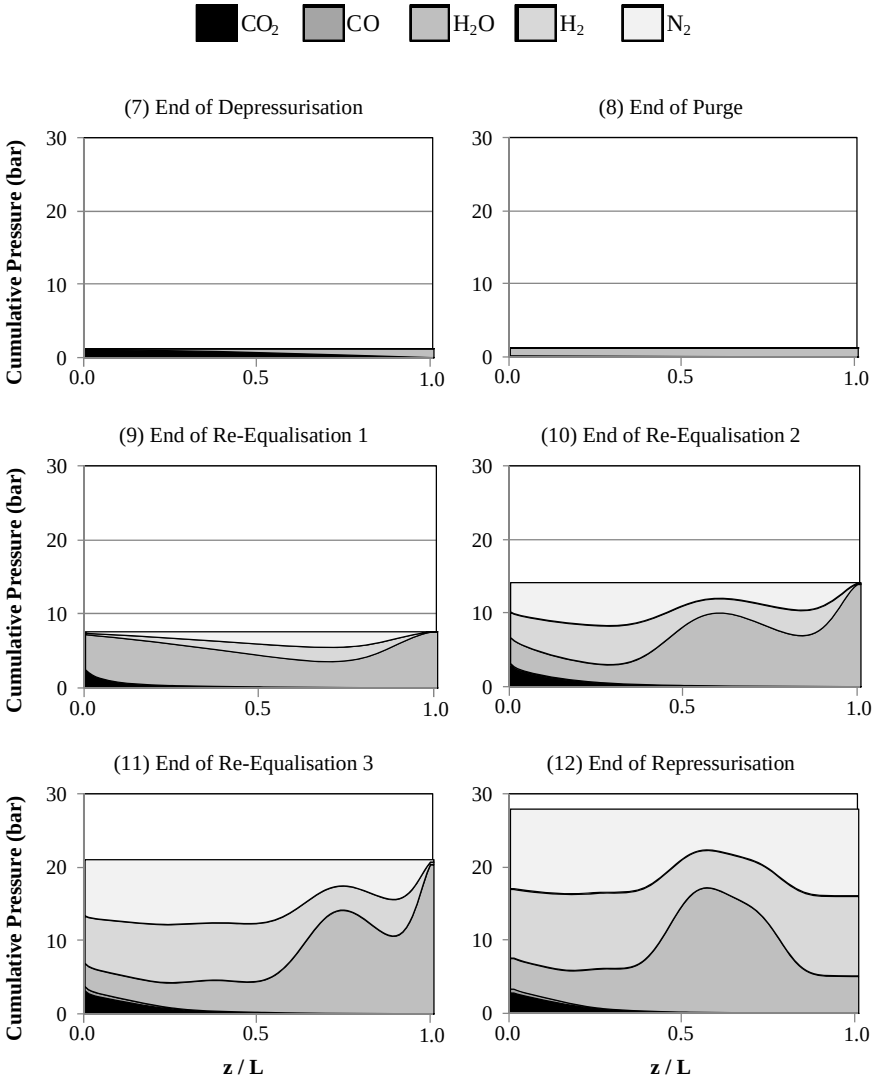

Simulation Results Showing Predicted Performance
of the SEWGS Cycle with a Counter-Current H_2O-Rinse Step

Carbon Dioxide Capture for Storage in Deep Geologic Formations, Volume 3
L.I. Eide (Ed.)

Chapter 14

DEVELOPING CHEMICAL LOOPING STEAM REFORMING AND CHEMICAL LOOPING AUTOTHERMAL REFORMING

Magnus Rydén[1], Anders Lyngfelt[1], Alexander Schulman[2], Luis F. de Diego[3], Juan Adánez[3], María Ortiz[3], Tobias Pröll[4], Johannes Bolhàr-Nordenkampf[4], Philipp Kolbitsch[4]
[1]Department of Energy and Environment,
Chalmers University of Technology, SE-412 96, Göteborg, Sweden
[2]Department of Chemical and Biological Engineering
Chalmers University of Technology, SE-412 96, Göteborg, Sweden
[3]Department of Energy and Environment, Instituto de Carboquímica (CSIC)
Miguel Luesma Castán 4, 50018 Zaragoza, Spain
[4]Institute of Chemical Engineering, Vienna University of Technology
Getreidemarkt 9/166, 1060 Vienna, Austria

ABSTRACT: Two methods for production of H_2 and power from natural gas with CO_2 capture utilizing chemical looping technologies have been examined within the framework of the CACHET project. Chemical looping steam reforming, CLR(s), is a process where conventional tubular reforming is used to convert steam and hydrocarbons into syngas, and chemical looping combustion (CLC) is used to provide heat for the endothermic reforming reactions and to capture CO_2. Chemical looping autothermal reforming, CLR(a), is a process where chemical looping is operated at understoichiometric conditions as an autothermal reformer. In this paper, the experimental results from this work are briefly presented. Ni-based oxygen carriers for CLR(a) manufactured by different methods have been carefully examined by experiments in thermo-gravimetric analyzer, batch fluidized bed reactor, semicontinuous pressurized fluidized bed reactor and three different continuously operating chemical looping units. This includes operation in a dual circulating fluidized bed pilot plant at a scale of 140 kW_{th} fuel power. The results show that CLR(a) is feasible, and that syngas with a composition close to thermodynamic equilibrium can be produced. The conversion of CH_4 was very high, in most cases complete. There were no problems with formation of solid carbon in the fuel reactor if the fuel was diluted with steam so that a steam to carbon ratio of 0.35-0.40 was obtained. Further, mixed-oxide oxygen carriers consisting of Fe- and Mn-based materials with addition of Ni-based catalyst have been examined as oxygen carrier for CLC/CLR(s), in batch experiments as well in a 300 W_{th} chemical looping combustor. It was found that addition of small amounts of Ni improved the fuel conversion considerably, and that the mixed-oxide concept is feasible. Also, novel oxygen carriers with the ability to release gaseous O_2 directly into the fuel reactor during operation have been developed, by addition of inert/semi-active/active support materials to Mn-based oxygen carriers, in order to stabilize Mn^{4+} in manganese dioxide by formation of manganese containing spinels.

INTRODUCTION

Chemical looping combustion

The concept of chemical looping combustion (CLC) was first proposed in the 1950s, in a patent aiming at production of carbon dioxide [1]. Early work includes a study from 1983 by Richter and

Knoche [2], who suggested a fuel oxidation reaction scheme involving two intermediate reactions with a metal oxide as oxygen carrier. Other pioneers include Ishida et al. [3], who in 1987 presented a novel combustion concept they called chemical looping combustion, which was similar to the idea put forth by Richter and Knoche a few years earlier. Further research was initiated in the 1990's as a result of increased awareness about the potential dangers of climate change due to CO_2 emissions. Occasionally the concept is referred to as unmixed combustion, see for example Lyon et al. [4].

In CLC, two separate reactors are used, one for air and one for fuel. A solid oxygen carrier performs the task of transporting oxygen between the reactors. Direct contact between fuel and air is avoided, so the combustion products are not diluted with N_2, see Figure 1.

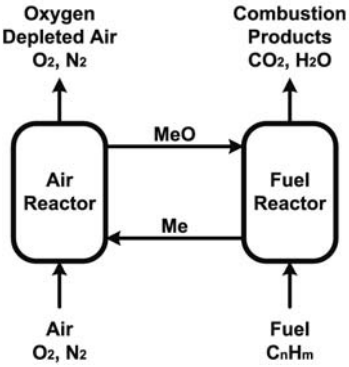

Figure 1. Schematic description of CLC.

Typically, the abbreviation MeO is used to describe the oxygen carrier in its oxidized form, while Me is used for the reduced form. This is because many potential oxygen carrier materials are metal oxides. The oxygen carrier circulates between the reactors. In the fuel reactor, it is reduced by the fuel, which in turn is oxidized to CO_2 and H_2O according to the reaction in Equation 1. In the air reactor, it is oxidized with O_2 from the combustion air according to the reaction in Equation 2.

$$C_nH_m + (2n+½m)\ MeO \rightarrow n\ CO_2 + ½m\ H_2O + (2n+½m)\ Me \qquad \text{Equation 1}$$

$$Me + ½\ O_2 \rightarrow MeO \qquad \text{Equation 2}$$

The amount of energy released or required in each reactor vessel depends on the nature of the oxygen carrier and the fuel. The reaction in Equation 2 is always strongly exothermic. For most oxygen carrier materials, the reaction in Equation 1 is endothermic if the fuel is a hydrocarbon. Therefore the flow of solid oxygen carrier must also be used to transport sensible heat from the air reactor to the fuel reactor. The net energy released in the reactor system is the same as in ordinary combustion. This is apparent since combining the reactions in Equations 1 and 2 yields the reaction in Equation 3, which is complete combustion of the fuel with O_2.

$$C_nH_m + (n+¼m)\ O_2 \rightarrow n\ CO_2 + ½m\ H_2O \qquad \text{Equation 3}$$

Compared to conventional combustion, CLC has several potential benefits. The exhaust gas from the air reactor consists mainly of N_2 and possibly some O_2. There should be very little thermal formation of NO_X since regeneration of the oxygen carrier takes place without flame and at moderate temperatures. The gas from the fuel reactor consists of mainly of CO_2 and H_2O. For some potential oxygen carriers there are thermodynamic constraints that limit the conversion of the fuel somewhat, see Jerndal et al. [5]. It is also possible that there will be incomplete conversion of

hydrocarbons due to slow reaction rate between fuel and oxygen carrier. However, in a properly designed system the fuel conversion should be complete and cooling in a condenser should be sufficient to obtain pure CO_2. This makes CLC a very attractive technology for power generation with CO_2 capture.

A CLC process could be designed in different ways, but circulating fluidized beds with oxygen carrier particles used as bed material are likely to have an advantage over other alternatives since this design is straightforward, provides good contact between gas and solids and allows a smooth flow of oxygen carrier particles between the reactors.

The oxygen carrier would need to consist of a material with high reactivity towards fuel and oxygen which is thermodynamically capable to convert the fuel to CO_2 and H_2O. Further, it should have sufficiently high content of oxygen which can react according to the reactions in Equations 1 and 2, so that the oxygen demand of the combustion can be satisfied with the desired rate of solids circulation. Finally, it should also have low tendency for fragmentation, attrition and agglomeration, and preferably be cheap and environmentally sound. Most experimental work have been focused on using oxygen carrier in the form of particles of metal oxides such as NiO, Fe_2O_3, Mn_3O_4 and CuO supported on inert materials such as Al_2O_3, $NiAl_2O_4$, $MgAl_2O_4$ or stabilized ZrO_2, see for example Johansson et al. [6], Cho et al. [7] and Adanez et al. [8].

Chemical looping with oxygen uncoupling

By using oxygen carriers with certain thermodynamical properties, it is possible to design a process in which gaseous O_2 is released in the fuel reactor according to the reaction in Equation 4.

$$2\ MeO \rightarrow 2\ Me + O_2 \qquad \text{Equation 4}$$

This process concept is referred to as chemical looping with oxygen uncoupling (CLOU). Fuel combustion occurs according to the reaction in Equation in 3 directly in the fuel reactor. The reduced oxygen carrier is recirculated to the air reactor where it is reoxidized according to the reaction in Equation 2. The overall reaction for CLOU is identical to the one for CLC, and encompasses complete oxidation of hydrocarbons. Possible advantages compared to CLC include faster reaction kinetics, particularly for combustion of solid fuels, which otherwise would have to rely on slow gasification reactions or even slower solid to solid reactions.

CLOU would require an oxygen carrier with specific thermodynamical characteristics. Oxide systems based on copper, manganese and cobalt all have suitable equilibrium pressures of gaseous O_2 at temperatures interesting for CLOU, i.e. 800-1200°C, see Mattisson et al. [9].

Chemical looping autothermal reforming

Chemical looping autothermal reforming, CLR(a), often referred to simply as chemical looping reforming, utilizes the same basic principles as CLC. The general idea was first presented in patent from the 1950's by Conrad Arnold, representing the Standard Oil Development Company [10]. The difference compared to CLC is that the products desired are not heat but syngas, i.e. a gas mix consisting mainly of H_2 and CO. CLR(a) could be described as a process for partial oxidation of hydrocarbon fuels, where a solid oxygen carrier is used as a source of undiluted oxygen. This would eliminate the need for expensive and power demanding air separation. The principles of CLR(a) are illustrated in Figure 2.

CLR(a) is operated at understoichiometric conditions, i.e. insufficient air is added to the air reactor to completely oxidize the fuel added to the fuel reactor. In the air reactor, the reaction in Equation 2 will occur, just as in CLC. All added oxygen will be consumed, so the depleted air will consist of

only N_2. In the fuel reactor, some fuel may become completely oxidized to CO_2 and H_2O via the reaction in Equation 1, but the larger share should react according to the reaction in Equation 5, partial oxidation using oxygen from the oxygen carrier.

$$C_nH_m + n\ MeO \rightarrow n\ CO + ½m\ H_2 + n\ Me \qquad \text{Equation 5}$$

The outlet from the CLR(a) fuel reactor consists of syngas, which could be used as feedstock for chemical processes or for production of H_2. Steam or CO_2 can be added to the fuel to enhance the relative importance of steam reforming, the reaction in Equation 6, or CO_2 reforming, the reaction in Equation 7, respectively. This could be useful if syngas with a H_2 to CO ratio that differs from the hydrogen to carbon ratio of the fuel is desired.

$$C_nH_m + n\ H_2O \leftrightarrow n\ CO + (n + ½m)\ H_2 \qquad \text{Equation 6}$$

$$C_nH_m + n\ CO_2 \leftrightarrow 2n\ CO + ½m\ H_2 \qquad \text{Equation 7}$$

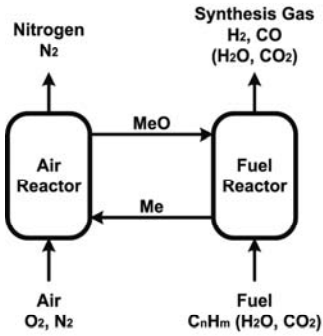

Figure 2. Schematic description of CLR.

The overall reaction energy of the CLR(a) system varies as the relative importance between the reactions in Equations 1 and 2 and the reactions in Equations 5-7 is altered. When the fuel and oxygen carrier reacts according to the reactions in Equations 1 and 2, heat corresponding to the lower heating value of the fuel is released. When the fuel reacts according to the reactions in Equations 5 and 2, heat corresponding to the reaction energy for partial oxidation of the fuel is released. The reactions in Equations 6 and 7 are strongly endothermic. Therefore, steam reforming and CO_2 reforming can not be allowed to dominate the process. This would result in a need for external heating, which would be technically unfavourable at relevant temperatures. Thus, for a thermally balanced process the oxygen supplied by the oxygen carrier would need to be in the order of or slightly below one third of what is needed for complete oxidation.

Due to thermodynamic constraints it is possible that there will be some unreformed CH_4 in the syngas if the reactor temperature is not sufficiently high. A fuel reactor temperature in the order of 800°C should be sufficient to achieve at least 99% conversion of CH_4 at atmospheric pressure. At elevated pressure, somewhat higher temperature may be necessary due to less favourable thermodynamics. Other potential obstacles include formation of solid carbon in the fuel reactor. This could be suppressed by dilution of the fuel with small amounts of steam. Carbon formation on oxygen carrier particles has been examined specifically by Cho et al. [11].

CLR(a) would require an oxygen carrier that produces CO and H_2 at understoichiometric conditions, rather than CO_2, H_2O and unreacted CH_4. According to Zafar et al. [12] and Mattisson et al. [13], oxygen carriers with NiO as active phase has suitable properties, while oxygen carriers based on Fe_2O_3, Mn_3O_4 and CuO do not.

Chemical looping and the CACHET project

Within the CACHET project, two different processes for H_2 production from natural gas which utilizes chemical looping as a way to achieve advantages compared to conventional technology have been examined:

- Chemical looping steam reforming, CLR(s), refers to a process where conventional tubular reforming is used to convert steam and hydrocarbons into syngas, and CLC is used as mean to provide heat for the endothermic reforming reactions and to capture CO_2. The reformer tubes are located in a fluidized bed heat exchanger connected to the chemical looping system, a procedure which provides very favourable conditions for the important heat transfer operation. Integrated with water-gas shift and pressure swing adsorption, CLR(s) would provide 100% CO_2 capture without efficiency penalty, and likely also considerable reduction in NO_X emissions. For details, see Rydén et al. [14, 15, 16].
- Chemical looping autothermal reforming, CLR(a), refers to a process where chemical looping is operated at understoichiometric conditions, possibly with addition of steam to the fuel. The conditions emulate those of conventional autothermal reforming of hydrocarbon fuels and could be used for production of syngas, H_2, or power with pre-combustion CO_2 capture. Compared to conventional autothermal reforming, CLR(a) utilizes chemical looping to provide oxygen undiluted with nitrogen, which reduces the need for expensive gas separation. For details, see the work of Rydén et al. [14, 15, 17].

The aims of the work presented in this article have been to develop these two technologies, and to examine their potential as means for power generation with pre-combustion CO_2 capture. To put it shortly, CLR(s) and CLR(a) have been considered for production of H_2 from natural gas, with CO_2 being captured within the process, and using the H_2 produced for power generation.

Summary of performed research

The experimental work concerning chemical looping technologies undertaken has included:

- Development of Ni-based oxygen carriers suitable for CLR(a), and showing that they work well in laboratory scale. Different production methods such as impregnation, freeze-granulation and spray drying have been used, as well as different inert support materials.
- Development of mixed-oxide oxygen carriers for CLC, suitable for the CLR(s) process. The idea has been to use cheap and environmentally benign materials that have high reactivity with CO and H_2, such as natural minerals or waste materials from the steel industry, in combination with small amounts of Ni-based materials, which can catalyze decomposition of hydrocarbons into reactive combustion intermediates such as CO and H_2.
- Examining the effect of pressure on the reactions between oxygen carriers and fuel. This is especially interesting for CLR(a) applications, since pressurized conditions would reduce the energy penalty for compression of produced H_2 considerably.
- Determine the reaction kinetics for various oxygen carriers materials, in order to be able to better understand the requirements of a large-scale chemical looping unit.
- Demonstrating CLR(a) in a comparably large (140 kW_{th}) chemical looping combustor and under conditions similar to those believed to be preferred in a real-world facility.
- Examining novel oxygen carrier materials for the CLOU process with the ability to release gaseous O_2 in the fuel reactor at relevant conditions. Examined materials were based on manganese oxide, which was transferred into spinel structure by addition of MgO, Fe_2O_3, NiO or SiO_2.

Further, the theoretical work has included:

- Setting up and optimizing process schemes for each process alternative, in order to determine suitable operating conditions and to identify upsides, downsides and critical process parameters.
- Calculating expected investment and operating cost, in order to make an estimation of the price for producing electricity with CO_2 capture using the processes examined.
- Making designs for certain novel, critical parts of the processes, such as the fluidized bed heat exchanger for CLR(s), in order to make sure that the concepts should be feasible for real-world applications.
- Modelling of a chemical looping system, in order to improve the general understanding and provide basis for scaling up.

In this paper, some of the more interesting findings, mainly from the experimental work, will be briefly presented.

PART 1: MIXED-OXIDE OXYGEN CARRIERS FOR CLC/CLR(s)

Of the most commonly suggested oxygen carrier materials, NiO has shown the highest reactivity with CH_4. When reduced by a fuel, NiO is converted directly into metallic Ni, which is known to catalyse decomposition of CH_4 and other hydrocarbons. Unfortunately, using NiO as oxygen carrier for CLC/CLR(s) has some drawbacks. It is relatively expensive compared to other possible oxygen carriers, and also a health hazard. Further, the conversion of hydrocarbons into H_2O and CO_2 at relevant temperatures will be limited to slightly above 99% due to thermodynamical constraints, see Jerndal et al. [5].

In contrast, materials such as Fe_2O_3, Mn_3O_4 and $FeTiO_3$ are cheap, abundant, non toxic and can convert hydrocarbons completely into CO_2 and H_2O. In general, the reactivity with CH_4 for such materials have been found to be low compared to NiO, but the reactivity with CO and H_2 is high. This is true even for cheap and abundant materials, such as natural minerals or waste products from the steel industry. For such oxygen carriers, the rate-limiting step for CLC/CLR(s) of hydrocarbons will be decomposition of CH_4 into reactive intermediates such as CO and H_2.

The mixed-oxide oxygen carriers examined within the CACHET project seeks to combine the low prize and high availability of materials such as Fe_2O_3, Mn_3O_4 and $FeTiO_3$ with the catalytic properties of metallic Ni. Small amounts of Ni would likely be sufficient to facilitate decomposition of hydrocarbons and CH_4 into CO and H_2. Such a mixed-oxide oxygen carrier could prove to have high reactivity, low cost and low environmental impact, compared to the alternatives.

Experimental

Oxygen carrier materials

A number of oxygen carrier materials were examined in a batch fluidized bed reactor (BFB), using Fe_2O_3, $FeTiO_3$ or Mn_3O_4 as active phase, in combination with NiO addition. The complete results are presented in three papers by Rydén et al. [18, 19, 20], where the first one deals with experiments with ilmenite, the second with synthetic Fe_2O_3 particles, and the third with waste materials from the steel industry. In this paper, only a few of the examined materials will be discussed, see Table 1.

Ilmenite is a naturally occurring mineral with the approximate composition $FeTiO_3$. Iron oxide scales and SSAB Red iron oxide are waste products from the steel industry and consists of more than 99% Fe_2O_3. Iron oxide scales are hard and non-porous and have simply been crushed into a

suitable size. SSAB Red is a powder which has been freeze granulated into particles. F6MZ1100, M4MZ1150 and N6AM1400 are synthetic particles produced by freeze granulation.

Table 1. Oxygen carriers for mixed-oxide experiments.

Oxygen carrier	Active phase	Inert phase	Density (g cm^{-3})	Crushing strength (N)
Ilmenite	$FeTiO_3$	-	3.7	3.7
Iron oxide scales	Fe_2O_3	-	4.0	8.3
SSAB red iron oxide	Fe_2O_3	-	2.1	0.8
F6MZ1100	60% Fe_2O_3	Mg-ZrO_2	2.3	1.1
M4MZ1150	40% Mn_3O_4	Mg-ZrO_2	2.3	0.7
N6AM1400	60% NiO	$MgAl_2O_4$	3.0	2.2

Chalmers batch fluidized bed reactor

The aim of the batch experiment was to examine the oxidation and reduction behaviour of various oxygen carrier materials, and to examine if the reactivity with hydrocarbons could be improved by addition of NiO. An 820 mm long quartz reactor with an inner diameter of 22 mm was used. A porous quartz plate, on which the oxygen carrier sample is applied, was located 370 mm above the bottom. During operation, the sample was fluidized by adding gas to the bottom of the reactor, and the porous plate acted as gas distributor. In order to reach suitable temperature the reactor was placed inside an electrically heated furnace. A picture of the reactor system can be found in Figure 3.

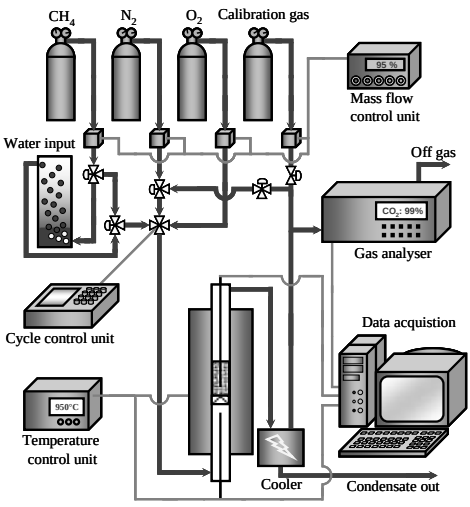

Figure 3. Experimental setup for Chalmers batch fluidized bed reactor.

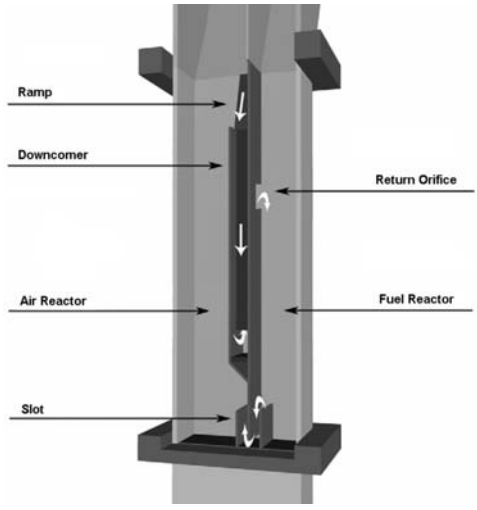

Figure 4. Chalmers 300 W_{th} continuous chemical looping combustor.

Reactor temperature was measured below and above the porous plate, using thermocouples enclosed in quartz shells. The pressure drop over the bed was measured with pressure transducers. The gas from the reactor was led to a cooler, in which steam was condensed and removed. Following this step the volumetric flow of gas was measured, and the composition analyzed.

Typically, the mass of the particle sample was 15 g. The reactor temperature was 800-950°C. Chemical looping conditions were simulated by alternating between reducing and oxidizing conditions. Firstly, the sample was reduced with fuel, typically 0.45 L_n/min CH_4. Following the reduction period, the sample was reoxidized with 1.0 L_n/min of a gas mix consisting of 5 vol.% O_2 and 95 vol.% N_2. After the oxidation period, the sample was ready to be reduced again and so on.

300 W_{th} continuous chemical looping unit

The continuously operating experiments were carried out in a small circulating fluidized bed reactor, see Figure 4. The reactor is 200 mm high. The base of the fuel reactor measures 25×25 mm. The air reactor is 25×40 mm in the bottom and 25×25 mm in the upper narrow part. Suitable flows are 0.20-0.75 L_n/min natural gas and 3-10 L_n/min air, with a solids inventory of 100-300 g. Fuel and air enter the system through separate wind boxes, located in the bottom of the reactor. Porous quartz plates act as gas distributors. In the air reactor the gas velocity is sufficiently high for oxygen carrier particles to be thrown upwards. Above the reactor there is a separate vessel for particle separation. Here the reactor widens and particles are allowed to fall back into the air reactor. A fraction of these particles falls into the downcomer, which is a J-type loop-seal. From the loop-seal, particles are ejected into the fuel reactor via the return orifice. Particles return to the air reactor through a U-type slot, and this way, a continuous circulation of oxygen carrier particles is obtained. The downcomer and the slot are fluidized with small amounts of inert gas. In order to make it possible to reach and sustain a suitable temperature, the reactor is placed inside an electrically heated furnace. The temperature in each reactor section is measured with thermocouples located 70 mm above the distributor plates. On the exit pipe from the fuel reactor there is a water seal that makes it possible to increase the pressure in the fuel reactor by altering the height of a water column. Along the reactor sections there are thirteen separate pressure measuring taps. By measuring differential pressures between these spots, it is possible to estimate where particles are located in the system, and to detect disturbances in the fluidization. Steam can be added to the fuel by means of a steam generator, or by bubble the fuel through hot water and cooling to the desired saturation temperature. The fuel-steam mix is transferred to the reactor in a heated tube with a temperature of 150ºC. It is also possible to dilute the fuel with N_2, Ar or CO_2. Prior to analysis, the gas from the reactor passes through particle filters, coolers and water traps. Therefore, all measurements are made on dry gas. CO_2, CO and CH_4 are measured using infrared analyzers, while O_2 is measured with paramagnetic sensors. The gas from the fuel reactor is also examined with a gas chromatograph, which measures H_2, CO_2, CO, CH_4, O_2 and N_2.

Results and Discussion

In general, addition of NiO to a sample of Fe_2O_3, $FeTiO_3$ or Mn_3O_4 improved the conversion of CH_4 into CO_2 and other products considerably, see Figure 5 for an example.

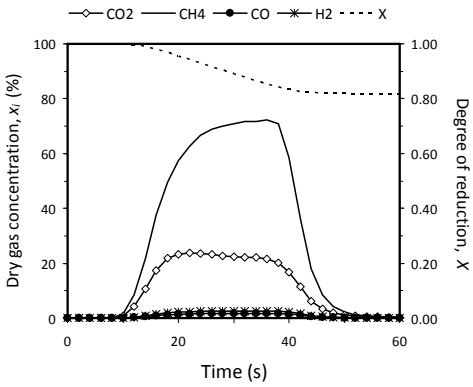

Figure 5a. Produced dry gas for reduction of 15 g ilmenite with 0.45 Ln/min CH_4 at 950°C.

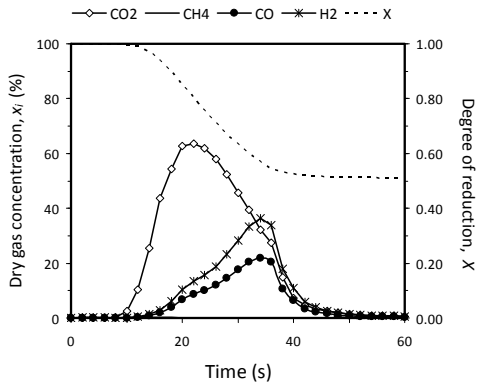

Figure 5b. As 5a, but for reduction of 14.25 g ilmenite and 0.75 g N6AM1400 at 950°C.

In Table 2, performance data derived from reduction such as those shown in Figure 5 are presented for the oxygen carriers from Table 1.

Table 2. Performance data for mixed-oxide systems in the batch reactor.

	T_{fr} (°C)	$\gamma_{eff,max}$ (%)	$\gamma_{eff,max,MO}$ (%)	$v_{CO_2,30s}$ (L_n)	$v_{CO_2,30s,MO}$ (L_n)	χ (%)	σ (%)
Ilmenite	950	33.3	85.4	0.038	0.126	78	142
Iron Oxide Scales	950	50.5	95.8	0.029	0.143	92	275
Iron Oxide Scales	850	47.1	89.9	0.027	0.129	81	251
SSAB Red	950	73.1	92.1	0.085	0.156	71	43
SSAB Red	850	41.4	88.3	0.020	0.105	80	254
F6MZ1100	950	75.3	95.9	0.096	0.128	83	-2
F6MZ1100	850	56.0	91.3	0.036	0.147	80	213
M4MZ1150	950	84.0	98.2	0.135	0.169	89	0

In Table 2, $v_{CO_2,30s}$ is the total volume of CO_2 produced during a 30 s of reduction of the base oxide, expressed in normal litres, and $v_{CO_2,30s,MO}$ is the corresponding number for the case with 5 wt.% N6AM1400 addition. $\gamma_{eff,max}$ is the highest combustion efficiency measured during reduction of the base oxide, while $\gamma_{eff,max,MO}$ is the peak value for the case with 5 wt.% N6AM1400 addition. The combustion efficiency, γ_{eff}, is defined in Equation 8, where, n_i is the molar flows of each component, while $H_{lhw,i}$ is its lower heating value.

$$\gamma_{eff} = 1 - \frac{n_{CH4,fr} \times H_{lhw,CH4} + n_{CO,fr} \times H_{lhw,CO} + n_{H2,fr} \times H_{lhw,H2}}{n_{fuel,in} \times H_{lhw,fuel}} \qquad \text{Equation 8}$$

χ describes the reduction in unconverted fuel passing through the reactor, when the reactivity is at its highest. χ is defined in Equation 9.

$$\chi = (\gamma_{eff,max,mo} - \gamma_{eff,max}) / (100 - \gamma_{eff,max}) \quad \text{Equation 9}$$

However, improved conversion of the fuel alone is insufficient proof that there is an actual synergy effect of mixing NiO and iron or manganese based oxygen carriers. Ni-based materials have higher reactivity and higher oxygen transfer capacity than other oxygen carriers, so addition of NiO should result in increased fuel conversion, even if there was no synergy effect. Therefore, a second expression σ which takes this into consideration is defined:

$$\sigma = 100 \times [(\nu_{CO_2,30s,mo} - \nu_{CO_2,NiO}) / \nu_{CO_2,30s} - 1] \quad \text{Equation 10}$$

σ describes the increase in the total amount of CO_2 produced during 30 s that is achieved by addition of 5 wt% NiO material. In Equation 10, $\nu_{CO_2,NiO}$ reflects the contribution of oxygen carrier capacity brought by the NiO addition, if it is assumed that added NiO is reduced to Ni by the fuel and that the products of this process are only CO_2 and H_2O.

In Table 2, It can be seen that adding 5 wt.% N6AM1400 clearly has a positive effect on fuel conversion. The fraction of unconverted fuel, χ, was reduced with 71-92%. As for the total production of CO_2 during 30 s with the addition of NiO taken into consideration, σ, the effect was not always equally obvious. Here only small improvements were obtained for SSAB Red at 950°C, and for M4MZ1150 and F6MZ1100 there was no effect. It is likely that this was a result of the chosen experimental conditions. At 950°C, the mentioned oxygen carriers already provided high fuel conversion, without addition of NiO. Therefore, the possible improvements probably just happened to be in the same order of magnitude as the extra oxygen carrier capacity provided by the NiO-particles. With less reactive oxygen carriers such as ilmenite and iron oxide scales, as well as at lower temperatures, it can be seen that there was a large improvement. Here, 2.4-3.5 times as much CO_2 was produced in a 30 s reduction compared to the base case plus contribution from NiO. This is a considerable improvement, which also proves that there is a considerable synergy effect of adding NiO to Fe_2O_3 or $FeTiO_3$. It was also possible to prove that there was a small synergy effect of adding NiO to M4MZ1150, by reducing the fraction of N6AM1400 to 3%.

In addition to the experiments in the batch reactor, a few oxygen carriers were also tested in the 300 W_{th} chemical looping unit. Some of these experiments turned out to be rather inconclusive, likely due to practical problems with the reactor. However, ilmenite was extensively examined with over 80 h of operation with fuel, using four separate batches and addition of two different kinds of NiO particles. An example of produced gas composition during operation can be found in Figure 6.

In Figure 6, it can be seen that the products were mostly CO_2, with some unconverted CH_4 and very small amounts of CO and H_2. N_2 was present since it was used as fluidization gas in the slot and downcomer. In Figure 7, the combustion efficiency is shown as function of temperature for experiments with and without NiO. It can be seen that 1 wt.% N6AM1400 improved the combustion efficiency 10-15 %-points, which is a considerable improvement.

Ilmenite was found to become more reactive and more porous during operation, up to a certain degree. The loss of fines was small and the particles did not appear to break apart. With decent stability and reactivity, very low price, and considerable synergy effects to be had by adding small amounts of NiO, ilmenite appears to be a promising oxygen carrier for CLC/CLR(s).

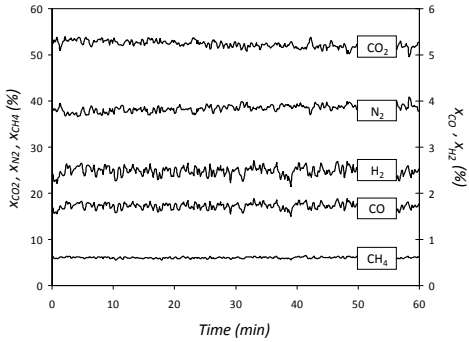

Figure 6. Dry-gas concentration, x_i, for CLC/CLR(s) of 0.49 L_n/min natural gas at 900ºC using 250 g ilmenite with 1 wt.% N6AM1400 as oxygen carrier. N_2 is present as fluidization gas to the particle seals.

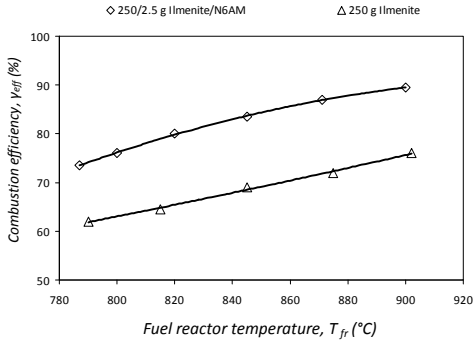

Figure 7. Combustion efficiency as function of fuel reactor temperature for CLC/CLR(s) of 0.49 L_n/min natural gas with 250 g ilmenite, with and without addition of 1 wt.% N6AM1400.

PART 2: BEHAVIOUR OF NICKEL-BASED OXYGEN CARRIERS FOR CLR(a)

Ni-based oxygen carriers prepared at ICB-CSIC by impregnation on alumina by two different methods, incipient wet impregnation and deposition-precipitation, were studied in a thermo-gravimetric analyzer (TGA) and in a batch fluidized bed reactor (BFB) in order to know its potential for CLR(a) of CH_4 [21]. In the TGA, the reactivity of the oxygen carriers was determined. In the BFB, the effect on the gas product distribution produced during reduction/oxidation cycles and on the carbon deposition of different operating conditions, as type of support, reaction temperature, H_2O/CH_4 molar ratio, and preparation method, was tested and analyzed.

It was found that the support material used to prepare the oxygen carriers had an important effect on the reactivity of the oxygen carriers, on the gas product distribution, and on the tendency for carbon deposition. The Ni-based oxygen carrier impregnated on γAl_2O_3 showed the lowest reactivity during reduction, while the Ni-based oxygen carrier impregnated on αAl_2O_3 showed the highest. All oxygen carriers exhibited very high reactivity during oxidation. The tests carried out in the BFB showed that Ni-based oxygen carriers prepared by incipient wet impregnation on γAl_2O_3, θAl_2O_3, and αAl_2O_3 are suitable for CLR(a) of CH_4 without carbon deposition, while oxygen carriers prepared by a deposition-precipitation method using urea had a higher tendency to carbon formation. Based in these findings, the Ni-based oxygen carriers prepared by incipient wet impregnation were selected for further analysis.

Experimental

Oxygen carrier materials

Two Ni-based oxygen carriers prepared by incipient wet impregnation on γAl_2O_3 and αAl_2O_3 were selected to be examined in a CLR(a) unit and in a semicontinuous pressurized fluidized bed reactor, the later operating at pressures up to 10 bar. NiO21-γAl_2O_3 [22] was prepared by impregnation over commercial γAl_2O_3 (Puralox NWa-155, Sasol Germany GmbH) and NiO18-αAl_2O_3 [23] was prepared by impregnation over αAl_2O_3 (obtained by calcination of γ-Al_2O_3 at 1150 ºC during 2 hours). The oxygen carriers were physically and chemically characterized by several techniques, see Table 3.

Table 3. Physical properties and solid composition of the oxygen carriers.

Oxygen carrier	Density ($g\ cm^{-3}$)	Crushing strength (N)	BET ($m^2\ g^{-1}$)	Porosity (%)	XRD
NiO21-γAl_2O_3	1.7	2.6	83.4	50.7	γAl_2O_3, $NiAl_2O_4$
NiO18-αAl_2O_3	2.4	4.1	7	42.5	αAl_2O_3, NiO, $NiAl_2O_4$

More details of the preparation and physical and chemical characterization of the oxygen carriers in Table 3 can be found elsewhere [21-24]. The oxygen carriers are designated with the metal oxide followed by its weight content and the inert material used as support.

900 W_{th} continuous atmospheric chemical looping unit

The 900 W_{th} CLR(a) unit was composed of two interconnected fluidized bed reactors, a riser for solids transport from the air reactor (AR) to the fuel reactor (FR), a solids valve to control the flow rate of solids fed to the fuel reactor, a loop seal and a cyclone, see Figure 8a for a schematic description. This design allowed variation and control of the solids flow rate between the reactors.

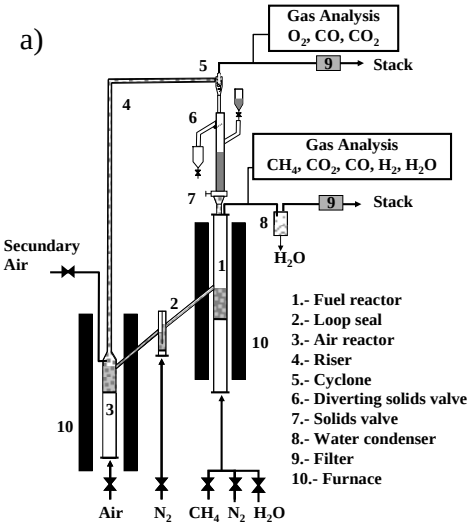

Figure 8a. 900 W_{th} continuous atmospheric chemical looping unit.

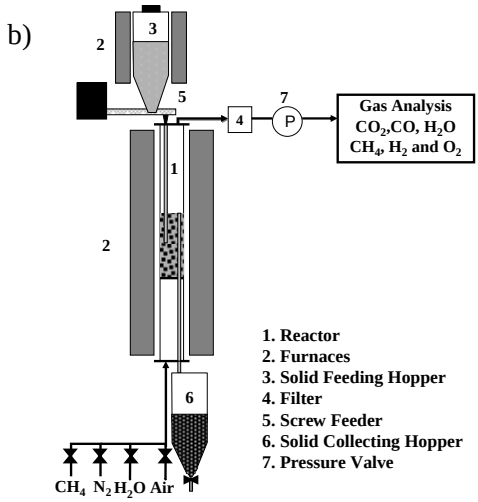

Figure 8b. Semicontinuous pressurized fluidized bed unit.

The FR (1) consisted of a bubbling fluidized bed with an inner diameter of 0.052 m and a bed height of 0.1 m. In this reactor, the NiO of the oxygen carrier was reduced by the fuel to Ni. Reduced oxygen carrier particles overflowed into the AR (3) through a U-shaped fluidized bed loop seal (2), to avoid gas mixing between fuel and air. The oxidation of the carrier took place in the AR, which consisted of a bubbling fluidized bed with an inner diameter 0.05 m and a bed height of 0.1 m, followed by a riser (4) with and inner diameter of 0.02 m and 1 m height. N_2 and unreacted O_2 left the AR passing through a high-efficiency cyclone (5) and a filter (9) before the stack. The oxidized oxygen carrier particles recovered by the cyclone were sent to a solids reservoir setting the oxygen carrier ready to start a new cycle. The regenerated oxygen carrier particles returned to the FR by

gravity from the solids reservoir through a solids valve (7) which controlled the flow rate of solids entering to the FR. A diverting solids valve (6) located below the cyclone allowed the measurement of the solids flow rates at any time. Fine particles produced by fragmentation/attrition in the experimental unit were recovered in the filters placed downstream of the FR and AR. The prototype had several thermocouples, pressure drop transducers etc at different points for measurement and system control. Specific mass flow controllers gave accurate flow rates of feeding gases and H_2O. The gas outlet streams of the FR and AR were drawn to respective on-line gas analyzers to get continuous data of the gas composition.

Semicontinuous pressurized fluidized bed unit

The semicontinuous fluidized bed reactor was basically composed of a system for gas feeding, a continuous system for solids feeding, a pressurized reactor and a gas analysis system, see Figure 8b. The gas feeding system had different mass flow controllers for different gases and water. The fluidized bed, with a bed height of 0.15 m, was placed inside a Kanthal reactor of 0.038 m inner diameter and 0.58 m height, with a preheating zone just under the distributor. The reactor was inside an electrically heated furnace. A pressure valve located at the gas exit line controlled the reactor pressure. There was a hot filter downstream from the fluidized bed reactor to recover the solids elutriated from the bed. The oxygen carrier was fed to the reactor using a screw feeder, with variable velocity, from a heated lock hopper. The reduced oxygen carrier overflowed into the solid collecting hopper. Different gas analyzers continuously measured the gas composition at each time.

Each experiment was divided into two tests, a reduction test and an oxidation test. During the reduction test, the oxidized oxygen carrier was loaded in the lock hopper and the whole system was locked and pressurized in nitrogen atmosphere until the desired pressure. Then, the oxygen carrier, water vapour and CH_4 were fed to the reactor to start the reduction test. After 20-40 minutes, depending of the operating conditions, the steady-state was reached. The steady-state was maintained at least for an hour in each test. When the reduction test finished the system was depressurized and the oxygen carrier was recovered. The oxidation of the carrier was carried out at atmospheric pressure in similar fashion.

Results and discussion

The two selected Ni-based oxygen carriers were tested in the CLR(a) unit in order to analyze their behaviour with respect to the reforming of CH_4. During operation the effect of different operating variables, like fuel reactor temperature (800-900ºC), H_2O/CH_4 molar ratio (0-0.5) and solid circulation rate (1-11 kg/h), on CH_4 conversion and gas product distribution was analyzed [25].

It was observed that at all operating conditions, with both oxygen carriers, the CH_4 conversion was very high (>98%). An increase in the reduction reaction temperature produced a slight increase in the CH_4 conversion and CO_2 and H_2O concentrations and a slight decrease in the H_2 and CO concentrations. An increase in H_2O/CH_4 molar ratio produced a small increase in the CO_2 and H_2 concentrations and a small decrease in the CO concentration. The most important operating variable affecting the gas product distribution was the oxygen carrier circulation rate, that is, the NiO/CH_4 molar ratio. An increase in the NiO/CH_4 molar ratio produced an increase in the CO_2 and H_2O concentrations and a decrease in the H_2, CO and CH_4 concentrations. Similar gas product compositions were obtained with both oxygen carriers although working with different oxygen carrier circulation rates. The NiO18-αAl_2O_3 oxygen carrier, due to its higher reactivity, needed lower solid circulation rate (lower NiO/CH_4 molar ratio) than the NiO21-γAl_2O_3 oxygen carrier to obtain almost the same gas product composition [25].

The best gas product composition was obtained for $NiO_{reacted}/CH_4$ molar ratios near 1, see Figure 9. However, a $NiO_{reacted}/CH_4$ molar ratio of ≈1.25 was calculated as needed for the fulfilment of the heat balance. In these operating conditions, a dry gas product composition of ≈65vol.% H_2, ≈25vol.% CO, ≈9 vol.% CO_2, and ≈1-1.5 vol.% CH_4 can be obtained in the autothermal CLR(a) process working with both oxygen carriers. With this composition, after water gas shift reactor, 2.5 moles of H_2 per mol of CH_4 can be obtained in this process.

Reforming tests, up to 10 bars, under different operating conditions, as reduction reaction temperature (800-900ºC) and NiO/CH_4 molar ratios (1-5), were also conducted in the semicontinuous pressurized fluidized bed facility using CH_4 as fuel to analyze the effect of the total pressure on the CH_4 conversion, gas outlet concentrations, and carbon formation in the CLR(a) process. To study the effect of the total pressure at a constant gas velocity and NiO/CH_4 molar ratio, experiments with a constant CH_4 partial pressure at the different total pressures were carried out. In this way, the solid feed flow rate, and so the mean residence time of the oxygen carriers in the fluidized bed reactor, were kept constant for a NiO/CH_4 molar ratio at the different total pressures.

Figure 10 shows the effect of the total pressure on the gas product concentrations measured during the reduction tests working with both oxygen carriers. It was found that at all operating pressures the CH_4 conversion was very high. An increase in the operating pressure did not produce any important change in the gas product distribution of the CLR(a) process. In addition, no carbon formation was detected at all operating pressures tested.

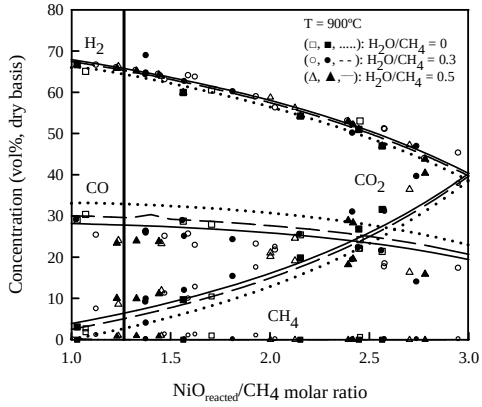

Figure 9. Effect of $NiO_{reacted}/CH_4$ molar ratio on the gas product composition. Filled dots: NiO18-αAl_2O_3. Empty dots: NiO21-γAl_2O_3. Lines: Thermodynamic equilibrium data.

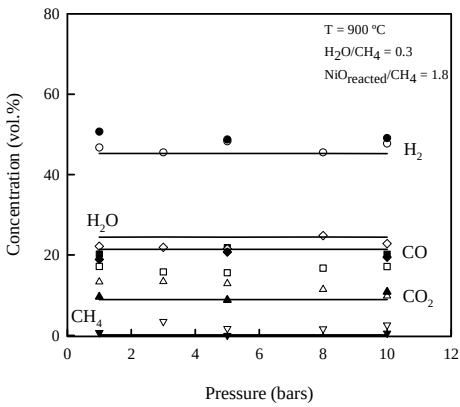

Figure 10. Effect of total pressure on the gas product composition. Filled dots: NiO18-αAl_2O_3. Empty dots: NiO21-γAl_2O_3. Lines: Thermodynamic equilibrium data.

The effect of the reactor temperature and NiO/CH_4 molar ratio during the reduction reaction at the different pressures was similar to those observed at atmospheric pressure. An increase in the reduction reaction temperature produced a slight increase in the CH_4 conversion and CO_2 and H_2O concentrations and a slight decrease in the H_2 and CO concentrations. An increase in the oxygen carrier to fuel ratio (NiO/CH_4) produced an increase in the CO_2 and H_2O concentrations and a decrease in the H_2, CO and CH_4 concentrations, very similar at all operating pressures. Finally, it was observed that the gas product compositions were close to thermodynamic equilibrium at all temperatures and pressures tested.

Important changes in the reactivity, surface texture and solid structure of the oxygen carrier particles were not detected after more than 100 hours of operation in both units with each oxygen carrier. In addition, the oxygen carriers did not show agglomeration or defluidization problems and the loss of fine solids due to attrition was negligible. These results suggest that these oxygen carriers could have a high durability, being suitable oxygen carriers for a CLR(a) system.

Other experiments with Ni-based oxygen carriers

In addition to the experiments conducted by ICB-CSIC, Ni-based oxygen carriers for CLR(a) have also been examined by Chalmers. The two impregnated oxygen carriers from Table 3, as well as two different freeze-granulated particles consisting of NiO supported on $MgAl_2O_4$ and Mg-ZrO_2 respectively, have been examined in the 300 W_{th} continuous chemical looping unit described in Figure 4. Each particle was used successfully for 40-60 hours of operation with fuel. Additionally, five more freeze-granulated oxygen carriers have been examined in Chalmers BFB. These experiments worked well and the results support the conclusions presented above. A detailed description of these experiments can be found in papers by Rydén et al. [26, 27].

PART 3: CLR(a) IN 140 kW_{th} DUAL CIRCULATING FLUIDIZED BED REACTOR

Experimental results

The dual circulating fluidized bed (DCFB) unit presented in [28] was used to investigate CLR(a). The tests were carried out at atmospheric pressure using natural gas (98.7 vol% CH_4) with a fuel power of 140 kW. Three experimental series were run using a mix of 50 wt.% OC-A and 50 wt.% OC-B as oxygen carrier, see [28] for information about these NiO-based particles. In each of the three campaigns, the fuel reactor temperature was kept constant at a certain value. This was achieved by proper adjustment of variable air reactor cooling devices. The global air/fuel stoichiometric ratio was varied step-wise from CLC conditions down to values around 0.5, where the system temperature was finally stable without deliberately cooling the reactor system.

Even though for low global air/fuel ratios equilibrium was reached at the fuel reactor exhaust also at temperatures as low as 750 °C, the clearest picture with respect to gas phase conversion is obtained at a fuel reactor operating temperature of 900°C, see Figure 11. The broken lines indicate the concentrations assuming thermodynamic equilibrium while the solid lines represent the measured gas composition. CH_4 conversion is high at this temperature even for high air/fuel ratios. The gas concentrations follow the equilibrium predictions within the range of measurement accuracy.

On the air reactor side it can be observed that O_2 is absorbed quantitatively by the particles for any air/fuel ratio below 0.95. H_2O is introduced into the air reactor from loop seal fluidization. Argon is present in air and its concentration is slightly increased because the total amount of gas decreases in the air reactor. This means that the air reactor exhaust consists only of N_2, Ar and some steam from the loop seals. Also, the concentrations of CO and CO_2 in the air reactor off gas have been monitored. No carbon species could be detected at all during the sets of experiments shown here. This is remarkable because no steam was added to the natural gas feed except for the part of the lower loop seal fluidization that might have been directed back into the fuel reactor. However, this would only amount to a global steam to organic carbon ratio of less than 0.4 in the worst case that all the lower loop seal steam would enter the fuel reactor, which is highly unlikely considering the direction of particle movement and the local pressure situation [29].

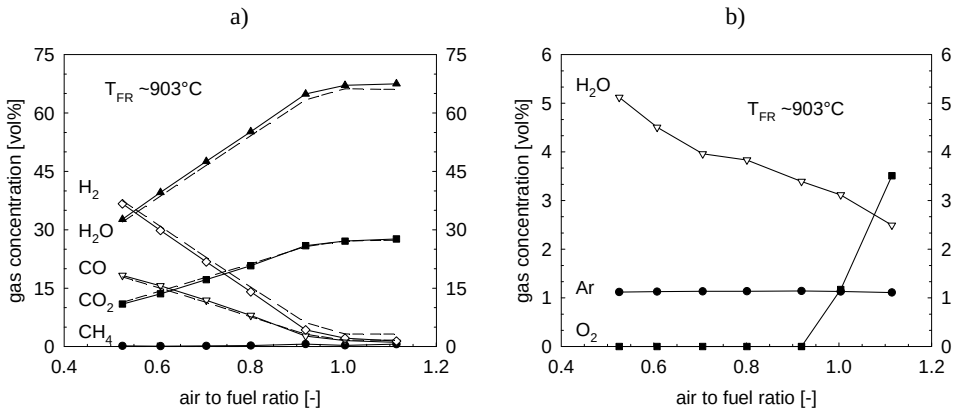

Figure 11. Gas compositions from fuel reactor (a) and air reactor (b) at a fuel power of 140 kW and a fuel reactor operating temperature of 900°C. The missing amount to 100% in (b) is N_2. Dashed lines in (a) is thermodynamic equilibrium data.

The minimum air/fuel ratio of 0.52 shown in Figure 11a is the steady state point where the reactor cooling was finally switched off completely. Neither air nor fuel could be preheated during the experiments due to technical reasons. Below this minimum air/fuel ratio shown, only non-steady state operation with the system continuously loosing temperature could be run. Such points are not shown here, but it can be reported that with the same parameters operated as for the points shown, i.e. no extra steam to the fuel, carbon formation started at global air/fuel ratios of 0.4. This was detected in a reproducible way by CO_2 measurements in the air reactor off gas.

Based on the experimental findings, the following assumptions are acceptable for the oxygen carrier used at least for air/fuel ratios between 0.4 and 0.7 and steam/carbon ratios larger than 0.4:

- the fuel reactor exhaust gas is in thermodynamic equilibrium
- the air reactor exhaust gas is practically free of oxygen
- no carbon is lost to the air reactor (no carbon deposition on the particles)

According to the experimental findings, it can be concluded that CLR(a) works well at atmospheric pressure.

PART 4: OXYGEN CARRIERS FOR CLOU/CLR(s)

Experimental results

In total, 26 novel oxygen carrier materials for CLOU applications based on combined oxide systems have been examined in the batch fluidized bed reactor described in part 2 above. These oxygen carriers were produced by combining manganese oxides with oxides of magnesium (with optional addition of calcium hydroxide and titanium dioxide), iron, nickel and silicon.

Addition of inert/semi-active/active supports was aimed at stabilization of Mn^{4+} in manganese dioxide by formation of manganese containing spinels with thermodynamic properties suitable for CLOU applications. This idea worked out as intended. In fact, all examined oxygen carriers demonstrated oxygen uncoupling properties in inert atmosphere at relevant temperatures, see Figure 12 for an example. Further, many of the examined particles also provided very high reactivity with CH_4, see Figure 13. A detailed description of these experiments can be found in the upcoming

papers by Shulman et al. [30, 31], where the former deals with reactivity evaluation of oxygen carriers based on Mn/Mg combined oxide systems with optional addition of calcium hydroxide and titanium dioxide, and the latter is devoted to investigation of reactivity of Mn/Fe, Mn/Ni and Mn/Si combined oxide systems.

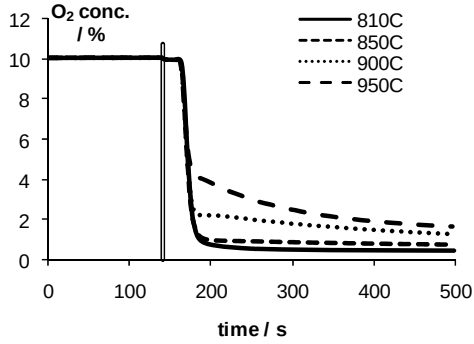

Figure 12. Oxygen concentration profile over the oxygen carrier M7MC1100 fluidized with 0.45 L_n/min N_2 at various temperatures. The double line marks the start of the inert period.

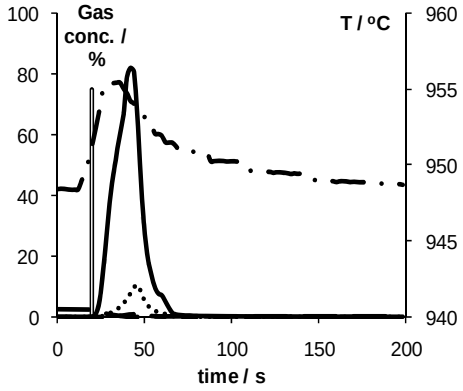

Figure 13. Produced gas concentration on dry basis (— CO_2, ··· CH_4, — · — Temperature) profiles for reduction of the oxygen carrier M7MC1100 with 0.45 L_n/min CH_4. Double line marks the start.

The oxygen carrier M7MC1100 referred to in Figures 12 and 13 was produced from fine chemical powders (67 wt.% MnO_2, 5 wt.% $Ca(OH)_2$, 28 wt.% MgO) by freeze granulation followed by sintering for 6 hours at 1100°C. The resulting particles were composed of Mg_2MnO_4, $CaMn_2O_4$ and $Ca_3Mn_2O_7$, as determined by powder XRD. This was one of the better of the 26 materials examined.

Figure 12 shows the outlet dry gas concentration for M7MC1100, when the reactor is fluidized with inert gas. It can be seen that although only inert N_2 is added to the reactor, the O_2 concentration does not drop to zero for several minutes. This means that gaseous O_2 is released from the particles, i.e. that oxygen is uncoupled. The amount of O_2 released clearly increases as a function of temperature.

Figure 13 shows the produced gas concentration for a reduction experiment using CH_4 fuel. It can be seen that the reactivity of M7MC1100 with CH_4 was high. The combustion efficiency was in the order of 90%, which is slightly better than what is obtained with more conventional Mn_3O_4-based oxygen carriers. It can also be seen that the concentrations of CO and H_2 are very low, i.e. that the products are almost exclusively CO_2 and unconverted CH_4.

While the examined oxygen carriers showed the intended behaviour, they did not have extraordinary oxygen uncoupling abilities. In no case, the total mass loss due to oxygen release in inert atmosphere did exceed 0.3 wt.% after 360 s. As comparison, typically 2-3 wt.% O_2 was released in less than 30 s when the sample was actively reduced with CH_4, i.e. as in Figure 13. This indicates that the O_2 release was slow compared to the gas-solids reactions between fuel and oxygen carrier.

It was possible to reoxidize all examined oxygen carriers at 950°C with 10% O_2 in N_2. From a thermodynamic point of view, this should be impossible for pure magnesium oxide system. This confirms the fact that the obtained spinels have different thermodynamic properties compared to pure magnesium oxides, and could possibly be used as oxygen carrier materials in the CLOU

process. The oxidation of the particles often proceeded comparably slowly, in contrast to conventional oxygen carriers, for which the oxidation typically proceeds very fast.

SUMMARY

A range of experiments has been conducted which examines the feasibility for production of H_2 and power from natural gas, utilizing chemical looping technologies.

It has been shown that addition of small amounts of Ni to Fe- and Mn-based oxygen carrier materials can improve the fuel conversion of such oxygen carriers considerably. The obtained mixed-oxide oxygen carrier would be attractive for CLC/CLR(s) and possibly for other applications. The phenomena have been studied in batch fluidized bed reactor as well in a 300 W_{th} chemical looping combustor. In many cases, the fraction of unconverted fuel was reduced by 70-90%. The likely mechanism is that Ni catalyzes decomposition of hydrocarbons into CO and H_2, which has high reactivity with Fe- and Mn-based oxygen carriers. Details about these experiments can be found in associated publications [18-20].

Further, it has been shown that CLR(a) of natural gas using Ni-based oxygen carriers should be feasible. Successful experiment have been conducted using thermo-gravimetric analyzer, batch fluidized bed reactor, semicontinuous pressurized fluidized bed reactor and three different continuously operating chemical looping units, including a 140 kW_{th} dual circulating fluidized bed pilot plant. In all instances, the conversion of CH_4 was very high, produced syngas had a composition close to thermodynamic equilibrium and there were no problems with formation of solid carbon if the fuel was diluted with some steam. Details can be found in associated publications [21-27] and [29].

Finally, novel oxygen carriers with the ability to release gaseous O_2 directly in the chemical looping fuel reactor have been developed. Such materials could be suitable for CLOU/CLR(s), as well as for applications with solid fuels. The examined materials were produced by addition of inert/semi-active/active support materials to Mn-based oxygen carriers, in order to stabilize Mn^{4+} in manganese dioxide by formation of manganese containing spinels. Most materials showed the desired behaviour, but did not have extraordinary oxygen uncoupling abilities. The total mass loss due to oxygen release in inert atmosphere did exceed 0.3 wt.% after 360 s. Nonetheless, the results were promising. These oxygen carriers were also highly reactive with CH_4. Details will be provided elsewhere [30, 31].

ACKNOWLEDGMENTS

The authors wish to thank our financers, supporters and co-workers within the CACHET project, which is an integrated research program funded by the European Commission (FP6 Contract No. 019972) with support from the CO_2 Capture Project Phase 2 (CCP2). Further, the oxygen carrier used in the 140 kW tests has been produced by the Flemish Institute for Research and Technology (VITO), Belgium under the guidance of Chalmers University of Technology, Sweden in the context of the EU financed project CLC GAS POWER (FP6 Contract No. 019800).

This Chapter contains figures that originally appeared in Energy Procedia Vol 1, Issue 1, Greenhouse Gas Control Technologies 9, Proceedings of the 9th International Conference on Greenhouse Gas Control Technologies (GHGT-9), 16-20 November 2008, Washington DC, USA, which was published by Elsevier Ltd.

NOMENCLATURE

AR, ar	Air reactor	MeO	Generic oxygen carrier, oxidized
BET	BET surface area (m^2 g^{-1})	n_i	Number of moles
BFB	Batch fluidized bed reactor	OC	Oxygen carrier
CLC	Chemical looping combustion	T, T_{fr}	Reactor temperature
CLOU	Chemical looping oxygen uncoupling	TGA	Thermo-gravimetric analyzer
CLR	Chemical looping reforming	v	Volume (L_n)
CLR(a)	Chemical looping autothermal reforming	Vol.%	Percentage by volume
CLR(s)	Chemical looping steam reforming	Wt.%	Percentage by weight
C_nH_m	Generic hydrocarbon fuel	X	Degree of oxidation of oxygen carrier *(%)*
DCFB	Dual circulating fluidized bed	XRD	X-ray diffraction
FR, fr	Fuel reactor	x_i	Dry gas concentration (%)
H_{lhv}	Lower heating value (J/mol)	γ_{eff}	Combustion efficiency *(%)*
L_n	Normal litres	χ	Reduction in unconverted fuel (%)
Me	Generic oxygen carrier, reduced	σ	Synergy effect by addition of NiO (%)

REFERENCES

1. W. K. Lewis, E. R. Gilliland. Production of pure carbon dioxide. US patent no 2665972, 1954.
2. H. J. Richter, K. Knoche. Reversibility of combustion processes. *ACS symposium series* 235, 71-85, 1983.
3. M. Ishida, D. Zheng, T. Akehata. Evaluation of a chemical-looping combustion power-generation system by graphic exergy analysis. *Energy* 12, 147-154, 1987.
4. R. K. Lyon, J. A. Cole. Unmixed combustion: An alternative to fire. *Combustion and Flame* 121, 249-261, 2000.
5. E. Jerndal, T. Mattisson, A. Lyngfelt. Thermal Analysis of Chemical-Looping Combustion. *Chemical Engineering Research and Design* 84, 795-806, 2006.
6. M. Johansson, T. Mattisson, A. Lyngfelt. Comparison of oxygen carriers for chemical-looping combustion. *Thermal Science* 10 (2006) 93-107.
7. P. Cho, T. Mattisson, A. Lyngfelt. Comparison of iron-, nickel-, copper-, and manganese-based oxygen carriers for chemical-looping combustion. *Fuel* 83 (2004) 1215-1225.
8. J. Adánez, L. F. de Diego, F. García-Labiano, P. Gayán, A. Abad. Selection of oxygen carriers for chemical-looping combustion. *Energy & Fuels* 18 (2004) 371-377.
9. T. Mattisson, A. Lyngfelt, H. Leion. Chemical-looping with oxygen uncoupling for combustion of solid fuels. *International Journal of Greenhouse Gas Control* 1 (2009) 11-19.
10. C. Arnold. Process for production of carbon monoxide and hydrogen. Patent specification 636,206, The Patent Office, London, United Kingdom, 1950.
11. P. Cho, T. Mattisson, A. Lyngfelt. Carbon formation on nickel and iron oxide-containing oxygen carriers for chemical-looping combustion. *Industrial & Engineering Chemistry Research*, 44, 668-676, 2005.
12. Q. Zafar, T. Mattisson, B. Gevert. *Industrial & Engineering Chemistry Research* 44 (2005) 3485-3498.
13. T. Mattisson, Q. Zafar, A. Lyngfelt, B. Gevert. Integrated hydrogen and power production from natural gas with CO_2 capture. Proceedings of the 15th World Hydrogen Energy Conference, Yokohama, Japan, 2004.
14. M. Rydén. Hydrogen production from fossil fuels with carbon dioxide capture, using chemical-looping technologies. Chalmers University of Technology, Göteborg, Sweden, 2008.

15. M. Rydén, A. Lyngfelt, T. Mattisson. Two novel approaches for hydrogen production; chemical-looping reforming and steam reforming with carbon dioxide capture by chemical-looping combustion. Proceedings of the 16th World Hydrogen Energy Conference, Lyon, France, 2006.
16. M. Rydén, A. Lyngfelt. Using steam reforming to produce hydrogen with carbon dioxide capture by chemical-looping combustion. *International Journal of Hydrogen Energy* 31 (2006) 1271-1283.
17. M. Rydén, A. Lyngfelt. Hydrogen and power production with integrated carbon dioxide capture by chemical-looping reforming. Proceedings of the 7th International Conference on Greenhouse Gas Control Technologies, Vancouver, Canada, 2004.
18. M. Rydén, M. Johansson, A. Lyngfelt, T. Mattisson. Ilmenite with addition of NiO as oxygen carrier for chemical-looping combustion. Submitted for publication.
19. M. Rydén, E. Cleverstam, M. Johansson, A. Lyngfelt, T. Mattisson. Fe_2O_3 supported on Ce-, Ca- or Mg-stabilized ZrO_2 as oxygen carrier for chemical-looping combustion using NiO as additive. To be submitted.
20. M. Rydén, E. Cleverstam, A. Lyngfelt, T. Mattisson. Waste products from the steel industry with NiO as additive as oxygen carrier for chemical-looping combustion. Submitted for publication.
21. L.F. de Diego, M. Ortiz, J. Adánez, F. García-Labiano, A. Abad, P. Gayán. Synthesis gas generation by chemical-looping reforming in a batch fluidized bed reactor using Ni-based oxygen carriers. *Chem. Eng. J.* 144 (2008) 289-298.
22. J. Adánez, L.F. de Diego, F. García-Labiano, P. Gayán, A. Abad. Transportador sólido de oxígeno de NiO/Al2O3 útil para el reformado de metano, procedimiento de obtención y sus aplicaciones. Patent PCT/ES2009/070023.
23. J. Adánez, L.F. de Diego, F. García-Labiano, P. Gayán, A. Abad. Transportador de oxígeno de NiO/Al2O3, procedimiento de obtención del mismo y sus aplicaciones. Patent PCT/ES2008/070146.
24. P. Gayán, C. Dueso, A. Abad, J. Adánez, L. F. de Diego, F. García-Labiano. NiO/Al_2O_3 oxygen carriers for chemical-looping combustion prepared by impregnation and deposition–precipitation methods. *Fuel* 88 (2009) 1016–1023.
25. L.F. de Diego, M. Ortiz, J. Adánez, F. García-Labiano, A. Abad, P. Gayán. Hydrogen production by chemical-looping reforming in a circulating fluidized bed reactor using Ni-based oxygen carriers. *J. Power Sources* (in press). doi:10.1016/j.jpowsour.2008.11.038.
26. M. Rydén, A. Lyngfelt, T. Mattisson. Chemical-looping combustion and chemical-looping reforming in a circulating fluidized-bed reactor using Ni-based oxygen carriers. *Energy & Fuels* 24 (2008) 2585-2597.
27. M. Rydén, M. Johansson, A. Lyngfelt, T. Mattisson. NiO supported on $Mg\text{-}ZrO_2$ as oxygen carrier for chemical-looping combustion and chemical-looping reforming. *Energy & Environmental Science*, in press.
28. T. Pröll, P. Kolbitsch, J. Bolhàr-Nordenkampf, H. Hofbauer, 2009 Demonstration of Chemical Looping Combustion at relevant operating conditions, in Eide, L.I. (ed.) 2009, Carbon Dioxide Capture for Storage in Deep Geologic Formations, Volume 3. CPL Press.
29. T. Pröll, P. Kolbitsch, J. Bolhàr-Nordenkampf, H. Hofbauer. A novel dual circulating fluidized bed (DCFB) system for chemical looping processes. Accepted for publication in AIChE Journal, 2009.
30. A. Schulman, E. Cleverstam, A. Lyngfelt, T. Mattisson. Chemical–Looping with Oxygen Uncoupling using Mn/Mg-based Oxygen Carriers for Methane Combustion. To be submitted.
31. A. Schulman, E. Cleverstam, A. Lyngfelt, T. Mattisson. Magnesium/Iron, Magnesium/Nickel and Magnesium/Silicon Oxides Used in Chemical–Looping With Oxygen Uncoupling (CLOU) for Combustion of Methane. Submitted for publication.

Carbon Dioxide Capture for Storage in Deep Geologic Formations, Volume 3
L.I. Eide (Ed.)

Chapter 15

ONE STEP DECARBONIZATION

Franco Mizia[1]; Stefano Rossini [1]; Mariangela Cozzolino[1]; Ugo Cornaro[1]
Stephen Tlatlik[2]; Ingeborg Kaus[3]; Egil Bakken[3]; Yngve Larring[3]
[1] ENI S.p.A Refining & Marketing Division, Via Maritano 26 -20097 San Donato – Italy
[2] Process Design Center B.V., Joseph-von-Fraunhofer-Str. 20, D-44227 Dortmund, Germany
[3] SINTEF Materials and Chemistry, Sem Sælands vei 12, 7465 Trondheim, Norway

ABSTRACT: In the framework of the European CACHET project, aiming to develop technologies to reduce greenhouse gas emissions from power stations by 90 %, the One Step Decarbonization (OSD) process is a highly innovative technology able to produce hydrogen from natural gas with simultaneous CO_2 capture. It belongs to the group of "chemical looping technologies" employing circulating fluidized beds and metal oxide particles for oxygen transfer, offering significantly reduced efforts and costs for gas separation. The OSD process is based on the use of a circulating "redox" solid material that can be oxidized via water splitting, thereby producing H_2, and reduced by a carbon-containing stream, typically hydrocarbons, producing CO_2. Ready sequestrable CO_2 is obtained within the redox loop after condensing water from the effluent stream purely composed by CO_2 and H_2O. Thus, any downstream energy intensive step, like transformations and/or separations, is avoided. The process design and its assessment lead to a high energy efficiency by integrating this process into a Hydrogen powered Combined Cycle energy production plant (H_2CC). The purity of both hydrogen and CO_2 yielded from the process should meet specifications for fuel-cells and for Enhanced Oil Recovery (EOR) applications. So, much attention is directed not only to the process design, in order to optimize the operative conditions, but also to the quality minimizing the presence of undesired by-products in the out-coming gas streams

INTRODUCTION

The One Step Decarbonization (OSD) process is a highly innovative chemical looping process that is being explored to produce hydrogen from natural gas with simultaneous CO_2 capture. It is based on the ability of a suitable material – either metal and metal oxides – to be oxidized by steam stoichiometrically releasing one mole of hydrogen per mole of water split. According to the scientific basis, the process affords two process streams: the first one is pure hydrogen to be sent to the energy production and the second one is pure carbon dioxide ready to be used directly in applications like Enhanced Oil Recovery (EOR) or injected into geological formations. Therefore any downstream energy intensive CO_2 capture step is avoided as well as any hydrogen enrichment. According to the basic idea, the OSD process has been designed to run a redox cycle where a solid acts as lattice Oxygen Carrier (OC). Such oxygen is released by the carrier in the flameless combustion step (fuel reactor) and subsequently taken up by the carrier in the water splitting step (hydrogen reactor). The oxygen exchange takes place in a different environment/reaction chamber in such a way that the OSD process belongs to the "chemical looping" process configuration.

Steam is provided to the redox cycle as the oxidizing agent while the typical reducing agent is a hydrocarbon like methane or natural gas, generating carbon dioxide and water. The process fits very well with a Circulating Fluidized Bed Reactor system (CFBR) which allows the movement of the

solid from one reactive environment to the other. This reaction pathway is however endothermic and additional heat is needed by combusting extra fuel or a quote of the hydrogen produced.

Subsequently, the OSD process configuration has been modified to admit a second (upper potential) redox pair in the OC cycle and therefore an additional redox reaction where the OC, once oxidized by steam, is further super-oxidized by air and the heat obtained via the exothermic reaction is utilized to fulfil the heat balance of the process. The products of this improved system would result into three separate streams of: (a) high purity H_2 for use in fuel cells, (b) sequestration ready CO_2 and (c) high temperature (pressure) oxygen depleted air for use in gas turbines. In this paper, we investigate the behaviour of the said two redox pairs: $MeO_{(x+y)}/MeO_x$ (upper pair) having a redox potential intermediate between the one of the pair O_2/O^{2-} and the other one of the pair H_2/H_2O and the pair MeO_x/MeO (lower pair) having a redox potential intermediate between the one of the pair H_2O/H_2 and the other one of CH_4/CO_2 as active phases of the OC.

THE OSD CHEMISTRY and PROCESS

The chemical concept

The OSD technology is based on a cycle which combines the oxidative potential of water and the reductive potential of a gaseous hydrocarbon fuel with the intermediate redox potential a metal oxide couple.

Water is the ideal raw material for hydrogen production, avoiding all the issues related to the exploitation of fossil fuels so the OSD technology is aimed to produce hydrogen from water while reducing to economically acceptable levels the cost of the capture of co-produced CO_2.

The added value of OSD is that hydrogen and pure CO_2 are obtained via a flameless combustion instead of reforming of natural gas. In this way it is possible to pass over the downstream operations usually needed in reforming operations to convert the intermediate syn-gas into the final products.

The OSD conceptual reaction pathway (see Figure 1), and the dual fluidized bed loop (see Figure 2) both depict a new Chemical Looping process characterized by 1) the oxidation chamber being a water splitting reaction (steam reactor) where the OC reduces water to hydrogen by uptake of oxygen; and 2) a flameless combustion chamber (fuel reactor) where the OC oxidizes the fuel to H_2O and CO_2 releasing oxygen.

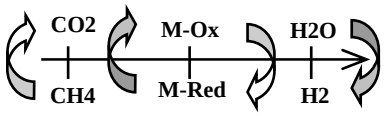

Figure 1. Conceptual reaction pathway.

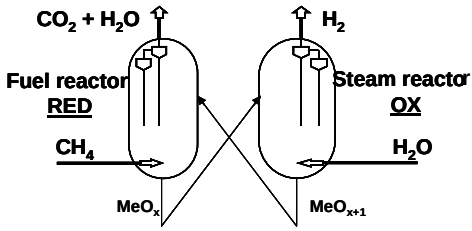

Figure 2. Conceptual reaction loop.

The large scale application of the OSD process is contingent to the availability of suitable oxygen carrier that has to be able to:

- release oxygen by reduction with hydrocarbons
- uptake oxygen by oxidation with water (splitting)

The main difficulty is to fit these two conditions by running the metal oxide stoichiometric reduction step under effective conditions like high lattice oxygen conversion because, in this case, the fuel partial combustion is favoured with respect the flameless combustion leading to the formation of syn-gas traces in the CO_2 stream.

Moreover, in terms of energy balance, it is worth to point out that, independently from the nature of the metal oxide chosen, in the OC reduction step the lattice oxygen extraction shows a strong positive reaction heat which is not balanced neither from the flameless combustion (Equation 1.a) nor from the negative reaction heat in the subsequent water splitting step (Equation 1.b):

$$4\ MeO_x + 4\ H_2O \rightarrow 4\ H_2 + 4\ MeO_{x+1} \qquad \text{Equation 1.a}$$

$$4\ MeO_{(x+1)} + CH_4 \rightarrow CO_2 + 2\ H_2O + 4\ MeO_x \qquad \text{Equation 1.b}$$

The overall reaction (1)

$$CH_4 + 2\ H_2O \rightarrow 4\ H_2 + CO_2 \qquad \text{Equation 1}$$

is endothermic (ΔH = 39.5 kcal/mol) and heat supply is needed to close the energy balance. Heat can be supplied burning a small amount of hydrogen (Equation 1.c)

$$x\ (H_2 + 0.5\ O_2 \rightarrow H_2O) \qquad \text{Equation 1.c}$$

or more generally via any other suitable exothermal reaction.

The overall reaction may be schematized as in Equation 2 whose thermal regime is controlled by the value of x. If x in Equation 1c is approximately 0.68 the overall reaction can be thermo-neutral, while it is endothermic at lower x values and becomes exothermic at higher x values

$$CH_4 + (2\text{-}x)\ H_2O + 0.5x\ O_2 \rightarrow (4\text{-}x)\ H_2 + CO_2 \qquad \text{Equation 2}$$

In order to overcome this thermal lack, making use of OC as an iron oxide system, see Figure 3, a third reaction step is admitted in the OSD and the essential redox pair (MeO_x/MeO) is extended to $MeO_{(x+y)}$ by further super-oxidation of magnetite/wuestite by air. This allows to supply lattice oxygen in the chemical loop with an higher potential redox redox pair ($MeO_{(x+y)}$/MeO).

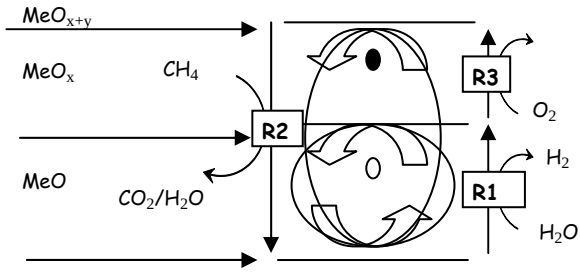

Figure 3. OSD – the OC pathway.

OSD reaction pathway

Several promising metal oxides were investigated as oxygen carriers. It turned out that the best candidate was the iron oxide based system. The iron species involved are: Fe_2O_3 (hematite), where the iron has the maximum oxidation state (Fe^{3+}); Fe_3O_4 (magnetite), a structure where part of the iron is formally in a Fe^{2+} state; FeO (wuestite), where all the iron atoms are formally in the Fe^{2+} state; Fe^0 (metallic iron), the lower oxidation state of the OC, whose formation should be avoided/minimized because it catalyzes the fuel pyrolysis and, therefore, the undesired formation of soot and/or iron carbides.

In terms of overall material balance, the three consecutive reaction steps, in a quite generalized and simplified manner, can be written as follow:

$4\ Fe_2O_3 + 1\ CH_4$	$\rightarrow$	$8\ FeO + 1\ CO_2 + 2\ H_2O$	Q = + 96.39 Kcal	Equation 3.a
$8\ FeO + 8/3\ H_2O$	$\rightarrow$	$8/3\ H_2 + 8/3\ Fe_3O_4$	Q = – 47.4 Kcal	Equation 3.b
$8/3\ Fe_3O_4 + 2/3\ O_2$	$\rightarrow$	$4\ Fe_2O_3$	Q = – 90.2 Kcal	Equation 3.c
$1\ CH_4 + 2/3\ H_2O + 2/3\ O_2$	$\rightarrow$	$8/3\ H_2 + 1\ CO_2$	Q = – 40 Kcal	Equation 3

The decoupling of the overall reaction (Equation 3) into three separate reactions (Equations 3a-c) allows for the following point:

- the process meets the heat balance and the overall reaction heat is even negative, because the super-oxidation of the whole magnetite to hematite phase has a remarkable negative reaction heat.
- the fuel takes up oxygen from the higher oxidation state such as hematite (eq. 3a) mainly forming a stream of CO_2/H_2O with negligible presence of reforming products.

Flameless combustion step

The reduction step of the iron oxides (Equation 3a) can be split into a net of consecutive reactions (concerning the oxidative iron oxides) and competitive reaction (concerning the reducing fuel gas). The six redox pairs which participate to the reactive system are: Fe_2O_3/Fe_3O_4; Fe_3O_4/FeO; FeO/Fe and CH_4/CO; CO/CO_2; H_2/H_2O. According to that, the fast irreversible reduction of hematite to magnetite (Equations 4.a; 4.d; 4.g) is followed by the slow reversible reductions of magnetite to wuestite (Equation 4.b) which affords partial oxidation products and by the slow parallel reversible reductions (Equations 4.e; 4.h) leading to combustion products. The net is then completed with the reversible reduction of wuestite to metallic iron (Equations 4.c; 4.f; 4.i) whose scheme can be described like the previous one. The description of this step is then completed with iron carbide formation (Equation 4.l) which consistently occurs if the combustion is carried out in the presence of such a molar excess of fuel.

$Fe_2O_3 + 1/12\ CH_4$	$\rightarrow$	$2/3\ Fe_3O_4 + 1/12\ CO_2 + 1/6\ H_2O$	Equation 4.a
$Fe_3O_4 + CH_4$	$\leftrightarrow$	$3\ FeO + CO + 2H_2$	Equation 4.b
$FeO + CH_4$	$\leftrightarrow$	$Fe + CO + 2H_2$	Equation 4.c
$Fe_2O_3 + 1/3\ CO$	$\rightarrow$	$2/3\ Fe_3O_4 + 1/3\ CO_2$	Equation 4.d
$Fe_3O_4 + CO$	$\leftrightarrow$	$3\ FeO + CO_2$	Equation 4.e
$FeO + CO$	$\leftrightarrow$	$Fe + CO_2$	Equation 4.f
$Fe_2O_3 + 1/3\ H_2$	$\rightarrow$	$2/3\ Fe_3O_4 + 1/3\ H_2O$	Equation 4.g
$Fe_3O_4 + H_2$	$\leftrightarrow$	$3\ FeO + H_2O$	Equation 4.h
$FeO + H_2$	$\leftrightarrow$	$Fe + H_2O$	Equation 4.i
$CH_4 + Fe$	$\rightarrow$	$FeC_X + 2H_2$	Equation 4.l

According to this overall reaction, both kinetics and thermodynamic aspects have to be considered in order to obtain a gaseous stream of undiluted CO_2 from the reduction reactor and a solid stream of wuestite minimizing, at the same time, the presence of both un-converted magnetite and metallic iron.

Operating conditions like Temperature, Pressure, feeding reactants molar ratio [$O_{lattice}/CH_4$] and reactor design should be appropriately selected.

Water splitting step

The oxidation (pre-oxidation) of the low iron oxidation state (Equation 3.b) can be described as a net of two reversible consecutive water splitting reactions, both producing hydrogen.

$$nFeC_x + n(1+x)\,H_2O \leftrightarrow nFeO + n(1+x)H_2 + nxCO \qquad \text{Equation 5.a}$$

$$3\,FeO + H_2O \leftrightarrow Fe_3O_4 + H_2 \qquad \text{Equation 5.b}$$

Although a sub-stoichiometric iron wuestite phase, where all the iron atoms are in the state between $Fe^{2,1+}$ and $Fe^{2,4+}$, is reported and the atomic ratio Fe/O in Equation 5.c ranges between 0,85 and 0,947.

$$FeO_{(1+x)} + (1-3x)\,H_2O \leftrightarrow Fe_3O_4 + (1-3x)\,H_2 \qquad \text{Equation 5.c}$$

In this paper we will refer to the stoichiometric iron wuestite for simplicity.

As previously discussed, the presence of iron carbides (Equation 4.l) is rather negligible and kept under control but, actually, the presence of CO traces (Equation 5.a) are unavoidable especially when the reduction of magnetite approaches the stoichiometric conversion degree. Under these conditions, the incipient reduction of wuestite is unavoidable. Operating conditions like temperature, H_2O/COD (Chemical Oxygen Demand of solid) feeding molar ratio (3 mols of FeO correspond to 1 mol of COD) and reactor design should be appropriately selected in order to manage the steam autogenic conversion and/or the physical-chemical stability of the OC, namely in terms of porosity and specific surface area, which is negatively affected by the presence of steam at high temperature.

Air regeneration step

The oxidation (super-oxidation) of the intermediate iron oxide (Equation 3.c) up to hematite can be decoupled as two fast irreversible consecutive reactions under the presence of molecular oxygen:

$$3\,FeO + 0.5\,O_2 \rightarrow Fe_3O_4 \qquad \text{Equation 6.a}$$

$$2\,Fe_3O_4 + 0.5\,O_2 \rightarrow 3\,Fe_2O_3 \qquad \text{Equation 6.b}$$

These equations can be written with a general formula

$$FeO_x + (y-x)\,O \rightarrow FeO_y \qquad \text{Equation 6.c}$$

where x ($1{,}0 \leq x \leq 1{,}3$) is a function of the average oxidation degree of the intermediate iron oxide (molar ratio of magnetite/wuestite) and thus, of the wuestite conversion in the previous water splitting and y ($1{,}0 < y \leq 1{,}5$) is a function of the average oxidation degree of the produced iron oxide (molar ratio of hematite/magnetite) and, thus, a function of the molar ratio between the molar ratio of atomic oxygen and iron fed to this addition step.

The process

As depicted in Figures 4.a and 4.b a Circulating Fluidized Bed Reactor (CFBR) configuration is the optimal choice [1 - 6], where the evolution of the gas and the solid phases (left side) is paired with a process based on a three vessels loop (right side).

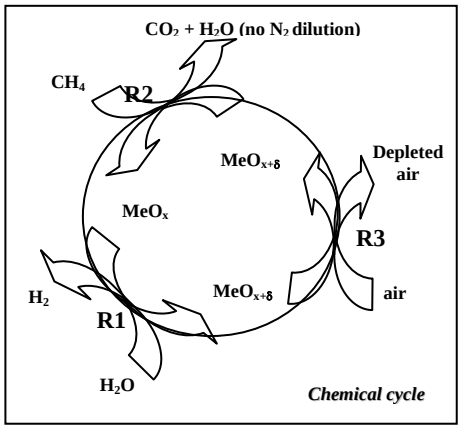

Figure 4.a the chemical evolution of the gas and solid reactants in the OSD process.

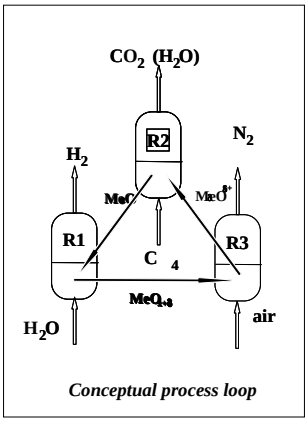

Figure 4.b the CFBR three vessels loop of the OSD process.

The amount and the rate of the exchanged oxygen per unit of mass of the OC are both of paramount importance, because they dictate the space time yield of the hydrogen production and because they govern the heat released during oxidation. The solid is also the heat carrier and this adds the basic constraint given by Equation 7 to the reactor loop. The sum of the adiabatic ΔT_i of reactions is dictated by the reaction kinetics, and the sum of reaction heats ($\sum$j=R1-R3 Qj) should be balanced with the solid circulation flow-rate (F_{OC}) of the solid (kg/hr) multiplied to the specific heat (Cp_{OC}) of the selected solid OC (Kcal x hr/kg x °C). The solid circulation controls the residence time of the solid in the reactors whose size depends on the needed productivity.

$$\sum_j\text{=R1-R3 } Q_j = Cp_{OC} \times F_{OC} \times (\sum_j\text{=R1-R3 } \Delta T_j) \qquad \text{Equation 7}$$

If the heat released exceeds an optimal value, the adiabatic temperature (ΔT_i) can be excessive while an optimal temperature profile through the cycle should be kept to reach the highest efficiency.

Thus the kinetics of the gas-solid reactions fixes the "REDOX" ratio, in other words the ratio between F_{OC} and the F_g mass flow rates in each reactor.

According to that, residence time distribution of the OC in each vessel must be carefully controlled to exploit its features at best, internals may be inserted in the fluidized bed reactors to avoid excessive solid mixing or channelling which lead to un-efficiency of the reaction chambers.

The efficiency of the system is a key parameter to evaluate a technology, the typical cold gas efficiency (η_{cg}) given in Equation 8 where Q_{H_2} and Q_{CH_4} are the molar fluxes of the hydrogen produced and fuel transformed.

Cold gas efficiency can be considered the starting point for the process assessment.

$$\eta_{cg} = \frac{QH_2 \times \Delta H_2}{QCH_4 \times \Delta HCH_4} \qquad \text{Equation 8}$$

The preliminary data obtained returned an efficiency for the OSD process (η_{OSD}) of the order of 72% versus a literature value of the Steam Methane Reforming ranging from 73% (no steam export valorization) to 76% (30% steam export valorization); a value of 72% gives zero value to the steam export, while it can be artificially increased to about 80% if a 100% valorization of the steam export is assumed. Anyway, in order to have a fair comparison, the SMR should be penalized for the CO_2 capture [7].

A thermogravimetric experiment can illustrate the whole solid redox cycle. In Figure 5 is shown a Theromogravimetric Analysis (TGA) profile of a iron oxide based solid at 800°C under methane flow is reported: the first slope is very steep – the derivative Δ(weight)/Δ(time) is the first step reduction step $Fe_2O_3 \rightarrow Fe_3O_4$ (Equations 4.a-d-g) and the outlet gas detection system shows the presence of carbon dioxide only. This reduction step is very fast and thermodynamics calculations show that CO_2 and H_2O are the only stable species formed. The Equations 4.a-d-g are shifted to the right, almost completely.

The second step, corresponding to reduction $Fe_3O_4 \leftrightarrow FeO$ (Equations 4.b-e-h), is not so fast as the previous one because the two redox pairs CO/CO_2 and H_2/H_2O in the gas equilibrates with the involved Fe_3O_4/FeO redox pair in the solid, so the contact with steam and CO_2 has to be limited since they could re-oxidize back the wuestite. The third step, corresponding to reduction $FeO \rightarrow Fe^0$ (Equations 4.f-i), is fast and the metallic iron formed may promote the auto-catalytic pyrolysis of CH_4 which leads to soot deposition and iron carbides formation (Equation 4.l) and an excess of hydrogen in the gaseous product.

Moreover, iron carbides in the subsequent water splitting reactor R1 can generate carbon monoxide, its allowed content depends upon the final use of hydrogen and the relative specifications. So even if the formation of metallic iron traces is un-avoidable, care must be taken to control the molar flow rate of the fuel avoiding its molar excess condition which causes the over-reduction of the OC.

The reduction pathway is very complex and only know-how built on experimental evidence can lead to an optimal reactor design and to the selection of appropriate operating conditions in order to ensure the best reduction potential and the preferred thermodynamic embodiment.

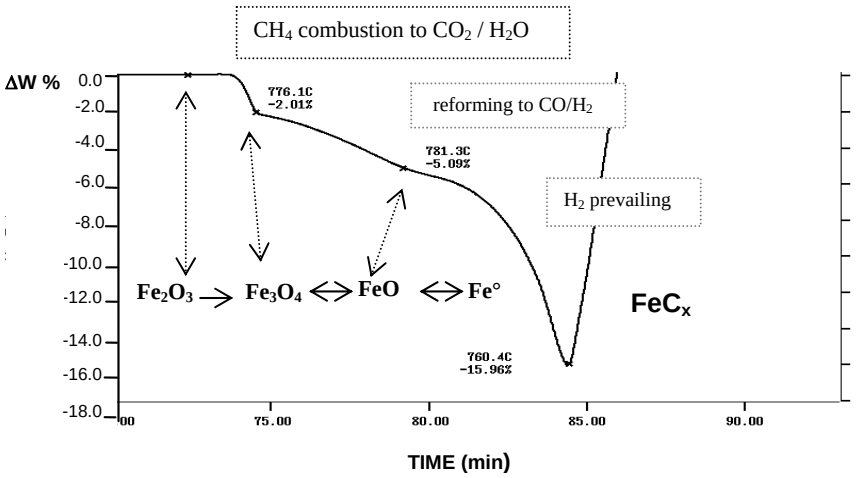

Figure 5. TGA measurement of the solid weight profile while the solid undergoes reduction and the fuel undergoes combustion-reforming-pyrolysis.

Figure 6 showns a thermogravimetry profile under steam and air flows. The first slope – the derivative Δ(weight)/Δ(time) – corresponds to the oxidation step by water splitting which leads to the quantitative conversion of FeO to Fe_3O_4 up to the first plateau. Under these conditions, no more hydrogen is attainable. This is due to the fact that TGA is a non-equilibrium set up because the steam is continuously fed to the splitting reaction.

The second slope is the super-oxidation step by air, which lead to the quantitative conversion of Fe_3O_4 to Fe_2O_3. The air is fed to the TGA up to the oxygen consumption stops. Under these conditions a second plateau is observed and solid weight is restored, at the initial value of the OSD cycle.

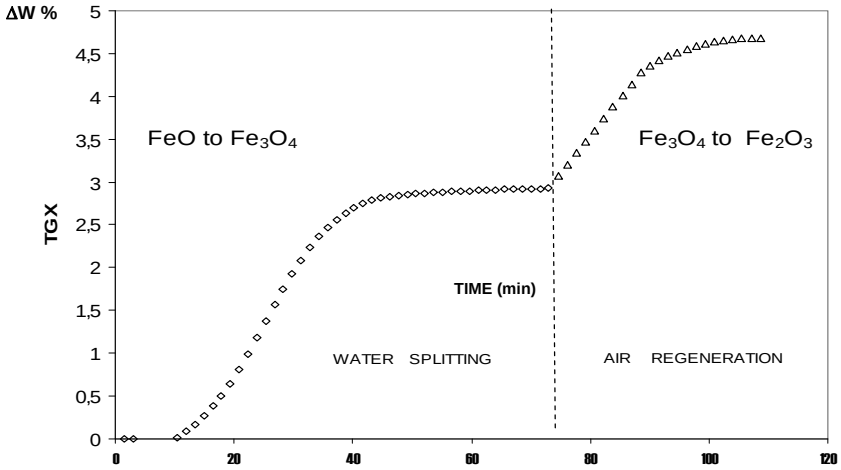

Figure 6. TGA measurement of the solid weight profile while the solid undergoes oxidation and the steam undergoes water splitting

OC reduction step

It was very soon recognized that the most critical step is the OC reduction taking place in the Natural Gas flameless-combution vessel (R2). From the fluidodynamic point of view, the Natural Gas Reactor can be set as an FBR operating in a counter current regime, where OC (hematite) flows downward and the fuel, which also acts as fluidization gas, flows upward. From the chemical point of view, it can be split into two separated reaction zones: an upper combustion zone where the fresh hematite quantitatively reacts with the unconverted NG and its partial oxidation products are quantitatively converted into CO_2/H_2O, and a lower reforming zone where magnetite reacts with fresh NG and it is converted to wuestite, nearly quantitatively.

According to this conceptual view, a plug-flow combustor like a Perforated Plates MultiStaged Fluid Bed Reactor (PPMSFBR) [8], which typically shows an axial conversion profile, should overcome thermodynamic constrains which limit the conversion of both oxygen and fuel. As observed in a continuous fluidized bed reactor having a homogenous axial profile, independently of contact time, the reduction stops at more or less the formation of Fe_3O_4, as it can inferred by the O_{rev} conversion of about 38%. The carbon dioxide formation is negligible, also because most of the methane is unconverted. The minimum number of the inserted plates, i.e. the number of reactive

steps in the multi-staged FBR, can be assessed at 800°C by simulation assuming a thermodynamic controlled reactor.

Therefore, according to Equation 3.a, Fe_2O_3 and CH_4 are fed to the counter current NGR observing a molar ratio equal to 4.

Then, assuming a series of cascade of homogeneous reactors where 2,66 mols of Fe_3O_4 are put in equilibrium with 1 mol of CH_4 (first reactor), the resulting gas output composition is equilibrated with the unconverted Fe_3O_4 (second reactor) and going in such way up to the conversion of magnetite is completed. The last reaction step of 4 mols of hematite with the residual unconverted CH_4 and/or with $CO/2H_2$ is assumed fast and irreversible and, therefore, it is assumed only one reactor stage.

According to this frame, the autogenic conversion of magnetite based on the K_p values at 800°C for the following equations:

$$K_{(1)} \equiv \frac{[CO_2]\times[H_2O]^2}{[CH_4]} \qquad \text{Equation 9}$$

$$K_{(2)} \equiv \frac{[CO]\times[H_2]^2}{[CH_4]} \qquad \text{Equation 10}$$

$$K_{(3)} \equiv \frac{[CO_2]}{[CO]} \qquad \text{Equation 11}$$

$$K_{(4)} \equiv \frac{[H_2O]}{[H_2]} \qquad \text{Equation 12}$$

The expected gas (shown in Figure 7a) and OC top-bottom axial composition profile (shown in Figure 7b) lead to the complete conversion of magnetite to wuestite after 4 reduction steps. An additional step is then needed to convert the residual reductants gas with hematite to combustion products. By concluding, 5 reactive stages are needed assuming an efficiency of 100% for each one.

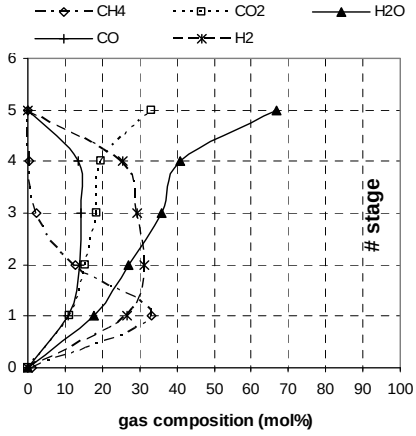

Figure 7a. Bottom to top gas composition.

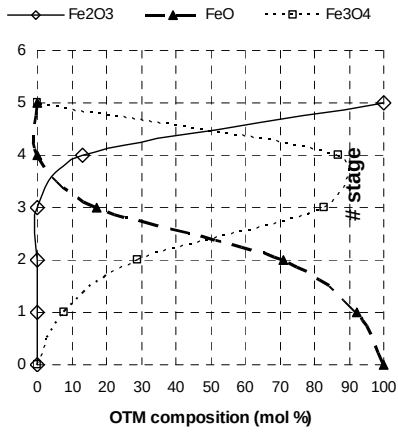

Figure 7b. Top to bottom OC composition.

Perforated plates, having hole diameter larger than particles, as inserted internals, should satisfy some main efficiency criterions like: lowest pressure drop, no risk of clogging, high contact efficiency, good thermal efficiency to control and minimize:

1. Gas and solid particles which bypass the reactive stage without reaching equilibrium condition
2. Back-mixing of solid particles which are not able to move properly in counter current way. So, they react with the reducing gas in a non-equilibrium condition, because:
    - Carried by the reducing gas up to the previous reactive stage (entrainment)
    - Hampered by the reducing gas to proceed to the subsequent reactive stage

PPMSFBR's fluid-dynamic regime needs to be studied making use of a Cold Flow Model to evaluate and improve the OC's residence Retention Time Distribution (RTD), which is a function both of the shape of perforated plates and of the ratio between solid and gas flow rates. The target would be to optimize the reactor design and obtain the expected reactor efficiency

OC oxidation steps

Water splitting

The water splitting step takes place into the steam reactor (R1), which can be set as a FBR operating in a counter current regime, the OC (wuestite) flows downward while the diluted steam, which acts also as fluidization gas, flows upward. From the chemical point of view, it can be assumed that is a homogeneous reactor limited by thermodynamics and therefore the splitting kinetcs will control its performance.

It follows from this that at the top of the reactor one obtains a water splitting gaseous mixture H_2/H_2O at equilibrium with wuestite/magnetite mixed oxides based solid phase, obtained from the bottom. So, according to thermodynamic constrains, converted and un-converted reaction species are present in both output reactor streams.

The thermodynamic profile of the splitting reaction (Equation 5.b) in the 500-900 °C range is described by the phase diagram (Figure 8a) of the reactive slurry at equilibrium. It is possible to observe a low steam molar fraction for splitting temperatures ranging from 500 to 600 °C. At higher temperatures (600-800°C), the dismutation of wuestite (Equation 5.d) as well as the splitting reactions (Equations 5.a-c) will take place .

$$4\,FeO \leftrightarrow Fe_3O_4 + Fe \qquad \text{Equation 5.d}$$

Finally at temperatures higher than 650°C conversions are negatively affected by thermodynamics.

This phase diagram can be re-written in term of $\log K_p$ and ΔG profiles (Figure 8b):

$$Kp \equiv \frac{[P_{H_2}]}{[P_{H_2O}]} \qquad \text{Equation 13}$$

observing, at that the ΔG values are negative and the equilibrium is shifted to the right temperatures lower than 800°C.

Likewise, the Kp equation (Equation 13), as depicted in Figure 9, can be re-written in terms of steam autogenic molar conversion (Xc) and becomes:

$$X_c \equiv \frac{[Kp]}{[1+Kp]} \qquad \text{Equation 14}$$

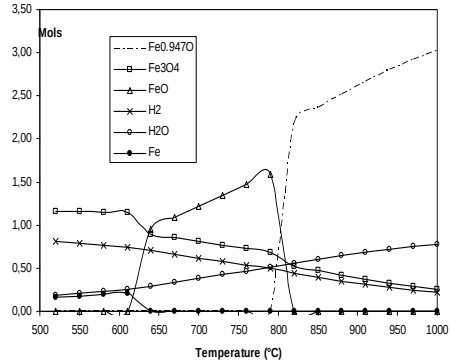

Figure 8a. Phase diagram of mixed equilibrium wuestite/steam

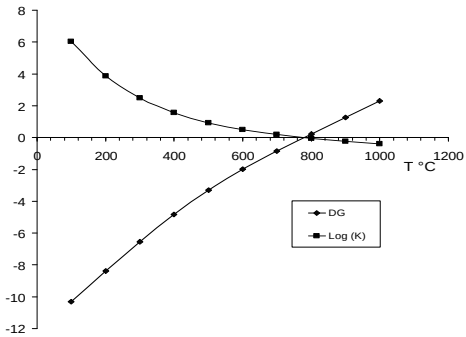

Figure 8b. Thermodynamic profile of mixed equilibrium wuestite/steam

Finally, on the basis of the phase diagram, a thermodynamically limited steam conversion can be assessed to about 50-40% in the temperature range 700-800 °C. Under such conditions, kinetics aspects are considerable and experimental practices are needed to define a reactor design able to maximize oxygen and hydrogen mass transfer to and from the oxygen carrier in the redox gas-solid reactive slurry.

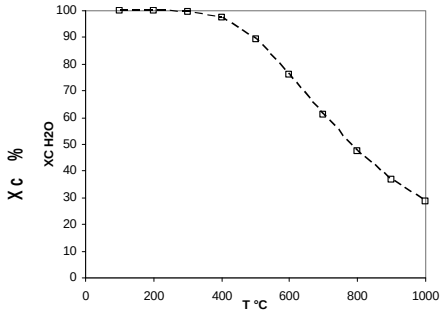

Figure 9. The autogenic steam molar conversion profile

Air regeneration

The air reactor (R3) is a riser. Thus, the OC (magnetite & wuestite based active phase), produced by the equilibrium in the water splitting step, and the air both flows upward.

The exothermal super-oxidation of the OC has two tasks:

- to supply heat to the solid in order to close the process's heat balance
- to restore the higher active phase (hematite) oxidation potential

As mentioned before, in the process the OC acts also as heat carrier. This allows to fulfil the constraint given by Equation 7. The adiabatic ΔT_i is dictated by the inlet air flow rate and the reaction heats ($\sum j$=R1-R3 Qj) should balance the OC's circulation flow-rate (F_{OC}) multiplied by its sensible heat Cp_{OC}. Therefore, the priority is given to the OC's circulation flow rate because it affects the contact times in each reaction vessel. Moreover, the air flow rate is tuned to keep the temperature of solid at the of top the raiser (R3) nearly equal to 832°C, in order to meet the above described tasks and, consequently, the exit temperatures of the solid from R2 and R1 reactors are 698°C and 718°C, respectively.

THE OSD OXYGEN CARRIER

The core of the technology is the Oxygen Carrier (OC) being required not only, to provide the thermal tonality into the loop to cover the chemical functionalities, but also to provide chemical functionalities like being easily oxidized by steam, neatly reducible by hydrocarbons and to be stable under the oxidation/reduction cycles. Since the configuration of this process is a solid circulation loop, similarly to the chemical looping redox technologies, it must be fulfilled the requirement of physico-chemical and fluidization properties like attrition resistance, optimal particle size distribution, suitable particle and skeleton density. The OC is required to meet a suitable chemical yield (amount of hydrogen per solid weight unit) which, together with kinetics of reaction, leads to the space time yield that covers an important role in the economics assessment (size and capital cost of the OSD plant) of the technology.

The deposition of the active phase can be carried out by incipient-wetness-impregnation on micro-spheroidal γ-alumina based support that has been pre-treated with a doping agent like di-valent magnesium or zinc [9] to form a $MeAl_2O_4$ based spinel layer. As consequence of the spinel modification, the migration of di-valent iron (wuestite) into the alumina structure forming the spinel $FeAl_2O_4$ has been observed. The di-valent iron atoms migrated into this structure are no longer oxidizable by steam splitting and, therefore, as a consequence of the lowered presence of reactive wuestite, the hydrogen production of H_2 is negatively affected. The doping of alumina inhibits such detrimental migration.

The oxygen transfer dynamic model

The performances of the Oxygen Carrier (OC) are closely correlated to the exchange phenomena which occur in the gas/solid slurry inter-phase between the gas (NG -Steam) and the iron oxides (oxygen releasing - demanding) and, likewise in the opposite sense between the so obtained reaction products and their corresponding iron oxides precursors. The Shrinking Core Model fits very well the realistic macroscopic interaction mechanism where both the reduction reaction and the splitting reaction can be split into four concurrent physical steps:

1. NG/Steam chemisorption on the surface
2. NG/Steam diffusion from surface to the core
3. Iron oxides reduction or oxidation
4. NG Combustion and/or reforming products and/or Hydrogen desorption from inner layer to the gaseous bulk

In Figure 10 these four steps are represented and the layering of the active phase concerning the reduction gradient which occurs from the outer to the inner solid layers is shown.

According to that, in the case of the NG combustion step, it is possible to define at microscopic level three rate determining reaction events (Equations 15.a-c), which are positively affected by fuel high partial pressure [CH_4] and negatively affected by both high particle molecular density (**ρ**) and length of the reactive layer (**R**).

$$Tr = \frac{\rho \times R}{B \times Kc \times [CH_4]} \qquad \text{Equation 15.a}$$

$$Td = \frac{\rho \times R}{B \times D \times [CH_4]} \qquad \text{Equation 15.b}$$

$$Tl = \frac{\rho \times R}{B \times Kg \times [CH_4]} \qquad \text{Equation 15.c}$$

Here, T_r is the resistence of the chemical reduction and it is controlled by the average reaction rate (Kc); T_d is the resistence of the NG diffusion through the reactive solid controlled by the diffusion coefficient (D); and T_l is the resistence of the NG chemi-absorption on the reactive surface it is also affected by the mass transfer coefficient (kg) from the bulk to the gas/solid interface.

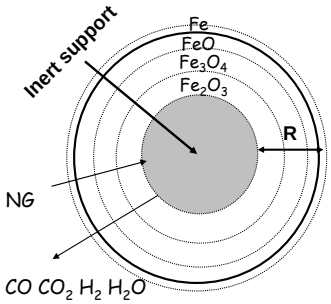

Figure 10. Shrinking Core Model.

Even if this representation is an almost qualitative picture, it suggests some of the physical features that must be meet designing the OC solid, which are:

- an high superficial area (to promote the gas chemisorption),
- a low density of the layer (to promote the gas diffusion),
- a good dispersion not to concentrate the un-avoidable superficial metal iron

According to this model, each single particle behaves as a fixed bed reactor. As a pre-requisite condition to design efficient reactors the fluidization of the gas/solid slurry is needed to promote the mass carrier from the bulk to the interphase of fresh NG and vice versa the reaction products desorption.

The Features

Physical-chemical features

The basic feature requested to the OSD material (30%$_w$ loading) is to be fluidizable at the lowest possible value of gas VMF (velocity of minimum fluidization). Solids on the base of their physical-chemical parameters (see table 1) are classified into 4 groups of fluidization attitude according to the Geldart [10] scale by matching their density parameters (as the difference between skeletal and particle density) against the mean particle size (D50).

Table 1. Physical-chemical parameters to define OSD oxygen carrier.

Sample	SA	VP	Pore avgdiam	Skd	Ptd	D10	D50	D90	<20micron	<45micron
	m2/gr	cc/gr	A	g/cc	g/cc	um	um	um	%	%
Carrier	213	0.59	92	3.25	1.11	26	73	122	7.5	22.3
Spinel	139	0.43	102	3.3	1.36	6	66	118	21.4	33.3
Redox solid	87	0.3	108	3.65	1.75	37	78	119	4.7	14.7

SA surface area; VP and Pore average diameter pore volume; Skd= Skeletal density; Ptd= Particle density; Dxx = size under which the specified (xx) % of particles is comprised; <xx micron = % of particle under the specified (xx) size; um= unit of mass; cc=cm^3

The corresponding fluidization curve (Figure 11) shows a knee at 0,5 cm/sec this value of gas superficial velocity where both solid bed expansion and pressure drop are stable. It defines the VMF value.

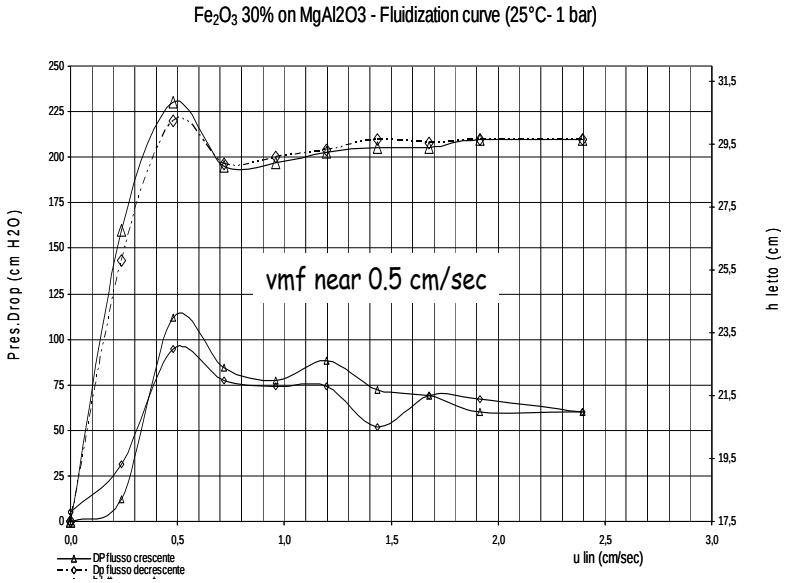

Figure 11. OC fluidization curve by air.

Chemical features

The basic solid chemical composition is shown in the following formulas as:

- atomic % of elements

  $[Fe_{20.44}\ Al_{56.37}\ Mg_{23.19}]O_{138.41}$

- weight % of oxides

  Fe_2O_3 30%; Al_2O_3 52.82%; MgO 17.18%

- weight and atomic composition % of the active redox component and of the support

  30% $[Fe_1O_{1.5}]$* 70% $[Al_{0.71}Mg_{0.29}O_{1.35}]$

The loading of Fe_2O_3 has a close relation with hydrogen productivity. Figure 12 shows the weight profile during the oxygen exchange of OC in the OSD process. When in R2 the lattice oxygen is released and the stoichiometric loss of weight is nearly -10%w. Vice versa, when in R1 the oxygen is taken up from steam the increasing of weight is nearly + 6,92%w and(in R3 the further taken up from air produce the remaining + 3,34%w to close the oxygen mass balance.

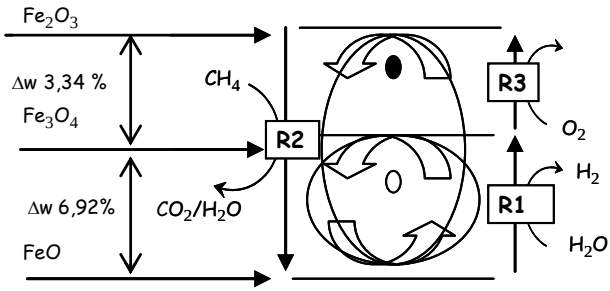

Figure 12. The productivity of the oxygen carrier.

From the productivity point of view, it is worth to underline that, starting from 1 kg of hematite, it is possible to obtain 900 g of pure wuestite. Consequently, on molar basis at normal conditions, 93,5 L_n of hydrogen in the splitting step and 35 L_n of CO_2 in the combustion step are obtained (the molar ratio H_2/CO_2=2,66).

Therefore, active phase loading is a critical issue and some aspects must to be taken into account and balanced: the higher the loading, the higher the hydrogen productivity. On the other hand, the higher the tendency of solid to lose active phase due to attrition under circulation, the lower is the reactivity/lattice oxygen conversion because the length of the phase layer (R) - see text below – represents a resistance factor and, consequently, it could negatively affect both conversion and kinetics of the oxygen exchange. The experimental evidences have demonstrated that 30% by weight of active phase is a good compromise to have a stable and reactive OC, able to afford per kilo of OC a chemical yield close to 30 L_n /kg of. H_2 and 10,5 L_n /kg of CO_2.

Reactivity features

The reactivity of OSD solids is experimentally assessed by TG/DTA measurements [11]. These are made with a TG/DTA220 module (Figure 13), which uses a horizontal differential system balance mechanism. Standard aluminium crucibles and sample size of 8-12 mg were used. The TG/DTA measurement device is interfaced with a home-built gas feeding system (multi-stream valve), located inside a box (stream selection box), kept under a continuous nitrogen flow (200 standard cm^3/min) during the thermogravimetric analyses.

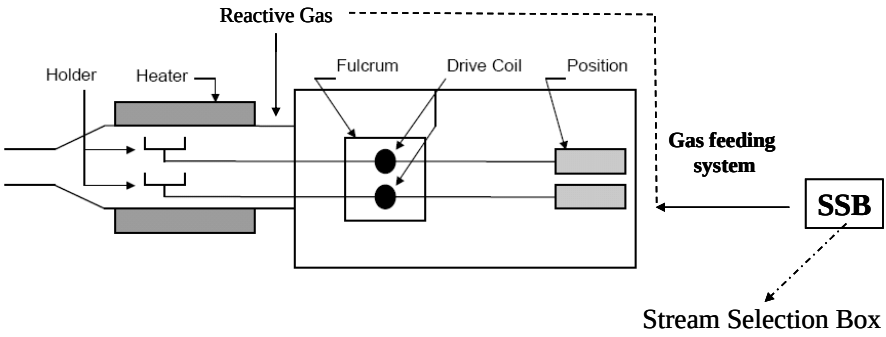

Figure 13. Thermo Balance module.

Each material is analysed in the following manner. A sample size of 8-12 mg is placed in the holder (Platinum/rhodium alloy) on the sample side and submitted to successive in-situ reduction treatments with methane (100 %) at different temperatures under a specified temperature program.

The TGA method define to carry out the reduction steps at different Tred (°C) according to the following sequence:

- 760 °C (1st cycle)
- 760 °C (2nd cycle)
- 720 °C (3rd cycle)
- 740 °C (4th cycle)
- 800 °C (5th cycle)
- 760 °C (6th cycle)

The change in both the weight of the sample and the difference of the temperature between the sample and the inert reference material were monitored and recorded simultaneously.

The raw experimental data, i.e. the time and the weight loss (%), exported from the data recording unit of the TG/DTA220 module, are treated in order to determine two parameters:

- τ (normalized time), defined as: $(t-t_0)/mgFe_2O_3$, where t is the current time-value and t_0 is the time at which the reduction step begins. This parameter can give information about the oxygen extraction kinetics and, consequently, about reactor size.
- **R (%)**= 100×dW/dWmax, where dW is the actual weight loss (%) and dWmax represents the maximum weight loss if all the hematite phase (Fe_2O_3), contained in the sample, was reduced to metallic iron (Fe0).

This parameter (R%) is defined as the reduction degree based on mass variation, ranging from 0 (Fe_2O_3, hematite) to -100 (Fe^0, metallic iron), and represents the ability of the material to release oxygen under reduction conditions, i.e., hydrogen productivity as before defined.

Both τ and **R(%)** are very useful parameters in order to compare the redox performances of any sample tested, with the performances given from the typical ENI OSD solid 30%w Fe_2O_3 supported on the Al-Mg spinel having formula $MgAl_2O_4$ labelled: **2011Fe$_3$0Mg08A200** which is assumed as the standard reference solid.

Experimental

The aim is to assess standard and doped materials on the basis of the following criteria:

- rate of reaction of the lattice oxygen with the NG
- ability of the materials to react oxygen before having coke deposition
- stability of OC performances after some NG/AIR cycling

The thermogram and the TG/DTA curves recorded for the OC standard material are shown in Figure 14. For shortness, we choose to report only the TG/DTA thermogram experimentally recorded at T_{red} = 760°C (2nd reduction cycle).

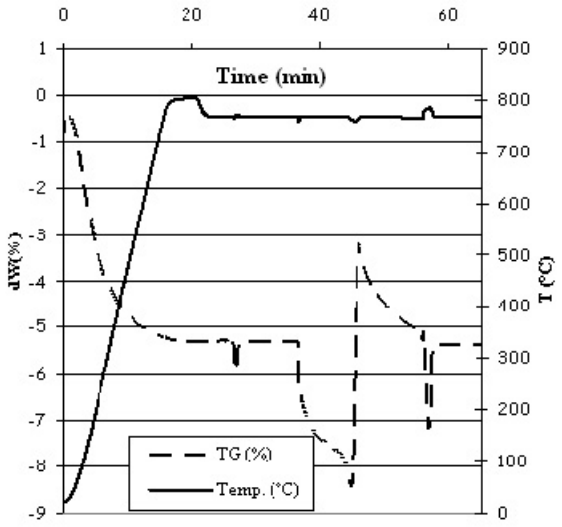

Figure 14. TG/DTA performed on **2011F30M08A200** sample (T=760 °C and P=1atm, 2nd cycle.

Figure 15 shows the whole set of the calculated reduction degree **R(%)** versus **τ** (normalized time) for the TG/DTA performed at different T_{red} values range from 720 to 800 °C . The position of the oxygen reduction (R%) maximum and the corresponding **τ** values (pointed out in the dotted ellipse) is an indication of reducibility degree and of reduction kinetics of the aged OC (5th TG/DTA run at 800°C as cited before).

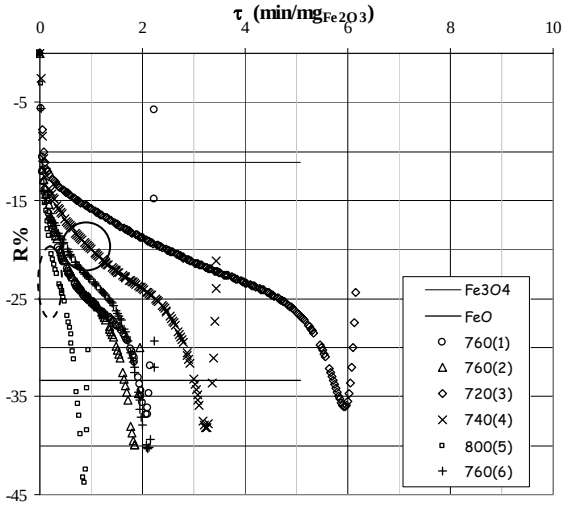

Figure 15. Plot of **R(%)** vs **τ** (normalized time) at different T_{red} of the TG/DTA test.

The position of R% vs τ values (pointed out in the circle) is an indication of the stability of the OC (1^{st}, 2^{nd},6^{th} TG/DTA runs at 760°C). The remaining two runs at 720 and 740°C (3^{rd}, 4^{th} runs) are taken to calculate then the effect of temperature (Figure 16a) and the corresponding Arrhenius plot (Figure 16b).

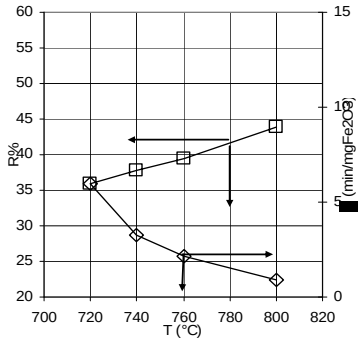

Figure 16a. Effect of temperature on the reducibility (%R) vs kinetics (τ)

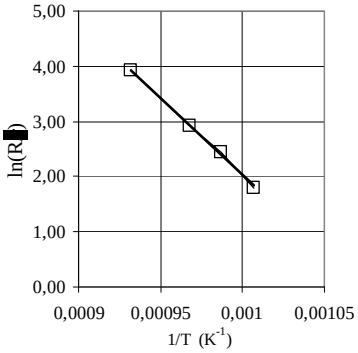

Figure 16b. Arrhenius plot.

From these figures, much information can be obtained in terms of:

- **stability of material**, i.e. in fig.16 shows good reproducibility of the position of the minimum of the curves (R% vs τ) corresponding to the reduction performed at T=760 °C.
- **ability of material to release oxygen**, i.e. in fig.16 which in the water splitting process step means hydrogen productivity - the (R%) reduction degree value obtained at T=760 °C is almost quantitative in the reduction gap from Fe_2O_3 to FeO and Fe^0 formation comes after so it can be put under control
- **rate of reaction**, i.e. in fig.16a the extraction time τ required at T=760 °C to get the maximum reduction degree is conveniently shortened increasing the temperature
- **The Arrhenius plot**, to assess the consistency of the achieved data

So, according to this procedure, one can carry out an evaluation of material according to their chemical composition and chemical-physical nature. As an example of this application, it were studied by TGA/DT a series of doped OSD materials with 100 ppm of Pt, Pd; Cu.

The observed beneficial effect on the rate of reaction by doping the standard material with noble metal is according to the scale Pt>Pd>Cu>Undoped. But this effect, due to the improved chemisorption of NG on the metal surface, is volatile (see Figure 17) because the noble metal migrate from the active surface to the inner layer of the phase loaded.

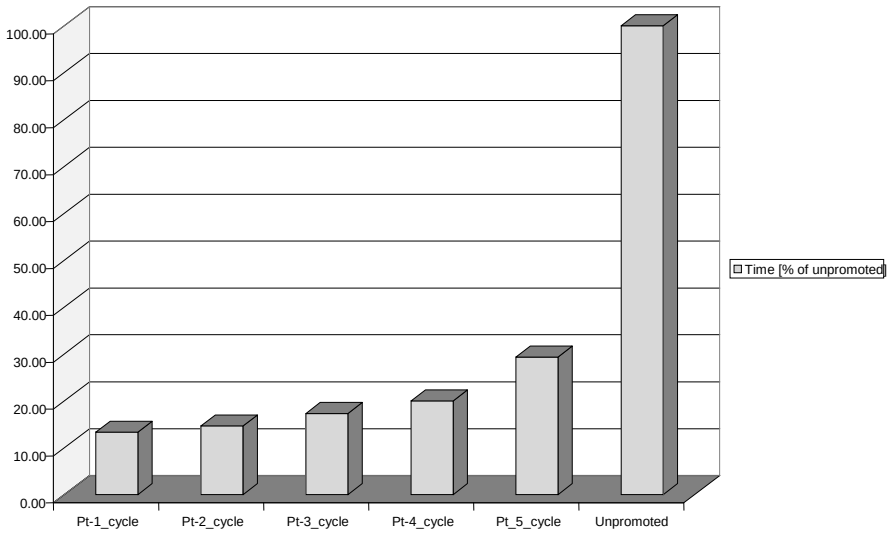

Figure 17. Ageing of a Pt doped OC – observed time in reduction cycles compared with the undoped OC.

CONCLUSIONS

The OSD process is a unique process that returns hydrogen and pure carbon dioxide without any further management. The process is based on a proprietary iron based material able to change the oxidation state within the three vessels loop where the hydrogen formation occurs via water splitting.

In the stand-alone hydrogen production, the OSD process with 100% CO_2 capture has better figures than cold gas efficiency with respect to a traditional steam reforming equipped with best available technologies allowing a 90% CO_2 capture. However the most promising perspectives come from an optimised integration with a H_2-Combined-Cycle plant where the net efficiency could peak up to 51%.

The process is complicated since the solid is not only a chemical partner but also the heat carrier. This poses many constraints to the viability of technological solutions whose final selection cannot avoid an economical evaluation which minimises the overall production costs and capture cost. Preliminary estimates for the OSD process places the capture cost in the 25-30 $/ton range.

The OSD process is part of the technological efforts of CACHET, a 3-year, integrated research project, led by BP and funded by the European Commission and by the CO_2 Capture Project consortium (CCP2), which aims to develop technologies to reduce greenhouse gas emissions from power stations by 90%. The objective of the project is to develop innovative technologies for hydrogen production from natural gas, halving the cost of low-carbon energy.

ACKNOWLEDGEMENTS

The authors wish to thank our financers, supporters and co-workers within the CACHET project, which is an integrated research program funded by the European Commission (FP6 Contract No. 019972), with support from the CO_2 Capture Projcet Phase 2 (CCP2). Further, the oxygen carrier used in the 140 kW tests has been produced by the Flemish Institute for Research and Technology (VITO), Belgium under the guidance of Chalmers University of Technology, Sweden in the context of the EU financed project CLC GAS POWER (FP6 Contract No. 019800).

REFERENCES

1. D. Sanfilippo, A. Paggini, V. Piccoli, R. Miglio, S. Rossini. Process for the production of hydrogen. Patent US 2001/0055559
2. D. Sanfilippo. One step Decarbonization: A new direct route by water splitting to hydrogen with intrinsic CO_2 sequestration. Proceeding of the AIDC Conference "H_2 – Age; When, Where, Why". Pisa, Italy, 2004
3. S. Rossini, U. Cornaro, F. Mizia. Hydrogen with intrinsic CO_2 sequestration: The ENI "One Step Hydrogen" Process. Proceedings of the conference "Innovation in the manufacture and use of hydrogen". Dresden, Germany, 2003
4. D. Sanfilippo *et al*. One step Decarbonization: A new direct route by water splitting to hydrogen with intrinsic CO_2 sequestration. Proceeding of the 7th Natural gas Conversion Symposium. Dalian, China, 2004
5. U,Cornaro, R.Miglio *et al*. Iron oxide based materials as oxygen carrier for hydrogen production from natural gas with inherent CO_2 sequestration. Poster Award of the Europacat-VI, Innsbruck, Austria, 2003.
6. D. Sanfilippo *et al*. One step Decarbonization: A new direct route by water splitting to hydrogen with intrinsic CO_2 sequestration. *Studies in surface science and catalysis*. 147 (2004) 91-96 Elsevier
7. S. Rossini, U. Cornaro, F. Mizia, A. Malandrino. Hydrogen from water splitting: The One Step Decarbonization Process of natural gas with inherent CO_2 capture. Submitted to the Congress "Rome 2007- Energy Future in an Interdipendent World". Rome, Italy, 2007
8. D. Sanfilippo, F. Mizia, a. Malandrino, S. Rossini. Process for the production of hydrogen and the co-production of carbon dioxide. Patent US 2005/0232859
9. D. Geldart. Types of gas fluidization. *Power technology*. 7 (1973) 285-292
10. D. Sanfilippo, U. Cornaro. Catalytic system and process for the production of hydrogen. Patent 2004/0152790
11. M. Cozzolino, U. Cornaro, F. Mizia, S. Rossini. Iron base solids as oxygen carrier for the The ENI "One Step Decarbonization" Process. Proceedings of the "XVII Congress of the Italian Chemical Society. Industrial Chemistry Division". Genova, Italy, 2008

Carbon Dioxide Capture for Storage in Deep Geologic Formations, Volume 3
L.I. Eide (Ed.)

Chapter 16

HYGENSYS: A NEW PROCESS FOR POWER PRODUCTION WITH PRE-COMBUSTION CO_2 CAPTURE

F.Giroudière[1], J.L. Ambrosino[1], B.Fischer[1], D.Pavone[1], E.Sanz-Garcia[1],
A. Le Gall[2], E. Soutif[2], H.Vleeming[3]
[1]IFP-Lyon-BP3-69360 Solaize, France
[2]TECHNIP 92973 Paris La Défense cedex, France
[3]PDC P.O. Box 7052 NL-4800 GB Breda, The Netherlands

ABSTRACT: This paper presents the HyGenSys process, its use for power production with pre-combustion CO_2 capture and developments carried out during the three years of CACHET project. The HyGenSys process is a steam reforming process producing mainly power as secondary product instead of steam. Actually, the heat necessary for the process comes from hot pressurized flue gases produced in a gas turbine instead of a conventional furnace. The overall efficiency is improved as the hot flue gases are used several times: to drive the air compressor within the first expander, to heat up the steam reforming process inside the HyGenSys reactor-exchanger, to produce power with the expander, and to produce process steam in a heat recovery section downstream the expander. The objective within CACHET project was to adapt and design the HyGenSys process to produce the hydrogen necessary for a 400 MW combined cycle as well as for the HyGenSys gas turbines. The process has been optimised to get the best possible efficiency with the best CO_2 recovery. The reactor-exchanger, heart of the process, has been studied and designed. A cost estimate has been done to evaluate the power and CO_2 cost. Different alternatives have been studied to reduce the methane slip in order to improve the CO_2 recovery.

INTRODUCTION

This work has been done in strong cooperation between all the partners and has required multidisciplinary skills between research institutes, universities, energy business, engineering and manufacturing companies, in order to develop all aspects of a new advanced SMR.

The most common H_2 production technology is steam reforming which can handle an important variety of feed stocks including natural gas, LPG and naphtha.

Steam methane reformers (SMR) are based on very mature technologies and are offered by a large number of licensors such as Haldor Topsoe AS, Technip, Linde, Lurgi, Davy, Foster Wheeler Corp, and Uhde. However SMRs are large and expensive to construct mainly because of their large fire box and upper convection section.

In conventional steam reforming, a pre-treated hydrocarbon feed is preheated in a convection section before being sent downwards through the nickel catalyst-filled tubes in the radiant section of the furnace. Here, the mixture is converted at a temperature of about 900°C and a pressure of 10 to 30 bars to reach an equilibrium mixture of H_2, CO, CO_2, H_2O and unreacted hydrocarbons.

As H_2 production is expected to increase in the near future, the energy efficiency of SMR units will become crucial. HyGenSys is a new SMR [12] process including a compact SMR reactor based on a

new heating concept and integration with a gas turbine. This new process arrangement leads to a co-generation of hydrogen and electrical power and can be easily integrated with CO_2 capture. This process has been further developed within CACHET.

In current SMR designs, the efficiency of the radiant section is quite low (about 50%), and the global energy efficiency is mainly linked to the on-site utilisation of steam, which is produced in the convection section to recover the low temperature heat in excess. If we consider a major development of hydrogen, the steam production will be difficult to valorise and an energy efficiency increase of the reaction section is needed. HyGenSys process is expected to meet this need thanks to the use of a high-efficiency compact reformer coupled with a power generation system. Moreover, with current SMRs it is difficult to recover CO_2 from the flue gas. Another possibility to produce hydrogen is the partial oxidation process; however, this process uses either air, which leads to dilution with nitrogen, and so higher sizes of all equipments, or oxygen which requires a very costly air separation unit.

HYGENSYS CONCEPT

Description of the reaction

The main equations involved are first the very endothermic steam reforming reaction

$$CH_4 + H_2O \Leftrightarrow 3H_2 + CO\,,$$

and the water gas shift reaction, which is exothermic

$$CO + H_2O \Leftrightarrow CO_2 + H_2\,.$$

In a conventional steam-reforming these reactions occur within catalyst tubes inside a furnace. In the case of HyGenSys, the heat source is an exchange with pressurized hot gas from a hot gas generator (part of a commercial gas turbine), as shown in Figure 1 and Figure 2. A gas turbine consists of an air compressor, followed by a combustion chamber in order to increase the air temperature prior to its feed into an expansion turbine. This expansion turbine will drive the air compressor and a power generator. In a two shaft gas turbine, the expansion turbine is separated in two parts: the first part drives the air compressor and the second one the power generator.
The flue gas at the outlet of the first turbine is still under pressure (about 3-5 bar) and still very hot (about 700°C). In the HyGenSys concept the hot pressurized gases are used as heat source for the steam reforming reaction and the second part driving the power generator is moved downstream.

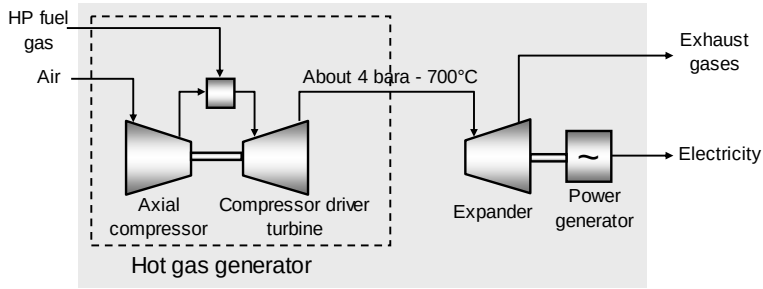

Figure 1. Gas generator used for HyGenSys process.

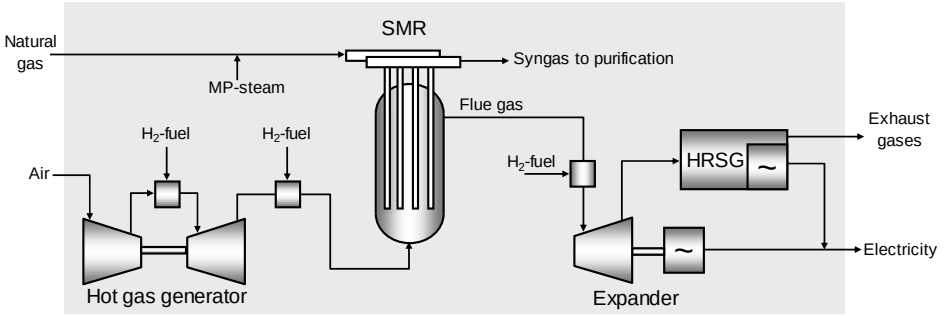

Figure 2. Principle of HyGenSys process: heat of reaction provided by hot pressurized gases.

The hot gas generator is fed with air and hydrogen in order to achieve a zero CO_2 emission process. The generated hot flue gases are reheated into an additional combustion chamber before entering the compact SMR. Downstream the SMR reactor the flue gases are reheated again thanks to a third combustion chamber before being expanded to generate power. The last flue gas valorisation step (steam production) is operated at lower temperature than in conventional SMR. Downstream the SMR, the process gas goes into classical high- and low-temperature shift reactors to increase the H_2 production, and finally into a gas purification unit including CO_2 capture.

The HyGenSys concept is expected to increase the energy use of the unit, thanks to the direct heat recovery of the flue gases in a gas turbine with reduced excess steam generation.

CO_2 CAPTURE WITH HYGENSYS

The HyGenSys process is especially well adapted to CO_2 capture. The gas turbines are fed with purified hydrogen, so that the turbine exhaust will be nearly free of CO_2. The hydrogen is diluted to 50% using steam or nitrogen, a composition confirmed by Siemens as feasible for at least one of their gas turbines. The CO_2 produced by the steam reforming and shift reactions is at high pressure and oxygen free, so it is relatively easy to capture with a conventional amine unit. CO_2 released to the atmosphere will mainly correspond to the not-converted methane in the reformer reactor, as the remaining amount of CO and CO_2 will be very low. The pressure of the process has been adjusted to feed directly the hydrogen to the gas turbine burner without recompression (Figure 3).

HyGenSys uses activated MDEA for CO_2 removal. In pre-combustion using SMR from natural gas or Autothermal Reforming (ATR) the oxygen is totally burned so there is no problem with oxygen at the outlet of syngas unit. At the inlet of the amine package the syngas contains CO_2 (about 15-19% mol) at high pressure so the driving force varies from 4.2 to 5.0 bars. For CO_2 capture the loading of the amine is directly related to that parameter, this is the reason activated MDEA is chosen. Moreover the energy needed for regeneration is lower with MDEA compared with MEA. This bigger heat use is due to the much stronger chemical bonds of the primary amine. In post combustion because of the very low pressure (the driving force is about 0.1-0.2 bar) the MEA is selected based on its high kinetic reactivity and high loading performance at such low pressure.

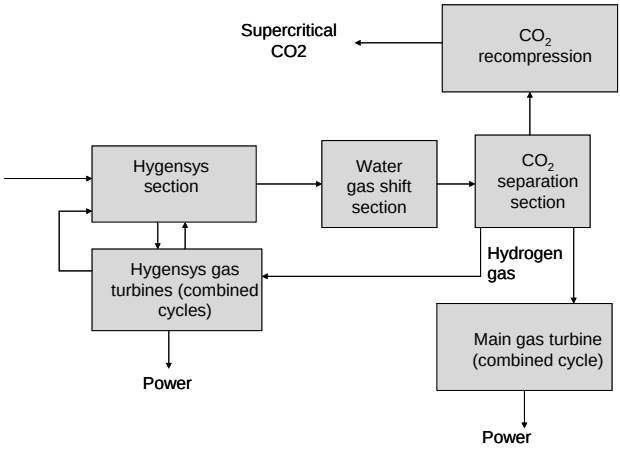

Figure 3. Block flow diagram: overall scheme for power generation with CO_2 capture.

DEVELOPMENT OF HYGENSYS REACTOR-EXCHANGER

Introduction of the solution

For thermodynamic reasons, a very high temperature is required to achieve a good conversion of natural gas and steam into syngas. Whereas in a conventional steam reformer furnace the conversion is achieved in single tubes filled with catalyst, the HyGenSys reactor concept is based on a vertically arranged double pipe (also called bayonet tubes). In the bayonet tube concept, natural gas and steam are fed to the annular section which is filled with steam reforming catalyst. The conversion of the feed into syngas is achieved in this annular section while the stream is being heated. The substantial heat required by the reaction is mainly brought by heat exchange through the wall of the outer tube, thanks to a hot flue gas stream which flows counter-currently to the process side. The resulting hot syngas provides additional heat to the catalytic section while being cooled flowing upwards through the internal pipe. Figure 4 shows the bayonet tube concept and the different flow streams.

The bayonet concept for steam reforming has been used by several actors in this domain. In particular Haldor Topsoe commercialises an industrial unit named HTCR (Haldor Topsoe convective reformer) since 1992 [3], but those reactors are limited to small capacity units. That reactor uses a tube-sheet at high temperature with a large pressure drop. That tube-sheet becomes very thick when the reactor diameter is large.

IFP has developed a new concept without tube-sheet allowing the design of large reactors of above 10 m diameter for large size SMR plants [4].

The bayonet tubes of HyGenSys reactor-exchanger are contained inside a pressurized and insulated shell (Figure 5). The bundle of tubes is fixed to the reactor upper cap and hangs vertically. The catalyst loading, the feed distribution and the syngas collection are ensured thanks to an ingenious arrangement of the upper part of the bayonet tube. The inner tube passing through the external pipe avoids the use of tube sheets and allows the connections to be carried out outside the reactor shell. Each bayonet tube is inserted in a flue gas sheath (or chimney) as shown in Figure 5. The narrow section between the chimney walls and the bayonet outer tube imprisons the hot flue gas around the bayonet tubes and induces high velocity. The high turbulence developed favours convective heat transfer to the bayonet tubes, containing the catalyst.

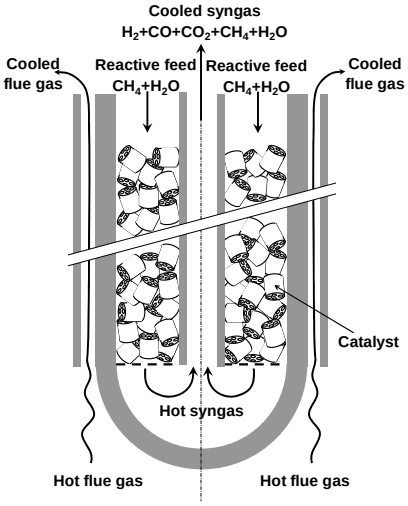

Figure 4. Bayonet tube concept.

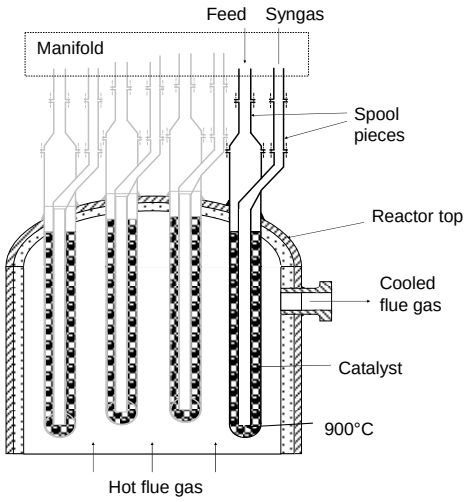

Figure 5. Reactor arrangement concept.

Constraints of the reactor-exchanger

HyGenSys process constraints

The reactor-exchanger concept described above has been adapted to the HyGenSys process characteristics: its maximum capacity is limited by the flue gas flow rate that can be provided by the biggest Siemens two-shaft gas turbine (SGT-700) that will be used as hot gas generator.

On the other hand, the heat input is provided by a hot and pressurized gas (turbine exhausts). Therefore, the reactor shall work with both process side and heating side in pressure. In addition, the pressure difference between process side and flue gas side is significant (about 30 bars). The reactor internals and tubes have to be suitable for the mechanical stress induced. On top of that the flue gas side pressure requires a pressure vessel design even if the pressure is low. As a consequence, for economical reasons, a compact arrangement of the reactor is welcome.

Materials constraints

The extreme operating conditions inside the reactor lead to very high thermal and mechanical constraints (flue gas temperature can achieve values of about 1300 °C). The materials selection is then essential. Metals and alloys are generally susceptible to carbon attacks when exposed at high temperature to an environment containing mixtures of CO, H_2 and hydrocarbons. Carbon attack refers to the metal damaging due to coke deposition, carburization and metal dusting. These three phenomena act at different temperature ranges between 400 and 1000°C, so each one will be an issue for a different part of the metallic bayonet tube. Specific studies have been carried out to find the most adapted alloys for the design.

Reliability and operability

As already stated, steam methane reforming is a very endothermic reaction. Especially, high temperature favours higher conversion. The reactor operating conditions are limited in practice by the highest acceptable temperature allowed by existing alloys. Hence, special attention must be paid

in keeping reactor operation as steady and uniform as possible: this is required to prevent reactor internals to be damaged by possible high temperature spots. Any leakage within the reactor would result in a self combustion of feed or product with oxygen. Consequently, the reactor design considers material testing of internals, leaks detection and replacement of any damaged parts to ensure safety and reliability. Catalyst management is also essential. Since no catalyst study has been done within CACHET project for the reactor development, the reactor concept has to be consistent with commercial catalyst requirements. This also applies to the process flow conditions across the pellets.

Finally, both the reactor overall design and the final operating conditions selection depend on an economical compromise between unit costs (such as material, construction, operating and maintenance costs) and unit performance and reliability.

Work to match the constraints

An iterative work has been realized to take into account all the factors described above, essentially to determine the optimum operation conditions, the materials selection, as well as the tubes and reactor geometry. Final results are shown in this section.

Selection of geometry and materials

Because of the chemical composition of the syngas which favours the metal dusting phenomenon, the material 602CA has been selected for the internal tube. As this tube is not under pressurised design conditions (same pressure inside and outside the internal tube), only the strength to its own weight has been considered.

The very high temperature is obviously the main constraint with regard to creep strength for the material selection of the external tube, associated with a corrosive environment. Several sections of Manaurite have been chosen, with different thicknesses with regard to the temperature variation.
Finally, the flue gas sheaths experience also a very high temperature (up to 1300°C) and very oxidizing conditions. A simple configuration using tubesheet (metallic and ceramic tubes) was dismissed due to thermal constraints, junctions feasibility and ceramic fragility. Technip and IFP have worked on a new hybrid concept: at the bottom of the tube, a concrete structure ensures the sheath support and a high temperature resistance. The main upper section of the sheaths, at lower temperature, can be constructed of metal.

Modelling of the heat-transfer and reaction

The objective of the simulator is to help the SMR tubes design in order to guarantee that the heat transfer from hot flue gas towards the SMR reaction section is high enough without leading to very high metal temperatures causing damage to the tube.

Because the SMR process is made of a bundle of identical SMR reactor tubes, only one tube has been simulated. The main tube geometry that has been used in the simulation is presented in Figure 6. The simulated part of the SMR reactor focuses on the tube section that includes the catalyst section plus the heating sections. On this figure it can be easily seen that the simulator takes 5 domains into account:

1. Dom1: The internal bayonet channel ("syngas" in the centre).
2. Dom2: The wall between the internal bayonet channel and the SMR catalyst ("Metal").
3. Dom3: The SMR catalytic bed for SMR reactions.
4. Dom4: The external wall of the overall tube ("Metal").
5. Dom5: The flue gas that heats up the tube.

At the centre of the cylindrical geometry lies the internal (bayonet) tube. It allows syngas that exits the SMR catalytic zone to go upwards and to transfer heat from the hot syngas in the centre towards the less hot SMR catalyst in the annular space. The main purpose of the bayonet tube is to heat the catalyst: no chemical reactions take place inside the bayonet tube. The internal wall between the inner canal and the catalyst conducts heat from the gas phase to the SMR catalytic section. This section is the heart of the process, its purpose is to convert the injected mixture of steam and methane into syngas. To be realistic, the simulator includes the chemical reactions, the gas temperature and the hydrodynamics in the catalytic bed. The components taken into account are respectively H_2, H_2O, CO, CO_2, CH_4 and C_2H_6. The chemical reactions are the standard shift reaction, steam methane reforming and steam ethane reforming. Apparent kinetics are used, the parameters have been fitted on published industrial results.

The metallic wall surrounding the catalytic bed is in contact with the very hot flue gas. This flue gas heats the metallic wall that conducts heating energy to the SMR reactions. Because SMR performances are closely connected to the energy provided for the chemical reactions, the modelling of this heating has been performed with great care especially because the flue gas flow is highly turbulent.

Most of the geometry variables have to be consistent with commercial equipment which limits the freedom to optimise the reactor size. For example, the radius of the bayonet central tube is given by the manufacturer because, due to fabrication constraints for welded tubes and strength given by its own weight, the minimum internal diameter for the tube is fixed at 30 mm.

The main degrees of freedom are the tube length and the space opened for the flue gas flow under the main following constraints: a 900° C syngas temperature at the exit catalytic bed, injected flue gas temperature not exceeding 1300 °C and the wall temperature compatible with the material limits.

It results from simulator optimisation that the section of the tube in contact with the flue gas should be 14 m in length to ensure the required heat transfer from the flue gas to the syngas. The space for the flue gas flow has been limited in radius to induce a high flue gas velocity necessary to achieve a high heat transfer. This space is enlarged at the entrance to reduce the flue gas velocity at that point and hence reduce the heat transfer. This results in lowering the wall temperature at bottom part of the bayonet. The result is that the injected flue gas temperature can be set at about 1290 °C. In the absence of this enlargement, the metallic wall would have to withstand a too high temperature.

According to the simulator, the flue gas temperature at the upper exit is closed to 660 °C. This temperature is in the good range to be directed outwards the reactor. The simulated SMR temperature complies with the expected 900 °C. Hence the syngas presents a high H_2 and CO_2 content as it is presented below (Table 1):

Table 1. Syngas composition.

Components	Composition (%)	Dry composition
H_2	49.8	72.2
H_2O	31.0	0
CO	11.0	16.0
CO_2	5.1	7.3
CH_4	3.1	4.5

The conversion of the CH_4 is not complete because it is limited by the thermodynamic equilibrium and the kinetics of the chemical reactions.

The temperature map is presented in Figure 6. Heat flux estimation shows that ¼ to ⅓ of the energy required for the SMR reactions comes from the syngas and the rest from the flue gas.

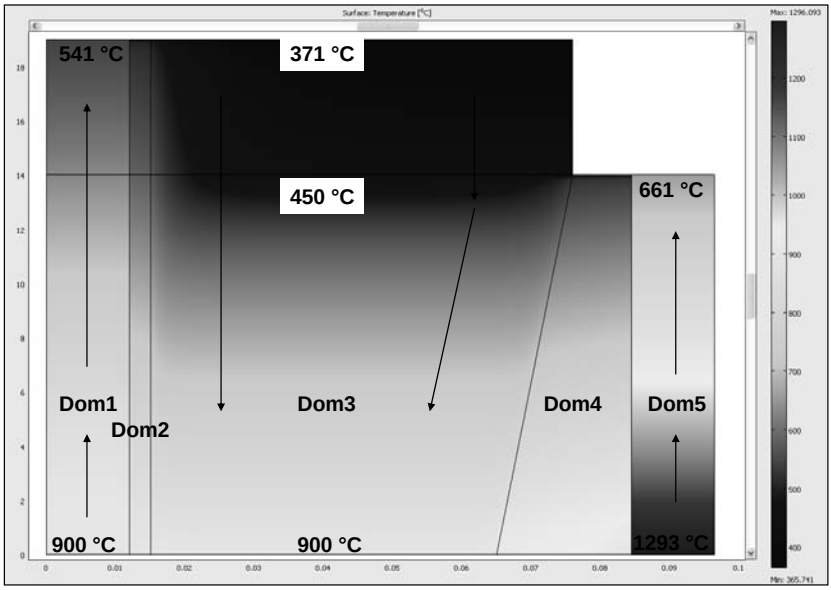

Figure 6. Temperature map in the SMR reactor.

To help understanding the temperature map, Figure 7 presents the radial temperature profile at the top of the reactor. The temperature in the gases is constant and exhibits a huge jump when crossing the interface between the gases and the walls. The feed temperature is 371 °C which is rather low compared to the objective of the SMR at 900 °C.

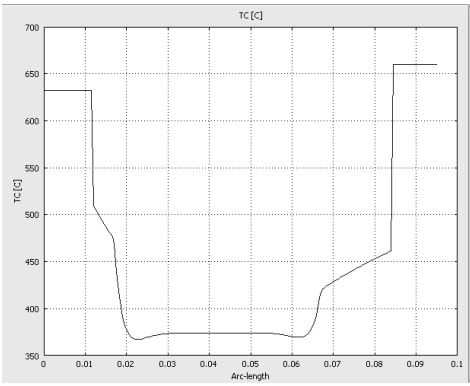

Figure 7. Radial temperature profile at the top of the SMR reactor.

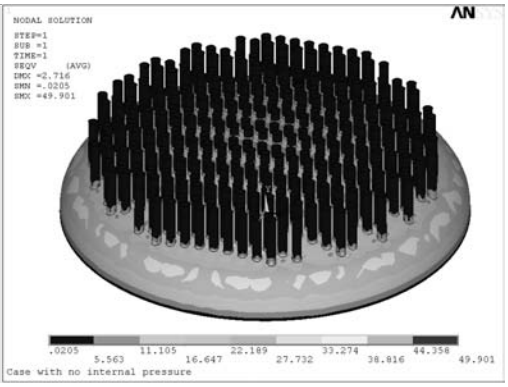

Figure 8. Von Mises stresses (MPa).

As a result, according to the simulator, with 981 tubes of 14 meters in length for the reactive section plus 5 meters for heat exchange purpose, it is possible to reach the expected conversion: the SMR temperature can reach the expected value of 900 °C to guarantee a high conversion. The syngas composition leads to more than 72% of H_2 in the dry syngas.

The flue gas and the syngas are able to provide enough heating energy to balance the energy necessary for the chemical reactions. The flue gas inlet temperature is equal to 1293 °C which is below the maximum temperature of 1300 °C that the equipment can withstand. In addition, the maximum metallic wall temperature is in agreement with the maximum temperature allowed by the material of construction.

Mechanical sizing

Numerical simulations using finite elements analysis have been carried out by Technip to optimise the mechanical sizing and design of the reactor. The reactor diameter has been determined with regard to the tubes layout. Two main criteria have been considered to implant the tubes:

- An operator should be able to access to each tube, for checking flanges for example.
- It should be possible to dismantle each tube independently.

The considered material of the reactor wall and support is P355GH. The reactor has been defined to match the design process conditions in terms of pressure (of around 5 bara) and temperature (of around 400°C). Furthermore, the ability of the top head to withstand the tubes bundle weight has been checked by Finite Element Analysis. Calculations have been done with ANSYS software to obtain the deformed shape of the top head and the Von Mises stresses maps, as shown in Figure 8.

The cold mock-up

The catalyst loading and unloading is crucial to enable long and effective operations. Indeed, any loading discrepancy or unevenness leads to a deviation in heating balance that may cause an early tube failure. A reliable loading method is considered as acceptable when the entire heated section is filled with catalyst with high uniform density, no bridging/void occurs and the flow distribution is kept uniform between each tube (a pressure drop variation of only ±5.0% is accepted).

Because of the central recirculation tube and the narrow annular space, the usual loading devices and procedures are not suitable for the HyGenSys reactor tubes. In addition, the catalyst settlement may differ in bayonet tubes in comparison with simple tubes.

Experimental tests have been done in a dedicated cold mock-up in order to investigate these loading and unloading questions. The cold mock-up consists of a single bayonet tube of 9 m length and 50 mm of annular space. The considered commercial catalyst in the cold mock-up was BASF SG-9301.

A loading procedure has been developed and successively modified to ensure a satisfactory loading. A vibrating platform feeds the catalyst to three separated channels. These channels connect the hopper to 3 feeding PVC pipes of 21 mm internal diameter which are equally separated. This feeding system ensures the same pellets flow into the 3 pipes, and a homogeneous distribution in the column. In order to provide a dense packing, a vibrator is attached to the column. Vibration of the reactor during the loading allows a better arrangement of the pellets inside it and thus a higher catalyst density.

The loading quality is then assessed by achieving several successive loadings. Measurements are performed in order to evaluate the loading quality (loading density estimation, visual inspection to detect possible catalyst bridging and pressure drop measurement for a given flow rate). Finally,

catalyst unloading is achieved using a vacuum system and a single suction hose. Special care has been taken to prevent catalyst damaging during catalyst unloading.

OPTIMIZATION OF HYGENSYS PROCESS

HyGenSys is part of the EU-funded CACHET Project [5,6]. The objective of CACHET is to develop technologies to halve the cost of CO_2 capture at a 90% capture rate. In order to compare four pre-combustion capture technologies identified as promising, a methodology alignment has been defined. Hence, a baseline was studied for the design and cost estimate of a combined hydrogen and power production facility. Two cases, named "Reference Case" and "Base Case", were selected. For results comparison this paper will focus on the HyGenSys process. Note that the Reference Case and the Base Case, as well as the approach to peformance and cost evaluations, are different from similar cases used by the CO_2 Capture Project Phase 2 (CCP2) to evaluate performance and cost of other capture technologies [7]. The Reference Case will produce about 400 MW (net) and correspond to a classical technology without CO_2 capture. A Combined Cycle Gas Turbine (CCGT) is selected to produce electricity without any CO_2 captured or hydrogen production. This Reference Case has been set by NTUA in close cooperation with Siemens and other partners.

The state-of-the-art technology for CO_2 capture is called the Base Case. The technologies used in this process are Auto Thermal Reforming (ATR) with a CO-shift reactor and a CO_2-absorber, a simplified description of this case is provided in the next section.

The target for technologies developed in the CACHET project is to avoid 90% of the carbon dioxide emission versus the Reference Case without any CO_2 capture. The CO_2 avoidance rate is calculated as shown in Equation 1 below:

$$Avoidance\ rate = \frac{\left(CO_{2Ref} / E_{Ref}\right) - \left(CO_{2Case} / E_{Case}\right)}{\left(CO_{2Ref} / E_{Ref}\right)} \cdot 100\% \qquad \text{Equation 1}$$

CO_{2Ref} CO_2 emission to the air, without taking into account the CO_2 in the air feed,
E Net power production,
Ref Reference case, CCGT without CO_2 capture,
Case Specific case, for example HyGenSys-1, CCGT with CO_2 capture.

Base Case study (400MW, 90% CO_2 capture) and comparison with existing technology (ATR with air)

Hereafter is presented a simplified description of the Base Case set by Technip in close cooperation with other partners. The Base Case process takes in account an available technology of air-blown ATR. In the ATR unit, reactions of partial oxidation and steam reforming take place. The inputs are preheated natural gas, steam and compressed air. The output is syngas. The syngas stream is treated in the high- and low-temperature (HT/LT) shift reactors to convert CO to CO_2. The CO_2 is then separated from the syngas by chemical absorption using an activated amine as solvent (MDEA) and finally compressed for export to storage (CO_2 capture). The hydrogen-rich stream is used as fuel for a gas turbine. The exhaust stream of the gas turbine goes into the Heat Recovery Steam Generation (HRSG) section, where steam and electricity are produced. The Base Case process is schematically represented in Figure 9.

Table 2 provides key performance data of the base case compared with the Reference Case.

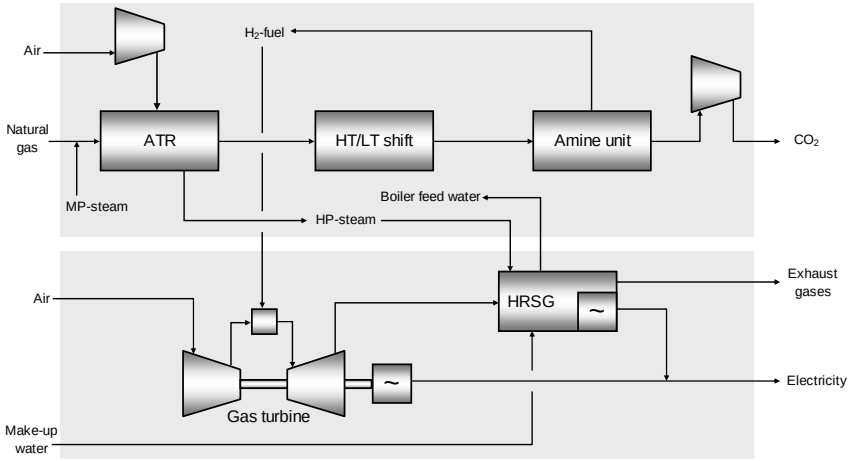

Figure 9. Schematic representation of the Base Case.

Table 2. Key performance data of the base case performance compared with the Reference Case.

	Reference Case	Base Case
H_2 production	no	ATR
Power production	CCGT	CCGT
Capture CO_2	no	yes
Total net power output (MW)	389.8	365.6
Overall efficiency	57.2	40.9
CO_2 capture rate (%)	0.0	94.7
CO_2 avoidance rate (%)	0.0	92.6

HyGenSys-1 description and results

The HyGenSys-1 scheme is the direct application of the HyGenSys basic concept. Its optimisation focuses in particular on:

- The determination of the number of HyGenSys trains required to produce enough hydrogen fuel to feed the main gas turbine (SGT5-4000F).
- The optimisation of each HyGenSys train: hot gas generator selection, reactor-exchanger process specification, power recovery expander selection, heat recovery steam generation design.
- The study of the influence of the operating parameters, such as, the steam to carbon ratio and the dilution rate of the hydrogen fuel with steam.

Several simulation iterations integrating data from Siemens were necessary to determine the number of HyGenSys trains. The result is that three parallel HyGenSys trains are necessary: equipments that are implemented in parallel are represented with A/B/C in the scheme Figure 10.

When the steam to carbon ratio is increased, the HyGenSys-1 net efficiency logically decreases as the Medium Pressure Steam (MPS) is consumed by the process instead of being sent to steam turbines generating power. The net efficiency drops with about 3.5 points when steam over carbon increases from 2.5 to 5. The final choice considers a value of 2.7 which reflects an operational proven minimum value for natural gas steam reforming. This value prevents coking of the catalyst and metal dusting corrosion.

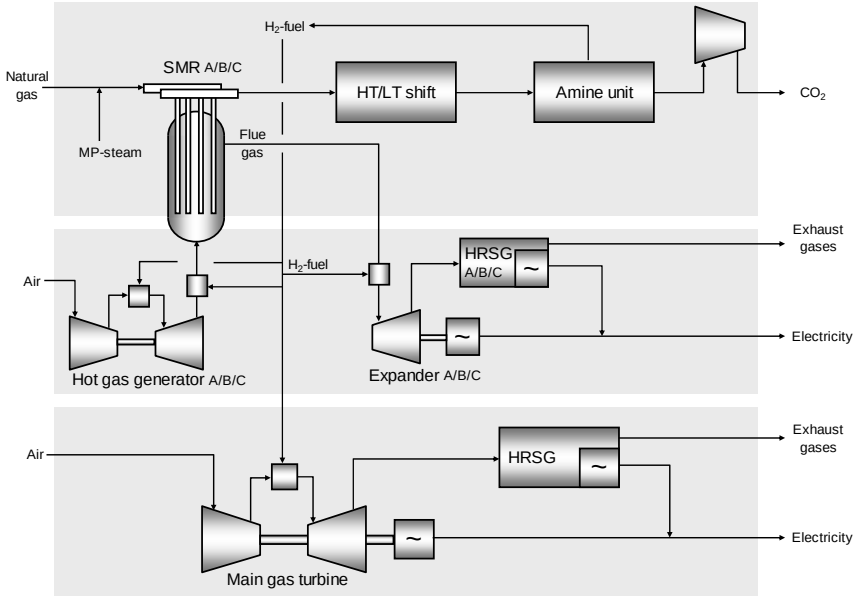

Figure 10. Schematic representation of HyGenSys-1.

The pressure of the SMR is derived from the required pressure of hydrogen rich fuel gas at the entrance of the combustion chamber of turbine (defined by gas turbine manufacturer) without recompression of hydrogen which is energy consuming and expensive.

The impact of hydrogen fuel dilution with steam is also investigated as the dilution is not favourable for the net efficiency of the global scheme. If technical developments are done on turbine burners' technology, a future dilution of 30%, instead of 50% as assumed at present, could increase the efficiency by 1.5 point.

For pressure drops reasons and so energy loss, the implementation of a common HRSG to treat the flue gases leaving the Fluid Catalytic Cracking FCC-kind expander and the large turbine was not feasible. Hence, a dedicated HRSG was used for each of them.

To summarize, HyGenSys-1 presented in Figure 10 consists mainly in a high thermal integration with:

- Three parallel HyGenSys heat-exchanger reactors, each one using a hot gas generator from Siemens (SGT-700) followed by an expander from Dresser-Rand (E-248) and a heat recovery steam generation system.
- The syngas is then treated in high and low temperature water gas shift reactors.
- The CO_2 is separated by an amine unit (activated MDEA) and compressed for storage.
- The hydrogen rich stream is partially used as fuel in a large turbine from Siemens SGT5-4000F (modified for hydrogen use), but also as feed for the different combustion chambers of the three parallel HyGenSys hot gas generators. Hydrogen-rich gas fuel is diluted with MP steam to respect a 50/50 mixture of fuel/inert at the turbine combustion chambers. This hydrogen dilution figure is coming from our Cachet partner Siemens. The idea is to use the existing gas turbine with minor modifications of the combustion chambers.

The CACHET objective of 400 MWe power generation is largely overreached with a total net power of 465.5 MWe (Table 3**)**. Compared with the CACHET base case the net power production is 27% higher. This is due to the additional power generated by expansion of the hot turbine exhaust gases leaving the flue gas side of the HyGenSys reactor.

This study shows that with HyGenSys-1 the efficiency is improved by about 8% compared to the base case. Nevertheless, it also shows a lower CO_2 capture rate and avoidance rate (78.2 % and 71.2 % respectively), which are below the CACHET target of 90%. These performances are mainly related to the fact that due to thermodynamic equilibrium, about 4 % of the methane remains in the syngas (which represent about 20% of the methane of the feed), and hence, at the amines unit outlet the H_2-rich fuel will also contain methane which is burned in the turbine combustion chamber with no CO_2 capture

From previous analysis two alternatives were investigated in order to improve the CO_2 capture rate:

- Increasing methane conversion thanks to a specific scheme considering a secondary reformer (ATR). This concept was named HyGenSys-2.
- Improving generated hydrogen's purity by adding a methane separation unit by adsorption with a recycle of the unconverted methane toward the SMR inlet. This option is called HyGenSys-3.

Potential of alternatives schemes HyGenSys-2 and HyGenSys-3

The HyGenSys-2 design differs from HyGenSys-1 in the use of an air-blown Auto Thermal Reforming within a specific scheme configuration for gas introduction, as illustrated in Figure 11.

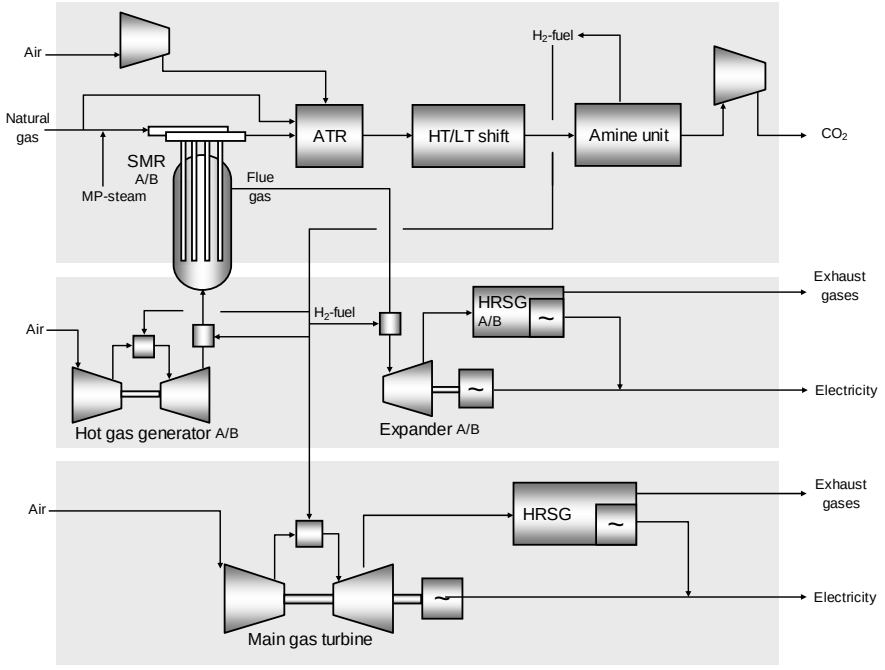

Figure 11. Schematic representation of HyGenSys-2.

After desulphurisation and preheating, the feed is split into three parts. Two parallel streams, corresponding to 65% of the total molar flow rate, are sent into two parallel HyGenSys reactor trains. The third stream bypasses the HyGenSys reactors; it is combined with the effluent of the HyGenSys reactor trains and is sent to the air-blown ATR reactor. The air is provided by a 3-stage electrical driven air compressor and adjusted in order to obtain 900°C at the outlet of the ATR (same value as in the base case). The reactor effluent is then cooled down to 385°C in a heat exchanger producing high-pressure steam. The design of the rest of the process is more or less identical to the HyGenSys-1 design.

Compared with HyGenSys-1, the net efficiency dropped from 44.1% to 42.1% (Table 3). The total cycle power of HyGenSys-2 is 14% higher, despite the fact that the design only uses 2 parallel reactor-expanders trains instead of 3 and the higher internal electricity consumption of the HyGenSys-2 process. The main reason for the higher total cycle power is that the steam cycle power almost doubled. This is primarily due to the lower steam dilution requirement for the hydrogen-rich fuel due to the presence of nitrogen, but also to higher steam production.

The total electricity consumption of the process increased significantly compared with the HyGenSys-1 design. This is due to the larger air and CO_2 compressor trains, because of the higher capture rate and natural gas import (8% higher).

The net power production of HyGenSys-2 is 481.4 MW, that is, 3% more than the HyGenSys-1 one. The CO_2 capture and avoidance rates improved considerably compared with HyGenSys-1, up to 93.4% and 91.1% respectively, which is better than the CACHET target of 90% capture rate.

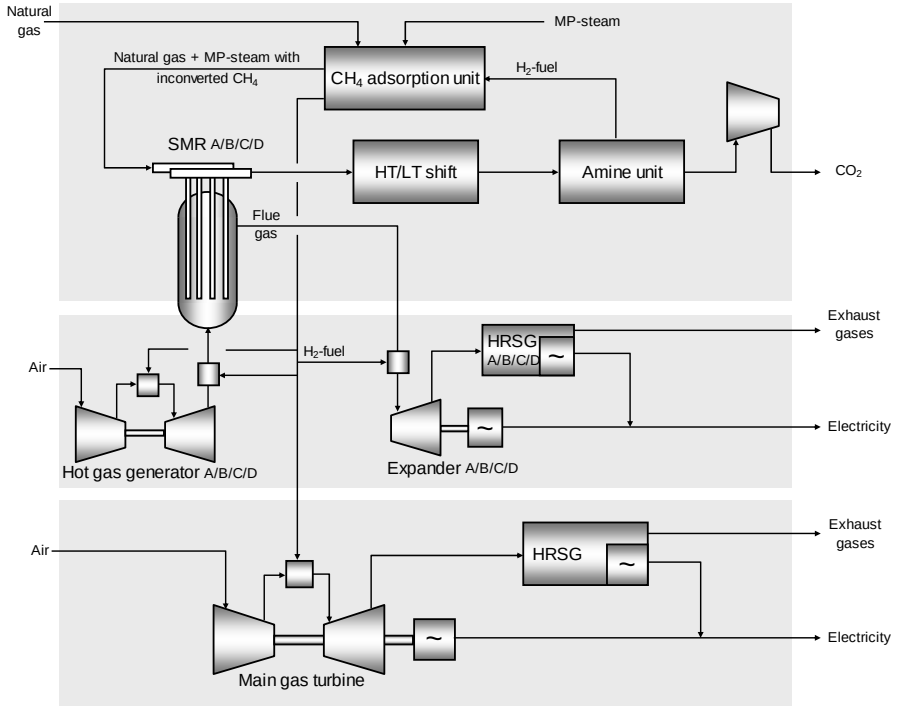

Figure 12. Schematic representation of HyGenSys-3.

The HyGenSys-3 scheme is based on HyGenSys-1 but includes an adsorption unit located downstream the amine unit (see Figure 12). The aim of this unit is to adsorb the unconverted methane in the steam methane reforming (SMR) in order to obtain methane-free hydrogen fuel. This hydrogen rich fuel diluted with steam feeds the combustion chambers of turbines SGT-700 and SGT5-4000F: the combustion of this gas will therefore be nearly free of CO_2.

The regeneration of the adsorbent is achieved by stripping with MP steam. The purge containing both the methane and the MP steam is recycled back to the SMR unit. The pressurization is obtained by using desulphurised natural gas which avoids the use of compressors and related energy consumption.

The key performance data of the Reference and Base Cases as well as HyGenSys-1, HyGenSys-2 and HyGenSys-3 are summarized in Table 3. The efficiency of HyGenSys-2 is in between the Base Case and HyGenSys-1, which is logical because the HyGenSys-2 design is a combination of both.

HyGenSys-3 results indicate a very high CO_2 avoidance rate (97.4%), but the efficiency dropped to 40.6%. On top of that, the higher methane conversion requires a higher heat flux and therefore this configuration would require four instead of three parallel HyGenSys trains. In combination with the additional methane adsorption unit, this results in substantially higher cost than HyGenSys-1 and HyGenSys-2. A discussion on the trade off between efficiency, CO_2 avoidance rates and cost is given in [7].

In conclusion, the alternative HyGenSys-2 is chosen in order to offer the best compromise between high performance and reduced cost.

Risk and reliability analyses were applied to the HyGenSys concepts in order to review and adjust the design.

Table 3: Key performance data of HyGenSys alternative cases compared with the Base Case and the Reference Case.

	Reference Case	Base Case	HyGenSys-1	HyGenSys-2	HyGenSys-3
H_2 production	no	ATR	SMR	SMR+ATR	SMR
Capture CO_2	no	yes	yes	yes	yes
Total net power output (MW)	389.8	365.6	465.6	481.4	484
Overall efficiency	57.2	40.9	44.1	42.1	40.6
CO_2 capture rate (%)	0.0	94.7	78.2	93.4	98.1
CO_2 avoidance rate (%)	0.0	92.6	71.2	91.1	97.4
CO_2 captured cost, €/ton		82.1	83.9	77.1	n.a
CO_2 avoided cost, €/ton		117.5	118.4	107.9	n.a
Cost of Electricity, €/MWh	47.5	86.6	78.0	82.7	n.a

CONCLUSION

Thanks to a strong cooperation between all the partners with multidisciplinary skills, this three years work results in major developments covering all aspects of a new advanced SMR. The main efforts concern: process study, turbine selection, reactor development, modelling and mechanical concept, cold mock-up for catalyst loading and un-loading testing, materials study, risk and reliability analysis.

This study demonstrates the feasibility of a new Steam Methane Reforming concept, HyGenSys, which is a promising process for conversion of gas into hydrogen and power with reduced carbon emissions.

ACKNOWLEDGEMENTS

The authors thank and acknowledge the European Commission (project no 019972) and every one of the 28 partners in the consortium [6] and especially to BP, NTUA, Technip and SIEMENS for their contribution in HyGenSys development in general and the risk and reliability analyses in particular. The authors acknowledge the support of the CO_2 Capture Project Phase 2 (CCP2) to CACHET

REFERENCES

1. Rojey A.,Minkkinen A., Arlie J.P, E.Lebas, (2003) *Combined Production of Hydrogen, Clean Power and Quality Fuels* In : *DGMK-Conference, Innovation in the Manufacture and Use of Hydrogen* proceedings, pp 102-114.
2. Giroudière Fabrice-CACHET-Hydrogen Generation System (HyGenSys) presentation. European Conference on CCS Research, Development and Demonstration, public workshop Oslo 2009-02-11.
3. Ib Dybkjaer, S.Winter, *Compact hydrogen plants*, Hydrocarbon Engineering Nov. 2004
4. WO 2009/024664 A1, Giroudière Fabrice *et al*.
5. Beavis, R., 2009. Introduction to CACHET, a pre-combustion technology development program co-funded by the EU and CCP, In Eide. L.I., 2009 Carbon Dioxide Capture for Storage in deep geological Formations, Volume 3. CPL Press.
6. Project CACHET partners: http://www.cachetco2.eu/partners.html
7. Melien, T. and S. Brown-Roijen, 2009. Economics. In Eide. L.I., 2009, Carbon Dioxide Capture for Storage in deep geological Formations, Volume 3. CPL Press.

Carbon Dioxide Capture for Storage in Deep Geologic Formations, Volume 3
L.I. Eide (Ed.)

Chapter 17

ECONOMICS

Torgeir Melien[1]* and Stefanie Brown-Roijen[2]**
[1]StatoilHydro, Oslo, Norway
[2]Shell, Houston, TX, USA

ABSTRACT: A main objective for the CO_2 Capture Project (CCP) is to identify and develop cost-efficient technologies to capture CO_2 from hydrocarbon processing plants. In the second phase of the project (CCP2) carried out between 2006 and 2008, the work focused on technologies applied to gas-fired power plants and refineries. As part of the project, external technology providers have delivered technology designs and solutions for several options and applications. Many of these were initiated and studied in phase 1 (2000-2004) of the program, whereas other technologies were included during the second phase. This chapter summarizes the cost estimation and the economic evaluation exercises on CO_2-capture technologies studied in CCP during the 2006-2008 period. The capture technologies are integrated, estimated and comparatively evaluated within the selected gas power plant and refinery scenarios as relevant industrial applications for the CCP-partner companies. The CCP-focus is technology R&D and comparison of developing technologies at different states of maturity. Near-term project realization is outside the scope of CCP2. Furthermore, evaluations are limited to CO_2-capture, and do not include the transport and storage part of a full CO_2-chain. Current CO_2-cost estimates mainly confirm the results for technologies pursued from the first phase of the program. Although new capture systems were introduced in phase 2, technologies further carried forward from phase 1, are still attractive.

PART I: GENERAL APPROACH

Introduction

CCP2 is a continuation of the CCP1-program carried out during the years 2000-2004. Several technologies from CCP1 were carried forward through CCP2 together with new technologies for CCGT gas power plant and refinery units' applications.

CCP2 incorporates an "umbrella" of capture technology sub-programmes with different funding sources;

- the EU Cachet program, focusing on pre-combustion capture from gas-fired power plants
- the Norwegian Research Council's Climit program, sponsoring pre- and post-combustion capture systems applied to gas-fired power plants
- CCP-partner's own funding, sponsoring additional capture studies applied to refinery heaters, boilers and FCC-units.

This chapter reports the comparative cost studies and economics for a selection of capture technologies for power plant and refinery applications, studied in these sub-programs.

*Responsible for Parts I and II
** Responsible for Parts III and IV

This chapter is split in three main parts. The first part outlines the main approach to the cost estimation and economic screening work. The second part summarizes the basic cost, performance and economic key data for the capture technologies applied to gas power plants. The last two parts provide similar summaries for capture technologies applied in refinery units.

The technical outline and descriptions of the capture technologies evaluated here, are given in [1], while the corresponding detailed cost estimate basis and breakdown is documented in [2].

Scenario-technology matrix

The capture technologies are developed and evaluated in the context of specific applications; capturing CO_2 from gas power plants, refinery emission sources, gasification units, etc. In CCP1, four main application scenarios were established:

- Combined Cycle Gas Turbine (CCGT) power plant in Norway
- Refinery heaters and boilers in the UK
- A coke gasification plant in Canada
- Distributed small gas turbines in Alaska

In CCP2 the following application scenarios are used as a basis for capture technology evaluations:

- Gas-fired power plant at a generic NorthWest-European (NWE) brown-site (generalized CCP1 scenario)
- Refinery heaters and boilers in the UK (CCP1 update)
- A refinery Fluid catalytic Cracker (FCC) unit in Brazil (new CCP2 scenario)

Table 1 summarizes the CCP1 and CCP2 application scenarios and activity.

Table 1. CCP1-2 application scenarios and activity.

CCP Scenarios	CCP1	CCP2	Cases	Main purpose
CCGT; Gas Power plant	Yes	CCP1-update	A-cases	2003 technical concept; pure 2003 -> 2008 cost escalation
CCGT; Gas Power plant		CCP2-developments	B-cases	2008 technical concept, 2008 cost estimates
Refinery Heather & Boiler retrofit	Yes	CCP1-update	C-cases	2003 technical concept; pure 2003 -> 2008 cost escalation
Refinery Heather & Boiler retrofit		CCP2-developments	D-cases	2008 technical concept, 2008 cost estimates
Refinery Single Boiler	No		E-cases	
Refinery Single Boiler		CCP2-developments	F-cases	2008 technical concept, 2008 cost estimates
Refinery FCC unit	No		G-cases	
Refinery FCC unit		CCP2-developments	H-cases	2008 technical concept, 2008 cost estimates
Coke gasification	Yes	No update	I-cases	
Coke gasification		No activity	J-cases	
Small gas turbines	Yes	No update	K-cases	
Small gas turbines		No activity	L-cases	

The individual capture technologies have been explored through a set of external technology provider-studies both during CCP1 and CCP2. The output from these studies has been aligned, cost estimated and economically compared in CCP. In CCP2 the work has been supported by the contracted process plant and cost estimator consultants; Teltek (Telemark Technology Center, Norway) and PDC (Process Design Center, Germany/ Netherlands). As in CCP1, TelTek acts as the main provider of cost estimates in this report. PDC has mainly been involved in estimating equipment and process costs for the EU Cachet-program, but has also estimated and verified selected technologies in the CCP2-program.

As indicated, the final CCP2-evaluation includes both updated cost estimates of the previous CCP1-technologies and a new set of estimates for the advanced and new capture technology concepts in CCP2. The cost update of the capture technologies from CCP1 pursued in CCP2 enables measurement of the progress in technical designs and performances for these technologies. Other capture technologies and variants have their first-time CCP-evaluation in phase 2.

Cost Estimation

In light of the scenario-technology matrix outlined above, the following describes the approach for the cost estimation.

Cost estimate scope

CO_2-chain; covering the CO_2 capture systems and CO_2-compression, but excl. CO_2-transport and storage

- In the gas power scenario, the cost of the CCGT power plant itself is part of the estimated scope, whereas in the refinery scenarios, the estimates basically cover the additional capture systems
- New-built plants are assumed; both for power and capture plants in the gas power scenario and the capture systems for the refinery applications.
- Plant location at industrialised site (e.g. NW-Europe for the gas power plant); assuming easy access to all necessary suppliers and delivery markets
- Capex vs. opex trade-off; basic power plant and capture systems are capex estimated, whereas all operating utility needs are opex estimated
- CO_2 capture systems include any pre-treatment, compression, additional separation/purification (if required), drying and pumping. Utility systems unique to the CO_2 separation plant are included. (i.e. oxygen plant, auxiliary steam plant, natural gas or exhaust gas purification plant etc.)

Capex estimate

The basic task in estimating plant construction costs, is to define the physical scope of the plant covering the required equipment, materials and labour, and cost these supplies with the corresponding prices and rates, to provide a complete cost estimate for the plant. The capex estimation work typically contains two main stages;

- To establish the cost estimates of the primary equipment required for CO_2 capture and processing
- To add the installation and indirect site costs necessary to establish the total cost of a complete, operative plant.

For the power plant scenario a reference document was established to provide the basic approaches and assumptions for this work [3]

Equipment costs are typically collected based on international market price trends, whereas the additional installation and completion costs are estimated by factorization methods. The sources of equipment cost data are either technology provider estimates/ quotes, or CCP/TelTek estimates produced by their estimation model (Aspen-IPM v.2006.5 software model) based on provided equipment lists. TelTek's estimation process is described in [3], and their CCP2 capex estimates and breakdowns are documented in [2], where the sum of

- equipment costs
- installation costs
- engineering and management overheads
- commissioning expenses
- and contingencies

provide the expected capex estimates applied in the economic screening of CCP2 capture technologies.

With its focus on R&D and capture technology comparison, the CCP capex estimates primarily include the basic capture processing systems, while the extent of upfront site and infrastructure costs, typically identified in site-specific realisation projects, is minimized here.

CCP2-cost estimates are referring to the actual mid-2008 supplier prices, when energy and supplier markets reached historic levels, hitting a record high of almost 150 USD/bbl for crude oil. In the economic screening exercises reported below, a sensitivity of 10% reduction in cost levels is also included, to reflect an indicated "normal" 2008-price level according to historic price trends. CCP2's NWE generic prices are regarded to be at the same level as US Gulf Coast-prices.

Technology maturity

The capture technologies addressed in CCP have different maturity levels; some are currently proven, though often accomplished on a smaller scale than necessary for industrial application. Others are early stage concepts and may require a long maturing and testing phase.

However, in CCP the basic comparison is made under the assumption that all technologies have reached the same maturity stage. R&D budgets and -time are disregarded, and cost contingencies are assumed to be the same (+20%) for all technologies. It is also assumed that early implementation problems are resolved, and capture systems are cost estimated as if they were well matured and commercialized technologies.

Alignment of cost estimates

The main challenge in R&D programs such as CCP, to establish cost and performance estimates enabling consistent and aligned techno-economic comparison of various technologies, should not be under-estimated. This can include alignment of primary technical assumptions, overall physical scopes and cost estimating methods and assumptions, across all the information delivered by the various technology providers. The process is illustrated in Figure 1.

Transforming a multitude of individual Technology studies into a comparable and quantified set of Scen-Tech options

- Integrating capture technologies into scenarios
- Calibrating physical scopes and capacities
- Capex vs. opex tradeoffs
- Capex & opex estimation methods and assumptions
- Consistent CO2-cost evaluation

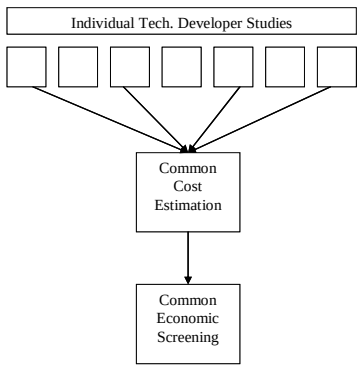

Figure 1. Alignment for comparative cost estimation and screening.

The current update of previous CCP1 estimates from 2003 ("A-cases") is a pure cost update based on the initial CCP1 designs and technical parameters. The CCP1 equipment costs, as estimated in 2003, are escalated to 2008 price levels by applying published processing plant cost indices, before computation of the Total Installed Costs by applying current factorizing assumptions. The updated and further developed technology designs for the "B-cases" are priced based on a full, bottom-up equipment/ total installed cost estimate process. Figure 2 illustrate the working process applied by TelTek, further described in [2].

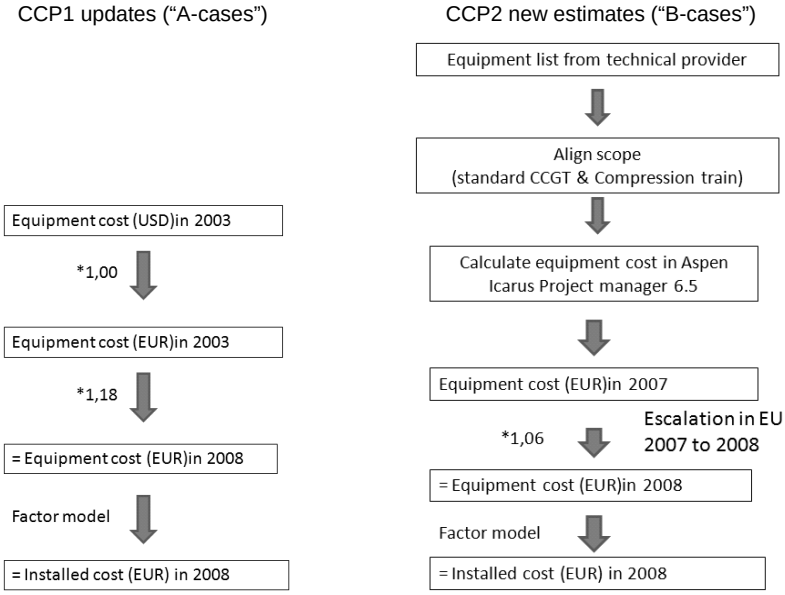

Figure 2. Main cost estimation process.

Operating cost

Based on the defined needs for plant operations in quantitative terms, regarding:

- operational manning
- operations and maintenance activity
- chemicals and utilities supplies

and a list of corresponding purchase prices and unit rates, annual operational (fixed and variable) costs are established by TelTek for the total plant and capture systems.

Economic screening

Key metrics

The economic screening of capture technologies is based on standard "Cost of Electricity" (COE)- and "CO_2 avoided cost" metrics calculated across the technology alternatives for each application scenario, as in CCP1 [4].

These calculations are based on aligned and standardised estimates and assumptions on technology process performance (energy efficiency, CO_2-generation and capture rates) and cost estimates (capex, O&M (operations and maintenance), fuel), and a set of general price and rate of return assumptions. All CCP2 calculations are furthermore carried out at:

- normalised, per unit (kWh) output from the base industrial (power) plant
- pretax, pre-financing basis
- annual cost basis, applying a capital charge factor corresponding to a standard discount factor and project time horizon.

Cost of electricity is calculated according to the formula:

$$COE = \frac{\left(accum.capex * capital\ charge\ factor + annual\ O\ \&\ M\ -\ cost + annual\ fuel\ cost\right)}{annual\ net\ power\ output}$$

Equation 1

CO_2 avoided cost is calculated according to the formula:

$$CO_{2-AC} = \frac{COE_{cap} - COE_{nocap}}{CO_2 / kWh_{nocap} - CO_2 / kWh_{cap}}$$

Equation 2

where:

$CO_{2\text{-}AC}$ = CO_2 avoided cost (EUR/t CO_2)

COE_{cap} / COE_{nocap} = Cost of Electricity for power plant with/ without CO_2 capture (EUR/MWh)

CO_2/kWh_{cap} / CO_2/kWh_{nocap} = CO_2-emission per KWh net output from power plant with/ without CO_2 capture

Regarding these metrics, it should be noted that:

- COE-levels are calculated both with and without the CO_2-emission cost. Equation 2 applies the COE without CO_2-emission cost
- The calculated CO_2-avoided cost implicitly accounts for the capture systems' own energy demand and its inherent CO_2-emissions
- For non-power or multi-product output plants, the standard COE-calculations may have to be substituted by transformed or aggregate product output measures for $CO_{2\text{-}AC}$ plant size normalization purposes
- The natural benchmarks for the calculated plant-technology COEs and $CO_{2\text{-}AC}$s in these evaluations are the corresponding market prices (national/ international) for power and CO_2 emission costs (emission quota prices or CO_2-taxes). Plant-technology COEs and $CO_{2\text{-}AC}$s lower than corresponding market prices indicate economic potentials at current price expectations, and vice versa.

Price assumptions

The final CCP2 economic evaluations for all cases (both updated, previous CCP1- and new CCP2-cases) are carried out using the set of long-term price level assumptions, energy conversion factors, discount rates and capital charges given in Table 2.

Table 2. General economic assumptions.

General assumptions		CCP2 2008
Fuel gas price	EUR/ MWh	15,0
	EUR/ GJ	4,17
	USD/mBtu	6,40
	NOK/Sm3	1,33
CO2 emission cost	EUR/tCO2	20
	USD/tCO2	29
	NOK/tCO2	160
Gas conversion	MWh/MMbtu	3,41
	kWh/Sm3 gas	11,1
	GJ/ MWh	3,6
	MJ/ Sm3	40
Exchange rates	NOK/USD	5,50
	NOK/EUR	8,00
	USD/EUR	1,45
Discount factor, real, pretax		10,00 %
Time horizon		25
Capital Charge factor		11,02 %

PART II: POWER SCENARIO

Scenario outline

CCGT gas power plant

This scenario has a standard 400 MW combined cycle gas turbine (CCGT) power plant as its underlying CO_2-emitting source. The reference CCGT-plant without CO_2 capture ("CCGT uncontrolled") is producing electric power at an overall efficiency of 58%.

Capture part of the CO_2-chain

The power scenario outlined in [3] for the CCP2-evaluations includes the power plant itself, the CO_2-capture process and necessary systems enabling delivery of export power and compressed CO_2 A full CO_2-delivery chain including transport and final delivery of CO_2 at a storage site or to a CO_2-EOR customer is outside the scope of these studies. The "baseline" for cost benchmarking of developing capture technologies is a CCGT power plant with a current state MEA-amine post-combustion capture system.

New-built plants

All power and advanced capture process systems are assumed new-built, providing maximum design and integration flexibility, and minimum restrictions from existing plant configurations, thereby enforcing focus on primary capture technology R&D. Implementing CO_2 capture systems in existing plants through retrofit projects should be evaluated additionally on a case-by-case basis.

The technical design basis for the amine baseline applied here (established in CCP1 before 2003) has however a design without a fully optimized integration with the basic CCGT power plant. The baseline cost and performance may thus be somewhat higher than an optimally integrated power plant with amine CO_2-capture.

Generic, brown-site location

The plant is assumed located at a non-specified NW European site with easy access to competitive markets and necessary supplies of:

- plant engineering and local construction capacities
- fuel gas
- other essential utility and supply requirements during construction and operations
- labour forces during construction and operations
- power export grid
- CO_2 storage options (storage sites and CO_2-EOR customers) within reasonable distance.

On the power side, it is assumed that all electricity consumed by the capture, compression and utility systems is supplied by the power plant itself.

All in all, these assumptions should enforce the focus on capture technologies both in the primary R&D-program and in cost estimation and technology screening, rather than the site and infrastructure development requirements emerging at specific locations.

Scenario-Technology Matrix

The capture technologies specifically applicable to the gas power scenario on which this chapter of the study reports, are listed in Table 3. They include the updated CCP1 ("A"-cases), and the new CCP2 ("B"-cases):

Table 3. Scenario-Technology matrix – CCGT scenario

CCP Scenarios	Cases	Sub-program		Capture	Technology Provider	Short-name
CCGT; 400 MW Gas Power plant	A1	CCP1 & 2	Reference without capture	No	Hydro	Uncontrol (2003)
	A2	CCP1 & 2	Amine Baseline	Postcomb	Fluor/ Hydro	MEA Amine Climit BL (2003)
	A3	CCP1 & 2	Amine Low Cost Nexant concept	Postcomb	Nexant	Nex.LowCost-MEA (2003)
	A4	CCP1 & 2	Amine Low Cost Integrated Nexant concept	Postcomb	Nexant	Nex.LowCostInt-MEA (2003)
	A5	CCP1 & 2	Best Integrated Technology, 50% Exhaust Gas Recycling, KS1-absorbent	Postcomb	Nexant	BIT-50%EGR-KS1(2003)
	A6	CCP1 & 2	Hydrogen Membrane Reforming (3-stage)	Precomb	Hydro	HMR-3stg (2003)
	A7	CCP1 & 2	Sorption Water Gas Shift, Airblown Auto Termal Reforming	Precomb	Air Products	SEWGS-AirATR (2003)
	B1	CCP2	Reference without capture	No	StatoilHydro/ Nexant	Uncontrol (2008)
	B2	CCP2	Amine Baseline	Postcomb	Nexant	MEA Amine Climit BL (2008)
	B3	CCP2	Best (heat) Unintegrated Technology, no Exhaust Gas Recycling, MEA-absorbent	Postcomb	GE/ Nexant	BUT (2008), noEGR-MEA
	B4	CCP2	Best (heat) Unintegrated Technology, 40% Exhaust Gas Recycling, MEA-absorbent	Postcomb	GE/ Nexant	BUT (2008), 40%EGR-MEA
	B5	CCP2	Best (heat) Integrated Technology, 40% Exhaust Gas Recycling, MEA-absorbent	Postcomb	GE/ Nexant	BIT (2008), 40%EGR-MEA
	B6	CCP2	Hydrogen Membrane Reforming (1-stage)	Precomb	StatoilHydro	HMR-1stg (2008)
	B7	CCP2	Hydrogen Membrane Reforming (1-stage) w/ Gas Heat Reformer	Precomb	StatoilHydro	HMR-1stg & GHR (2008)
	B8	Cachet	Cachet Baseline, AutoThermalReforming	Precomb	PDC	ATR-BL (2008)
	B9	Cachet	Sorption Water Gas Shift, Airblown Auto Thermal Reforming	Precomb	PDC	SEWGS-AirATR (2008)
	B10	Cachet	Membrane Water Gas Shift	Precomb	PDC	MWGS (2008)

Performance and capex estimates

An aligned set of key performance and cost data for the power for the following results:

- specific capex; total power and capture plant capex per kW installed
- energy efficiency; net power output in percent of fuel gas input (LHV-basis)
- CO_2 capture rate; CO_2 captured in percent of CO_2-generated.

is illustrated in Figures 3 – 5.

Cost estimate details for each technology are reported in [2].

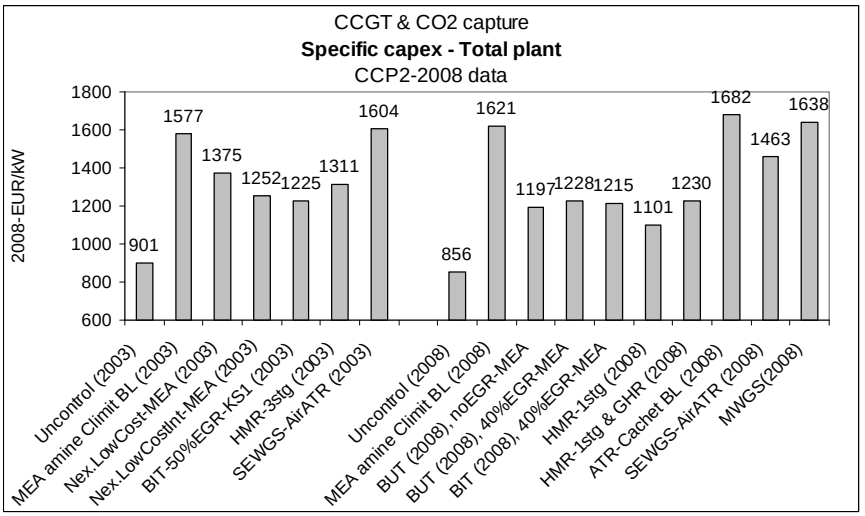

Figure 3. Specific Capex, Power plus Capture Plant, A- and B-cases.

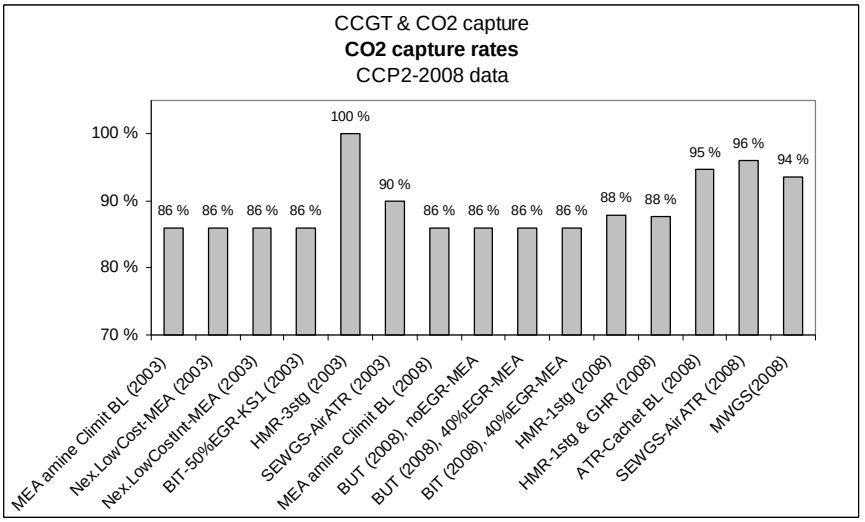

Figure 4. CO_2 capture rates, A- and B-cases.

Some observations that can be made for Figures 3-5 are summarized in Table 4 regarding CCP1 (2003->2008 escalated estimate) -> CCP2 (2008-new estimate) developments for the capture technologies included in both phases of CCP.

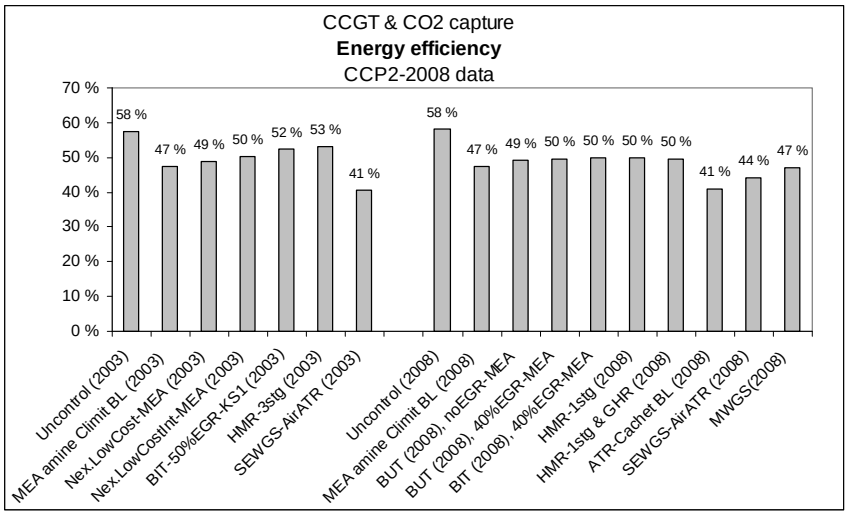

Figure 5. Energy efficiency, A- and B-cases.

Table 4. CCP1-> CCP2 developments, selected CCGT cases.

A-case; CCP1 design basis, updated/ escalated cost estimate	B-case; CCP2 design basis, new cost estimate	Specific capex; EUR'08/kW	Energy Efficiency	CO_2 capture rate	Comments
A1) Uncontrol (2003)	B1) Uncontrol (2008)	901 -> 856	58 %	0 %	
A2) Amine Baseline	B2) Amine Baseline	1577 -> 1621	47 %	86 %	
A3) Nex.LowCost-MEA (2003)	B3) BUT (2008), noEGR-MEA	1375 -> 1197	49 %	86 %	
A4) Nex.LowCostInt-MEA (2003)	B4) BUT (2008), 40%EGR-MEA	1252 -> 1228	50 %	86 %	
A5) BIT-50%EGR-KS1(2003)	B5) BIT (2008), 40%EGR-MEA	1225 -> 1215	52,5 -> 50%	86 %	CCP1; KS1 -> CCP2; MEA
A6) HMR-3stg (2003)	B6) HMR-1stg (2008)	1311 -> 1101	53 -> 50%	100 -> 88%	Revised concept
A6) HMR-3stg (2003)	B7) HMR-1stg & GHR (2008)	1311 -> 1230	53 -> 50%	100 -> 88%	As B6), incl Gas Heat Reformer
A7) SEWGS-AirATR (2003)	B9) SEWGS-AirATR (2008)	1604 -> 1463	41 -> 44%	90 -> 96%	Improved concept

Economic Screening

Main results and findings

The final economics for the capture technologies applied to the 400 MW CCGT power plant, are measured in terms of COE (Cost of Electricity generated) and CO_2 avoided cost based on the:

- energy efficiency, CO_2 capture rates and capex estimates, shown in Figures 3-5, as well as in Tables 5 and 6
- estimated capex, fixed and variable O&M-costs, documented in [2]
- fuel consumption, established from performance data, documented in [2]
- fuel gas price and CO_2 emission cost, as given in Table 2
- a common annual load factor of 95%, corresponding to 8322 hrs/yr, as applied in the CCP1- power scenario.

The main input data and resulting key metrics are given in Table 5 and 6 for the A- and B-powergen cases, respectively.

Table 5. Summary inputs and results - CCP1 updated technologies (A-cases).

Scenario-Technology case		A1	A2	A3	A4	A5	A6	A7
	Units	CCGT Ref case Uncontrol (2003)	CCGT w/Capt Post BL MEA amine Climit BL (2003)	CCGT w/Capt Post BL Nex.LowCost-MEA (2003)	CCGT w/Capt Post BL Nex.LowCostInt-MEA (2003)	CCGT w/Capt Adv.tech BIT-50%EGR-KS1 (2003)	CCGT w/Capt Adv.tech HMR-3stg (2003)	CCGT w/Capt Adv.tech SEWGS-AirATR (2003)
Net power out	MW	392	323	332	343	357	361	358
Fuel consumption	MW	681	681	681	681	681	681	880
Efficiency	pct	**57,6 %**	**47,4 %**	**48,8 %**	**50,4 %**	**52,5 %**	**53,0 %**	**40,7 %**
Total capex	MEUR 08	**353,3**	**509,1**	**456,5**	**429,6**	**437,5**	**473,2**	**574,6**
Specific capex	EUR/kW net	**901**	**1577**	**1375**	**1252**	**1225**	**1311**	**1604**
O&M total	MEUR/yr	**14,8**	**29,1**	**26,8**	**25,9**	**23,8**	**20,6**	**25,1**
Fuel cost	MEUR/yr	**85**	**85**	**85**	**85**	**85**	**85**	**110**
CO2-capture	pct	0 %	86 %	86 %	86 %	86 %	100 %	90 %
	mton/yr	0,00	1,05	1,05	1,05	1,05	1,22	1,41
CO2 emission	mton/yr	**1,22**	**0,17**	**0,17**	**0,17**	**0,17**	**0,00**	**0,16**
	kg/kWh	0,37	0,06	0,06	0,06	0,06	0,00	0,05
CO2 avoidance rate	pct		83,0 %	83,5 %	84,0 %	84,6 %	100,0 %	85,7 %
COE excl CO2 emiss.cost	EUR/MWh	**42,5**	**63,4**	**58,7**	**55,4**	**52,8**	**52,5**	**66,5**
COE incl CO2 emiss.cost	EUR/MWh	**50,0**	**64,6**	**59,9**	**56,6**	**53,9**	**52,5**	**67,6**
CO2 avoided cost	EUR/tCO2		**67,4**	**51,9**	**41,2**	**32,6**	**26,8**	**75,1**
	% ch rel to Amine BL			**-23 %**	**-39 %**	**-52 %**	**-60 %**	**11 %**
COE excl CO2 emiss.cost	USD/MWh	**61,8**	**92,1**	**85,3**	**80,6**	**76,8**	**76,4**	**96,7**
COE incl CO2 emiss.cost	USD/MWh	**72,7**	**94,0**	**87,1**	**82,4**	**78,5**	**76,4**	**98,3**
CO2 avoided cost	USD/tCO2		**98,0**	**75,5**	**60,0**	**47,4**	**39,0**	**109,2**

Table 6. Summary inputs and results - CCP2 technologies (B-cases)

Scenario-Technology case		B1	B2	B3	B4	B5	B6	B7	B8	B9	B10
	Units	CCGT Ref case Uncontrol (2008)	CCGT w/Capt Post BL MEA amine Climit BL (2008)	CCGT w/Capt Adv.tech BUT (2008), noEGR-MEA	CCGT w/Capt Adv.tech BUT (2008), 40%EGR-MEA	CCGT w/Capt Adv.tech BIT (2008), 40%EGR-MEA	CCGT w/Capt Adv.tech HMR-1stg (2008)	CCGT w/Capt Adv.tech HMR-1stg & GHR (2008)	CCGT w/Capt Pre BL ATR-Cachet BL (2008)	CCGT w/Capt Adv.tech SEWGS-AirATR (2008)	CCGT w/Capt Adv.tech MWGS(2008)
Net power out	MW	395	322	367	360	361	373	379	366	367	392
Fuel consumption	MW	681	681	745	725	726	745	763	895	828	832
Efficiency	pct	**57,99 %**	**47,28 %**	**49,26 %**	**49,66 %**	**49,72 %**	**50,07 %**	**49,67 %**	**40,89 %**	**44,30 %**	**47,10 %**
Total capex	MEUR 08	**338,2**	**521,9**	**439,2**	**442,0**	**438,5**	**410,7**	**466,1**	**615,6**	**536,7**	**642,0**
Specific capex	EUR/kW net	**856**	**1621**	**1197**	**1228**	**1215**	**1101**	**1230**	**1682**	**1463**	**1638**
O&M total	MEUR/yr	**17,2**	**32,6**	**35,7**	**34,5**	**32,6**	**20,7**	**22,9**	**29,0**	**28,6**	**36,4**
Fuel cost	MEUR/yr	**85**	**85**	**93**	**90**	**91**	**93**	**95**	**112**	**103**	**104**
CO2-capture	pct	0,0 %	86,0 %	86,0 %	86,0 %	86,0 %	87,9 %	87,7 %	94,8 %	96,0 %	93,5 %
	mton/yr	0,000	1,045	1,144	1,113	1,114	1,169	1,194	1,514	1,419	1,389
CO2 emission	mton/yr	**1,22**	**0,17**	**0,19**	**0,18**	**0,18**	**0,16**	**0,17**	**0,08**	**0,06**	**0,10**
	kg/kWh	0,37	0,06	0,06	0,06	0,06	0,05	0,05	0,03	0,02	0,03
CO2 avoidance rate	pct		82,8 %	83,5 %	83,7 %	83,7 %	86,0 %	85,6 %	92,6 %	94,8 %	92,0 %
COE excl CO2 emiss.cost	EUR/MWh	**42,4**	**65,3**	**58,0**	**58,0**	**57,1**	**51,2**	**53,7**	**68,5**	**62,6**	**64,7**
COE incl CO2 emiss.cost	EUR/MWh	**49,8**	**66,6**	**59,2**	**59,18**	**58,3**	**52,2**	**54,8**	**69,0**	**63,0**	**65,3**
CO2 avoided cost	EUR/tCO2		**74,7**	**50,4**	**50,2**	**47,4**	**27,6**	**35,7**	**76,0**	**57,5**	**65,4**
	% ch rel to Amine BL			**-33 %**	**-33 %**	**-37 %**	**-63 %**	**-52 %**	**2 %**	**-23 %**	**-12 %**
COE excl CO2 emiss.cost	USD/MWh	**61,7**	**95,0**	**84,4**	**84,3**	**83,1**	**74,5**	**78,2**	**99,6**	**91,0**	**94,1**
COE incl CO2 emiss.cost	USD/MWh	**72,5**	**96,9**	**86,1**	**86,1**	**84,8**	**76,0**	**79,7**	**100,4**	**91,6**	**95,0**
CO2 avoided cost	USD/tCO2		**108,7**	**73,2**	**73,1**	**68,9**	**40,1**	**51,9**	**110,5**	**83,7**	**95,1**

The key COE and CO_2-$_{AC}$ metrics and breakdowns are illustrated in Figures 6 and 7.

From the CCP2 economic evaluations of capture technologies applied to CCGT gas power plants, the following main conclusions can be drawn:

- CCP2 confirms CCP1 CO_2-avoided cost ($CO_{2\text{-}AC}$) levels;
  a. CCP1 technologies update ("A-cases"): 27-75 EUR/ tCO_2
  b. CCP2 technologies ("B-cases"): 28-76 EUR/tCO_2

- Power generation cost (COE) levels excluding CO_2-emission cost for CCP2 technologies are estimated at the following levels:
  a. CCGT no capture: 42 EUR/MWh
  b. CCGT w/amine baseline capture: 65 EUR/MWh
  c. CCGT w/advanced technologies (ex. ATR-BL): 51-65 EUR/MWh
  d. i.e. additional capture-generated COE from: 9-23 EUR/MWh

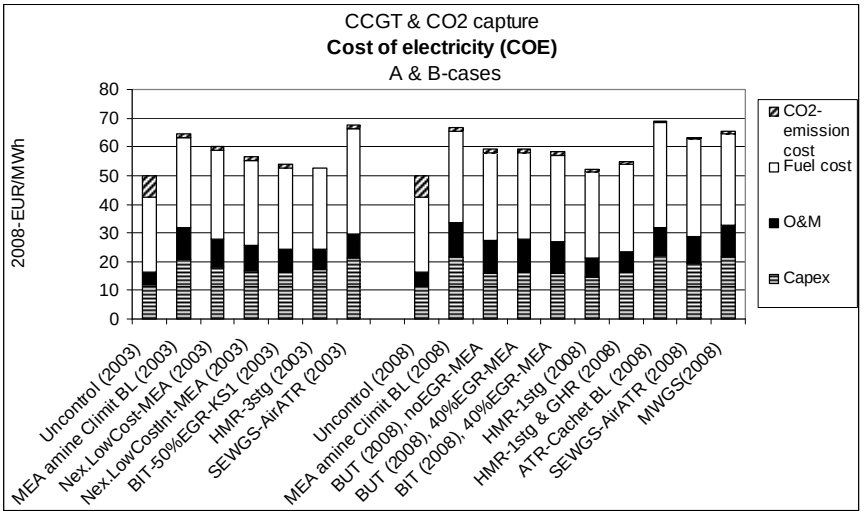

Figure 6. Cost of Electricity, CCGT Power Scenario; A- and B-cases.

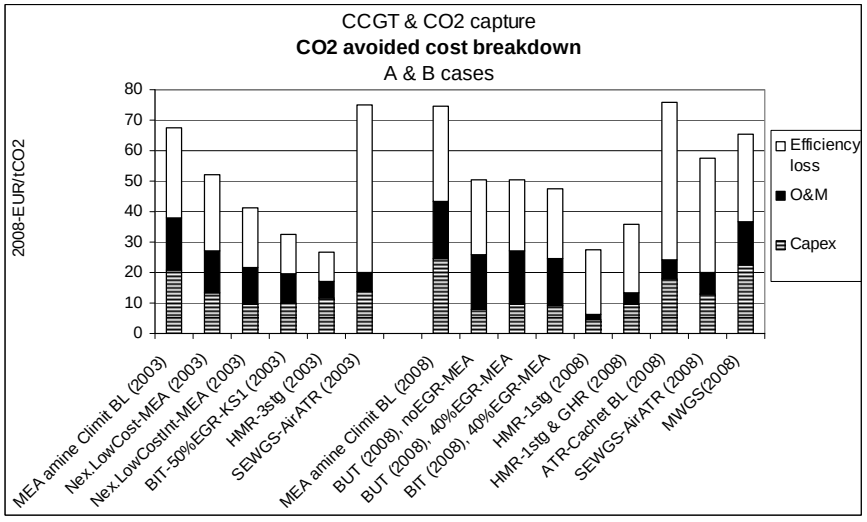

Figure 7. CO_2 avoided cost, CCGT Power Scenario; A- and B-cases.

- Power generation cost (COE) levels including the 20 EUR/ton CO_2-emission cost (the relevant, stand-alone COE-metric) for CCP2 technologies are estimated at the following levels:
  a. CCGT no capture: 50 EUR/MWh
  b. CCGT w/amine baseline capture: 67 EUR/MWh
  c. CCGT w/advanced technologies (ex. ATR-BL): 52-65EUR/MWh
  d. i.e. additional capture-generated COE from: 2-15 EUR/MWh

- The current amine baseline technology applied here is basically established before 2003 during CCP1. General technology developments since 2003 have obviously also improved amine capture systems. If regarding the "BUT-2008-noEGR-MEA"-case as a cost-updated "2008 state of art" baseline, only the HMR and BIT-cases demonstrate CO_2 avoided cost levels below this adjusted baseline reference.

Most industrial supplier markets, also those relevant to capture processing plants, have experienced significant price increases over the last 3-5 years. The cost estimates in this report refer to mid-2008 price levels, representing a point of peak prices in energy and raw material markets. If extending historic price trends mid 2008-supplier prices could potentially have been 5-10% lower than actual levels. A 10% reduction in capex levels in our calculations, would give CO_2-$_{AC}$ levels 1-3 EUR/tCO_2 lower than those reported above.

Sensitivities and discussion

Cost drivers

All the variables used to quantify the realisation and operation of the various capture systems affect the resulting final cost of CO_2 capture to some degree, when measured as incremental cost of electricity (COE), or CO_2-avoided cost ($CO_{2\text{-}AC}$).

The xy-plots in Figures 8 – 10 covering all technologies among the B-cases (in Table 6) indicate covariation trends between the calculated CO_2 avoided costs and assumed cost drivers as energy efficiency, capture rate and capex-levels Such potential correlations should basically be investigated for the individual capture technology, however, such exercises are not made in these studies.

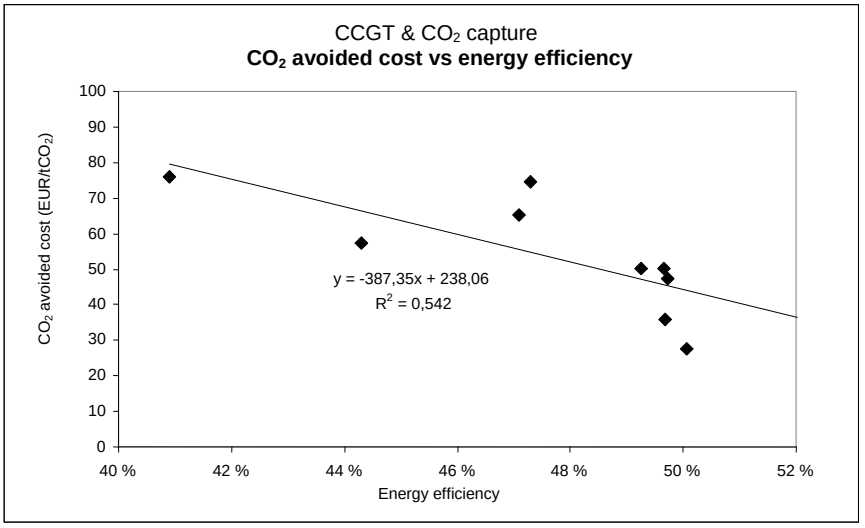

Figure 8. CO_2 avoided cost vs. energy efficiency.

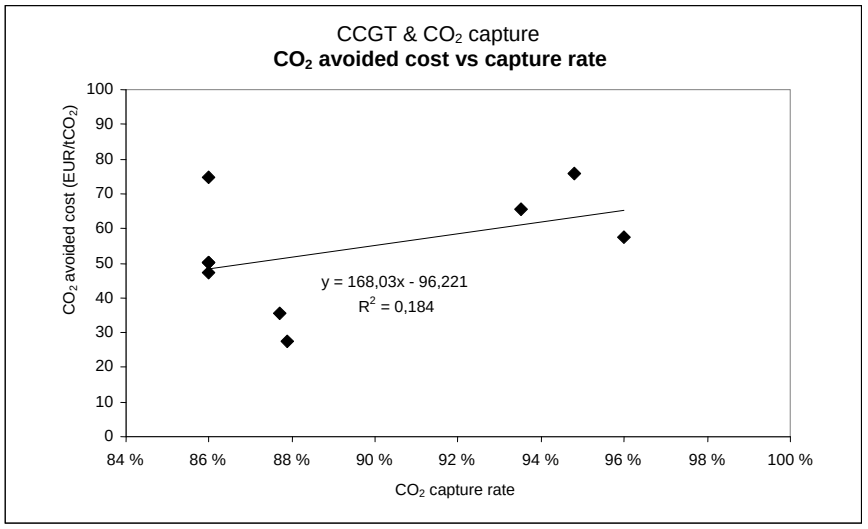

Figure 9. CO_2 avoided cost vs. CO_2 capture rate.

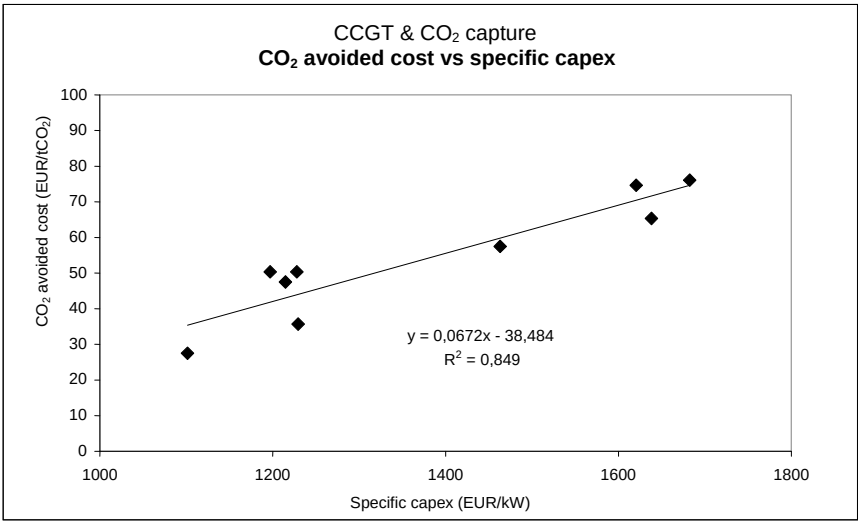

Figure 10. CO_2 avoided cost vs specific capex.

As indicated in figures 8 - 10 covering a number of capture technologies, one can observe the following correlative trends between CO_2 avoided cost levels and important cost drivers;

- a negative covariation vs. energy efficiency
- a weak, but positive correlation vs. CO_2 capture rate
- a strong positive correlation vs. specific capex levels.

Table 7 summarizes technology rankings according to efficiency, capture rates, specific capex levels, and the final COE and $CO_{2\text{-}AC}$-measures. As illustrated in Figure 8, it shows a strong influence of energy efficiency on the total economic rankings of capture technologies.

Table 7. Screening summary current CCP2-technologies ("B-cases") according to technical and cost criteria (ranking no.1 =1, no.2=2, ….,no.9=9)

	Energy efficiency	CO_2 capture rate	Specific capex - tot.plant	COE, incl emiss.cost	CO_2-AC	Sum (non-weighted)
HMR-1stg (2008)	1	4	1	1	1	8
HMR-1stg & GHR (2008)	3	5	5	2	2	17
BIT (2008), 40%EGR-MEA	2	6	3	3	3	17
BUT (2008), 40%EGR-MEA	4	6	4	4	4	22
BUT (2008), noEGR-MEA	5	6	2	5	5	23
SEWGS-AirATR (2008)	8	1	6	6	6	27
MWGS(2008)	7	3	8	7	7	32
MEA amine Climit BL (2008)	6	6	7	8	8	35
ATR-Cachet BL (2008)	9	2	9	9	9	38

Partial sensitivities

At an individual technology level, typical sensitivities on each key techno-economic parameter, are illustrated below for the CCP2 Amine Baseline case B2. Figure 11 shows the percentage reductions of the basic $CO_{2\text{-}AC}$ (at 75 EUR/tCO_2), of a marginal 1% favourable (increase or reduction) change in each of the main variables, while keeping the others constant. The uniform change is chosen to illustrate the relative importance of the key variables, even if the relevant variation ranges for these may vary. The partial sensitivities indicate first order effects of such parameter variations. The potential impacts of capture rate or energy efficiency changes on technical designs and costs were not addressed in this limited exercise.

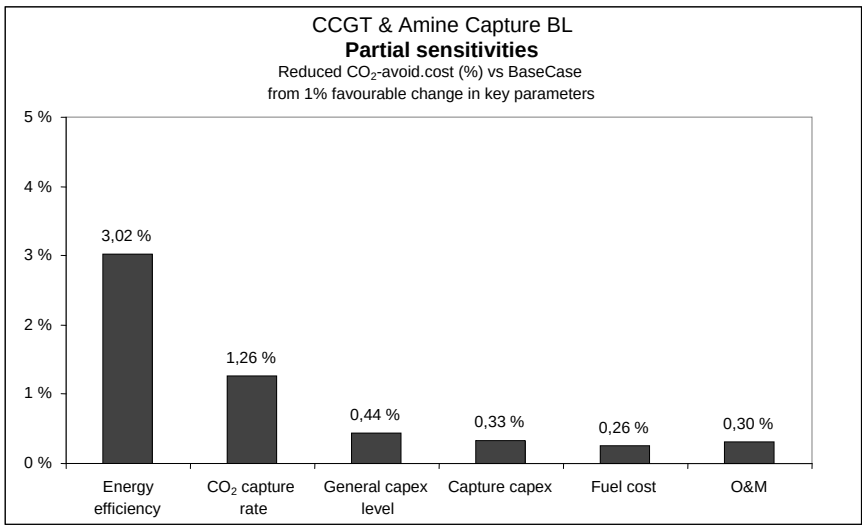

Figure 11. Partial parameter changes on CO_2-avoided cost.

The calculations show that a 1% increase in energy efficiency (from 47,3 to 47,8%) reduces the $CO_{2\text{-}AC}$ by 3,0%. A similar increase in the CO_2-capture rate (from 86 to 86,9%), reduces the Baseline $CO_{2\text{-}AC}$ by 1,3%. These superproportional sensitivities are due to the pass-through impacts changes in these parameters have on all unit cost elements (per kWh- or per ton CO_2 emitted) in the COE- and CO_2-AC-calculations. On the other side, the 1% changes in capex and opex variables have lower than 1% impact on $CO_{2\text{-}AC}$, as illustrated below.

Energy efficiency

Given the importance of energy efficiency, efforts to develop more efficient capture solutions should be given high priority. Since the capture process itself demands energy, questions like the following could be asked:

- is there an optimal capture rate for capture technologies?
- if so, how does this vary across technologies?
- what are the efficiency vs. capture rate tradeoffs for various capture technologies?
- what is the impact of various efficiency-capture rate levels on scope, capacities, designs and costs of the overall capture system?

The xy-plot in Figure 12 indicates a correlation trend between CO_2 capture rate and energy efficiency again across all capture technologies, referred in Table 6. The potential capture rate vs. efficiency tradeoffs should be explored at the individual technology level, in order to identify the shapes of marginal cost-curves for CO_2 capture for various technologies, as basis for optimization of technology designs.

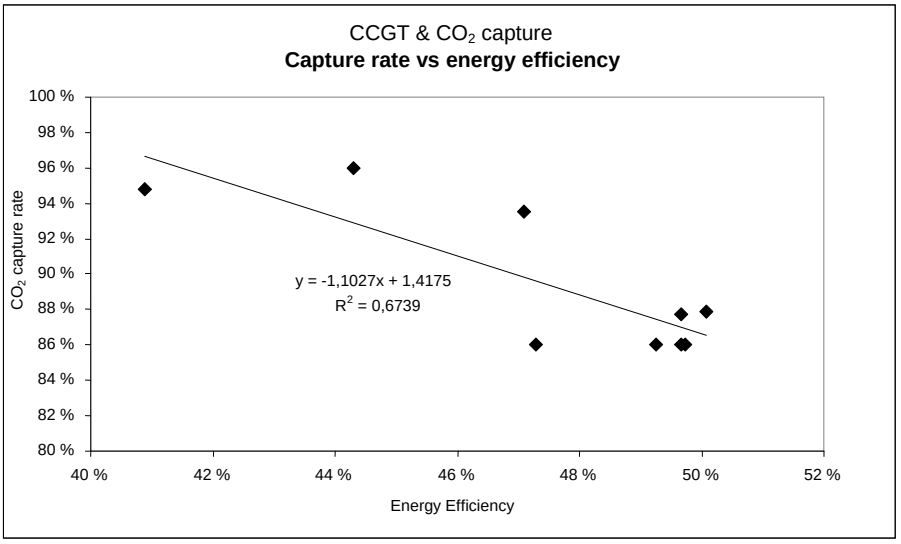

Figure 12. CO_2 capture rate vs energy efficiency.

PART III: REFINERY SCENARIO - HEATERS AND BOILERS

Scenarios outline

Refinery, Heaters and boilers

This scenario outlines technology alternatives to evaluate CO_2 capture from selected heaters and boilers (H&Bs) in an existing refinery, by installing new-built, centralized capture systems at the plant site. Three capture routes are evaluated;

- Post combustion capture system using a MEA solvent
- Oxy-firing capture with flue gas recycle and a conventional cryogenic air separation unit to supply high purity oxygen
- Pre-combustion capture system, with an oxygen fired autothermal reformer coupled to a membrane water gas shift system to provide hydrogen fuel.

The original CCP1-evaluations of this scenario were based upon heaters and boilers in an existing UK refinery, fed with refinery oil and gas. Of a total CO_2 emission of 4 mill.tons/year, a target capture of about 2 mill.tons/year from a selected subset of H&Bs was established for this scenario.

The post-combustion baseline was prepared by Fluor in 2001 using state-of-the-art MEA washing (Econamine technology).

The oxy-fired alternative with cryogenic Air Separation Unit (ASU) was prepared by Air Products in collaboration with Mitsui-Babcock (boiler retrofit) and Foster Wheeler (heater retrofit) using two world scale ASUs in parallel (3700 MTPD of oxygen each).

The advanced pre-combustion case was prepared by BP using metallic hydrogen membranes and cost data developed in the frame of EU and DOE co-funded research projects.

The scenario set strict limitations to available utilities based upon the actual refinery set-up. Unavailable utilities are generated on-site in this scenario, using additional equipment fed by natural gas. The CO_2 footprint of this utility supply is included in the calculation of the CO_2 avoided cost. For instance, a 107MW gas turbine system is included in the oxy-fired case to supply the required energy for air separation and CO_2 purification (and exporting 11MW).

This scenario was originally established in CCP1, and the capture technology alternatives above have been cost updated from 2003 to June 2008-price levels in CCP2.

Refinery, New single boiler

This sub-scenario represents a new-built single boiler located in an existing refinery in North West Europe. The boiler produces approximately 210 tonne steam/hr. For this scenario, three capture routes were also evaluated here;

- Post combustion capture using a MEA solvent
- Oxy-firing with flue gas recycle, and a conventional cryogenic air separation unit to supply high purity oxygen
- Oxy-firing using a Chemical Looping Combustion (CLC) boiler.

This sub-scenario was introduced during CCP2 to obtain a fair evaluation of the CLC technology, using a completely new type of boiler with built-in capture system. While the CLC case is regarded fully as a new-build case, the comparison cases were scaled down from the above retrofit scenario under the following assumptions

- Post-combustion system scaled down to a smaller unit capturing about 350,000 Mtons/year of CO_2 (15% of the full H&B-scenario). The necessary steam for the amine regeneration reboiler is valued as additional fuel (natural gas) needed for its production. The smaller unit (exponent scale-down) was necessary to obtain a fair comparison with the CLC option.

- Oxy-firing capture with oxygen purchased from a large external ASU-unit based on an oxygen-pricing reflecting a 10% discount rate, 10 year lifetime and an O_2/CO_2 consumption rate of 1.21 kg/kg.

The additional CO_2 footprint for imported utilities is considered in the CO_2 avoidance cost. The power to drive the ASU in the oxyfired case was assumed supplied from a new natural gas combined cycle engine, with a CO_2 –content of 0.37 tCO_2/MWh.

All of the other utilities are delivered from the refinery.

At the current cost of nickel oxide, the replacement rate of the solid oxygen carrier due to chemical and mechanical degradation is a key factor in defining economics. Two cases were thus considered for CLC, reflecting different carrier replacement frequencies:

- case 1: carrier replacement every 50000 hr
- case 2: carrier replacement every 8000 hr.

Generic, brown-site location

The plant is assumed to be located at a non-specified NW European site (similar to Rotterdam) with easy access to competitive markets and necessary supplies of:

- plant engineering and local construction capacity
- fuel gas deliveries
- other necessary utility and supply needs during construction and operations
- labour force during construction and operations
- power grid
- CO_2 offset options (storage sites and CO_2-EOR customers) in reasonable circumference.

Scenario-Technology Matrix

The specific set of capture technologies applied to the refinery heater and boiler, and new boiler scenarios is given in Table 8.

Final performance and cost estimates

An aligned set of key cost and performance data for the refinery boiler cases are illustrated in Figures 13 and 14.

Cost estimate details for each technology are reported in [2].

Table 8. Scenario-Technology Matrix for Refinery Heaters and Boiler Retrofit and New Boiler Cases

Case				Tech provider
C1	Refinery H&B	Reference	Uncontrol (2008)	Fluor/ BP (2001)
C2	Ref. H&B w/Capture	Post	MEA amine (2008)	Fluor/ BP (2001)
C3	Ref. H&B w/Capture	Adv.tech	MWGS (2008)	BP (2003)
C4	Ref. H&B w/Capture	Adv.tech	Oxy-FGR-ASU (2008)	AirProducts (2003)
F1	New Ref Gas Boiler	Reference	Uncontrol (2008)	Alstom
F2	New Ref Gas Boiler	Post Baseline	MEA amine single boiler	Internally scaled down from C2
F3	New Ref Gas Boiler	Adv.Tech	Oxy-Boiler 1	Internally scaled down from C4
F4	New Ref Gas Boiler	Adv.Tech	Oxy-Boiler 2	Internally scaled down from C4
F5	New Ref Gas Boiler	Adv.Tech	Oxy-Boiler 3	Internally scaled down from C4
F6	New Ref Gas Boiler	Adv.Tech	CLC1	Alstom
F7	New Ref Gas Boiler	Adv.Tech	CLC2	Alstom

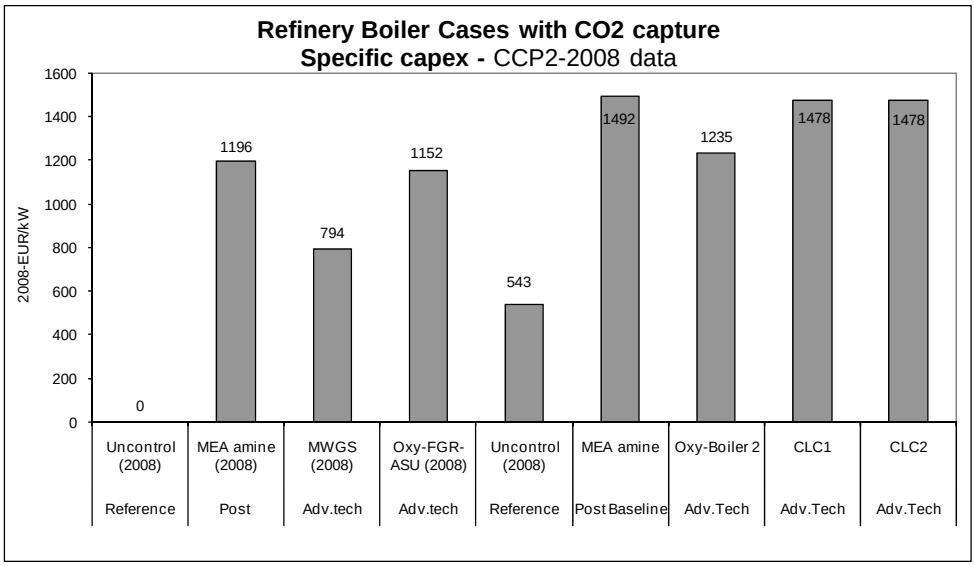

Figure 13. Specific capex, Refinery Heater and Boiler and Refinery Boiler cases.

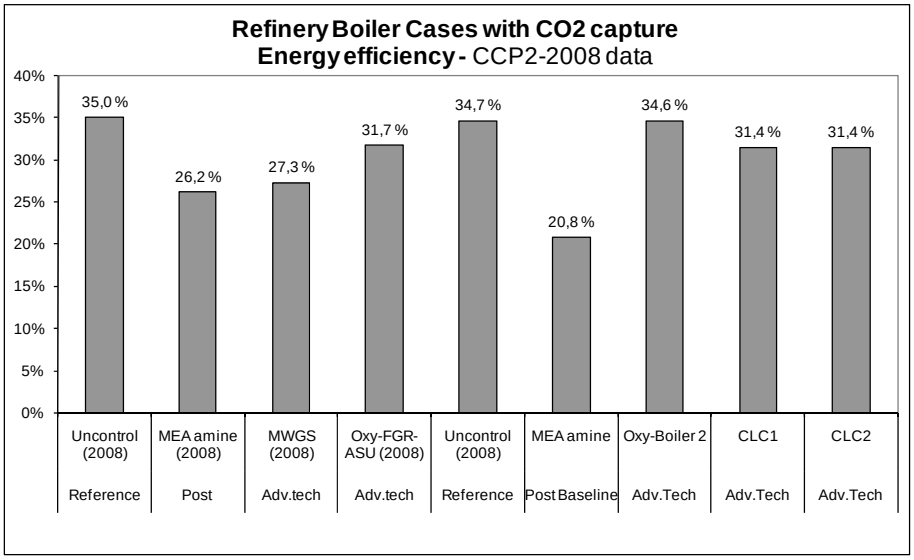

Figure 14. Energy efficiency (LHV-basis), Refinery Heater and Boiler and Refinery Boiler cases.

Economic Screening

Main results & findings

Tables 9 and 10 and Figure 15 summarize the main findings.

Table 9. Summary inputs and results – Refinery Heaters and Boilers Cases.

			CCP1-update	*2003 technical concept; pure 2003 -> 2008 cost escalation*		
Scenario-Technology case			**C1**	**C2**	**C3**	**C4**
		Units	Refinery H&B Reference	Ref. H&B w/Capture Post	Ref. H&B w/Capture Adv.tech	Ref. H&B w/Capture Adv.tech
			Uncontrol (2008)	**MEA amine (2008)**	**MWGS (2008)**	**Oxy-FGR-ASU (2008)**
Net power out		**MW**	473	354	369	428
		GWh	3935	2946	3069	3564
Internal power consumption/ loss		MW		119	104	45
Gross power capacity installed		MW	473	473	473	473
Fuel consumption		MW	1351	1351	1351	1351
		GWh/yr	11243	11243	11243	11243
		MSm3/yr	1012	1012	1012	1012
Efficiency		**pct**	**35,0 %**	**26,2 %**	**27,3 %**	**31,7 %**
Capex	Technology system	MEUR	0	423	293	493
	Capture system	MEUR		0	0	0
	Enng, Adm, other	MEUR				
	Total	**MEUR**	**0**	**423**	**293**	**493**
		EUR/kW ne	0	1196	794	1152
		MUSD	**0**	**616**	**426**	**717**
		USD/kW	0	1740	1155	1675
O&M fixed		MEUR/yr		15,46	11,88	18,42
O&M variable (at 100% basis)		MEUR/yr		16,76	3,60	2,46
O&M transport & storage		MEUR/yr		0,0	0,0	0,0
Fuel cost		MEUR/yr	169	169	169	169
CO2 generation		mton/yr	2,57	2,57	2,57	2,57
CO2-capture		**pct**	0%	**86%**	**90%**	**90%**
		mton/yr	0,00	2,21	2,31	2,31
CO2 emission		**mton/yr**	**2,57**	**0,36**	**0,26**	**0,26**
		kg/kWh (ne	0,65	0,12	0,08	0,07
COE excl CO2 emiss.cost		EUR/MW	**42,9**	**83,7**	**70,4**	**68,4**
COE incl CO2 emiss.cost		EUR/MW	**55,9**	**86,2**	**72,1**	**69,8**
CO2 avoided cost		EUR/tCO2		**77,0**	**48,5**	**43,9**
COE excl CO2 emiss.cost		USD/kWl	**62,3**	**121,8**	**102,5**	**99,5**
COE incl CO2 emiss.cost		USD/kWl	**81,3**	**125,4**	**104,9**	**101,6**
CO2 avoided cost		USD/tCO2		**112,0**	**70,5**	**63,9**

Table 10. Summary inputs and results – Refinery Boilers Cases.

Scenario-Technology case			F1	F2	F4	F6	F7
		Units	New Ref Gas Boiler Reference	Ref Gas Boiler Post Baseline	Ref Gas Boiler ef Adv.Tech	Gas Boiler ef Adv.Tech	Gas Boiler Adv.Tech
			Uncontrol (2008)	**MEA amine**	**Oxy-Boiler 2**	**CLC1**	**CLC2**
Net power out		**MW**	68	66	66	62	62
		GWh	568	549	548	515	515
Internal power consumption/ loss		MW		4	4	8	8
Gross power capacity installed		MW	70	70	70	70	70
Fuel consumption		MW	197	318	190	197	197
		GWh/yr	1638	2646	1581	1638	1638
		MSm3/yr	147	238	142	147	147
Efficiency		**pct**	**34,7 %**	**20,8 %**	**34,6 %**	**31,4 %**	**31,4 %**
Capex	Technology system	MEUR	37	29	29	59	59
	Capture system	MEUR		44,6	29	14	14
	Enng, Adm, other	MEUR		24,6	23,0	19,2	19,2
	Total	**MEUR**	**37**	**99**	**81**	**91**	**91**
		EUR/kW ne	543	1492	1235	1478	1478
		MUSD	**54**	**143**	**118**	**133**	**133**
		USD/kW	789	2171	1797	2149	2149
O&M fixed		MEUR/yr	1,5	2,6	1,9	2,3	2,3
O&M variable (at 100% basis)		MEUR/yr	0,0	2,8	7,7	0,6	3,8
O&M transport & storage		MEUR/yr		0,0	0,0	0,0	0,0
Fuel cost		MEUR/yr	25	40	24	25	25
CO2 generation		mton/yr	0,35	0,38	0,40	0,34	0,34
CO2-capture		**pct**	**0%**	**86%**	**90%**	**98%**	**98%**
		mton/yr	0,00	0,33	0,32	0,34	0,34
CO2 emission		**mton/yr**	**0,35**	**0,05**	**0,08**	**0,01**	**0,01**
		kg/kWh (ne	0,62	0,10	0,14	0,01	0,01
COE excl CO2 emiss.cost		EUR/MW	**53,1**	**102,9**	**77,2**	**72,9**	**78,8**
COE incl CO2 emiss.cost		EUR/MW	**65,5**	**104,8**	**80,1**	**73,1**	**79,1**
CO2 avoided cost		EUR/tCO2		**95,6**	**50,4**	**32,6**	**42,4**
COE excl CO2 emiss.cost		USD/kWh	**77,3**	**149,7**	**112,3**	**106,0**	**114,6**
COE incl CO2 emiss.cost		USD/kWh	**95,3**	**152,5**	**116,6**	**106,4**	**115,0**
CO2 avoided cost		USD/tCO2		**139,1**	**73,3**	**47,5**	**61,7**

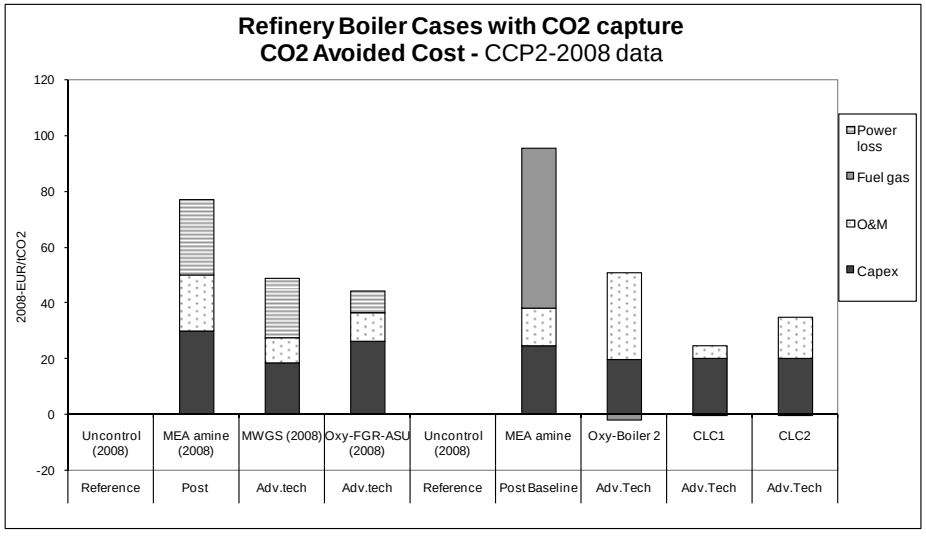

Figure 15. CO_2 Avoided Cost, Refinery Heater and Boiler, and Refinery Boiler cases.

Refinery, Heaters and boilers

From the CCP2 economic evaluations of heaters and boilers capture technologies, the following main conclusions can be drawn:

- CCP2 2008 updates to the CCP1 refinery heaters and boiler CO_2-avoided costs are:
  a. Amine: 77 EUR/tCO_2
  b. Membrane water gas shift: 49 EUR/tCO_2
  c. Oxy-FGR-ASU: 44 EUR/tCO_2
- The CO_2-avoided cost savings over amine post combustion capture are:
  a. Membrane water gas shift: 36%
  b. Oxy-FGR-ASU: 43%

In the full retrofit heaters and boilers case, the capex of the MWGS is lower than for the oxy-fuel fuel gas recycle with the air separation unit (Oxy-FGR-ASU) case. However, the oxy-fuel case has a higher efficiency than MWGS, and lower operating cost. The cost savings for the MWGS over the amine system are in line with CCP1 findings of 28-34%.

The new technologies in the refinery heater and boiler scenario have fairly similar economics. At this stage they seem more attractive than the amine solution as outlined here, unless a technical hurdle is revealed in the further development. It must however be highlighted that the MEA baseline does not include any technical advancements claimed over the past five years by technology providers.

Refinery, New single boiler

From the CCP2 economic evaluations of new single boiler capture technologies; the following main conclusions can be drawn:

- CCP2 new scenario of single refinery boiler CO_2-avoided costs are:
  a. Amine update: 96 EUR/ tCO_2
  b. Oxy-boiler update: 50 EUR/ tCO_2
  c. Chemical Looping Combustion update: 33-42 EUR/tCO_2
- The CO_2-avoided cost savings over amine post combustion capture are:
  c. Oxy-boiler: 48%
  a. CLC: 56-66%

Some assumptions in the evaluation may have penalized post-combustion on one side and favored conventional oxy-firing on the other. The scale factor is penalizing post-combustion from the the capex viewpoint. Efficiency is also lower than in the full retrofit case since the power output is assumed constant and additional steam is produced from natural gas at relatively low efficiency. In the oxyfired case, on the contrary, efficiency does not include oxygen generation and is therefore kept artificially high (see for comparison the C cases). This scenario however confirms the potential of the CLC., with high efficiency and capture rate levels. However, a better understanding of the carrier losses and excess air is needed. The development of cheaper carriers would also help in further decreasing costs.

In the oxy-fuel case, the imported power needed to drive the ASU is assumed supplied from a new natural gas combined cycle engine. With coal or a heavy fuel oil generating this power supply, would increase CO_2-footprints and avoided costs.

Sensitivities & discussion

Single Boiler –Oxygen production costs

The new built single boiler cases (F1-F7) include three cases for oxy-fuel where the production cost of the oxygen was calculated by:

- Oxy Case 1: NPV with a discount rate of 7.5% and 25 year time horizon; O_2/CO_2 ratio is 1.21 kg/kg
- Oxy Case 2: NPV with a rate of 10% and 10 year life; O_2/CO_2 ratio is 1.21 kg/kg
- Oxy Case 3: NPV with a rate of 10% and 10 year life; O_2/CO_2 ratio is 1.42 kg/kg

The oxygen needed for the oxy-fuel case is 20% more than the CO_2 captured. The oxy Case 3 reflects the same oxygen ratio as a CLC case; the refinery fuel oil uses less oxygen to combust.

The results of the sensitivity calculations are shown in Figure 16. A shorter operating life and higher discount rate for cases 2 and 3 will have higher costs than if oxygen is assumed to be produced over a longer time horizon. Producing more oxygen, as excess to burn fuel in Case 3 is also more expensive than a lower O_2/CO_2 ratio in Cases 1 and 2 (F3 and F4). Case 3 (F5) results in the highest operating costs. All the scenarios have the same CAPEX as the new single boiler is the same. Case 2 (F4) was used in the baseline comparison for the refinery boiler cases.

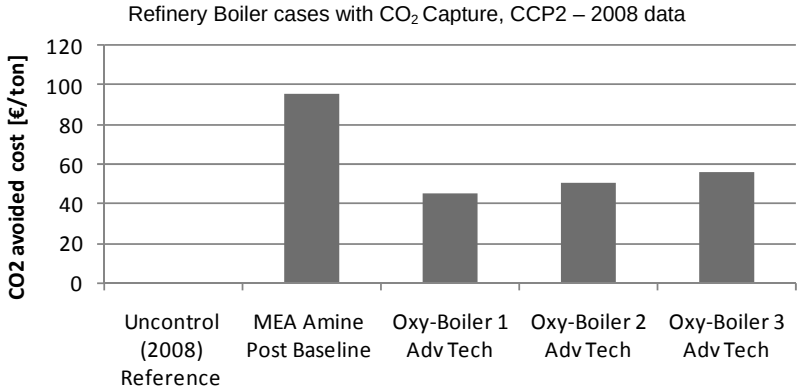

Figure 16. CO_2 Avoided Cost, Refinery Boiler Sensitivities Cases.

The CLC process scheme gives a CO_2 stream of about 94% vol. purity with main impurities being H_2 and CO. An afterburner system fed with 16 t/day of oxygen would burn 75% of the above impurities leading to 98%CO_2 purity The impact of this purification system on the CO_2 avoidance cost is estimated at < 3€/ton of CO_2.

PART IV: REFINERY SCENARIO - FLUID CATALYTIC CRACKER (FCC) UNIT

Scenario outline

Refinery, Fluid Catalytic Cracking Regeneration

The Fluid Catalytic Cracker (FCC) studied here, is located in a refinery in South America and generate approximately 1 million tonne CO_2 per year. All of the utilities are delivered to the refinery. Two capture routes were evaluated:

- Post-combustion capture of CO_2 from the FCC regenerator flue gases using a MEA absorption system
- Oxy-firing with flue gas recycle (FGR)

Generic, brown-site location

The plant is assumed to be located at a non-specified South American site with easy access to competitive markets and necessary supplies of:

- plant engineering and local construction capacity
- fuel gas deliveries
- other necessary utility and supply needs during construction and operations
- labour force during construction and operations
- power export grid
- CO_2 offset options (storage sites and CO_2-EOR customers) in reasonable circumference.

Technical Design Basis

This scenario is based on a 62,000 bpd FCC unit located in South America.

The uncontrolled (without capture) case emits 1 mill.tons of CO_2 per year. The amine capture baseline is based on a conventional MEA absorption unit, with a capture rate above 90%. ABB designed the qxy-fired FCC-application., with an air separation unit (ASU) and a required capacity of 2400 tonnes/day. All the utilities are delivered from the refinery site; including oxygen. The capture rate for an oxyfired FCC is very high at >99%.

To establish the energy and CO_2 import-export balances, the CO_2 content for imported power is assumed at 0.37 tCO_2/MWh., and 12t CO_2/t steam for all steam pressure options.

Scenario-Technology Matrix

The specific set of capture technologies applied to the refinery FCC case is given in Table 11.

Table 11. Scenario-Technology Matrix for Refinery FCC scenario.

Case				Tech Provider
		Reference case		
H1	Refinery FCC unit		Uncontrol (2008)	ABB Lummus/ Randall
H2	Refinery FCC unit	Post Baseline	MEA amine (2008)	ABB Lummus/ Randall
H3	Refinery FCC unit	Adv.Tech	OxyFuel 99,5%O2	ABB Lummus/ Randall

Final performance and cost estimates

Figures 17 and 18 summarize the performance and the capital investment estimates for the amine and Oxy-fuel options.

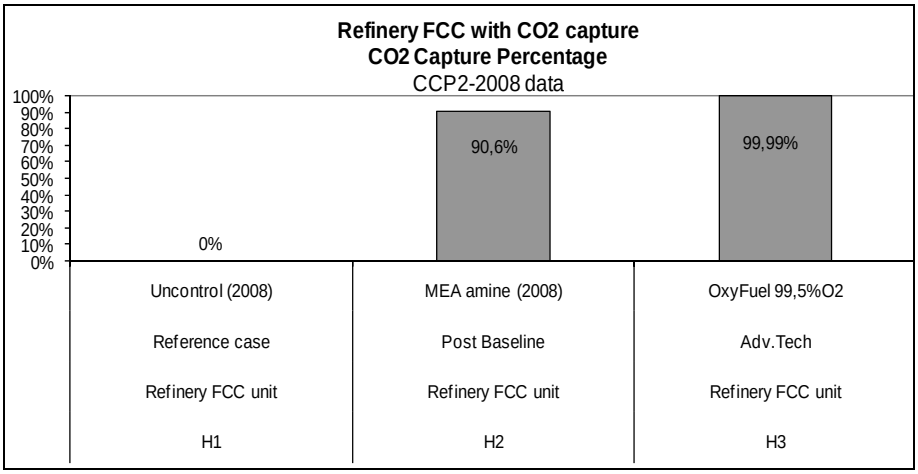

Figure 17. CO_2 Capture Rates, Refinery FCC case.

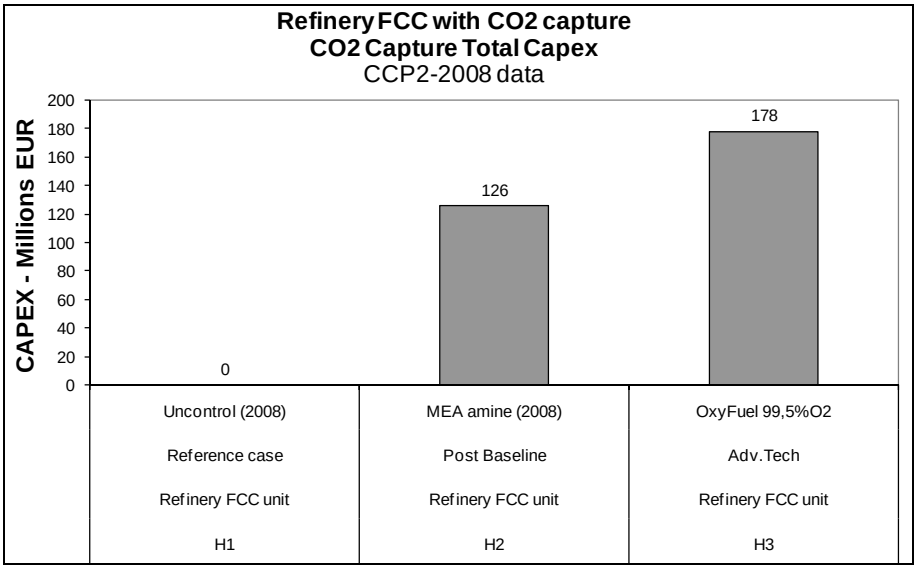

Figure 18. Total Capex, Refinery FCC case.

Economic Screening

Main results & findings

Table 12 and Figure 19 summarize the main findings.

Table 12. Summary inputs and results – Refinery FCC Cases.

H-cases		CCP2-tech & cost update	2008 concepts, 2008 cost estimates	
Scenario-Technology case		**H1**	**H2**	**H3**
	Units	Refinery FCC unit Reference case **Uncontrol (2008)**	Refinery FCC unit Post Baseline **MEA amine (2008)**	Refinery FCC unit Adv.Tech **OxyFuel 99,5%O2**
Power Consumption	**MW**	0	16	74
Capex Total	**MEUR**	**0**	**126**	**178**
	MUSD	**0**	**183**	**259**
Fuel cost	MEUR/yr		**23**	**18**
O&M fixe Manning	MEUR/yr		0,66	0,66
Maintenance	MEUR/yr	0,00	5,03	7,11
O&M var (Chemicals, utilities	MEUR/yr		3,90	1,46
O&M transport & storage	MEUR/yr			
O&M total	MEUR/yr	**0,0**	**9,59**	**9,23**
Capture plant O&M cost	MEUR/yr		32,8	27,5
Power Consumption	mton/yr		**0,051**	**0,240**
HP steam	mton/yr		**0,065**	**-0,109**
MP steam	mton/yr		**0,000**	**0,003**
LP steam	mton/yr		**0,227**	**0,000**
Total Utilities			**0,343**	**0,134**
FCC CO2 generation	mton/yr	**0,98**	**0,98**	**0,98**
CO2-capture	pct	0%	**90,6%**	**99,99%**
CO2-capture	mton/yr		0,89	0,98
CO2-avoided	mton/yr		**0,55**	**0,85**
CO2 capture cost	EUR/tCO2		52,4	47,9
CO2 avoided cost	EUR/tCO2		**85,3**	**55,4**
CO2 capture cost	USD/tCO2	**0,0**	**76,2**	**69,7**
CO2 avoided cost	USD/tCO2		**$124**	**$81**

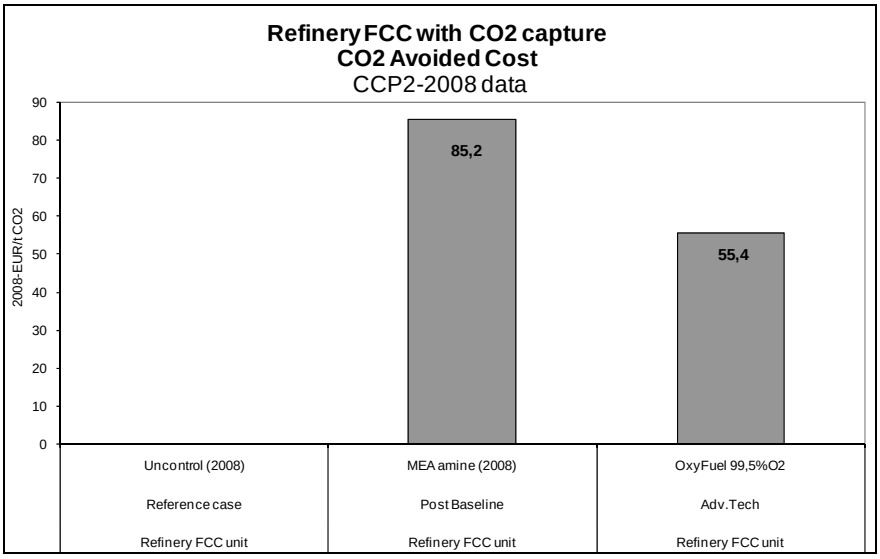

Figure 19. CO_2 Avoided Cost, Refinery FCC case.

From the CCP2 economic evaluations of refinery Fluid Catalytic Cracking capture technologies, the following main results can be observed:

- CCP2 2008 refinery Fluid Catalytic Cracking CO_2 avoided costs for Oxy-fuel are:
  a. Amine: 85 EUR/ tCO_2
  b. Oxy-fuel: 55EUR/ tCO_2
  c. The CO_2-avoided cost savings over amine: 35%

In the FCC scenario, the oxy-firing system demonstrates a favourable energy and CO_2 balance compared to the Amine system, and explains its lower CO_2-avoided cost, despite its higher capex-level.

Sensitivities & discussion

Plant size

For the oxy-fired case, a 2400 MTPD of oxygen ASU was required for a 62,000 bpd FCC unit. Considering the maximum size of a single train ASU to be 4000 MTPD, single train oxy-firing is applicable up to 100,000 bpd FCC units. However, the largest FCC units produce up to 180,000 bpd. Consequently, for world scale FCC units, two parallel ASUs would be needed.

Considering the post-combustion MEA absorption option, CO_2 concentration (~13% vol) is similar to a coal fired power station. In this case up to 8000 MTPD of CO_2 may be captured on a single train. For the largest world scale FCC units, economies of scale will work in favor of post-combustion MEA over oxy-firing.

CO_2 from associated steam generation

The CO_2 avoided cost is dependent upon the amount of CO_2 generated by additional steam used in capture system. FCC oxy-firing consumes less high pressure steam than the uncontrolled case while the base case amine consumes additional high, medium and low pressure steam. As a consequence, assuming higher levels of CO_2 generation associated to steam production favors oxy-firing compared to post-combustion. The following two alternative assumptions were made:

- All steam pressures emit 0.12t CO_2/t steam– used as the main case in computations
- High pressure emits 0.193t CO_2/t steam, medium pressure steam emits 0.178 tCO_2/t steam and low pressure steam emits 0.171 tCO_2/t steam.

The effects of the different assumptions are shown in Table 13.

Table 13: Steam generation effects on cost of CO_2 capture and avoidance.

Scenario	Cost (Eur/yr)	Amine	Oxyfired
All CO2/steam emis	Capture	52	48
ratio=0.12	Avoided	85	55
CO2/steam emis	Capture	52	48
ratio range=0.19-0.17	Avoided	112	52

Differently from the oxy-fired case, results for the post-combustion case are strongly affected by the above assumptions. Though the ranking is not modified, detailed verification of these assumptions will be necessary before taking decisions in an actual case, also considering the continuous progress in post-combustion systems opex claimed by the main technology providers. A simplified sensitivity was also performed considering a much lower steam consumption for the amine unit, in line with most recent claims (1.5 kg/kg of CO_2 washed). In this case the advantage of the oxy-fired case is

reduced, but still consistent, in the 20% zone (avoidance cost for the amine case would be reduced to about 70 €/ton).

ACKNOWLEDGEMENTS

Members of the CO_2 Capture Project Phase 2 (CCP2) capture team, CCP's Advisory Board, the external referees and the editor of this book deserve all our great thanks for providing valuable comments and advice in preparing this chapter of the CCP2 final report.

REFERENCES

1. Miracca, I. 2009, Introduction to the CCP2 Capture Technology Portfolio, in Eide, L.I. (ed.), 2009, Carbon Dioxide Capture for Storage in Deep Geologic Formations, Volume 3. CPL Press
2. CCP-2 Cost Estimate Report (confidential). TelTek, Porsgrunn, Norway, February 2009
3. CCP-2 Gas Power Plant Scenario – Reference document (Hydro, 2006)
4. Melien, T., 2005. Economic and Cost Analysis for CO_2 Capture Costs in the CO_2 Capture Project Scenarios, in Thomas, D. C. (ed) Carbon Dioxide Capture for Storage in Deep Geologic Formations – Results from the CO_2 Capture Project (phase 1), Vol.1, Chapter 3 (Elsevier 2005)

Carbon Dioxide Capture for Storage in Deep Geologic Formations, Volume 3
L.I. Eide (Ed.)

Chapter 18

OVERVIEW OF THE CanmetENERGY CO_2 R&D CONSORTIUM – PHASE 9

Kourosh E. Zanganeh[1,2] (Overview)
Milenka Mitrovic[2], Ahmed Shafeen[2] and Kourosh Zanganeh[2] (Project 1, Task 1)
Ashkan Beigzadeh[2], Peter L. Douglas, Eric Croiset[3] and Kourosh Zanganeh[2] (Project 1, Task 2)
Kourosh Zanganeh[2], Ahmed Shafeen[2] and Carlos Salvador[2] (Project 2, Task 1)
Carlos Salvador[2], Kourosh Zanganeh[2] and Ahmed Shafeen[2] (Project 2, Task 2)
Carlos Salvador[2] and Milenka Mitrovic[2] (Project 3)
Kourosh Zanganeh[2], Ahmed Shafeen[2] and Carlos Salvador[2] (Project 4, Task 1)
Yewen Tan[4], Dennis Y. Lu[4], Robert Dureau[5] and Edward J. Anthony[4] (Project 4, Task 2)
ZET Team[2] (Project 5)
[1] Consortium's Program Manager and the Corresponding Author
[2] Zero Emission Technologies Group, Clean Electric Power Generation, CanmetENERGY, Natural Resources Canada, 1 Haanel Drive, Ottawa, Ontario, K1A 1M1, Canada
[3] Department of Chemical Engineering, University of Waterloo, 200 University Avenue West, Waterloo, Ontario, N2L 3G1, Canada
[4] Gasification & FBC Group, Clean Electric Power Generation, CanmetENERGY, Natural Resources Canada, 1 Haanel Drive, Ottawa, Ontario, K1A 1M1, Canada
[5] Analytical Laboratory, Clean Electric Power Generation, CanmetENERGY, Natural Resources Canada, 1 Haanel Drive, Ottawa, Ontario, K1A 1M1, Canada

ABSTRACT: CanmetENERGY in Ottawa's near-zero emission oxy-fuel combustion program involves research, development and demonstration of efficient and clean fossil fuel combustion technologies in an oxygen-enriched environment with multi-pollutant control and CO_2 capture for storage. In an oxygen-enriched environment, the product of combustion comprises mainly CO_2, water and minor impurities. This CO_2-rich flue gas stream can be dried, pre-treated to the desired level, and processed to capture and compress CO_2 for transport to industrial end user or for permanent storage in suitable geological formations. In 1995, CanmetENERGY commissioned its world class, advanced pilot-scale oxy-fuel Vertical Combustor Research Facility (VCRF) with the aim of developing efficient and clean combustion technologies as a means for harnessing energy from fossil fuels with near-zero emission environmental performance. Shortly thereafter, a CO_2 R&D Consortium was formed to direct a pre-competitive research program in the areas of oxy-fuel combustion and CO_2 capture. This Consortium is comprised of national and international industry and government partners. The on-going program is supported by a strong team of CanmetENERGY's research scientists, engineers and technologists, and is complemented by national and international participants from industry, academia and other research institutes. This section provides an overview of the range of innovation activities proposed and completed under the work program for Phase 9.

INTRODUCTION

Since 1995, eight phases of R&D have been completed under the CanmetENERGY CO_2 R&D Consortium, whose accomplishments include a range of innovative concepts, processes and technologies for clean combustion of fossil fuels with multi-pollutant control and CO_2 capture for storage.

Extensive studies and pilot-scale testing under the previous phases of this program have led to the design and development of:

- Advanced CFD tools for studying oxy-fuel combustion and flame characteristics;
- Process models to study feasibility of, and to optimize the operation of oxy-fuel combustion technologies under various retrofit scenarios;
- Concepts for adapting oxy-fuel combustion technologies to gas turbine cycles;
- Oxy-fuel burners that significantly lower NO_x emissions as compared to low-NO_x burners, which use air as the oxidant;
- A CO_2 capture and compression process simulator and pilot-scale CO_2 compression research facility to study and optimize capture and compression processes for CO_2; and,
- Process development for new and advanced gas turbine and high-efficiency fuel cell-based power generation cycles.

In addition to the above development, with funding initially provided by the Canadian Federal Government's Climate Change Technology & Innovation (T&I) program, CanmetENERGY started on a path to develop the next generation of near-zero emission combustion systems that may prove to be less costly than conventional combustion technologies. These developments have been supported by CanmetENERGY's world class pilot-scale oxy-fuel combustion and CO_2 capture facilities. These pilot-scale facilities have been evolved in recent years to the state-of-the-art combustion test platforms with advanced capabilities to implement new near-zero emission fossil fuel combustion processes.

WORK PROGRAM AND RESEARCH GOALS

The 1st generation of oxy-fuel combustion systems with flue gas recycle are ready for pilot demonstration and recent initiatives such as the 30 MW_{th} oxy-fuel pilot demonstration project by Vattenfall in Germany, the Australian Callide-A oxy-fuel demonstration project in Australia, projects supported and funded by the US Department of Energy, and EU funded projects, have drawn considerable interest in the international community towards this effective CO_2 capture technology pathway.

Some of the main technology gaps for oxy-fuel combustion with CO_2 capture for storage are:

- System integration and cycle development for oxy-fuel with flue gas recycle processes, pure O_2 combustion, and hydroxy-fuel combustion of fossil fuels in advanced power cycles;
- Better understanding of the combustion, heat transfer, and emissions in oxy-fuel combustion;
- Development of integrated multi-pollutant control strategies for NO_x, SO_x, Hg, and particulate with optimization, integration and low-grade heat recovery;
- Development of oxygen chemical looping combustion cycles;
- Design and development of high-temperature tolerant materials;
- Improved air separation units with lower energy demand for oxygen production;
- Development of larger-scale adsorption or membrane technology with lower energy penalty for oxygen production with higher purity; and,
- Improved CO_2 capture and compression processes with lower energy demand.

It is obvious that the work program for Phase 9 of the CanmetENERGY CO_2 R&D Consortium cannot address all the gaps identified above within the short time span of this Phase. However, the range of innovation activities under Phase 9 cover further technology developments for large-scale deployment of the near-zero emission plants that can either burn coal or low-value fuels, through optimization and system integration as well as developing enabling technologies for the clean oxy-combustion of fossil fuels with CO_2 capture for storage. The work program under Phase 9 and the range of research and development activities aim at improving the overall economics and performance of oxy-fuel technologies with focus on advanced supercritical oxy-coal power plants, CO_2 capture and compression, utilizing opportunity fuels such as petroleum coke, and processes and designs with strong potential for integration with other technology areas, such as advanced zero-emission turbines. This work program also includes extensive pilot-scale investigation of oxy-fuel combustion and CO_2 capture and compression processes, including studying the effect of impurities.

CONSORTIUM MEMBERS

The following is the list, in alphabetical order, of the members in Phase 9:

- Alberta Energy Research Institute (AERI)
- Babcock & Wilcox Power Generation Group Inc. (B&W)
- CO_2 Capture Project (CCP) – managed by BP Corporation North America Inc.
- Ontario Power Generation Inc. (OPG)
- Saskatchewan Power Corporation (SaskPower)
- US Department of Energy (DOE) - The National Energy Technology Laboratory (NETL)

RESEARCH AND DEVELOPMENT ACTIVITIES AND PROJECTS

The work program for Phase 9 focuses its research on evaluating an expanded array of new technologies and process options for application in new, clean fossil power plants with CO_2 capture. The projects for this phase are summarized in the following sections:

Project 1: Modeling and Analysis of Advanced Supercritical (ASC) Oxy-Coal Plants

This project includes two main tasks: Task 1) Modeling and analysis of advanced supercritical oxy-coal plants with CO_2 capture; and Task 2) Economic evaluation of these plants.

Under Task 1, CanmetENERGY is developing an integrated advanced supercritical (ASC) oxy-coal power plant model and investigating the following:

- The integration of demonstrated technologies for oxygen production, supercritical steam boilers and turbines, and CO_2 capture and compression;
- The impact of oxygen purity and oxygen partial enrichment on the oxy-fuel boiler performance;
- The impact of air-combustion on the oxy-fuel boiler and overall plant performance.

Figure 1 shows an example of a simplified oxy-fuel combustion process. The plant overall model includes detailed sub-models for Air Separation Unit (ASU), boiler, integrated pollution control units, balance-of-plant (BOP), and the CO_2 Capture and Compression Unit (CO_2CCU). Only steady-state simulations were performed and Saskatchewan lignite was used in the plant model. The pollution control devices integrated in the model included an electrostatic precipitator (ESP) and a wet flue gas desulfurization unit (FGD). Cryogenic air separation system for on-site supply of oxygen was modelled in Aspen HYSYS® process simulation software yielded an electrical consumption of 213.5 kWh per metric ton of oxygen produced. Approximately 10,000 tons per day of oxygen are required for a 500 MW_e oxy-coal power plant with CO_2 capture. Two boiler island

configurations were investigated in order to assess the impact of air leakage and plant mechanical layout. The CO_2CCU was modelled in Aspen HYSYS® process simulation software as well.

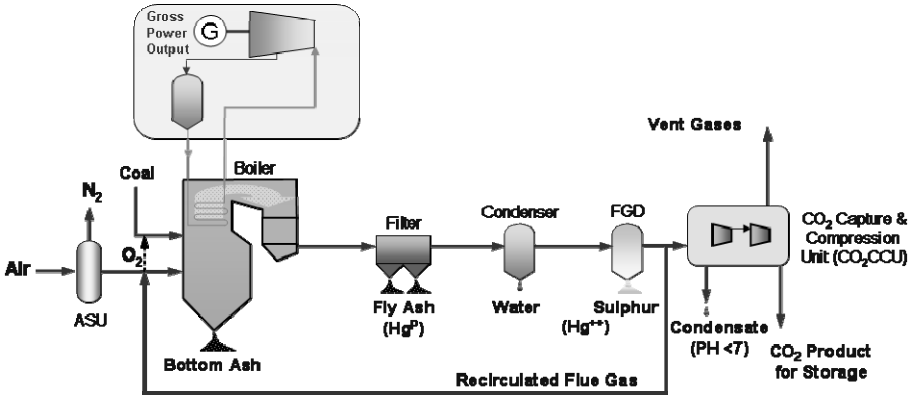

Figure 1. Oxy-fuel pulverized coal combustion.

Under Task 2, economics of an Advanced Supercritical (ASC) oxy-coal power plant was investigated. One of the main objectives of this study was to develop a financial toolbox that would allow users to change different parameters and tailor the model to perform proper cost estimations of their processes at hand. The study of the economics of the (ASC) oxy-coal power plant shows that a levelized cost of electricity (LCOE) of 131\$/$MWhr_{net}$ along with a CO_2 avoidance cost of 68\$/tonne. Employing the detailed financial toolbox developed in-house, several sensitivity case studies were carried out illustrating the sensitivity of the process economics to different parameters, such as fuel price, plant cost index variations, and capacity factor. Large uncertainty bounds were calculated for the cost estimations in this study. The largest contributors to uncertainties in the estimation of the overall cost estimates were the boiler and balance of plant cost estimations for which large variations were observed in the reported literature. Detailed case specific information was deemed crucial to improving the accuracy of the cost estimations.

Project 2: Performance Testing of CO_2 Capture and Compression Pilot-Scale Unit and Experimental Investigation of Phase Change in CO_2 Gas Mixtures

This project has two tasks: Task 1) Development and performance testing of an optimized CO_2 Capture and Compression Unit (CO_2CCU); and 2) Experimental investigation of phase behaviour in CO_2 mixtures.

Task 1 includes the design and development of an efficient CO_2 capture process and the CanmetENERGY's pilot-scale CO_2 capture and compression unit (CO_2CCU). This unique pilot-scale unit provides an excellent test platform to study the CO_2 capture processes and the impact of flue gas impurities on these processes. The CO_2CCU is first-of-a-kind pilot-scale unit that represents an integrated approach to near-zero emission oxy-fuel combustion of coal and other fossil fuels. In this approach, the incoming CO_2-rich gas stream is pre-treated and sent to CO_2CCU in order to separate and capture CO_2 by compression and cooling. The outputs of the CO_2CCU are the so-called CO_2 product stream, process condensate, and the vent stream which is a mixture of gases containing non-condensable impurities and minor amount of CO_2. A major advantage for the CO_2CCU technology is that it can receive the gas stream from different fossil fuel energy conversion systems, such as gasifiers, oxy-fuel combustors or boilers, fluidized bed combustors,

refineries' off gases, or other similar industrial processes. Figure 2 depicts the final product based on a trailer-mounted configuration.

(b) (a) (c)

Figure 2: (a) The trailer-mounted CO_2CCU; (b) Finished Internal: (c) During Fabrication.

Task 2 includes an experimental investigation of the phase change behaviour of CO_2 at liquid and supercritical states in the presence of impurities. Depending on the adopted combustion technology, the flue gas composition and the end-user's requirement, the optimum CO_2 capture and compression process will vary in each case. Moreover, the design and subsequent optimization of such a technology is limited to or dependent on a clear understanding of the phase behaviour of the flue gas compositions, i.e., the mixture of CO_2 and such gas phase impurities as N_2, O_2, SO_x, NO_x, and Ar. Such knowledge would assist in the specification of the proper equations of state to model and subsequently design such systems and would also prove useful in establishing corrosion limit for pipelines and piping systems. As a consequence, CanmetENERGY in Ottawa has designed and developed a bench-scale apparatus to study of phase behaviour of CO_2 mixtures with emphasis on the pressures and temperatures that apply to CanmetENERGY's CO_2CCU. The knowledge obtain will assist in the specification of the proper equations of state to model and subsequently design such systems and would also prove useful in establishing corrosion limit for piping systems.

Project 3: Testing and performance optimization of a novel multi-function oxy-fuel/steam burner

A consequence of oxy-fuel combustion is that the fuel burnt in the presence of nearly pure oxygen results in elevated flame temperatures that are significantly higher than those for air combustion. In order to utilize existing and proven technologies, the common method of alleviating this condition is to recycling a portion of the CO_2-rich flue gas, approximately 60-70%, back to the combustion zone to dilute the flame. While this approach has been the subject of much research it limits the potential improvements that could be made on the boiler system, namely, constraining the size of the combustion system before the recycle point. If, however, the recycled flue gas could be minimized or an alternative moderator, such as water or steam, could be used to control the flame temperature, substantial reductions in the physical size of the boiler can be achieved, which could ultimately reduce the scale, capital, and operating costs of the oxy-fuel plants. For this reason, CanmetENERGY in Ottawa has developed a novel multi-function burner for performance testing in its pilot-scale oxy-fuel combustion facility. The objective of this project is to establish the operational envelop and optimize the performance of this CanmetENERGY proprietary burner in both oxy-fuel and oxy-steam combustion modes.

The multi-function burner designed to operate under various firing modes and to fire both solid and liquid fuels. It is a swirl stabilized burner with whose primary operation modes are air, O_2/recycled flue gas, O_2/steam, and oxygen enriched air. It is also possible to combine multiple modes to produce unique oxidant streams such as O_2/steam/recycled flue gas.

Physically the burner consists of a centrally located coal gun surrounded by secondary and tertiary annuli. The burner has also been designed with secondary and tertiary swirl block generators, which allow for the swirl number of each annulus to be independently varied. The mass flow rate and oxygen content in each annulus may also be varied. The result is the ability to exert a great deal of control over the flame envelop and ultimately combustion process.

This work has enabled a better understanding of the impact of the swirl number and the oxygen content on the flame envelop and emissions. The experimental data generated may be used to validate the CFD models for these flames and to test combustion of difficult fuels due to the flexibility of the burner design and the ability to control selected parameters at a time.

Project 4: Development of an Efficient Mercury Removal Process and Analysis of Multi-Pollutant Control Strategies for Oxy-Coal Fired Power Plants

This project has two tasks: Task 1) Analysis of multi-pollutant control strategies for oxy-coal fired power plants; and Task 2) Development of an efficient mercury removal process from coal flue gas.

Task 1 focused on analysis of multi-pollutant control strategies for oxy-coal fired power plants. In general, control technologies that are capable of simultaneously reducing emissions of multiple pollutants offer the potential to achieve flue gas clean up at lower cost and reduced footprint when compared to conventional emission control technologies. For the new oxy-coal fired power plants, multi-emission control technologies can help designers of these plants select effective and less expensive compliance strategies, compared with compliance choices made when the requirements are addressed individually.

There are two main approaches to control multi-pollutant emissions from oxy-coal power plants. The first approach relies on the conventional air pollutant control devices that can be used in the oxy-coal plant without the need for major changes to the plant. The successful implementation of this approach depends on many factors including the plant configuration, coal type and the flue gas recycle pathway. The second approach uses the CO_2CCU to remove acid gases and mercury during the CO_2 capture and compression process. A set of pilot-scale testing was completed to study the latter approach as a multi-pollutant control strategy for advanced oxy-coal plants. Initial results are promising and further analysis is underway to better understand the fate of Hg and other acid gases in flue gas stream of the oxy-coal plants.

Task 2 had the objective to assess the effectiveness of Hg removal from coal combustion flue gas using the Fenton reactions and sodium sulphide with the help of the newly acquired Hg CEM (continuous emission monitor). The Hg CEM is an invaluable tool in this kind of research as it can provide “almost real time’ results on the effects on Hg of various changes such as changes in scrubbing solution and air pollution control equipment. The use of the Hg CEM could also provide further insight into the evolution of Hg at various stages during the coal combustion process.

The mercury scrubbing was performed in a condensing heat exchanger (CHX) with flue gas generated by coal combustion in CanmetENERGY’s Vertical Combustor Research Facility (VCRF). Previous results using the same approach obtained with the combustion of three different pulverized coals, namely, eastern bituminous, western sub-bituminous (Highvale), and SaskPower’s lignite, showed that the CHX was effective in removing oxidized mercury (Hg(II)). These results also

showed that better Hg removal results was achieved by combining sulphur removal and Hg removal in the same stage of the CHX.

Based on results from previous Phases, it was concluded that the CHX can be a very effective tool to remove Hg from coal combustion flue gas. Hence, it was planned to further explore means to use the CHX for this purpose. A short test done showed that a very small amount (~ 5 grams) of Na_2S effectively removed all the Hg from the flue gas generated by burning a lignite coal using the VCRF, although Hg was subsequently released back into the flue gas stream. Overall, using Na_2S for Hg removal is a viable and very effective approach. The main obstacle is to find a way to safely handle the chemical and to prevent the release of H_2S, and a pilot-scale test plan is mow being developed. As an alternative, there are indications from literature that sodium tetra-sulfide can also be a very effective agent for mercury removal. Most of the work reported so far, involved injecting or spraying sodium tetra-sulfide into the flue gas duct. We proposed to test the effectiveness of using sodium tetra-sulfide in the condensing heat exchanger. Tests have been performed in the VCRF and results are pending.

Project 5 Development of advanced pulverized coal combustion processes for oil sands petroleum coke in air and oxygen-enriched environment.

Canada possesses sizable fractions of global hydrocarbon resources. The province of Alberta is home to the world's largest known natural bitumen reservoir. This reservoir is located in the Western Canadian Sedimentary Basin (WCSB) and comprises the Athabasca, Peace River, and Cold Lake oil sands fields. The estimated ultimate reserves of bitumen in the WCSB are in the order of 400 billion cubic meters (2516 billion bbl). Petroleum coke is one of the major by-products of oil sands upgrading process (see Figure 3).

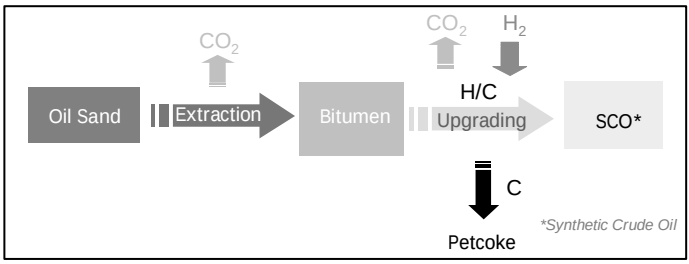

Figure 3. Typical stages of an oil sands extraction and upgrading process.

With the massive expansions in Canadian oil sands operations, every year large inventories of oil sands petroleum cokes are being built up in Alberta, Canada. These petroleum cokes have high fuel value, however owing to high concentrations of sulphur, heavy metals and carbon they require special attention so as to exploit their fuel values leaving minimum environmental foot prints. CanmetENERGY at Ottawa is pursuing a research initiative to investigate the oxy-fuel combustion of petroleum coke as a potential fuel in place of natural gas to facilitate the efficient supply of in-situ energy needs in oil sands operations in an environmentally sustainable manner, integrated with CO_2 capture and storage (CCS).

A set of experiments involving different coal to petroleum coke ratio was conducted. Saskatchewan lignite coal and delayed petroleum coke from Suncor's upgrading operations at Fort McMurray were used in these tests. The coal to petroleum coke ratio varied from 0 to 100 %, while maintaining the firing rate of 0.21 MW_{th} (~0.7 MMBtu/h), and the stable flame conditions were established.

Figure 4a and 4b show a snapshot of 100 % Saskatchewan lignite coal firing and 100% petroleum coke combustion in oxy-fuel firing modes with O_2/CO_2 recycle.

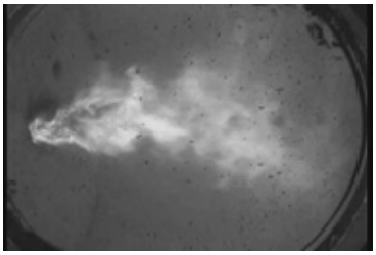

Figure 4a. Flame propagation for coal-to-coke ratio at 100%.

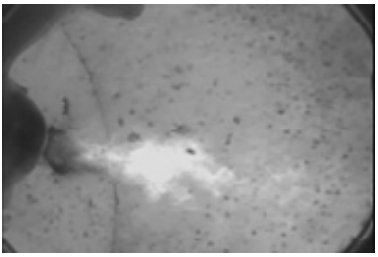

Figure 4b. Flame propagation for coal-to-coke ratio at 0%.

The trace metals analysis in the first few tests reveals that negligible amount of heavy metals (including the *Ni* and *V*) were detected after the baghouse for coal-to-petroleum coke ratios less than 25% (*w/w*). This indicates some kind of relationship between particulate control and heavy metals reduction. Non-traceable observations for heavy metals after the baghouse indicated that these metals are mostly adsorbed by the particulates and as the particulates are trapped by filter media, so as the most trace metals. Thus, the *Ni* and *V* appear to be captured with the particulate morphology. As the ratio of coal-to-petroleum coke reduced from 100% to 0%, significant rise in SO_3 concentrations was observed in the flue gas.

These are early conclusions from data collected and additional analysis is currently underway. Impacts of suitable sorbent injection on sulphur capture before the recycle point have been investigated as well.

ACKNOWLEDGEMENTS

The authors contributed to this chapter would like to thank the members of the Consortium's Steering Committee (Surindar Singh – AERI; Kevin McCauley - B&W; Linda Curran, Mark Bohm and Michael Desmond – CCP; Ron Wilson – OPG; Bob Stobbs – SaskPower; Timothy Fout - NETL) for their valuable support and technical guidance regarding the Work Program and performance of tasks in Phase 9. The authors also express their gratitude for technical assistance provided by staff at Clean Electric Power Generation Unit, Characterization laboratory, and Analytical Laboratory of CanmetENERGY in Ottawa. Special thanks to Dr. Daryoush Emadi for his coordination and assistance in preparation of this report.

The financial contributions of the CanmetENERGY CO_2 R&D Consortium members listed above, Natural Resources Canada's Program for Energy Research and Development (PERD), Technology and Innovation (T&I) and ecoETI Funds is gratefully acknowledged. Also, the Saskatchewan lignite coal samples and delayed petroleum coke samples were provided by SaskPower and Suncor, respectively. The contributions from these two organizations in supplying the fuels for pilot-scale combustion tests are greatly appreciated.

Carbon Dioxide Capture for Storage in Deep Geologic Formations, Volume 3
L.I.Eide (Ed.)

Chapter 19

CO_2 CAPTURE: KEY FINDINGS, REMAINING GAPS, FUTURE PROSPECTS

Ivano Miracca
Saipem S.p.A., Viale De Gasperi 16, I-20097 San Donato Milanese, Italy

ABSTRACT: This chapter summarizes the key findings that may have modified the way CCP member companies look at future prospects for the application of CCS and to outline gaps in need of further R&D during next years.

POWER GENERATION FROM NATURAL GAS

The CO_2 Capture Project Phase 1 (CCP1) identified pre-combustion as the preferred approach for mid- and long-term application of CO_2 capture from power station based on natural gas combined cycle (NGCC). This conclusion was based on the very positive results achieved for the Hydrogen Membrane Reforming (HMR) technology. The extensive work that CCP Phase 2 carried out in the frame of the CACHET project however highlighted several hurdles, summarized below, that may delay large scale implementation of pre-combustion capture to power generation and keep post-combustion as the preferred option, also in the new-built case, at least until 2020.

- Low energy efficiency: a state-of-the-art power station has an overall efficiency of about 58%. Post-combustion capture including the latest advancements claimed by technology owners may decrease this value by 8-10 % points (or to 48-50% efficiency). A power station based on today's state-of-the-art pre-combustion technology may achieve an efficiency in the 42-44% range, depending on the assumptions. Novel technologies or improvements of currently available technologies in a mid-term prospect (2015-2020) may increase achievable efficiency by 4-5% points, maybe not yet enough to compete with post-combustion.
- A parallel development of turbo-machinery is necessary to improve prospects of pre-combustion with particular reference to:
    - Hydrogen concentration at turbine inlet, currently limited to 40-50% vol. Current research on new generation burners may be able to increase the concentration up to 70%, but commercialisation seems some years away.
    - Turbine inlet temperature, currently limited to 300-400°C. If higher temperatures can be achieved, the efficiency will.
    - Metal dusting that occurs with high temperature syngas streams, limiting heat recovery options.

A very innovative technology like HMR still shows high potential in the long term, but even with continuing development, commercialisation may not occur until after 2020.

CCP Phase 1 identified Exhaust Gas Recycle (EGR) as a promising technology for improving the economics of post-combustion capture, even at the 400 MW level (typical scale for a single line 9-type turbine) since, among other features, EGR allowed size reduction of the amine unit to a single

train. However, vendors of post-combustion capture technology now claim ability to design single trains up to capacities in the 550-600 MW equivalent range for NGCC power stations. A consequence is that EGR is unlikely to show advantages over traditional post-combustion technology for power stations delivering less than 800 MW, the approximate size where EGR can capture CO_2 using a single MEA train. This reduces possible field of application for EGR, as the number of 800 MW NGCC power stations is limited.

Several novel solvents have shown promise in large scale pilot tests applied to flue gas from coal power stations. Availability of novel solvents or sorbents with a steep variation in specific energy consumption with CO_2 concentration may increase chances for application of EGR. A recycle level in the 40-50% range may double CO_2 concentration in the effluent bringing it closer to the typical concentration of coal combustion effluents.

Though the first batch of large scale demonstrations of CCS is likely to focus on coal power stations, CO_2 capture from NGCC power stations still remains an interesting option for future application, since, in spite of higher specific CO_2 capture costs, the efficiency advantage of NGCC plants above coal power station is increased by CO_2 capture by 2-4% points. They also have less increase in the cost of electricity by about 10% with state-of-the-art technology than capture from coal. A screening of novel and emerging technologies specifically targeting this application is necessary to identify the path forward that may lead to further cost reduction in the mid-term.

REFINERY

For the retrofit of selected islands, including process heaters and boilers in a refinery, oxy-firing remains the approach with potential for lowest capture costs. Several vendors are in the process of developing and commercializing oxy-burners for both process heaters and boilers. The option of dilution through internal gas re-circulation, rather than external flue gas recycle may lead to further cost reduction. Acceptance of a network of oxygen pipelines in a refinery from the view point of HSE considerations is a prerequisite for future implementation.

The same considerations may be applied to the application of CO_2 capture to the effluent from the regenerator of a Fluid Catalytic Cracking (FCC) unit.

Scale considerations may favour post-combustion since a single amine train may now treat larger capacities than the largest cryogenic air separation units. This applies, for instance, to the largest world scale FCC units, representing however a small fraction of the total existing units.

Further studies are needed to assess the potential of pre-combustion in the refinery since this approach may include the hydrogen production unit and may be applied to the whole set of refinery sources of CO_2.

OTHER ASPECTS

The required CO_2 purity for transportation and storage is a remaining gap that may play a key role in the selection of technologies. Should very pure (> 99% vol.) CO_2 be required or should oxygen concentration in transportation and reservoir storage be limited to very low concentrations, the required purification systems might increase the cost of capture with oxy-firing techniques to a level that might favour post- or pre-combustion applications.

From this point of view development and optimization of CO_2 purification systems may become an important part of the overall R&D effort in CCS over the next years.

For new-built applications (for example steam generation for heavy oil product) Chemical Looping Combustion shows a very high potential for cost reduction coupled to some positive strategic features when compared to “conventional” oxy-firing:

- No presence of free oxygen, which mitigates HSE concerns.
- No need for air separation units, favouring implementation in remote locations.

The development of the CLC technology should be pursued to mitigate the remaining gaps in knowledge, optimizing the solid carrier from the view point of cost, chemical and mechanical duration, and environmental impact, and start implementation of a demo unit as soon as possible.

REFERENCES

1. Miracca, I. 2009, Introduction to the CCP2 Capture Technology Portfolio, in Eide, L.I. (ed.), 2009, Carbon Dioxide Capture for Storage in Deep Geologic Formations, Volume 3. CPL Press

SECTION 2:
STORAGE, MONITORING AND VERIFICATION

Carbon Dioxide Capture for Storage in Deep Geologic Formations, Volume 3
L.I. Eide (Ed.)

Chapter 20

CCP2 STORAGE, MONITORING AND VERIFICATION: INTRODUCTION AND OVERVIEW

Scott Imbus[1], Dan Kieke[1], Linda Curran[2] and Lars Ingolf Eide[3]
[1]Chevron Energy Technology Co., 1500 Louisiana St. Houston, TX 77002 USA
[2]BP Alternative Energy 150 W. Warrenville Road, Naperville, IL 60563, USA
[3]Stian Kristensens vei 33, N-1348 Rykkinn, Norway

ABSTRACT: This paper provides introduction to and overview of the CCP2 (CO_2 Capture Project) work related to geological storage of CO_2. The background for choosing individual research projects and their key results are described.

INTRODUCTION

The CO_2 Capture Project Phase 2 (CCP2) Storage Monitoring and Verification (SMV) program (2005-2008) aimed to develop promising CO_2 storage technologies identified in CCP1-SMV (2001-2004) [1] while addressing emerging technical gaps, identifying high impact opportunities and meeting member company priorities. At the start of CCP2 (2004/2005), the SMV Team identified priority research and development (R&D) topics that would address key CO_2 storage assurance gaps, simplify assessment protocols or improve cost-effectiveness. The identified assurance gaps included the geomechanical stability of reservoirs / caprocks and wellbore integrity. This was also the time when regulatory efforts were initiating and guidance from industry was needed on how to simplify and systematize complex assessment protocols. CO_2 Capture and Storage (CCS) will always incur costs. The guiding principles in project selection for CCP2-SMV funding included relevance to addressing cost-effectiveness, technical gaps, urgency and likelihood of CCP2-SMV achieving a substantial and unique contribution to the scientific and engineering disciplines directly applicable to geologic storage. As outcome the CCP2 decided to further develop the most pressing storage issues, with emphasis on:

- Risk assessment and a certification guidelines and protocols
- Wellbore integrity
- Geomechanical stability of reservoirs and caprocks
- Other opportunities to improve cost-effectiveness (e.g., monitoring)

The CCP2 portfolio of storage monitoring and verification (SMV) consists of seven technologies. Table 1 lists the technologies together with the involved R&D co-institutions. The portfolio consists of an integrated platform for site certification for CO_2 permitting, operation and decommissioning; well integrity logging, sampling, modelling, history matching and simulation of post-closure sealing capability over extended time; testing the capability of a standard logging tool to detect a sharp interface between free-phase CO_2 and brine; coupling of geochemical and geomechanical models; simulation of safe and effective operational constraints and monitoring for CO_2 injection in coal beds; and a field test of airborne remote sensing technologies.

Table 1. List of major SMV projects for phase II of CCP.
Underscore indicates the leading institutions

Project Name	**Involved institutions**	**Starting Date**	**Duration**
Certification Framework	Lawrence Berkeley National Laboratory (LBNL), Univ. Texas (UT), Univ. California, Berkeley (UCB)	April 2006	33 months
Wellbore Integrity Field Study	BP, Schlumberger, Los Alamos National Laboratory (LANL)	April 2006	33 months
Bench Scale Reservoir Saturation Tool (RST) Logging to detect CO_2	Schlumberger	April 2006	18 months
Coupled Geochemical-Geomechanical Simulation	Univ. Bergen and University of Catalonia, Spain	April 2006	33 months
Simulation study of methane and CO_2 migration and leakage in connection with Enhanced Coal Bed Methane (ECBM) operations	Sproule Associates,	April 2006	33 months
Non-seismic monitoring of ECBM	LBNL	June 2005	43 months
Remote Sensing of CO_2 and Methane Leakage	University of California Santa Cruz (UCSC)	June 2005	43 months

CERTIFICATION FRAMEWORK

The objective was to develop a simple, transparent framework for assessing, operating and decommissioning storage sites.

The framework is intended for certifying operation and decommissioning of Geologic CO_2 Storage (GCS) systems. It will provide a single, streamlined platform for integrating site assessment, field development/operation and risk assessment of proposed CO_2 storage programmes for use in project permitting, operating and decommissioning. The CF was developed in conjunction with an independent stakeholder advisory board.

The project is described in more detail in [2].

In 2005, the United States Environmental Protection Agency (US EPA) launched a series of workshops to better understand the role of industry and other (e.g., national labs) assessment protocols and modelling techniques in CO_2 storage project regulation. It was noted by the SMV Team that the complexity of the assessment processes and the use of sophisticated and/or proprietary software might hinder the development of workable regulations. Furthermore, the particular requirements of CO_2 storage ("indefinite" immobilization of large volumes of CO_2 in subsurface formations that might not have closed structures) are different from those of hydrocarbon exploration. The SMV Team worked with LBNL and UT to develop a generic framework that would organize input of geologic data, process such data using accessible numerical methods and perform risk calculations. The Certification Framework (CF) Team, which eventually included several researchers from multiple institutions, developed an assessment approach that would provide a single, streamlined platform for integrating site assessment, field development / operation and risk assessment for CO_2 storage programs. The CF, therefore, aimed to develop "a simple, transparent and accepted basis for regulators and stakeholders to certify that the risks of geologic carbon capture and storage (CCS) projects to Health Safety and Environment (HSE) and resources are acceptable".

The CF combines site data, simulations of plume migration, estimates of probability of intersection of the CO_2 plume with conductive wells and faults, and model calculations of fluxes and concentrations in compartments to calculate CO_2 leakage risk. The theory and philosophy of the certification framework includes the following generalized elements:

1) Effective trapping requirement – the CO_2 leakage risk over the period of review is below specified threshold flux levels (agreed upon by the proponent and regulator).
2) CO_2 Leakage Risk (CLR) – probability that storage volume of CO_2 (source) will migrate from the target reservoir (source) to impact a receptor compartment via preferential pathways or conduits (faults / fractures and wells). Safety and effectiveness of GCS are achieved if injected CO_2 does not impact underground sources of drinking water (USDW), nor migrate to the shallow subsurface and seep out into the atmosphere.

Simplicity in the CF is achieved by assuming that the main potential leakage pathways at carefully chosen GCS sites are wells and faults. Further, it is assumed that all of the vulnerable entities (protected resources) reside within a handful of compartments, and that impacts to compartments can be represented by proxy CO_2 fluxes and concentrations affecting the compartments. Transparency is achieved by making use of a precise terminology and a logical work flow. The CF allows screening of sites through use of a pre-computed catalogue of simulation results that a non-specialist user can query to estimate plume locations and pressures. This feature also enables interactive use of the CF to examine sensitivities of leakage risk to operating parameters or site properties. For site-specific simulations, the Certification Framework can use the results of commercial simulations developed with detailed geologic data.

In addition to developing the framework, the authors generated a catalogue of simulation results, implemented a simple well-flow model, initiated development of atmospheric dispersion capabilities and an improved well-flow model, and applied the CF approach to two case studies: (1) a hypothetical large-scale (24 million tonnes) GCS site in the Texas Gulf Coast; and (2) a one-million tonne pilot project in California that is part of the U.S. Regional Carbon Sequestration Program (WESTCARB Phase 3). The Texas site is in an area of historical hydrocarbon production and has a high density of deep exploration wells. This resulted in a 100% certainty that at least one abandoned well will be intersected by the CO_2 plume. While the California site will have a small enough plume that intersection with existing exploration wells is not predicted based on simulations, fault density is high enough to make plume intersection with faults likely. The faults are expected to be sealing features due to high shale-gouge ratio.

The dual objectives of encouraging the use of GCS as one of many climate-change mitigation strategies while simultaneously protecting the environment from unintended CO_2 injection-related impacts have motivated the development of a novel and practical risk-based framework for certifying that the leakage risk of a potential GCS site is below agreed-upon thresholds. The approach proposes a standardized way for project proponents, regulators, and the public to analyze and understand risks and uncertainties of GCS in a simple and transparent way. The CF considers both physical and chemical impacts as well as impacts to emission-reduction credits due to CO_2 leakage. Through its generality, the CF endeavours to contribute to the CO_2 and brine leakage-risk part of the certification process for licensing and permitting (e.g., start up or decommissioning) of GCS sites around the world regardless of the specific regulations in place in any given country.

WELLBORE INTEGRITY FIELD STUDY

This project was a well "autopsy" and "prognosis" study with the objectives to provide quantitative information on the extent of alteration in wells that have been exposed to CO_2, to history match the observed alteration, forward project the long-term barrier performance; and to develop appropriate engineering solutions to improve well integrity.

The project is described in more detail in [3].

Early in the CCP2 timeframe, stakeholders were hearing conflicting messages on well integrity ranging from rapid (weeks) deterioration of cement (based on aggressive laboratory conditions) to "not a significant problem" (decades-long CO_2 enhanced oil recovery (EOR) experience in West Texas). Encouraging data has been presented on the West Texas SACROC (Scurry Canyon Reef Operations Committee; majority of the Kelly-Snyder Field now operated by Kinder-Morgan), carbonate reservoir study (LANL) showing that cements are indeed altered by CO_2 exposure but that mineral replacement and void-fill mineral precipitation may maintain the fluid barrier [4]. The long-term integrity of wellbores in a CO_2-rich environment is a complex function of material properties and reservoir conditions including brine and rock compositions, CO_2 pressure, and formation pressure and temperature gradients. Laboratory experiments can provide essential information on rates of material reaction with CO_2. However, field data are essential for assessing the integrated effect of these factors in subsurface conditions to provide a basis for validation of numerical models of wellbore behaviour and precipitation reactions may limit the chemical and mechanical vulnerability of well materials.

A comprehensive study and conclusions from an investigation of a 30-year old well from a natural CO_2 production reservoir in Colorado, was conducted in 2006-2008. The wellbore had been exposed to a 96% CO_2 fluid from the time of cement placement. This site is considered "extreme" as CO_2 was co-produced with water and the clastic reservoir-caprock system affords little buffering capacity. The well produced CO_2 for a total of 20 years with the first 13 years averaging 7000 standard cubic feet per day (SCF/D) of CO_2 with associated water production of 0.75 barrel per 1000 SCF. The final 7 years of production was intermittent due to increased water production. Some conclusions are:

- The wellbore remains an effective hydraulic seal to CO_2
- Conventional cement-fly ash systems can inhibit CO_2 migration even after carbonation of the cement, i.e. carbonated cement remains an adequate seal
- Permeability and capillary resistance of the cement are at levels sufficient to act as barriers to CO_2 migration
- CO_2 migration within and above caprock did occur but are less significant with increasing distance from the reservoir

- Cement interfaces appear to be the preferential CO_2 migration path (as opposed to matrix diffusion)
- Current technologies effectively evaluate the barrier system

The CO_2 production well study illustrates that current technologies can be used to determine wellbore barrier condition. The barrier system in this well provides hydraulic isolation across the caprock based on formation pressure measurements made during this survey. Effective placement of the Portland-fly ash cement system was a key element in the performance of the barrier system to prevent or limit migration along cement interfaces with casing/borehole. Whereas carbonation of cement has increased permeability and porosity with mixed effects on capillary properties and compressive strength, the cement still provides an effective barrier. Conventional well systems, therefore, are suitable for long-term CO_2 storage operations if good practices are employed during well construction. Examples of such practices include: centralization of casing and efficient borehole mud removal for cement placement. The data acquired from the CO_2 production well will be incorporated into a model amenable to simulation of CO_2-fluid-rock-cement alteration over the near- (production) to long (post production) timeframes.

BENCH SCALE RESERVOIR SATURATION TOOL (RST) LOGGING TO DETECT CO_2

The objective was to develop, construct, and bench test a new well design that allows accumulation and detection of CO_2 leaking from wells and surrounding rock.

The project is described in more detail in [5].

The study tested the capability of standard logging tools to detect multiple phases of CO_2 originating from leakage through wells. A slightly modified well architecture could obviate the need for down hole samplers and sensors to detect plume arrival and well bore leakage. The pressurized test vessel constructed for this study is amenable to additional experiments including variable water salinity and multiphase fluids.

The concept of a modified well construction design, capable of accumulating CO_2 leaking through well annuli and amenable to detection by conventional logging tools, was proposed by British Petroleum (BP). Schlumberger was contacted to test the ability of their RST tool in detecting CO_2 under various fluid types and CO_2 pressures. A bench scale pressurized chamber, which could be loaded with sediments / water, charged with CO_2 and tested for RST tool response, was constructed for the study. Analysis of study results (based on a sand loaded tank with pore space filled with 2/3 brine and 1/3 CO_2) indicate that the RST (resistivity logging tool) contrast readings (with pre-CO_2 charge) are too small using inelastic capture mode (relative carbon yield and carbon / oxygen ratios), but sufficient using sigma mode (detection of decay response to neutron pulses, specific for fluid types) to detect a brine / free phase CO_2 contact.

As the scope of the study was limited, i.e., testing the bench scale chamber and the most basic sediment, brine and CO_2 charging conditions, the threshold of detection was based on CO_2 saturation and not extent of dissolution. Forward work might include calibrating dissolved CO_2 saturation to RST detectability limits and distinguishing between dissolved and residual phases.

GEOCHEMICAL-GEOMECHANICAL SIMULATION

The objective was to develop a robust, coupled simulation tool capable of predicting CO_2-induced alteration of reservoir and seal rocks over time and space.

The project is described in more detail in [6].

Injection of CO_2 into geological formations may result in geochemical reactions and pressure effects that may affect the performance of the flood or increase the likelihood of containment failure. To address these concerns, the CCP2 Storage Team commissioned development of a simulation tool that evaluates the mechanical stability of both the reservoir and seal rocks by modeling the evolution of stresses and other geomechanical parameters induced by the geochemical reactions that take place between the rock minerals and the CO_2-enriched wetting phase. In this interdependent and transient problem, the reactive transport simulation (geochemistry) and rock deformation modeling (geomechanics) need to be coupled. In other words, a single set of equations -generally a large system of nonlinear coupled partial differential equations- incorporating all of the relevant physics needs to be derived.

The coupled software developed in the study, RetrasoCodeBright (RCB), is comprised of two existing models: CodeBright, which calculates the mechanical deformation and solves the transport of mass and heat, and Retraso, which is the geochemical solver. Both these codes were adapted to the specific problem. The nonlinear algebraic systems of equations are solved through a Newton-Raphson iteration method. The governing equations and solution algorithms in CodeBright and in the geochemical solver in Retraso can be found in the project's final report.

The code was intended to have a user-friendly interface to enable an efficient and relatively fast set up of new systems through *Visual Retraso* and provision of a graphical interface for kinetic reaction models that allows testing for sensitivity in the characterization of the different reactions. The results from the two sections of the code are stored in common blocks and transferred to a graphical output format which enables the creation of figures and animations for the whole structure or for segments of the structure at any time step of the progress.

The simulation tool was applied to a simplified test case [6].

The RetrasoCodeBright simulator is the first to feature implicit coupling of geochemical and geomechanical simulator code. Thus, the development of a simulator with these capabilities and implicit coupling represent an important modeling effort. However, it remains to be seen whether the code is numerically stable as it has not been benchmarked with other codes nor calibrated with laboratory data. The example used to assess the software and provide results is very simple in terms of geology, geomechanics, and the injection processes. A successful simulation of a real case would be much more convincing.

CO_2 ECBM FLOW SIMULATION

The objective of this task was to establish safe and effective operating parameters for CO_2 injection and methane (CH_4) production processes in deep, unmineable coals.

The project is described in more detail in [7].

CO_2 enhanced coal bed methane (ECBM) recovery with CO_2 storage was widely considered prospective in the early CCP2 timeframe. Given that the methane release and CO_2 trapping in coals was (and continues to be) incompletely understood and that coal beds are usually situated in complex sedimentary systems that may be shallow (<800m or below the CO_2 critical point), the safe and effective operation of CO_2 floods in coals was uncertain. The "operability" study was commissioned to assess conditions under CO_2 ECBM that might be both effective (performance) and safe (contained).

This is the first of three projects co-funded by the CCP2 and the U.S. Department of Energy (DOE). The projects aimed to advance CO_2 sequestration monitoring, verification and risk assessment technology to include coal beds. The three projects dealt with:

- Simulation of CBM and CO_2 ECBM recovery processes and operating practices that could lead to leakage of methane or CO_2
- Modelling the resolution of inexpensive non-seismic geophysical monitoring tools to detect gas behaviour within coal seams and generically in the rock overburden
- Direct, remote detection of methane and CO_2 leakage from a coal (mining, EBM or CO_2 ECBM) or other geologic storage

The geologic model and simulations developed in the first task were necessary to construct a rock geophysical model to conduct the second task.

The project plan called for development of an operational simulation approach to optimize CH_4 production and CO_2 storage while investigating the potential for CO_2 leakage from a coalbed. A SECARB (Southeast Regional Carbon Sequestration Partnership, one of seven such organizations led by the US DOE) proposed small scale injection (900 tonnes) of CO_2 into the Deerlick Creek coal field in Alabama was chosen as the case study for the simulations.

The model of the Deerlick Creek Field consists of 27 layers including 14 coal seams in the three major groups of coal beds found in the field. The model includes thirteen intervening shale layers and nine wells. In order to enable modelling of leakage of CO_2 from the coal seams to upper horizons and the surface, a model of the entire overburden has also been developed.

Gas and water production have been successfully history matched by adjusting the fracture permeability and fracture porosity. Short term and long term injection of CO_2 into three coal seams have been successfully simulated.

Longer term injection scenarios included:

- A base case with no CO_2 injection
- Continuous CO_2 injection for 27 years with continuous operation of production wells
- Continuous CO_2 injection for 30 years with production wells shut-in after CO_2 breakthrough
- Continuous CO_2 injection for 13 years, production wells shut-in, CO_2 injection continued for an additional 20 years
- Continuous CO_2 injection for 13 years, production wells shut-in, CO_2 injection continued for an additional 16 years at a higher injection rate

Simulation results showed CO_2 sequestration amounts that varied by a factor of about five between the scenarios but almost similar volumes of methane produced.

The simulation case study results indicated that a trade-off exists between sequestration efficiency and methane recovery. CO_2 ECBM should not necessarily be expected to lead to increased recovery of methane. While CH_4 saturations were reduced significantly in those areas swept by CO_2, CH_4 saturations remained high in unswept or poorly swept areas. Sequestration volumes could be increased by (1) increasing the CO_2 injection rate after production well shut-in or (2) perforating additional coal seams. Conducting simulations on a range of coal bed settings and operating conditions would help identify guidelines for optimizing CH_4 production and CO_2 storage.

The results from the study evaluating the potential for leakage of CO_2 indicated that CO_2 is unlikely to migrate to the surface through natural fissures over a period of centuries. Other vulnerable features such as wells or induced fractures could provide pathways for leakage to the surface or groundwater resources. However, evaluation of these features was outside the scope of this project.

NON-SEISMIC MONITORING OF ENHANCED COAL BED METHANE (ECBM)

The objective of this task was to develop cost effective monitoring technologies to assess CO_2 flood performance and detect low seepage rates.

The project is described in more detail in [8].

This is the second of three projects co-funded by the CCP2 and the U.S. Department of Energy (DOE). It uses the geologic model and flow simulation results from the first project described above.

CO_2 ECBM and storage, if feasible, will likely involve numerous wells and the need for cost effective monitoring. Whereas conventional surface seismic is feasible for monitoring CO_2 injection in coal beds, likely settings for CO_2 ECBM operations in the Eastern US will include hilly, forested terrane, making logistics for acquisition and interpretation of data difficult and expensive. A previous analysis of non-seismic geophysical techniques for monitoring CO_2 injection was carried out as part of the "Novel geophysical monitoring" project of CCP1 [9]. The results from that study showed that electromagnetic (EM) and gravity measurements could, under certain circumstances, be used as a lower cost alternative to seismic geophysics. However, the reduction in cost is accompanied by a reduction in spatial resolution so the utility of non-seismic techniques would be site dependent. This project adapted the novel geophysical concepts developed for saline aquifers under CCP1 to include coal beds.

The simulation studies conducted in the task described above of CO_2 injection into coal beds in the Deerlick Creek pilot area were used to develop geophysical models to simulate gravity and EM responses from coal beds containing CO_2 and to predict the utility of these non-seismic detection methods for monitoring the presence and migration of CO_2 in the geologic setting. Laboratory measurements, carried out independently from this project, of electrical resistivity and seismic velocity as a function of CO_2 saturation on a coal core sample were used as a link between the coal bed CO_2 injection flow simulation results described above and the geophysical models.

Simulation results indicated that CO_2 injected into a coal seam should be detectable using gravity or EM non-seismic detection methods. Even the small volumes planned for the Deerlick Creek field test should be detectable. Inversion of gravity data accurately predicted the location of the CO_2 plume. Synthetic time-lapse seismic AVA analysis showed that by inverting seismic and EM data jointly much better estimates of CO_2 saturation can be obtained compared to those obtained from the inversion of seismic data only.

This study's results coupled with results from a previous CO_2 Capture Project study [9] simulating gravity and EM monitoring of CO_2 injected into the Schrader Bluff field on the North Slope of Alaska indicate that gravity and EM methods have potential as lower cost alternatives to seismic measurements. Field surveys of an actual CO_2 injection would confirm these studies' conclusions.

REMOTE SENSING OF CO_2 AND METHANE LEAKAGE

The objective was to evaluate aerial hyperspectral monitoring as a means of directly detecting CO_2 and CH_4 leakage over large areas, eliminating the need for extensive ground based monitoring infrastructure and thereby providing significantly lower operational costs.

The project is described in more detail in [10].

This is the third of three projects co-funded by the CCP2 and the U.S. Department of Energy (DOE).

At the start of the study, remote hyperspectral detection of CO_2 was limited to indirect, chronic effects on vegetation and soils. Developing a remote sensing application capable of detecting leakage of CO_2 and other gases (particularly methane) from storage sites would have advantages in the ease of large area coverage with elimination of most expenses and environmental impact of field-based instrumentation and crews. The CCP1-SMV study [11] on remote (satellite and aerial) geobotanical detection of CO_2 was inconclusive. UCSC proposed to use the instrument (re-tuned) for an aerial survey of field sites known to emit CO_2 and methane. The Rocky Mountain Oilfield Technology Center (RMOTC) Teapot Dome Field site in Wyoming was chosen as a site for detection work using the MASTER (airborne modification of NASA's satellite (MODIS / Advanced Spaceborne, Thermal Expansion and Reflection Radiometer), as test facilities were available for releasing CO_2 and methane through perforated pipes at the surface and in the shallow subsurface. Overflights in August 2006 traversed "engineered" leaking sites and an adjacent control site.

Seven experimental leak sites were used in this experiment, laid out to simulate leaks from a pipeline. Four sites were used as sources of methane/natural gas, and three were used as sources of CO_2.

Results obtained from the evaluation of remote, hyperspectral monitoring for direct detection of CO_2 and CH_4 leaks showed the MASTER instrument to be unsuitable as it is currently configured. It appears likely that the MASTER instrument could detect large ground leaks of CH_4 with its present configuration. However, the MASTER instrument could not reliably detect CO_2 from ground based leaks.

The difficulty inherent in this type of application is trying to detect small changes in CO_2 or CH_4 concentrations through a large column of the atmosphere. In general, the MASTER spectral resolution is too broad. Successful application of hyperspectral monitoring for direct detection of CO_2 and CH_4 will require advances in instrument design**.**

CONCLUSIONS

The CCP2-SMV program includes a diverse portfolio of projects aimed at addressing technical gaps surrounding CO_2 storage assurance and cost effectiveness. The Wellbore Integrity Field Study, through an assessment protocol using existing technology, broke new ground in our understanding of the rate, extent and origin of alteration in CO_2-exposed wells. The Certification Framework provides a simple and transparent approach identifying and assessing risk associated with prospective CO_2 storage sites. The Geochemical-Geomechanical Simulation study provides a new numerical approach to depicting impacts of CO_2 injection on reservoir and cap rocks. The CO_2 ECBM flow and geophysical modelling studies offer an understanding of operational tradeoffs between CO_2 storage and methane production as well as a cost-effective monitoring approach. The remote sensing study provides lessons-learned on sensor selection and surveying techniques.

REFERENCES

1. Benson, S.M., ed., 2005, Carbon Dioxide Capture for Storage in Deep Geologic Formations - Results from the CO_2 Capture Project, Vol. 2: Geologic Storage of Carbon Dioxide with Monitoring and Verification, Elsevier Publishing, UK. 654 pp
2. Oldenburg, C.M., S. L. Bryant, J-P. Nicot, N. Kumar, Y. Zhang, P. Jordan, L. Pan, P. Granvold, F. K. Chow, 2009. Model Components of the Certification Framework for Geologic Carbon Storage Risk Assessment, in: Eide, L.I. (ed.), 2009. Carbon Dioxide Capture for Storage in Deep Geologic Formations Vol. 3, CPL Press, UK

3. Crow, W., D. Brian Williams, J. W. Carey, M. Celia and Sarah Gasda, 2009. Well Integrity Evaluation of a Natural CO_2 Producer, in: Eide, L.I. (ed.), 2009. Carbon Dioxide Capture for Storage in Deep Geologic Formations Vol. 3, CPL Press, UK
4. Carey, W., M. Wigand and S. Chipera *et al.*, Analysis and performance of oil well cement with 30 years of CO_2 exposure from the SACROC Unit, West Texas, USA, *International Journal of Greenhouse Gas Control* (2007), pp. 75–85
5. Climent, H. 2009. CO_2 Detection – Response testing of RST in Sandstone Formation Tank Containing CO_2 and Water-based Fluid, in: Eide, L.I. (ed.), 2009. Carbon Dioxide Capture for Storage in Deep Geologic Formations Vol. 3, CPL Press, UK
6. Kvamme, B. and S. Liu, 2009. A new reactive Transport Reservoir Simulator for Aquifer Storage of CO_2 – with implicit Geomechanical Analysis, in: Eide, L.I. (ed.), 2009. Carbon Dioxide Capture for Storage in Deep Geologic Formations Vol. 3, CPL Press, UK.
7. Galas, C., V. Savenko, and DE. Kieke 2009. Simulation Study of Methane and Carbon Dioxide Migration and Leakage during Normal and Enhanced Field Operations to recover Coal Bed Methane from Coal Seams, in: Eide, L.I. (ed.), 2009. Carbon Dioxide Capture for Storage in Deep Geologic Formations Vol. 3, CPL Press, UK.
8. Gasperikova, E. and J. Chen, 2009**.** A Resolution Study of Non-seismic Geophysical Monitoring Tools for Monitoring of CO_2 Injection into Coal Beds**,** in Eide, L.I. (ed.), 2009. Carbon Dioxide Capture for Storage in Deep Geologic Formations Vol. 3, CPL Press, UK.
9. Hoversten, G.M. and E. Gasperikova, 2005. Non-Seismic Geophysical Approaches to Monitopring, in Benson, S.M., ed., 2005, Carbon Dioxide Capture for Storage in Deep Geologic Formations - Results from the CO_2 Capture Project, Vol. 2: Geologic Storage of Carbon Dioxide with Monitoring and Verification, Elsevier Publishing, UK. 654 pp.
10. Pickles, W.L., E.A. Silver and J. Jacobson, 2009. Monitoring and Verification of Controlled releases of CO_2 and CH_4 Using airborne Remote Sensing in: Eide, L.I. (ed.), 2009. Carbon Dioxide Capture for Storage in Deep Geologic Formations Vol. 3, CPL Press, UK.
11. Pickles, W.L., Cover, W.A., 2005. Hyperspectral Geobotanical Remote Sensing for CO_2 Storage Monitoring, in: Benson, S.M., ed., 2005, Carbon Dioxide Capture for Storage in Deep Geologic Formations - Results from the CO_2 Capture Project, Vol. 2: Geologic Storage of Carbon Dioxide with Monitoring and Verification, Elsevier Publishing, UK. 654 pp.

Carbon Dioxide Capture for Storage in Deep Geologic Formations, Volume 3
L.I. Eide (Ed.)

Chapter 21

MODEL COMPONENTS OF THE CERTIFICATION FRAMEWORK FOR GEOLOGIC CO_2 STORAGE RISK ASSESSMENT

Curtis M. Oldenburg[1], Steven L. Bryant[2], Jean-Philippe Nicot[3], Navanit Kumar[2,5], Yingqi Zhang[1], Preston Jordan[1], Lehua Pan[1], Patrick Granvold[4], Fotini K. Chow[4]
[1]Earth Sciences Division, 90-1116, 1 Cyclotron Rd.,
Lawrence Berkeley National Laboratory, Berkeley CA 94720
[2]Department of Petroleum and Geosystems Engineering, The University of Texas at Austin,
1 University Station C0300, Austin, TX 78712
[3]Bureau of Economic Geology, Jackson School of Geosciences, The University of Texas at Austin,
University Station, Box X, Austin, Texas 78713
[4]Department of Civil and Environmental Engineering, University of California,
Berkeley, Berkeley, CA 94720
[5]Shell Oil and Production Company, 200 North Dairy Ashford, Houston, TX 77079

ABSTRACT: We have developed a framework for assessing the leakage risk of geologic CO_2 storage sites. This framework, known as the Certification Framework (CF), emphasizes wells and faults as the primary potential leakage conduits. Vulnerable resources are grouped into compartments, and impacts due to leakage are quantified by the leakage flux or concentrations that could potentially occur in compartments under various scenarios. The CF utilizes several model components to simulate leakage scenarios. One model component is a catalog of results of reservoir simulations that can be queried to estimate plume travel distances and times, rather than requiring CF users to run new reservoir simulations for each case. Other model components developed for the CF and described here include fault characterization using fault-population statistics; fault connection probability using fuzzy rules; well-flow modeling with a drift-flux model implemented in TOUGH2; and atmospheric dense-gas dispersion using a mesoscale weather prediction code.

INTRODUCTION

We have developed a novel and practical risk-based framework for certifying that the leakage risk of a potential geologic CO_2 storage (GCS) site is below agreed-upon thresholds [1, 2, 3]. The approach we developed, known as the Certification Framework (CF), proposes a standardized way for project proponents, regulators, and the public to analyze and understand risks and uncertainties of GCS in a simple and transparent way. The CF goes beyond the scope of regulations of deep underground injection permitted by the U.S. Environmental Protection Agency (EPA) which protect underground sources of drinking water (USDW) to consider risks to a broader set of resources and environmental assets as well as loss of emission-reduction credits due to CO_2 leakage. The CF uses physically grounded models for the movement of injected CO_2 and brine, and for assessing the likelihood that CO_2 or injection-related pressure perturbation will intersect wells and faults. The CF and an example case study have been fully described elsewhere [3]. This paper describes the essential model components that we have developed for carrying out a CF analysis. These model components include the catalog of simulation results, fault population statistics, fault connectivity analyses, well-bore flow, and dense gas dispersion.

BRIEF OVERVIEW OF THE CF

The goal of the CF is to evaluate the degree to which a GCS site is expected to be safe and effective. In the risk-assessment context, the word "safe" means that impacts to humans and other living things, the environment, and other resources resulting from injection are acceptably low over both short and long time periods. The word "effective" means that the site will contain indefinitely the vast majority of injected CO_2 [4]. The approach we take in the CF is to simplify the system into a tractable and logical form amenable to modeling and analysis. We achieve simplicity in the CF by assuming that sedimentary basins share common concerns such as the presence of wells and faults as potential leakage pathways.

The CF uses the concept of "effective trapping" [3] in acknowledgment of the enormous volumes of CO_2 that will be injected into the non-leak-proof deep subsurface. If small amounts of injected CO_2 escape to the atmosphere, the net mitigation of CO_2 emissions is still substantial. Furthermore, effective trapping is intended to recognize the fact that migration of injected CO_2 can significantly increase the amount stored in secure forms (e.g., dissolved in brine, or trapped as a residual phase) [5]. Of course, harmful leakage of CO_2 (or brine) into USDW, into other resources, or even out of the ground is also possible. Analyses with the CF distinguish benign from harmful migration so that the risk management can focus on the latter.

The CF approach uses a precise terminology. Before leakage of CO_2 can be discussed, it must be defined. To this end, the following definitions are established:

- *Effective Trapping* is the proposed overarching requirement for safety and effectiveness.
- *Storage Region* is the three-dimensional volume of the subsurface intended to contain injected CO_2.
- *Leakage* is migration across the boundary of the Storage Region.
- *Compartment* is a collection of vulnerable entities (e.g., environment and resources).
- *Impact* is a consequence to a compartment, evaluated by proxy concentrations or fluxes.
- *Risk* is the product of probability and consequence (impact).
- *CO_2 Leakage Risk* is the product of the probability and negative impact to compartments arising from CO_2 migration.
- *Effective Trapping* is achieved if CO_2 Leakage Risk is below agreed-upon thresholds.

The purpose of the CF is to evaluate the CO_2 Leakage Risk (CLR) for each compartment to determine whether the Effective Trapping threshold will be met for a proposed GCS site. Given the large amounts of brine that will be pressurized and displaced by injected CO_2, we further define the brine leakage risk (BLR) as the product of the probability and consequences to compartments of brine migration.

Wells and Faults are the Conduits

We assume in the CF that wells and faults are the only potential leakage conduits. This assumption is made to simplify the analysis and is predicated on the assumption that GCS sites will be well chosen so as to avoid sites with potentially discontinuous cap-rock seals. Under this assumption, the injected CO_2 and the associated over-pressured brine comprise the source of fluids that can potentially leak through the conduits.

Impacts Occur to Compartments

The consequence of upward leakage of CO_2 or brine is impact to compartments, which the CF uses to represent the vulnerable entities. For example, USDW, taken collectively at a site, forms a single compartment. In the CF, we define five compartments in which impacts will be evaluated.

- ECA = Emission Credits and Atmosphere
- HS = Health and Safety
- NSE = Near-Surface Environment
- USDW = Underground Source of Drinking Water
- HMR = Hydrocarbon and Mineral Resources

The compartments have general locations within the system but are abstract in the sense that they are collections and may include disconnected pieces. For example, there may be multiple zones of USDW and yet the CF would consider only one USDW compartment. Similarly, the HS compartment is abstract in that safety could refer to both a resident in a home or a worker in an office building. The ECA compartment is even more abstract in that emission credits are not physical entities.

We present in Figure 1a a cross section of a generic GCS site showing a deep structure potentially suitable for use in sequestering CO_2, sealing formations, an oil-bearing formation, faults, wells, USDW, vegetation, and a residence with water well. This conceptualization of common elements of a GCS system is further abstracted to consist of the source, conduits, and compartments of Figure 1b. In summary, the CF simplifies the GCS system so that the CO_2 (and brine) form a potential source of hazard, wells and faults comprise the potential leakage pathways, and impacts occur to compartments.

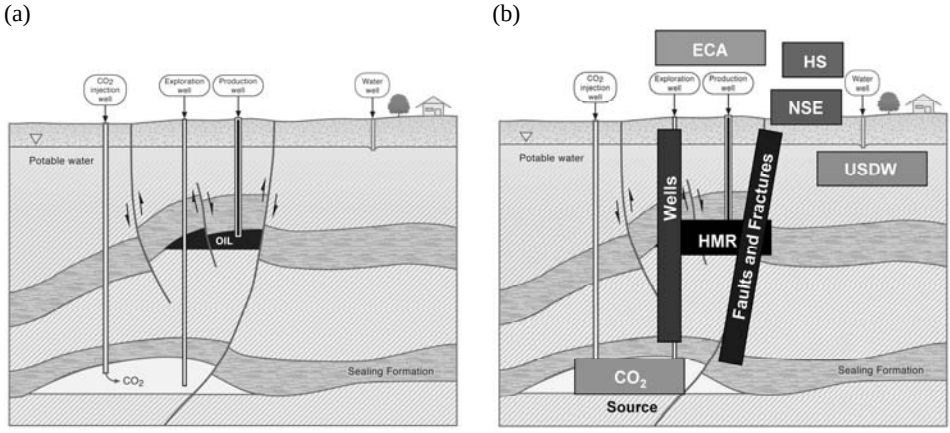

Figure 1. (a) Generic geologic cross section of potential GCS site showing reservoir and sealing formations, faults, wells, USDW, and near-surface and surface environments. (b) Generic cross section with CF source and compartments overlaid.

Evaluating Impacts

Impacts of CO_2 to compartments are evaluated by modeling and simulation of proxy concentrations or fluxes. The CF assumes that there are established limits on CO_2 or brine concentrations within the compartment as a whole, or on fluxes into the compartment, that ensure acceptable impact to the compartment. The numerical value of these limits will be specified in regulations that may vary by country. Whether a concentration- or flux-based limit is appropriate depends on the context and compartment. For example, for modeling CO_2 impact to the HS compartment, it may be most convenient to set a concentration-based limit since the safety standards for CO_2 exposure are given in terms of concentration of CO_2 in air. In contrast, the ECA compartment impacts will be best

modeled using a flux-based limit. In all cases, the time over which the high concentration or flux persists is important to calculate the associated impact. Reservoir simulation results (e.g., from a catalog of pre-computed results) are used to calculate fluxes and concentrations resulting from the CO_2 source and brine displacement process, and well and fault flow models are used for leakage up the conduits.

Likelihood of Impact and Risk

The CF uses the likelihood of intersection of the CO_2 (or brine) source with a conduit, and the likelihood of intersection of the conduit and a compartment to generate the probability of the given source-to-compartment leakage scenario. The risk associated with that leakage is the product of the likelihood of leakage and the impact of that leakage event. Acceptable risks from CO_2 or brine leakage will be those below a threshold provided by external sources such as regulators or carbon credit insurers.

Work Flow

The overall work flow of the CF approach is summarized in Figure 2. External inputs are required to characterize the site and define the reservoir, injection plan, and time frame. These inputs constrain the conditions and properties needed to estimate the CO_2 (source) plume location, footprint size, and pressure perturbation, e.g., by reservoir simulation. These characteristics of the plume change during injection and after injection ends. Values at times deemed significant by regulators, e.g. at end of injection, 25 yr and 100 yr after injection ends, can be extracted from the simulations. Next the CF uses external inputs on wells and faults, typically the plan-view spatial density of abandoned wells and conductive faults.

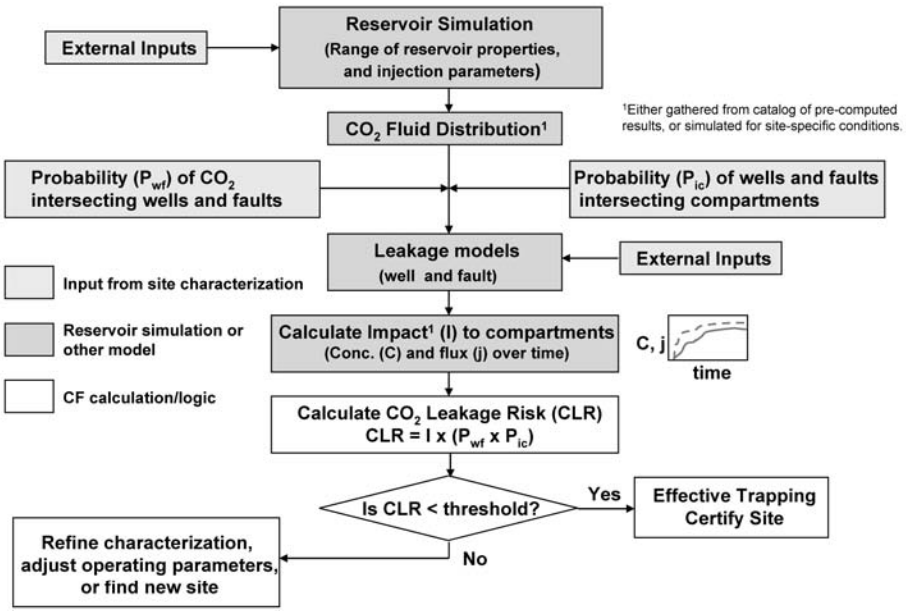

Figure 2. Flow chart of CF-CLR process showing logic and inputs and outputs.

The likelihood of the plume intersecting the conduits is a function of the plume size and conduit spatial density. The output of the reservoir simulation is fed to the conduit flow model to calculate fluxes and/or concentrations within compartments under the assumption that they intersect. The fluxes and/or concentrations calculated by the CF either exceed the limit or fall below the limit (are not impacts). The risk can then be calculated as the product of the impact and the likelihood of the corresponding intersection with conduits (leakage scenario). Comparing the calculated CLR to the externally provided threshold, the CF determines whether the leakage risk is acceptable. If the CLR is above the threshold, changes to the injection plan or refinements in site characterization may be made, resulting in decreased CLR. Although written in terms of CLR for brevity, the CF analysis of BLR follows the same flow process. Greater detail of the CF and a case study can be found in [3].

As outlined above, the CF relies on model components and approaches for calculating risk. Specifically, physical process models (reservoir simulation, conduit leakage flow, and atmospheric dispersion) and model approaches (fault density, likelihood of fault intersection) are required to carry out a CF analysis. In the remainder of this chapter, we describe the five critical model components that we have developed for use in the CF. These components are particular examples for demonstration and application of the CF approach. Any of them could be replaced with a functionally equivalent model or approach without changing the fundamental framework or workflow of the CF.

MODEL COMPONENTS IN THE CF

Simulation Catalog

To facilitate use of the CF by a wide range of people, we have developed a catalog of reservoir simulation results that can be queried by users to obtain estimates of plume size and pressure perturbation at various times [6]. The reservoir simulations in the catalog were carried out using the CMG-GEM (Computer Modelling Group (Calgary), Generalized Equation of state Model) numerical reservoir simulator with the equation of state tuned to the CO_2/brine system [7, 8]. A large number of cases were simulated with a range of combinations of key reservoir properties such as thickness, dip, porosity, permeability, permeability anisotropy, injection interval, and injection rate. In the simulations, constant-rate injection is specified at the center of the generic model reservoirs, with constant-pressure conditions imposed at the model boundaries. The significant output extracted from the simulations and stored in the catalog includes time for CO_2 to migrate to the top of the reservoir, size of CO_2 plume and fraction of the CO_2 that is still mobile as functions of time, and pressure in the reservoir.

Parameter Ranges

Ranges of parameters for typical saline formation targets are presented in Table 1. As the initial attempt to construct such a catalog, simulations were carried out on a subset of these parameters indicated by shading in the table. The output is post-processed to provide a much reduced dataset in terms of the response variables for use in the CF. The risk parameters (time to hit top, maximum lateral extent, and total mobile gas) can be extracted from these simulations and interpolated for cases that do not exactly match catalog input parameters [9].

Table 1. Formation and operating parameters and their general range of values for aquifers. Shaded terms were used in this study.

FORMATION ROCK/FLUID PROPERTIES		Units	Range of values		
			High	Medium	Low
Anisotropy	k_v/k_h	--	1	0.03	0.001
Residual nonwetting phase saturation	$S_{g,r}$	--	0.8	0.5	0.2
Average saturation of CO_2 between injection well and injection front	S_{mean}	--	1	0.6	0.2
Relative permeability of CO_2 at displacement front	$k_{CO_2,disp}$	--	1	0.5	0.1
Lateral correlation length of permeability	λ	m	∞ (layered)	100	0 (uncorrelated)
Dip angle (from horizontal)	α	°	20	5	0
Thickness	h	m	300	50	10
Average permeability (horizontal)	$<k_h>$	mD	1000	100	10
Average porosity	ϕ	--	0.40	0.20	0.10
Spacing of natural fractures (see spacing of faults)	w_{frac}	m	∞ (unfractured)	100	1
Fault permeability relative to matrix permeability	k_{fault}/k_h	--	100	1	0.01
FORMATION CHARACTERISTICS					
Depth	Z	m	3000	1000	100
Spacing of existing wells	w_{well}	m	∞ (no wells)	500	50
Spacing of faults	w_{fault}	m	∞ (no faults)	1000	100
Lateral distance from injector to top of nearest anticline	L	m	∞ (no structure)	2000	200
Thickness of caprock	h_{cap}	m	1000	100	10
OPERATIONAL PARAMETERS					
Number of vertical injection wells	N_{vert}	--	10	1	0
Number of horizontal injection wells	N_{horiz}	--	10	1	0
Mass of CO_2 to be injected	M	ton	10^8	10^7	10^6
Injection period	t_{inj}	y	50	10	5
Fraction of formation thickness in which vertical well is completed	f_{perf}	--	1	0.5	0.25

Response Variables

To constrain the CO_2 leakage potential, we consider the three response variables illustrated in Figure 3, namely (1) total mobile CO_2 in the aquifer, (2) maximum lateral distance traveled from the injector, and (3) time the plume takes to reach the top seal.

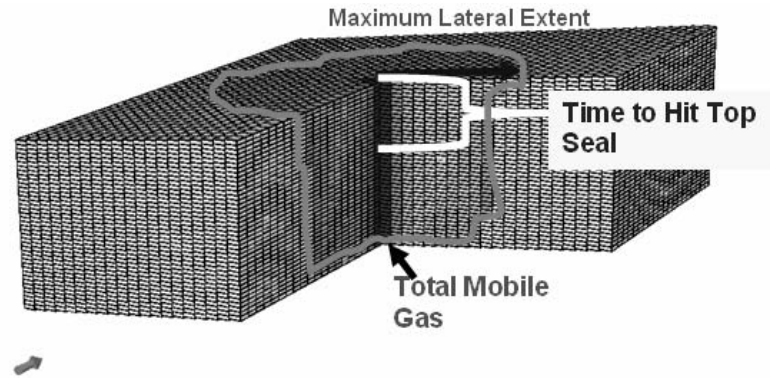

Figure 3. Schematic showing aquifer system with a vertical injector in center. Well is perforated in bottom half section of thickness. Three response variables (time to hit top seal, maximum lateral extent and total mobile gas) are shown.

Total mobile CO_2 is the CO_2 that has not been trapped by dissolution, residual trapping, or mineral trapping. The mobile CO_2 is calculated from phase saturations in grid cells in which relative permeability of CO_2 phase is greater than zero. Total mobile CO_2 is expressed as percent of total CO_2 injected.

Maximum lateral distance is the distance the CO_2 plume (defined as region in which CO_2 phase saturation is nonzero) travels in the (sub-) horizontal or up-dip direction from the injector in 1000 years. The longer the distance the plume travels, the higher is its probability to intersect leaky faults or abandoned wells. Some plumes reach the edge of the simulation domain, and in these cases the lateral extent can be estimated by calculating the plume velocity in the up-dip direction and multiplying by 1000 years.

Time to reach the top seal is calculated as the time when any of the top layer grid blocks have non-zero CO_2 phase saturation. If CO_2 is injected across the entire thickness of the aquifer, time to reach top is zero. If CO_2 is injected in the lower regions of the aquifer, CO_2 will move vertically until it is either trapped or reaches the top seal. If CO_2 is still mobile, the plume will move laterally under the top seal.

Risk Parameters Correlated by Gravity Number

The catalog results are observed to be correlated to the Gravity number (N_{gv}), which is the dimensionless ratio of gravity forces to viscous forces in a reservoir. In general, the gravity number determines the shape of the CO_2 plume in an aquifer and is a convenient way to parameterize the CF catalog results. The various properties of the simulations carried out to generate the catalog can be grouped into the Gravity Number

$$N_{gv} = \frac{k_v \Delta\rho g \cos\alpha}{\mu u_{inj}} \qquad \text{Equation 1}$$

Here k_v is vertical permeability, $\Delta\rho$ is density difference between brine and CO_2 at aquifer temperature and pressure, α is the dip angle, μ is CO_2 viscosity, and u_{inj} is the injection velocity.

The injection velocity is computed at the wellbore/formation interface by

$$u_{inj} = \frac{Q}{A_w} = \frac{Q}{2\pi r_w h_p} \qquad \text{Equation 2}$$

where Q is the volumetric injection rate, A_w is the circumferential area of the well, r_w is the well radius and h_p is the perforation interval.

Figure 4 shows an example simulation result of saturation profiles after 20 years for two different gravity numbers. The aquifer is 500 ft (150 m) thick and horizontal permeability is 100 md in both the cases. The gravity number is varied by changing injection rate and vertical permeability. In Case "a" the injection rate is 15 MMscfd (8.8 kg/s) and vertical permeability is 3 md, yielding N_{gv} = 0.013. In Case b the corresponding values are 10 MMscfd (5.9 kg/s), 10 md and 0.07. The higher gravity number case (Case b) has more gravity override of CO_2 and the CO_2 travels a longer distance beneath the top seal reaching 6000 ft (1800 m) in 20 years. In Case a the flux distribution along the perforated interval is almost uniform resulting in the plume contacting more rock and brine in the lateral direction and thus enhancing trapping. The gravity override is very small and the lateral distance traveled in 20 years is 2750 ft (840 m). As this example shows, higher gravity number is detrimental to CO_2 trapping efficiency. The ability to capture general trends such as this one is an advantage of using a catalog in the CF.

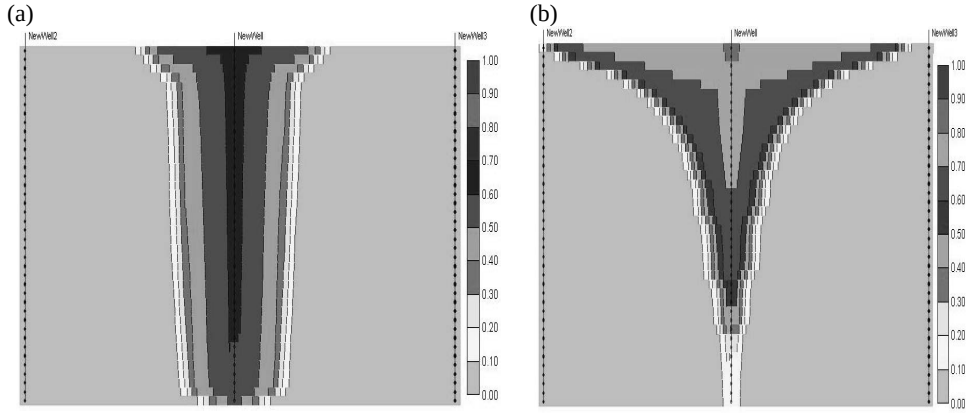

Figure 4. a) CO_2 plume for lower gravity number (N_{gv} = 0.013) after 20 years of injection. The plume moves almost uniformly away from the well in the lateral direction.
b) CO_2 plume for higher gravity number (N_{gv} = 0.07) after 20 years of injection. There is preferential vertical movement of the plume and greater gravity override.

Example of Time to Hit Top Seal

To demonstrate the use of parameterizations derived from the catalog, we present an example of the time to hit the top seal. The data were extracted from the simulations carried out to generate the catalog. The correlation improves if time t to hit top seal is normalized by a characteristic time t^* given by

$$t^* = \frac{(H - h_1) h_2 r_w \varphi}{Q} \qquad \text{Equation 3}$$

where H is the formation thickness, h_1 is the distance to the top perforation in the vertical well from the aquifer bottom, h_2 is the perforation interval, and ϕ is porosity. In short, t^* is the time for the plume to arrive at the top seal if it were traveling at constant velocity v corresponding to the radial velocity at the wellbore:

$$v = \frac{Q}{\varphi A_w} = \frac{Q}{2\pi r_w h_2 \varphi} \qquad \text{Equation 4}$$

For large gravity number, the plume travels almost vertically and t/t^* approaches unity. For small gravity number, the plume travels more in the lateral direction, and $t/t^* << 1$. Thus dimensionless time (t/t^*) is correlated inversely to gravity number.

For the simulations included in the catalog, the plot of dimensionless time to hit the top vs. gravity number, Figure 5, shows considerable scatter, but an inverse relationship is evident as expected from the above discussion. The data points on the plot correspond to various simulations run with varying porosity, permeability, permeability anisotropy, thickness, depth, and perforated interval.

Higher gravity number generally has these effects:

- Preferential vertical movement and thus smaller time to hit the top.
- In a dipping aquifer, once the plume reaches the top seal it travels faster.
- Trapping is reduced as the plume does not come in contact with as much rock and brine in the direction transverse to plume movement.
- In large perforated sections, only a fraction of perforations contribute to injection.

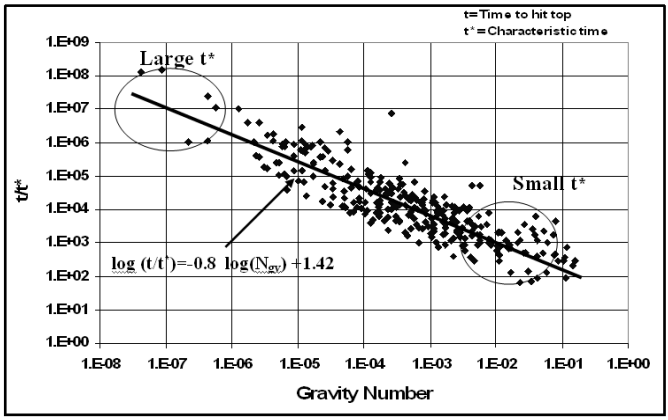

Figure 5. Plot of dimensionless time to hit top seal vs. gravity number. The data points are from simulations carried out by varying porosity, permeability, permeability anisotropy, thickness, depth, and perforated interval.

Using catalog for estimating risk parameters for actual aquifer

The simulation catalog includes cases for low, medium and high values of the shaded properties listed in Table 1. Most aquifers will not have all properties similar to any one case in the database. For a particular aquifer, we can estimate the risk parameters with simple correlations, or by interpolation from the closest database case. As an example of the former, the time to hit the top seal can be estimated by calculating the gravity number and characteristic time (t^*) for the target

aquifer, then using the trend line in Figure 5. Examples of interpolation for lateral extent and fraction of mobile CO_2 are described in [9].

FAULT POPULATION STATISTICS

In order to calculate the likelihood of intersection of the CO_2 plume (or brine pressure perturbation) with conductive faults, we developed a method based on fault population statistics [10, 11]. These statistics can be measured from available fault coverages (geologic or structure maps) near or at a prospective site. Combining this information with an estimate of the anticipated plume size, shape, and orientation (obtained from the reservoir simulation catalog) allows calculation of the probability of the plume encountering a fault of a particular size.

Fault Population Statistics

Numerous investigators have found that fault length and displacement populations evolve with increasing strain, but typically follow a power-law distribution from low to moderate strains. This finding is based upon field research (e.g., [12]), physical modeling (e.g., [13]), and numerical simulations (e.g. [14]). Power-law distributions are of the form

$$N_d \propto d^{-C_d} \qquad \text{Equation 5}$$

where N_d is the number of faults with displacement greater than d, and C_d is the power law exponent.

Fault Density

Values of N_d are dependent upon the area of interest. The areal density of faults, F, is more useful as it is not dependent on area, which is based on CO_2 plume size in the current application. Values of F can be accurately calculated by measuring the length of faults with greater than a certain displacement in an area and dividing by the area. Structure contour maps are a typical source for such data. Because values of N_d are defined based on scan-line intersections and therefore contain length information, F can be substituted for N_d in Equation 5 [11] and follows the same pattern as of N_d. This substitution yields

$$F \propto d^{-C_d} \qquad \text{Equation 6}$$

and

$$\log F \propto -C_d \log d \qquad \text{Equation 7}$$

Equation 7 indicates a log-log plot of F against d will be linear if the fault population follows a power-law distribution. In addition, F approaches infinity as d approaches 0. This implies F becomes very large at the actual lower limit of d. This suggests a high probability that a given CO_2 plume will encounter a fault of some size. Of course, most such faults will have such small displacements as to not be of serious concern for leakage. This suggests that the concern for leakage should be on faults of a certain size (large enough to have a high probability of leakage) rather than on all faults encountered.

Fault Encounter Probability Estimation

The method used by the CF to calculate the probability of a CO_2 plume encountering a fault proceeds by the following steps:

1) Identify fault coverage(s) (fault-map data) relevant to a proposed site.

2) Measure fault lengths, orientations, and displacements from the coverage(s).
3) Define fault orientation modes through plotting and/or statistical analysis.
4) Calculate *F* at various *d* for each orientation mode.
5) Plot *F* versus *d* in log-log and semi-log space.
6) Model *F* distribution as power-law (or exponential, characteristic, or some combination if necessary) with consideration of resolution limit and possible sampling bias.
7) Use the modeled *F* distribution to define a distribution specific to the proposed site.
8) Calculate the encounter probability at the *d* of interest from site-specific *F*-distribution model, fault orientation modes, and CO_2 plume area, aspect ratio, and orientation estimated from reservoir simulation.

Fault Coverage(s), Measurements, and Calculations

Fault coverage(s) relevant to a proposed site can consist of oil or gas field structure maps, gas storage facility structure maps, or regional geologic maps. Measurement proceeds by fault segment, rather than by fault. To calculate *F* for a given *d*, the total length of the fault segments with displacement greater than *d* (displacement cutoff) must be calculated. Using the measured fault lengths, displacements, and areas, log-log plots are constructed of fault density versus displacement cutoff as shown in the example for the Kimberlina site in the southern San Joaquin Valley, California (Figure 6). Note this example uses throw truncation (vertical offset cutoff) instead of displacement cutoff because most of the faults are normal and near vertical, so the available structure maps show only throw, not displacement.

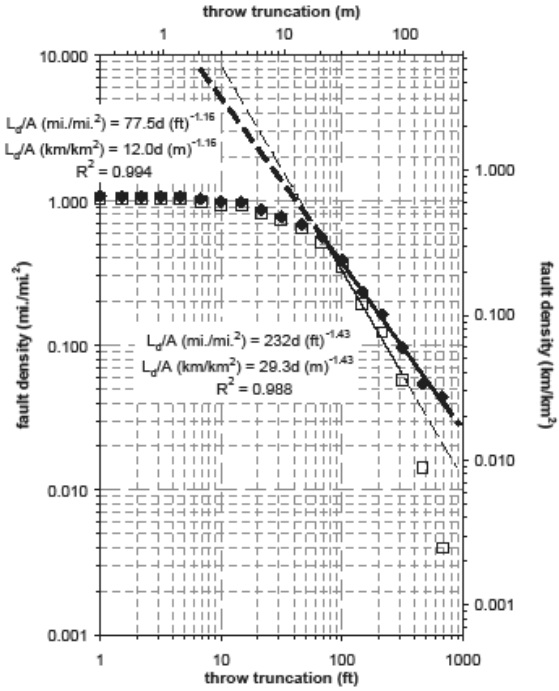

Figure 6. Measured data on throw truncation and fault density for the Kimberlina site in the southern San Joaquin Valley, California. Open boxes are raw data and filled boxes are data adjusted to account for the "finite-range effect."

Selected data on Figure 6 are fit to a power-law distribution. The data appear exponential, with the data departing from a power-law fit at a throw cutoff of approximately 65 ft (20 m). This value is consistent with the resolution of the oil and gas field structure maps, however. The departure is due to the resolution limit inherent in mapping rather than reality. Consequently, the linear fit appears more likely to represent the actual fault population in the vicinity of the Kimberlina site, indicating that the fault population follows a power-law distribution. The power law fit also yields higher fault density estimates, which makes it more conservative than the exponential fit for estimating leakage risk. Adjusted data and associated power law are also shown on Figure 6 to account for the "finite-range" sampling effect [15].

Calculating Plume Fault Encounter Probability

Consider 100 randomly located plumes and a single randomly located fault of size L_f as shown in Figure 7. In this case, the probability of intersection, *g*, is given by

$$\Pr(g) = A_f \,/\, A_0 \qquad \text{Equation 8}$$

where A_0 is the area of interest and A_f is the area of the fault. This approach assumes that the fault or faults cross the entire area of interest (A_0), and that each plume only encounters one fault. The first condition is equivalent to assuming that faults are large relative to A_0, and the second condition is equivalent to assuming the spacing between faults is large relative to the plume diameter. As the spacing between large faults is generally greater than between small faults, these assumptions are qualitatively in agreement. With these assumptions, if a plume is centered within a distance equal to the plume radius, *r*, the plume will intersect the fault (an event represented by *g*). Given that the fault has two sides

$$A_f = 2rL_f \qquad \text{Equation 9}$$

where L_f is the length of fault in the study area (shown as *L* on Figure 6). L_f can also be written as the areal fault density *F* times A_0:

$$L_f = FA_0 \qquad \text{Equation 10}$$

Substituting Equation 10 into 9, 9 into 8, and canceling terms gives

$$\Pr(g) = 2rF \qquad \text{Equation 11}$$

The value of *F* is measured from fault maps (as discussed), and the value of *r* can be approximated by numerical simulation. If the plume margin is some shape other than circular, then Equation 8 can be generalized to any plume shape by substituting half the plume dimension perpendicular to the fault, *s*:

$$\Pr(g) = 2sF \qquad \text{Equation 12}$$

The value of *s* can be measured directly from plots of the area swept by mobile CO_2 as modeled by numerical simulation.

If the relationship between *F* and *d* is power law, then

$$\Pr(g) = 2sBd^{-C_d} \qquad \text{Equation 13}$$

where *B* is a proportionality constant. For elliptical plumes, the plume dimension perpendicular to the fault (*s*) can be calculated from the plume area, aspect ratio (eccentricity), and the acute angle between the long axis of the plume and the fault orientation of interest [11]. As mentioned, this approach assumes the fault-perpendicular plume dimension is considerably less than the distance between faults (fault spacing). As the plume dimension approaches the fault spacing, this approach

will overestimate Pr(g) because the chance a plume will encounter two faults will be non-negligible. Consequently, this approach is more prone to false positives than false negatives for risk mitigation.

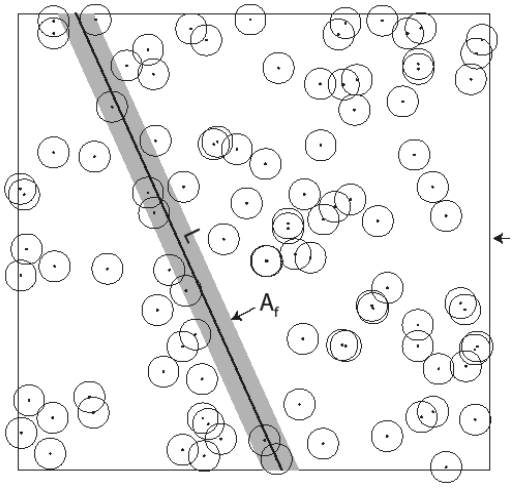

Figure 7. Diagram of 100 randomly located, circular plumes and a randomly located fault. Any plume geometrically centered within the shaded area will encounter the fault.

Numerical simulation indicates the CO_2 plume at the Kimberlina Pilot site in the San Joaquin Valley, California, will be elliptical due to the dipping reservoir. The sealing formation over the storage target at the site has a vertical thickness of approximately 180 m (590 ft). A throw truncation equal to the seal thickness is one threshold of concern (although such a fault may not be a leakage conduit due to its reservoir properties). The adjusted fault density equation on Figure 6 indicates the average fault density, F, at this throw truncation is 0.028 km/km^2 (0.046 mi./mi.^{2}). This is a low density, so the condition that the fault-perpendicular plume dimension is much smaller than the spacing between faults is sufficiently met to use the probability estimation of Equation 12. The distribution of Pr(g) at this fault density and simulated plume area, but varying plume aspect ratios and orientations, is shown on Figure 8. The simulated plume has an aspect ratio of 1.32 and a plume axis to predominant fault angle of 70°. Given these values, the Kimberlina plume Pr(g) for a fully seal-offsetting fault is 3.3%.

Summary

The probability of CO_2 leakage via a fault is the product of the probability a plume will encounter a fault and the probability of flow occurring along the fault through the seal. As described, the former probability can readily be calculated. The latter probability is dependent on the reservoir properties of the fault zone with respect to CO_2 flow (permeability, relative permeability, porosity, residual saturation, capillary entry pressure, etc.). The probability distribution of these properties are currently poorly constrained, and are a critical research area for GCS, as well as oil and gas exploration and production, nuclear waste repository selection and design, and groundwater hydrology.

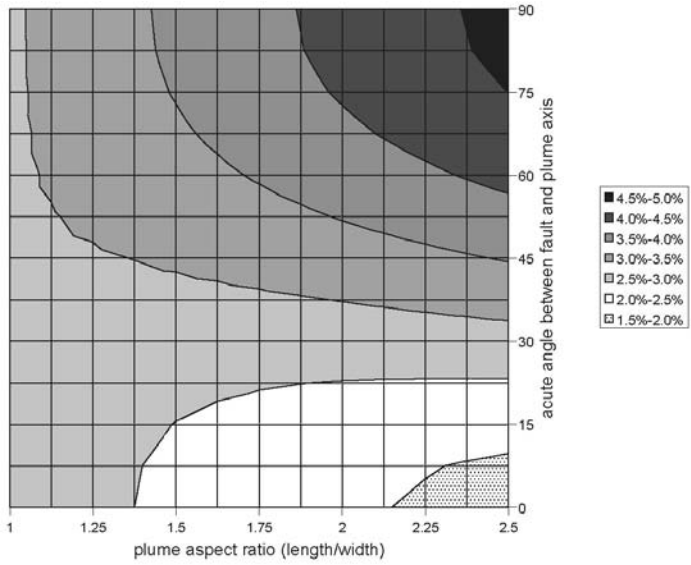

Figure 8. Probability the Kimberlina plume will encounter a fault fully-offsetting the seal as a function of the plume aspect ratio and the angle between the plume axis and the fault.

PROBABILITY OF FAULT CONNECTIVITY

The objective of the fault connectivity model component is to provide a methodology for calculating P_{leak}, the probability that a CO_2 plume will encounter a system of conduits that is connected to a compartment that may be impacted by leakage and cause potential health, safety and environmental issues [16, 17]. The fundamental problem addressed by the approach is presented graphically in Figure 9. The fault population statistics approach described above allows estimation of the likelihood of a CO_2 plume encountering a fault large enough to be a leakage conduit. However, it does not address the question of the likelihood of that conduit connecting to a compartment much higher in the stratigraphic column, e.g., to USDW. Nor does it account for the likelihood of that conduit connecting to another conduit, e.g., another conductive fault. To address this issue, analysis of the likelihood of existence of a fault network must be considered as discussed in this section.

The probability that the CO_2 plume leaks into a compartment through faults or fractures is related to (1) the geometric characteristics of the system of conduits (i.e., distribution and connectivity of faults and fractures) between the storage reservoir and the compartment, and (2) the size and location of the CO_2 plume. For a site (which includes the storage formation and the geological formation above it) to be selected for GCS, some fault and fracture distribution data are expected to be available. However, the information on the conduit system is usually limited and highly uncertain. Moreover, the location and size of the CO_2 plume is also highly uncertain given the uncertain properties of the deep storage reservoir. Therefore, it is a challenge to predict (1) whether the conduits are connected, and if so, (2) the probability that a CO_2 plume will encounter the connected pathways.

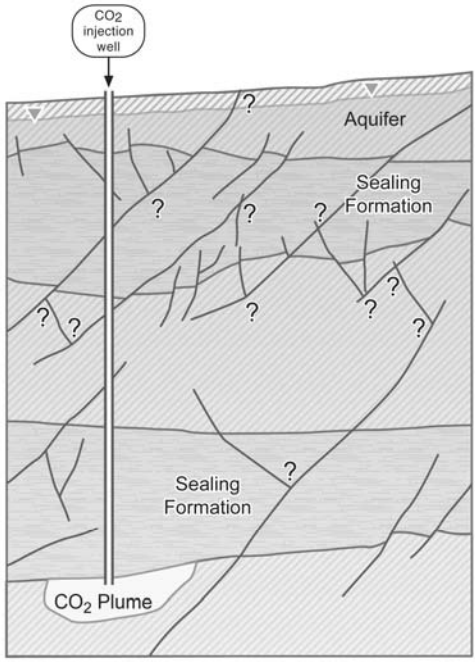

Figure 9. Schematic geologic cross section (not to scale) showing CO_2 injection well, CO_2 plume, reservoir, sealing formation, overlying formations, and potable ground water, along with conductive faults that may or may not intersect as indicated by the question marks.

Methodology

The proposed approach includes four steps: (1) estimate a critical value (α_c) for the parameter α, which is related to the density of conduits (faults and fractures), such that when this critical value is reached, the system is on average connected between the storage formation and a compartment; (2) estimate the probability that the CO_2 plume will encounter the connected conduits for a system with $\alpha \geq \alpha_c$, for various distributions of conduits, system sizes and CO_2 plume sizes; (3) construct fuzzy rules that relate information about the conduit system and CO_2 plume size to leakage probability; and (4) for given system characteristics, predict the probability that a CO_2 plume will escape from the storage formation to a compartment through connected conduits.

We make the following assumptions:

- The system under investigation is a square, two-dimensional (2D) cross section with sides of length L.
- Faults/fractures are randomly oriented.
- Faults/fractures considered are conductive.
- Faults/fractures follow a power-law length distribution.

The third assumption means this method provides an upper bound estimate of leakage probability. The method assumes if a "conductive" pathway exists, leakage along the pathway will occur, which discounts flow dynamics. For instance, flow may not reach the compartment given the limited duration of any actual injection and/or matrix permeability along the pathway.

Estimation of Critical Value α_c

Among different models for describing fault length distributions, the power-law distribution is the most widely used [18, 19, 20]:

$$n(l, L) = \alpha(L) l^{-a} \qquad \text{Equation 14}$$

where $n(l, L)dl$ is the number of faults having a length in the range $[l, l+dl]$, $\alpha(L)$ is a coefficient of proportionality that reflects fault density and depends on the system size L (assuming a square system with sides of length L), and a is an exponent, which typically varies between 1 and 3. It is apparent from Equation 14 that the power-law distribution contains no characteristic length. This is the key argument for using power laws to describe fault growth processes [21].

Percolation theory [22] has been applied to study the connectivity of fault systems. In percolation theory, a parameter p is used as an average measure of the geometric properties, generally related to the density of elements, which also provides information on the connectivity of the system. The percolation threshold p_c is defined as the critical p value below which (on average) the fault system is not connected, while when p is above the critical value p_c, the system is connected. In other words, 50% of the systems at the percolation threshold are connected. Bour and Davy [22] presented an analytical expression for the percolation threshold for a fault system following a power-law length distribution as:

$$p_c(L) = \int_{l_{\min}}^{L} \frac{\alpha_c(L) l^{-a} l^2}{L^2} dl + \int_{L}^{l_{\max}} \alpha_c(L) l^{-a} dl \qquad \text{Equation 15}$$

If $l_{max} < L$, the second term on the right-hand side drops out and the first term integrates to l_{max} instead of L.

Bour and Davy [22] also demonstrated that the percolation threshold $p_c(L)$ does not present significant variations with L. For a power-law fault length distribution with any value of a, the computed values of $p_c(L)$ are around 5.6 in two dimensions. By setting p_c to 5.6, an expression for the critical fault density $\alpha_c(L)$ can be obtained. Equation 15 can be normalized with respect to l_{min}, where $\alpha_{cs}(L_s) = \alpha_c(L) l_{\min}^{-a+1}$.

The subscript s indicates normalized values with respect to smallest fault size l_{min}.

For a given system, we can calculate the critical parameter $\alpha_{cs}(L_s)$ and compare it to the actual parameter $\alpha_s(L_s)$. If the actual density is much smaller than the critical value, we can conclude that the system is not connected and the CO_2 plume will not be able to leak out through the fault system.

Generation of Conduit Network

To estimate the probability that a CO_2 plume escapes through the connected conduits and reaches compartments for a system with $\alpha(L) > \alpha_c(L)$, we vary system parameters to generate discrete fracture networks and perform Monte Carlo simulations. Three types of uncertainty are considered. The first results from our lack of knowledge of the system properties. This uncertainty is considered by using fuzzy-rule-based modeling to propagate the uncertainty of the input parameters in estimating P_{leak}. The second is the uncertainty in the generation of the discrete fracture network itself. Even for systems with the same parameters (e.g., system size and fracture distribution), the generated network could have very different connectivities. This uncertainty is considered by conducting Monte Carlo simulations. The third uncertainty is in the size and location of the CO_2

plume. In the simulation, we will vary CO_2 plume size and use a moving average to consider the uncertain location of the plume.

The parameters varied in the fracture network generation and P_{leak} calculations are the normalized system size L_s, the normalized maximum fracture length $l_{max\ s}$, the exponent a, the ratio of $\alpha_s(L_s)/\alpha_{cs}(L_s)$, and the normalized plume size M_s.

For each of the realizations of the generated network, the outcome has the following format:

IF $L_s = L_1$, $l_{max\ s} = l_1$, $a = a_1$, $r = \alpha_s(L_s)/\alpha_{cs}(L_s) = r_l$, and $M_s = M_1$

THEN the probability that a CO_2 plume escapes from the storage reservoir through a connected network of conduit (P_{leak}) is b.

where L_1, l_1, a_1, r_1 ($r_1 \geq 1$), and M_1 are the numerical values of the varying parameters in the simulation (crisp numbers) which should cover all possible values considered.

Construction of Fuzzy Rules for Calculating P_{leak}

Fuzzy set theory, introduced by Zadeh [23], has been used to deal with approximate (rather than exact) reasoning. In a fuzzy statement, A_i is a fuzzy number that reflects vagueness. Membership functions of a fuzzy number can have different shapes. Typically, triangular, trapezoid, or Gaussian memberships are used. Fuzzy rules can be used to model systems with imprecise or uncertain information. These rules can be developed using expert opinions, existing data, and qualitative information. Alternatively, fuzzy rules can be generated through numerical simulations. In our case, we use results from the fault network generation as a training set to construct fuzzy rules of connectivity.

An example of a fuzzy-rule statement using triangular membership functions is as follows (the numbers in this statement are dimensionless numbers that are normalized with respect the smallest fracture size):

IF a = (1.1, 1.5, 2.0) AND L_s = (50, 100, 200) AND l_{maxs} = (50, 100, 200)

AND r = (0.75, 1.0, 1.25) AND r_p = (0.2, 0.4, 0.6)

THEN P_{leak} = (0.01, 0.12, 0.18)

where $r_p = M_s/L_s$. Using the centroid method, the final defuzzified P_{leak} for this rule (when it is fulfilled) is 0.1.

Calculation of P_{leak} for a Given System

For a given system, the first step is to calculate $\alpha_{cs}(L_s)$ and compare it to $\alpha_s(L_s)$. If the latter is smaller, $P_{leak} = 0$. Otherwise, the above fuzzy rules are used to infer P_{leak}. To aggregate fuzzy rules, one option is to use the normalized sum combination method proposed by Bardossy and Duckstein [24]. Another option is to use the Mamdani-type inference system provided by the Matlab Toolbox, which uses a maximum combination method to aggregate fuzzy rules.

To demonstrate the approach, we use fuzzy rules to predict P_{leak} as a function of r_p (CO_2 plume size divided by system size) for a system with a of approximately 1.5, $l_{max\ s}$ of approximately 100, L_s of approximately 100, and a few values of $r = \alpha_s(L_s)/\alpha_{cs}(L_s)$. The final defuzzified P_{leak} are shown in Figure 10. Details of the method are presented in Zhang et al. [17].

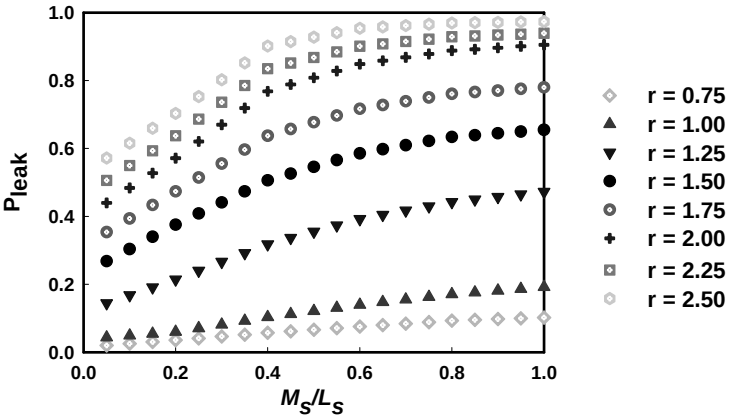

Figure 10. Fuzzy-rule based prediction of P_{leak} as a function of normalized CO_2 plume size for a system with a = 1.5, $l_{max\ s}$ = 100, L_s = 100, and different values of $r = \alpha_s(L_s)/\alpha_{cs}(L_s)$.

Summary

This fuzzy rule-based model component of the CF is used to estimate the probability (P_{leak}) of the plume intersecting a connected network of faults or fractures that also intersects a compartment in which impact may occur. The main computational effort of the approach lies in the numerical generation of the fracture networks. However, this only needs to be done once to provide the basis for constructing the fuzzy rules; predictive simulations are then performed very efficiently using these fuzzy rules. The uncertainty of P_{leak} is predicted by propagating the uncertainty in the input parameters. The method can be extended to apply to brine leakage risk by using the size of the pressure perturbation above some cut-off value as the effective plume size. The method can also be extended to account for non-random fault/fracture orientations, stratigraphic connections between faults/fractures, and three rather than two spatial dimensions.

WELLBORE FLOW

The wellbore flow model component is used in the CF to model leakage up wells [25]. The focus of this work in on the upward (or downward) flow in the well occurring either in the tubing, within an annular region between casings, or between the casing and the rock, all of which fall into non-Darcy flow regimes. Regardless of the region in which flow is occurring, physical processes involving viscous or turbulent flow, phase change, and advective and diffusive mass and heat transfer are relevant. In this work, we focus on two-phase flow of CO_2 and brine with non-isothermal effects and neglect well cement degradation and geomechanics.

Methodology and Verification

The approach we use for describing wellbore flow is based on the drift-flux model (DFM) [26] for transient two-phase non-isothermal flow of CO_2-water mixtures. Conservation equations for mass, momentum, and energy under different flow regimes in the wellbore are solved numerically while wellbore heat transmission is handled semi-analytically. We implement the DFM in TOUGH2 [27] with the ECO2N equation of state module [28]. The conventional approach for calculating the mixture velocity in the DFM is often based on the steady-state pressure loss equation for wellbore flow [29]. To improve simulation performance in wellbore flow processes involving high fluxes,

we have extended the DFM to include the transient terms of the momentum conservation equations in calculating the velocity from the pressure gradient.

To calculate the mixture velocity, we use the transient momentum conservation equation with the steady-state assumption about the wall shear stress

$$\frac{\partial}{\partial t}\left(\rho u_m\right)+\frac{\partial}{\partial L_w}\left(\rho u_m{}^2\right)=-\frac{\partial P}{\partial L_w}-\frac{f\,\rho u_m^2}{4r_w}-\rho g\cos\theta \qquad \text{Equation 16}$$

where u_m is the mixture velocity in the wellbore, L_w is a length of the wellbore section (positive upward), ρ is the mixture density, and θ is the local angle between wellbore section and the vertical direction. The friction coefficient (f) is a function of the Reynolds number (Re) for laminar and turbulent flows (Re = $\rho u_m d/\mu$ where μ is the mixture viscosity and d is the wellbore diameter) and is given by

$$f=\frac{64}{\mathrm{Re}}\ \text{for Re} < 2400, \text{ and } \frac{1}{\sqrt{f}}=-2\log\left[\frac{2\varepsilon/d}{3.7}-\frac{5.02}{\mathrm{Re}}\log\left(\frac{2\varepsilon/d}{3.7}+\frac{13}{\mathrm{Re}}\right)\right]\ \text{for Re} > 2400$$

Equation 17

[29]. When the system reaches steady state there is no mass accumulation, and Equation 16 reduces to the pressure loss equation [30] given by

$$-\frac{dP}{dL_w}=\frac{f\,\rho\,u_m^2}{4r_w}+\rho\,u\frac{du_m}{dL_w}+\rho\,g\cos\theta \qquad \text{Equation 18}$$

To verify the wellbore flow solution approach, we simulated a case of steady-state single-phase water flowing up the wellbore at 25 ^{o}C at a rate of approximately 2 kg/s and compared the result with the theoretical pressure profile along the well as calculated from the steady-state pressure loss equation. A sketch of the model system used for this verification problem and for the test problem that follows is shown in Figure 11a. The initial conditions are hydrostatic pressure, temperature varying linearly from 15-45 ^{o}C, and 100% water in the well. In the verification problem, we set a higher pressure at the bottom boundary and ran the model to steady state (at ~2 kg/s) under isothermal conditions (25 ^{o}C). Shown in Figure 11b are the theoretical and calculated pressures along the wellbore, along with the relative error showing a very close match. This verification problem confirms the ability of the code to solve a steady-state single-phase flow up the well.

(a)

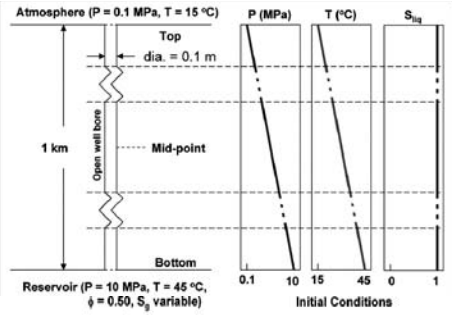

(b)

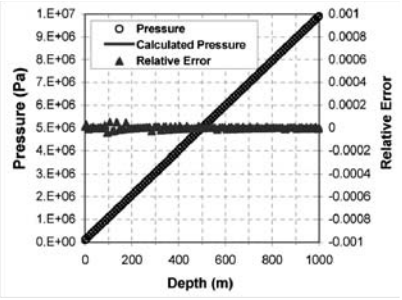

Figure 11. (a) Wellbore boundary and initial conditions.
(b) Steady-state pressure and relative error in flowing well for verification.

Example Results

We present here results for a case of two-phase flow up an open wellbore. The scenario envisioned is that of the encounter of the edge of a migrating CO_2 plume at 10% phase saturation encountering an open well initially filled with water. The focus is on flow in the wellbore, and we assume residual gas saturation in the reservoir is 0.05. Starting from hydrostatic conditions, an overpressure of 0.1 MPa (1 bar) is applied to the reservoir.

With reference to Figure 12, we observe in this test problem the early-time upward flow within the well of water at all depths as driven by the 0.1 MPa pressure perturbation at the bottom. Gas flow does not begin until approximately t = 20 s when gas is present at the bottom. By t = ~500 s, gas flows at the middle and top of the well. The flow rate of CO_2 reaches approximately 1.4 kg/s in this open wellbore case and the final Reynolds numbers are between 5.1 x 10^5 (at bottom) and 4.7 x 10^6 (at top).

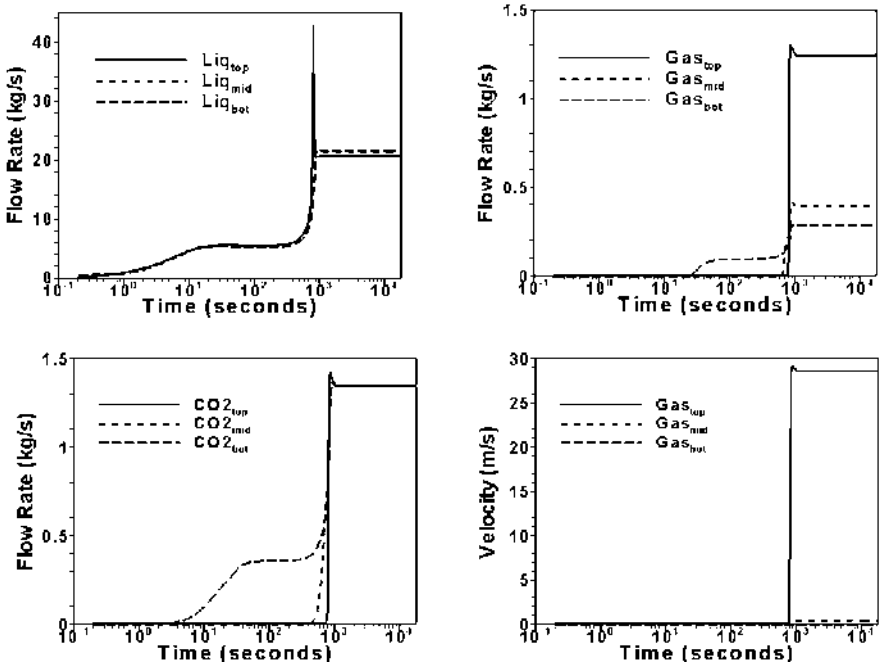

Figure 12. Flow rates and velocities of CO_2 and water at three levels in the well (bottom, middle, and top).

Further insight into the processes modeled can be obtained from Figure 13 which shows gas saturation, gas density, pressure, and temperature throughout the well as a function of time. As shown, the well is initially filled with water and gas progressively fills the well from the bottom up. After 30 minutes (1800 s), gas is fairly evenly distributed throughout the well from 10% at the bottom to nearly all gas at the top. The reasons for this increase in gas saturation are (1) the exsolution of gas from the liquid as pressure drops and (2) the large expansion that CO_2 undergoes as it transitions from supercritical to gaseous conditions. This transition occurs around the critical pressure of 7.4 MPa (74 bar), at a depth of approximately 800 m. The gas density plot in Figure 13 shows the sharp decrease in gas density at depths around 800 m. Temperature also affects CO_2

solubility, but temperature becomes relatively constant as steady flow develops, resulting in decreasing CO_2 mass fractions being controlled mostly by pressure. The temperature contour shows the evolution from a conductive profile controlled by the geothermal gradient to an advective profile controlled by upward fluid flow. In between the initial and steady states, there are some local maxima and minima arising from expansion and dissolution of CO_2 as gas phase rises upwards.

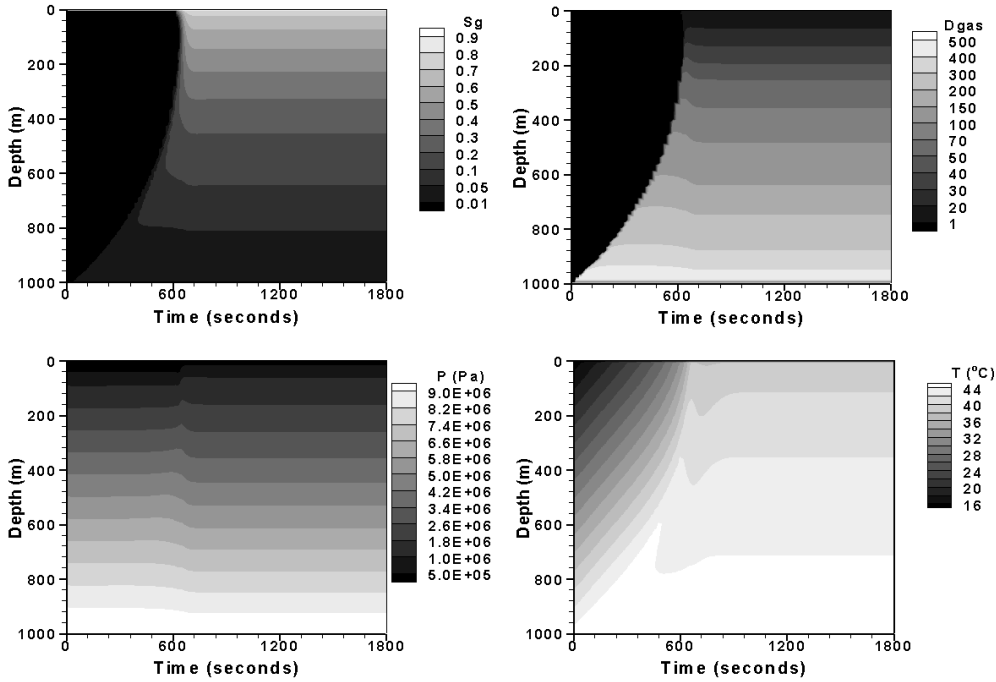

Figure 13. Profiles of gas saturation, gas density, pressure, and temperature in the wellbore as a function of time.

Summary

We have developed a wellbore flow simulator that models two-phase CO_2-brine mixtures for use in GCS leakage and injection studies [25]. This simulation capability was developed for quantifying potential leakage up wells using pressures and gas saturations at depth of CO_2 migration and pressure propagation that are calculated by reservoir simulation. Although the test problem is based on flow up an open borehole, the approach can be used for flow in an annulus region by suitable modifications of roughness coefficients and geometric parameters. The fundamental elements of advection, diffusion, and phase change are independent of the particular flow geometry. Similarly, the approach can be applied to leakage in non-vertical and horizontal wells with the caveat that flow in the well is always 1-D.

DENSE GAS DISPERSION

Dense gas dispersion capabilities were developed for the CF by modification of an existing numerical weather simulation model [31]. This component of the CF is intended to allow quantification of CO_2 concentrations in the NSE compartment. Because atmospheric dispersion of

CO_2 is driven by gravity (gas-density contrast) and wind, the danger from CO_2 is greatest in regions with topographic depressions where the dense gas can pool, or under stably-stratified background atmospheric conditions which further inhibit mixing and dilution of the gas.

We have used the new capability to demonstrate the ability of common topographic depressions to trap accumulated CO_2 for extended periods and at concentrations that exceed limits allowable for continuous or instantaneous exposure; accumulated CO_2 can persist for shorter periods even under high ambient winds. A variety of simulations of different release strengths and background atmospheric conditions allows the generation of a catalog of results analogous to the reservoir simulation catalog that can be queried to identify hazardous scenarios.

Approach

We extended a mesoscale atmospheric model (Advanced Regional Prediction System (ARPS)) to predict dispersion of releases of dense CO_2 gas. ARPS allows specification of complex terrain, land-surface fluxes, heterogeneous land cover, time-dependent weather forcing, etc. and can be run as a large-eddy simulation (LES) code that solves the three-dimensional, compressible, non-hydrostatic, filtered Navier-Stokes equations. ARPS is described in detail by Xue et al. [32, 33].

ARPS was modified to include a scalar-advection diffusion equation for dense gas transport described by the equation

$$\frac{\partial \rho X_c}{\partial t} + u\frac{\partial \rho X_c}{\partial x} + v\frac{\partial \rho X_c}{\partial y} + w\frac{\partial \rho X_c}{\partial z} = \frac{\partial}{\partial x}\left(\kappa_T \frac{\partial \rho X_c}{\partial x}\right) + \frac{\partial}{\partial y}\left(\kappa_T \frac{\partial \rho X_c}{\partial y}\right) + \frac{\partial}{\partial z}\left(\kappa_T \frac{\partial \rho X_c}{\partial z}\right)$$

Equation 19

where X_c is the mass fraction of the gas in a particular cell, u, v, and w are the velocity components in the x, y, and z directions, respectively, κ_T is the turbulent eddy diffusivity, and ρ is the total density in kg/m^3. Note that the entire quantity ρX_c is solved for at each time step (i.e., the two quantities are not calculated separately). Active scalar (i.e., dense gas) transport required modifying two areas of the model: (1) calculation of density, and (2) calculation of buoyant forcing in the w-equation. This allows incorporation of the total density (due to air and the dense gas) into the buoyancy forcing, which appears in the vertical momentum equation. The density field thus couples the equation describing transport and dispersion of the dense gas with the momentum equations, causing the model to feel the effects of density-driven flow. Note that the ARPS system of governing equations does not allow for large mass fluxes across a boundary, hence the current formulation can accommodate instantaneous releases only.

Passive vs. Dense Gas Dispersion

The behavior of dense gases such as CO_2 can be quite different from that for passive tracers (with neutral buoyancy) due to density effects [34]. For example, a plume of CO_2 will spread laterally over flat terrain even in the absence of wind because it is denser than the surrounding air. Driven by density effects, a CO_2 plume will spread more quickly than a neutrally-buoyant gas which spreads only through diffusion, giving the counter-intuitive result that ground-level concentrations can drop more quickly for a dense gas than for a passive gas tracer under calm conditions. The hazard of prolonged exposure to CO_2 at high concentrations, however, lies in the fact that topographical depressions or basins provide preferential sites for accumulation and immobilization. The presence of negatively buoyant gas in sufficient amounts can prevent the scouring of the gas from a basin by ambient winds.

The impact of topography and ambient conditions on scalar dispersion can be illustrated through examination of a two-dimensional idealized basin described by mirror sigmoid functions.

Simulations using the new capability were performed on a computational domain of 200 x 60 grid cells, with Δx = 5 m and a stretched grid in the vertical with a minimum resolution of Δz = 0.25 m and an average resolution of 2 m. The top and bottom boundaries are rigid, and there is a Rayleigh damping layer beginning at z = 80 m. An instantaneously released mass of CO_2 is initialized at the bottom of a depression. A logarithmic wind profile is initialized across the domain and held constant as an inflow condition on the left, as shown in Figure 14. The passive scalar is quickly transported out of the basin (solid lines), while the CO_2 plume (gray contours) lingers in the basin even under strong winds (~5 m/s).

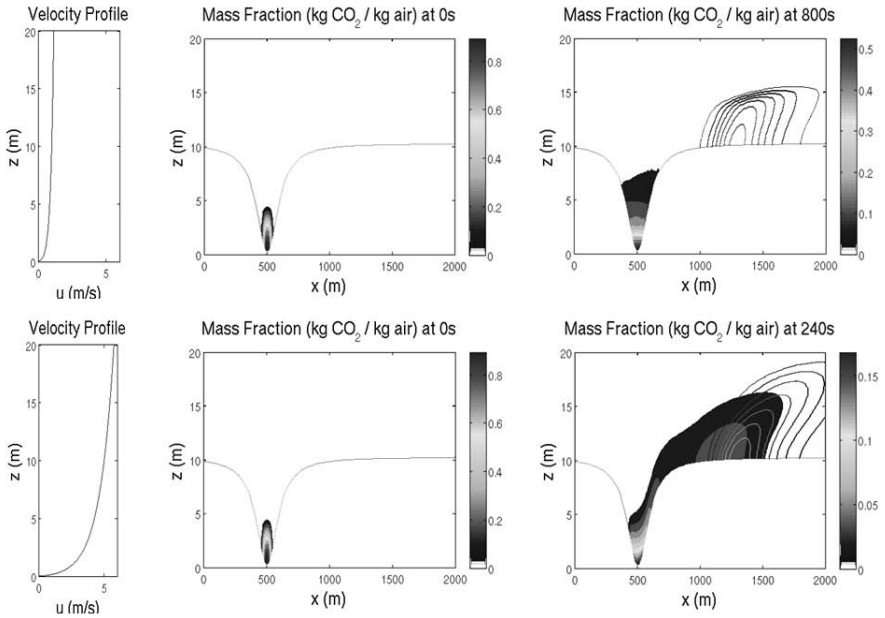

Figure 14. Scouring from a 2D trench. Shaded contours show mass fraction of CO_2 (CO_2 mass fraction is highest at the deepest part of the trench) and solid lines show passive tracer. Profiles on left indicate driving wind at left edge of domain.

CO_2 Atmospheric Dispersion Catalog

A catalog of CO_2 dispersion and accumulation scenarios, analogous to the reservoir simulation catalog, was created for different topographies, release scenarios, and meteorological conditions.

Four types of terrain were used in the simulation scenarios: (A) completely flat ground, (B) flat ground interrupted by a long trench of depth 10 m, (C) flat ground interrupted by a step change in elevation (shelf) of 10 m (a half-trench), and (D) a set of rolling hills of maximum amplitude 50 m (see Figure 15). The domain size is (203, 143, 43) grid points in the x, y, and z directions, respectively, for all cases except the rolling terrain where it is (163, 203, 43). The simulations all use the same grid spacing ($\Delta x = \Delta y$ = 5 m, Δz_{avg} = 2.5 m, Δz_{min} = 0.25 m near the ground, stretched above) and time steps (Δt = 0.02 s, $\Delta \tau$ = 0.002 s). Lateral boundary conditions are zero-gradient. Top and bottom boundaries are rigid walls, with a log-law condition specified at the bottom boundary to account for surface drag (as is typical in all mesoscale prediction models). A Rayleigh damping layer is used at the top of the domain above 80 m. All simulations use a 1.5 order turbulent kinetic energy formulation for the large-eddy simulation turbulence closure.

Wind speeds were chosen from the following set: 0 m/s (calm conditions), 0.5 m/s, 1 m/s, 2 m/s, and 4 m/s. Winds were initialized uniformly over the domain. Shear develops at the ground after the simulation is started due to drag at the surface (corresponding to an effective roughness height of 0.1 m). A range of wind directions can be selected but winds from the west were applied in the cases shown here. Neutral stratification and weakly stable conditions (with a vertical potential temperature gradient of approximately 0.01 K/m) were chosen. Releases are considered to be instantaneous, with a magnitude of either 1,000 kg (1 tonne) or 10,000 kg (10 tonnes) of CO_2 at the surface. A uniform hemispherical instantaneous release is specified, with a radius of 15 m in *x* and *y* and 6 m in *z* for the 1,000 kg release, or 30 m in *x* and *y* and 14 m in *z* for the 10,000 kg release.

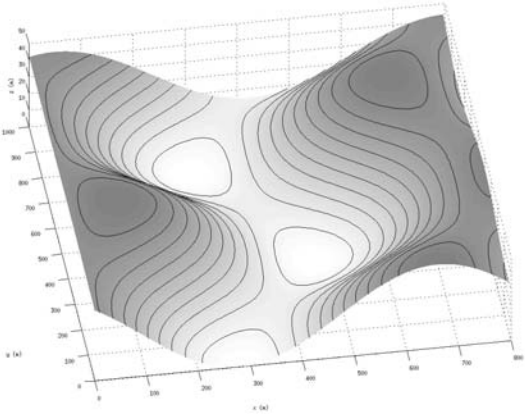

Figure 15. Rolling terrain used for catalog of ideal simulations.

For each case scenario, a number of parameters are extracted for analysis of plume extent and dilution time. Three concentration threshold levels are chosen which correspond to a Short-Term Exposure Level (STEL) for 15 minutes. The thresholds are based on mass fractions (i.e. kg CO_2/kg air) of 0.01, 0.03, and 0.1, which correspond to concentrations of 10,000 ppm (1%), 30,000 ppm (3%), and 100,000 ppm (10%). Severe headaches, diffuse sweating, and labored breathing begin at 30,000 ppm. The OSHA (U.S. Occupational Safety and Health Administration) occupational exposure standards are 0.5% CO_2 for a 40-hour work week average and 3% for a 15-minute exposure. The maximum instantaneous limit is 4%. All three exposure standards must be satisfied [5]. In addition to plume extent, local exposure times (in seconds) are provided for each of the chosen thresholds. Thus, if the overall exposure time is greater than 900 s (15 min) for the 0.03 mass fraction threshold, the STEL will have been exceeded. A series of three figures showing ground level concentration at 300 s, 600 s, and 900 s is provided for each simulation. A second series of three figures shows the amount of time spent above the three threshold concentrations as a function of *x*,*y* location, indicating which portion of the domain is at risk for exceeding the STEL.

Two examples of catalog results are given in Figures 16 and 17 for the rolling hills: Case D1 with no ambient winds and Case D1 with a 1 m/s westerly wind. Both are initialized with a 10 tonne release of CO_2. The source location is marked with an 'x'. With no winds, the CO_2 flows downhill and collects in the valley. With a 1 m/s wind, the primary direction of plume spreading is still down-gradient (perpendicular to the mean wind direction), with significant accumulation in the valley. A portion of the plume even travels upwind of the source location. A large area in the valley exceeds the 0.01 threshold, and a smaller area exceeds the 0.03 concentration threshold for more than 15 minutes. Note that the threshold contours and statistics are calculated based on data at 60 s intervals.

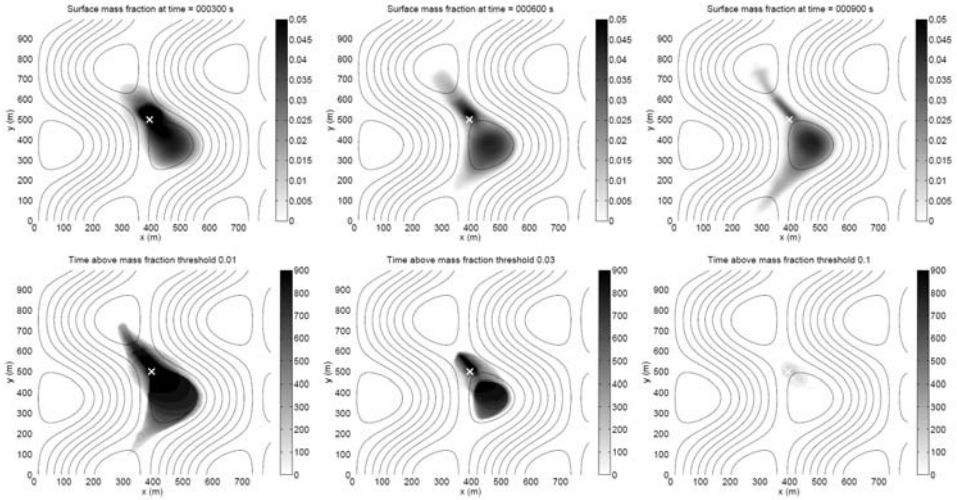

Figure 16. Case D1. Rolling hills with no winds, 10,000 kg release (marked by 'x'). Top panel shows surface CO_2 mass fraction contours. Bottom panels show exposure time above each threshold level (in seconds). Black lines show terrain contours.

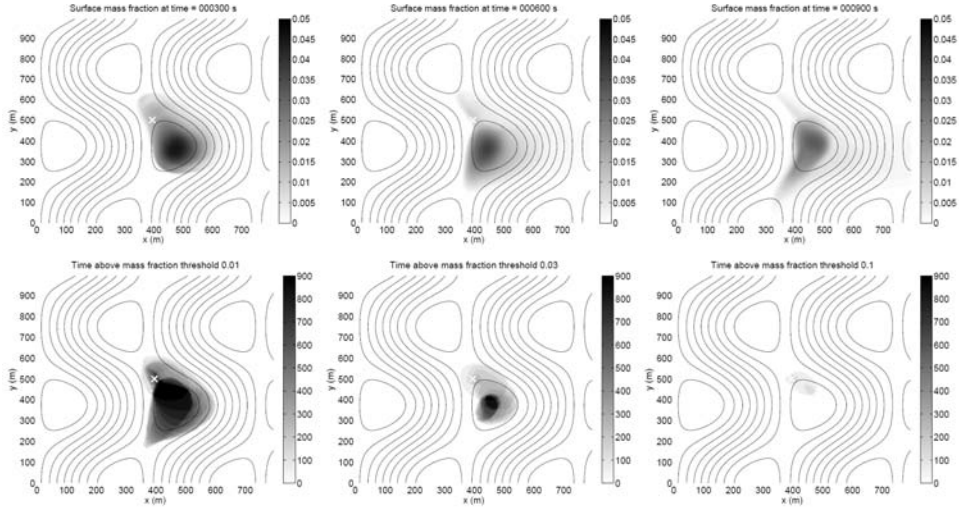

Figure 17. Case D2. As in Figure 16 but for 1 m/s background winds.

Summary

The model component on atmospheric dispersion in the CF allowed the generation of a catalog of idealized simulation results to demonstrate features of dense gas dispersion and to create a tool to allow stakeholders to carry out risk assessment for a particular CO_2 storage site by querying a database. A set of 22 simulations was performed to investigate the parameter spaces described above, including topography type, wind speed, stability, and release strength. It was found that

topographic depressions of only 10-50 m in depth can lead to accumulation of CO_2 at hazardous exposure levels. Future work will be directed at adding a flux-type boundary condition capability to ARPS to handle incipient CO_2 leakage.

CONCLUSIONS

Although the CF invokes major simplifications of an actual GCS system, it requires sophisticated model components to carry out the analysis. We have presented above brief summaries of the five significant model components we have developed for the CF. Further details of the methods can be found in the references. Although the approaches described here are anticipated to be effective in many cases, undoubtedly applications of the CF to additional sites will reveal shortcomings and more effort in developing model components and/or underlying assumptions will be needed as the number and scale of GCS projects increase.

ACKNOWLEDGMENTS

We thank H.H. Liu (LBNL) for internal review and Scott Imbus (Chevron) for support and encouragement. This work was supported in part by the CO_2 Capture Project (CCP) of the Joint Industry Program (JIP), and by Lawrence Berkeley National Laboratory under U.S. Department of Energy Contract No. DE-AC02-05CH11231.

This Chapter contains figures that originally appeared in Energy Procedia Vol 1, Issue 1, Greenhouse Gas Control Technologies 9, Proceedings of the 9th International Conference on Greenhouse Gas Control Technologies (GHGT-9), 16-20 November 2008, Washington DC, USA, which was published by Elsevier Ltd.

REFERENCES

1. C.M. Oldenburg, S.L. Bryant, Certification Framework for Geologic CO_2 Storage, Sixth Annual Conference on Carbon Capture and Sequestration, National Energy Technology Laboratory, Pittsburgh, PA, May 7-10, 2007.
2. C.M. Oldenburg, J.-P. Nicot, S.L. Bryant, Case studies of the application of the Certification Framework to two geologic carbon sequestration sites, *Energy Procedia*, GHGT9 conference, Nov. 16-20, 2008, Washington DC. LBNL-1421E.
3. C. M. Oldenburg, S.L. Bryant, J.-P. Nicot, Certification Framework for Geologic Carbon Sequestration Based on Effective Trapping, *Int. J. of Greenhouse Gas Control*, in press, 2009.
4. R.P. Hepple, S.M. Benson, Geologic storage of carbon dioxide as a climate change mitigation strategy: performance requirements and the implications of surface seepage, *Environ. Geol.* **47**(4) (2005) 576.
5. Intergovernmental Program on Climate Change (IPCC) Special Report on carbon dioxide capture and storage, ISBN 92-969-119-4, http://www.ipcc.ch/activity/srccs/index.htm, 2005.
6. N. Kumar, CO_2 Sequestration: Understanding the plume dynamics and estimating risk, Univ. of Texas, Austin, Master's Thesis, 2008.
7. A. Kumar, R. Ozah, M. Noh, G.A. Pope, S. Bryant, K. Sepehrnoori, and L.W. Lake, Reservoir Simulation of CO_2 Storage in Deep Saline Aquifers, *Society of Petroleum Engineers Journal* **10**(3) (2005) 336.
8. L. Nghiem, P. Sammon, J. Grabenstetter, H. Ohkuma, Modeling CO_2 storage in aquifers with a fully-coupled geochemical EOS compositional simulator. Paper SPE 89474 presented at 2004 SPE/DOE Symposium on Improved Oil Recovery, Tulsa, Oklahoma, 17-21 April, 2004.
9. N. Kumar, S.L. Bryant, J.-P. Nicot, Simplified CO_2 plume dynamics for a Certification Framework for geologic sequestration projects, *Energy Procedia*, GHGT-9 conference, Nov. 16-20, 2008, Washington DC.

10. P.D. Jordan, C.M. Oldenburg, J.P. Nicot, 2008, Characterizing fault-plume intersection probability for geologic carbon sequestration risk assessment, *Energy Procedia*, Proceedings of GHGT-9, Washington, D.C., Nov. 17-20, 2009.
11. P.D. Jordan, C.M. Oldenburg, J.P. Nicot, Calculating the probability of injected carbon dioxide plumes encountering faults. In preparation.
12. J. Watterson, J.J. Walsh, P.A. Gillispie S. Eaton, Scaling systematics of fault sizes on a large-scale range fault map. *Journal of Structural Geology* **18**(2-3) (1996) 199.
13. R.V. Ackerman, R.W. Schlische M.O. Withjack, The geometric and statistical evolution of normal fault systems: an experimental study of the effects of mechanical layer thickness on scaling laws. *Journal of Structural Geology* **23**(11) (2001) 1803.
14. P.A. Cowie, D. Sornette, C. Vanneste, Multifractal scaling properties of a growing fault population. *Geophysical Journal International* **122**(1) (1995) 457.
15. G. Pickering, J.M. Bull, D.J. Anderson, Sampling power-law distributions, Tectonophysics No. 248 (1995) 1-20.
16. Y. Zhang, C.M. Oldenburg, P.D. Jordan, S. Finsterle, K. Zhang, Fuzzy Rule-Based Probability Estimation of Fault Leakage at Geologic Carbon Sequestration Sites, Energy Procedia, GHGT9 conference, Nov. 16-20, 2008, Washington DC. LBNL-1415E.
17. Y. Zhang, C.M. Oldenburg, S. Finsterle, Percolation-Theory and Fuzzy Rule-Based Probability Estimation of Fault Leakage at Geologic Carbon Sequestration Sites, *Environmental Geology*, in press.
18. G. Gudmundsson, Geometry, Formation and Development of Tectonic Fractures on the Reykjanes Peninsula, Southwest Iceland, *Tectonophysics* **139**(3-4) (1987) 295.
19. H. Scholz, P.A. Cowie, Determination of Total Strain from Faulting Using Slip Measurements, *Nature* **346**(1990), 837.
20. P. Segall, D.D. Pollard, Joint Formation in Granitic Rock of the Sierra-Nevada, *Geological Society of America Bulletin* **94**(5) (1983), 563.
21. E. Bonnet, O. Bour, N.E. Odling, P. Davy, I. Main, P. Cowie, B. Berkowitz, Scaling of Fracture Systems in Geological Media, *Reviews of Geophysics* **39** (3) (2001) 347.
22. O. Bour, P. Davy, Connectivity of Random Fault Networks Following a Power Law Fault Length Distribution, *Water Resources Research* **33** (7) (1997) 1567.
23. L.A. Zadeh, Fuzzy Sets, *Information and Control* **8**(3) (1965) 338.
24. A. Bardossy, L. Duckstein (1995), Fuzzy Rule-Based Modeling with Applications to Geophysical, Biological and Engineering Systems, CRC Press.
25. L. Pan, C.M. Oldenburg, Y.-S. Wu, K. Pruess, Wellbore flow model for carbon dioxide and brine, *Energy Procedia*, GHGT9 conference, Nov. 16-20, 2008, Washington DC. LBNL-1416E.
26. H. Shi, J.A. Holmes, L.J. Durlofsky, K. Aziz, L.R. Diaz, B. Alkaya, G. Oddie, Drift-flux modeling of two-phase flow in wellbores, *Soc. Pet. Eng. J.* **10** (2005) 24.
27. K. Pruess, C.M. Oldenburg, G.J. Moridis. TOUGH2 User's Guide Version 2. E. O. Lawrence Berkeley National Laboratory Report LBNL-43134, November 1999.
28. K. Pruess, N. Spycher, ECO2N – A fluid property module for the TOUGH2 code for studies of CO_2 storage in saline formations, *Energy Conversion and Management* **48** (2007) 1761.
29. J.P. Brill, H. Mukherjee, *Multiphase Flow in Wells*. Monograph Volume 17, SPE Henry L. Doherty Series, 1999.
30. F.K. Chow, P.W. Granvold, C.M. Oldenburg, Modeling the effects of topography and wind on atmospheric dispersion of CO_2 surface leakage at geologic carbon sequestration sites, *Energy Procedia*, GHGT-9 conference, Nov. 16-20, 2008, Washington DC., LBNL-1420E.
31. N. Zuber, J.A. Findlay, Average volumetric concentration in two-phase flow systems, J. Heat Transfer ASME, 87(4), 453-468, 1965.

32. M. Xue, K.K. Droegemeier, V. Wong: The Advanced Regional Prediction System (ARPS): A multi-scale nonhydrostatic atmospheric simulation and prediction model. Part I: Model dynamics and verification, *Meteorol. and Atmos. Phys.* **75** (2000) 161.
33. M. Xue, K.K. Droegemeier, V. Wong, A. Shapiro, K. Brewster, F. Carr, D. Weber, Y. Liu, D. Wang: The Advanced Regional Prediction System (ARPS): A multi-scale nonhydrostatic atmospheric simulation and prediction tool. Part II: Model physics and applications, *Meteorol. and Atmos. Phys.* **76** (2001) 143.
34. R.E. Britter, Atmospheric Dispersion of Dense Gases, *Annual Reviews of Fluid Mechanics* **21** (1989) 317.

Carbon Dioxide Capture for Storage in Deep Geologic Formations, Volume 3
L.I. Eide (ed.)

Chapter 22

WELL INTEGRITY EVALUATION OF A NATURAL CO_2 PRODUCER

Walter Crow[1], D. Brian Williams[1], J. William Carey[2], Michael Celia[3], Sarah Gasda[4]
[1] BP Alternative Energy, 501 Westlake Park Blvd., Houston Texas, 77079, USA
[2]Los Alamos National Laboratory, Los Alamos, New Mexico 87545, USA
[3] Princeton University, Princeton, New Jersey, 08544, USA
[4]University of North Carolina, Chapel Hill, North Carolina, 27514, USA

ABSTRACT: The long-term integrity of wellbores in a CO_2-rich environment is a complex function of wellbore material properties, brine and rock compositions, CO_2 pressure, and pressure gradients. Laboratory experiments provide essential information on rates of material reaction with CO_2. However, field data are essential for assessing the integrated effect of these factors and for providing a basis for validation of numerical models of wellbore behavior. Each well system provides a barrier composed of tubulars, Portland cement and other material to isolate them and the borehole. The objective of this survey is to collect and analyze samples and data in order to characterize the isolation performance of the wellbore barrier system.

INTRODUCTION

This paper is an extended and modified version of a paper submitted to the 9th International Conference on Greenhouse Gas Control Technologies [1]. A field study of a 30-year old well from a natural CO_2 reservoir was conducted to determine the effect of CO_2 on the well barrier system defined as the tubulars and cement including its contact with casing and the formation. When CO_2 combines with moisture in the reservoir, carbonic acid is created which may corrode metal and Portland cement used in well construction. Fluid samples, cores and pressure response data were collected and analyzed to determine the potential effect of CO_2 on the barrier system. This information is used to provide benchmark data for modeling of the long term effects of injected CO_2 on the well system. The field survey was conducted in a well completed in the Dakota Sandstone formation found at 4561' True Vertical Depth (TVD) and had an estimated original reservoir pressure of 1624 psi and temperature of 136 ^{o}F at that datum. The CO_2 in the reservoir is a supercritical fluid under those conditions. This zone produces 96% CO_2 and has an average permeability of 59 millidarcies (mD), with a mineralogy that includes 69% quartz, less than 10% carbonate and water saturation of 20% based on original drill core analysis from this interval. The caprock confining layers in this well that overlie the Dakota formation are the Graneros Shale (135' vertical thickness) and Greenhorn Shale/Limestone (75' vertical thickness) formations (Figure 1).

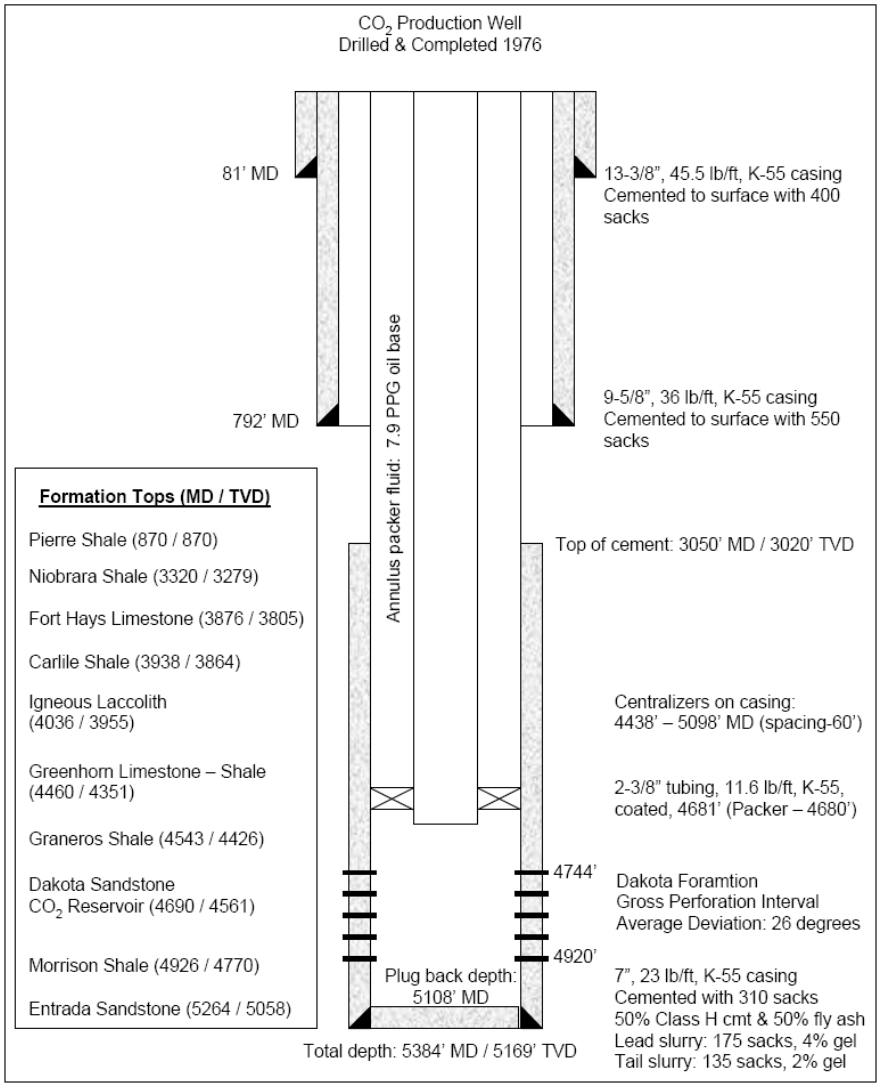

Figure 1. Schematic diagram outlining the type, size and grade of tubulars used in the well construction. Production tubing was plastic-coated carbon steel and cement was a Portland cement system with 50% fly ash.

The well was drilled in 1976 but production was deferred 9 years until 1985 due to pipeline availability. The well produced a total of 20 years and the first 13 years averaged 11 million standard cubic feet per day (SCF/D) of CO_2 with associated water production of 0.75 barrel per million SCF. The final 7 years of production were intermittent with associated increase in water production. Produced water from this interval is less than 5000 parts per million total dissolved solids (TDS). There was no casing pressure observed over the 30 year life of the well. The well

was drilled with an oil-based mud and the barrier system consisted of 7-inch diameter casing cemented with a Portland-cement-fly ash system. The casing was carbon steel, K-55 grade and was centralized in the borehole. The cement was 310 sacks (391 ft^3) of Class H Portland cement with 50% fly ash, 3% bentonite gel mixed at a density of 14.2 pounds per gallon (specific gravity: 1.71). The top of the cement (behind casing) was 3050' measured depth (MD) which extended 1640' above the CO_2-bearing reservoir. The casing was pressure tested to 1000 psi for 30 minutes after a 24 hour waiting period when the estimated cement compressive strength was 2000 psi. Production tubing was plastic-coated, K-55 grade material that showed no signs of corrosion during its production life.

Solid and fluid samples were collected from outside the casing within the CO_2 reservoir and from the caprock shale. Sidewall cores were cut through the casing to recover casing, cement and formation samples. Cement samples were analyzed at 2400 psi confining pressure for permeability, porosity and Young's Modulus (Figure 2). Capillary pressure properties and formation factor were deteremined at atmospheric pressure. Cement cores taken near the CO_2 reservoir have higher average permeability (21 μD) with average porosity of 41% compared to cores collected near the top of the caprock of 1 μD permeability and approximately 44% porosity (typical values of permeability and porosity for fresh cement are in the nanoDarcy range and 25-40% porosity, e.g., [2]). Cement core mineralogy (Figure 3) determined by X-ray diffraction indicates the relative amount of original unaltered cement paste compared to the amount converted to calcium carbonate due to CO_2 exposure over the life of the well. Cement samples taken in and near the CO_2 reservoir have been almost completely converted to calcium carbonate. Samples at the top of the caprock retain more of the original cement mineralogy but have had some minimal alteration. Cement evaluation log information given by raw acoustic impedance map (Figure 2) indicates generally good cement quality with the highest near the top of the shale at 4560' MD (shown by the darker color in the log strip). However, there are possible channel features above and below that area based on the lighter coloration which represents lower acoustic impedance. Visual observation of the cement interfaces with casing and with caprock show apparently tight contacts with no debris or other indications of porosity (Figures 4 and 5) and only very thin deposits (< 0.1 mm) of calcium carbonate (Figure 6). All 20 carbon steel casing samples recovered were in excellent condition with limited corrosion. Fluid samples were collected with a test tool that isolated formation pressure from the wellbore, drilled a hole through the casing, collected a fluid sample and recorded formation pressure and temperature data (Figure 2). The fluids had a surface-measured pH range of 5.2 to 6.1 and are slightly acidic. The measured formation pressure suggest that wellbore system provides hydraulic isolation between the CO_2 production zone and the upper caprock intervals based on the 1000 psi pressure difference sustained across the shale.

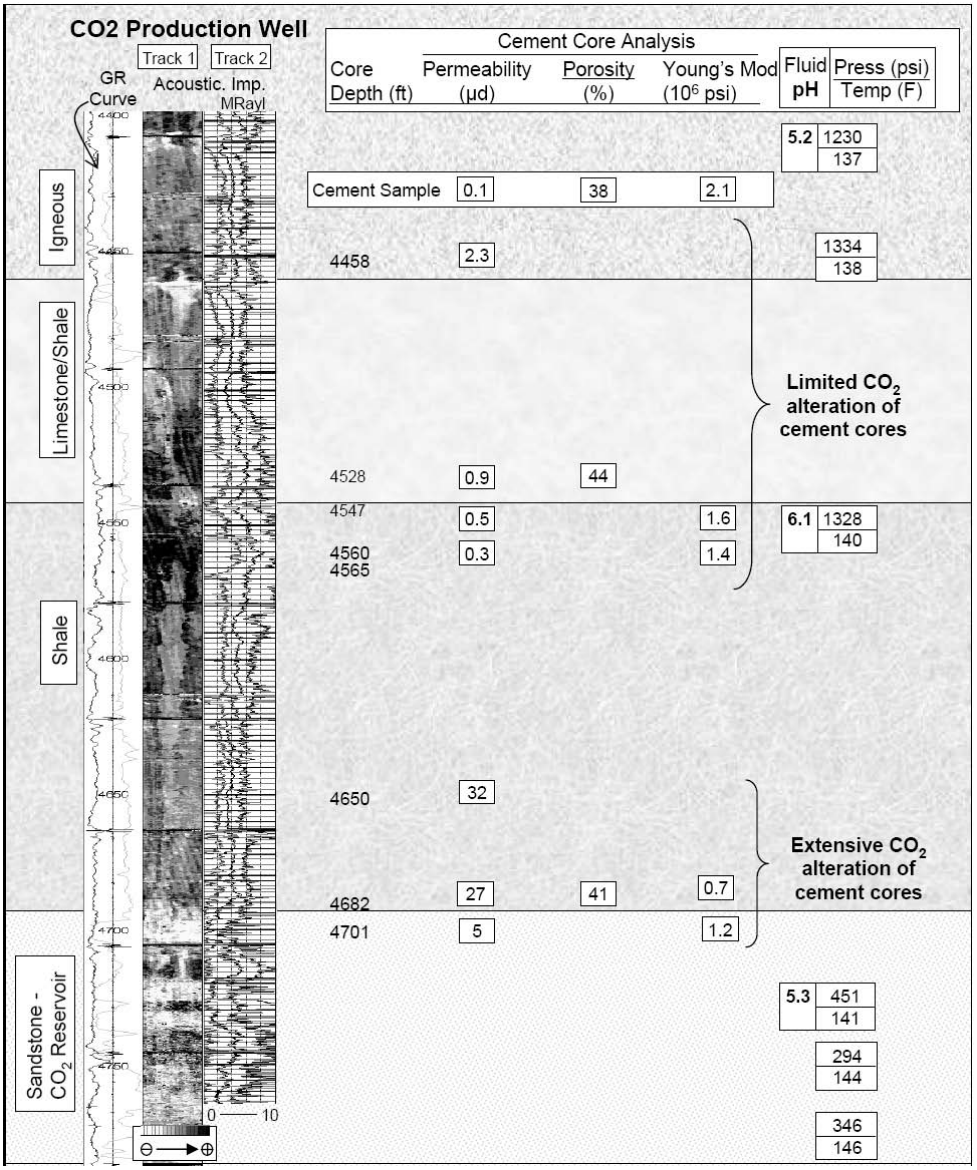

Figure 2. Comparison of cement core petrophysical properties with well log data, pressure data and fluid pH. Raw Acoustic Impedance map from the Ultrasonic Imaging Tool provides qualitative reference of cement condition (darker = better casing-cement bond).

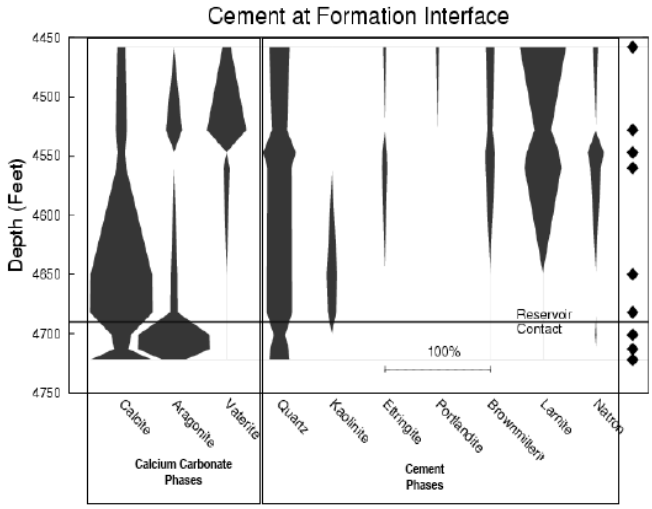

Figure 3. Mineralogy of cement cores measured at the interface with the formation as a function of depth. Original cement phases on the right are compared with CO_2 induced of alteration to calcium carbonate phases. The amount of calcium carbonate is greatest within and near the CO_2 reservoir and original cement phases are more abundant further from the reservoir. Aragonite is the most common calcium carbonate within the reservoir; calcite is common in the region just above the reservoir contact and vaterite is limited to regions far from the reservoir.

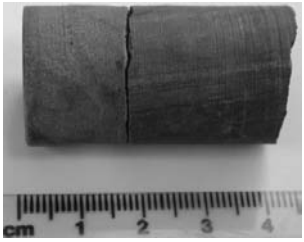

Figure 4. Core from 4682' of cement (left) and formation (right) indicates a tight fit at the interface.

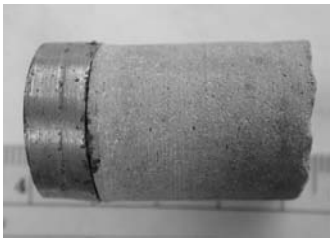

Figure 5. Core from 4650' with an intact contact between casing and cement.

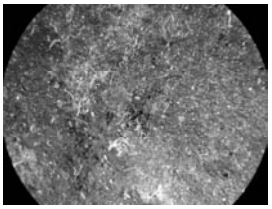

Figure 6. Core from 4722' in contact with the CO_2 formation has a thin layer of calcium carbonate crystals (view is 4 mm in width).

CAPILLARY PRESSURE MEASUREMENTS

The capillary pressure properties of the cement cores were analyzed by centrifuge (Figure 7) to determine the resistance to displacement of brine by air under differential pressure up to 300 psi. (The difference in the interfacial properties of the air-water and supercritical CO_2-water systems suggests that the capillary entry pressure for supercritical CO_2 is about half of that of air [3,4].) The estimated total pressure differential drive at the wellbore is approximately 90 psi (CO_2 buoyancy + non-hydrostatic gradient) which indicates that the capillary pressure measurements cover the expected range experienced by this wellbore system.

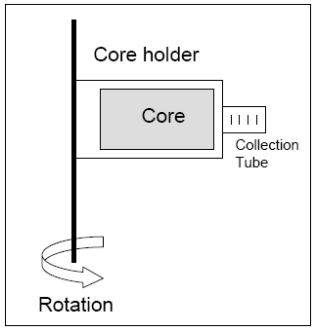

Figure 7. Schematic of a capillary pressure centrifuge.

The capillary pressure measurements are summarized in Figure 8 and compared to a laboratory sample of cement prepared according to the original wellbore specifications and cured under reservoir conditions. The capillary resistance is so high for fresh, unaltered cement that air entry is not possible at pressures higher than 200 psi. These results suggest that for fresh cement, CO_2 penetration of the cement matrix would not occur and that diffusion is the only mechanism for CO_2 migration through the cement matrix which is extremely slow. Similar results were observed by Kutchko et al. [5] and Carey et al. [6] in which carbonation of cement by supercritical CO_2 under static confining pressure or flow-through conditions was limited to diffusion processes. By contrast, the capillary pressure curves of relatively unaltered cement cores collected far from the CO_2 reservoir (shown by circles, squares and triangles in Figure 8) showed that only about 5% of the available pore space was accessible at pressures > 50 psi and < 300 psi. The effect of more complete carbonation as shown in samples collected from within and near the CO_2 reservoir further reduces the capillary resistance such that about 25% of the available pore space was accessible at pressures > 50 psi and < 300 psi. Interestingly, complete carbonation produces on average a small increase in capillary entry pressure resistance over the relatively unaltered samples.

Years of downhole aging may have led to the difference in capillary pressure between laboratory samples and relatively unaltered cement samples. Our hypothesis is that for fresh cement, migration of CO_2 in the wellbore can only occur by passing through a defect in the barrier system (channel or cement interface transmission pathway) and thus alteration of the cement could only occur by diffusion of CO_2 from the defect into the cement matrix. However, it also possible that with aging of the cement, the capillary resistance decreases and a limited volume (5%) of the available pore space could be accessible by CO_2, if the entry pressure exceeds 50 psi. Alteration could then occur by diffusion from the 5% pore space occupied by CO_2. Once the cement has been carbonated, however, it still retains relatively high capillary resistance to CO_2. These observations should be qualified by noting that the capillary pressure measurements were conducted at laboratory conditions and *in situ* confining pressure may further modify/reduce the cement permeability. In addition, the capillary pressure measurements do not address the percolation threshold for movement of CO_2: a saturation of 5% CO_2 may be insufficient for connected flow through the cement. In summary, the capillary pressure measurements suggest that separate phase CO_2 migration through the cement matrix is unlikely at the pressure conditions for the wellbore.

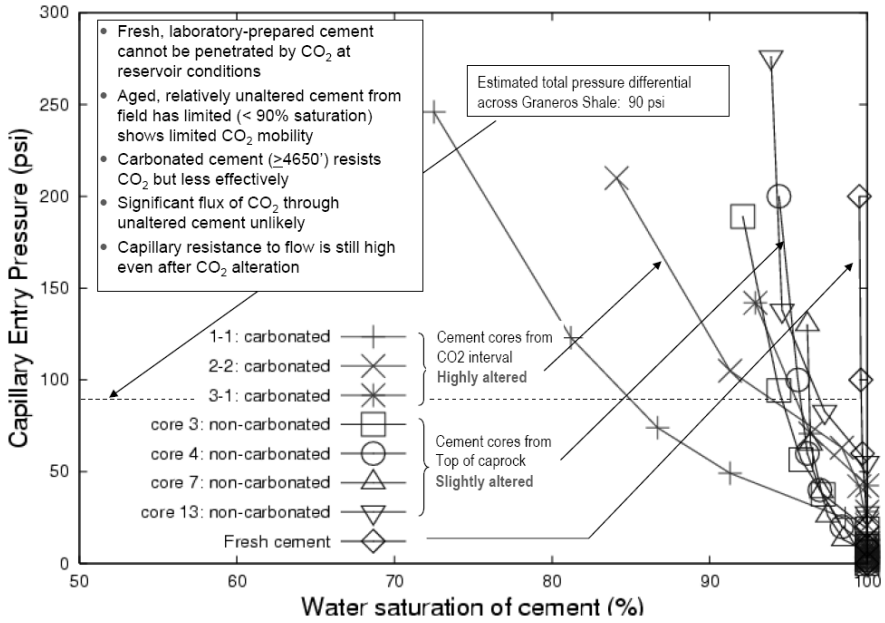

Figure 8. Capillary pressure properties of seven cores and a laboratory prepared cement sample. The fresh cement (diamonds) shows great capillary resistance such that no displacement of brine was possible at air pressures < 200 psi. An estimated pressure differential at the caprock-reservoir contact of 90 psi (dashed line) limits capillary displacement of brine to 20% of pore space for the most carbonated cores (crosses) and to 5% for the slightly altered cores near the top of caprock (circles, squares and triangles).

LOG ANALYSIS

An ultrasonic evaluation log was run to provide an indication of the cement quality and its bond to the casing measured by attenuation of the acoustic signal. Log results are presented in Tracks 1 and 2 in Figure 2. Acoustic impedance decreases from the top of the shale to the CO_2 interval (Track 2) from 8 to 0 MRayl over the interval from 4560' to 4700'. This general trend is consistent with a decrease in cement core hydrologic properties from the top of the caprock (1μD permeability) to the CO_2 interval (21μD permeability). For this well, the log measurement is relatively capable of detecting differences in the quality of the cement that is attached to, and surrounding the casing.

A multi-arm mechanical caliper was used to inspect the inner casing diameter and indicated minimal wall thickness loss between the perforations and packer where the casing was exposed to CO_2 and produced water. The corrosion log data is consistent with actual casing samples collected with the coring tool and showed limited or no corrosion.

There was no gas saturation evident in the caprock or other overlying layers based on results of a pulsed neutron log. This suggests limited migration along the barrier system. All gas shows from the survey are within the CO_2 formation and are consistent with presence of gas from the completion.

VERTICAL INTERFERENCE TEST ANALYSIS

A Vertical Interference Test (VIT) was conducted at the interface of the Greenhorn Limestone/Shale and the Graneros Shale between two perforated intervals at 4522' and 4533' (Figure 9). A wireline tool isolates the lower perforated interval from applied casing pressure. The applied pressure from the surface passes through the casing wall at the upper perforated zone to the cement barrier and shale interval. The pressure signal is recorded by the upper strain gauge (MRPS) and the lower quartz gauge (MRPA) adjacent to each perforation interval. The results from this test indicate the extent of hydraulic communication along the exterior of the well casing between the two perforations and are a measure of the effective permeability of the barrier system. Here, the barrier system is defined as the region outside of the casing that includes the following components: the cement that was placed between the casing and the shale (wellbore), the zone of shale that may have been damaged by drilling, and any annuli (interfaces) that may exist between the cement and the casing or the cement and the shale. The effective permeability of this system is a bulk measure of permeability but does not distinguish individual flow paths within the different components of the barrier system. Therefore, effective permeability is an integrated measure of the overall competence of the barrier system to prevent fluid and gas migration along the wellbore.

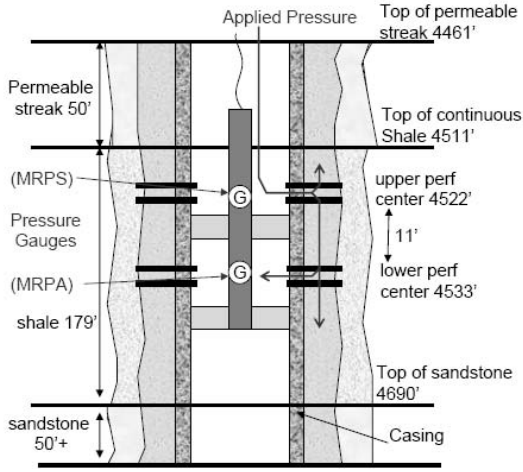

Figure 9. Configuration of VIT includes an isolation tool with pressure gauges (MRPS & MRPA) positioned in the wellbore. The model describes perforations in a shale interval with sand (permeable) intervals above and below the shale.

The approach taken in the VIT analysis is to use a numerical model developed for this analysis to simulate the physical test data. The effective permeability assigned to this region in the model is then tuned until the simulated data sufficiently matches the test data. This approaches requires that other system parameters can be reasonably estimated, which include the permeability and compressibility of the shale and other geologic formations within the domain, the compressibility of cement, and the effective permeability of other sections of barrier system along the wellbore.

The raw VIT data (shown in Figure 10) were normalized to a dimensionless scale between 0 and 1. On this scale, a value of 1 means that 100% of the pressure change imposed in the upper perforation is detected in the lower perforation. Likewise, a value of 0 means that no pressure change is detected in the lower perforation. This normalization is achieved by taking the ratio of the relative pressure changes recorded in the lower and upper gauges using Equation 1. An initial pressure

($MRPA_0$) of 1940 psi is used, which is the value recorded in the lower perforation at 5,600 seconds that corresponds to the wellbore fluid hydrostatic pressure (equivalent to a gradient of 0.439 psi/ft at 4417' TVD). Similarly, the relative pressure change in the upper perforation is the average sustained pressure (2725 psi) minus $MRPA_0$. Since the perforations are so close together, this is an appropriate approximation. The normalization formula is as follows:

$$MRPA_{norm} = \frac{MRPA(t) - MRPA_0}{2725 - MRPA_0} \qquad \text{Equation 1}$$

Governing Equation

The governing equation for this system is the continuity equation for compressible flow of a single fluid in porous media,

$$c_f \frac{\partial p}{\partial t} - \nabla \cdot \frac{k}{\mu}(\nabla p - \rho \mathbf{g}) = 0 \cdot \qquad \text{Equation 2}$$

In the above equation, c_f is the compressibility, p is the fluid pressure, k is the permeability, μ is the fluid viscosity, ρ is the fluid density, and **g** is the gravity vector. Equation 2 is a transient equation that describes the evolution of pressure in space and time. For this model, compressibility and permeability can vary, but the fluid viscosity and density are assumed to be constant in the near-well environment. In Equation 2, the pressure response depends on the ratio k/c_f (permeability to compressibility) at each point in space. A set of values is chosen for k and c_f at each point in space. Thus, although the focus of the modelling is on permeability, the dependency on compressibility is implied.

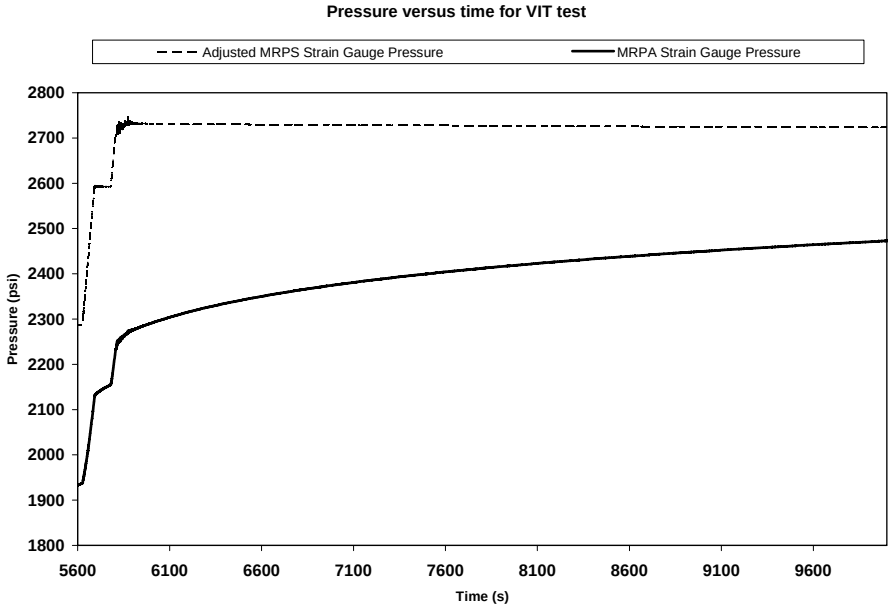

Figure 10. Raw data from VIT showing pressure in the two gauges; MRPS in the upper perforation, MRPA in the lower perforation which are separated by an isolation packer.

Numerical Method

A numerical model was developed that solves the governing equations for compressible flow of a single fluid in porous media in space and time. This model solves the system in a radially symmetric coordinate system. As in the physical system, the domain that is modeled consists of two sandstone formations separated by a low-permeability shale layer. The model domain measures 256' in the vertical and 27,000' in the radial direction. The inner boundary of the domain coincides with the outer casing radius (OD) and is impermeable to flow. At the outer boundary, a hydrostatic pressure condition is imposed. The top and bottom boundaries of the domain are also impervious to flow. The perforations are modeled as very high permeability regions at the same location within the shale as in the physical system. Pressure is imposed in the upper perforation to a value of 2725 psi, which is the average applied pressure measured by the MRPA gauge in the physical system. During the VIT simulation, the pressure was recorded in the lower perf for 10,000 s and compared with the actual VIT data.

Based on original drill core measurement, the horizontal permeability value of the sandstone formations are estimated to be 0.1 D (1 Darcy = 10^{-12} m^2) and are assumed to be isotropic. The permeability of the shale is assumed to be anisotropic and estimated to be 0.1 nD (horizontally) and 0.0001 nD (vertically) where 1 nD = 10^{-18} D. Based on survey sidewall core measurement, the compressibility of the sandstone is estimated to be 10^{-10} m^2/N, while the shale compressibility is assumed to be higher and is estimated to be 10^{-9} m^2/N. For reference, the compressibility of water is 4.6×10^{-10} m^2/N, where 1 m^2/N = 1 Pa^{-1}= 6,895 psi.

The distance from the outer radius of the casing to the inner wall of the borehole is 1.75 in. This region corresponds to the barrier system as discussed above, where it is assumed that the shale outside this zone is undamaged. Determining the effective permeability of this 1.75 in wide zone is the objective of this analysis, and the value can be tuned in the model until a sufficient match is found to the test data.

Method of analysis

Using the model, numerical simulations were performed using different values of effective permeability assigned to the barrier system. After testing numerous values, the comparison with the VIT data was best for a limited number of cases. Three representative cases are discussed here. The values of the assigned effective permeability and the horizontal permeability in the shale for each case are listed in Table 1.

Table 1. Simulation cases that present the best matches to test data using variation of barrier system effective permeability with shale permeability.

Case	Effective Permeability	Shale horizontal permeability
1	7 mD	0.1 nD
2	10 mD	0.1 nD
3	4 mD	1 nD

Results

The simulated VIT results for all cases are compared with the actual VIT test data (Figure 11). For all the following cases, the temporal dimension is presented in log-space so as to examine both the early time and late time comparisons between the simulated and test data. In addition, the temporal values of the test data are scaled so that time $t = 0$ corresponds to the start of the VIT when the well is pressurized, which occurs at 5,600s in Figure 10.

In Figure 11, the test data begins to slowly increase between t = 0.1 s and t =1 s, as the first part of the pressure signal reaches the gauge in the lower perforation (Figure 10, MRPA line). From 1 to 10s, the test data undergoes a rapid increase in pressure before decreasing abruptly. At around 11 s, there is a jump in the test data followed by a steady increase until the end of the test at 10,000 s. The erratic data during this period is due to the way pressure is applied at the surface by a pump that does not have constant rate control.

The simulated data for each of the three cases are reasonably close to the test data, but no single case can emulate the full test response from early to late time. Cases 1 and 3 compare best to the test data at early time, t < 1 s. Case 2 matches better between 10 s and 100 s. However, none of the cases compare well with the test data at late time. For all of the simulated cases, the slope in the response curve is less than the test data from 1000 s to 10,000 s.

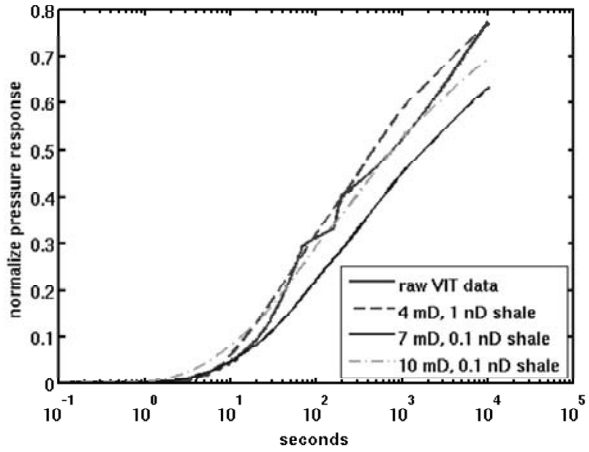

Figure 11. Comparison of IT data (upper unbroken line) to numerical simulations under differing assumptions of cement permeability (4-10 mD) and shale permeability (0.1-1 nD).

Discussion

It appears from the VIT analysis that the effective permeability of the zone is close to one of the three simulated cases, though it is difficult to determine which case is the best comparison. There is a possible channel noted on the Acoustic Impedance curve (Figure 2) that could contribute to communication along the cement interface where the VIT was conducted. The fact that the simulated data does not match perfectly with the test data is to be expected given that the simulated system is only an approximation of the real physical system. Two key assumptions that may contribute to the discrepancy in the simulated results are radial symmetry and homogeneous permeability in the cross-section of the barrier system. In addition, uncertainties in system parameters, such as the shale permeability and compressibility, are also important factors in how well the simulated data is able to match the test data. Given this discussion, the VIT analysis is limited to estimating the effective permeability of the barrier system within an order of magnitude, between 1 and 10 millidarcy. Further investigation is required of the test method and geomechanical properties of the near-wellbore environment in order to reduce uncertainty in the analysis.

The cement core collected from 4528' MD has a matrix permeability of 0.9-μD (at 2400 psi confining stress) and thus the estimated permeability from the VIT data may be approximately 3

orders of magnitude greater than cement core. The enhanced permeability observed in the VIT is likely due to communication at the interfaces and thus the most likely path of any CO_2 migration would be these interfaces. The possible channel noted on the Acoustic Impedance curve (Figure 2) could contribute to the communication along those interfaces.

CONCLUSIONS

The primary conclusions from this investigation are:

a. Conventional cement-fly ash systems can inhibit CO_2 migration even after carbonation of the cement because permeability remains relatively low and capillary resistance relatively high. Effective placement of the cement system was a key factor in the barrier performance to prevent or limit migration along cement interfaces with the casing and formation. These interfaces are the areas of greatest concern for migration potential, but in this well, they provide sufficient flow restriction between formations based on the VIT results, the lack of corrosion in the well, and the lack of sustained casing pressure.

b. Cement carbonation has been observed in varying degrees in cores from this well. Compared to the lab cement sample, the carbonated cement cores have increased permeability and porosity and decreased capillary resistance and mechanical strength. In spite of the changes in the cement properties in this well, it still provides an effective hydraulic barrier and resistance to CO_2 migration.

c. The casing is in very good condition, consistent with good cement coverage and limited circulation of reservoir fluids along the casing-cement interface.

d. Cement interfaces with casing and formation appear to be tight and do not have significant calcium carbonate deposition.

e. The effective permeability of the barrier system including the cement interfaces was evaluated by numerical modelling of the Vertical Interference Test (VIT) data, which is the preferred method to analyze in-situ migration potential. The VIT data analysis indicates the permeability may be as much as 1-10 millidarcies. This is approximately 3 orders of magnitude greater than the cement core permeability of 1 microdarcy that was taken from the same interval. Although further investigation is required to reduce uncertainty in this analysis, the results indicate that the cement interfaces with casing and/or formation are the primary path for potential CO_2 migration compared to the cement matrix.

f. Our interpretation of the data suggests that the CO_2 that has caused carbonation of cement and acidification of fluids adjacent to the caprock originated in the CO_2 reservoir (Dakota formation). The alteration could come from either or a combination of CO_2 diffusion into the caprock or by migration along defects (primarily cement-caprock and cement-formation interfaces) within the wellbore system. History matching the survey data and results will be conducted to distinguish between these two alternatives.

g. Current technologies can be used to determine wellbore barrier condition. Logging results from this survey correlate with the performance measurement of the large scale vertical interference test (VIT) and the small scale cement core properties.

Evidence from this investigation suggests that Portland-based cement systems can be used effectively in creating suitable barrier systems for long-term CO_2 storage operations, if good practices are employed during well construction. Examples of required good practices include: centralization of casing and efficient borehole mud removal for cement placement.

ACKNOWLEDGEMENTS

The authors express their appreciation to the management of CO_2 Capture Project Phase 2 member companies for support of this project. CCP2 member companies are: BP Alternative Energy, Chevron, ConocoPhillips, Eni, StatoilHydro, Petrobras, Shell Global Solutions US Inc. and Suncor Energy Inc. The conclusions in this report are those of the authors and are not necessarily the view of the other member companies.

Special thanks to Charles Christopher, BP Alternative Energy, for the guidance in creating this comprehensive program. Special thanks also to Ray Wydrinski, BP America for support with petrophysical analysis. Special thanks also to Andrew Duguid, Ph.D., and Matteo Loizzo of Schlumberger Carbon Services for their support in this project.

This Chapter contains figures and excerpts that originally appeared in Energy Procedia Vol 1, Issue 1, Greenhouse Gas Control Technologies 9, Proceedings of the 9th International Conference on Greenhouse Gas Control Technologies (GHGT-9), 16-20 November 2008, Washington DC, USA, which was published by Elsevier Ltd.

REFERENCES

1. W. Crow, D. B. Williams, J. W. Carey, M. Celia, S. Gasda, (2008), 9th International Conference on Greenhouse Gas Control, Wellbore integrity analysis of a natural CO_2 producer.
2. Taylor, H. F. W. (1990) Cement Chemistry. Academic Press, London, 475 pp.
3. Chiquet, P., Broseta, D., and Thibeau, S. (2007) Wettability alteration of caprock minerals by carbon dioxide. Geouids 7: 112-122.
4. Chiquet, P., Daridon, J. L., Broseta, D., and Thibeau, S. (2007) CO_2/water interfacial tensions under pressure and temperature conditions of CO_2 geological storage. Energy Conversion and Management 48: 736-744.
5. Kutchko, B., Strazisar, B., Dzombak, D., Lowry, G., and Thaulow, N. (2007) Degradation of well cement by CO_2 under geologic sequestration conditions. Environmental Science and Technology 41: 4787-4792.
6. Carey, J. W., Svec, R., Grigg, R., Lichtner, P., Zhang, J., and Crow, W. (2008) Wellbore integrity and CO2-brine ow along the casing-cement microannulus. In 9th International Conference on Greenhouse Gas Control Technologies, November 16-20, 2008, Washington, DC, USA.

Carbon Dioxide Capture for Storage in Deep Geologic Formations, Volume 3
L.I.Eide (Ed.)

Chapter 23

CO_2 DETECTION – RESPONSE TESTING OF RST IN SANDSTONE FORMATION TANK CONTAINING CO_2 AND WATER-BASED FLUID

Helene Climent*
Schlumberger Sugar Land Product Center,
110 Schlumberger Drive MD5, Sugar Land, TX77478, USA

ABSTRACT: A set of experiments has been performed at Schlumberger's Environmental Effects Calibration Facility (EECF) as part of the CO_2 Capture Project experimental phase. The objective was to evaluate the ability of Schlumberger's Reservoir Saturation Tool (RST) to detect the presence of CO_2 in a brine-saturated sandstone formation. The RST measurements were made in a tank that was built especially for these experiments. RST offers two different measurement modes that have the potential for detecting the presence of CO_2 in the formation. Inelastic-Capture (IC) mode measurements provide the relative amount of carbon (yield) and the ratio of carbon to oxygen present in the wellbore and surrounding formation. This is particularly useful in detecting and quantifying hydrocarbon concentrations in the reservoir. Sigma mode provides measurements of the capture cross-sections of the formation and borehole along with count rate ratios that help determine the types of fluids present. Inelastic-Capture mode experiments show that the increase in carbon yield when CO_2 is injected into the formation is detectable in certain circumstances but is too small compared to the statistical uncertainty to be a practical indicator. Because of the large difference between the capture cross sections of a brine-saturated sandstone formation and a formation containing CO_2, the presence of CO_2 is easily detected in sigma mode. When the formation is saturated with fresh water or oil instead of brine, the large capture cross-section difference disappears. In this case the sigma mode count rate ratios show promise in differentiating CO_2. More modeling and experiments will be needed to better understand RST response in these circumstances.

INTRODUCTION

In the last few years, there has been a growing interest in the capture of CO_2 and its storage in depleted oil and gas reservoirs. This has motivated several projects to study the use of current oilfield technology for this purpose (see references [1] and [2]). One aspect of this is the monitoring of the location of CO_2 injected into the reservoir using well logs. The Reservoir Saturation Tool (RST) with its ability to measure carbon concentrations and neutron capture cross-sections can potentially provide key measurements to help detect the presence of CO_2 in formations.

As part of the CO_2 Capture Project, a set of experiments was performed at Schlumberger's Environmental Effects Calibration Facility (EECF) aimed at evaluating the ability of the RST to detect the presence of CO_2 in a brine-saturated sandstone formation. The RST measurements were made in a tank that was built especially for these experiments (see Figure 1). The tank housed a sandstone formation constructed to have a porosity of approximately 30 p.u. with a borehole passing through. RST response was recorded with various saturating fluids including brine and CO_2. This paper summarizes the results of these experiments.

* Present address: 4730 Stoney Point Court, Sugar Land, TX 77479, USA (helene.climent@gmail.com)

Some initial modeling was carried out to help understand what RST responses to expect in the experiments and is presented first. After that, the experiments themselves are described and interpreted and conclusions are drawn about RST's suitability to detect CO_2 in this environment.

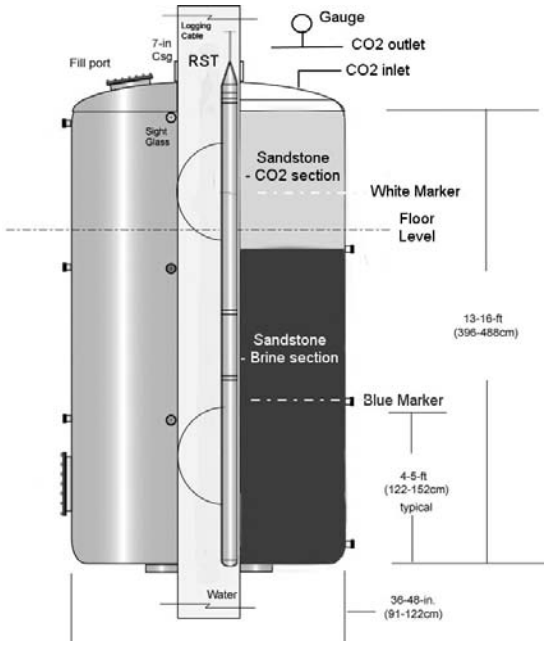

Figure 1. Experimental Setup.

THEORY OF MEASUREMENT

RST offers two different measurement modes that have the potential of detecting the presence of CO_2 in the formation. Inelastic-Capture mode measurements provide the relative amount of carbon (yield) and the ratio of carbon to oxygen present in the wellbore and surrounding formation. Sigma mode provides measurements of the capture cross-sections of the formation and borehole along with count rate ratios that help determine the type of fluids present. The two types of interactions are illustrated in Figure 2.

The RST measures the energy spectra and the time decay of neutron induced gamma-rays. The Pulsed Neutron Generator generates pulses of high-energy neutrons also called fast neutrons. Some of these fast neutrons collide with the nuclei of elements present in the formation and transfer part of their energy to these nuclei through inelastic collisions. The excited nuclei promptly revert back to their original energy levels and by doing so emit gamma-rays. The energies of the gamma rays emitted are specific to the nucleus of the isotope involved. An analysis of the spectrum of gamma-rays reaching the detectors reveals the elements present in surrounding environment. This inelastic gamma ray spectrum is used to determine the relative contributions or yields of carbon, oxygen and other elements and to compute the carbon/oxygen ratio helpful in detecting hydrocarbon presence in reservoirs. This measurement type is provided by using RST's Inelastic-Capture mode.

As neutrons slow to thermal energy levels, they are eventually captured by the nuclei present in the formation, the borehole and the tool. This leaves a new nucleus with its captured neutron in a highly

excited state and the excess energy is promptly given off in the form of one or more gamma rays. The average time that the neutron stays at the thermal energy level before being captured is determined by the capture cross section of the formation and the borehole. The tool indirectly measures the rate at which thermal neutrons are absorbed by measuring the decay rate of gamma rays produced by this absorption. The capture cross section of the formation (Sigma) is then determined from the decay rate. Sigma is strongly affected by the type of fluid that is present in the formation. This measurement type is provided by using RST's Sigma mode.

More details on the RST data processing are given in references [3] and [4].

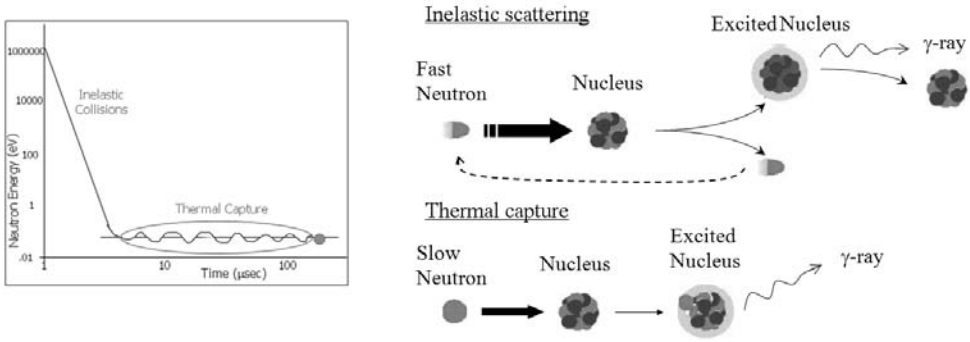

Figure 2. Illustration of neutron inelastic scattering and thermal capture.

PRELIMINARY CALCULATIONS

Before considering the data collected from the experiments, it is helpful to understand what the effects the various environments will have on key tool response parameters. To do this, a special Schlumberger internal code called Schlumberger Nuclear Parameter (SNUPAR) was used. SNUPAR is a deterministic modeling code that uses the neutron and gamma ray cross-sections of the various elements to compute various nuclear parameters. The nuclear response parameters of interest for this study are:

- The macroscopic thermal-neutron capture cross-section (Σ in capture units (c.u.)) - measured by RST in the Sigma mode – formation fluid type has a large effect on the Σ value;
- The neutron epithermal slowing-down length (Ls in cm) - the average distance fast neutrons travel in a material as they slow down to thermal energies;
- The hydrogen index (HI) - measure of the amount of hydrogen in the formation;
- The diffusion length (D) – correlated to temperature for moderators like water and oil that contain large amounts of hydrogen.

These parameters are very helpful in confirming our baseline measurements for sandstone saturated with brine, sandstone with air and sandstone with CO_2. Ls and HI are not directly measured by RST but have a strong effect on the gamma ray count rates measured by the detectors. Since hydrogen is the most effective element in slowing down fast neutrons (because its nuclear mass is almost the same as the neutron mass), Ls is highly correlated with HI. Larger values of Ls mean that neutrons can travel deeper into the formation and closer to the detectors before being absorbed. This produces higher gamma ray count rates at the detectors at lower HI.

Additionally, the slowing-down length proves to be helpful in

- Determining the density of CO_2;
- Comparing the nuclear tool response of CO_2 versus hydrocarbon.

The main materials present in these experiments are sandstone (SiO_2), CO_2, brine (H_2O + NaCl) and iron (Fe). The SNUPAR computation is based on the fraction and density of each component. Table 1 displays the results obtained for a 30 p.u. sandstone formation, then the same formation filled with air, with brine at 196.8 ppk and with CO_2 gas and liquid. The last line shows the values for liquid CO_2 alone (not in sandstone) with a density of 1.032 g/cm^3. The values in this Table indicate a large difference between the values of sandstone with air or CO_2 (Σ=3.2 c.u., Ls=43 cm) and sandstone saturated with brine ($\Sigma_{sand+brine}$=46 c.u., Ls=12 cm). The capture cross-section values for sandstone with air and sandstone with CO_2 are very similar.

Table1. Benchmark of Capture Cross-Sections (Σ), Diffusion Length (D), Slowing-Down Lengths (Ls) and Hydrogen Index (HI) with SNUPAR

	Σ (c.u.)	**D (cm)**	**Ls (cm)**	**HI**
Sandstone	4.55	1.47	28.81	0.00
Sandstone + air	3.20	2.10	42.81	0.00
Sandstone + H_2O	9.85	0.40	10.91	0.30
Sandstone + brine at 196.8 ppk	32.94	0.41	11.15	0.28
Sandstone + CO_2 (0.001 g/cm^3)	3.19	2.10	42.81	0.00
Sandstone + CO_2 (1.032 g/cm^3)	3.20	1.61	33.32	0.00
Liquid CO_2	0.06	2.05	48.31	0.00

During the experiment, the temperature ranged from 77 to 88 ºF and the CO_2 pressure from 0 to a maximum of 1060 psi. Under these pressure and temperature conditions, CO_2 is in either a gaseous or vapor-liquid state (see Figure 3).

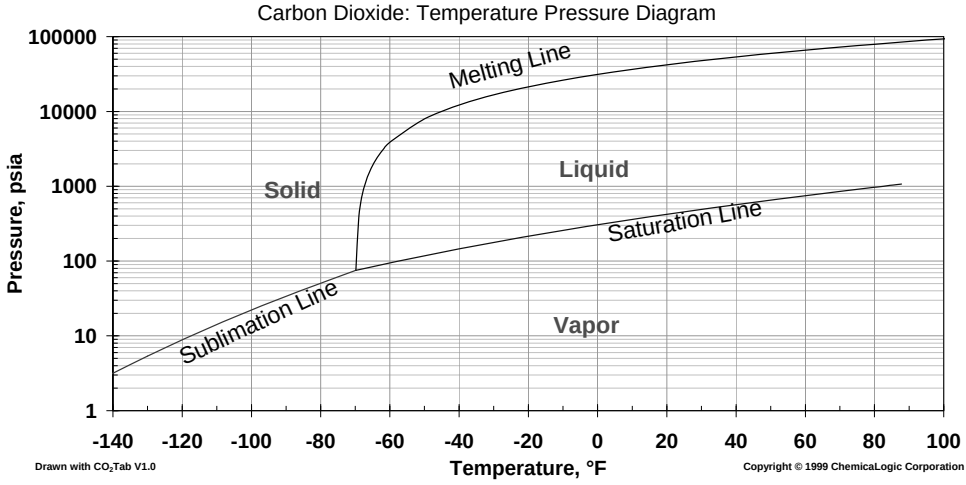

Figure 3. CO_2 Phase diagram.

SNUPAR has been used to predict the response to CO_2 compared to hydrocarbon such as ethylene (CH_2) and methane (CH_4). For calculation purposes, the densities of CH_2, CH_4 and CO_2 have been assumed to range between 0.001 (gaseous at atmospheric pressure) and 1.03 g/cm^3 (liquid at higher pressure). The results are displayed in Figure 4 to Figure 6.

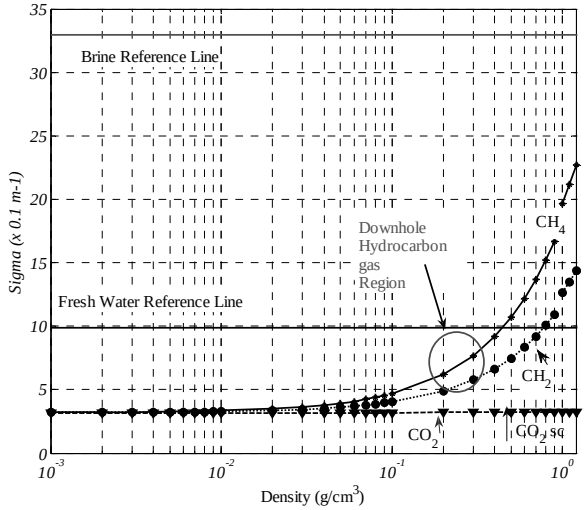

Figure 4. Calculated Capture Cross-Section (Sigma) versus CH_2, CH_4 and CO_2 densities in Sandstone.

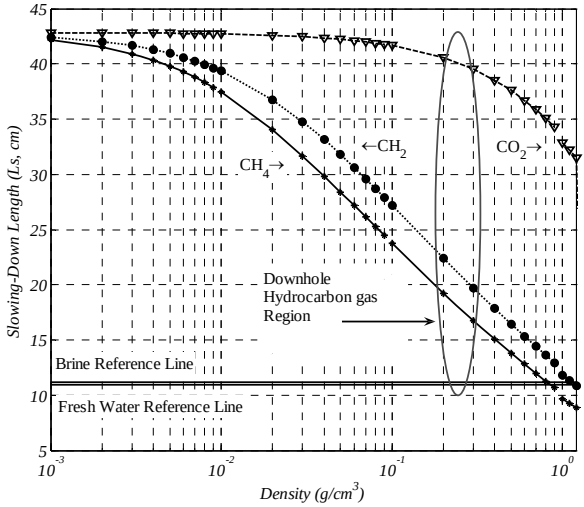

Figure 5. Calculated Slowing-Down Length (Ls) versus CH_2, CH_4 and CO_2 densities in Sandstone.

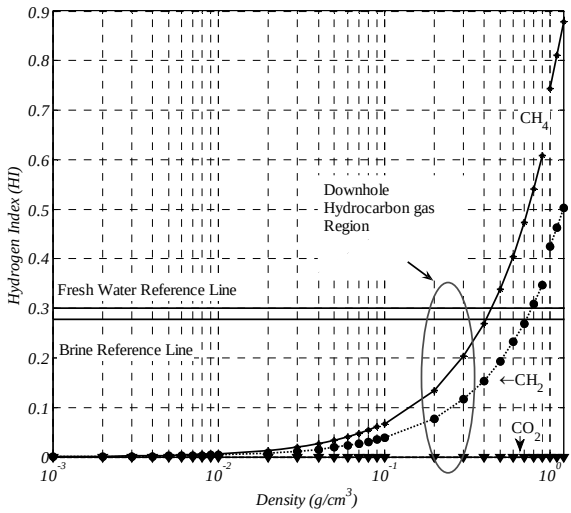

Figure 6. Calculated Hydrogen Index (HI) versus CH_2, CH_4 and CO_2 densities in Sandstone.

The slowing-down length Ls in Figure 5 suggests that liquid CO_2 behaves similar to light hydrocarbon gas for slowing down neutrons from the count rate point of view. The expected hydrocarbon density for CH_4 downhole is usually in the range of 0.2 to 0.3 g/cm^3. For this density interval, the Ls and Σ values are very different between CO_2 and hydrocarbon. The capture cross-section (Σ) and the slowing-down length (Ls) are good indicators of the presence of CO_2 in the formation. The hydrogen index (HI) of CO_2 in a sandstone (SiO_2) formation is zero: there is no hydrogen (see Figure 6). Thus a low value of HI can also be a good indicator of the presence of CO_2.

EXPERIMENTAL SETUP

The experiment setup is shown in Figure 1. The custom tank described in the first stages of the CO_2 Capture Project experimental phase has been setup in the pit area of the Schlumberger Environmental Effect Calibration Facility (EECF). It has been filled with Flint Silica #12 from US Silica. This is a quartz containing 99.8% SiO_2 with a density of 2.65g/cm^3. The fines are white round grains with an AFS grain fineness of 22. The packing of these grains in this experiment produces a porosity of about 30%. Preliminary measurements have been taken with RST with dry sandstone in the tank in order to measure the baseline.

Two thirds of the tank volume has been saturated with brine. The brine has a salinity of 196.8 ppk NaCl. The brine has been pumped into the tank from the bottom, keeping the upper one third volume of sandstone dry. Baseline measurements have been run in the brine section of the tank. The borehole fluids are air or fresh water or brine at 195 ppk NaCl.

The CO_2 injection has been done from the CO_2 inlet located in the upper part of the tank. The CO_2 pressure can be monitored with the gauge at the top of the tank. The CO_2 pressure was increased in steps allowing several measurements to be carried out for each step. These measurements are described and interpreted later in this report.

RST MEASUREMENTS

RST Measurements in Sigma Mode

In order to determine which RST measurement (or which combination of measurements) is useful in detecting the presence of CO_2 in the formation, several channels have been studied:

- Sigma Formation Near Apparent - SFNA
- Sigma Formation Far Apparent - SFFA
- Near/Far Capture Ratio - TRAT (TRAT is strongly influenced by Hydrogen Index)
- Inelastic Far/Near Ratio - IRAT (IRAT is influenced by both HI and density)
- Sigma Borehole Far Apparent - SBFA
- Sigma Borehole Near Apparent - SBNA

The four sigma channels are determined from the measured gamma ray decay rate. These measurements have an additional decay component due to neutron loss through diffusion. They are called "sigma apparent" because of this. The true decay rate due to just neutron capture cross-section is slightly different.

Two cases of interest taken from the RST sigma characterization database are given in Table 2. They are for a water-saturated, 34.4 p.u. sandstone formation with an 8-in. borehole including a 7-in. 32 lb/ft casing. They are included for comparison purposes to indicate how the tool responds in the environment of the characterization database that is closest to the environment of the experiments here. These values are a good benchmark of how the RST will respond in our experiments.

Table 2. RST Sigma Characterization Database relevant values.

Lith.	BHS (in)	Por (p.u.)	FSAL (ppk)	BSAL (ppk)	TRAT	SFNA (c.u.)	SFFA (c.u.)	SIGM (c.u.)	SBNA (c.u.)	SBFA (c.u.)
Sand.	8	34.4	208.5	10	1.09	28.06	30.45	38.96	41.13	36.08
Sand.	8	34.4	208.5	211.2	0.88	41.72	41.38	38.96	79.45	70.69

Two types of measurements have been carried out in Sigma mode. The first is made up of 20 minutes stationary measurements. Most of them are taken opposite the formation in the CO_2 section (referred as "white marker" in Figure 1) others in the brine section (referred as "blue marker" in Figure 1) to obtain a baseline. The second type of measurements is logging up from the brine section to the CO_2 section. These measurements are meant to show the contrast between the two sections.

Sigma mode stationary logs

Figure 7 displays the results of the sigma mode measurements taken in the tank at the CO_2 section level versus CO_2 pressure. As a reference, the values extracted from the database and the baseline formation data measured in the brine section are also plotted on the left side of the graph (at P_{CO_2} = 0 psi). When the borehole fluid is fresh water, the large contrast between thermal capture cross-section of CO_2 and formation water gives a clear indication of the formation content. The measurement of the apparent thermal capture cross section from the RST database when the formation contains brine varies depending on the borehole fluid (fresh water or brine). The values with brine as the borehole fluid are higher than the values with fresh water in the borehole. When CO_2 is in the formation instead of brine, this tendency is reversed due to the diffusion effect. The diffusion length (see Table 1) is larger for a sandstone formation containing CO_2 than the one for a

sandstone formation saturated with brine. Note that although the EECF formation is of very good quality (quartz containing 99.8% SiO_2), the presence of some trace elements has an effect on the capture cross-section. The Snupar calculations predicted $\Sigma_{sand+air)snupar} = 3.199$ c.u., the measured is $\Sigma_{(sand+air)meas} = 9.667$ c.u.. Formations are typically not as clean and larger differences in the capture cross-sections are to be expected.

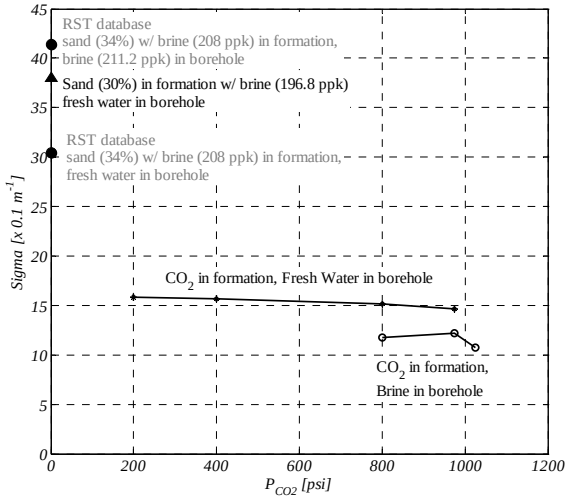

Figure 7. Sigma Formation Far Apparent (SFFA) versus CO_2 pressure.

The near/far capture ratio (TRAT, Figure 8) and the inelastic ratio (IRAT, Figure 9) show trends similar to the formation capture cross-sections. Typically, when there is gas in the formation the far detector count rates increase making the near/far ratio decrease. Note that the use of TRAT and IRAT as indicators in a monitoring program require base passes without CO_2 in the system, as a reference point.

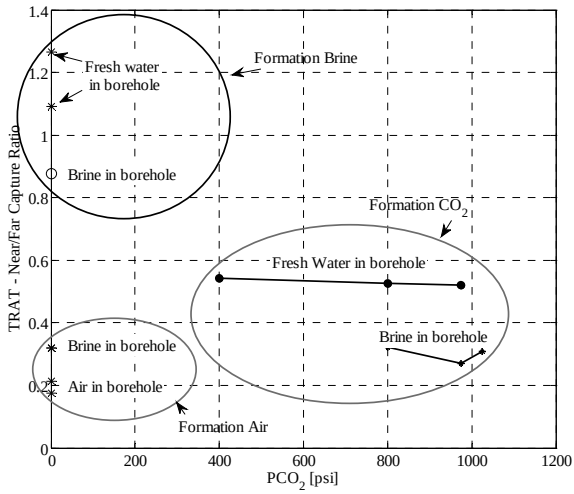

Figure 8. Near/Far Capture Ratio (TRAT) versus CO_2 pressure.

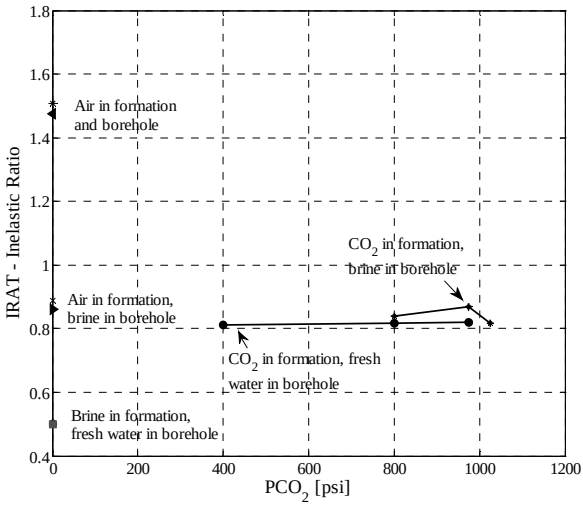

Figure 9. Inelastic Ratio (IRAT) versus CO_2 pressure.

The apparent sigmas from the borehole are similar to the ones of the database. As expected, sigma values with fresh water in the borehole are lower than the ones with brine in the borehole confirming the borehole signal of our measurements. SBFA and SBNA essentially read the sigma of the borehole fluid especially for brine in the borehole.

The thermal capture cross-section is the main RST measurement in Sigma mode to consider for CO_2 detection and monitoring.

Sigma mode logging from the brine to the CO_2 section

In these measurements, the tool is moving at 300ft/h from the formation brine to the formation CO_2 section. The depth control on these logs is only approximate so some of the logs where manually shifted for better depth matching.

The apparent formation capture cross-sections for the far detector SFFA (Figure 10) display a large contrast between the brine and the CO_2 section. Roughly, from 1 to 8 ft is the brine section; and from 9 ft is the CO_2 section. The distance between stations is 6 in. The same borehole fluid effect is observed as in the stationary measurements. However, although we see a large brine/gas contrast, no real difference between the measurements at different values of CO_2 pressure appears. For instance, with CO_2 pressures respectively of 400 psi and 800 psi, have SFFA in the same range of values. This is in agreement with the expected change in sigma shown in Table 1. A variation of the CO_2 concentration from 0.001 to 1.032 g/cm^3 produces a very small change in sigma from 3.186 to 3.203 c.u. and thus no significant conclusion can be drawn. Such small variations in the field might be due solely to trace elements in the formation.

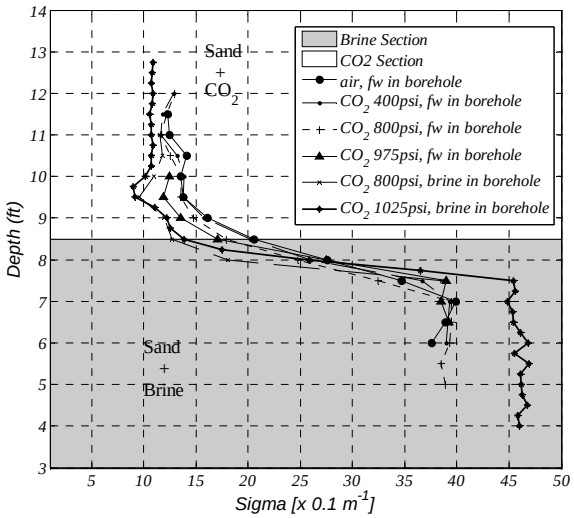

Figure 10. Logging Sigma Formation Far Apparent (SFFA).

Figure 11 displays the inelastic ratio (IRAT) and Figure 12 the near/far capture ratio (TRAT). The understanding of these results requires more modeling and/or experiments. The departure to the left at the transition between brine and CO_2 reflects the effect of carbonation and/or chlorine.

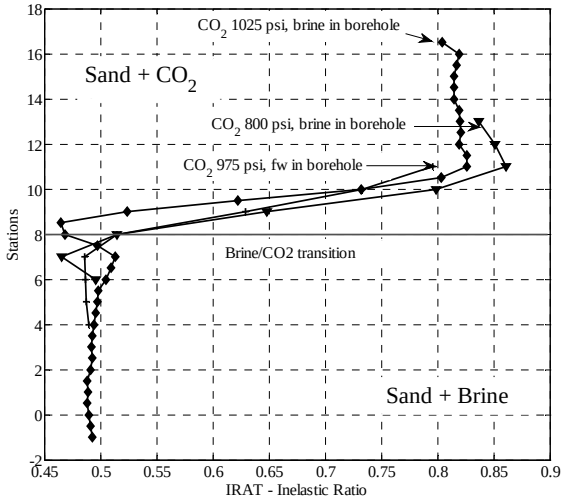

Figure 11. Logging Inelastic Ratio (IRAT).

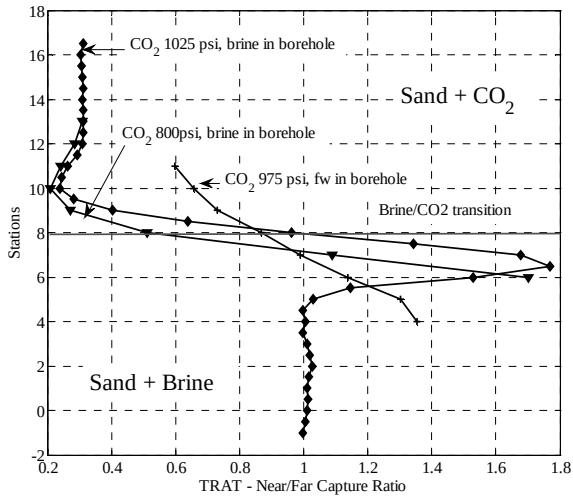

Figure 12. Logging Near/Far Capture Ratio (TRAT).

RST Measurements in Inelastic-Capture Mode

The Inelastic-Capture mode measurements are:

- The far inelastic spectra A - FSPA (inelastic-capture spectra acquired during the neutron burst)
- The inelastic carbon yield
- The inelastic oxygen yield
- The Near/Far Net Inelastic Count Rate Ratio - NICR
- The Far Carbon/Oxygen Ratio - FCOR

As with the Sigma mode measurements, the Inelastic-Capture mode measurements have been taken in two different situations. The first situation is made up of one hour stationary measurements. Most of them are taken in the CO_2 section (referred as "white marker"). Some measurements are taken in the brine section (referred as "blue marker") to acquire a baseline. The second type of measurement is logging between the brine section and the CO_2 section stopping the tool for a 5-minute log every 6 inches between the brine and the CO_2 marker. These measurements are meant to display the contrast at the transition between the two sections.

Inelastic-Capture mode stationary logs

The RST Far Inelastic Standard Spectra are displayed for reference in Figure 13. Note the carbon triple peaks (full energy, first and second escape) between channel 105 and channel 142 and the signature of the oxygen triple peaks between channel 151 and channel 194.

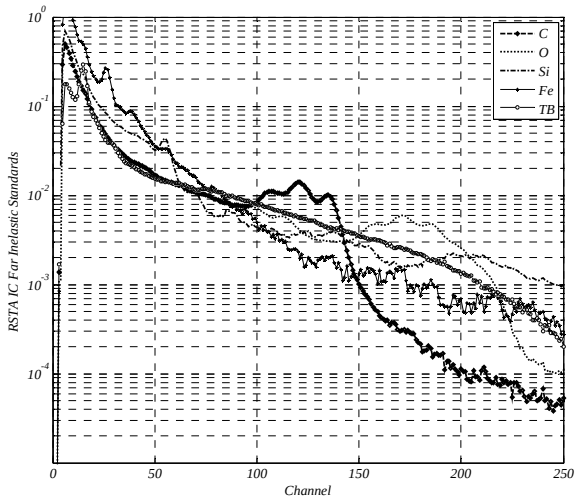

Figure 13. RST Far Inelastic Standard Spectra A (FSPA).

The Far Inelastic Spectra measured are displayed in Figure 14.

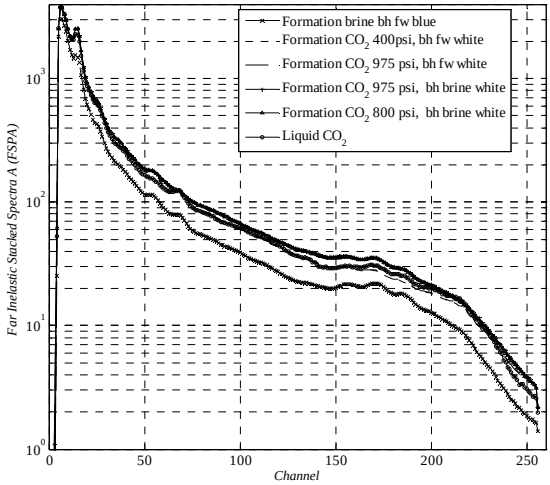

Figure 14. Far Inelastic Spectra A (FSPA).

The Near/Far Net Inelastic Count Rate Ratio (NICR), the Far Carbon/Oxygen Ratio (FCOR) and the carbon and oxygen yields values corresponding to the previous measurements are summarized in Table 3. In the case where RST is surrounded with liquid CO_2 the carbon yield mean value is 0.029. The carbon/oxygen ratio (FCOR) and the carbon yield indicate the presence of carbon in the formation when the CO_2 pressure increases. Although the values are very small, carbon is detected.

Table 3. Inelastic-Capture Mode Near/Far Inelastic Count Rate Ratio (NICR), Far Carbon/Oxygen Ratio (FCOR), Carbon and Oxygen Far Inelastic Yields.

	NICR	FCOR	Carbon Far Yield	Oxygen Far Yield
brine section, fresh water in borehole	2.17	-0.0154	-0.0050	0.35
CO_2 400psi, fresh water in borehole	1.32	-0.0145	-0.0026	0.20
CO_2 975psi, fresh water in borehole	1.34	-0.0055	-0.0008	0.19
CO_2 975psi, brine in borehole	1.39	0.0069	0.0018	0.18
CO_2 800psi, brine in borehole	1.38	0.0076	0.0018	0.19
CO_2 liquid	1.43	0.0970	0.0290	0.30

FCOR, the carbon and oxygen yields are also displayed in Figure 15. The oxygen yield is higher in brine than in CO_2 gas and then increases again when liquid CO_2 is present.

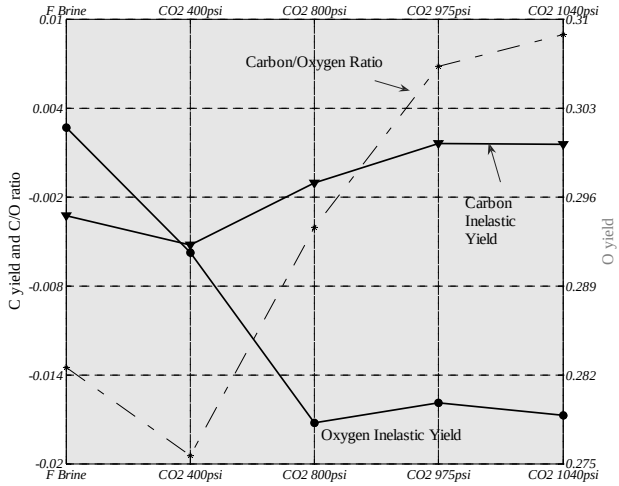

Figure 15. Far Carbon/Oxygen Ratio (FCOR), Carbon Far Inelastic Yield and Oxygen Inelastic Yield.

Although the values are still very small, an increase in carbon is observable here. If the carbon present is due exclusively to CO_2, then it might be possible to detect it with protracted stationary measurement.

Inelastic-Capture mode logging up from the brine section to the CO_2 section

The Near/Far Net Inelastic Count Rate Ratio (NICR) when logging up from the brine to the CO_2 section is displayed in Figure 16. The values are in agreement with the values measured with the tool stationary. Usual NICR field values are 2 for liquid in the formation. Typical downhole hydrocarbon gas densities range from 0.2 to 0.3 g/cm^3 corresponding to HI of 0.135 to 0.203 for CH_4 and 0.0772 to 0.116 for CH_2 (see Figure 6). The corresponding NIRC for hydrocarbon gas in the formation is 1.4. If we were in the presence of hydrocarbon instead of CO_2, the values in the CO_2 section would be representative of a hydrocarbon gas. However, we saw evidence that liquid

CO_2 was present in the tank. First, the pressure behavior during the tank filling: a steady increase and then a slower increase in pressure indicating liquid formation. Then, during the venting out of the tank of the CO_2, liquid came out. The tank was probably not filled with a 100% liquid CO_2 but liquid CO_2 was present in the bottom CO_2 section where the measurements were carried out.

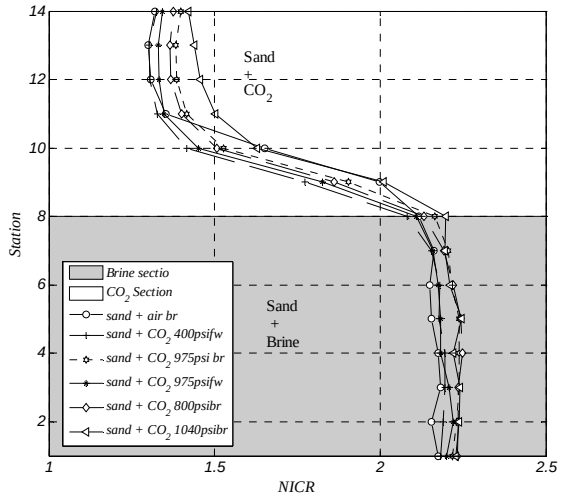

Figure 16. Logging Near/Far Net Inelastic Count Rate Ratio (NICR).
Note: Stations 1 to 8 are in the brine section; stations 9 to 17 are in the CO_2 section.

The carbon yields displayed in Figure 17 show an increase of carbon content when the CO_2 pressure increases.

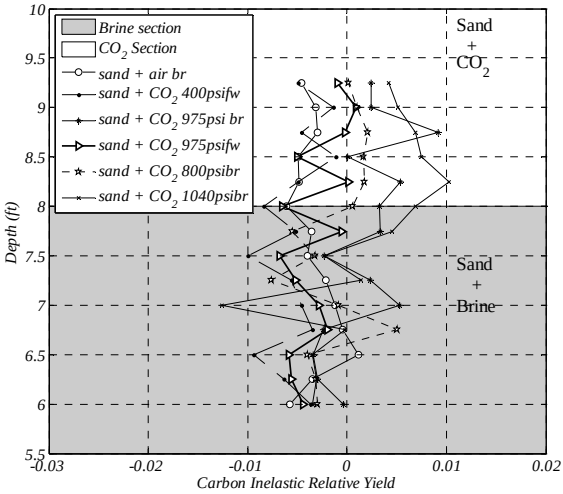

Figure 17. Logging Carbon Far Inelastic Yield.
Note: Stations 1 to 8 are in the brine section; stations 9 to 17 are in the CO_2 section.

The oxygen yield decreases in Figure 18 due to the lower density of CO_2 in the formation compared to brine.

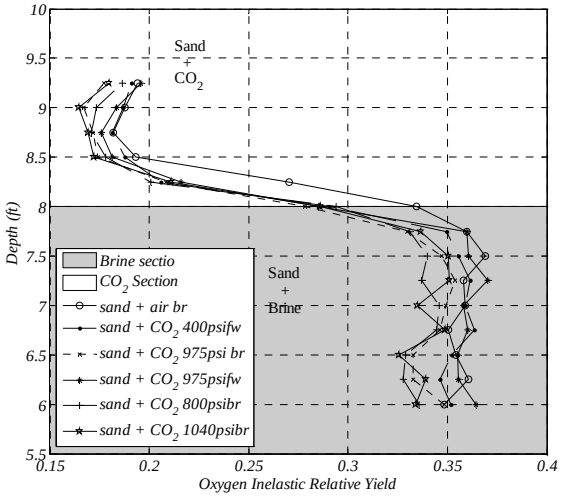

Figure 18. Logging Oxygen Far Inelastic Yield.
Note: Stations 1 to 8 are in the brine section; stations 9 to 17 are in the CO_2 section.

These trends are confirmed by the Far Carbon/Oxygen ratio (FCOR, Figure 19). The carbon from CO_2 is detected by RST. However, it clearly appears only at CO_2 pressures greater than 975 psi.

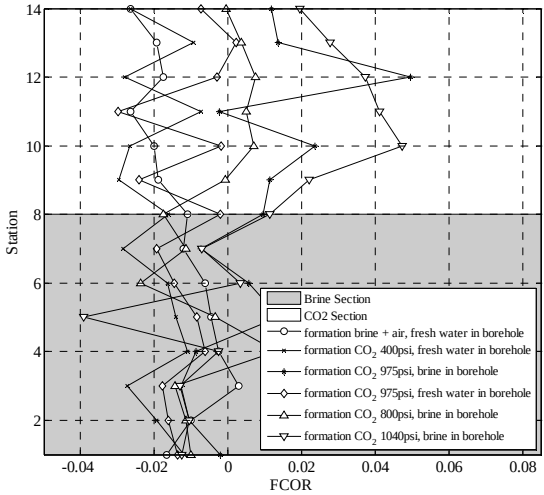

Figure 19. Logging Far Carbon/Oxygen Ratio (FCOR).
Note: Stations 1 to 8 are in the brine section; stations 9 to 17 are in the CO_2 section.

In these experiments, the sequence of 5 minute IC stations spaced 6 inches apart is equivalent to continuous logging at a speed of 6 ft/hr. Typical IC logging speeds are in the range of 50 – 100 ft/hr. At these speeds the statistical uncertainty that would exist in the logs would make it impossible to identify any changes in carbon yield.

FUTURE WORK

These experiments have focused on detecting CO_2 in brine-saturated reservoirs. The study may be expanded to other types of reservoirs or to other types of measurements. Here is a non exhaustive list of the future work that could be accomplished in the frame of the CO_2 Capture project:

- RST response at oil/CO_2 contacts, fresh-water/CO_2 contacts and brine/CO_2 contacts with different NaCl concentrations;
- Sigma 5-min station logs to better characterize response at the boundary; we can get a good idea of some of these from the sigma characterization database;
- Sigma sand measurement from external laboratory;
- RST response to CO_2 in a supercritical fluid state;
- Modeling to simulate RST response to CO_2 in environments difficult to study in the laboratory;

Because RST has a neutron generator source and gamma-ray detectors, its response is both density and neutron like. Logs in the CO_2 section should be correlated with a density tool and a porosity tool. The measure of density through casing remains difficult with gamma-rays only, a measurement of Ecoscope type would be interesting to compare with the RST measurements.

Finally, RST is a tool for oil and gas applications. Its application to CO_2 detection requires work on the interpretation side especially because of the similarity of response in partially CO_2 saturated water reservoirs and saturated methane reservoirs. These similarities imply careful baseline measurements in real life CO_2 capture situations where RST can be used to locate potential reservoirs, monitor the injection and finally check for CO_2 leaks.

CONCLUSIONS

For the brine-CO_2 systems studied in this work, the RST Sigma measurement provides the best means of detecting CO_2 present in brine-saturated formations. The large contrast in the capture cross-section between formations with brine and formations with CO_2 gives us a reliable way to locate CO_2.

For lower salinity fluid, fresh water or oil in the formation, the contrast between zones with and without CO_2 decreases substantially. In this case, formation sigma may not be adequate. The use of count rate ratios provides the contrast necessary to detect CO_2. However, the use of count rate ratios as indicators in a monitoring program will require base passes without CO_2 in the system as a reference point.

The RST Inelastic-Capture measurements also have the potential for locating CO_2. The carbon yield will increase when CO_2 is present in the formation. Except in protracted stationary logging situations, the statistical uncertainty in the inelastic measurements is too large for the small yield increase to be detectable.

ACKNOWLEDGEMENTS

The author would like to thank Frank Morris (Schlumberger contractor), Mike Evans (Advisor, Schlumberger Sugar Land Product Center), Chris Stoller (Advisor, Schlumberger Princeton Technical Center) and Tim Quinlan (Senior, Kuala Lumpur, Malaysia) for their help in preparing this article. This work was funded by the CO_2 Capture Project Phase 2 (CCP2).

REFERENCES

1. Sakurai, S., T.S. Ramakrishnan, A. Boyd, N. Mueller and S. Hovorka (2005) Monitoring Saturation Changes for CO_2 Sequestration; Petrophysical Support of the Frio Brine Pilot Experiment SPWLA 46th Annual Logging Symposium held in New Orleans, Louisiana, United States, June 26-29, 2005.
2. Bennaceur, K., N. Gupta, M. Monea, T.S. Ramakrishnan, T. Randen, S. Sakurai and S. Whittaker (2004) CO_2 Capture and Storage-A Solution Within Oilfield Review 16, no. 3 (Autumn 2004): 44–61.
3. Plasek, R.E., R.A Adolph, C. Stoller, D.J Willis, and E.E Bordon: Improved Pulsed Neutron Capture Logging With Slim Carbon-Oxygen Tools: Methodology SPE 30598.
4. Stoller, C., H.D Scott, R.E Plasek, A.J Lucas, and R.A Adolph. Field Tests of a Slim Carbon/Oxygen Tool for Reservoir Saturation Monitoring SPE 25375.

Carbon Dioxide Capture for Storage in Deep Geologic Formations, Volume 3
L.I. Eide (Ed.)

Chapter 24

A NEW REACTIVE TRANSPORT RESERVOIR SIMULATOR FOR AQUIFER STORAGE OF CO_2 - WITH IMPLICIT GEOMECHANICAL ANALYSIS

Bjørn Kvamme and Shunping Liu
University of Bergen, Allégt. 55, N-5007 Bergen, Norway

ABSTRACT: The motivation for the work reported here have been to develop a CO_2 storage simulator which is able to address geochemical and geomechanical reservoir stability concerns within one ***implicit*** software package. This paper presents a rewritten and extended version of RetrasoCodeBright (RCB) for simulations of CO_2 storage in saline aquifers. The code has been rewritten to account for non-ideal gas through corrections of gas density and gas solubility in all transport terms. Newton-Raphson method used to solve the flow and mechanics in RCB has been improved so as to improve convergence even under high gas injection pressures. Two 2D hydro-chemical-mechanical problems are used to illustrate the modified RCB code. The purpose of the first test case has been to demonstrate implications of geochemical buffering in systems containing very high portions of rapidly dissolving calcite. The second test case gives examples of fracture descriptions using the classical approach of defining a fracture through extremely high permeability. While this is being used in the example the code also have another option of defining a fracture through a hydrodynamic description. This feature is briefly discussed but is yet at an evaluation stage. The reactive transport parts are at a state of the art level since it is based on the most acknowledged data bases for fundamental thermodynamic properties. This also includes a comprehensive library of reaction constants for different mineral reactions as well as a visual interface for incorporation of new parameters for specific reactions. In the present version the Soave Redlich Kwong (SRK) equation of state has been applied for compressibility factors and fugacity coefficients but can easily be replaced with more accurate equations of state for CO_2. Finally some future extension plans are discussed.

INTRODUCTION

The objective of this project has been to develop a new reservoir simulator for theoretical evaluation of CO_2 storage scenarios which also contains geomechanical analysis. From an operator's point of view two specific needs could be brought forward as examples of specific needs for geomechanics. The first is the need for evaluation of the geomechanical stability of a given geological formation for CO_2 storage, given the needed overpressure for desired rates. While the overpressure is at its largest close to the injection the geomechanical stability throughout the reservoir depends on the geology (and corresponding local tensile strength) as well as local stresses and pressures. Evaluation of possible fracturing and corresponding creation leakage paths in all parts of the reservoir will be important. A second class of examples are situations of promising storage reservoirs with low permeability. A common approach to increase injectivity in these types of reservoirs is local hydraulic fracturing in the vicinity of the injection point(s). In this case an analysis of the geomechanical stability of the whole formation after the fracturing will be needed in order to evaluate the risk of undesired fracturing, and corresponding creation of leakage paths, in other parts of the formation. Geomechanical stability is also a part of the overall storage integrity.

Documentation of storage stability for several years ahead is likely to be required from governmental institutions and other licensing institutions involved in the process of giving the necessary permissions for injection projects. Long term effects of geochemical reactions on the geomechanical stability of a given reservoir depend on the specific mineral compositions and mineral distributions. Carbonates calcite and magnesite will dissolve rapidly in low pH environment (which can be caused by dissolved and partly dissociated CO_2). On the other hand, released carbonate ions from the dissolution, will buffer the system and contribute to an increase in pH. In some composite minerals these rapidly dissolving minerals may even act as a "glue" and dissolution of these minerals may release other mineral particles. The complexity in the balance between erosion (and also potential particle release) and buffering in the reservoir close to the injection zone makes it desirable to have an *implicit coupling* between the reactive flow and the corresponding consequences on geomechanical stability of the reservoir. Dissolved ions will precipitate in zones of higher pH and this will also changes flow patterns and local pressure gradients, which also makes it necessary to verify the local geomechanical stability.

A limited number of reactive transport models for theoretical studies of CO_2 storage scenarios are available worldwide. An intercomparison study of some of these simulators is reported by Pruess et.al [1]. An even smaller number of these reactive transport simulators have a built-in table of finite elements which can be used to export estimated properties for subsequent explicit geomechanical analysis using external couplings to geomechanical codes like for instance FLAC. Lawrence Berkeley National Laboratory (LBNL) activities are examples of this type of approach [2, 3], in which the TOUGH simulator is coupled with the FLAC software for the geomechanics. The primary drawback of an explicit scheme is that the changes in properties of the soil are not directly updated in an implicit way, and as such may not reflect the correct dynamics of geomechanical processes. For this reason it was decided to choose a different software platform in this project.

In the work reported here code RCB (RetrasoCodeBright) has been chosen as the software platform. RCB is the result of coupling two codes: CodeBright and Retraso. CodeBright (COupled DEformation of BRIne Gas and Heat Transport) was designed for the thermo-hydraulic-mechanical analysis of three-dimensional multiphase saline media [4 - 6]. In other words, CODE-BRIGHT permits the modeling of deformation, mechanical processes and heat transport in multiphase. Retraso (REactive TRAnsport of SOlutes) is a code for solving reactive transport problems [7, 8]. The design of implicit coupling between Retraso and CodeBright makes the code RCB perfect for CO_2 injection calculations. The limitations of the original RCB is that it was written for ideal gas and all terms containing densities of gas needed to be corrected over to realistic fluid properties using the SoaveRedlichKwong (SRK) equation of state [9]. Dissolution of CO_2 into the aqueous phase also needed to be upgraded through implementation of fugacity coefficient from the equation of state.

In an implicit solution of the geomechanics and the governing equations for fluid flow the total stress as well as the pore water pressure will be available in all directions in all nodes for each time step in the integration. Breakdown conditions can therefore be analyzed directly using the criteria that the Terzaghi effective stress (total stress minus pore water pressure) equals the tensile strength at breakdown condition. As for hydraulic fractioning the main criteria would be to ensure that the pressure in the wellbore is less than the minimum horizontal stress for the caprock(s) sealing the storage.

The extension of a hydro-geological simulator from ideal gas assumption into a high pressure CO_2 storage simulator appeared to be far more challenging than just implementing corrections for densities and gas solubility. Numerical algorithms have been extensively rewritten in order to increase the convergence qualities of the code.

Note: Fractures will be treated as thin elements of constant thickness but varying permeability which should reflect varying real fracture size. A brief example is included as test case number 2 below. An alternative method involves the definition of fracture through a 1D element (line) in a 2D model or a 2D element in a 3D structure. This fracture is then denoted a transmissibility representative for the expected impact of the specific fracture. This option is yet being evaluated and is expected to appear in a subsequent publication.

Also note that shale will have different geomechanical characteristics than the rest of the reservoir but variation of this is not included. Geomechanical parameters for shale will be fixed according to best available values from literature.

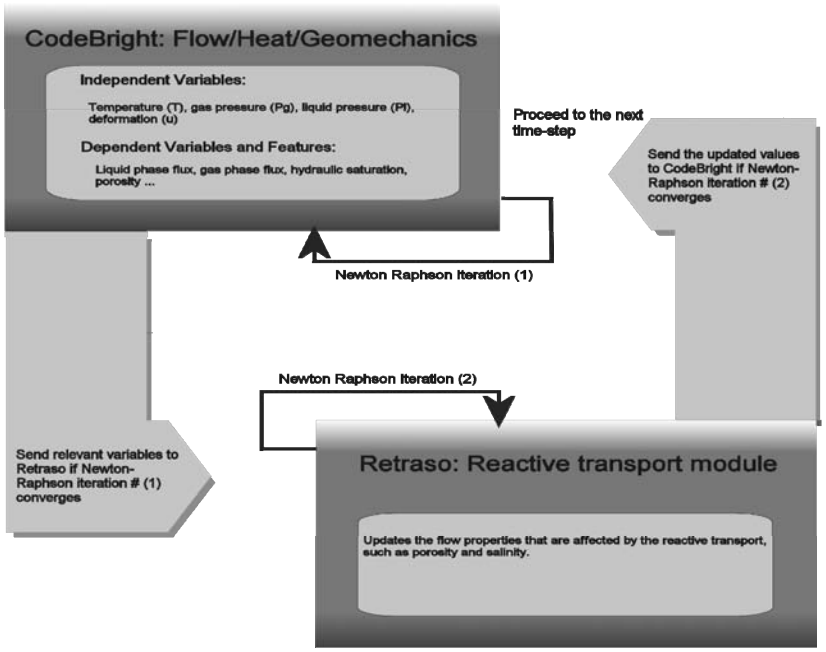

Figure 1. RCB solves the integrated equations sequentially in one time step.

THE NUMERICAL TOOL RCB

As briefly mentioned in the introduction the software consists of two coupled modules, CodeBright and Retraso. Briefly described the coupling between the two parts is as follows: In one time step, which is pre-described by user, CodeBright module first calculates the mass flow, heat transport and geomechanical deformation. All these properties, well as physical properties and state conditions like liquid pressures (Pl), gas pressures (Pg), temperatures (T) and deformations (u), flux of liquid, flux of gas, hydraulic saturation are transported to Retraso part. The initial integration time step defined in CodeBright is divided into a smaller subdivision for integration over the fluxes of individual molecules and ions, taking into account possible reactions between fluids and solid in either equilibrium approximation or reaction kinetic formulation [10]. Porosity is updated according to mineral erosion or mineral precipitation and permeability is updated according to commonly used correlations [11]. All detailed results from the individual fluxes and phase properties are then transferred back to the CodeBright module for next time step. Both CodeBright module and Retraso

module adopt Newton-Raphson iteration method to solve the linear algebraic systems of governing equations. Since extensive modifications of the original code have been implemented through this project we describe the current algorithms in sufficient details in a separate section below for reference. The coupling between the two modules is also schematically illustrated in Figure 1 below.

GOVERNING EQUATIONS AND SOLUTION ALGORITHMS IN CODEBRIGHT MODULE

The governing equations for non-isothermal multiphase flow of water and gas through porous deformable saline media have been presented by Olivella et al. [4]. These equations can be categorized into four main groups, which are balance equations, constitutive equations, equilibrium relationships and definition constraints.

Equations for mass balance were established following the compositional approach. That is, mass balance is performed for water, air and salt species instead of using solid, liquid and gas phases. Equation for balance of energy is established for the medium as a whole. The equation of momentum balance for the porous medium is reduced to that of stress equilibrium.

Mass balance of solid

$$\frac{\partial}{\partial t}(\theta_s(1-\phi)) + \nabla\bullet(j_s) = 0 \qquad \text{Equation 1}$$

where θ_s is the mass of solid per unit volume of solid, j_s is the flux of solid and ϕ is porosity. From this equation, an expression for porosity variation is obtained as:

$$\frac{D_s\phi}{Dt} = \frac{1}{\theta_s}[(1-\phi)\frac{D_s\theta_s}{Dt}] + (1-\phi)\nabla\bullet\frac{du}{dt} \qquad \text{Equation 2}$$

where u is solid displacements.

Mass balance of water

$$\frac{\partial}{\partial t}(\theta_l^w S_l\phi + \theta_g^w S_g\phi) + \nabla\bullet(j_l^w + j_g^w) = f^w \qquad \text{Equation 3}$$

where θ_l^w and θ_g^w are respectively water in liquid and gas phase, *Sl*, *Sg* is degree of saturation of liquid and gaseous phases i.e., fraction of pore volume occupied by each phase, f^w is the external supply of water.

Mass balance of gas

$$\phi\frac{D_s(\theta_l^a S_l + \theta_g^a S_g)}{Dt} + (\theta_l^a S_l + \theta_g^a S_g)\frac{D_s\phi}{Dt} + ((\theta_l^a S_l + \theta_g^a S_g)\phi)\nabla\bullet\frac{du}{dt} + \nabla\bullet(j_l^{'a} + j_g^{'a}) = f^a \qquad \text{Equation 4}$$

where θ_l^a and θ_g^a are respectively mass of air in liquid phase and gaseous phase, $j_l^{'a}$ and $j_g^{'a}$ are total mass flux of air in liquid phase and gaseous phase relative to the solid phase, and f^a is air supply.

Momentum balance of the medium

The momentum balance reduces to the equilibrium of stresses if the inertial terms are neglected:

$$\nabla \bullet \sigma + b = 0 \qquad \text{Equation 5}$$

where σ is stress tensor and b is the vector of body force.

Internal energy balance of the medium

The equation for internal energy balance for the porous medium is established taking into account the internal energy in each phase (*Es, El, Eg*):

$$\frac{\partial}{\partial t}(E_s \rho_s (1-\phi) + E_l \rho_l S_l \phi + E_g \rho_g S_g \phi) + \nabla \bullet (i_c + j_{Es} + j_{El} + j_{Eg}) = f^Q \qquad \text{Equation 6}$$

where i_c is energy flux due to conduction through the porous medium, the other fluxes (j_{Es}, j_{El}, j_{Eg}) are advective fluxes of energy caused by mass motions and f^Q is an internal/external energy supply. In this case this term accounts, for instance, energy dissipation due to medium deformation which is not explicit because it is negligible in most cases. The use of the material derivative allows obtaining an equation formally similar to the mass balance of water. The reason for the similarity is that both water and internal energy are considered present in the three phases.

CONSTITUTIVE EQUATIONS AND EQUILIBRIUM RESTRICTIONS

Associated with this formulation there is a set of necessary constitutive and equilibrium laws. Table 1 is a summary of the constitutive laws and equilibrium restrictions that should be incorporated in the general formulation. The dependent variables that are computed using each of the laws are also included. Here we need to explain some of the most important constitutive and equilibrium laws.

Generalized Darcy's law is used to compute the advective flux, q, of the α phase ($\alpha = l$ for liquid, $\alpha = g$ for gas). It is expressed as:

$$q_\alpha = -\frac{\mathrm{k}k_{r\alpha}}{\mu_\alpha}(\nabla P_\alpha - \rho_\alpha g) \qquad \text{Equation 7}$$

where k is the tensor of intrinsic permeability (m^2), $k_{r\alpha}$ is the relative permeability of the phase, μ_α is the phase's dynamic viscosity (Pa s) and g is the gravity vector(ms^{-2}). Her we need to point

out that the dynamic viscosity μ_α highly depends on temperature (T) and the relative permeability ($k_{r\alpha}$).

Table 1. List of constitutive equations and equilibrium restrictions in CodeBright.

Constitutive equations	**Variable name**	**variable**
Darcy's law	Liquid and gas advective flux	q_l, q_g
Fick's law	Vapor and gas non-advective flux	i_g^w, i_l^a
Fourier's law	Conductive heat flux	i_c
Retention curve	Liquid phase degree of saturation	S_l, S_g
Mechanical constitutive model	Stress tensor	σ
Phase density	Liquid density	ρ_l
Gas law	Gas density	ρ_g
Equilibrium restrictions	**Variable name**	**variable**
Henry's law	Mass fraction gas dissolved	ω_l^h
Psychometric law	Vapor mass fraction	ω_g^w

The Van Genuchten's [12] retention curves expressing saturation as a function of liquid or gas pressure is used. It is:

$$S_l = (1 + (\frac{P_g - P_l}{P_0})^{\frac{1}{1-n}})^{-n} \text{ where } S_g = 1 - S_l \qquad \text{Equation 8}$$

where P_0 and n are scale pressure and shape parameters. The relative permeability $k_{r\alpha}$ depends on saturation (S_l) which in its turn depends on P_l and P_g.

The relative permeability ($k_{r\alpha}$) in eq. (7) is a function of the saturation. In various expressions, the Van Genuchten is the most widely used, which is:

$$k_{rl} = \sqrt{S_l}(1 - (1 - S_l^{1/n})^n)^2 \qquad \text{Equation 9}$$

Where n is still the shape parameter, but it does not necessarily have the same value.

The independent variables

The governing equations for non-isothermal multiphase flow of liquid and gas through porous deformable saline media have been established. Variables and corresponding equations are tabulated as in Table 2.

Table 2. Equations and independent variables.

Equation	Variable name	Variable
Equilibrium of stresses	Displacements	u
Balance of liquid mass	Liquid pressure	Pl
Balance of gas mass	Gas pressure	Pg
Balance of internal energy	Temperature	T

After the spatial discretization of the partial differential equations, the residuals that are obtained can be written (for one finite element) as:

$$\begin{pmatrix} r_u \\ r_{Pl} \\ r_{Pg} \\ r_T \end{pmatrix} = \frac{d}{dt}\begin{pmatrix} d_u \\ d_{Pl} \\ d_{Pg} \\ d_T \end{pmatrix} + \begin{pmatrix} a_u \\ a_{Pl} \\ a_{Pg} \\ a_T \end{pmatrix} + \begin{pmatrix} b_u \\ b_{Pl} \\ b_{Pg} \\ b_T \end{pmatrix} = \begin{pmatrix} 0 \\ 0 \\ 0 \\ 0 \end{pmatrix} \qquad \text{Equation 10}$$

where **r** are the residuals, *d***d**/*dt* are the storage or accumulation terms, **a** are the conductance terms, and **b** are the sink/source terms and boundary conditions. After time discretization a more compact form can read as:

$$r\left(X^{k+1}\right) = \frac{d^{k+1} - d^{k}}{\Delta t^{k}} + A\left(X^{k+\varepsilon}\right)X^{k+\theta} + b\left(X^{k+\theta}\right) = 0 \qquad \text{Equation 11}$$

where *k* is the time step index, : $\mathbf{X}=[(ux,uy,uz,Pl,Pg,T)_{(1)}, ..., (ux,uy,uz,Pl,Pg,T)_{(n)}]$, is the vector of unknowns (i.e. a maximum of seven degrees of freedom per node), **A** represents the conductance matrix. The Newton-Raphson scheme of solution for this non-linear system of AE's is:

$$\frac{\partial r\left(X^{k+1}\right)}{\partial X^{k+1}}\left(X^{k+1,l+1} - X^{k+1,l}\right) = -R\left(X^{k+1,l}\right) \qquad \text{Equation 12}$$

where *l* indicates iteration. In the present approach, the standard Galerkin method is used with some variations in order to facilitate computations.

The mathematical equations for the system are highly non-linear and they will be solved numerically. The numerical approach can be viewed as divided into two parts: spatial and temporal discretizations. Finite element method is used for the spatial discretization while finite differences are used for the temporal discretization. The discretization in time is linear and the implicit scheme uses two intermediate points, $t^{k+\varepsilon}$ and $t^{k+\theta}$ between the initial t^{k} and final t^{k+1} times. The Newton-Raphson method is adopted to find an iterative scheme. This scheme has been modified through the introduction of a relaxation factor approach according to the algorithms of Nakata and Fujiwara [13 - 16], in which we obtain the proper relaxation factors by combining the general tendency method [13 - 16] and time step reduction method.

Time subdivision in CodeBright

Both code CodeBright and code Retraso adapt Newton-Raphson iteration method to solve the highly non-linear equations. Nevertheless the method to subdivide the time in one time step in code CodeBright and code Retraso is different.

Time adaption in CodeBright is performed as a function of several convergence criteria. If we consider the iteration at time t, and time $t+1$, the time interval is dt. So we have $dt_{next} = dt_{updated} * factor_{next}$, where dt_{next} is the next time interval, $dt_{updated}$ is the adjusted dt according to the value of residuals at time $t+1$, and $factor_{next}$ is the predicted next time factor which is bigger than 0. $factor_{next}$ should be reasonable which means that $factor_{next}$ lies always between 1.4 and 0.1 which are empiric numbers.

$factor_{next}$ is predicted from the relative error in variables of the previous time increment. If the relative error is less than a prescribed value, time increment is reduced according to error deviation. There are different ways to calculate the relative error. From a lot of testing CodeBright uses an equation to get it, which can be written as $factor_{next} = dtol / r_{relative}$, where $dtol$ is a small number, like 0.001, and $r_{relative}$ is the norm of relative residual.

For each independent variable, four parameters as error tolerance present the convergence criteria. They are maximum absolute error ($delmx$), maximum relative error (fac), maximum mass balance error ($delqmx$) and maximum correction per iteration (dmx). The four parameters combined together on the best effective way will decide the $dt_{updated}$. If the residual at time $t+1$ is big enough, $dt_{updated}$ will be reduced, otherwise, if the residual at time $t+1$ is small enough, $dt_{updated}$ will be increased.

Boundary conditions

In CO_2 injection scenario, the injecting pressure is relatively high. If such high pressure is directly used as boundary condition, it causes the pressure of some elements and nodes in model to be too high to make the Newton iteration trend to convergence. From this consideration, a lower pressure is always put initially as boundary condition, and then the code will take a pressure ramp loading in one or more time intervals to get the supposed injecting pressure. In the example that will be explained later, we will demonstrate the usage of the function of pressure ramp loading. Here we focus on the boundary condition equations.

In CodeBright which is in charge of thermo-hydraulic calculations P_l, P_g and T are always used as boundary conditions, plus some prescribed parameters which given by user are the specific requirements from the user for the thermo-hydraulic system. Boundary conditions and expressions for the source/sink terms (f^w, f^a and f^Q in Equations 3, 4 and 6, respectively) have to be written for mass balance equation for water, air and heat. CodeBright expresses nodal flow rates for every component (water, air and heat) and every phase (liquid, gas) as function of the state variables (P_l, P_g and T) and some prescribed values, specified by the user.

The mass flow rate of water as a component of the gas phase and liquid phase are:

$$j_g^w = (\omega_g^w)^0 (j_g^0 + \Delta j_g^0 \frac{dt}{\Delta t}) + (\omega_g^w)^0 \gamma_g ((P_g^0 + \Delta P_g^0 \frac{dt}{\Delta t}) - P_g) + \beta_g ((\rho_g \omega_g^w)^0 - (\rho_g \omega_g^w))$$

Equation 13

$$j_l^w = (\omega_l^w)^0 \left(j_l^0 + \Delta j_l^0 \frac{dt}{\Delta t} \right) \qquad \text{Equation 14}$$
$$+ (\omega_l^w)^0 \gamma_l \left(\left(P_l^0 + \Delta P_l^0 \frac{dt}{\Delta t} \right) - P_l \right) + \beta_l \left((\rho_l \omega_l^w)^0 - (\rho_l \omega_l^w) \right)$$

where the superscript $()^0$ stands for the prescribed values and the terms $\Delta(.)$ $dt/\Delta t$ allow for imposing a linear variation of the variable (.) during the time step. This general form of boundary condition includes three terms. The first one is the mass inflow or outflow that takes place when a flow rate of gas (j_g^0) or liquid (j_l^0) is prescribed. The second term is the mass inflow or outflow that takes place when gas phase pressure (P_g^0) or liquid phase pressure (P_l^0) is prescribed at a node. The coefficients γ_g or γ_l are leakage coefficients, i.e., parameters that allows a boundary condition of the Cauchy type. The third term is the mass inflow or outflow that takes place when vapour or water in liquid phase mass fraction is prescribed at the boundary. This term naturally comes from the nonadvective flux (Fick's law). Mass fraction and density prescribed values are only required when inflow takes place. For outflow the values in the medium are considered. The fluxes of different phase of a component are summed (Equation 13 + Equation 14) to obtain the total boundary condition of water, which is:

$$j^w = j_g^w + j_l^w \qquad \text{Equation 15}$$

Similarly, the mass flow rate of air as a component of the gas phase and liquid phase are:

$$j_g^a = (\omega_g^a)^0 \left(j_g^0 + \Delta j_g^0 \frac{dt}{\Delta t} \right) \qquad \text{Equation 16}$$
$$+ (\omega_g^a)^0 \gamma_g \left(\left(P_g^0 + \Delta P_g^0 \frac{dt}{\Delta t} \right) - P_g \right) + \beta_g \left((\rho_g \omega_g^a)^0 - (\rho_g \omega_g^a) \right)$$

$$j_g^a = (\omega_g^a)^0 \left(j_g^0 + \Delta j_g^0 \frac{dt}{\Delta t} \right) \qquad \text{Equation 17}$$
$$+ (\omega_g^a)^0 \gamma_g \left(\left(P_g^0 + \Delta P_g^0 \frac{dt}{\Delta t} \right) - P_g \right) + \beta_g \left((\rho_g \omega_g^a)^0 - (\rho_g \omega_g^a) \right)$$

The total boundary condition of air is:

$$j^a = j_g^a + j_l^a \qquad \text{Equation 18}$$

For the energy balance equation, the boundary condition has a similar form

$$j_e = \left(j_e^0 + \Delta j_e^0 \frac{dt}{\Delta t} \right) + \gamma_e \left(T^0 + \Delta T^0 \frac{dt}{\Delta t} - T \right) \qquad \text{Equation 19}$$
$$+ E_g^w \left(j_g^w \right) + E_l^w \left(j_l^w \right) + E_g^a \left(j_g^a \right) + E_l^a \left(j_l^a \right)$$

REACTIVE TRANSPORT IN RETRASO PART

The Retraso part of the code has a built in state of the art geochemical solver and in addition capabilities of treating aqueous complexation (including redox reactions), adsorption, precipitation-

dissolution of minerals and gas dissolution. Precipitation-dissolution and aqueous complexation can be modelled in equilibrium or according to kinetic laws [8].

In the current version we have extended the code from ideal gas to realistic fluid description using an equation of state. Calculations of densities and fugacity coefficients can either be handled through an interface which calls an equation of state, or through interpolation in tabulated values for pure CO_2. In all examples illustrated in this paper the SRK equation of state have been used [9]. More accurate equations of state for pure CO_2, like for instance the equation of Span & Wagner [17], are available although the simple equations of state may offer the advantage of being able to treat gas mixtures more conveniently. This equation of state is used for density calculations as well as the necessary calculations of fugacity for the CO_2 phase as needed in the calculation of dissolution of CO_2 into the groundwater. See also Hellevang & Kvamme [18] for more details. The dissolution and precipitation of minerals in CO_2 injection scenarios are slow natural processes, where the kinetic law [10] is applied in RCB. The mathematical equations for the system are highly non-linear and are solved numerically [7, 8].

Aqueous species and stoichiometric coefficients in Retraso

Components of a system are chemical entities independent from each other that completely describe the system. In Retraso, a set of aqueous species namely the primary species is used to represent the system. From a mathematical point of view, defining a set component amounts means to define a vector space of chemical species. In a system made up of N_s chemical species, any of the N_R reactions taking place can be presented as a linear combination such as

$$\sum_{j=1}^{N_s} v_{ij} Q_j = 0 \qquad i = 1, ..., N_R \qquad \text{Equation 20}$$

where Q_j is the chemical formula of the j-th species, and v_{ij} is its stoichiometric coefficient in reaction i. If the reactions are independent, the stoichiometric coefficient matrix S contains a non-singular square $N_R \times N_R$ sub-matrix and S has the range of N_R. We note as:

$$S = (S_1 \mid S_2) \qquad \text{Equation 21}$$

where S_2 is the square matrix of size N_R and S_1 is a rectangular $N_R \times (N_S - N_R)$ sub-matrix. This equation reflects that the chemical reactions in equation (20) can be rewritten so that a subset of N_R species can be expressed as linear combinations of the remaining $(N_S - N_R)$ species, namely the primary species. These N_R species are secondary species according to the primary species. The entries of matrix S are:

$$S = \begin{bmatrix} v_{11} & v_{12} & .. & v_{1N_c} & -1 & 0 & .. & 0 \\ v_{21} & v_{22} & .. & v_{2N_c} & 0 & -1 & .. & 0 \\ . & . & .. & . & . & . & .. & . \\ v_{N_R1} & v_{N_R2} & .. & v_{N_RN_c} & 0 & 0 & .. & -1 \end{bmatrix} \qquad \text{Equation 22}$$

In Retraso the entries v_{ij} of matrix S are read from one of the possible databases. Each database has a set of primary aqueous species. The rest of chemical species, the secondary species (aqueous complex, minerals, gases, surface complex) are expressed as linear combinations of primary species. Through matrix computation, a new set of secondary species will be found.

The choice of primary species is arbitrary. Secondary species correspond to the -1 columns of matrix S in equation (22). If other species are selected as primary, the corresponding stoichiometric coefficients will be different.

Concentration of total aqueous species and ion strength

When local equilibrium is assumed among chemical species of the system, at a given pressure and temperature, the Gibbs free energy of the system reaches a minimum, and the system cannot spontaneously carry out any chemical work. The mass action law is expressed as:

$$a_j^{-1} \prod_{i=1}^{N_c} a_i^{v_{ji}} = K_{j(p,T)} \qquad \text{Equation 23}$$

where K_j is the equilibrium constant which depends on the pressure and temperature of the system. a_j and a_i are the thermodynamic activity of the j th and i th species, N_c is the total number of primary species and v_{ji} is the stoichiometric coefficient of the i th primary species in the dissociation reaction of the j th species. From equation (23) we have:

$$\ln \mathrm{K_a} = -\ln \mathrm{a_2} + \mathrm{S_a} \ln \mathrm{a_1} \qquad \text{Equation 24}$$

where $\mathrm{a_1}$ and $\mathrm{a_2}$ are vector containing the thermodynamic activities of the primary and secondary aqueous species, respectively, and $\mathrm{S_a}$ is the matrix with stoichiometric coefficients. This equation allows one expressing the concentration of secondary species or aqueous complex $\mathrm{C_{a_2}}$ in terms of primary species concentration $\mathrm{C_{a_1}}$ (both in mol/kg water):

$$\mathrm{C_{a_2}} = -\ln \mathrm{k_a} - \ln \gamma_{\mathrm{a_2}} + \mathrm{S_a} \ln \mathrm{C_{a_1}} + \mathrm{S} \ln \gamma_{\mathrm{a_2}} \qquad \text{Equation 25}$$

where $\gamma_{\mathrm{a_1}}$ and $\gamma_{\mathrm{a_1}}$ are vectors with thermodynamic activity coefficients of primary and secondary aqueous species, respectively.

The value of the activity coefficient of the i th aqueous species can be calculated according to the extended Debye-Hückel formula:

$$\log \gamma_{a_i} = -\frac{Az_i^2 (I)^{\frac{1}{2}}}{1 + Ba_i (I)^{\frac{1}{2}}} + bI \qquad \text{Equation 26}$$

where I is the ionic strength of the solution; z_i and a_i are the electric charge and the ionic radius in solution of the i th aqueous species, respectively; A and B are constants which depend on temperature and dielectric constant of water, and b is a constant determined from fitting experimental data. The values of A, B and b at different temperatures are tabulated in Helgeson and Kirkham [19].

The value of the ionic strength is calculated as:

$$I = \frac{1}{2} \sum_{i=1}^{N_c} C_{a_i} z_i^2 \qquad \text{Equation 27}$$

The vector of total aqueous concentration of the components $\mathrm{u_a}$ can be written in an explicit form as a function of the concentration of the N_c primary species:

$$\mathrm{u_a = C_{a_1} + (S_a)^T C_{a_2} = C_{a_1} + (S_a)^T \exp(-\ln k_a - \ln \gamma_{a_2} + S_a \ln C_{a_1} + S \ln \gamma_{a_2})} \qquad \text{Equation 28}$$

Kinetic rate laws

In RetrasoCodeBright the rates of mineral dissolution or precipitation is calculated according to the general expression of Lasaga et al. [10] (see also Saaltink et.al. [7]):

$$r_m = \sigma_m \zeta_m \exp\left(\frac{E_{a,m}}{RT}\right) \sum_{k=1}^{N_k} k_{mk} \prod_{i=1}^{Ns} acc_i^{P_{mki}} \left(\Omega_m^{\theta_{mk}} - 1\right)^{\eta_{mk}} \qquad \text{Equation 29}$$

Where r_m is the mineral dissolution rate (moles of mineral per volume of rock and unit time), k_m is the experimental rate constant (in the same unites), Ω_m is the saturation ratio, which is the ratio between the ion activity product and the solubility product defined in Equation 30.

$$\Omega_m = \frac{1}{K_m} \prod_{i=1}^{Nc} a_{i,actual}^{\nu_{mi}} \qquad \text{Equation 30}$$

$$K_m = \prod_{i=1}^{N_c} a_i^{\nu_{mi}} = \prod_{i=1}^{N_c} c_i^{\nu_{mi}} \gamma_i^{\nu_{mi}} \qquad \text{Equation 31}$$

where the log Ω_m value is known as the saturation index SI_m. The system reaches the minimum free energy at equilibrium when Ω_m = 1 or SI_m = 0. The parameters θ and η must be determined from experiments. The term inside the parenthesis in Equation 29, called the far-from-equilibrium function, decreases the reaction rate in a non-linear way, as the solution approaches to equilibrium. The extra subscript "actual" on the activity *a* in equation (30) distinguishes the actual non-equilibrium activity for the equilibrium activity in equation (31). *c* in equation (31) is either concentration or mole-fractions depending on the actual units used for the K-values. and a similar consistent formulation will occur in equation (30) for the real concentrations and corresponding activity coefficients γ for actual non-equilibrium conditions. The term $acc_i^{p_i}$ accounts for the catalytic effect of some species (particularly of H+) and the value of p_i is determined by fitting experimental data. For reactions which are slow at ambient conditions the experiments are carried out at temperatures which are sufficiently high to result in dissolution within reasonable reaction times.

Scaling of the rate constants are normally done through the Arrhenius equation:

$$k_m = k_0 \exp(\frac{-E_{a,m}}{RT}) \qquad \text{Equation 32}$$

where k_0 is a constant and $E_{a,m}$ is the apparent activation energy of the overall reaction process, which for most minerals range from 30 to 80 kJ/mol [10]. Parameters k_0 and $E_{a,m}$ are determined from experiments performed at different temperatures.

Reactive transport for CO_2 injection scenario

The mathematical formulation for reactive transport in the CO_2 injection scenario is written as:

$$U_a \frac{\partial \phi S_l \rho_l c_a}{\partial t} + U_m \frac{\partial (1-\phi)\rho_s c_m}{\partial t} + U_g \frac{\partial \frac{\phi S_g}{Z_{co_2} RT} P_{co_2}}{\partial t} = U_a L_l(c_a) + U_g L_g(P_{co_2}) + U S_k^t r_m(c_a) \qquad \text{Equation 33}$$

Equation (33) are the Nc overall reactive transport equations, where Nc means the numbers of primary species in the system. Vectors c_a, c_m (mol kg^{-1}) are the concentrations of aqueous species, and mineral species. P_{co_2} is the partial pressure of CO_2. Matrices U_a, U_m and U_g are named the component matrices for aqueous, mineral and gaseous species. They relate the concentrations of the species with the total concentrations of the components. ϕ is the porosity in media. S_l and S_g are respectively liquid and gas saturation. R is the gas constant, T is temperature, and Z_{co_2} is the compressibility factor for CO_2. The matrix U is the component matrix for all the species, together with U_a, U_m and U_g, all these matrices can be calculated from the stoichiometric coefficient of the chemical reactions. Matrix S_k and vector r_k contains the stoichiometric coefficients and the rates of the kinetic reactions, which can be considered as functions of all aqueous

concentrations. L_l and L_g are linear operators for the advection, dispersion/diffusion and non-chemical sink-source terms for the liquid and gas phase, which are written as:

$$L_l() = -\nabla\bullet(q_l\rho_l()) + \nabla\bullet(D_l\phi S_l\rho_l\nabla()) + m_l \qquad \text{Equation 34}$$

$$L_g() = -\nabla\bullet(q_g\frac{1}{Z_iRT}()) + \nabla\bullet(D_g\phi S_g\nabla\frac{()}{Z_iRT}) + m_g \qquad \text{Equation 35}$$

where m_l and m_g are the non-chemical source-sink (mol m^{-3} s^{-1}) and D_l and D_g are the dispersion/diffusion tensors (m^2 s^{-1}). Z_i is the compressibility factor for i th gas.

The absorption term is dropped in Eq. (33), because the absorption reactions are not taken into consider for current CO_2 injection scenario, which will be part of the future work.

Time subdivision in Retraso

Both code CodeBright and code Retraso adapt Newton-Raphson iteration method to solve the highly non-linear equations. Nevertheless the method to subdivide the time in one time step in code CodeBright and code Retraso is different.

After one Newton iteration at time $t+1$ code Retraso will judge whether this iteration is successful by compare the residual of solutions of time $t+1$ and time t, noted as r_{t+1}, is within the prescribed error accepted area. If not, next time interval will be reduced to dt / fd, where dt is the last time interval, fd is the time decrease factor which is bigger than 1.0. Then calculation goes back to repeat the iteration of time $t+1$.

If convergence has been achieved, Retraso will judge whether the number of iteration $niter$ is within the prescribed area, that is $(thr\min, thr\max)$. If $niter$ is bigger than $thr\max$, $dt = dt / fd$. If $niter$ is smaller than $thr\min$, meaning that it has taken a very few iteration steps to converge, dt will be increased to $dt * fi$, where fi means the time increasing factor, which is bigger than 1.0. Otherwise, $niter$ is between the accepted areas. No matter which routine is taken, calculation will go to the next time step.

Boundary conditions

Since we have taken the pressure ramp loading method in CodeBright part and code Retraso, in its turn, does not allow varying boundary injection pressure, we have to instead use the CO_2 molar fraction as the boundary condition. No matter how different the injecting pressure is changed, the CO_2 molar fraction will be kept to be a constant.

For every chemical component a boundary condition equation in Retraso is to be written for the mass balance. Retraso permits two types of boundary conditions. In the first type, a component mass flux is calculated by multiplying the boundary flux of a phase (j_l , liquid, j_g , gas) by a total concentration of a component, which is that of the node of the boundary (u_a , concentration of total

aqueous species, or u_g, concentration of gas) or an externally specified one ($(u_a)^0$ or $(u_g)^0$), depending on whether the phase enters or leaves the medium:

$$m_l = j_l (u_a)^0 \qquad j_l > 0 \qquad \text{Equation 36}$$

$$m_l = j_l u_a \qquad j_l < 0$$

$$m_g = j_g (u_g)^0 \qquad j_g > 0 \qquad \text{Equation 37}$$

$$m_g = j_g u_g \qquad j_g < 0$$

The second one is a mixed condition according to the following expressions:

$$m_l = \gamma_l ((u_a)^0 - u_a) \qquad \text{Equation 38}$$

$$m_g = \gamma_g ((u_a)^0 - u_a) \qquad \text{Equation 39}$$

where γ_l and $\gamma_g a$ are leakage coefficients. A fixed concentration can be simulated by giving these leakage coefficient very high values. The first type is more preferred for advection dominated cases, whereas a fixed concentration is more preferred for diffusion dominated cases.

The values of the external total concentrations ($(u_a)^0$ or $(u_g)^0$) should be given for every component. For the aqueous phase, Retraso first calculates the concentrations of the primary species by choosing one of the equations in Table 3. Then the total aqueous concentrations will be calculated by equation (28).

Table 3 Options for calculating the chemical composition of the boundary

Option	Equation
Total aqueous component	$(u_a)^0$ = fixed
Charge balance	$\sum_i z_i (c_{ai})^0 = 0$
Activity	$(a)^0$ = fixed
Equilibrium with mineral	$(\Omega_m)^0 = 1$
Equilibrium with gas	$(p_f)^0$ = fixed

SIMPLIFIED MODEL SYSTEM FOR DEMONSTRATION OF BUFFERING EFFECT

During the duration of the project the efforts have been made to find realistic scenarios for which sufficient data on the reservoir were available. Unfortunately the search was unsuccessful within the time frame of the project.

In lack of real field data for relevant systems with significant reactivity we present one example from a simplified model. A 2D example is made up with gravity acceleration equal to -9.81, working on Y direction. We will respectively introduce the geometry and material properties, initial and boundary conditions and chemical species components. At last we will illustrate the evolution

results of gas pressure, liquid saturation, stress and pH values at three different time points, 10 years, 50 years, and 100 years.

It is emphasized that the simplified model is meant to demonstrate the model capabilities and not to represent a realistic scenario.

Geometry and material properties

Figure 2 schematically shows the vertical profile of this 2D example which lies 1000m under ground in X-Y plane. It is 1000m long in X direction and 200m high in Y direction where injection formation which consists of homogenous aquifer is 150m high and caprock is 50m high. CO_2 will be injected in the right-down corner. The material properties are given in Table 4 and correspond to sandstone aquifers mainly calcite with a caprock mainly quartz. Table 5 shows the initial and boundary conditions, and Table 6 shows the chemical species.

Figure 2. Graphical representation of the model and its formation zones.

Table 4. Material properties.

Property	**Caprock**	**Aquifer**
Young's modulus, E(GPa)	0.3	0.3
Poisson's ratio, v(-)	0.2	0.2
Permeability (mD)	1	100
Porosity (-)	0.1	0.2
Saturated rock density, ρ_s (kg / m^3)	2.26	2.26
Zero stress porosity, ϕ_0 (-)	0.1	0.2
Zero stress permeability, k_0 (m^2)	1.0e-15	1.0e-13
Irreducible gas saturation, S_{rg} (-)	0	0
Irreducible liquid saturation, S_{rl} (-)	0.3	0.3
Van Genuchten's air-entry pressure, P_0 (kPa), (at zero stress)	196	19.6
Van Genuchten's exponent, m	0.457	0.457

Table 5. Initial and boundary conditions. Initial values are given as a range because they vary with depth in each formation. CO_2 injection pressure is raised from initially 12.3 MPa to 14.8 MPa in 146 days, after that it is kept at 14.8 MPa.

Parameter	**Caprock**	**Aquifer**
Pressure, *P*(MPa)	10-10.5	10.5-12
Mean Stress, σ (MPa)	22.28-23.39	23.61-26.49
CO_2 initial injection pressure, P_g (MPa)	-	12.3
CO_2 final injection pressure P_g (MPa)	-	14.8
Gas and liquid outgoing pressure, *P*(MPa)	10	12

Table 6. Chemical species in different formations.

Species	Caprock	Aquifer
Aqueous species	'ca+2'	'ca+2'
	'h2o'	'h2o'
(Primary+Secondary	'hco3-'	'hco3-'
Aqueous species)	'h+'	'h+'
	'sio2(aq)'	'sio2(aq)'
	'caco3(aq)'	'caco3(aq)'
	'cah2sio4(aq)'	'cah2sio4(aq)'
	'cahco3+'	'cahco3+'
	'caoh+'	'caoh+'
	'co2(aq)'	'co2(aq)'
	'co3-2'	'co3-2'
	'oh-'	'oh-'
	'h2sio4-2'	'h2sio4-2'
	'hsio3-'	'hsio3-'
Mineral volume fraction	Calcite (0.1), Quartz(0.8)	Calcite(0.7), Quartz(0.1)
Mineral reactive surface	Calcite (100), Quartz(800)	Calcite (700), Quartz(100)
Gas	CO_2	CO_2

The method for specifying the primary and secondary species is based on that devised by Peter Lichtner for the code MPATH and used by Carl Steefel for the code 1DREACT [20, 21]. The code RCB requires the user to specify a set of aqueous primary species (or component species) to determine the number of independent components of the system. The choice of aqueous primary species is not unique, and the set of most abundant species for each component is recommended to avoid numerical problems. The calculation of volume fraction and surface reactive area of calcite and quartz in the whole formation is adapted according to the paper by S.P.White [22]. Kinetic geochemical reactions are assumed for all fluid-mineral reactions.

As explained above in the discussion of boundary condition in the CodeBright part the CO_2 injection pressure is a pressure ramp loading in order to smoothen out otherwise initially steep gradient changes in the system. This eases the convergence of the Newton iteration process. In this specific example, injection pressure is initially 12.3 MPa, then it is raised to 14.0 MPa in about 73 days, after that it is raised again to 14.8 MPa in another 73 days. The final injection pressure after this time is constant 14.8 MPa over the duration of the injection 100 years. So far no efforts have been made to evaluate minimum time for the upscaling to final injection pressure.

Estimated gas pressure after 100 years of injection is plotted in Figure 3. Norm of gas phase flux is plotted in Figure 4. Liquid saturations are plotted in Figure 5. The estimated principal stresses in xx and yy directions are plotted in Figures 6a and 6b respectively. Positive stress is for tension while negative values are for compressions. Since this example is artificial we do not have any real measured material properties for which we could evaluate fracturing but the analyses will obviously be easier than an explicit analyze since the pressure and stress in given directions can be directly compared to experimentally measured breakdown pressures for a real system. Initial stress is set to uniform values of 23.8 MPa. The yy stress is lower than xx and for most regions lower than 4 MPa.

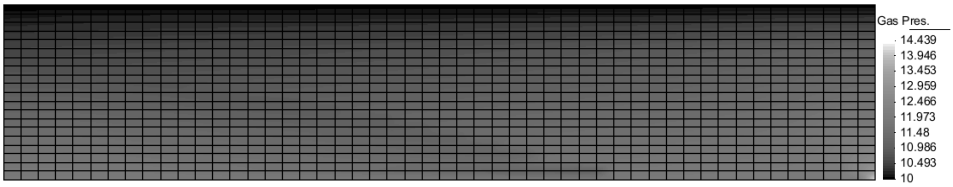

Figure 3. Simulated results of gas pressure (MPa) after 100 years of CO_2 injection. The displacements in the elements and boundaries reflect the deformation of the formation. It applies also for the following figures.

Figure 4. Simulated results of gas phase flux (m/s) after 100 years of CO_2 injection**.**

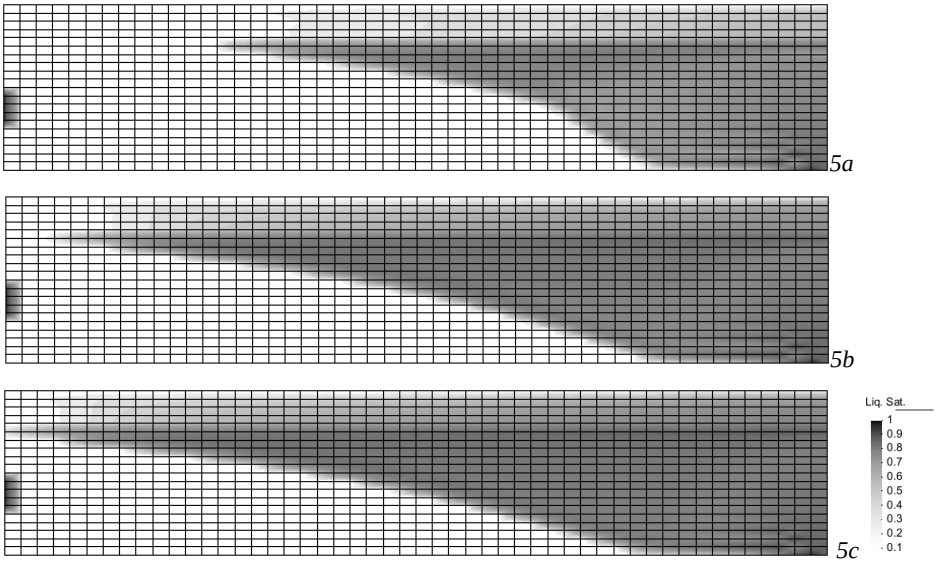

Figure 5. Simulated results of liquid saturation at the time points of 10 (a) 50(b) 100(c) years, after CO_2 injected.

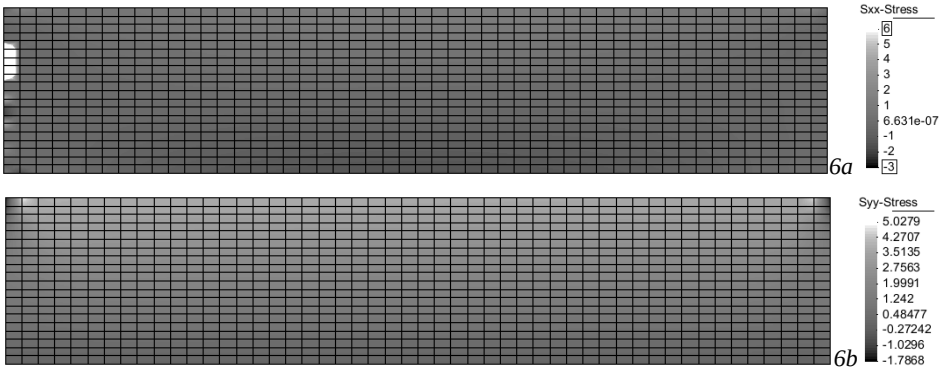

Figure 6. Simulated results of stress on XX direction (6.a) and YY direction (6.b) (MPa) at the time point 100 years after CO_2 injected.

The system will be geochemically buffered through the release of carbonate ions form the dissolved minerals. As expected from this test case for the actual injection conditions, Figure 7 shows that the pH do not drop below 7 for any region of the formation and it is even so that the released and transported carbonate ions creates an increase in pH for some regions.

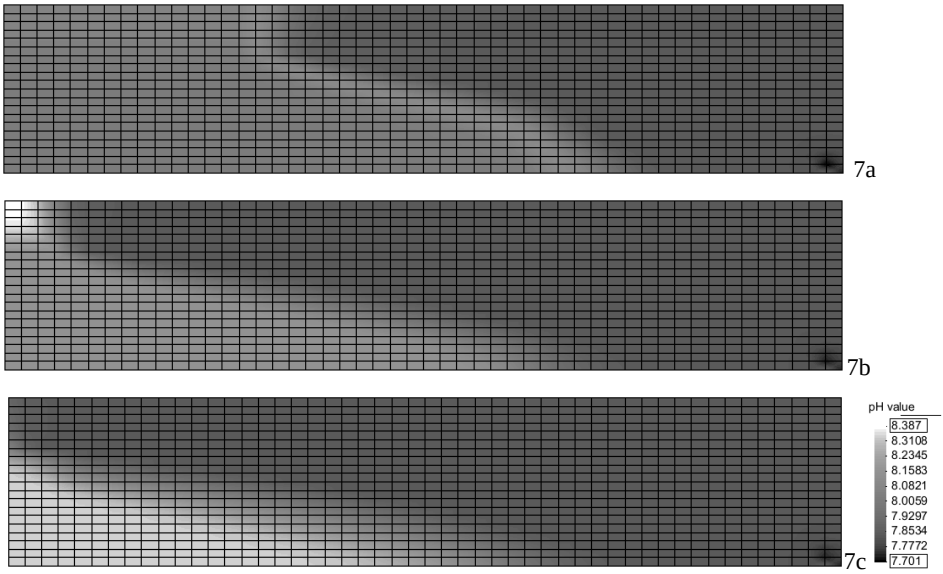

Figure 7. Simulated results of pH values after the time points of 10 (a) 50(b) 100(c) years after CO_2 injected.

The density of CO_2 plumes which cumulate under traps of low permeability shale or soft clay depends on depth and local temperature in each unique storage scenario. The difference in density and the density of the groundwater results in a buoyancy force for penetration of CO_2 into the cap rock. And even if the solubility of water into CO_2 is small dissolution of water into CO_2 may also

lead to out-drying. Mineral reactions between CO_2 and shale minerals are additional effects which eventually may lead to out-drying and embrittlement. Linear geo-mechanics may not be appropriate for these effects. In particular clay is expected to exhibit elastic non-linear contributions to the geo-mechanical properties. Different types of non-linear models are already implemented in the CodeBright part of the code and the structure of the code makes it easy to implement new models derived from theory and experiments.

A MODEL SYSTEM WITH FRACTURE

The two-dimensional geometry is limited to a 1000 m long and 250 m high model, of which the vertical and horizontal axis are respectively divided into 50 and 25 elements. Each element is 20 m long and 10 m high. In order to define the width of the fracture, there was added an additional 4m-wide element. The fracture zone is situated in the middle of the geometry, enabling the gas to flow from the injection aquifer through the cap rock and into the top aquifer. A schematic overview of the system is illustrated in Figure 8 below. Again, the idealized model is meant to demonstrate model capabilities only.

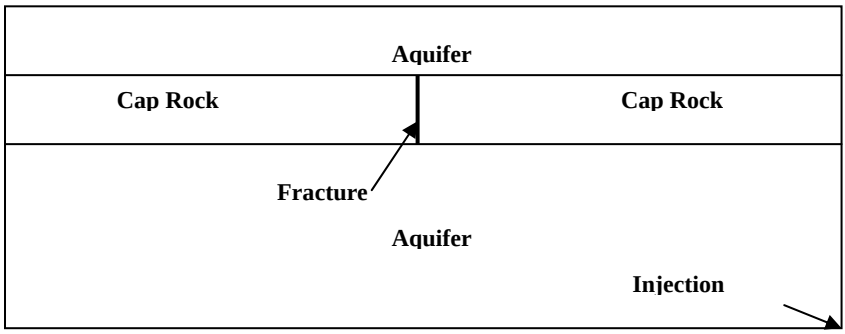

Figure 8. Geometry zone layouts

The lower boundary of the injection aquifer is located at -1200 meters below the sea floor. Similar depths are found in a range of aquifers including the Utsira formation off the coast of Norway. From the lower boundary, the aquifer extends 150m to the cap rock located at -1050m. Contributing with an additional 50m to the total thickness, the cap rock divides the injection aquifer from the upper aquifer. The 50m thick upper aquifer is placed upon the cap rock in order to observe the gas plume that will form as the gas seeps through the fracture. The injection point of carbon dioxide is located on lower the right hand side of the bottom aquifer.

In the process of defining the zone properties the initial temperature, pressure and stress can either be specified as constant or in a field approach. While the gradients of both stress and the fluid pressures are solved in the presented simulation, the temperature remains constant. The initial approach was to define the reservoir uniformly at 25 ^{o}C, however with a simple operation the reservoir temperatures have also been appended with vertical gradients. This extension will allow a more realistic description of the dissolution and precipitation occurring in the aquifer since the retrograde temperature dependence of calcite will be considered.

The geometry is simulated with linear gradients for the pressure and stress. The structure is closed in top and bottom and kept open on the right and left hand side. As such the initial reservoir boundary pressures are constant at 12 MPa in the bottom boundary and 9.5 MPa in the upper boundary. This case is run with realistic gravity and initial pressure defined according to pressure of initial fluid

column. The average density is estimated to be 2.26 kg/m^3 and the initial stresses are given in absolute values in a range from 21.17 MPa to 26.5 MPa. The temperatures range from 34.2 - 43.2 ^{o}C

At initial conditions the injection pressure of CO_2 is set to 12.3 MPa. The injection pressure is then increased in four stages during the 10 first months of the simulation to a pressure of 27.0 MPa. These steps are necessary in order to let the simulation converge. A high initial injection pressure would crash the simulation because the integrations would go towards infinity. The injection point is located on lower the right hand side of the bottom aquifer.

The aquifers are initially modeled as 4% Calcite and 96% Quarts with porosities ranging from 0.01 to 0.1 depending on the respective zones. During the simulation the geometry is subject to change in mineral dissolution and mineral precipitation. The calculation of volume fraction and surface reactive area of calcite and quartz in the formation is adapted according to the paper by White et al. [22]. Initially the water concentration is equal in all the geometry zones.

Parameters for the five zones (the injection aquifer, the top aquifer and two cap rock zones separated by a fracture zone) are shown in Table 7 and data for permeability dispersion and diffusion for the different zones can be found in Table 8. All the geometry zones are simulated with different permeabilities. Most of the values for the fracture zone are estimates with no physical source. The goal is to be able simulate the fracture hydrodynamically instead of defining the given parameters in Tables 7 and 8.

Table 7. Mineral volume fractions in the 5 zones at 4 percent calcite.

Zone	Aquifer	Aquifer	Caprock	Caprock	Fracture
Vol. fraction of calcite and effective area	0.036 36	0.036 36	0.0396 39.6	0.0396 39.6	0.038 38
Vol. fraction of quartz and effective area	0.864 864	0.864 864	0.9504 950	0.9504 950	0.912 912
Porosity	0.1	0.1	0.01	0.01	0.05

Table 8. Permeability, dispersion and molecular diffusion.

Zone	Aquifer	Caprock	Fracture
Permeability (D)	1e-13	1e-17	1e-12
Longitude dispersion factor (m)	11	11	11
Transverse dispersion factor (m)	21	21	21
Molecular diffusion(m)	1e-10	1e-10	1e-10

In the simulation we have used a poroelastic model with Young Modulus equal to 3000 MPa for the Aquifer and Cap Rock, while the corresponding value for Fracture is set to 1500 MPa. All the zones in the geometry are operating with a Poissons ratio equal to 0.2. Kinetic geochemical reactions are assumed for all fluid-mineral reactions.

A few figures will be used to illustrate the specific behavior related to the fracture. The gas phase flux through the fracture is steadily increasing until breakthrough of carbon dioxide through the fracture, after which there will be continuous channels of carbon dioxide, as indicated in Figure 9 in units of m/s. The corresponding flux in kg per square meter and second is available by multiplying with the corresponding carbon dioxide density. This vary of course locally with pressure and temperature and is varying substantially in the fracture during the breakthrough but order of magnitude values can be achieved by multiplying with a density of carbon dioxide equal to 750 kg/m^3. A snapshot of the gas phase flux profile through the formation after 15 years is plotted in Figure 10.

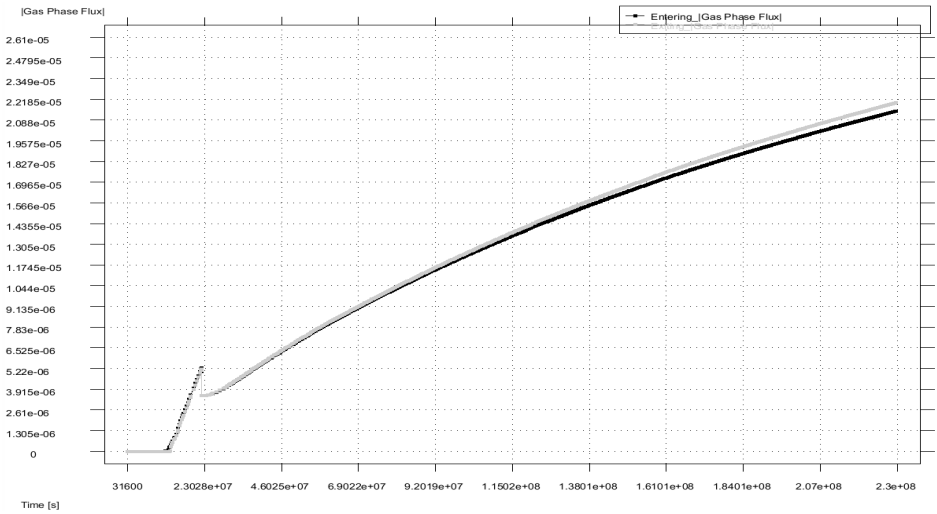

Figure 9. Estimated carbon dioxide fluxes for the model system with fracture in m/s. Maximum and minimum on the flux scale is ($6.21 \cdot 10^{-5}$, 0) and the time axis corresponds to 7.2 years.

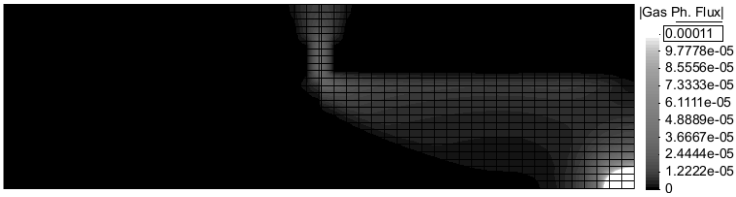

Figure 10. Carbon dioxide flux (m/s) profile after 15 years of injection.

The estimated lateral stresses are limited and consistently expansive (positive) with values below 9 MPa. The estimated overbearing stress profile after 100 years is plotted in Figure 11. As expected also these stresses are limited and with the highest stress above the fracture close to the top of the formation. The corresponding estimated gas pressure profile is plotted in Figure 12.

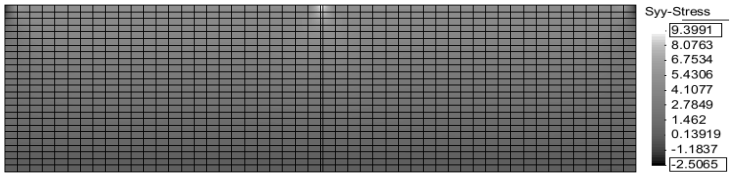

Figure 11. Estimated bearing stress after 100 years of injection.

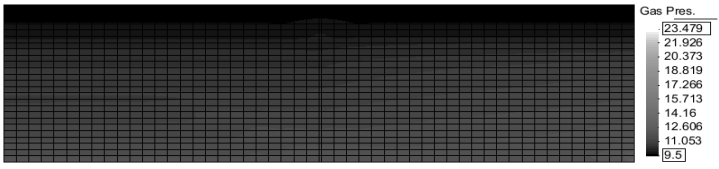

Figure 12. Estimated gas pressure profile after 100 years of injection.

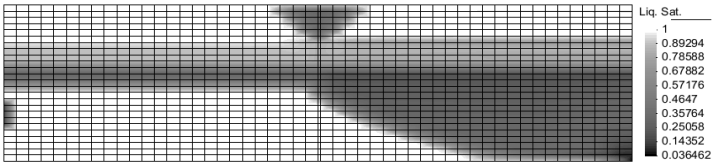

Figure 13. Estimated liquid saturation after 100 years of injection.

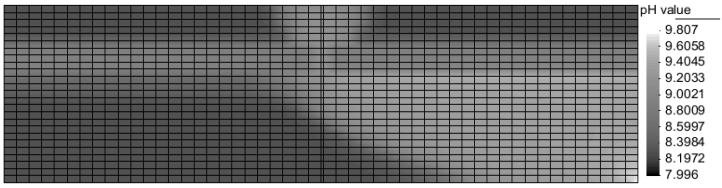

Figure 14. Estimated pH profile after 100 years of injection.

As expected the liquid saturation profile (Figure 13) is dominated by the fracture, which leaves large portion of the reservoir practically "unused" for storage of carbon dioxide since the flow through the fracture has such a dominating role of redirecting the carbon dioxide flow. The buffering of the system is substantial, as illustrated by the pH plot in Figure 14. Within 100 years of injection the dissolution of the quartz based minerals is very small.

In addition to the theoretical advantages of an implicit scheme for geomechanics, the geomechanical stability analysis becomes fairly easy since the sum of the local pressure (Figure 12) and the local stress can be directly compared to the tensile strength of the material. This allows for detection of possible times and places for potential fracturing or collapse, and also easy analysis of the impact of local fracturing on geomechanical stability of the formation as a whole.

CHANGES IN POROSITY

The presented case above did not show any significant changes in porosity other than relatively small variations in the cap rock. In order to better illustrate the abilities of the reactive module and porosity updates, the data from a similar case will be presented below. The only difference between these two cases is larger volume fraction (16%) of calcite throughout the reservoir. Hence the remaining specifications will be equal to that found in Tables 7 and 8.

After thirty to fifty years of carbon dioxide injection there are noticeable changes in the porosity right below the fracture and in the surrounding area of the injection point as shown in Figure 15. The areas marked in black are the sections of the reservoir which have an initial porosity equal to 0.1, whereas the remaining white areas represent porosities outside the set scale of the graphical representation. The white belt stretching across the figure is due to the lower porosity of the cap rock and fracture.

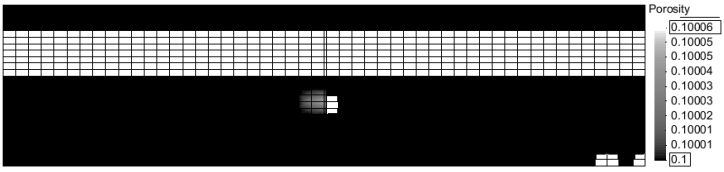

Figure 15. Change in porosity after 50 years.

The white spots within the aquifer are much more interesting as the porosity is initially uniform at 10%. Any significant changes to this zone would be related to dissolution and precipitation of carbonates. Contribution from dissolved quartz is negligible as the reaction rate is low and would require a reaction times equivalent to several thousands of years compared to the much more rapid dissolution rate of calcite [7]. Although the change in porosity is noticeable, the increment is rather small ranging from 0.0 to 0.00006 which is less than $6x10^{-3}$ percent. The white regions in figure 15 represents values outside the set scale of porosity. The largest increment due to precipitation is only a tenth of the equivalent change due to dissolution.

A small area around the injection point is experiencing a reduction in porosity. Figure 16 below is a graphical representation of the precipitation in the lower right hand side corner of Figure 15. The precipitation peaks within 2 to 5 years and steadily decreases as the simulation approaches 30 years. The change of porosity in this section is present at an early stage, whereas the increments in the porosity of figure 15 and 16 first appear after 30 years.

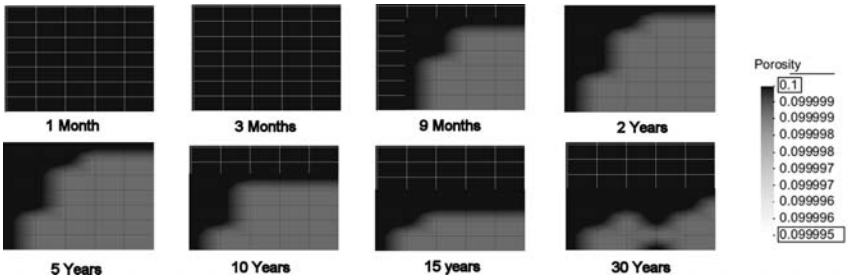

Figure 16. Change in porosity around the injection zone over 30 years.

The significantly higher pressure and large gradients in the injection zone is most likely responsible for the precipitation of calcite in the surrounding elements. As the pressure drops, less calcite will be soluble in the formation water due to the impact of pressure on carbon dioxide solubility and the couplings to calcite through carbonate ions.

With respect to the anomaly in porosity below the fracture the mechanism is probably related to the phase fluxes in the region. By examination of the gas and liquid phase flux after 50 years, Figure 17 indicates that areas of significant porosity changes are located directly between the flux interface of liquid and gas.

The water within the gas phase flux is saturated by dissolved gas and calcite. The buffering from calcite increases the pH value to above 8 and prevents further dissolution of minerals and gas. At the interface shown in Figure 17, the conditions are quite different. CO_2 gas is continuously transported into low saturated liquid and dissolved. The dissolution of CO_2 lowers the pH and shifts the chemical reactions in favor of dissolved calcite.

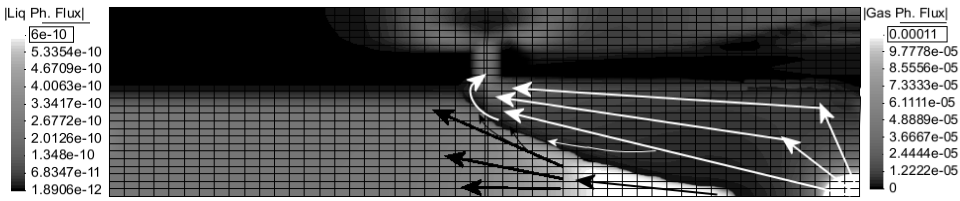

Figure 17. Liquid and gas phase flux after 50 years. Black arrows: Liquid flux, White arrows: Gas flux. The flow above the cap rock is liquid phase flux.

A constant dissolution of carbon dioxide at the interface, combined with the buoyancy of gas, creates a flux vector of acidic water that flows through the very area of the porosity changes illustrated in Figure 15. At the same time some of the saturated acidic water will move into the high pH zone with in the gas flux and cause precipitation of carbonates. The reduction in pressure also has an impact on the magnitude of porosity increments. The described movements are indicated with black and white arrows in Figure 17.

FUTURE EXTENSIONS

Some of the most immediate things that will be worked into the code after this project are summarized in the sections below. There are likely to be additional features which might be of specific interest to industry and/or governmental institutions so this list is limited to features for which extension plans are formulated and different options for funding are yet being considered.

Real Cases

A secondary goal of the project was to apply this software to specific test cases for which sufficient information was available. Unfortunately the only cases with sufficient details in level of information, like for instance Utsira and Frio, have very limited mineral reactivity for time scales less than ~ 1000 years and it was decided to conduct a sensitivity study. This work is in progress but was delayed substantially due to unexpected numerical convergence problems.

Gas mixtures

One of the simplest extensions is to include gas mixtures since the code has an integrated general equation of state. The density corrections are already in place and the only difference in that part will be to use the estimated mixture compressibility factor. The database in RetrasoCodebright is also able to handle reaction which involves dissolved H_2S. So the essential working task is to rewrite the gas solubility part from pure CO_2 solubility to mixed gas solubility. The primary targets will be to include H_2S since CH_4 solubility into water is very small and in the case of exhaust gas nitrogen and oxygen dissolves even less. The latter components may be readily approximated by a Henry's law type of approach. A secondary target would be to include SO_2 and NO_x provided that there is enough industrial interest for a combined governmental and industrial support.

Fracturing dynamics

As discussed above there are two ways to define fractures in the current state of the code, as a geological element of high permeability or as an element of a dimension lower that the simulation system and the use of a transmissibility for definition of flow through the fracture. A third option is the rigorous treatment of fractures as hydrodynamic boundary conditions coupled to the reservoir flow equations. This will open up for an extension to the inclusion of fracturing dynamics. Logistically this implies that when the stress plus pore pressure in a certain point in the structure exceeds the tensile strength of that section of the geology a fracture analysis will be called. This will involve the fracturing as well as the relaxation hysteresis after the pressure release due to the fracturing.

Relative permeability hysteresis

Unlike many other academic codes RetrasoCodebright do have built-in capabilities of changing permeabilities and relative permeabilities in every time step. In the present version this is used to update permeabilities as function of changed porosities due to mineral dissolution or mineral precipitation. As such it should be possible to include relative permeability hysteresis effects without substantial efforts (less than half a year of manpower). The built-in adsorption facility will

also enable more realistic description of surface reactions as well as wetting preference characteristics of different minerals on residual pore saturations.

Injection well modelling

Most academic simulators do not have any rigorous description of the injection wells and may as such miss important dynamic features of the immediate surroundings. The rigorous description of fractures also opens up for realistic injection wells through definition of these as "fractures" with given geometry and zero flux boundary conditions, except the boundaries of the injection section at the reservoir side which then will be treated in the usual fashion as boundary condition between the hydrodynamics of the well and the reservoir flow. This is not actually something that requires new implementation but it needs to be tested and evaluated.

Hydrate sealing effects

Some relevant reservoirs for storage of CO_2 are located in regions of low seafloor temperatures and at depths which facilitates the formation of hydrate (ice-like solid with up to 12 mole per cent CO_2) between CO_2 and water. These hydrates do not close pore space since they are unable to attach to mineral surfaces due to hydrogen bonding limitations. But they reduce the permeability to very low levels and may as such provide more time for the CO_2 plume below to dissolve into surrounding groundwater and sink. A special feature of clay is that ionic double layers on the mineral surfaces may facilitate a bridging to hydrate which is "glued" to the clay sections. As such the extra sealing achieved may actually promote the search for storage reservoirs in which hydrates may form. Within RetrasoCodeBright this can be treated as a pseudo mineral reaction in which hydrates form at the CO_2 water interface and my dissolve again towards water lean on CO_2. This dynamic is very often controlled by mass transport, as investigated and published in several papers from the group behind this report. Another reason for implementing it in this fashion is to capture the dynamics of the formation (roughly 10% volume increase compared to liquid water) and dissociation and the potential geomechanical impact on the geological structure. This is priority area for which further funding will be applied for. Offshore Norway Utsira is too warm for hydrate formation while Snøhvit injection is cold enough in the upper section if the CO_2 plume reaches the upper layers. The injection location is very deep and due to lack of open data on the formation it has not been possible to simulate possible migration patterns for the CO_2 so far.

CONCLUSIONS

A new reservoir storage simulator for CO_2 have been developed on the RetrasoCodeBright platform by inclusion of non-ideal gas description using an equation of state for calculation of gas solubility and incorporation of realistic fluid densities as function of local pressures and temperatures. The simulator contains state of the art geochemical descriptions and a great advantage is the implicit geomechanical module which enables simultaneous analyses of possible geomechanical implications for every time step and every region of the reservoir in consideration. Using the Terzaghi criteria the combinations of calculated pressures and stresses in different directions will immediately give a value which can be evaluated against the tensile strength of the actual formation. Numerical algorithms have also been modified so as to ensure converged solutions for the high pressures relevant for storage of CO_2. Different features of the simulator have been studied through two test cases, of which one has a fracture. The most important impact of the fracture is, as expected, a substantial redirection of the flow towards the fracture. The result is that large portions of the potential storage volume are not actively in use. Given that it is extremely difficult to detect fractures below certain lower limits by standard geophysical method, and from comparing the injection flux with estimated flux through fracture it is quite obvious that methods and techniques which are able to characterize sealing properties to a more detailed level are crucial for the further

success and acceptance of reservoir storage of carbon dioxide. Among a number of proposed extensions two alternative approaches for representing fractures will be investigated: 1) fracture as a hydrodynamic section with velocity boundaries towards the reservoir flow model; and 2) fracture as a zone of lower dimension. Practically the latter option would imply that the fracture is represented as a line without extension but given flow conductivity. This option has been evaluated for low pressure systems but to our knowledge not for high pressure carbon dioxide systems. Representation of fractures as hydrodynamic zones is the most rigorous approach and can also be used for rigorous representation of wells. This option will therefore have a high priority in future work on this simulator. Modelling of hydrate kinetics as a pseudo reaction also allows for implementation of the couplings between hydrate dynamics and geomechanics. Hydrate volume is in the order of 10% larger than liquid volume, which means that hydrate formation and dissociation can lead to fracturing or collapse. Changes in porosity with hydrate formation/dissociation and impact for flow properties can be corrected for through an extended version of the implemented correlations for fluid/mineral. These qualities will also come to use in the accelerating interest for natural gas hydrate reservoirs as an energy source.

ACKNOWLEDGEMENT

This study was funded by the CO_2 Capture Project Phase 2 (CCP2) and the Research Council of Norway through its CLIMIT program. A special thank also goes to Lars Ingolf Eide for his dedication and good advises.

REFERENCES

1. Pruess, K., J. García, T. Kovscek, C. Oldenburg, J. Rutqvist, C. Steefel, and T. Xu, Code intercomparison builds confidence in numerical simulation models for geologic disposal of CO_2, Energy, 29, 1431-1444, 2004.
2. Rutqvist J., Y.-S. Wu, C.-F. Tsang, and G. Bodvarsson A Modeling Approach for Analysis of Coupled Multiphase Fluid Flow, Heat Transfer, and Deformation in Fractured Porous Rock *Int. J. Rock Mech. & Min. Sci.* 39**,** 429-442 (2002).
3. Rutqvist J. and Tsang C.-F. TOUGH-FLAC: A numerical simulator for analysis of coupled thermal-hydrologic-mechanical processes in fractured and porous geological media under multi-phase flow conditions. Proceedings of the TOUGH symposium 2003, Lawrence Berkeley National Laboratory, Berkeley, May 12–14 (2003).
4. Olivella, S., J. Carrera, A. Gens, E.E. Alonso, “Non-isothermal Multiphase Flow of Brine and Gas through Saline Media”, Transport in Porous Media, 15, pp. 271-293, 1994.
5. Olivella, S., A. Gens, J. Carrera, E. E. Alonso, “Numerical Formulation for a Simulator (CODE_BRIGHT) for the Coupled Análisis of Saline Media”, Engineering Computations, vol. 13, No.7, pp.87-112, 1996.
6. Olivella, S., A. Gens, J. Carrera, CodeBright User’s Guide. Barcelona, E.T.S.I. Caminos, Canales y Puertos, Universitat Politecnica de Catalunya and Instituto de Ciencias de la Tierra, CSIS, 1997.
7. Saaltink, M., Benet, I., Ayora, C., RETRASO, Fortran Code for Solving 2D Reactive Transport of Solutes, Users´s guide. Barcelona, E.T.S.I. Caminos, Canales y Puertos, Universitat Politecnica de Catalunya and Instituto de Ciencias de la Tierra, CSIC, 90 pp. 1997.
8. Saaltink, M., Batlle, M., Ayora, C., “RETRASO, a code for modeling reactive transport in saturated and unsaturated porous media”, Geologica Acta, Vol.2, No 3, pp. 235-251, 2004.
9. Soave, G., “Equilibrium constants from a modified Redlich-Kwong equation of state” Chem. Eng. Sci., 27, 1197-1203, 1972.
10. Lasaga, A.C., “Chemical kinetics of water-rock interactions”, Journal of Geophysical Research, B6, 4009–4025, 1984.

11. Kozeny, J. **(**1927), Uber kapillare Leitung der Wasser in Boden, Sitzungsber. Akad. Wiss. Wien, 136, 271–306.
12. van Genuchten, M. Th. Mass transport in saturated-unsaturated media: One-dimensional solutions, Research Report 78-WR-11, Princeton Univ., Princeton, NJ, 102 p., 1978.
13. Nakata, T. and Fujiwara, K., "Method for determining relaxation factor for modified Newton-Raphson method", IEEE TRANSACTIONS ON MAGNETICS, vol. 29, No. 2, MARCH 1993.
14. Nakata, T, Takahashi, N., Fujiwara, K., Olszewski, P., and Muramatsu, K. "Analysis of magnetic fields of 3-D non-linear magnetostatic model (Problem 13)," Proceedings of the European TEAM Workshop and International Seminar on Electromagnetic Field Analysis, pp. 107-1 16, 1990.
15. Nakata, T, Takahashi, N., "Summary of results for benchmark problem 13 (3-D nonlinear magnetostatic model)," COMPEL, James & James, vol.11, 1992.
16. Nakata, T, Takahashi, N., Fujiwara, K., Okamoto, N. and Muramatsu, K. "Improvements of convergence characteristics of Newton-Raphson method for nonlinear magnetic field analysis," IEEE Trans Magn., vol. M 28, no.2, pp. 1048-1051, March 1992.
17. Span, R., Wagner, W., J. Phys. Chem. Ref. Data 25, 1509, 1996.
18. Hellevang, H., Kvamme, B, "An explicit and efficient algorithm to solve kinetically constrained CO_2-water-rock interactions", 2007, WSEAS TRANSACTIONS on Mathematics, 6, issue 5, 681 – 687.
19. Helgeson, H. C., Kirkham, D. H., Theoretical prediction of the thermodynamic behavior of aqueous electrolytes at high pressures and temperatures; I, Summary of the thermodynamic/electrostatic properties of the solvent, 1974, American Journal of Science, Vol. 274, 1089-1198.
20. Steefel, C.I., 1993. 1DREACT User Manual.
21. Steefel, C.I., Lasaga, A.C., 1994. A coupled model for transport of multiple chemical species and kinetic precipitation/dissolution reactions with applications to reactive flow in single phase hydrothermal system., 1994, Am. J. Sci. 294, 529-592.
22. White, S. P.; Allis, R. G.; Moore, J.; Chidsey, T.; Morgan, C.; Gwynn, W.; Adams, M. Injection of CO_2 into an unconfined aquifer located beneath the Colorado, Central Utah, USA. *Proc. Annu. Conf. Carb. Seq., Alexandria, VA* 2003; p 15.

Carbon Dioxide Capture for Storage in Deep Geologic Formations, Volume 3
L.I. Eide (Ed.)

Chapter 25

SIMULATION STUDY OF METHANE AND CARBON DIOXIDE MIGRATION AND LEAKAGE DURING NORMAL AND ENHANCED FIELD OPERATIONS TO RECOVER COAL BED METHANE FROM COAL SEAMS

C. M. F. Galas[1], V. Y. Savenkov[1] and D. Kieke[2]
[1]Sproule International Limited
[2]Chevron Corp 1500 Louisiana St. Houston, TX 77002

ABSTRACT: A simulation model of nine wells in the Pratt, Mary Lee and Black Creek coal zones in the Deerlick Creek field was constructed. The primary production of methane from the coal seams was history matched. The history-matched model was used to investigate the injection of CO_2 into the coal seams. Under continued primary production, the methane recovery was 81.7% of the original gas-in-place (OGIP) to 2040. Injection of CO_2 with continued production led to roughly the same recovery with some acceleration. The effect of shutting-in the production wells and continuing injection was also investigated. It was found that there is a trade-off between recovery of the original methane and efficient storage of the CO_2. Furthermore, the possibility of leakage of the sequestered CO_2 was investigated using a model which included all of the overburden. The risk of CO_2 migrating to the surface or sources of potable water is very low for centuries.

INTRODUCTION

The CO_2 Capture Project (CCP), started in 2000, is an international effort intended to address the issue of reducing CO_2 emissions resulting from the combustion of fossil fuels. The CCP seeks to develop new technologies to reduce the cost of capturing CO_2 from combustion sources and safely store it underground. The objective is to reduce the impact of continued fossil energy use by implementing these new technologies while cleaner energy sources are being developed.

Three critical areas identified that required further study for the second phase of the project (CCP2) were (1) the integrity of coal bed methane (CBM) geologic and engineered systems, (2) the optimization of the coal bed storage process, and (3) reliable monitoring and verification systems appropriate to the special conditions of CO_2 storage and flow in coals.

This report covers the numerical simulation work aimed at the optimization of the coal bed storage process and CO_2 storage, as well as examining the leakage of CO_2 out of the coal beds through natural fractures and fissures – note that an investigation of leakage from shut-in or abandoned wells is outside the scope of this study.

To achieve these goals, the work reported herein consisted of the following tasks:

- Selection of study area
- Data collection
- Construction of coal bed methane (CBM) model
- Calibration of model using historical production data
- Prediction of future performance of CBM production

- Examination of CO_2 storage in study area
- Examination of potential for enhanced CBM production
- Construction of CBM model with overlying strata
- Examination of CO_2 leakage out of coal beds

The simulation software used is GEM, which is a compositional model with CBM capabilities developed by the Computer Modelling Group (CMG). GEM is the industry's leading coal bed methane (CBM) simulator, as it can provide accurate early-time water and methane production predictions, as well as multi-component production predictions for enhanced CBM (ECBM) recovery. The ECBM features include extended Langmuir Isotherms to model the preferential adsorption of CO_2 and other gases and models for coal shrinkage and swelling.

FIELD DATA

Alabama – Black Warrior Basin

A CO_2 storage field test was being planned by the "Southeast Regional Carbon Storage Partnership" (SECARB) in the Black Warrior Basin in Alabama, and it was decided to use data from this area. A major advantage is that considerable data is available for the project and future results can be used to update and evaluate this work [1-14].

The well selected for the SECARB field test is the Jobson 24-14 No. 11 well (State Oil and Gas Board of Alabama permit number 4001-C) [8,15]. A map showing the well and the offsetting CBM wells is shown in Figure 1, which also indicates the cumulative gas production from each well. This area was selected for the remainder of the study.

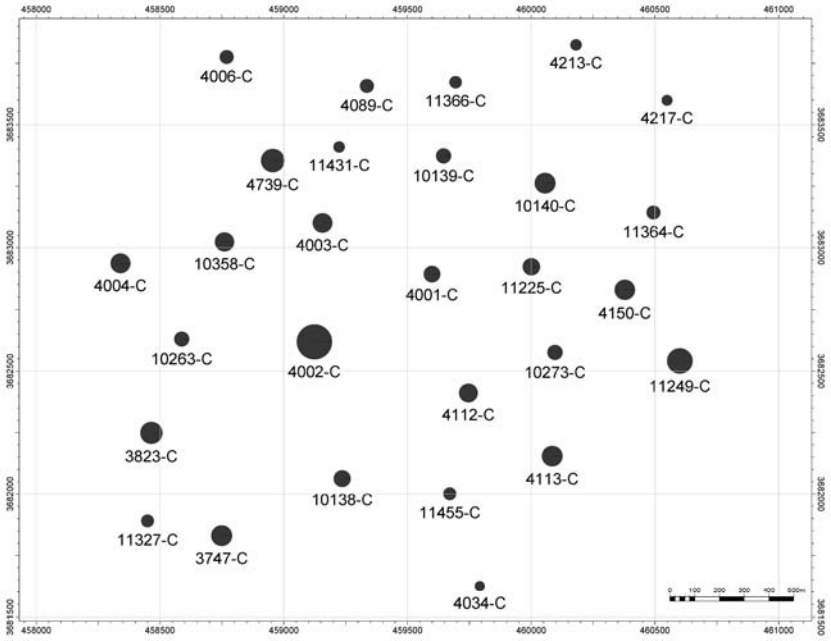

Figure 1. Well Locations and Cumulative Gas Production– Deerlick Creek Field.

CBM SIMULATION MODEL DEVELOPMENT AND CALIBRATION

Data Collection

Additional data acquired includes:

- Well location data
- Well tickets
- Well production data
- Tops of formations at each well
- Thicknesses of all coal seams in each well
- Gas sorption data for the Blue Creek Field
- Coal property data

The wells within a mile of the 4001-C well were identified. Raster images of the logs of these wells were obtained and several cross-sections were generated from these to evaluate the continuity of individual coal seams.

Well Logs

The logs of the wells in the study area were analysed by hand. Each coal seam which met the cut-off criteria was identified and included in the model with its top and thickness honored. The criteria used were:

- Density less than 1.75 g/cc
- Thickness of the seam greater than 0.4 ft exceeding the density cut-off
- Less than 100 API on the gamma ray log.

The log data was read into the Petrel geological modeling software and a 3-D geological model was created using the tops and thicknesses of the coal seams. This model grid was exported to the simulation model.

Adsorption Isotherms

Isotherm data for the Deerlick Creek field was not available. In its place, it was assumed that data from the Blue Creek field would be a close approximation since they are from the same basin and the field boundaries are arbitrary.

Langmuir isotherms for the Blue Creek field for both methane and carbon dioxide were obtained from lab data from the EPBC well. Figures 2 and 3 show the methane and carbon dioxide isotherms respectively. The differences between the Pratt, Mary Lee and Black Creek isotherms were judged to be insignificant, therefore the average isotherms were used for all three coal zones.

The isotherms are calculated on a “dry, ash-free” basis (DAF), therefore the gas content was corrected for the ash content which was calculated from the density of the individual coal seams.

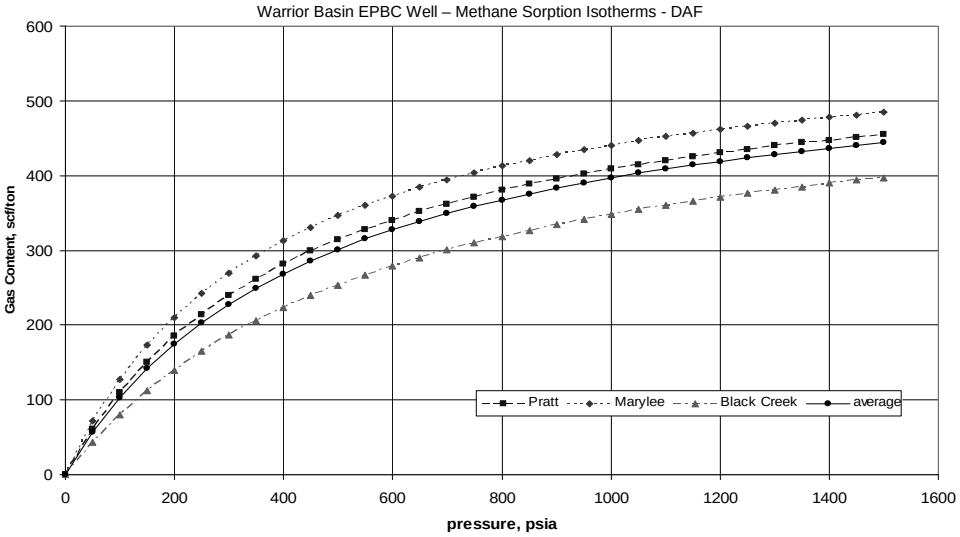

Figure 2. Langmuir Isotherms for Methane.

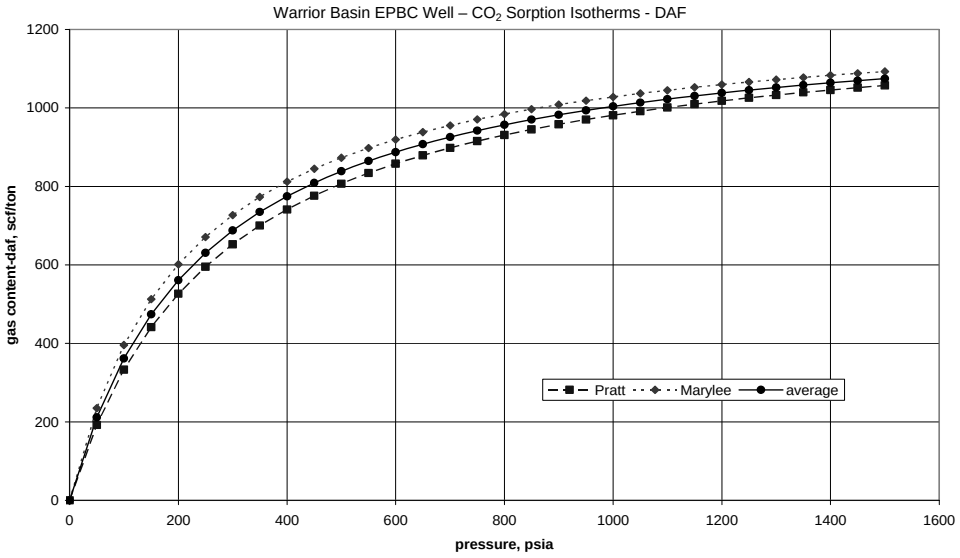

Figure 3. Langmuir Isotherms for CO_2.

Other Coal Properties

The coalbed methane literature was searched for data on the coals in the Black Warrior basin. A number of sources had relevant data, though the original source of the data was rarely available.

Table 1 shows some of the data available (note that the data in the references was provided in "oilfield" units – for ease in comparison, no conversion to SI have been made).

Table 1. Black Warrior Basin Coal Data.

SPE Paper No.		24359	26201	24358	24358	24358	20666	20666	20666	16420	16420	16420	30734	30734	75519
Author		Soot	Seidle	Seidle	Seidle	Seidle	Ely	Ely	Ely	Zuber	Zuber	Zuber	Sparks	Sparks	Seidle
Year		1992	1993	1992	1992	1992	1990	1990	1990	1987	1987	1987	1995	1995	2002
Reference		10	11	12	12	12	5	5	5	9	9	9	6	6	13
Coal							Mary Lee	Black Creek	Pratt						
Thickness	ft	7	11	12.2	6	9.7				6.8	6.8				6.8
Gas Content	scf/ton	396	733	480	835	541				375					616
Langmuir Pressure	psi		270.3	354.6	427.4	243.9				258					147
Initial Pressure	psi	430	530	466	500	550				431					440
Cleat Porosity	fraction		0.02	0.005	0.01	0.01				0.02	0.04	0.01-0.05			0.19
Cleat Permeability	md	20	18	28	10	20	0.35	1.4	4.4	11	10	1-30	46		10
Fracture Half Length	ft	290								287	200	50-500			
Well Spacing	acres	80	160	80	160	160				40					40
Initial Gas Saturation	fraction		0	0	0	0				0					0
Temperature	°F		90							68					70
Skin Factor			0	0	0	-3	-3.2	-4.2	-5.9						-4.3
Well Flowing Pressure	psi			20	100	20									
Coal Compressibility	10^{-4} psi^{-1}												4.73	4.69	2.00

Note that the coal compressibility (C_p) reported by Sparks [6] was determined from interference tests where the product of the cleat porosity and compressibility is measured. The reported values assumed a porosity of 0.01, thus if a different porosity is used in the model, the compressibility should be adjusted accordingly.

The effect of stress on the permeability of coals was examined by Sparks [6] and Seidle [16]). As the stress increases, the permeability is decreased. Thus deeper coals will tend to have a lower permeability than shallower coals. This is not the only factor affecting the coal permeability, but it serves as a good starting point for the initial permeability of the individual coals. Using the data from Sparks, on average, the permeability in the Mary Lee coals will be a factor of 0.776 lower than the permeability in the Pratts coals due to the greater depth. For the Black Creek coals the equivalent factor is 0.603. The variation of permeability with pressure was modelled using the Palmer-Mansoori model [17].

Published coal seam relative permeability data are of two types: lab-measured and simulation history-matched. Gas-water relative permeabilities for the San Juan Basin have been published by Gash [18] and Reeves [19], and show distinctly different character. Five sets of data from Australian coal seams derived by history-matching and ten from transient laboratory testing have been presented by Meaney and Patterson [20]. The wide variability is readily apparent.

The variability of the relative permeability and the lack of any laboratory data for the Deerlick Creek field result in this being a history-matching parameter. Any reasonable set of relative permeability curves can be used as a starting point. A set of unpublished history-matched curves from the Mannville coals in Alberta, Canada were selected as a suitable starting point.

Other properties for the modelling of the cleat and matrix systems were taken from the published data listed in Table 1. In many cases there are several different values for the parameters cited by different authors. Table 2 lists the values used in the model. Note that some of the parameters are not physical, but are required inputs for the specific simulation software (for example, the matrix porosity and permeability).

Table 2. Coal Properties in Model.

Cleat Porosity	0.05	
Cleat Permeability (Pratt)	20	md
Cleat Permeability (Mary Lee)	15.5	md
Cleat Permeability (Black Creek)	12.1	md
Matrix porosity	0.005	
Matrix permeability	5.00E-07	md
Initial Water Saturation	0.95	
Temperature	30	C
Cleat Cp	9.0	10^{-5} kPa^{-1}
Matrix Cp	3.0	10^{-5} kPa^{-1}
Water Viscosity	0.6	mPa.s
Initial Pressure (Pratt)	4364	kPa
Initial Pressure (Mary Lee)	5961	kPa
Initial Pressure (Black Creek)	7550	kPa

Construction of Deerlick Creek Model

The production history of each well was downloaded from the Alabama State Oil and Gas Board website and imported into the simulation model.

The final Deerlick Creek model covers an area of 1200 metres square, with grid block dimensions of 50 metres by 50 metres. There are 27 layers in the model – 14 coal seams with 13 intervening shale layers. These intervening layers consist predominantly of shales but may also have silts, sandstones and other lithologies; for simplicity, they shall be referred to as "shales" throughout this report. Figure 4 shows a 3-D view of the model, clearly showing the Pratt, Mary Lee and Black Creek coal zones (the Pratt is in the depth interval from 203-344 mss, Mary Lee 391-486 mss and the Black Creek from 533 to 675 mss).

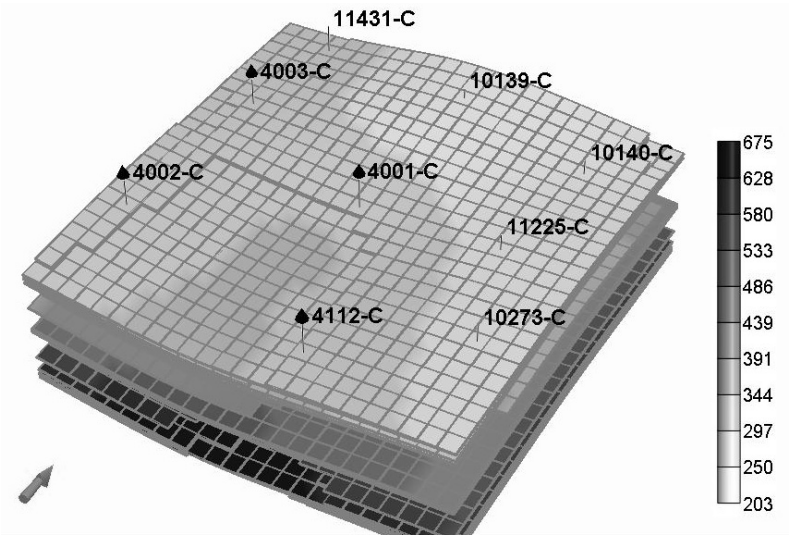

Figure 4. 3D View of Model – Grid Top (mss).

The model includes the 4001-C well and 8 surrounding wells. Although the SECARB field test is focused on the 4001-C well, including the offsetting wells enables CO_2 storage and ECBM options to be examined in detail.

Each well in the model was completed over the historical completion interval. Not all of the coals in each well were completed. In reality, the fracture stimulation of the wells may have connected some unperforated coals to the wells but there is no data to confirm this.

The coal zones are thin compared to their separation, as shown in Figure 5. On the scale of the figure, the coals appear as lines, and the intervening spaces are the shales separating the coals. The figure also shows the perforations of the 4001-C well – not all of the coals have been perforated.

Model Initialisation

The initial pressure in the cleat system was estimated using the normal hydrostatic gradient of 10 kPa/m. No field pressure measurements were available and none of the literature sources specified the depths at which the quoted pressure data were obtained so the validity of the hydrostatic pressure assumption could not be verified.

The coals were assumed to be saturated with methane, so the matrix pressure was set equal to the cleat pressure. The adsorbed gas was assumed to be 100% methane, and its properties were taken from the internal values in the simulator.

History Matching

The model was run several times with different parameters. In all cases, the historical gas rate could not be matched. Figure 6 shows the cumulative gas production from such a run compared to the field data.

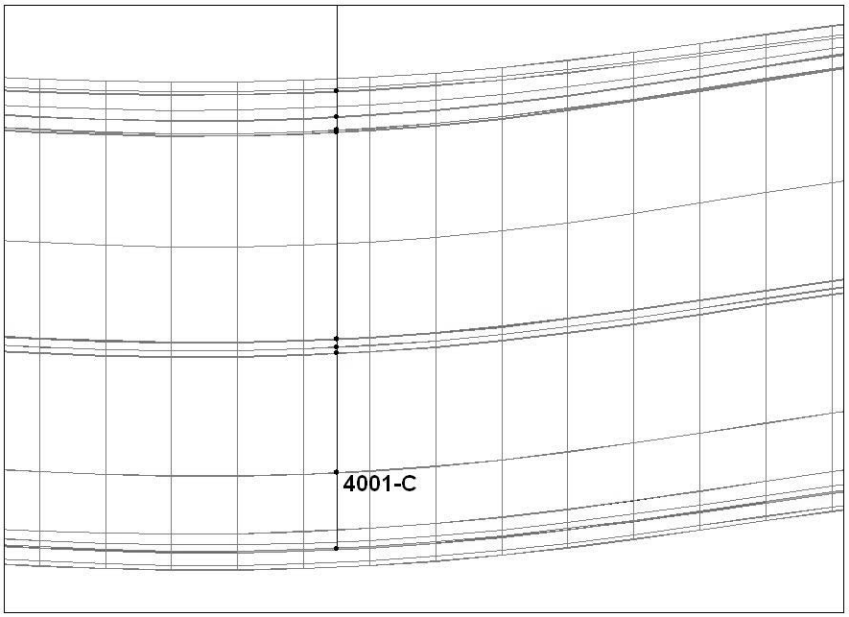

Figure 5. Cross-Section Through Model.

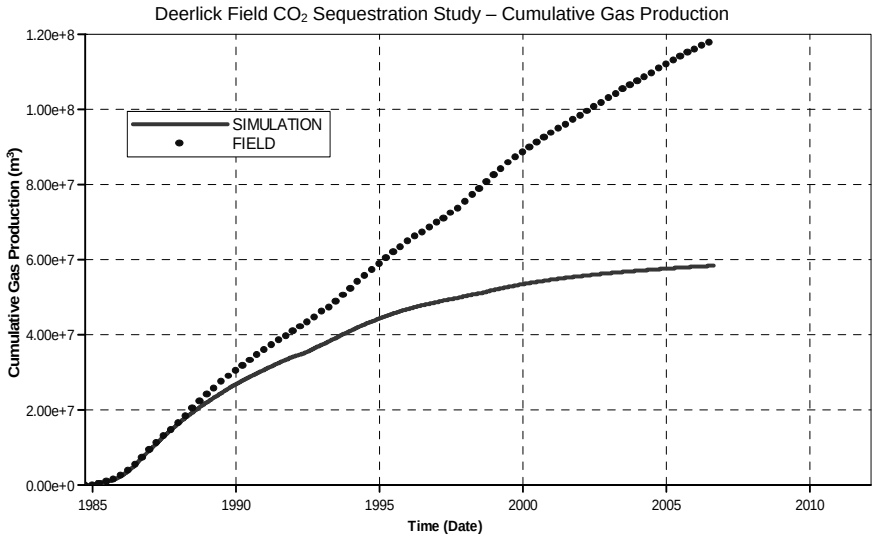

Figure 6. Comparison of Predicted and Actual Cumulative Gas Production (Initial Runs).

Closer examination of the data showed that the original gas-in-place (OGIP) in the model was less than the cumulative gas production. Underestimating the methane content is a common problem in the analysis of CBM projects and has been the subject of numerous papers [21,22,14]. Although the "best practices" were adopted in this study, there are still a number of reasons why this situation could occur:

- Inflow of gas from outside the model area
- Gas content of coals under-estimated
- Net pay of coals too low
- Minor coals not included in model
- Part of produced gas originated in adjacent lithologies (carbonaceous shales, silts, sandstones etc.)

Inflow of Gas From Outside The Model Area

A 2-D model of an area considerably larger than the coal model was built, centered on the 4001-C well. This model included the nine wells of the original model and 43 off-setting wells. Each well was set at its average gas rate and the model was run. The output was put into the "Results" post-processor and stream lines were generated. This indicated the drainage area of each well. All of the wells in the model had a drainage area which extended beyond the area of the model.

Since the drainage area changes as the rates change and new wells are added, the model was run for three time slices. The start of each time-slice coincided with a major addition of new wells. Figure 7 shows the streamlines for the period up to 1992, which is the earliest time slice.

The areas of each drainage area were planimetered and the contributions from outside the coal model area were subtracted from the production data. The rationale for this procedure is that when the wells are in steady state production, the drainage area of each well is proportional to its production rate. Thus the ratio of the areas is a good indicator of the contribution of each area to the total production, providing there are no major pressure gradients. The preliminary runs indicated that the pressure gradients in the coal seams were small, hence the methodology is sound.

Final History Match

The reduced production was introduced into the coal model. The history match was closer, but there was still inadequate gas in the coals to match the field production.

Re-evaluation of the logs with less stringent cut-off criteria increased the net pay in each coal and provided the necessary original gas-in-place. Several thinner coals which had not met the previous cut-off criteria were added which increased the number of layers in the model to 35 – 18 coal seams with 17 intervening shale layers. There were nine coals in the Pratt, five in the Mary Lee and four in the Black Creek coal zones.

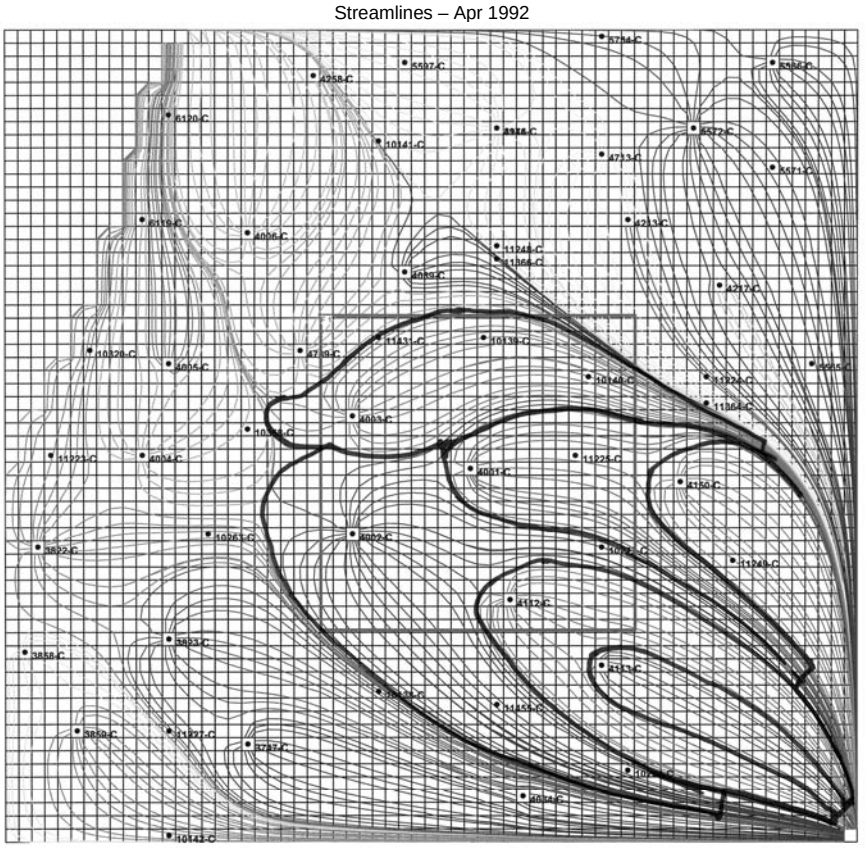

Figure 7. Streamlines for the Drainage Area for the Period up to 1992.

The model was finally history-matched mainly by adjusting the cleat permeability and cleat porosity. Figures 8 and 9 show the match of the gas rate and water rate respectively. The cleat permeability controlled the production rates while the cleat porosity controlled the water production.

There is still considerable uncertainty in the history match. The absence of pressure data means that the true depletion level of the field is not known. The lack of any production logging means that the contribution of each individual coal seam in each well is not known.

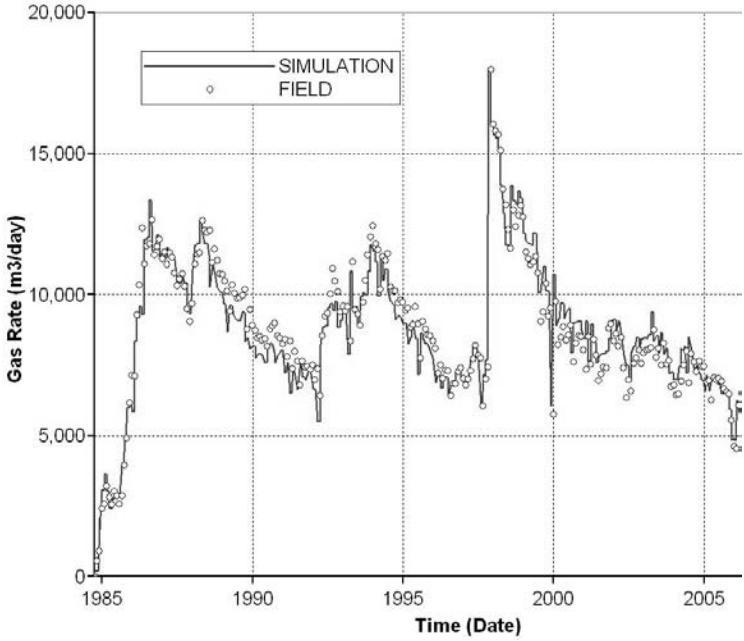

Figure 8. Gas Production Rate (m3/d) – Deerlick Creek Model Area.

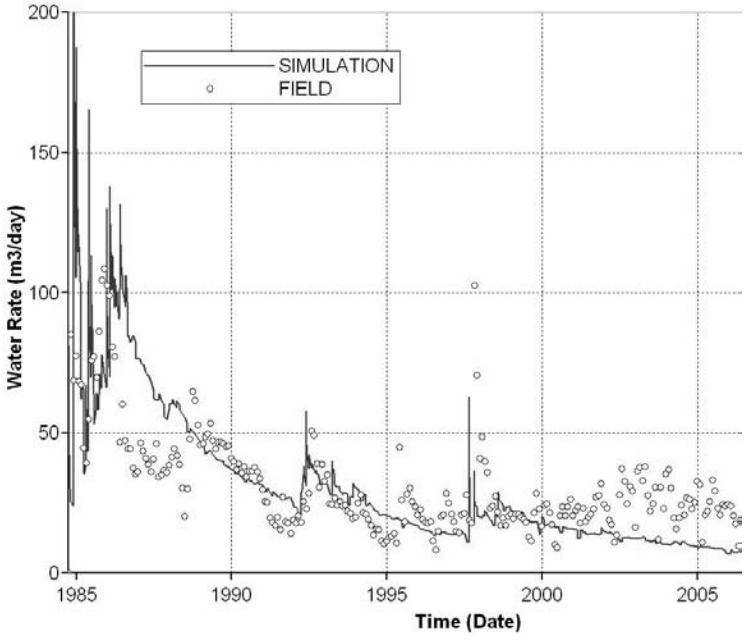

Figure 9. Water Production Rate (m3/d) – Deerlick Creek Model Area.

In the final model, the cleat permeability varied from 12 to 144 md, with the bulk of the reservoir at the lower end of the scale (12 – 20 md). The cleat porosity was 0.05 in those coals which produced considerable water and 0.005 in those with little water production (Coal 3 in the Pratt, Coals 1 and 4 in the Mary Lee and Coal 5 in the Black Creek).

The gas-water relative permeability curves in the final model are shown in Figure 10.

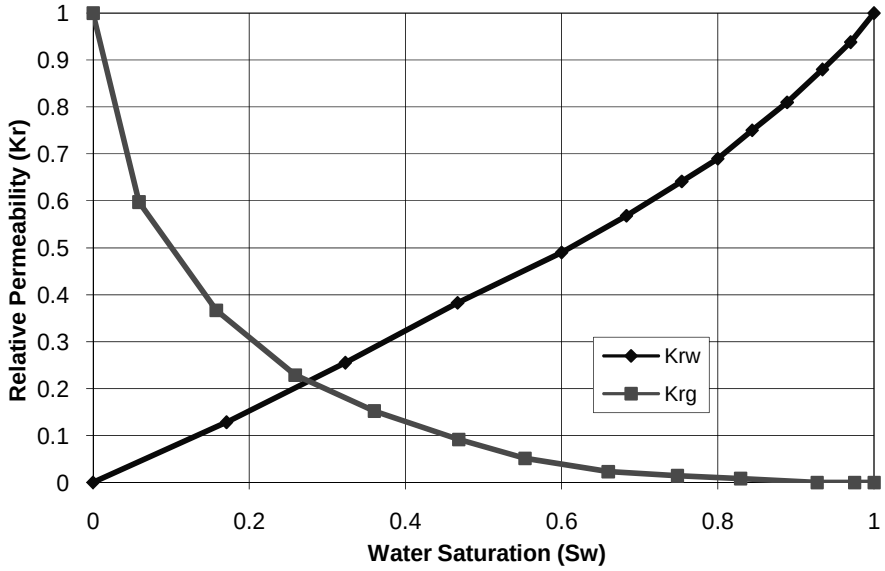

Figure 10. Gas-Water Relative Permeability.

The volumetrics of the final model are shown in Table 3. Note that a small initial gas saturation was included in the cleats (fractures) to improve the numerical performance of the model – this added about 1% to the gas-in-place (i.e. the difference between the "adsorbed gas" and "total gas" in the table above).

Table 3. Deerlick Creek Model Volumetrics.

		FIELD	Black Creek	Mary Lee	Pratt	MATRIX	FRACTURE
Adsorbed Gas	10^6 sm^3	105.6	39.0	34.1	32.6	105.6	0.0
Gas at Surface	10^6 sm^3	106.8	39.0	34.1	32.6	105.7	1.1
Water at Surface	10^3 sm^3	340.2	0.0	0.0	0.0	0.0	340.2
CH4	10^6 moles	4469.2	1648.4	1441.0	1379.8	4469.2	0.0
Average Pressures		FIELD	Black Creek	Mary Lee	Pratt	MATRIX	FRACTURE
Total PV Ave.	kPa	6052.8	7549.9	5961.9	4364.7	5911.6	6053.1
HC PV Ave.	kPa	6046.5	7549.9	5961.9	4364.7	5911.6	6053.1
Ave. Saturations		FIELD	Black Creek	Mary Lee	Pratt	MATRIX	FRACTURE
Gas						1.000	0.050
Water						0.000	0.950

CARBON DIOXIDE STORAGE

CO_2 Injection at Deerlick Creek – SECARB Test

The SECARB plan was described in the "Project Design Package" [23] and this was used as input into the model. The revised plan involves separate injection into the three coal zones. First injection is into the Black Creek coals with 40 tons injected. After a 16 day "pressure stabilization" period, 280 tons will be injected into the same coals. Similar volumes will then be injected into the Mary Lee and Pratt coal zones.

This scheme was input into the model. The pressure and the adsorbed CO_2 distribution in the Black Creek coal zones are shown below in Figures 11 – 12:

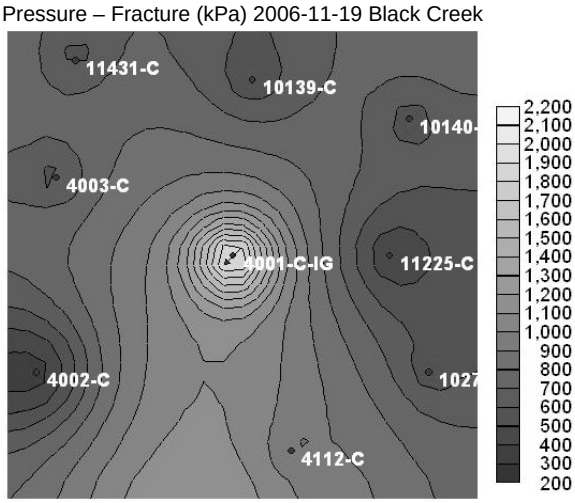

Figure 11. Pressure Distribution in Black Creek Coal Zone Following Injection of 320 tons CO_2.

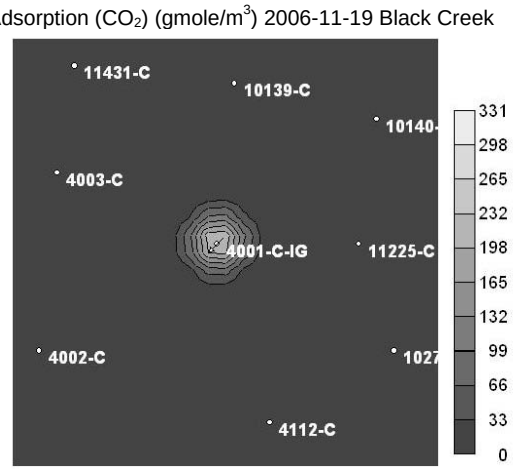

Figure 12. CO_2 Distribution in Black Creek Coal Zone Following Injection of 320 tons CO_2.

The Mary Lee and Pratt zones are similar. In all three zones the amount of CO_2 injected was small but increased the pressure significantly; however it did not result in CO_2 breakthrough at the producing wells.

ECBM at Deerlick Creek

Longer term CO_2 storage was also investigated, with continuous injection into 4001-C (though the well was modelled as separate injectors into each of the three zones). The following cases were run:

- Base Case; no CO_2 injection; 4001-C continuing as a production well.
- CO_2 injection; production throughout to 2040.
- CO_2 injection; production until CO_2 breakthrough, injection continued until 2040.
- CO_2 injection; production until 2020, injection continued to 2040.
- CO_2 injection; production until 2020, injection continued to 2040 at a higher rate.
- Base Case, but all coals with thickness > 0.2 m perforated
- CO_2 injection; production until 2020, injection continued to 2040 at a higher rate, but all coals with thickness > 0.2 m perforated

The results are summarized in Table 4, below:

Table 4. Summary of CO_2 Storage Simulations.

Case No.	Case Description	End Date	Cum. Methane Production (10^6 m^3)	Cum. Water Production (10^3 m^3)	Cum. CO_2 Injection (10^6 m^3)	Cum. CO_2 Production (10^6 m^3)	Net CO_2 Sequestration (tonnes)
0	History	2006-09	69.67	241.3	0	0	0
1	Base Case; no CO_2 injection; 4001-C continuing as a production well.	2040	87.28	262.3	0	0	0
2	CO_2 injection; production throughout to 2040.	2034	87.09	263.9	136.9	32.96	192905
3	CO_2 injection; production until CO_2 breakthrough, injection continued until 2040.	2040	75.71	248.3	168.5	0.00	315028
4	CO_2 injection; production until 2020, injection continued to 2040.	2040	83.52	258.1	177.4	11.12	308237
5	CO_2 injection; production until 2020, injection continued to 2040 at a higher rate.	2038	83.52	258.1	228.9	11.02	407182
6	Base Case, but all coals with thickness > 0.2 m perforated	2040	90.80	302.2	0	0	0
7	CO_2 injection; production until 2020, injection continued to 2040 at a higher rate, but all coals with thickness > 0.2 m perforated	2040	85.91	275.4	233.8	13.34	412022

Note that two cases did not reach 2040 due to numerical problems – results can show the trends compared to the other cases. Figure 13 shows the cumulative methane production for each case. Figure 14 shows the total mass of CO_2 in the model area with time.

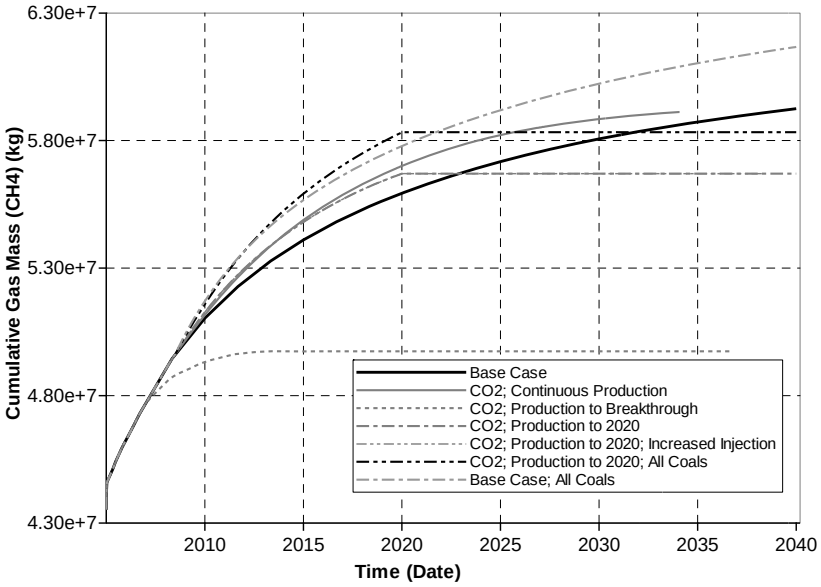

Figure 13. Predicted Cumulative Methane Produced.

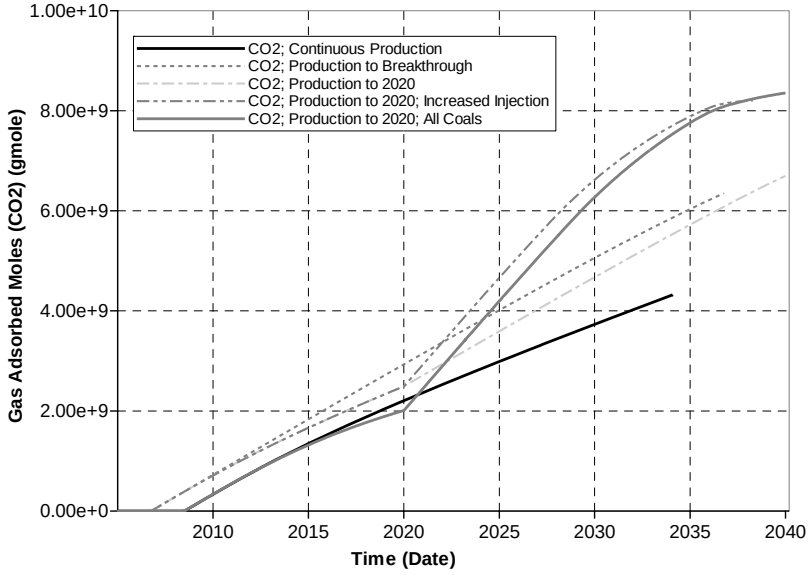

Figure 14. Predicted Cumulative CO_2 Adsorbed.

In the Base Case, the total production to 2040 was 87.3 x 10^6 sm^3, for an incremental production of 17.6 x 10^6 sm^3 (622 MMscf). This corresponds to a recovery factor of 81.7% of the original gas-in-place (OGIP). The high recovery is largely due to the relatively high cleat permeability which results in a fairly constant pressure across the field.

CO_2 breakthrough at the production wells is quite rapid and, if the producers are shut-in when breakthrough occurs, there is significant loss of methane production.

If production is continued after CO_2 breakthrough, the production of methane is enhanced by a small amount, though this appears to be mainly an acceleration effect (see Figure 12).

Shutting-in the producers in 2020 while continuing injection leads to an increase in the CO_2 adsorption rate. There is little loss of methane production. Nevertheless, with the selected injection rate, the coals are not saturated with CO_2 even in 2040, after 33 years of injection.

Increasing the injection after 2020 from 30 ton/d (14600 m^3/d) to 60 ton/d (29300 m^3/d) does saturate the coals with CO_2 by 2040, as indicated by the flattening-off of the cumulative CO_2 adsorption in the model area in Figure 13.

ECBM does not appear to be successful in increasing the recovery of the methane. Closer inspection of the model shows that the methane recovery is increased where the coal has been swept by CO_2, however there are areas which have been poorly swept. Figures 15 and 16 show the distribution of the adsorbed methane in the second coal of the Mary Lee in 2040 with CO_2 injection and without, from cases 6 and 7.

With CO_2 injection, the adsorption at the 4001-C well has been reduced from 362.8 gmole/m^3 to 0, while with no CO_2 injection, the adsorption has been reduced to just 50.3 gmole/m^3.

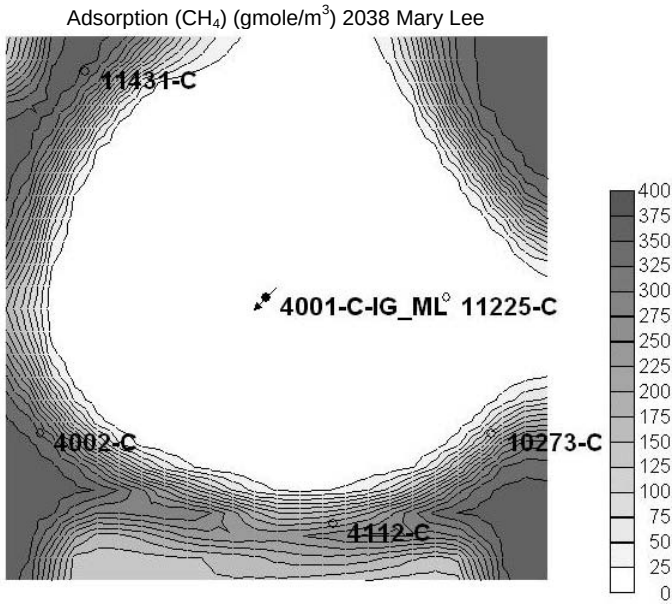

Figure 15. Methane Adsorption in Mary Lee Coal 2 in 2040 – With CO_2 Injection.

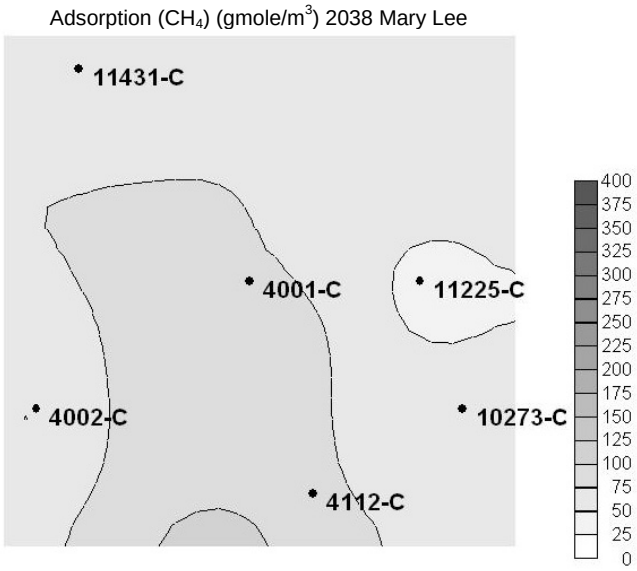

Figure 16. Methane Adsorption in Mary Lee Coal 2 in 2040 – Without CO_2 Injection.

Comparing the two figures clearly shows that considerable methane is trapped along the edges of the model. This is the result of stopping the production early. However, if the producers had not been shut-in, much of the injected CO_2 would have been produced. This would have prevented the pressure from rising to its original value, reducing the CO_2 storage. Figure 17 shows the pressure in a single coal (same coal as in the figures above) under primary, CO_2 injection with continuous production and CO_2 injection with production stopped in 2020.

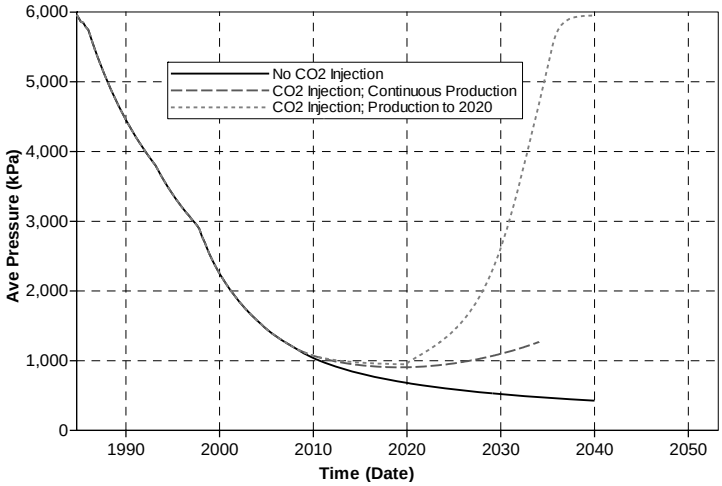

Figure 17. Pressure in Mary Lee Zone.

Figure 18 shows the amount of CO_2 sequestered in the same coal. Continuous production clearly decreases the storage.

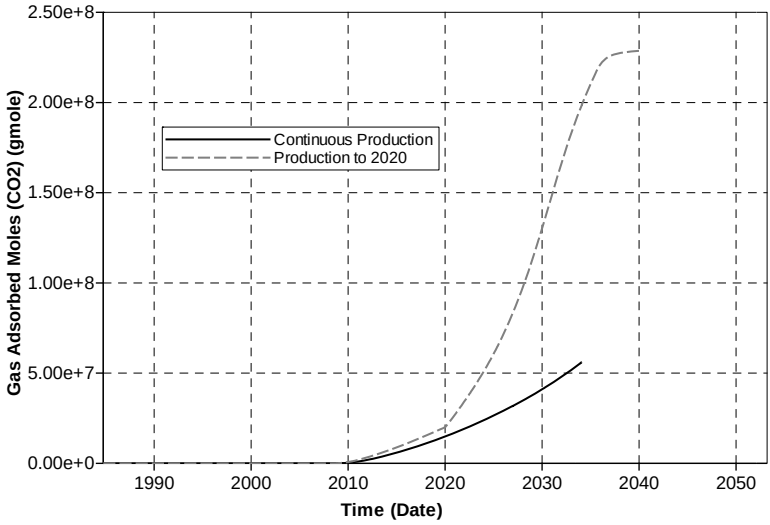

Figure 18. Adsorbed CO_2 in Mary Lee Zone.

Table 4 shows that over 400000 tonnes of CO_2 can be sequestered with the pressure returned to close to the original pressure. Since the model area is 1.44 km^2, the sequestered CO_2 is 286000 tonnes/km^2 or 12.8 tons/acre. This is somewhat lower than the 390000 tonnes/km^2 storage capacity predicted for the coal in the area. There are several reasons for this. The first is that not all of the area has been swept by the CO_2 as shown in the previous figures. Secondly, even with the increased injection rates, the entire area is not re-pressured to the original level. Figure 19 shows the pressure distribution in 2038 for a Mary Lee coal.

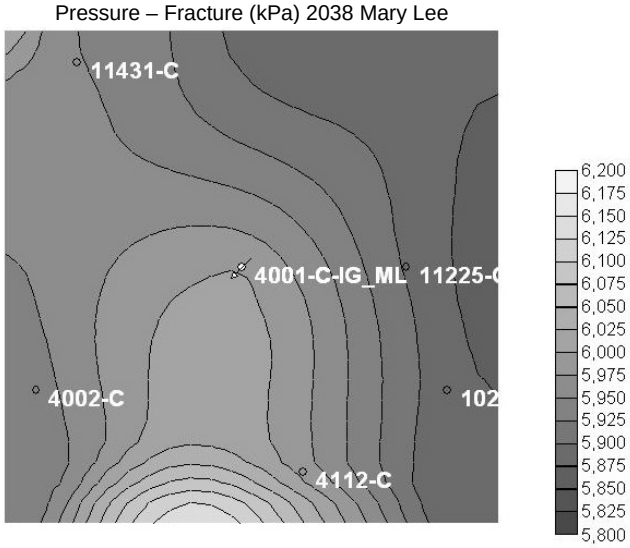

Figure 19. Pressure Distribution in Mary Lee Coal 2 in 2038.

Thirdly, not all of the water in the cleats had been produced. With CO_2 injection, this water can be trapped in areas of low pressure gradient and will prevent CO_2 from adsorbing in those areas. In the model, these areas are along the edges of the model and are artifacts of the model boundaries. Nevertheless, this phenomenon is likely to occur in the reservoir and will serve to reduce the storage capacity. Figure 20 shows the water saturation in the cleats in the Mary Lee coal zone (coal 2) in 2038.

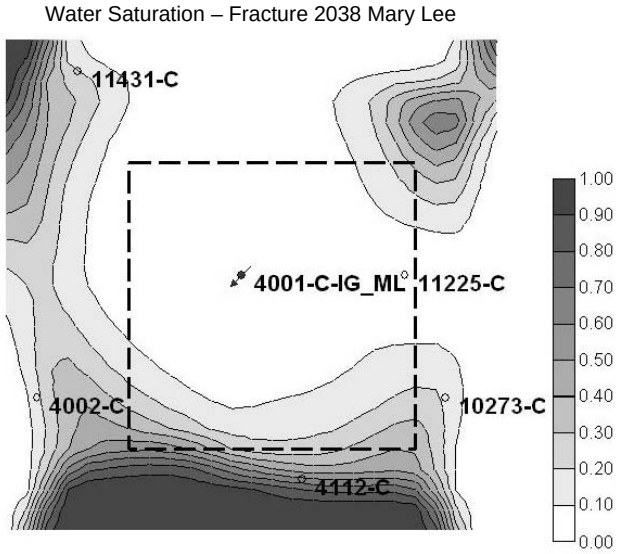

Figure 20. Water Saturation Distribution in Mary Lee Coal 2 in 2038.

If only a 0.5 km^2 region around the 4001-C well as shown in Figure 20 is considered (black dashed box), the CO_2 storage is equivalent to 285164 tonnes/km^2. The methane recovery from this area is 97.9%.

CARBON DIOXIDE SEEPAGE

Development of Overburden Model

In order to model the leakage of the CO_2 from the coal seams to upper horizons and the surface, a model had to be developed which includes the coals and the entire overburden.

The concept of such leakage is that there are natural fissures in the rocks which allow the CO_2 to escape [24-26]. Such fissures can be considered to have an effective vertical permeability, which is a combination of the conductivity of an individual fissure and the frequency of their occurrence.

The logs for the Reichold Chemicals Inc. Research Waste Disposal #1 well were obtained. The location of the well is in section 3, township 21S, range 9W in Tuscaloosa County, Alabama.

The geological zones in the overburden were identified and are listed in Table 5 below, together with the depth intervals.

Table 5. Tops of Overburden Zones.

Zone	Top (ft)	Top (m)
Utley Coal	0	0
Shale/Sand	200	61
Gwin Coal	440	134
Shale/Sand	540	165
Cobb Coal	685	209
Shale/Sand	770	235
Pratt Coal	1090	332
Shale/Sand	1430	436
Mary Lee Coal	1740	530
Shale/Sand	1920	585
Reem Coal	2090	637
Shale/Sand	2160	658
Black Creek Coal	2240	683
Shale/Sand	2460	750
Package 7 Coal	5060	1542
Shale/Sand	5620	1713
Package 6 Coal	5830	1777

The logs were analysed on a 0.15 m basis, with the porosity, volume of shale and a coal indicator calculated.

Overburden Model

A model with 2m layers and one layer for each coal zone was created. Areally the model was coarsened to 5 by 5 blocks.

A cross-section through part of the model is shown in Figure 21.

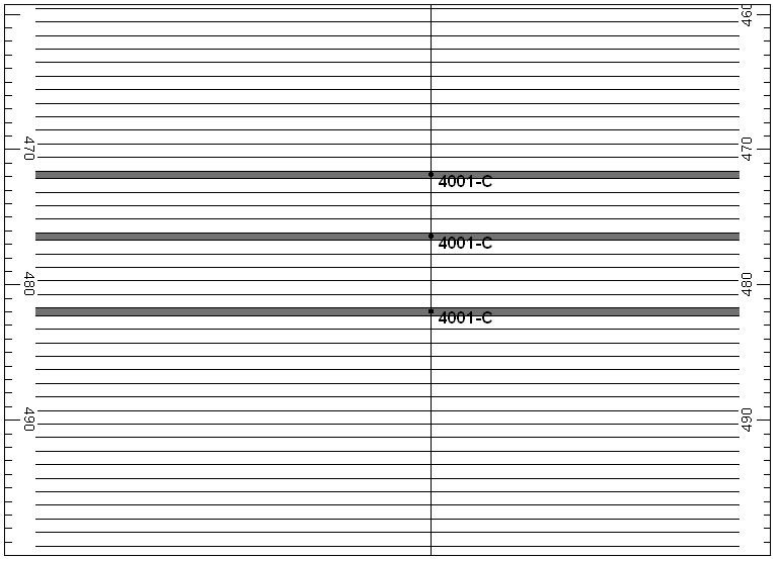

Figure 21. Close-Up View of Overburden Model Showing Grid.

The model includes the coals in the upper zones, namely the Utley, Gwin and Cobb. These have been given the same properties as the lower coals except that the cleat permeability has been set to 10 md. The model has 786 layers and goes from the surface to the base of the Black Creek coal zone. The vertical permeability of the non-coal zones has been initially set to 1 x 10^{-5} md. There are no high quality sands in the upper zones. The porosity distribution peaks at 0.004 and the maximum porosity value is about 0.04. The V_{shale} distribution shows a bi-modal character with a minimum at 0.55.

The original gas-in-place in the producing coals has been adjusted to match the volume in the history-matched model. The historical period was run and the results are comparable to the history match, though not identical. Nevertheless, the model is suitable for modeling the leakage of CO_2 out of the injection zones.

A simulation run was set up with injection of CO_2 to 2030, followed by a 70-year shut-in period. The coal pressure had reached the original pressure in about 2030, so injection was stopped at that time. The run showed some leakage of the CO_2 out of the coals and into the non-coal zones.

Three sensitivities were run using this model, setting the vertical permeability of the non-coal zones to 0.00001, 0.0001 and 0.001 mD.

Note the decline in the pressure after injection was stopped which indicates the loss of CO_2 to the caprock. Figure 22 shows the average pressure in the Mary Lee zone as a function of time for the three cases.

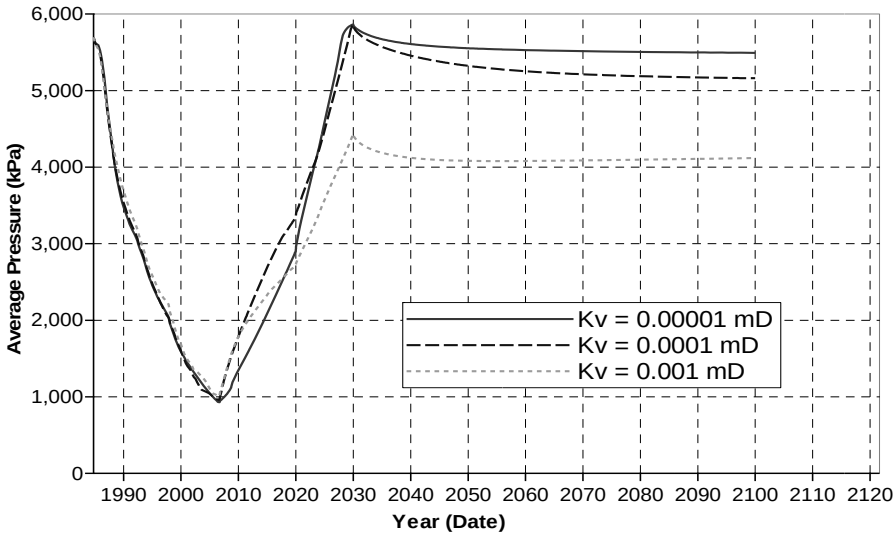

Figure 22. Pressure in Mary Lee Zone to 2100.

Each of these cases had to be run to include the historical production. The results clearly show that the water production rises rapidly as the vertical permeability is increased. Figures 23 and 24 show the gas production rate and the cumulative water production rate for the three vertical permeability values. Clearly only the 0.00001 md case provides a reasonable history match. This puts an upper limit on the effective vertical permeability and hence on the density of the fissures which are responsible for the effective permeability of the non-coal zones.

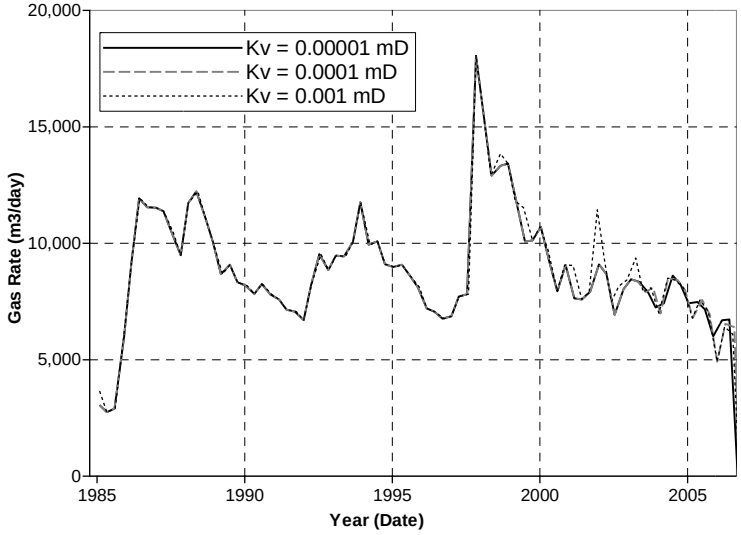

Figure 23. Gas Production Rate – History Match with Leakage to Caprock.

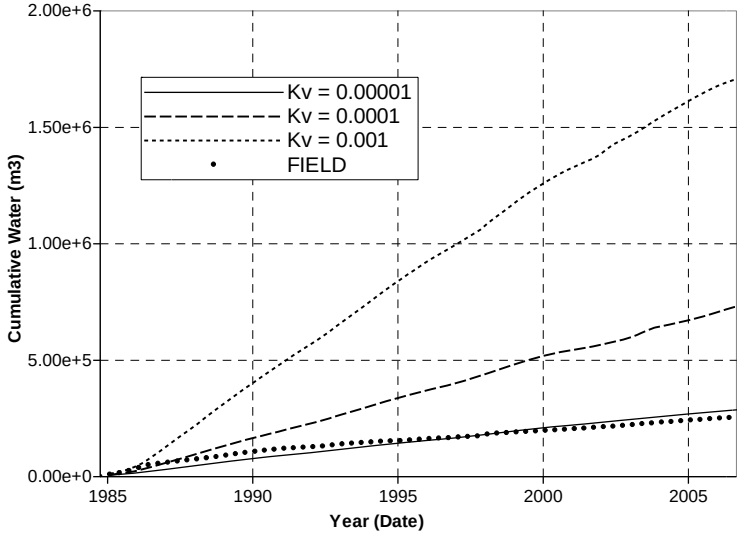

Figure 24. Cumulative Water Production – History Match with Leakage to Caprock.

With the low vertical permeability, there was some leakage of gas out of the coals. Figure 25 below shows the gas saturation in the cleats at the end of the simulation. Since the rock outside the coals is initially water saturated, any reduction in the water saturation represents an increase in the gas saturation, i.e. migration of CO_2 out of the coal. Even by 2100, the gas has not migrated more than 10 m from the coals. Note that no "threshold pressure" for entry of the gas into the shales was assumed, so the results are probably over-estimating the migration.

The conclusion is that migration of the injected CO_2 through natural fissures to the surface is highly unlikely, even over centuries. Other sources of leakage are outside the scope of this project and have not been investigated.

The effect of injecting above the initial reservoir pressure has also not been investigated; if the pressure is high enough, geomechanical effects (e.g. induced fracturing) may increase the migration. This is also outside the scope of the project and would require the addition of geomechanical modeling.

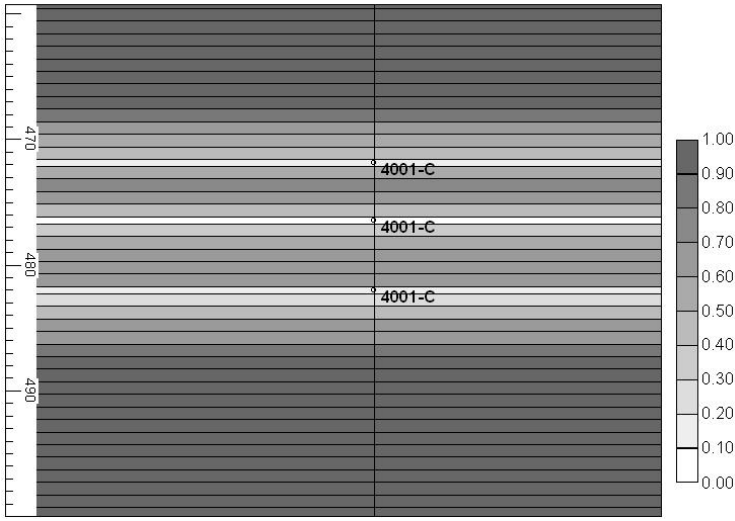

Figure 25. Gas Saturation in Mary Lee Coal Zone – 2100 End of Simulation.

CONCLUSIONS

The coals in the Pratt, Mary Lee and Black Creek coal zones in the Deerlick Creek field in Tuscaloosa County, Alabama have been highly depleted since the start of methane production in 1985. Within the study area, 65.2% of the OGIP has been produced.

Continued primary production to 2040 will increase the recovery to 81.7% of OGIP. If additional coal seams within the same coal zones are completed, the recovery will increase to 85.0% of the OGIP. Note that in the area around each well, the recovery can be as high as 97.9% of OGIP. The difference is the result of non-uniformity in the final pressure distribution and, to a lesser extent, remaining water saturation in the cleats.

The SECARB CO_2 injection test should easily inject the planned volumes of CO_2 into the coal seams, but due to the small volume relative to the size of the resource, the effect will be very local and will not be observed at the offsetting wells.

Continued injection of CO_2 will result in roughly the same methane recovery to 2040 as without CO_2, with some acceleration of recovery. Due to the continued production, the pressure in the coal seams will not increase significantly, and CO_2 storage will be inefficient. Within the model area, only 193000 tonnes of CO_2 will be sequestered, or 134000 tonnes/km^2. Thus the expectation that injection of CO_2 will result in significant "Enhanced Coal Bed Methane" (ECBM) production is not justified. ECBM will presumably be more effective in coal seams which have not been as depleted

in pressure as those in the Deerlick Creek field or where the bottomhole flowing pressure cannot be reduced to a very low value.

Continued injection of CO_2 will also result in rapid breakthrough of CO_2 at the production wells. If the wells are shut-in when breakthrough occurs, then the recovery of the methane will be reduced to 70.9% of OGIP. However, the pressure in the coals will increase and the storage will increase to about 219000 tonnes/km^2.

Clearly, there is a trade-off between storage efficiency and methane recovery. Shutting-in the production wells in 2020 is a suitable compromise. The methane recovery increases to 78.2% of OGIP, while the storage to 2040 increases to 218000 tonnes/km^2.

With the injection rates selected, the CO_2 injection rate is constant throughout the period to 2040, implying that the coals are not saturated with CO_2 after this time. Doubling the injection rate from 2020 to 2040 causes the pressure in each coal seam to rise to close to the original pressure and the injection rate is decreased. Under these circumstances, the storage is increased to 283000 tonnes/km^2. Perforation of additional coal seams can increase this further to 286000 tonnes/km^2.

The amount sequestered is somewhat less than expected from analytical calculations. This is due to non-uniform pressure in the cleat system, pockets of high water saturation in the cleats and lack of continuity in some coal seams.

Modelling leakage of the sequestered CO_2 from the coal seams through the overburden to surface was examined using a model where the entire overburden was included. The model was run with three different effective vertical permeabilities. It was found that, if the effective permeability was greater than 10^{-5} mD, the primary production would have resulted in considerably more water production than was observed. Thus this value of the vertical permeability represents an upper limit for the overburden.

To examine the migration of the CO_2 out of the coals, the model was run with CO_2 injection into the coals to 2030, when the coals are roughly re-pressurized, shutting-in the injection well and continuing the simulation to 2100. The migration of the CO_2 out of the coals was observed in the model, but even in the timeframe modelled, the CO_2 did not migrate more than 10 m above the coal zone. The conclusion is that there is very little risk that the CO_2 will migrate significantly through the fissures to the surface (or sources of potable water) in centuries.

ACKNOWLEDGEMENTS

The CO_2 Capture Project Phase 2 (CCP2) is funded by the industry partnership of BP, Chevron, ConocoPhillips, Eni, StatoilHydro, Petrobras, Shell, and Suncor with additional support being obtained from the U.S. Department of Energy (DOE), the European Union, the Norwegian Research Council, and CCP2 Associate Members Repsol and the Electric Power Research Institute (EPRI).

REFERENCES

1. Graves S. L., A. F. Patton and W. M. Beavers, 1982, "Multiple Zone Coal Degasification Potential in the Warrior Coal Field of Alabama", SPE 10816,presented at the Unconventional Gas Recovery Symposium held in Pittsburg, Pa. May 16-18, 1982.
2. Groshong, R.H. 1998 International Journal of Coal Geology, 38, 89-113.
3. Groshong, R. H. ,M.H. Cox, J.C. Pashin and M. R. McIntyre, 2006 Relationship Between Gas and Water Production and structure in the Southeastern Deerlick Creek Coalbed Methane Field, Black Warrior Basin, Alabama, , Paper 0306, 2006 International Coalbed Methane Symposium.

4. Jin, G, J. C. Pashin and J. W. Payton, 2006 Application of Discrete Fracture Network Models to Coalbed Methane Reservoirs of the Black Warrior Basin, , Paper 0321, 2006 International Coalbed Methane Symposium.
5. Ely, J. W., R. L. Zbitowsky and M. D. Zuber, 1990, "How To Develop a Coalbed Methane Prospect: A Case Study of an Exploratory Five-Spot Well Pattern in the Warrior Basin, Alabama", SPE 20666, prepared for presentation at the 65th Annual Technical Conference and Exhibition of the Society of Petroleum Engineers held in New Orleans, LA, September 23-26, 1990.
6. Sparks, D. P., J. L. Saulsberry and S. W. Lambert, 1995, "The Effects of Stress on Coalbed Reservoir Performance, Black Warrior Basin, U.S.A.", SPE 30734, presented at the Annual Technical Conference and Exhibition held in Dallas, Texas, 22-25 October, 1995.
7. Stremal, K., "Alabama Coalbeds: Ignited by the Section 29 Tax Credit, Drilling Activity in the Black Warrior Basin is Exploding".
8. Lambert, S. W. and S. L. Graves, "Warrior Basin Drilling, Stimulation Covered".
9. Zuber, M. D., W. K. Sawyer, R. A. Schraufnagel and V. A. Kuuskraa, 1987, "The Use of Simulation and History Matching To Determine Critical Coalbed Methane Reservoir Properties", DPE/DOE 16420, prepared for presentation at the SPE/DOE Low Permeability Reservoirs Symposium held in Denver, Colorado, May 18-19, 1987.
10. Soot, P.M., 1992 ,"Coalbed Methane Well Production Forecasting","SPE 24359, prepared for presentation at the SPE Rocky Mountain Regional Meeting Held in Casper, Wyoming, May 18-21, 1992.
11. Seidle J. P. and D. J. Erickson, 1993, "Use of Vogel's Inflow Performance Relation for Coal Wells", SPE 26201, prepared for presentation at the SPE Gas Technology Symposium held in Calgary, Alberta, Canada, 28-30 June 1993.
12. Seidle, J. P., 1992, "A Numerical Study of Coalbed Dewatering","SPE 24358, prepared for presentation at the SPE Rocky Mountain Regional Meeting Held in Casper, Wyoming, May 18-21, 1992.
13. Seidle, J. P. , 2002, "Coal Well Decline Behavior and Drainage Areas: Theory and Practice", SPE 77519, prepared for presentation at the SPE Gas Technology Symposium held in Calgary, Alberta, Canada, 30 April-2 May 2002.
14. Nelson, C. R., 2000, "New Methods for Coalbed Reservoir Gas-In-Place Analysis: Results from Case Studies in the San Juan, Powder River, Black Warrior and Central Appalachian Basins", Gas Research Institute.
15. Pashin, J. C. and P. E. Clark, 2006, "SECARB Field Test for Carbon Dioxide Sequestration in Coalbed Methane Reservoirs of the Black Warrior Basin, Alabama", Paper 0630, 2006 International Coalbed Methane Symposium.
16. Seidle, J. P., M. W. Jeansome and D. J. Erickson, “Application of Matchstick Geometry to Stress Dependent Permeability in Coals”, SPE 24361, presented at the 1992 SPE Rocky mountain regional meeting.
17. Palmer, I. and J. Mansoori, 1996, “How Permeability Depends on Stress and Pore Pressure in Coalbeds: A New Model”, SPE 36737, 1996 ATCE of SPE, Denver, Colorado.
18. Gash, B. W., 1991, “Measurement of ‘Rock Properties’ in Coal for Coalbed Methane Production”, SPE 22909, 66th ATCE of SPE, Dallas, Texas.
19. Reeves, S., “The Coal-Seq Project: Field Studies of ECBM and CO_2 Sequestration in Coal”, 2002, Coal Seq Forum, March 14-15, Houston, Texas.
20. Meaney, K., and L. Paterson, “Relative Permeability of Coal”, 1996, SPE 36986, 1996 Asia Pacific Oil & Gas Conference, Adelaide, 28 October.
21. Mavor, M. J., T. J. Pratt, C. R. Nelson and T. A. Casey , 1996, "Improved Gas-In-Place Determination for Coal Gas Reservoirs", SPE 35623, prepared for presentation at the Gas Technology Symposium held in Calgary, Alberta, Canada, 28 April to 1 May 1996.

22. Weida, S. D. and S. W. Lambert, 2005, "Challenging the Traditional Coalbed Methane Exploration and Evaluation Model","SPE 98069, prepared for presentation at the 2005 SPE Eastern Regional Meeting held in Morgantown, W. V., 14-16 September 2005.
23. Pashin J. C., M. R. McIntyre, P. E. Clark and R. A. Esposito, “Project Design Package, SECARB Black Warrior Test Site Deerlick Creek Field, Tuscaloosa County, Alabama”, August 2007.
24. Klusman, R. W., “Geochemical Perspective And Assessment Of Leakage Potential For A Mature Carbon Dioxide-Enhanced Oil Recovery Project And As A Prototype For Carbon Dioxide Sequestration; Rangely Field, Colorado”, AAPG Bulletin, V. 87, No. 9, September, 2003 PP. 1485-1507.
25. Klusman, R. W., “Detailed Compositional Analysis of Gas Seepage in the National Carbon Storage Test Site, Teapot Dome, Wyoming, USA”, Applied Geochemistry 21, (2006), 1498-1521.
26. Riaz, A. and H. A. Tchelepi, 2006, "Dynamics of Vertical Displacement in Porous Media Associated with Carbon Dioxide Sequestration",SPE 103169, prepared for presentation at the 2006 SPE Annual Technical Conference and Exhibition held in San Antonio, Texas, USA, 24-27 September 2006.

Carbon Dioxide Capture for Storage in Deep Geologic Formations, Volume 3
L.I. Eide (Ed.)

Chapter 26

A RESOLUTION STUDY OF NON-SEISMIC GEOPHYSICAL MONITORING TOOLS FOR MONITORING OF CO_2 INJECTION INTO COAL BEDS

Erika Gasperikova[1] and Jinsong Chen[1]
[1]Lawrence Berkeley National Laboratory, One Cyclotron Road, MS 90R1116, Berkeley, CA 94720

ABSTRACT: We conducted a sensitivity study of gravity and electromagnetic (EM) techniques, and an amplitude versus angle (AVA) analysis for CO_2 movement in coal beds, based on a pilot test planned in the Black Warrior basin in Alabama. Density, sonic and resistivity well logs from a nearby well were used to create background (pre-injection) models. Our laboratory measurements of seismic velocity and electrical resistivity as a function of CO_2 saturation on coal core samples were used to provide a link between the coalbed CO_2 flow simulation models and the geophysical models. The sensitivity study shows that while the injection of the 300 tons of CO_2 into a single layer does not produce a measurable surface response for either gravity or EM, the response to an industrial-size injection would produce measurable surface signals for both techniques. Thus, gravity and EM measurements could be used as a low-cost alternative/supplement to seismic measurements under certain circumstances. Gravity inversion results illustrate that, with high-quality field data and some a priori information about the reservoir depth, we can correctly estimate the spatial location of the CO_2 plume, although with the smoothing constraint of the inversion, the area is slightly overestimated, resulting in an underestimated value of density change. AVA analysis shows that by inverting seismic and EM data jointly, much better estimates of CO_2 saturation can be obtained, especially in the third of three injection zones, where seismic AVA data alone fail to detect the high CO_2 saturation.

INTRODUCTION

Cost-effective monitoring of CO_2 movement during sequestration is a necessary part of a practical geologic sequestration strategy. Previous analysis of the spatial resolution and detectability limits of non-seismic geophysical techniques found that surface and borehole based electromagnetic (EM) and gravity measurements could, under certain circumstances, be used as a lower-cost alternative to seismic geophysics [1]. An analysis of the cost of gravity and EM surveys needed for monitoring of enhanced oil recovery (EOR) projects showed that they are ten times less expensive than conventional 3D seismic surveys [2]. However, the reduction in cost is accompanied by a reduction in spatial resolution, and thus the applicability of non-seismic techniques depends on site specifics and the monitoring questions needed to be addressed.

Significant potential exists for carbon sequestration and enhanced methane recovery in coalbed methane (CBM) production scenarios. However, in order to assure the safety and security of CO_2 storage in unmineable coal beds, one of the necessary tasks is to develop reliable monitoring and verification tools appropriate to the special conditions of CO_2 flow and storage in coal. Our study was motivated by a pilot test planned in the Black Warrior basin in Alabama. The coal seams in the Black Warrior basin are distributed through a thick stratigraphic section and are clustered in a series of coal zones within the Lower Pennsylvanian Pottsville Formation. Assessment of the CO_2

sequestration and enhanced recovery potential of CBM in this area indicate that more than 5.9 Tcf of CO_2 could be sequestered, while increasing CBM reserves by more than 20% [3]. Within the Black Warrior basin, coalbed methane is produced mainly from the Black Creek, Mary Lee, and Pratt coal zones, at depths between 400 m and 700 m with an average thickness of ~3 m. The coal permeability in the Black Warrior basin decreases exponentially with depth as the overburden stress increases: permeability of the top layer is 100 mD; permeability of the deepest layer is around 1 mD. The pilot field test will include injecting a total of 1,000 tons of CO_2 into these three coal zones (~300 tons for each zone).

In connection with the Southeastern Regional Carbon Sequestration Partnership (SECARB) pilot test, we evaluated gravity and EM techniques, as well as an amplitude versus angle (AVA) analysis for monitoring of CO_2 enhanced CBM production. We studied responses for three different models: (1) the background (pre-injection) model, (2) CO_2 injection into one coal zone, and (3) CO_2 injection into three coal zones. Flow simulations were provided by Sproule Associates, Ltd. [4]. Laboratory measurements of seismic velocity and electrical resistivity as a function of CO_2 saturation on a coal core sample [5] were used as a link between the coalbed CO_2 injection flow simulation results and the geophysical models. The experimental data showed that seismic P- and S-wave velocities were reduced on the order of 10% by the CO_2 flood. Electrical resistivity increased by 160% in the core when flooded by CO_2. These experimentally determined values were used as end members of an assumed linear trend for velocity and resistivity over the range from 0 to 100% CO_2 saturation. The inversion of gravity data is very important, since construction of density contrast models significantly increases the amount of information that can be extracted from the gravity data. Therefore, we used a new gravity inversion algorithm that uses depth of reservoir as *a priori* information and solves for a smooth density variation within the reservoir [6]. Simulated seismic data were imaged using industry-standard seismic processing techniques, followed by acoustic AVA inversion to obtain reservoir fluid properties. The CO_2 content predicted from the seismic AVA data was compared to those obtained from joint inversion of seismic AVA and EM data.

RESULTS AND DISCUSSION

Gravity monitoring

Gravity methods are sensitive to density change. For most of the depth intervals of interest for sequestration, CO_2 is less dense than water or coal. The reduction in the vertical component of gravity is caused by increased CO_2 saturations reducing the bulk density of the coal layer. The spatial pattern of the change in the vertical component of gravity is directly correlated with the net change in density of the coal bed.

One of the factors that affects the feasibility of any geophysical technique is the magnitude of the change in the measured geophysical property, in this case a surface gravity response, produced by increasing CO_2 saturation. Hence, calculating the expected gravity response for different sequestration scenarios is an essential part of a survey design. A simplified model was created to investigate whether a variation in CO_2 saturation within a coal layer would produce a measurable surface gravity response. The model consisted of a 3 m thick coal layer with a density of 1,435 kg/m^3 at a depth of 400 m. A plan view of the model is shown in Figure 1a; a section view is shown in Figure 1b. The undisturbed coal layer is on the left; a coal layer containing CO_2 is on the right.

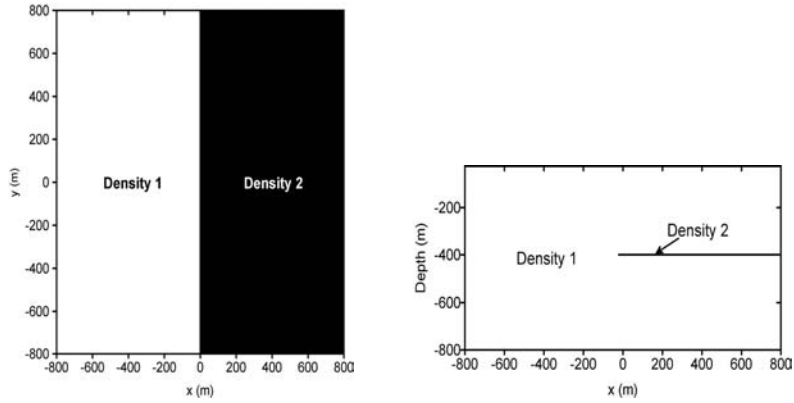

(a) (b)

Figure 1. (a) Plan view and (b) cross-section of a density model with a coal layer with no CO_2 on the left and with CO_2 on the right.

We calculated the density of CO_2 using the NIST14 code [7] at a temperature of 35°C (i.e., 308°K or 95°F) and a pressure of 600 kPa, given that those were used in flow simulations. Under these conditions, the density of CO_2 is 10.6 kg/m^3. If we define CO_2 saturation as S_{CO2}, then the layer bulk density is given by:

$$Density = \left(1 - S_{CO_2}\right) * Density\left(coal\right) + S_{CO_2} * Density\left(CO_2\right)$$

Resulting density values and their corresponding peak gravity responses for 0, 10, 20, 50, 70, 80, and 90% of CO_2 saturation are listed in Table 1. The presence of CO_2 reduces the coal density and thus causes a decrease in the gravity response. Adsorption of CO_2 into coal can affect the matrix density, and hence the total density change could be smaller than we predicted, because changes in the matrix density were not considered.

Table 1. Coal layer density and peak gravity response as a function of CO_2 saturation at temperature of 35°C and pressure of 600 kPa.

% CO_2	Density (kg/m^3)	Peak gravity response (μGal)
0	1435.0	0
10	1292.6	-9
20	1150.1	-18
50	722.8	-46
70	437.9	-64
80	295.5	-73
90	153.0	-82

The vertical component of the gravity response is defined as the difference between the models with and without CO_2. Figure 2 shows the surface gravity response (in μGal) for 20% of CO_2 saturation. The maximum gravity response is -18 μGal. The contact between areas with and without CO_2 is clearly visible, and the surface gravity response can be measured using current technologies. A 5-7 μGal and 3.5 μGal survey accuracy has been reported for gravity surveys at Prudhoe Bay, Alaska [8, 9]. A repeatability of 3 μGal and detection threshold of 5 μGal for time-lapse variations was observed in gravity monitoring surveys at the Sleipner CO_2 sequestration site and the Troll gas field in the North Sea [10, 11]. For the model with 50% CO_2 saturation, the maximum gravity

response is -46 μGal, while for the model with 90% CO_2 saturation, the maximum gravity response is -82 μGal. The surface gravity response decreases with increased CO_2 saturation. The presence of CO_2 reduces the layer density and thus decreases the gravity response.

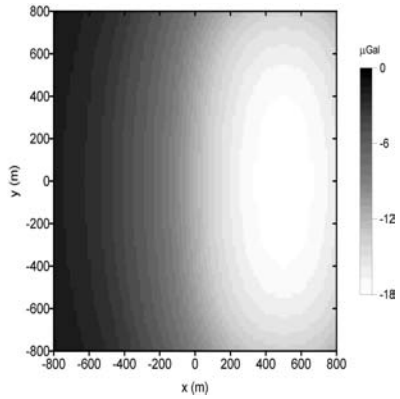

Figure 2. Surface gravity response (in μGal) for the coal layer in Figure 1 with 20% CO_2 saturation.

In the proposed pilot test, the amount of injected CO_2 into three coal layers is limited. Flow simulation models showed that the highest CO_2 mole fractions and the largest spatial extent of CO_2 exist in the upper two coal layers (see Figure 5). CO_2 in the deepest layer hardly moved from the injection well, presumably due to very low permeability. Guided by these simulations, our reference density model was a coal layer with 95% water saturation and 5% residual gas saturation. Assuming that the water in fractures is replaced by CO_2, and neglecting any changes in the matrix density, we calculated the surface gravity response for each of the three layers independently and then for all of them together. Figure 3a shows a plan view and Figure 3b a section view of the model. The coal layer at the depth of 400 m was 3 m thick, and the CO_2 anomaly was 300 × 200 m wide, with 50% CO_2 saturation.

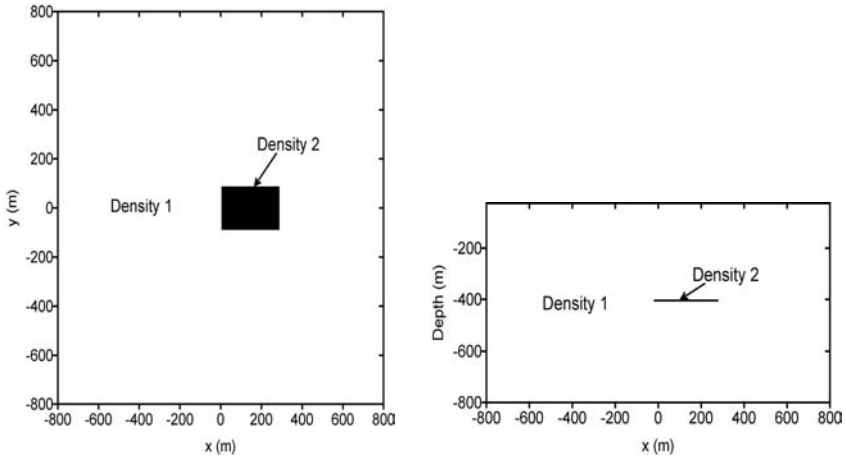

(a) (b)

Figure 3. (a) Plan view and (b) cross section of a density model based on a flow simulation model.

Figure 4 shows the surface gravity response for the CO_2 plume at a depth of 400 m. The maximum response is -5 μGal, which is on the edge of detectability in the field. Gravity anomalies decay with the inverse square of the distance from their source; hence, the same plume at 600 m or 750 m produced an even smaller surface gravity response (not shown), one that would be difficult to detect in the field. However, if the layer thickness at a depth of 400 m would be 6 m, instead of 3 m, and the CO_2 plume had the same lateral extent (300×200 m), the maximum surface gravity response would be -10 μGal. This anomaly response is above the detection threshold and therefore would be measurable in the field. The deepest coal layer, at a depth of 750 m, with the same lateral extent and properties as described above, would be detectable by surface gravity only if its thickness was 18 m. Similarly, surface gravity measurements would be above the detection threshold when all three layers are present. In this case, the thickness of each layer would be 3 m, the lateral extent 300×200 m, with each layer containing 50% of CO_2, the depths of 400, 600, and 750 m, respectively. As mentioned earlier, the surface gravity response decreases with the square of the distance to the source. Hence, while the model contains identical CO_2 anomalies in three different layers, most of the response comes from the layer at 400 m, with less from the layer at 600 m and lesser still from the layer at 750 m.

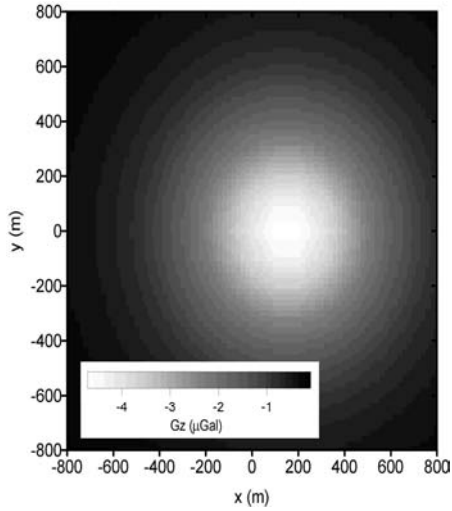

Figure 4. Surface gravity response (in μGal) for the model in Figure 3. The coal layer at 400 m depth is 3 m thick; the CO_2 plume is 300×200 m wide and contains 50% CO_2.

Gravity inversion

Inversion of gravity data is very important, since construction of density contrast models significantly increases the amount of information that can be extracted from the gravity data. However, one substantial difficulty with the inversion of gravity data is its inherent non-uniqueness and lack of inherent depth resolution. This difficulty can be overcome by introduction of *a priori* information. We adopted the approach described by [12] for magnetotelluric data inversion, in which the top and base of the reservoir are assumed to be known, and we invert for a smooth density variation inside the reservoir. The inversion result is a cumulative density change in the reservoir as a function of x and y coordinates. To illustrate this approach we took the CO_2 mole-fractions model shown in Figure 5 and created the density model shown in Figure 6. We first calculated the surface gravity response to this model (Figure 7) and then ran the inversion.

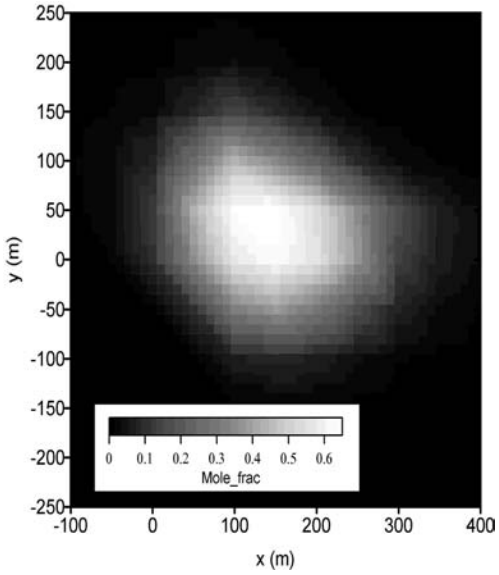

Figure 5. Plan view of CO_2 mole fractions in the coal layer at a depth of 400 m (from Sproule Associates).

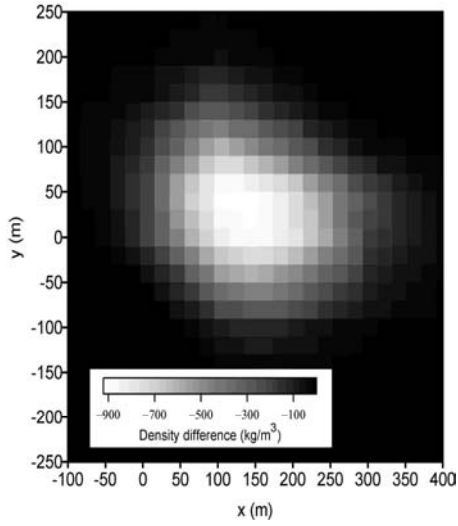

Figure 6. Plan view of a density model (kg/m^3) based on the flow simulation model in Figure 5.

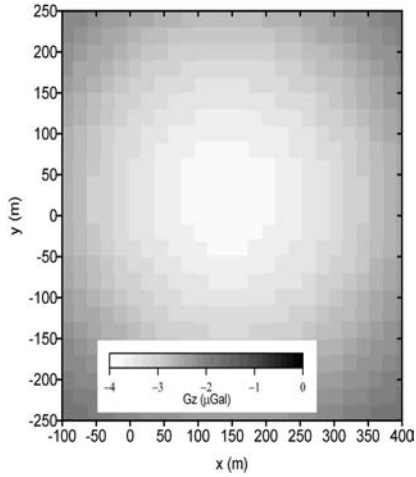

Figure 7. Surface gravity response (μGal) of the model in Figure 6.

Figure 8 shows inversion results from the surface gravity data shown in Figure 7. The true density difference is shown by the white contours. CO_2 plume location was recovered correctly, although with the smoothing constraint of the inversion, the area was slightly overestimated, resulting in an underestimated value for density change (Figure 8a). The inversion of gravity data from Figure 7 with 1 μGal random noise (25% of peak value) added results in the correct location of the CO_2 plume; however, the density contrast is not resolved (Figure 8b). We believe that this would be a realistic noise level if new instruments were able to measure such low response in the field. Gravity inversion results illustrate that, with high-quality field gravity data and some a priori information about the depth of the reservoir, the spatial location of CO_2 plume and density contrast can be recovered. However, as we concluded above, this model response is too small to be detected in the field.

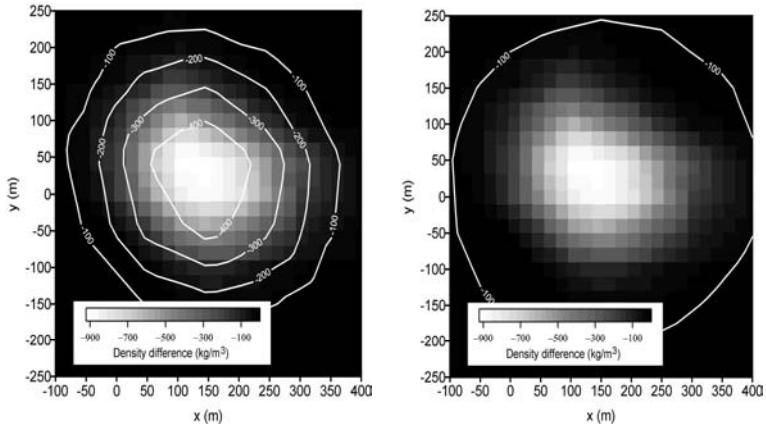

Figure 8. Density change (kg/m^3) as a function of x and y coordinates recovered by inversion of (a) the noise free, and (b) with 1 μGal random noise (25% of peak response) added to the data shown in Figure 7. The true density difference is shown by the white contours.

EM monitoring

The electrical resistivity of reservoir rocks is highly sensitive to changes in water and gas saturation. This high sensitivity can be exploited by EM techniques, in which the response is a function of the electrical resistivity of the medium. One possible technique employs a grounded electric dipole energized with an alternating current at a given frequency (e.g., 1 Hz) to produce time-varying electric and magnetic fields that can be measured on the ground surface. In this configuration, the electric dipole consists of two steel electrodes (1 m^2 plates or sections of drill pipe) buried at a shallow depth (1–10 m), separated by 100 m, and connected by cables to a low-power generator (typically a portable 5,000 W generator is sufficient). A setup schematic is shown in Figure 9a, and instruments photos are shown in Figure 9b. The measured data consist of the electric field at a given separation from the transmitter, acquired on the ground surface or within the near surface.

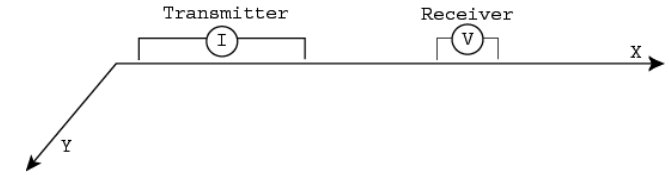

(a)

(b)

Figure 9. EM survey: (a) schematic, (b) equipment photos.

As described earlier, the pilot study area contains three main coal layers: Pratt, Mary Lee, and Black Creek. According to the annotated coal lithology log of J.D. Jobson 24-14 #11 Well, a part of the SECARB II project design package, the top of the Pratt zone is located at 396 m depth with injection zone between 405 and 442 m; the top of the Mary Lee zone is located at 574 m depth, with injection zone between 592 and 610 m; and the top of the Black Creek zone located at 673 m depth, with injection zone between 750 and 760 m. Decreased water saturation resulting from CO_2 injection should lead to a change in the electrical resistivity of the reservoir rock. We used the resistivity log from a deep disposal well (located a couple of miles from the pilot test site) to build our background resistivity model. We also used results from our previous laboratory measurements to estimate how the presence of CO_2 influences coalbed resistivities. Our laboratory results show that CO_2 can cause up to 150% resistivity increase in coal. Assuming that the layers within each injection zone will be influenced by the presence of CO_2 in a manner similar to that in the laboratory measurements, we created our CO_2 models. Resistivity values as a function of depth for both the background and CO_2 models are plotted in Figure 10. The solid line represents the background model; the dashed line represents the CO_2 model.

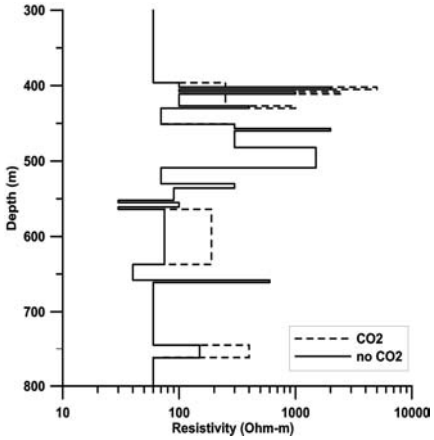

Figure 10. Resistivity profiles as a function of depth for the background model (solid line), and CO_2 model (dashed line).

We calculated 1D responses of both models using an electric point dipole as a source (transmitter) and an electric point dipole as a receiver. Both "in-line" and "broad-side" responses were calculated for transmitter-receiver offsets up to 4 km. The transmitter was oriented in the x-direction. When both the transmitter and receivers are on the same line (i.e. y(Tx)=0 and y(Rx)=0), the configuration is referred to as an "in-line" configuration. When the transmitter is on a different line from the receivers (e.g. y(Tx)=0 and y(Rx)=150), the configuration is referred to as a "broad-side" configuration. Since the in-line responses were much smaller than the broad-side responses, we present here the broad-side responses only. The amplitude and phase plots for the broad-side electric field Ex-component for models with and without CO_2 are presented in Figure 11. The solid curves represent the responses of the background model, while the dashed curves represent the response of the model with CO_2 presence.

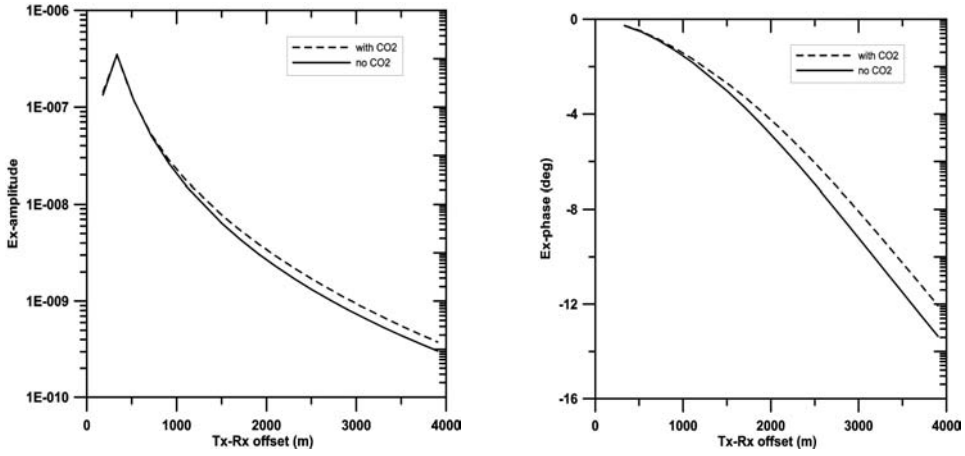

(a) (b)

Figure 11. (a) Amplitude and (b) phase of Ex field for models in Figure 10.

These results show the maximum responses at the offsets larger than 2 km. Responses to individual injections zones (not shown) were smaller than those to all three zones together. The ability to observe this difference in the field would depend on the signal-to-noise ratio of the data. While this technique has been successfully used in the offshore environment, it has not been tested for a CO_2 sequestration scenario on land. Future plans should incorporate field demonstration of the EM technique to verify its feasibility.

Amplitude vs. Angle (AVA) Analysis

Monitoring field-scale CO_2 saturation is important for CO_2 sequestration. Time-lapse geophysical methods, for example surface seismic and EM, have the potential of providing such information, and hence they can be considered as candidate monitoring tools. In this section, we investigate, through synthetic case studies, the feasibility of using time-lapse seismic AVA and EM data to monitor CO_2 injection into coal beds. We assume that the background information, such as the thickness of each layer, seismic P- and S-wave velocities, density, and electrical resistivity can be obtained from borehole logging.

Seismic data

Synthetic seismic data were generated using a 2D finite-difference staggered-grid code, which models elastic wave propagation in arbitrarily inhomogeneous media [13]. Using a 18 Hz Gaussian derivative source wavelet, we simulated the responses of three different cases: (1) a background (pre-injection) model (referred to as Mod0) using the well logs from a nearby well, (2) a model with a 10% decrease in P-wave velocity and a 5% decrease in density in the top injection zone (referred to as Mod1), and (3) a model with a 10% decrease in P-wave velocity and a 5% decrease in density in all three injection zones (referred to as Mod2). The wavelet contains frequencies up to 60 Hz, and since we work with differential data, we can detect very subtle changes even though the choice of the source wavelet frequency might seem low. The decrease in P-wave velocity and density resulting from the presence of CO_2 was based on our laboratory measurements of coal samples [5]. Figure 12a shows the seismic P-wave velocity cross-section when CO_2 is injected into the top injection zone, whereas Figure 12b shows the seismic P-wave velocity cross section when CO_2 is injected into the three injection zones. The CO_2 plume was 300 m wide from x = 850 m to x= 1,150 m.

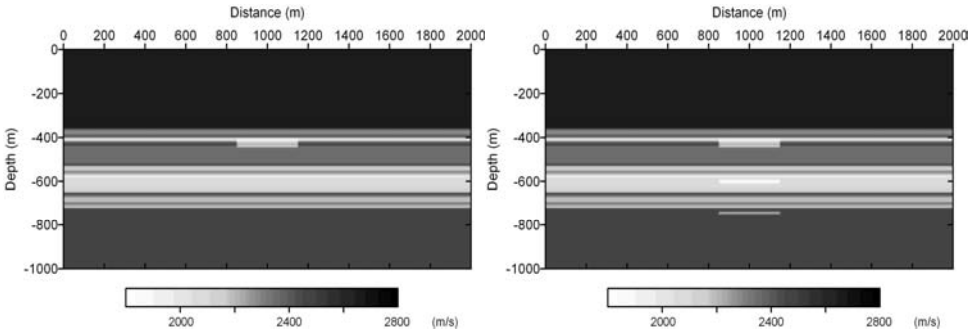

(a) (b)

Figure 12. 2D seismic P-wave velocity models for CO_2 injection (a) into the top injection zone, and (b) into the three injection zones.

After normal move-out (NMO) correction, we created a common depth point (CDP) stack and AVA data. We generated seismic AVA first for the background model, and then for the injection zone(s) with 95% CO_2 saturation. The seismic data were normalized by the maximum amplitude. The normalized differences in seismic AVA responses between the model with CO_2 plume and the background model were considered as time-lapse AVA data. Because only the first four incident angles (corresponding to 0, 1.9, 3.8, and 5.7 degrees, respectively) had responses to all the zones, we used them only for the inversion. At this point, the AVA inversion was carried out using a 1D numerical code (justified by comparison of the 1D approximation with the 2D data, shown below). The same source wavelet as in the 2D forward code was used in the 1D seismic code in the AVA inversion. The 1D seismic data were calculated by convolving seismic reflectivity with a Gaussian derivative wavelet having a center frequency of 18 Hz. Seismic AVA reflectivity is an explicit function of seismic P- and S-wave velocities and density in the given layers, and is calculated using the Zoeppritz's equations [14].

A comparison of normalized differences in seismic AVA data for the model with a CO_2 plume in the top injection zone, calculated using the 1D approximation and 2D numerical methods, is shown in Figure 13a. The same comparison for the model with CO_2 present in the three injection zones is shown in Figure 13b. Figure 13 shows that the 1D convolution model provides a good approximation of the 2D data for the four small angles.

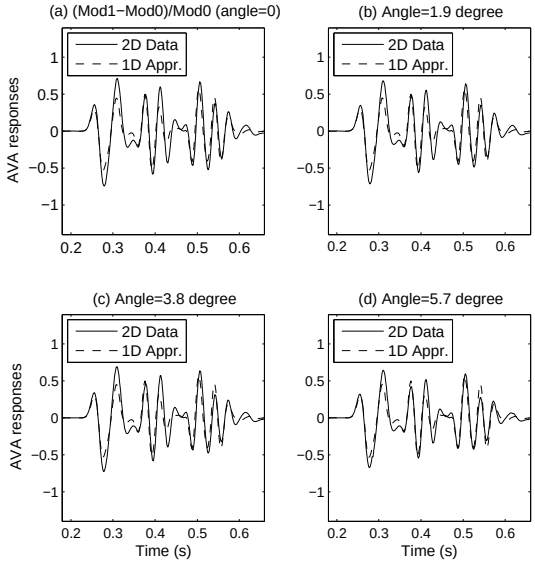

Figure 13a. Comparison of differences in normalized seismic AVA data, (Mod1-Mod0)/Mod0, for four incident angles, where the solid curves are calculated using 2D numerical methods and the dashed curves are calculated using 1D convolution method.

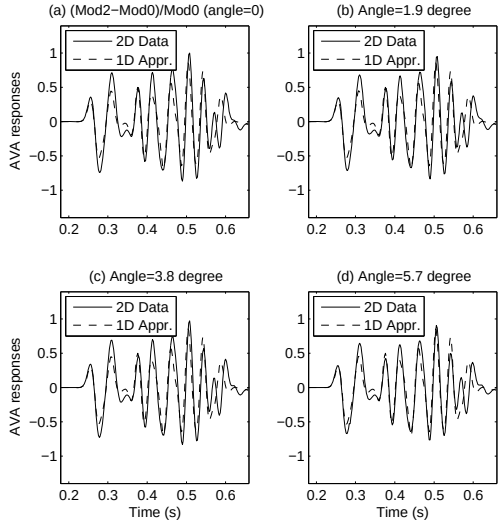

Figure 13b. Comparison of differences in normalized seismic AVA data, (Mod2-Mod0)/Mod0, for four angles, where the solid curves are calculated using 2D numerical methods and the dashed curves are calculated using 1D convolution method.

EM data

Synthetic EM data were generated using 2D numerical methods [15] at two frequencies (1 Hz and 10 Hz), with five transmitter locations (-2000 m, -1900 m, -1800 m, -1700 m, and -1600 m), and 60 receivers located from -1000 m to 1900 m with a separation of 50 m. Again, three cases were considered: (1) the background (pre-injection) model (referred to as Mod0) using the resistivity log from the nearby well, (2) the model with a 150% increase in resistivity in the top injection zone (referred to as Mod1), and (3) the model with a 150% increase in resistivity in the three injection zones (referred to as Mod2). The increase in resistivity caused by the presence of CO_2 was based on our laboratory measurements of coal samples [5]. Figure 14a shows the resistivity cross section when CO_2 was injected only into the top injection zone, whereas Figure 14b shows the resistivity cross section when CO_2 was injected into all three injection zones. Again, the CO_2 plume was 300 m wide from x = 850 m to x= 1,150 m.

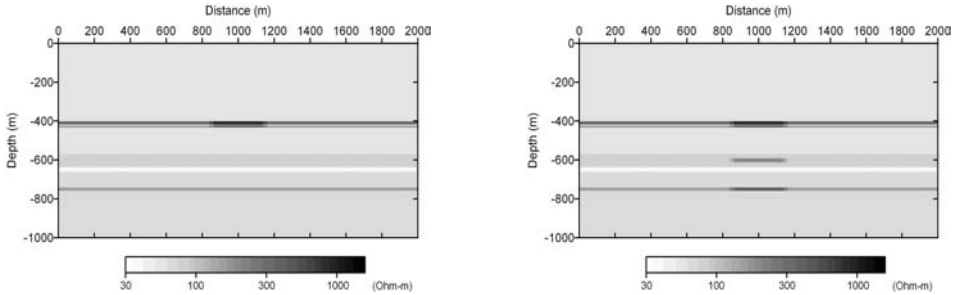

Figure 14. 2D resistivity models for CO_2 injection
(a) into the top injection zone, and (b) into all three injection zones.

Figure 15a compares the ratios of Mod1/Mod0 EM responses calculated using the 2D numerical method (solid curves) with those using the 1D method (dashed curves). Similarly, Figure 15b compares the ratios of Mod2/Mod0 EM responses calculated using the 2D numerical method (solid curves) with those using the 1D method (dashed curves). The values obtained from the 1D method are significantly larger than those obtained by the 2D method. This is understandable, because in the 1D model, we assume that the entire layer (an infinite extent) is CO_2 saturated, whereas in the 2D model, the CO_2 zone is only 300 m wide (a finite extent). The 2D EM responses clearly identify the lateral boundaries of the injection zones, located between 850 m and 1,150 m. If we focus on the EM data within the injection zones, we find that the slopes in the 1D and 2D data show some similarities, even though the slopes from the 2D calculation are sharper than those obtained from the 1D method. Further studies are needed to better understand this approach advantages and limitations.

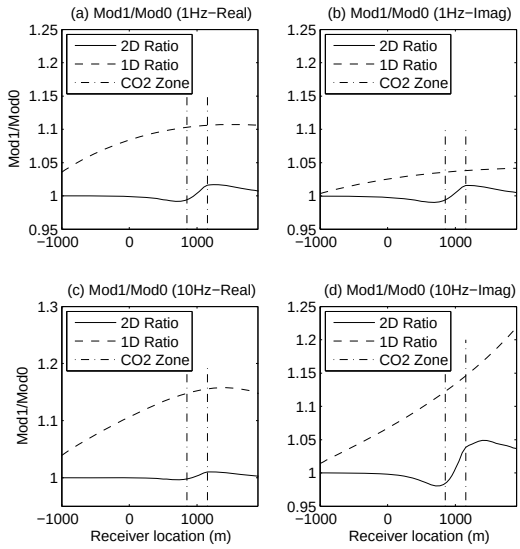

Figure 15a. Comparison between the real and imaginary components of EM data (ratio of Mod1/Mod0) calculated using the 2D numerical model (solid curves) and those calculated using the 1D model (dashed curves). The response for a frequency of 1 Hz is shown in (a) and (b), and the response for a frequency of 10 Hz in shown in (c) and (d). The regions within the dashed-dotted vertical parallel lines are CO_2 injection zones.

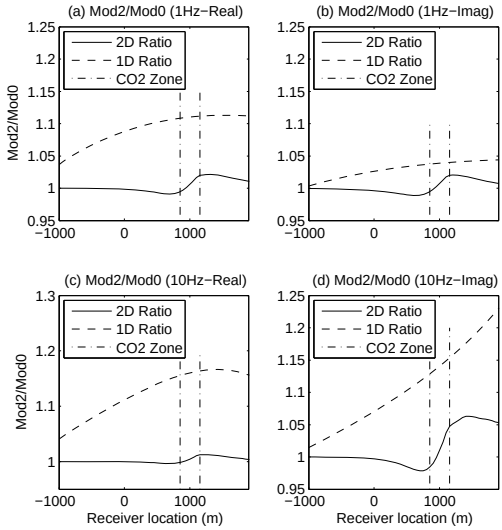

Figure 15b. Comparison between the real and imaginary components of EM data (ratio of Mod2/Mod0) calculated using the 2D numerical model (solid curves) and those calculated using the 1D model (dashed curves). The response for a frequency of 1 Hz is shown in (a) and (b), and the response for a frequency of 10 Hz in shown in (c) and (d). The regions within the dashed-dotted vertical parallel lines are CO_2 injection zones.

AVA Analysis

Our current AVA analysis uses a Bayesian model with 1D seismic and EM codes. This model is a revision of the joint inversion model given by [16]. As discussed above, the 1D seismic convolution model provides a good approximation to the 2D seismic data at small incident angles. The 1D EM model provides a fair approximation to the 2D EM data for those receivers directly above the injection zones. After jointly inverting the time-lapse seismic AVA and EM data for CO_2 saturation, we compared the inversion results with those obtained from the inversion of seismic AVA data only. The statistics of the estimated parameters for the model with CO_2 injection into the top injection zone is summarized in Table 2, and their marginal posterior probability distribution functions (pdfs) are given in Figure 16. Figure 16a shows the estimated probability density function (pdf) of the unknown CO_2 saturation using seismic AVA data alone, whereas Figure 16b shows the estimated pdf using both seismic AVA and EM data. In both cases, the inversion correctly predicts the presence of high CO_2 saturation in the injection zone. However, incorporation of EM data significantly reduces inversion uncertainty. The pdfs obtained using both seismic AVA and EM data are much sharper than those obtained using seismic AVA data alone. As shown in Table 2, both the standard error and the 95% predictive intervals of the unknown CO_2 saturation are lower if EM data are incorporated into the inversion.

Table 2. Comparison between the CO_2 saturation estimated using seismic AVA data alone, and that estimated using both seismic AVA and EM data for the case of one injection zone.

	Median	**Mean**	**Mode**	**Standard deviation**	**95% Predictive Interval**
CO_2 saturation (seismic AVA data alone)	0.9844	0.9791	0.9891	0.0183	(0.9341, 0.9994)
CO_2 saturation (both seismic AVA and EM data)	0.9999	0.9999	0.9999	0.0001	(0.9995, 1.0000)

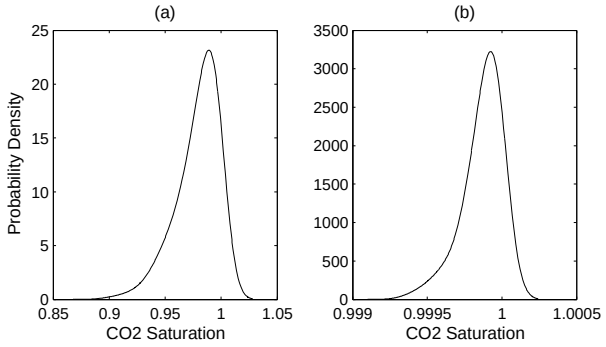

Figure 16. Estimated marginal posterior probability density functions (pdfs) of CO_2 saturation in the top injection zone (a) using seismic AVA data alone, and (b) using both seismic AVA and EM data.

The results for the model with CO_2 injection into three injection zones are given in Table 3 and Figure 17. Figures 17a-c show the estimated pdfs of the unknown CO_2 saturation using seismic AVA data alone, while Figures 17d-f show the estimated pdfs using both seismic AVA and EM data. Again, for the top two injection zones, the estimated CO_2 saturations are close to 1.0 with a small uncertainty; the joint inversion of seismic AVA and EM data improves the estimation by significantly reducing uncertainty (Figures 17a-b, 17d-e). The advantage of EM data is clearly illustrated in Figure 17c and Figure 17f. Inversion of seismic AVA data gives misleading results and shows the injection zone with a low CO_2 saturation (Figure 17c). This is far from the true value of 95% CO_2 saturation. However, the inversion results after incorporating EM data clearly show a high CO_2 saturation zone (Figure 17f).

In all cases, the joint inversion of seismic AVA and EM data gives higher CO_2 saturation than the corresponding true value (95%). This is possibly because the 1D approximation of the 2D EM data underestimates the slopes in the EM data sets. To obtain more accurate results, and to account for the effects of finite-sized target zones, we may need to use 2D EM forward codes in our inversion approach.

Table 3. Comparison between the CO_2 saturation estimated using seismic AVA data alone, and that estimated using both seismic AVA and EM data for the case of three injection zones.

	Zones	Median	Mean	Mode	Standard deviation	95% Predictive Interval
Seismic AVA data alone	Zone-1	0.9900	0.9855	0.9931	0.0140	(0.9495, 0.9997)
	Zone-2	0.9419	0.9303	0.9646	0.0528	(0.8217, 0.9976)
	Zone-3	0.1067	0.1152	0.0813	0.0781	(0.0046, 0.2611)
Seismic AVA and EM data	Zone-1	0.9996	0.9995	0.9997	0.0005	(0.9979, 1.0000)
	Zone-2	0.9984	0.9978	0.9987	0.0020	(0.9928, 0.9999)
	Zone-3	0.9993	0.9991	0.9994	0.0008	(0.9972, 1.0000)

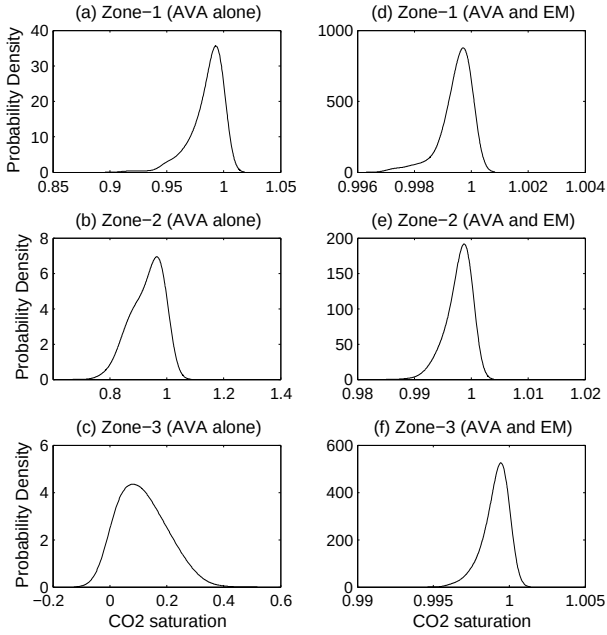

Figure 17. Estimated probability density functions (pdfs) of CO_2 saturation into three injection zones (a-c) using seismic AVA data alone, and (d-f) using both seismic AVA and EM data.

CONCLUSIONS

The presence of CO_2 reduces the bulk density of the coal layer, causing a decrease in the gravity response. Adsorption of CO_2 into coal can affect the matrix density, and hence the total density change could be smaller than we predicted. The spatial pattern of the change in the vertical component of gravity is directly correlated with the net change in density of the coalbed. Gravity inversion results illustrated that, with high-quality field gravity data and some a priori information about the depth of the reservoir, we can recover the spatial location of CO_2 plume correctly, although with the smoothing constraint of the inversion, the area was slightly overestimated, resulting in an underestimated value of density change. The CO_2 injection decreases the water saturation, causing an increase in the coalbed electrical resistivity. There is a direct one-to-one correspondence between the change in the water saturation and the change in the electric field

amplitude. The ability to observe these differences in the field would depend on the signal-to-noise ratio of the data. While this technique has been successfully used in the offshore environment, it has not been tested for a CO_2 sequestration scenario on land. Future plans should incorporate field demonstration of the EM technique to verify its feasibility. The sensitivity study showed that while the response to the 300 tons of CO_2 injected into a single layer would not produce a measurable surface response for either gravity or EM, the response due to an industrial-size injection (several million tons of CO_2) would produce measurable surface signals for both techniques, assuming the accuracy of the EM measurements is 1–2%. Hence, gravity and EM measurements could, under certain circumstances, be used as a lower-cost alternative/supplement to seismic measurements. Even though uncertainty in the rock-physics models exists, as well as discrepancies between the 1D approximation and 2D numerical models, we found that by inverting seismic and EM data jointly, much better estimates of CO_2 saturation could be obtained, especially in the third injection zone, where seismic AVA data fail to detect the high CO_2 saturation. Our synthetic studies show that time-lapse surface seismic and EM methods are a promising tool for CO_2 injection monitoring in the scenario presented in this study; however, further studies are certainly needed for more complicated scenarios.

ACKNOWLEDGMENTS

This work was supported in part by a Cooperative Research and Development Agreement between BP Corporation North America, as a part of the CO_2 Capture Project of the Joint Industry Program, and the U.S. Department of Energy, and by the Lawrence Berkeley National Laboratory under contract DE-AC02-05CH11231. The flow simulations models were provided by Sproule Associates, Ltd. We thank Gregory Newman for running 2D EM models and Valeri Korneev for running 2D seismic models.

This Chapter contains figures (10 and 11) that originally appeared in Energy Procedia Vol 1, Issue 1, Greenhouse Gas Control Technologies 9, Proceedings of the 9th International Conference on Greenhouse Gas Control Technologies (GHGT-9), 16-20 November 2008, Washington DC, USA, which was published by Elsevier Ltd.

REFERENCES

1. Gasperikova, E., and M. Hoversten, 2006, A Feasibility Study of Non-seismic Geophysical Methods for Monitoring Geologic CO_2 Sequestration: The Leading Edge, **25,** 1282-1288.
2. Benson, S.M, Gasperikova, E., and Hoversten, M., 2004, Overview of monitoring requirements for geologic storage projects, LBNL report.
3. Pashin, J.C., and P.E. Clark, 2006, SECARB Field Test for CO_2 Sequestration in Coalbed Methane Reservoirs of the Black Warrior Basin: Tuscaloosa, Alabama, University of Alabama, College of Continuing Studies, 2006 International Coalbed Methane Symposium Proceedings, paper 0630.
4. Galas, C.M.F., V.Y. Savenkov, and D. Keike, 2009, Simulation study of methane and carbon dioxide migration and leakage during normal and enhanced field operations to recover coal bed methane from coal seams. In Eide, L.I. (ed.) 2009, Carbon Dioxide Capture for Storage in Deep Geologic Formations, Volume 3. CPL Press
5. Kneafsey, T, Gritto, R., and Tomutsa, L., 2005, Coalbed methane laboratory experiments, LBNL report.
6. Gasperikova, E., and Hoversten, M., 2008, Gravity monitoring of CO_2 movement during sequestration: Model Studies: Geophysics, 73, WA105-WA112.
7. NIST Mixture Property Database, NIST Standard Reference Database #14, 1992, U.S. Department of Commence, National Institute of Standards and Technology (NIST).

8. Ferguson, J.F., Klopping, F.J., Chen, T., Seibert, J.E., Hare, J.L., and Brady, J.L., 2008, The 4D microgravity method for waterflood surveillance: Part 3 - 4D absolute microgravity surveys at Prudhoe Bay, Alaska: Geophysics, **73**, WA163-WA171.
9. Brown, J. M., T. Chen, T. M. Niebauer, F. J. Klopping, J. Ferguson, and J. Brady, 2003, Absolute and relative gravity integration for high precision 4D reservoir monitoring: EAGE Expanded Abstracts, A26-A26.
10. Nooner, S.L., M.A. Zumberge, O. Eiken, T. Stenvold, and G.S. Sasagawa, 2003, Seafloor Micro-gravity Survey of the Sleipner CO_2 Sequestration Site: EOS Trans. AGU, **84**(46), Fall Meet. Suppl., Abstract GC31A-01.
11. Eiken, O., Stenvold, T., Zumberge, M., Alnes, H., and Sasagawa, G., 2008, Gravimetric monitoring of gas production from the Troll field: Geophysics, **73**, WA149-WA154.
12. Smith, J.T., G.M. Hoversten, E. Gasperikova, and H.F. Morrison, 1999. Sharp Boundary Inversion of 2-D Magnetotelluric Data: Geophysical Prospecting, **47**, 469-486.
13. Levander, A.R., 1988, Fourth-order finite-difference P-SV seismograms: Geophysics, 53, 1425-1436.
14. Aki, K., and Richards, P.G., 1980, Quantitative Seismology: Theory and methods: W.H. Freeman and Co.
15. Newman, G., and D. L. Alumbaugh, 1997, Three–dimensional massively parallel electromagnetic inversion - I. Theory: Geophysical Journal International, **128**, 345-354.
16. Chen, J., M. Hoversten, D. Vasco, Y. Rubin and Z. Hou, 2007, A Bayesian model for gas saturation estimation using marine seismic AVA and CSEM data, Geophysics, **72**, WA85-WA95.

Carbon Dioxide Capture for Storage in Deep Geologic Formations, Volume 3
L.I. Eide (Ed.)

Chapter 27

MONITORING AND VERIFICATION OF CONTROLLED RELEASES OF CO_2 AND CH_4 USING AIRBORNE REMOTE SENSING

William L. Pickles, Eli A. Silver and James Jacobson[1]
[1]University of California, Santa Cruz
Earth and Planetary Sciences Department 1156 High Street Santa Cruz, CA 95064

ABSTRACT: Storage of CO_2 in subsurface geologic formations is a potential Green House Gas mitigation strategy and monitoring of gas storage sites will be an important component of assuring the safe operation and maintenance of these facilities. Surface detection methods will most likely constitute a critical component of any monitoring protocol because of the environmental impact and safety concerns associated with leakage of CO_2 to the surface. Airborne monitoring of CO_2 and CH_4 has the advantage over ground-based methodologies in that it allows large areas to be evaluated over short periods of time.

The NASA AMES airborne multispectral imaging system called MASTER was tested to monitor engineered gaseous CO_2 and CH_4 releases. The experiments were done at the Naval Petroleum Reserve Site #3 (NPR3). NPR3 is operated by the US DOE Rocky Mountain Oil Test Center (RMOTC) facility in Casper Wyoming. The MASTER sensor was flown on August 3, 2006, in a Sky Research Cessna Caravan flying at heights of approximately 1000m and 2000m above ground level (AGL). The MASTER was configured to have 50 wavelength bands between the wavelengths of 0.4 μm and 13 μm. The pixel size was 2.5 m for the images acquired from 1000m AGL and 5m from 2000m AGL. . The field test showed no conclusive detection for CO_2, but apparent detection of CH_4 at a release rate of 142 m^3/h.

INTRODUCTION

Above ground monitoring for gaseous atmospheric CO_2 and CH_4 concentrations can be an important component of the successful operation of underground sequestration sites. While there are many methods of detecting gas leaks, airborne and satellite remote sensing are unique in their ability to monitor large land-surface areas. If carbon dioxide gas percolates to the surface along faults, joints, cracks, or well heads from the storage formation below, it will generate a localized gas plume and increase ambient CO_2 levels in the region. Monitoring techniques that target CH_4, another important GHG, are important since CH_4 emissions may accompany CO_2 leakage. Similarly, fugitive leaks of CO_2 and/or CH_4 from pipelines may occur during transport. Sensors in an aircraft or satellite are ideal for detecting localized plumes, because the speed and distances covered will make these forms of detection efficient.

Both multi-spectral and hyper-spectral remote sensing can detect elevated concentrations of gases in the atmosphere. All atoms and molecules absorb, reflect, or emit radiation at well known, narrow wavelength regions. Gaseous molecules of CO_2, CH_4 and other greenhouse gases absorb energy at various wavelengths throughout the electromagnetic spectrum due to their vibrational and rotational modes of internal oscillation, as explained in [1], where one can also find the relation between absorption as function of length for various gases. In an airborne image, any elevated concentrations of CO_2 and/or CH_4 between the plane and the ground will strongly absorb light reflected from or

thermally emitted by the earth's surface. By comparing images created with bands that are exactly on the narrow wavelength absorptions to images created with wavelength bands not on the narrow absorption bands it is possible to map areas of elevated CO_2 or CH_4 concentrations.

Most studies on using remote sensing to detect gas leaks have focussed on CH_4. An assessment of several technologies for this purpose can be found in [2]. An airborne active interrogation remote sensing systems that are based on imaging Differential Absorption LIDAR, called DIAL, has been shown to be very effective at mapping even small CH_4 leaks from pipelines networks [3]. DIAL uses a laser to measure absorption on and off the absorption resonances for various gases between the aircraft and the ground. The imaging capability allows pinpointing the exact location and extent of the gas effluent. We have been encouraging the development of a similar airborne DIAL system to image CO_2.

This study included detection of CO_2 in addition to CH_4. MASTER, a NASA AMES airborne multi-spectral imager, [4], was used to map CO_2 and CH_4 engineered controlled leaks which were created within the boundaries of Naval Petroleum Reserve #3 (NPR#3) in Wyoming, USA. Master images from earlier experimental flights using the same instrumentation over sites with natural CO_2 leaks (Kilauea, HI; Mount Saint Helens, WA; and Mammoth Mountain, CA) were studied during the planning for the field test. Flights in 2004 using five systems over the same area as in the present experiment showed that these systems had limited capabilities to image CH_4 plumes [5].

The objective of the present study was to acquire further data on the ability of MASTER to detect CO_2 and CH_4 leaks under controlled conditions. Cost evaluation was not included in the scope.

EXPERIMENTAL METHODS

The NASA AMES MASTER Instrument (Multispectral Imager)

The MODIS/ASTER Airborne Simulator (MASTER) was developed by the NASA Ames Research Center in cooperation with the Jet Propulsion Laboratory and built in 2001. This instrument combines properties of both the MODIS and ASTER systems. MODIS and ASTER are space-borne imaging instruments installed on the first Earth Observing System (EOS) platform launched in late 1999. A description of the MASTER system can be found in [4].

MASTER has 50 bands or channels that cover wavelengths from 0.4 to 13 μm. The angular resolution (2.5 mrad) is excellent. The spatial resolution depends on the altitude at which it is flown and can be as good as 0.5 m.

MASTER (Figure 1) has been used in many locations around the globe, including well known sites of natural CO_2 and/or CH_4 off-gassing such as Kilauea, Hawaii; Mount St. Helens, Washington; and Mammoth Mountain, California.

The Experimental Design

MASTER was flown over a line of engineered CH_4 and CO_2 releases created on the Rocky Mountain Oilfield test Center of the NPR#3 site. The site is in the historic Teapot Dome oil field in Natrona County, Wyoming, approximately 35 miles north of the city of Casper. The test site facilities are described in [6].

(a) (b)

Figure 1. (a) NASA AMES MASTER imaging optics and
(b) data acquisition electronics installed in a Caravan single engine aircraft.

Seven experimental release sites were used in this experiment. The locations of each of the numbered release sites are shown on the map of the NPR#3 in Figure 2a. Four release sites were used as sources of methane, and three were used as sources of carbon dioxide. The release sites used were the same that were used for the previous remote sensing experiment which studied CH_4 pipeline leak detection [5]. Locally produced natural gas and trucked in CO_2 were used as the gas sources for the release sites. The flow rates for the gas were altered to achieve the range of CH_4 and CO_2 concentrations desired for this experiment.

MASTER Image Acquisition

On August 3, 2006, a Sky Cessna Caravan carrying the modified MASTER payload flew over the NPR3 RMOTC NPR#3 site on one of two flight-lines, nine times. The flight path transected the site from SSE to NNW, approximately following the line of release sites The plane was flown at 1000 m and 2000 m, above ground level (AGL) giving an image pixel size of 2.5m and 5m respectively. The flight lines and the release locations are shown in Figure 2b below. The flight line for the higher flights is the straight line from N43 21.370 W106 14.548 to N43 13.913 W106 10.939. The flight line for the lower flights is in two segments almost parallel to the higher flight fine.

The MASTER sensor was configured to have 50 bands between 0.4 μm to 13 μm for this experiment.

The over flights started around 09:00. The skies were clear and the air was about 75 deg F, dry, and the wind was very light. The release rates were measured by the RMOTC release equipment. There were no other ground measurements.

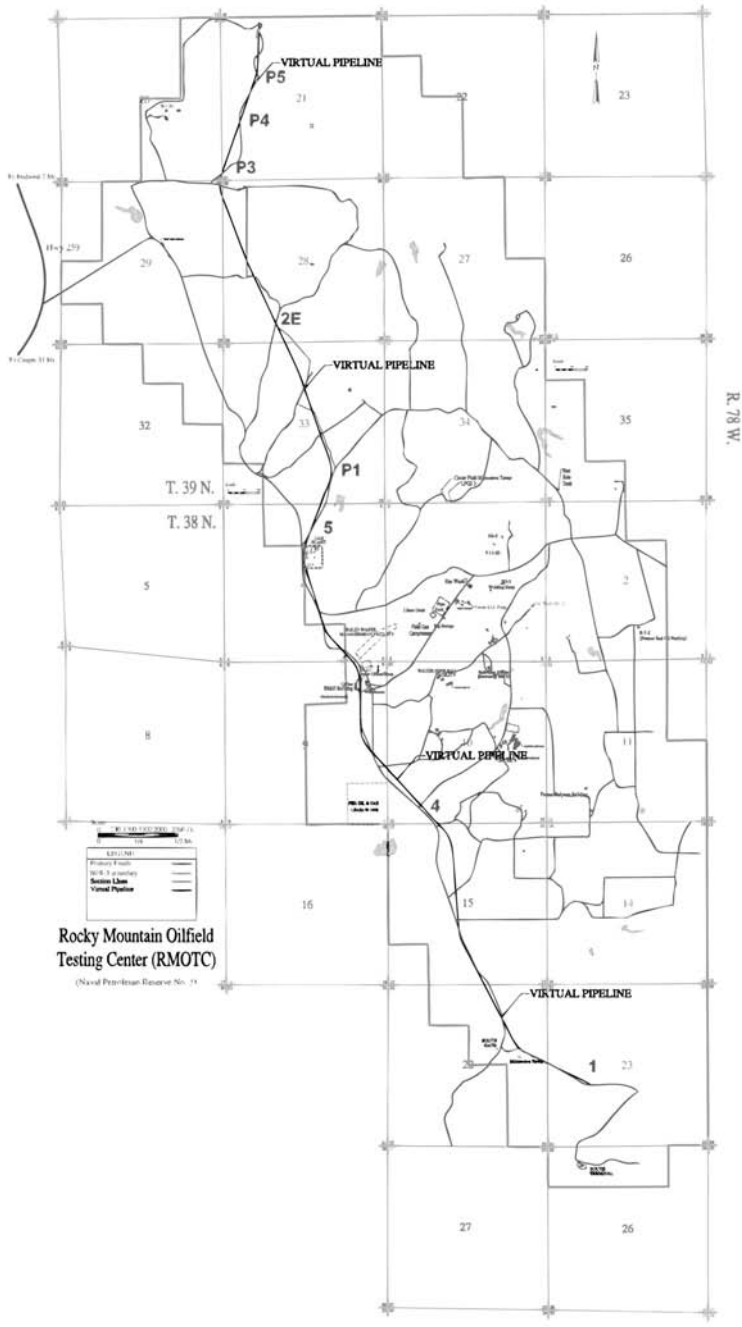

Figure 2a. Map of the NPR#3 site showing the locations of the engineered releases. The engineered releases are located by the numbers 1, 4 and 5, and the numbers P1, P2, P3, and P5 on the site map.

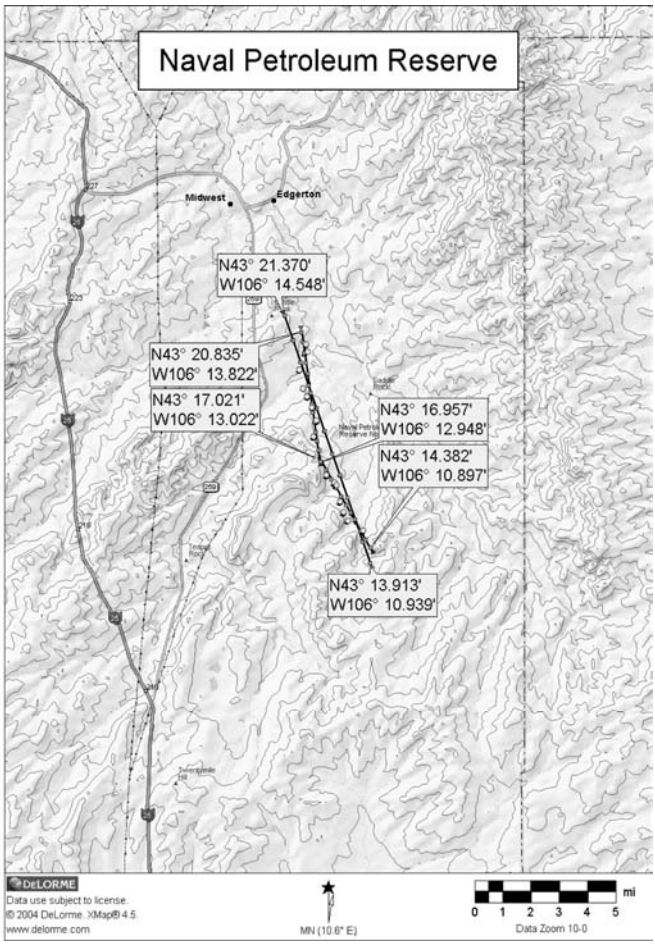

Figure 2b. Flight path and gas release sites.

MASTER Image Processing

MASTER data was provided by NASA Ames in Hierarchical Data Format (.hdf), and all files were imported into ENVI version 4.1 for processing. For each flight line image, a Geographic Lookup Table (GLT) was produced from latitude and longitude data in the .hdf file. This GLT was then applied to the MASTER flightline imagery to georectify the image. The resultant image has all pixels placed in their correct geographic location. In the georectified image specific points can be located using map coordinates.

CO_2 and CH_4 have well documented spectra in the visible and near-infrared (VNIR) and short-wavelength infrared (SWIR). The bands needed for imaging CO_2 include the vibrational-rotational absorption bands located at 2.06 μm, 2.7 μm, 4.3 μm, 9.4 μm, 10.4 μm, and 15.0 μm. Due to the mechanical limits of MASTER, we are forced to ignore the deep absorption bands at 2.7 μm, and

15.0 μm. The absorptions at 9.4 μm and 10.4 μm are likely too faint for MASTER to detect with confidence, which leaves the 2.06 μm and 4.3 μm bands. Unfortunately MASTER has a very low signal to noise ratio in the channels associated with wavelengths from 3.1 μm to 5.1 μm. CH_4 has three well-defined absorption bands within the sensory range of MASTER: one at 1.7 μm, one near 2.4 μm, and another close to 7.5 μm. Table 3 lists the absorption bands associated with each molecule and the MASTER band which overlaps it. Only the MASTER bands used for this experiment are included in Table 1.

Modtran

Modtran (moderate spectral resolution atmospheric transmittance algorithm and computer model), [7], calculates atmospheric transmittance and radiance for frequencies from 0 to 50,000 cm^{-1} at moderate spectral resolution. Modtran was created to provide an atmospheric correction model with high spectral resolution and great accuracy. Modtran 4.0 code was used to model atmospheric conditions with elevated gas concentrations at the surface using "PCModWin4.0", a graphical user interface for Modtran distributed by the Ontar Corporation.

The goal was to predict effects of increased concentrations of gasses in the atmospheric column between the sensor and the ground. PCModWin4.0 was used to estimate the transmission of radiation through the atmosphere while controlling parameters like sensor height, gas mixing ratios, sun angle, time of year, and height of target.

This portion of the MASTER investigation focused on the 4.3 μm absorption feature. The spectral response curve of MASTER bands close to the 4.3 μm CO_2 feature overlap the graph of atmospheric transmission of radiation as it is absorbed with increasing CO_2 concentration. CO_2 has the greatest effect on transmission in this region, but the Modtran model predicts little change with increases in concentration up to 572 parts per million by volume (ppmv). For analysis of CO_2, MASTER bands were subset from 15 to 25 around the 2.06 μm CO_2 absorption, and from 30 to 38 around the 4.3 μm CO_2 absorption. From the Modtran model MASTER Bands 33, 34, and 35 appear to cover the breadth of the 4.3 μm CO_2 absorption. Unfortunately, band 34 is unsuitable to detect differences in CO_2 concentrations on this sensor scale due to the saturation effect in this part of the spectrum. Band 35 is centered over a minor peak that appears to be influenced by the absorption effect of CO_2.

Methane (CH_4) has major absorption features at both 1.7 μm and 2.4 μm. However, we focused the attention on the 2.4 μm methane absorption feature due to the influence of water absorptions near 1.7 μm. For CH_4 analysis MASTER bands were subset from channel 21 to channel 27 around the 2.4 μm absorption feature.

Table 1. CO_2/CH_4 absorption features and their MASTER bands.

Molecule	Wavelength Location of Molecular Absorption Feature	MASTER Band Enveloping Absorption Feature (Band Center Wavelength)
CO_2	1.63 μm	Band 12 (1.6060 μm)
	2.06 μm	Band 20 (2.0806 μm)
	4.3 μm	Band 35 (4.3786 μm)
	9.4 μm	Band 45 (9.7004 μm)
CH_4	1.7 μm	Band 14 (1.7196 μm)
	2.3 μm	Band 24 (2.3284 μm)
	7.4-7.58 μm	Band 41 (7.7599 μm)

RESULTS AND DISCUSSION

Figure 3 shows MASTER images of the three CO_2 release locations (P5, 4, and P1) viewed in Band 1 (Blue Visible, 0.45 μm), Band 35 (CO_2 absorption feature in mid-infrared, 4.52 μm), and Band 42 (thermal infrared, 8.16 μm). Band 1 and band 42 have no molecular resonances in them and are not included in Table 1.

Site P5 had the smallest of the three CO_2 leaks (8 m^3/h). The site included a small stream channel with standing water in the topographic low and healthy green vegetation in surrounding areas. The channel shows a dark vertical strip in Figure 3, Site P5, Band 1. Bands 35 and 42 confirm the local topography, and Band 35 has a cluster of slightly darker pixels around the leak location.

Site 4 was intended to have a moderately sized leak (23 m^3/h), but due to technical difficulties, became the highest rate CO_2 leak site (approximately 566 m^3/h). The topography is relatively flat with two dirt roads intersecting in the left of the image (clearly visible in Band 1 and 42). The Band 35 (CO_2 Resonance) and Band 42 (thermal) images appear to contain a small cluster of darker pixels at the leak site, and in Band 42 (thermal), this cluster appears to trend Northeast away from the source location.

Site P1 was intended to be the largest leak (142 m^3/h). Its topography slopes gradually uphill to the north with a single road trending NW-SE and approximately 10 meters away Northeast of the CO_2 tanker truck used as the source of our CO_2 leak. The grey arrow indicates the location of the end of the 4 inch diameter hose that was our leak location, approximately 15 meters south of the tanker. The tanker is the bright white linear set of pixels in Band 1 and the black pixels in Band 35 images of Site P1. The tanker is cool due to expansion of the released CO_2 and so appears dark in the thermal image band 35. While there are no clear indications of a CO_2 plume from browsing the images, attention should be given to the Band 42 image of Site 04. At this site there appears to be a temperature effect related to the gas plume which can be seen in the band 42 data (at approximately 8 microns, thermal infrared). This is discussed in further detail below.

One difficulty of remote sensing of gas plumes is the heterogeneity of the ground surface. Variations in geology, vegetation, moisture, and dust can all drastically affect the irradiance in a given pixel. The goal is to detect reduction in light transmission over pixels covered by the gas plume, but this goal becomes complicated without knowing precisely how the ground will appear spectrally, without the interference of gas plumes. This is normal and is the primary determinate in how well a signature can be extracted in all remote sensing applications. These effects are not known precisely until the imagery is acquired and processed. This is why it is best to just do the experiment if the signature detection probability is marginal. These effects cannot be calculated effectively in advance.

In comparing the MASTER images for effects of CO_2, there were no consistent differences that could be attributed solely to CO_2 absorption by the gas plume. In one case (Site 04), MASTER appeared to record a thermal signature of cooling at the site of CO_2 gas expansion (Figure 3). The planned release rate at this location (23 m^3/h) was compromised by the cooling effect of the rapidly expanding CO_2 gas. As the CO_2 expanded, ice formed and plugged the leak hoses. The leak setup was re-evaluated and changed to accommodate the ice formation. The result was an ice-generating cold gas plume of CO_2 being released at approximately 566 m^3/h. The gas plume and the frozen trailer-mounted gas tanks are clearly visible in the thermal imagery (Figure 4).

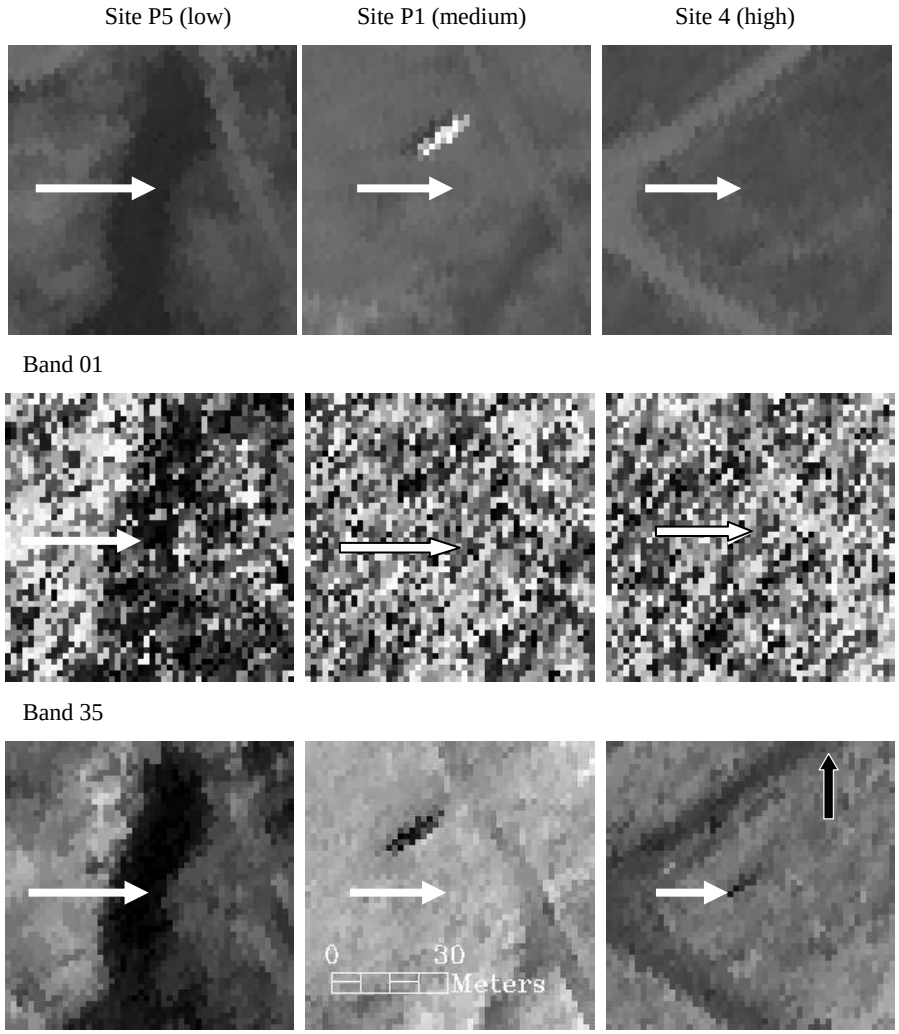

Figure 3. Three experimental CO_2 leak sites visualized at three different wavelengths from the visible (Band 01, 0.45µm) to the absorption band for CO_2 in the mid IR Band 35 to thermal infrared (band 42, 8.16µm). Release rates were 8 m^3/h (left), 23 m^3/h (right) and 142 m^3/h (centre). White arrows indicate the approximate locations of the releases. Scale and North arrow (in black) are shown in the lower image. They are the same for all the images.

Detailed Pixel Comparisons around Release Points

To test MASTER's ability to detect CO_2 through very small changes in pixels near the source point, a method was developed to quantify reductions in light transmission relative to the immediate background. This method uses a collection of a contiguous linear transect of background pixels from north to south across the leak source (8 pixels total: 4 north and 3 south of the leak location pixel), and then individually subtracting each background pixel spectra from the leak source pixel. Pixels in

this image are 1.5m on a side. All pixel transects are north to south for consistency, and to minimize the effect of winds.

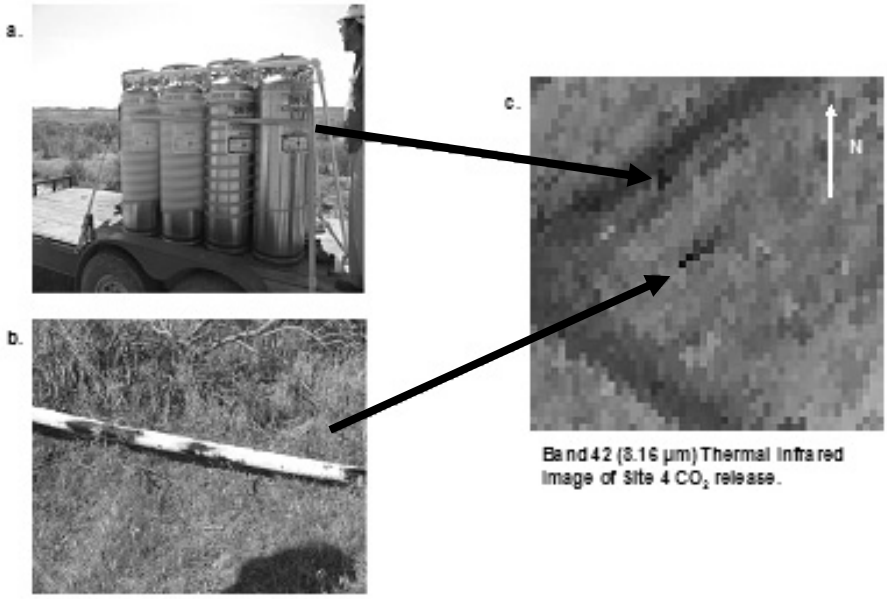

Figure 4. Thermal effect of CO_2 release seen by MASTER. Images are: a. Liquid CO_2 storage tanks, b. ice-covered release site hose, and c. Site 4 viewed in MASTER Band 42 (8.16 µm).

The ideal output from the neighboring pixel subtraction technique would be a series of negative numbers occurring in the MASTER channels sensitive to the absorption bands of the target gas. The spectral subsets for all the CO_2 analyses include MASTER bands 31 through 38, digitally calibrated as radiance at the sensor (in units of watts per square meter). For CO_2, our MASTER channels of interest include channel 35, and 37, but channel 34 was excluded due to the noise inherent in this band. An example of the results of the pixel subtraction technique is shown in Figure 5.The pixel subtraction for P5 (Figure 5) shows that the release outlet pixel had a lower transmission than the other 7 pixels. The medium volume leak site (P1) transmission was lower in the outlet pixel than in 3 out of the 7 background pixels. While this result is consistent with the expected effects of CO_2 on the pixel spectra, the result also brings doubt into the viability of leak detection at this site. In the same pixel subtraction technique across the Site 04 release, all seven of the background pixels for Site 4 indicate a drop in transmission in bands 35 and 37.

At all three CO_2 leak sites there was a consistent decrease in transmission of outlet pixels compared to nearby background pixels in both MASTER band 35 and 37. This indicated that MASTER used in this way has the sensitivity to detect gaseous CO_2 leaks between 8 and 566 m^3/h.

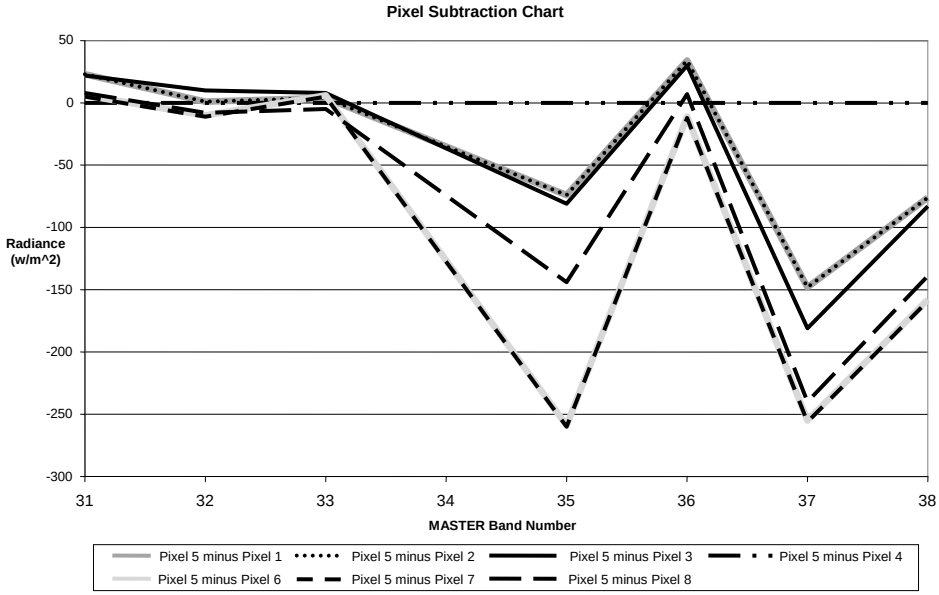

Figure 5. Site P5 (8 m3/h) pixel subtraction graph. Line "Pixel 5 minus Pixel 1" is overlain by line "Pixel 5 minus Pixel 2". Line "Pixel 5 minus Pixel 6" is overlain by line "Pixel 5 minus Pixel 7".

Analysis of MASTER CH_4 Detection

The Modtran model showed that MASTER bands 24 and 25 both overlap the absorption feature for methane at 2.4 microns. Figure 6 is the results of pixel subtractions on CH_4 site 5, following the example of the pixel subtractions performed on the three CO_2 leak sites.

The largest leak site for CH_4 was Site 5 at a release rate of 142 m^3/h. All six Site 5 pixel subtraction lines record typical drops in transmission for MASTER bands 24 and 25. Each of the four CH_4 pixel subtraction graphs show values that range from 1 to -1.5 rather than the range of 200 to -400 seen in the pixel subtractions for CO_2. With so dramatic a difference in pixel subtraction ranges, noise may be an issue in interpreting the CH_4 data.

At site 5, a potential plume can be seen in imagery formed with MASTER channels 24 and 25. After applying ENVI 4.1's "equalization enhancement" tool: an area of slightly darker pixels begins at the leak source pixel and off to the west-southwest which is consistent with the wind speed and direction of August 3, 2006 (NOAA, 2006), see Figure 7 (a) and (b).

Modtran modelling was used to calculate expected drops in transmission for both CH_4 and CO_2 leaks at each leak location. In all but one case the Modtran predictions were for 1% or less drop in transmission which would be difficult to detect. For the one other case, the highest leak rate CH_4 site, Modtran predicted a 6% decrease in transmission and this compared favourably with the observed decrease in the MASTER data at this site.

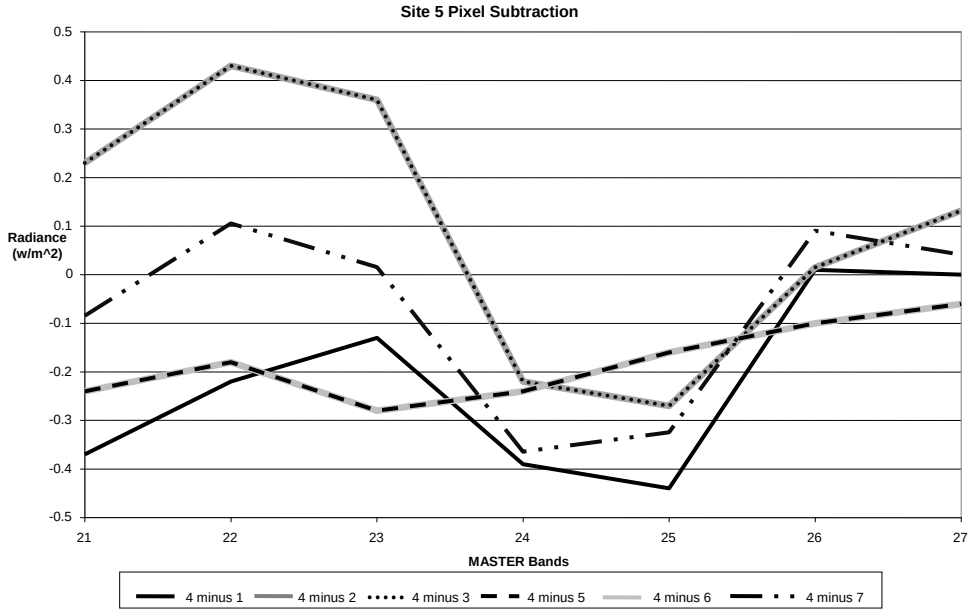

Figure 6. Site 5 (142 m3/h) pixel subtraction graph. Line “Pixel 4 minus Pixel 3” is overlain by line “Pixel 4 minus Pixel 2”. Line “Pixel 4 minus Pixel 6” is overlain by line “Pixel 4 minus Pixel 5”.

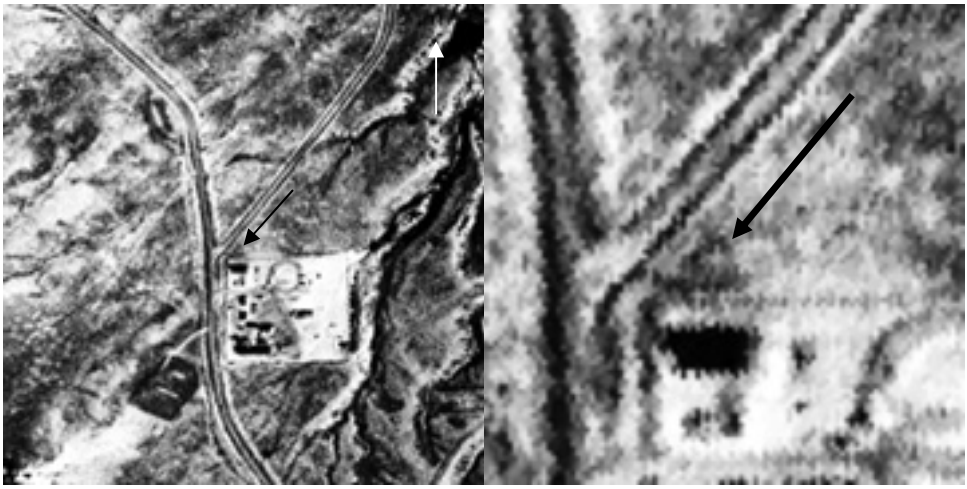

(a) (b)

Figure 7. Potential methane plume near the location of the Site 5 leak. (a) General view. (b) Enlargement of immediate area of leak outlet. Black arrows indicate the pixel containing the leak. The structures to the south are the RMOTC Gas plant. White arrow indicates North direction.

Possible improvements

Future experiments would benefit from an instrument that has additional spectral response from at least the short wave infrared (3 to 5 microns) through the thermal wavelengths (8 to 14 microns), with channels whose widths are significantly narrower than those of MASTER. Ideally we would need channel widths as narrow as possible, down to only a nanometer or less, if available. In this way, it will still be possible to image the larger wavelength overtones of the absorption effects of CO_2 and CH_4. Instruments that have a spectral range from around 0.4 to 2.5 μm would be valuable. This makes them better for imaging the absorption for CO_2 at 2.06 μm, but incapable of imaging the absorption features beyond 2.5 μm in the mid and far infrared. MASTER and similar multispectral instruments have the capability to image in the mid and far infrared, but for MASTER the signal-to-noise ratio combined with undesirably wide band widths make imaging absorption features in this range extremely difficult.

CONCLUSION

These experiments have shown that the NASA AMES MASTER airborne multispectral imager is unlikely to be an efficient or accurate system for the kinds of global monitoring and verification systems that are needed. Although the MASTER results indicate potential for detection of both CO_2 and CH_4, there are ambiguities in all but one case that limit the usefulness of the results. The results showed that MASTER was inadequate for direct CO_2 detection over wide areas, but there are indications that the techniques have potential for small areas under controlled circumstances. Results for CH_4 appear promising for leaks at rates higher than 142 m^3/h or more than 64.4 ppmv. In general, the MASTER spectral resolution is too broad, and the spatial resolution too coarse to confidently detect and map variations of greenhouse gas release on a scale significant to CO_2 sequestration site managers.

Although the results presented here show that it is unlikely that the MASTER instrument as currently configured could reliably detect gaseous CO_2 from ground based leaks, the data do suggest that the MASTER instrument can detect large-scale CH_4 ground leaks.

ACKNOWLEDGEMENTS

This project was funded by the CO_2 Capture Project Phase 2 (CCP2). We want to thank Lyle Johnson, Doug Tunison, Judith Johnston, Jim States and rest of the DOE RMOTC staff in Casper Wyoming for providing the engineered gas leaks at NPR3. We want to thank the NASA AMES Airborne Sensor Facility for providing the MASTER overflights.

REFERENCES

1. Stephen C. Porter & Daniel Botkin Brian J. Skinner, The Blue Planet, ISBN: 9780471161141, John Wiley and Son, 1999.
2. Stearns, Steven V., Raymond T. Lines, Christian J. Grund and C. Russell Philbrick, “Active Remote Detection of Natural Gas Pipeline Leaks,” Technology Status Reports of NETL Department of Energy (http://www.netl.doe.gov/technologies/oil-gas/NaturalGas/Projects_n/TDS/TD/T%26D_A_41877AdvAirborne.html).

3. Lenz, D., R.T. Lines, D.Murdock, J. Owen, S. Stearns and M. Stoogenke (2005) Flight Testing of an Advanced Airborne Natural Gas Leak Detection System. ITT Industries Space Systems, LLC Final Report DOE Award No. DE-FC26-03NT41877 (http://www.netl.doe.gov/technologies/oil-gas/NaturalGas/Projects_n/TDS/TD/T%26D_A_41877AdvAirborne.html).
4. http://asapdata.arc.nasa.gov/dscrptns.htm
5. Southwest Research Institute (2004) Field Testing of Remote Sensor Gas Leal Detection Systems. Final Report DOE Contract –DE-AC01-04R01058 (http://www.netl.doe.gov/technologies/oil-gas/NaturalGas/Projects_n/TDS/TD/T%26D_A_41877AdvAirborne.html).
6. http://www.rmotc.doe.gov/
7. "US Air Force Fact Sheet: Modtran 4 Software" Kirkland Air Force Base. http://www.kirtland.af.mil/library/factsheets/factsheet.asp?id=7915

Carbon Dioxide Capture for Storage in Deep Geologic Formations, Volume 3
L.I. Eide (Ed.)

Chapter 28

CCP2-SMV PROGRAM KEY FINDINGS, TECHNOLOGY GAPS AND THE PATH FORWARD

Scott Imbus[1] and Linda Curran[2]
[1]Chevron Energy Technology Co., 1500 Louisiana St. Houston, TX 77002, USA
[2]BP Alternative Energy 150 W. Warrenville Road, Naperville, IL 60563, USA

KEY FINDINGS OF THE CCP2-SMV PROGRAM

The initial CCP-SMV Phase (200-2004) assessed some 30 technologies along the themes: Integrity (of natural and engineered systems), optimization (synergies with CO_2 capture and transportation and enhanced hydrocarbon recovery; injection operations efficiencies), monitoring and verification and risk assessment [1]. The second Phase (CCP2-SMV; 2005-2009) was intended to develop these and other technologies towards deployment-ready status in the third and final phase (CCP3-SMV; 2009-2013). The overarching objective of all studies through the three phase program is to improve confidence in safe and effective storage of CO_2 at scale.

The CCP2-SMV program began at a time (2004-2005) when site assessment and other regulation development was emergent, well integrity was thought to be a potential CO_2 storage "showstopper" and there was a major focus on coal beds as a major potential venue for CO_2 storage. The program was developed to address these issues and, insofar as was possible, continued to evolve with landscape changes since then. Key findings of the program include:

- The Certification Framework (CF) has developed a simple workflow for assessing CO_2 storage sites. Tool development and case studies to illustrate utility and limitations of the CF.
- The Well Integrity Field Study has put into perspective the containment risk of CO_2-exposed wells. The results of the two cases studies illustrate that a well's barrier performance is not necessarily compromised by alteration and that good drilling and installation practices are important for long-term well stability.
- The Geochemical-Geomechanical Simulation project has succeeded in implicitly coupling rock mechanical and reactive transport code but further development and real world case studies are required to assess its applicability and robustness.
- The Bench Scale RST Logging experiment illustrates the utility of sigma mode for detecting CO_2.
- The CO_2 ECBM flow simulation / containment and monitoring studies identifies CO_2 injection / storage and methane production optimization scenarios consistent with containment and detection using cost-effective techniques.
- The Direct, Remote Detection of CO_2 and Methane study showed that the chosen technique was unsuitable to detect these gases.

Other products / activities of the CCP2-SMV team maintained stakeholder communication (NGO forums, conferences), added to the technical literature (project publications) and confidence of industry E&P approaches as applied to CO_2 storage ("Technical Basis for Carbon Dioxide Storage" document).

TECHNOLOGY GAPS IN CO_2 STORAGE ASSURANCE

A number of "real" and "perceived" technical gaps remain in achieving stakeholder confidence in the security and effectiveness of large scale CO_2 storage assurance. Real technical gaps include incomplete understanding of details of subsurface processes occurring during the operational and post operational phases and their impact on flood performance and storage security. Perceived technical gaps include the applicability of existing E&P technology to CO_2 storage such as workflows and technology selection. These real or perceived gaps, however, would not be detrimental storage assurance in properly sited and operated CO_2 storage projects. Progress made towards addressing technical gaps would, however, enhance the ability of the proponent to optimally manage the site assessment, development, operations and decommissioning process.

Real technical gaps:

- CO_2-fluid-rock geochemical and geomechanical interactions over time and their impact on near wellbore, reservoir and cap rock stability
- Analytical and experimental basis for plume dynamics simulations (including rate and extent of trapping mechanisms; brine displacement and pressure transients)
- Fault connectivity and transmissivity systematics
- Long-term integrity of existing wells under CO_2-enriched conditions and cost-effective mitigation approaches

Perceived technical gaps:

- Suitability of Exploration and Production (E&P) workflows and assessment protocols to the CO_2 storage project lifecycle
- That monitoring and verification (M&V) programs should involve deployment of extensive, redundant instrumentation aimed at quantifying CO_2 state or insignificant out of reservoir migration over the storage project lifecycle
- That the risk associated with CO_2 storage is more extreme or less manageable than other commonplace endeavors such as large civil engineering projects

For CO_2 storage to maintain its status as a leading option for mitigating GHG emissions, the real technical gaps should be addressed through focused RD&D. Perceived gaps should be addressed through data integration and tool development with two-way communication between technical experts and stakeholder groups.

CCP3-SMV RD&D PROGRAM

Many of the real and perceived gap issues outlined above are addressed in whole or in part by CO_2 storage joint industry projects (JIPs), project developers and individual companies. The CCP3-SMV program seeks to develop appropriate RD&D work that will address remaining technical gaps and release key results to technical and stakeholder groups. The following outlines the proposed program:

Theme 1 – Storage Assurance R&D - Address real and perceived uncertainties, risks and opportunities associated with CO_2 storage through prioritized R&D programs culminating in conclusive study results or field demonstrations / deployments (field trialing).

A. Well Integrity – Field-based protocol for assessing well material alteration and forward simulation of well barrier stability over time; Develop cost-effective engineering solutions to well design, construction, completion, monitoring and intervention.

B. **Subsurface Processes** – Physico-chemical phenomena associated with CO_2 injection and impact on flood behavior and containment; Conduct laboratory and field experiments to understand such processes with development of numerical code that can be used with commercial simulators.

C. **Monitoring & Verification** – Relative value assessment of monitoring technology and feasibility of verification (quantification); Development of M&V "platform" suitable for most storage project settings.

D. **Storage Optimization** – Field development concepts for flood optimization and framework for lifecycle certification. Development of an integrated platform that can be used by technical specialist and communicated to stakeholders.

Theme 2 – Field Trialing - Identify and demonstrate Theme 1 concepts and/or instrumentation in one or more field projects to reduce subsurface process uncertainty and build confidence in emerging, cost-effective monitoring tools.

Theme 3 – Stakeholder Issues - Understanding of public perception of CO_2 storage risk with strategies to put such risk in perspective and technical support of Policy and Communication teams .

REFERENCES

1. Benson, S.M., ed., 2005, Carbon Dioxide Capture for Storage in Deep Geologic Formations - Results from the CO_2 Capture Project, Vol. 2: Geologic Storage of Carbon Dioxide with Monitoring and Verification, Elsevier Publishing, UK. 654 pp

SECTION 3:
POLICY & INCENTIVES AND COMMUNICATION

Carbon Dioxide Capture for Storage in Deep Geologic Formations, Volume 3
L.I. Eide (Ed.)

Chapter 29

ASSESSING ISSUES OF FINANCING A CO_2 TRANSPORTATION PIPELINE INFRASTRUCTURE

Ioannis Chrysostomidis[a], Paul Zakkour[a], Mark Bohm[b], Eric Beynon[b],
Renato de Filippo[c], and Arthur Lee[d]*
[a]Environemtal Resources Management, London, United Kingdom
[b]Suncor Energy, Calgary, Alberta, Canada
[c]Eni SpA, Milan, Italy
[d]Chevron Corporation, 6001 Bollinger Canyon Road, San Ramon, California 94583, USA

ABSTRACT: For carbon dioxide capture and geologic storage to be deployed commercially and in a widespread manner will require well thought out approaches for transporting the CO_2 in a pipeline system from the capture facility to the injection site. This paper outlines the results of a study, commissioned by the Carbon Capture Project (CCP) and completed by Environmental Resources Management (ERM) that evaluated the benefits and risks of two approaches to developing CO_2 pipeline systems. The two basic approaches are described in the paper as:

1. On a point-to-point basis, which matches a specific source to a specific storage location; or
2. Via the development of pipeline networks, including backbone pipeline systems, which allow for common carriage of CO_2 from multiple sources to multiple sinks.

While point-to-point pipelines may be readily funded on a project-by-project basis by individual developers, there may be a need for public policy to encourage the development of optimized networks. An optimized network could offer the potential to significantly reduce the per unit costs of transportation and reduce the barriers to entry when compared to point to point systems, Development of optimized networks can help to broaden participation and deepen deployment of CCS.

Establishing a widespread CO_2 transportation infrastructure will require strategic long-term planning, adopting a paradigm that takes into account the potential magnitude of future deployment scenarios for CCS, up to a scale of infrastructure that could be comparable to the scale of oil & gas infrastructure.

This paper describes preliminary findings from a CO_2 Capture Project study that looked at issues of financing the development of a hypothetical CO_2 transportation pipeline infrastructure. These issues include debt and equity structure, loan guarantees, government bonds, and the role of public-private partnerships.

* Corresponding author. Tel: +1-925-842-7421; Fax: +1-925-842-7555.
E-mail address: rlas@chevron.com.

INTRODUCTION

For carbon dioxide capture and geologic storage to be deployed commercially and in a widespread manner will require well thought out approaches for transporting the CO_2 in a pipeline system from the capture facility to the injection site. This paper outlines the results of a study, commissioned by the Carbon Capture Project in Phase 2 (CCP2) and completed by Environmental Resources Management (ERM) that evaluated the benefits and risks of developing CO_2 pipeline systems.

The approach of the research is based on a view that pipelines for CO_2 transport could evolve in two basic ways:

1. On a point-to-point basis, which matches a specific source to a specific storage location; or
2. Via the development of pipeline networks, including backbone pipeline systems, which allow for common carriage of CO_2 from multiple sources to multiple sinks.

A combination of the two will likely prove to be the most optimised approach, with individual projects driving the scope for development on a network basis. However, establishing such a network of CO_2 transportation infrastructure will require long-term planning and adopting a strategy that takes into account the potential magnitude of future deployment scenarios for CCS (i.e. 100s $MtCO_2$ being transported over long distances).

STRATEGIES FOR DEPLOYMENT OF INFRASTRUCTURES

Future strategies for private business and policy-makers should take account of the following:

- That while point-to-point pipelines may be readily funded on a project-by-project basis by individual developers, there may be a need for public policy that encourages the development of optimized networks. Development on this basis can help to broaden participation and deepen deployment of CCS;
- The incremental cost of building optimized networks ahead of point-to-point pipelines may not pass project-specific commercial evaluation criteria;
- Consequently, other forms of financial support which overcome commercial barriers may be needed to ensure optimized development of CO_2 pipelines networks.

Two further elements were also considered to influence the way pipeline networks are promoted and deployed, namely: geography and geo-political factors; and, the nature of policy tools used to incentivise CCS.

The approach taken to address these issues was as follows:

- To review the rationale, models and mechanisms used to promote and finance large oil & gas backbone pipelines;
- To review public/private infrastructure project financing models via case studies, such as large rail or road transport projects
- To undertake economic analysis of the relative risks and opportunities associated with developing point-to-point pipelines or backbone pipeline networks; and,
- To hold discussions with a range of potential financiers for CO_2 pipeline development.

RESULTS

Point-to-point pipelines will be funded on project-by-project basis by individual developers because of certainty over capacity utilisation. The study found that integrated backbone pipeline networks may be the most efficient long-term option. At the same time, such integrated backbone pipeline networks will need "guaranteed" capacity utilization in order to be economically viable. Therefore,

public policy that encourages development of optimised networks with some support of capacity utilization will be needed. Government support in the first years when capacity is ramping up will be important to commercial viability. Government incentives or loan guarantees are also needed to support a backbone infrastructure.

In interviews with staff from banks and financial institutions[2], the key conclusion is that CO_2 pipeline projects, if they can be reduced in terms of carbon price risks, will become the same in terms of risks similar to any other oil & gas pipeline project. At the same time, these same banks and financial institutions view such projects as having significant regulatory and market risks associated with the carbon price, in addition to the typical geopolitical and commercial risks associated with other oil and gas projects.

POINT TO POINT PIPELINES COMPARED WITH BACKBONE PIPELINE

In this study, economic modeling was done to attempt answering some basic questions potentially posed to a project developer (or project consortium) in considering the option of developing a backbone CO_2 pipeline infrastructure. The key question faced by a developer is whether to develop a backbone system ahead of a point-to-point pipeline, and what are the commercial considerations in this context. Thus, the questions that the modeling exercise aims to answer include:

- Is a backbone system the most optimized way of deploying CO_2 pipelines?
- Are there technical and commercial advantages to deploying a backbone system?
- Are there commercial barriers to deploying backbone pipelines?
- Are there options to overcome any commercial barriers?

In order to try and answer these questions, a methodology was developed based on several potential deployment scenarios, with each scenario tested using a pipeline financing model to test the most appropriate option, as described below.

The modelling approach adopted to undertake the analysis consists of two core components, namely:

1. The modelled scenario: consisting of the physical (i.e. sources of CO_2, storage site availability; and distance between the two) and temporal (i.e. the timeline for development) aspects of a hypothetical CCS value chain development. This also includes the different options for connecting sources and storage sites; and
2. The economic assumptions: in terms of the construct of the underlying economic model used to appraise the two options (i.e. the basis of the pipeline cost model).

The Modeled Scenario

The hypothetical scenario consists of possibly 10 new coal-fired power plants being developed over a seven year period, by four different independent power producers. Developer “One” will bring on stream four new plants together in year one, with subsequent tranches of plant following in later years. All operators are assumed to be suitably incentivised to deploy CCS under the types of policy regimes described above. Each tranche of deployment is assumed to be clustered close together, although collectively, the tranches are dispersed over approximately a 60-120 mile radius.

[2] Staff from six financial institutions were interviewed. One is an institution with a charter to carry out strategic investments for the European Union.

A saline formation suitable for CO_2 storage has been identified within 600 miles or so of all the power plants. The formation has an estimated 2000 Mt CO_2 storage capacity, sufficient to take all the CO_2 from all the plant for 40 years.

In terms of connecting the power plants to the storage formation, two options exist, namely:

1. Point-to-point pipelines: each tranche of power plants independently develops a pipeline, designed to only take the CO_2 from that tranche to the storage formation at 98% capacity utilisation.
2. Backbone pipeline: the developer of tranche 1 develops a backbone network with the option for subsequent tranches to connect, so as to reach 95% capacity utilisation after year 7 when the final tranche of plants are completed. See Figure 1.

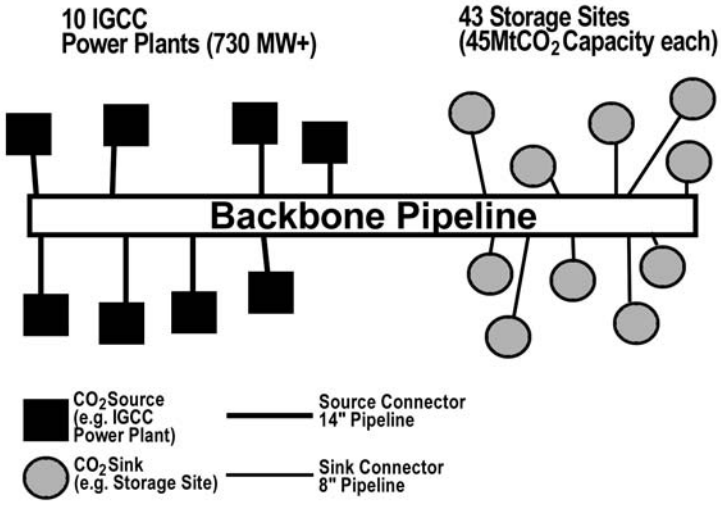

Figure 1. Scenario Overview - Showing the Backbone Pipeline Option.

Details of the characteristics of the hypothetical scenario are outlined below (Table 1). While what is described here will not necessarily play out in reality, the scenario provides a useful basis with which to test the two options for pipeline development in the context of advantages and barriers, as well as options to overcome those barriers.

Table 1. Summary of the Scenario Characteristics and the Two Options.

Feature	**Characteristics**
CO_2 source	10 x 730MW Integrated gasifier combined cycle (IGCC) coal-fired power plants, ~5 $MtCO_2$/year/plant [1, Table 3.10, new IGCC power plant using current technology]
Timeline for deployment	The projects will be developed over an 8 year period as follows: • Year 1. Tranche 1: 4 x IGCC in close proximity completed • Year 3. Tranche 2: 2 x IGCC in close proximity completed. • Year 5. Tranche 3: 2 x IGCC in close proximity completed. • Year 7. Tranche 4: 2 x IGCC in close proximity completed. Each tranche is being developed by different developers.

Feature	Characteristics
Timeline for operation	• All plants are assumed to operate for a 40 year+ period. • During design of tranche 1, it is not assured that subsequent tranches will be realised i.e. there is uncertainty over whether new power plants will come on stream.
Total CO_2	• Tranche 1: 20 million tonnes CO_2/year • Tranche 2: 10 million tonnes CO_2/year • Tranche 3: 10 million tonnes CO_2/year • Tranche 4: 10 million tonnes CO_2/year Total CO_2 per annum in year 7 = ~ 50/year Total CO_2 following 40 years operation = ~2000 $MtCO_2$
CO_2 store	• Large saline formation with around 2000 $MtCO_2$ storage capacity. • Each injection well has a capacity of 1 Mt/year, which means 45 injection wells will be needed in total.
CO_2 pipeline	All plants with an average distance from the formation = 600 miles Interconnectors detailed below.
Options for pipeline development	*Option 1. Point to point:* Each new tranche of plant seeks to connect directly to the storage formation in isolation of earlier or subsequent tranches. Tranche 1 builds a backbone pipeline (operating at 97.5% capacity utilisation), operating with an inter-connecting hub on average 60 miles away. In addition, a centralised receiving hub is built at the storage formation, with inter-connectors built to individual wells with an average distance of 10 miles from the hub. Tranche 2 builds a small backbone pipeline to take-up CO_2 from the two power plants in year 3 and with an interconnecting hub similar as the one for Tranche 1. Tranche 3 and 4 follow the same pattern as Tranche 2. *Option 2. Backbone:* Tranche 1 builds a backbone pipeline system in year 1 (operating at ~40% capacity utilisation), with a view to take up CO_2 from all the new potential tranches coming on stream through an inter-connecting hub, on average 120 miles away. In addition, a centralised receiving hub is built at the storage formation, with inter-connectors built to individual wells with an average distance of 20 miles from the hub. This is necessary to avoid interference between each injector.

The project revenues form the basis for comparing different options. A summary of financing assumptions is provided below (Table 2).

Table 2. Assumptions Underpinning Financial Analysis.

Feature	Characteristic and assumptions
Project financing structure	Debt to equity ratio: 70:30 Based on analysis of oil and gas pipeline case studies also conducted as part of the study. The ratio used here is a reasonable one based on interviewing staff from these projects.
Timeline for financial appraisal	20 years (financial)
Cost of equity	15% - typical rate
Cost of debt	9.57% (US libor + 4%) – London Interbank Offered Rate (LIBOR) is the interest rate at which banks can borrow funds, in marketable size, from other banks in the interbank market.
Discount rate	7.5% - Discount rate is the weighted average cost of capital (WACC), a combination of equity and debt for this scenario that also accounts for inflation

Comparative Analysis

In this section we compare the two options using as metrics the cost of service associated with their use and the capital investment required for their development.

Cost of Service (Tariff Charge to Breakeven)

Table 3 shows the average cost of service for Option 1 and Option 2 for the whole system (i.e. for all tranches) and from a first mover perspective (i.e. in year 1).

Table 3. Average Cost of Service for Option 1 and Option 2.

	Cost of Service (for all tranches)	**Cost of Service (in year 1)**
Option 1	$10.5	$8.1
Option 2	$7.7	$11.3

Key findings of the research can be summarized as:

- The cost of service for Option 2 (i.e. backbone pipeline) presents the cost effective scenario for the system.
- Cost of service for the system is higher for Option 1 than Option 2 because additional smaller pipelines are developed separately for Tranches 2, 3 and 4.
- From a first mover perspective the reduction to the cost of service for the operator of Tranche 1 (cost of service in year 1) that follows Option 2 is small $0.4 ($8.1 vs. $7.7).
- There is a risk that if the first mover opts for Option 1 then additional tranches may not be able to carry out CCS due to prohibitive costs, absent of a backbone pipeline (i.e. Option 2).

Capital Expense

Table 4 presents the capital required for the development of Option 1 and Option 2 for the whole system (i.e. for all tranches) and from a first mover perspective (i.e. in year 1).

Table 4. Capital expense required for the development of Option 1 and Option 2 ($thousand).

	Capex (for all tranches)	**Capex required (in year 1)**
Option 1	$3,112,747	$1,030,942
Option 2	$2,321,779	$1,560,622

Key findings of the research can be summarized as:

- The capital required for the deployment of the Option 1 system is almost 35% more when compared with Option 2.
- From a first mover perspective the operator of Tranche 1 would need to raise an additional $500 million in year 1 to develop Option 2.

Capacity Utilisation

A sensitivity analysis was undertaken in order to understand the economic risks for a first mover (i.e. Tranche 1) pursuing a backbone pipeline with excess capacity (Option 2), when some or all subsequent tranches are not deployed. Figure 2 shows that the above scenario effectively results in an increase in the cost of service due to under-utilisation of the backbone pipeline capacity.

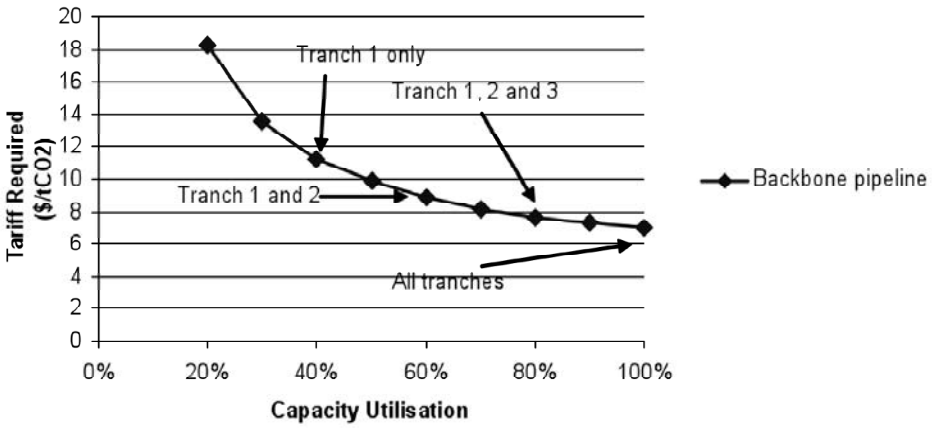

Figure 2. Cost of Service for Different Capacity Utilisation for Option 2.

The above results are summarised along the equivalent cost of service for Option 1 in Table 5 in order to understand the risk in the context of the both scenarios.

Table 5 describes the following:

- Under Option 1: The cost of service for Tranche 1 and for the system when more tranches build separate pipelines.
- Under Option 2: The cost of service for the backbone pipeline depending on how many tranches eventually connect to the system.

Table 5. Average Cost of Service of Deployment of Option 1 and 2 (in $/tCO$_2$).

	Tranche 1 only	**Tranches 1 and 2 only**	**Tranches 1, 2 and 3 only**	**All Tranches**
Option 1	$8.1	$9.2	$9.8	$10.5
Option 2	$11.3 (40% capacity utilisation)	$9.2 (60% capacity utilisation)	$8.2 (80% capacity utilisation)	$7.7 (Full capacity utilisation)

Table 5 shows that it would be cheaper for a first mover (i.e. Tranche 1) to pursue Option 1 for $8.1/tCO$_2$ over Option 2 unless they are sure that all tranches will eventually connect to the backbone as this will bring the cost down to $7.7/tCO$_2$ for Option 2.

In this sense, the Tranche 1 operator would need to weigh the probability of future capacity realisation, along with the marginal cost benefit that will be received in this scenario, versus the probability of non-realisation along with the associated costs.

Financing Structure

Different financing structures influence the cost of capital and can subsequently affect the cost of service. For this reason the model was run for alternative financing structures in order to evaluate the cost of service in relation to Option 2.

The alternative financing scenarios that were studied are presented below in Table 6.

Table 6. Financing Scenario.

Scenario	Financing Sources	Comments
Baseline Scenario (typical)	70% Debt, 30% Equity	Projects are typically leveraged with 70/30 debt to equity ratios or higher.
Balanced	50% Debt, 50% Equity	Similar to the base scenario the medium scenario is structured with less debt and more equity.
High equity	30% Debt, 70% Equity	As the cost of debt is usually cheaper that that of equity this can be considered as the pessimistic scenario where the project company could only partially raise the necessary debt to finance the project.
PPP	40% Debt, 10% Equity, 50% Government Guaranteed Bonds	Public private partnership scenario where the government would agree to guarantee bonds issued by the project company in the capital markets.
Government funding	100% Government Guaranteed Bonds	Government entirely funds the project.

The cost of service for different capacity utilisation for Option 2 under various financing scenarios is presented in Figure 3.

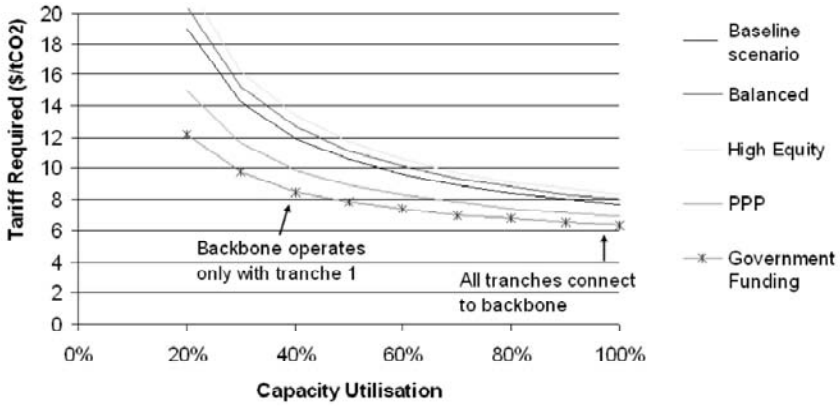

Figure 3. Cost of Service for Different Capacity Utilisation for Option 2 under Various Financing Scenarios.

Government funding can enable the project to operate commercially at a comparative cost of service (~8 t/CO_2) to Option 1 even when Tranches 2, 3 and 4 are not realised (i.e. see Figure 4.4 at 40% capacity utilisation). In this sense, governments through favourable financing or other types of support can provide security to first mover over future capacity up-take and mitigate risks in order to promote optimised deployment options for a CCS scenario such as the one modelled.

Deployment Challenges for a Backbone Pipeline

The three main deployment challenges for the development of a backbone pipeline can be summarised as:

- System Capacity Utilisation: A backbone pipeline would need a sufficient utilisation of its capacity in order to be economical. It was highlighted in the model that it is still

marginally cheaper for Tranche 1 to pursue a smaller pipeline with no excess capacity, (i.e. Option 1) unless all tranches connect to the backbone pipeline (i.e. Option 2).

- Marginal benefits for a first mover might be relatively small compared to potential losses: The potential reduction of cost of service for a first mover in building a backbone might be relatively small in comparison to potential losses from unrealised capacity. It was shown in the model if all tranches connect to the backbone pipeline the operator of Tranche 1 benefits from a cost reduction of $\$0.4/tCO_2$ (see Table 4.10). On the other hand their potential losses from unrealised capacity stand at four times more at $\$3.2/tCO_2$ if Tranches 2, 3 and 4 are not realised.
- Financeability issues: Financing could present challenges because investment decisions (especially project finance) for high capital outlay are justified by economic analysis based on revenue certainty as was highlighted during the review of oil and gas pipeline case studies.

Risk mitigation options that can manage the challenges presented above may be required to promote successful deployment of backbone pipelines.

Our analysis suggests that there is an opportunity for governments to provide the support that is needed in the first few years of operation to help first mover operators to build pipelines with excess capacity for future users and realise economies of scale.

This support can come in many forms such as:

- Favourable financing options
- Project revenue guarantees or cost of service subsidies
- Project sponsorship and delivery by State

Favorable financing options could enable the financeability of a pipeline network and take up some of the risks associated with excess capacity as was shown earlier Figure 3. An example of this is the Maghreb–Europe Natural Gas Pipeline Project (Gazoduc Maghreb Europe; GME) pipeline where the Spanish public sector, during the initial phase of the project, guaranteed the Spanish section of the pipeline by assuming a 91 percent share to the project company to insulate the pipeline from project risks.

Financing support can be provided in the form of capital grants, earmarked revenues generated by auctioning allowances in cap and trade systems (e.g. EU-ETS) and/or low cost government financing like guaranteed bonds, etc. Bonds could be very well-suited for pipelines given the regularity and predictability of cash flows, and the long life and large size of required investment.

Project revenue guarantees or cost of service subsidies for an operator that builds a pipeline with excess capacity in order to accommodate future users could be another type of support. Under this arrangement governments would guarantee the revenue, or alternatively cover the additional cost of the operator when subsequent tranches do not come into the system. In our model governments could guarantee the revenue of the first mover (Tranche 1) if Tranches 2, 3 or 4 are not realised through a cost of service subsidy (i.e. represented as a red line in Figure 4).

A project example where revenue guarantees were used by the UK government is the Channel Tunnel Rail Link.

Lastly, direct government involvement, as another type of support, could be an option where the government would assume the project entirely. An infrastructure that would help mitigate climate change could be developed and delivered by states to kick-start large scale CCS deployment and help them achieve their international reduction obligations. Additionally, government's ROI requirements that are generally lower than those of the private sector would effectively translate into

lower CO_2 transportation tariff charges giving this way a competitiveness boost to the rest of the CCS value chain.

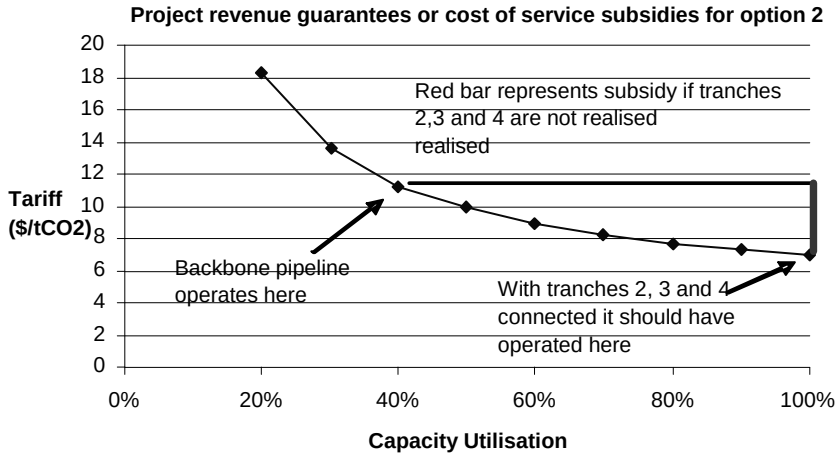

Figure 4. Revenue Guarantee or Cost of Service Subsidy.

Any adopted fiscal incentives have to be long term, as investors will be reluctant to participate in the development of CO_2 infrastructure if there is uncertainty that these can be changed during the project lifetime. In principle, once the price of carbon is stable and high enough to cover the aforementioned risks, the incentives would no longer be needed.

INTERVIEWS WITH FINANCIAL INSTITUTIONS

The key conclusion from the interviews with financial institutions is that CO_2 pipeline projects, if they can be reduced in terms of carbon price risks, will become the same in terms of risks as any other oil & gas pipeline project. At the same time, these same banks and financial institutions view such projects as having significant regulatory and market (carbon price) risks. None expressed any specific, strong interest to fund such projects at the time of the completion of the study.

Altogether, six financial institutions were interviewed for this study. While the authors cannot quote the answers of specific institutions here, a sample of the questions asked is shown below.

1. What are the key factors that your organization assesses in order to determine the financeability of infrastructure schemes?
2. What do you think are the main associated risks, uncertainties, information requirements and other issues that you would need to know about before investing in such pipelines?
3. What types of funding mechanisms do you think may be appropriate for CCS pipelines that either your or other institutions could assist with?
4. What aspects of a CO_2 CCS chain you would feel more comfortable providing finance for?
5. What specific funds (e.g. “Green” or emerging technology funds) are currently available for financing such projects, either through yourselves or other institutions? If relevant, associated details would be appreciated.
6. To what extent are your organisation and other similar institutions likely to be interested in helping to finance CCS pipelines, and in what way?

CONCLUSIONS

This paper describes preliminary findings from a CO_2 Capture Project study that looked at issues of financing the development of a hypothetical CO_2 transportation pipeline infrastructure. These issues include debt and equity structure, loan guarantees, government bonds, and the role of public-private partnerships.

We conclude that:

- Point-to-point pipelines will be funded on project-by-project basis by individual developers because of certainty over capacity utilisation.
- Integrated backbone pipeline networks may be the most efficient long-term option.
- At the same time, such integrated backbone pipeline networks will need "guaranteed" capacity utilization in order to be economically viable. Therefore, public policy that encourages development of optimised networks with some support of capacity utilization will be needed.
- Government support in the first years when capacity is ramping up will be important to commercial viability. Government incentives or loan guarantees are also needed to support a backbone infrastructure.
- Banks and financial institutions view CO_2 transport projects as having significant regulatory and market risks associated with the carbon price, in addition to the typical geopolitical and commercial risks associated with other oil and gas projects.

ACKNOWLEDGEMENT

The authors acknowledge the very helpful discussion and input from Frede Cappelen (StatoilHydro) and Richard Rhudy (Electric Power Research Institute).

This Chapter contains figures, portions and excerpts that originally appeared in Energy Procedia Vol 1, Issue 1, Greenhouse Gas Control Technologies 9, Proceedings of the 9th International Conference on Greenhouse Gas Control Technologies (GHGT-9), 16-20 November 2008, Washington DC, USA., which was published by Elsevier Ltd.

REFERENCES

1. Intergovernmental Panel on Climate Change (2005) IPCC Special report on Carbon Dioxide Capture and Storage, Cambridge University Press.

Carbon Dioxide Capture for Storage in Deep Geologic Formations, Volume 3
L.I. Eide (Ed.)

Chapter 30

COMMUNICATIONS SUMMARY

Simon Taylor[1], Iain Wright[2]
[1]Pulse Brands Ltd, Berkshire House, 168-173 High Holborn, London WC1V 7AA, UK
[2]BP, plc, Sunbury-on-Thames, UK

ABSTRACT: The activities of the Communications Team of the CO_2 Capture Project Phase 2 (CCP2) are summarized.

CONTEXTS

CCP communications undertaken during Phase 2 of the Carbon Capture Project (CCP2) reflect not only the progress of the CCP itself – but also the profound changes that took place in broader awareness and interest in the environment during this period – and the consequences that that has had for CO_2 capture and storage.

Until the Kyoto Summit in 1997 environmental issues had had only a limited impact on the public consciousness. Certainly, industry, NGOs, consumers and governments had all been active on a number of environmental fronts over the previous 50 years. As public awareness grew from that point, so came the accompanying realisation that society needed to act at a concerted level to address the number one threat of climate change, by actively reducing man-made CO_2 emissions.

Until the publication of the fourth assessment report of the IPCC into climate change in 2007, CO_2 capture and storage as a subject was largely unheard of by the wider world. Since then, interest has grown enormously as the technology increasingly is viewed as one of the more practical options to make emissions reductions almost immediately.

The first phase of CCP (CCP1) communications from 2000-2004 had seen much foundation work taking place to establish the new organisation, create a voice and begin to outreach to key audiences such as industry and NGOs. It was also a critical phase in the formation of relationships both within the CCP itself and without, to a network of organisations – such as academia, industry bodies, government – who would become critical to furthering the aims of the CCP over time.

To achieve this, a communications strategy was formulated early in the period, with the initial, overarching objective being to *increase awareness and understanding of the role and value of the CO_2 Capture Project and to build broad-based support for its success*. It had the following specific communications objectives:

1. To develop information that effectively and efficiently communicates the benefits of CO_2 capture and storage to all key audiences
2. To maximise internet resources and applications that afford access to information and CO_2 capture
3. To enhance public awareness about the benefits of CO_2 capture by developing positive media exposure and credibility for the CCP and its activities

4. To establish partnerships to extend the reach of the CCP and its member companies for the purposes of both advocacy and furthering technological understanding and its applications
5. To evaluate the reach and success of CCP communication activities

To begin to meet these, and support the work of the CCP, a number of activities were undertaken, including the creation of CCP website framework and engagement with a number of key audiences to begin to tell the CCP story. This included participation in technical conferences, the publication of technical brochures and a peer reviewed findings book that covered the progress made during the first four years of CCP activity.

CCP2 - REFINING THE COMMUNICATIONS APPROACH, INCREASING ENGAGEMENT

CCP's work since 2004 has continued the development of the most promising capture and storage technologies identified in Stage 1. It has focused on the advancement of cost-effective, next-generation capture technologies and on ensuring the framework for the CO_2 Geological Storage, monitoring and long-term verification tools and processes.

Communications has naturally evolved to reflect these activities and requirements, building on the foundation work laid during Phase 1. However, the changing environmental and political landscape that began to emerge during Phase 2 meant that the approach would also need a degree of realignment.

As interest in climate change escalated, so the potential role of CCS became more important. As far as communications was concerned a pivotal moment occurred in 2005/06, when CCP became involved in the EU-funded CACHET programme. This three-year, integrated research project aims to develop technologies to reduce greenhouse gas emissions from power stations by 90% and comprises a strong and diverse international consortium of highly experienced research institutes, universities, energy businesses, engineering and manufacturing companies.

With CCP now firmly established and participating in projects such as CACHET, the time was right to review the communications approach and increase engagement.

At their Gleneagles summit in July 2005, the G8 leaders asked the International Energy Agency (IEA) and the Carbon Sequestration Leadership Forum (CSLF) to work together to accelerate the development and commercialization of CO_2 Capture and Geological Storage (CCS) technology. Article 14(a) of the Gleneagles communiqué encouraged IEA/CSLF to "work with broader civil society to address the barriers to public acceptability of CCS technology". To further this effort, the UK government Department of Trade and Industry (DTI) commissioned the CCP to prepare a report on public perception of CCS and to make a prioritised assessment of issues and concerns that could be used to formulate a CCS Communications Strategy

The resulting report was well received by the IEA and CSLF and provides a prioritized assessment of perceptions and issues affecting the deployment of CCS. It recommends strategies to address those issues and to develop regulatory and policy frameworks for CCS. Perceptions and issues were surveyed by region (North America, Europe, Australia and New Zealand, China and other countries) and by stakeholder group (Non-Government Organisations -NGOs, Public, Government, Industry, and Research and Development - R&D organisations). Regional reports are provided as appendices. A prioritized, regional database of opinion-formers and policy-makers was also prepared.

The maturity of understanding of CCS varies widely between regions and stakeholder groups, however, the perceptions and issues affecting the deployment of CCS are (in order of priority):

The perceptions and issues affecting the deployment of CCS at that time were found to be:

1. **Cost of deployment**: CCS projects are large compared to some other low-carbon options (solar panels, hybrid cars) and therefore require high capital investments, though on a unit basis, their cost (per tonne CO_2 avoided) may be significantly lower.
2. **Scale of deployment**: Small-scale CCS deployment will have little impact, but the feasibility of deployment and effects on the energy system (at a scale that would make a significant difference to climate change), are not well understood.
3. **Perceived risks (to local health and safety)**: There are so few operational CCS projects in the world that any perception of local risks, even those not viewed as serious by experts, such as catastrophic leakage of CO_2 from storage, are nevertheless vital to address even at the very earliest stages of development.
4. **Lack of accessible information**: There is relatively little information on CCS that is expressly aimed at the general public. Research has shown that focus groups become more supportive of the technology once they have received basic information and understand the context better.
5. **Supporting policies**: Views on this are the most divided. Those who focus on the potential to reduce the CO_2 impact of fossil fuels, or who believe that fossil fuels will be required to raise living standards in the developing world advocate policies to support CCS. Others see CCS threatening to delay the deployment of renewables.
6. **Adequacy of regulatory frameworks to address the perceived risks**: No region has a comprehensive regulatory framework governing CCS, but several processes are now under consideration.

The report recommended a number of strategies to address these issues:

1. Implement appropriate commercial incentives for industrial deployment
2. Demonstrate comprehensive regulatory frameworks
3. Implement industrial-scale demonstration projects
4. Resolve long-term liability issues for geologically stored CO_2
5. Clarify the role of CCS within a portfolio of climate change mitigation options
6. Increase education efforts (media, policy makers)
7. Exploit opportunities for international collaboration

Clearly, CCP communications had the potential to support a number of these areas. The Communications Team at CCP, working in conjunction with the CCP's three technical teams - Capture, SMV (storage, monitoring and verification), Policy and Incentives - identified where resources could be deployed most efficiently to support CCP's revised aim of *helping make carbon capture and storage a practical reality for carbon mitigation*.

CCP members still wished to retain principal control over the communications of CCP's work but it was felt that a change in approach was needed to reflect changing times and the progress of CCP itself after Phase 1. Thus it was agreed to shift from an existing base level of communications, which was largely reactive in nature, to a more proactive approach acting both as a 'scientific publisher' and as an 'authoritative source' with a point of view. This would involve delivering the CCP/CCS story more widely to members and externally (e.g. NGOs, media) and creating materials specifically to do this.

A communications strategy for CCP2 was developed which focused on delivering objective and authoritative information on the science, engineering, economics and policy/regulation of

CCS/CCP, alongside the deep practical experience of its members. It also aimed to focus on demonstrating CCS viability and correcting misconceptions, rather than just projecting CCP findings.

The following objectives were set to achieve this:

- Develop and sustain CCP as the authoritative global source of science, engineering, economics and policy/regulatory information in the matter of CCS
- From a solid technology base, actively promote CCP technical and policy work
- Raise awareness (internal and external) of CCP and the deep practical experience of its members
- Provide strategic communications counsel and feedback to CCP teams to shape their work
- Join up the technology development work (C&S) with the Policy Principles work.

COMMUNICATIONS ACHIEVEMENTS DURING CCP2

During Phase 2, the CCP has become critical in building up the technical support and expertise to make CCS a practical reality. Effective communications has become increasingly important in this, providing the link between members themselves and outwards to participating organisations and the outside world. This extension of activities to the outside world is likely to become more pronounced with the passage of time.

The huge amount of expertise available from member organisations is shared to good effect among these groups. Since the beginning of the CCP, its participants have undertaken more than 150 projects to increase understanding of the science, engineering, application and economics of CCS. This has often been achieved by working alongside research institutions, universities and commercial organisations, which total over 50 in number.

In addition, members have contributed the results of proprietary research as well as data obtained from existing CO_2 capture and geological injection and storage operations and demonstrations globally, which are shared with the wider academic and industrial community through a range of communications channels, outlined below.

The task of the Communications team has been to take the rich content from this ongoing work and deliver it in a relevant and understandable way to an increasing range of audiences who are becoming interested in the CCS story. Much – though not all - of the focus for this work in CCP2 has been on showing that geological storage is safe and can be delivered now. Audiences therefore range from industry to policy makers and regulators, from CCP members to the broader energy industry, and from NGOs to media and the audiences that they in turn serve.

Allocation of communications resources to this work during this Phase has prioritised several areas including website development, collateral, NGO engagement and technical conferences. Key deliverables achieved during CCP2 include:

- **Website** Following feedback from members and users, the CCP website – www.co2captureproject.org – was reviewed and redesigned to aid usability and to allow CCP to project itself as the authoritative source of technical information on CCS. The site was streamlined and redesigned into 5 user-oriented areas – *Who are we?; What is CCS?; Activities Summary: Publications and Media & Resources.* Added functionality such as Search and Links components were built in as was the capability to stream CCP video footage.

Since its relaunch in November 2008 prior to the GHGT-9 conference, further improvements have been made with the site now migrated to a more flexible server to allow for rapid updates, better content management and closer supervision by the content developers.

The results of these changes have been striking with hundreds of hits recorded each week since the relaunch, including repeat visits and downloading of many key documents and publications. Daily unique visitors to the site at the beginning of 2009 averaged 500-700, generating 1200-2600 page views a day.

- **Literature**
  - *Technical basis book* - one of the most recent outputs has been the publication of the most definitive work yet on subsurface storage of CO_2, *"The Technical Basis for CO_2 Storage"*, aimed at policy makers and industry. This major study provides a guide to the main technical issues related to safety in the subsurface geological storage of carbon dioxide. It provides guidance on how to identify and regulate suitable locations for industrial-scale CO_2 Geological Storage (CGS) projects, to ensure the right injection, monitoring and sealing techniques are employed
  - *In-depth storage brochure* – a clever, concertina-style guide that was created to provide an at-a-glance explanation of the principles of CO_2 storage. This has proved extremely useful and popular with a range of audiences from policy makers to teachers and at the start of 2009 was the most popular download from the website
  - Further summary booklets on Storage and on Capture are planned, drawing upon the case studies and examples contained in the '*Technical basis...*' book
- **Technical conferences** CCP has participated in a number of key technical conferences during Phase 2 of the Project, delivering presentations, seminars and with CCP brand presence (including posters, literature booth, collateral). These have been crucial events to share progress and findings from the work of the CCP and engage with experts and peers on the subject of CCS as part of the greater climate change debate. Key events have included:
  - US DoE NETL (National Energy Technology Laboratory) conferences: these events bring together wealth of scientific and engineering talent to discuss commercially viable solutions to US/international energy and environmental problems
  - IEA GHGT (Greenhouse Gas Control Technologies) conferences 8 and 9: the GHGT conference series has established itself as the principal international conference on greenhouse mitigation technologies. CCP participation in GHGT-9 included presentations on *Technical Basis for CO2 Storage Practices and Regulations*, (Cal Cooper); *Financing a CO2 Transportation Pipeline Infrastructure* (Arthur Lee) and *Field Study of a Wellbore from a Natural CO_2 Reservoir* (Walter Crow)
- **NGO events** CCP has hosted bi-annual engagement events in the US and Europe in recent years, bringing together key NGOs to debate CCS. Discussion topics have included: the regulatory treatment of CO2; the contribution CCS could make to climate change; who would pay for CCS and how much; the launch of a Certification Framework. During these events the role and work of CCP has also been presented.

  Healthy discussions have evolved during the course of these debates with a range of views presented. This has led to ongoing relationships being formed with these groups which are helping shape the work of the CCP and the future of CCS. Attendees have included:
  - US: *Environmental Defense Fund; World Resources Institute; Natural Resources Defense Council; Bellona Foundation; American Water Works Association; Illinois Geological Survey; US DoE*

- Europe: *Bellona Foundation; Greenpeace; Carbon Capture & Storage Association; EU Commissioner for Energy; Strategic Energy Technology SET Plan; ETP-ZEP*

- **Communications campaigns** A series of communications campaigns was initiated to meet the need to proactively raise awareness among internal and external audiences of the work of the CCP. Template materials were produced to support the '*Technical basis...*' book, including key messages, Q&As, articles and a press release. These were provided to communications teams at member companies for use with their internal and external audiences. Further campaigns are planed for future CCP projects
- **Video** A half hour video was released in 2004 to introduce the projects and results of the CO_2 Capture Project. Now available on the CCP website it includes background information on climate change, an overview of CCP Projects at the time, and interviews with representatives of NGOs, government organisations and companies who are developing a new generation of carbon dioxide capture and storage technologies.

CHALLENGES AHEAD

As the CCP moves into its third phase and CCS technologies enter full pilot and development stage, demand for more information about the practical potential of CCS will increase. As outlined earlier, the range of audiences with an interest in CCS can only grow, thus it will become even more important to ensure that their needs are met.

CCP3 communications will therefore need to continue to build the organisation's role as the 'scientific publisher' and 'authoritative source' on CCS. This will necessarily involve the continuation of proactive outreach and engagement with a range of different audiences with different levels of information need, as well as the continued development and improvement of key communications tools such as the website.

AUTHOR INDEX

SUBJECT INDEX